UNIVERSITY OF ADELAIDE
18·6·98
LIBRARY

A New Fuzzy Logic Based Sensorless Rotor Position Estimation Algorithm for Switched Reluctance Motor Drives

Adrian David Cheok

Submitted to the Faculty of Engineering for the degree of
Doctor of Philosophy

Department of Electrical and Electronic Engineering
The University of Adelaide
Australia

January 1998

THE UNIVERSITY OF ADELAIDE
AUSTRALIA

Abstract

Switched reluctance (SR) motor drives can be advantageous in many applications due to a number of inherent advantages. The drives require a position sensor to operate, because excitation of the motor phases needs to be synchronised with the rotor position. Rotor position information has traditionally been derived from sensors that are mechanically mounted on the motor shaft and physically measure the angle of the rotor. However, in practice the use of these sensors can lead to disadvantages in the SR drive system. Therefore in recent years there have been extensive research activities to eliminate direct position sensors, using indirect, or sensorless, position estimation methods.

Although many sensorless position estimation methods have been proposed for the SR motor, some problems with sensorless position estimation have not generally been solved in the methods developed up to this date. This is due to the fact that the previous methods have limitations in providing accurate rotor position measurements under all operating speeds and conditions found in SR motor drives. Moreover, no previous research specifically addressed the problem of the robustness and reliability of the SR motor drive operation with sensorless position estimation.

In this thesis a new fuzzy logic based rotor position estimator is described to address these issues. The estimator implemented in this research can be used under all operating speeds and conditions, including transients, stand-still, and start-up. The method does not require any external testing circuitry or test signals. In addition no complex mathematical model is required, whilst no simplifying assumptions about the motor's non-linear behaviour are made. The scheme takes into account non-ideal motor operating effects such as mutual inductance and eddy currents. This is achieved by using a non-parametric fuzzy logic motor model which builds up rules from two sources of motor characteristic test data: The static magnetisation curves, as well as dynamic real time operating data.

In this research a major consideration was the robustness and reliability of the new sensorless scheme. This is because motor drives are usually electrically noisy environments, with noise often being induced on any measurement circuitry. Therefore, fuzzy logic theory was utilised in order to satisfy the requirement that the algorithm is not affected significantly by deviations and error in the input data. This is because it has been demonstrated that modelling and estimation using fuzzy set theory is more tolerant to noise and errors than crisp methods.

To provide extra reliability against noise and error, two additional fuzzy logic based error correction routines were used in the algorithm. The first error correction routine uses a fuzzy logic rule base to determine if a signal is corrupted, whilst the second uses a predictor to predict values of flux linkage and angle at future sample times.

NAME: **COURSE:** PhD

This work contains no material which has been accepted for the award of any other degree or diploma in any university or other tertiary institution and, to the best of my knowledge and belief, contains no material previously published or written by another person, except where due reference has been made in the text.

I give consent to this copy of my thesis, when deposited in the University Libraries, being available for photocopying and loan.

SIGNATURE: ..... **DATE:** PhD 4/5/98

Adrian David Cheok
27th March 1998

Acknowledgment

Firstly, I wish to thank my supervisor Dr. Nesimi Ertugrul for the guidance, inspiration, support, and knowledge that he has shown over the years. Working with him has been a most enjoyable and challenging chapter of my life. Above all he has shown great warmth and friendship, and for that I am very grateful.

I would also like to thank all the technical staff for their help and assistance during my long hours in the power projects laboratory. Their practical insights were often invaluable.

I would like to acknowledge Mr. George Karolyi, former lecturer in the Department of Electrical and Electronic Engineering, who sparked my interest in power electronics during my final year of undergraduate studies, and also Dr. Michael Gibbard who first introduced me to fuzzy logic. This thesis derived from the merging of these two major interests of mine.

The Australian Research Council provided me with a scholarship during my studies, for which I am grateful. Additionally I am grateful to Mitsubishi Electric, who have provided support and time for me to finish my thesis.

Thanks to my family for all your support and teaching me the value of study. Thanks a million mum for always being there, and also to Nick my brother and friend.

Ευχαριστο ψιαψια κε παπου.

Thanks Melanie for being there over the years. Thanks for the good times and friendship Anthony and Tricia Tuennison, Mark Giglio, John Cross, Emma Hack, dj Rob, the Hong Kong crew (Annie, Jennifer Cheng, Jennifer Wong, Victor), Peter Drapaniotis, Patrick Veitch, Nik Gaffney, and hmc (Carmello) for the soundtrack.

みなこ、ずっとあいしてる

Abbreviations

Abbreviation	Variable Name	Unit
$\mu_F(u)$	*Membership* Function	-
$\bar{y}^i$	Peak of Fuzzy Set	-
θ	Rotor Position	degrees
θ_c	Conduction Angle	degrees
θ_{off}	Turn Off Angle	degrees
θ_{on}	Turn On Angle	degrees
θ_q	Angle at which Current Decays to Zero	degrees
$D_{\theta i}$	Density of Angle Variation with Current	degrees/A
$D_{\theta\psi}$	Density of Angle Variation with Flux Linkage	degrees/Wb
Dq	Angle Variation Between Position Samples	degrees
ΔT	Sample Period	s
f	Frequency of Test Signal	Hz
F	Fuzzy Set	-
GMP	Generalized Modus Ponens	-
GMT	Generalized Modus Tollens	-
i	Instantaneous Phase Current	A
$i(n)_{1,2,3,4}$	Four Phase Motor Currents	A
i_e	Excitation Current of Powering Phase	A
i_t	Test Phase Current	A
J	Moment of inertia	$kg.m^2$
$l(\theta,i)$	Incremental Inductance	H
$L(\theta,i)$	Phase Inductance	H
LED	Light Emitting Diode	-
L_t	Test Phase Inductance	H
M	Mutual Inductance	H

M_2	Largest Value of the Second Derivative of a general function $x(k)$.	-
M_2^*	Smallest Value of the Second Derivative of a general function $x(k)$.	-
N	Speed of Motor	rpm
n	Sample Number	-
PM	Permanent Magnet	-
q	Number of SR Motor Phases	-
$\theta_e(n)$	Single Weighted Value of Position	degrees
$\theta_e(n)_{1,2,3,4}$	Estimated Position from All Motor Phases	degrees
$\theta_p(n+1)$	Next Step Predicted Angle	degrees
R	Phase Winding Resistance	Ω
R.F.	Radio Frequency	-
SR	Switched Reluctance	-
T	Torque	Nm
t	Integration Time	s
T_{avg}	Average Torque	Nm
T_l	Load Torque	Nm
U	Universe of Discourse	-
v	Instantaneous Phase Winding Voltage	V
$v(n)_{1,2,3,4}$	The four phase voltages of the SR motor	V
v_t	Test Phase Voltage	V
ω	Speed of Rotation	degrees/s
$\psi(\theta,i)$	Motor Phase Flux Linkage	Wb
$\psi^*(n-1)_{1,2,3,4}$	Corrected Four Phase Flux Linkage	Wb
$\psi_e(n)_{1,2,3,4}$	Estimated Four Phase Flux Linkages	Wb
ψ_{mn}	Flux Linking the Phase m with Phase n due to Current in the n'th Phase	Wb

Table of Contents

ABSTRACT i

SIGNED STATEMENT iii

ACKNOWLEDGMENT v

ABBREVIATIONS vii

TABLE OF CONTENTS ix

Chapter 1:

1. INTRODUCTION 1

1.1 OVERVIEW AND BACKGROUND 1
1.2 THE POSITION ESTIMATION PROBLEM 1
1.3 SUMMARY OF CONTRIBUTIONS 3

Chapter 2:

2 SWITCHED RELUCTANCE MOTOR PRINCIPLES AND CONTROL 7

2.1 INTRODUCTION 7
2.2 SWITCHED RELUCTANCE MOTORS: AN INTRODUCTION 8
2.3 ADVANTAGES AND DISADVANTAGES OF SWITCHED RELUCTANCE MOTORS 10
2.4 SWITCHED RELUCTANCE MOTOR VARIABLE SPEED DRIVE APPLICATIONS 15
2.5 SR MOTOR AND DRIVE DESIGN OPTIONS 17
2.6 OPERATING THEORY OF THE SWITCHED RELUCTANCE MOTOR (I): LINEAR MODEL 22
2.7 OPERATING THEORY OF THE SR MOTOR (II): MAGNETIC SATURATION AND NON-LINEAR MODEL 32
2.8 MAGNETISATION CHARACTERISTIC MEASUREMENT 37
2.9 CONTROL PARAMETERS OF THE SR MOTOR 39
2.10 CONTROL METHODS 42
2.11 POSITION SENSING 44
2.12 CONCLUSION 46

Chapter 3:

3. A SURVEY OF POSITION ESTIMATION TECHNIQUES IN SR MOTORS 49

3.1 INTRODUCTION 49
3.2 ELECTRO-MECHANICAL POSITION SENSORS 50
3.3 PREVIOUS SENSORLESS POSITION ESTIMATION METHODS 53
3.3.1 Test Signal Methods 53
3.3.1.1 Test Signals with Current Pulses 55
3.3.1.2 Calculating Instantaneous Inductance 60
3.3.1.3 Frequency Injection 61
3.3.2 Passive Waveform Monitoring 65
3.3.2.1 Monitoring Chopping Mode Current Waveform 65
3.3.2.2 Measurement of Mutually Induced Voltages 67
3.3.2.3 Using Flux Linkage 69
3.3.2.4 Observer Based Methods 71
3.4 CONCLUSION. 75

Chapter 4:

4. A NEW ROTOR POSITION ESTIMATION SCHEME: INTRODUCTION AND TRAINING PHASE....77

4.1 INTRODUCTION....77
4.2 INTRODUCTION TO FUZZY LOGIC SYSTEMS....78
4.2.1 Fuzzy Sets and Classical Sets....80
4.2.2 Fuzzy Logic Reasoning Concepts....82
4.3 A NEW FUZZY LOGIC BASED ROTOR POSITION ESTIMATION ALGORITHM: INTRODUCTION....93
4.4 TRAINING PHASE: DEVELOPMENT OF AN SR MOTOR FUZZY LOGIC BASED MODEL....96
4.4.1 SR Motor Model Training Scheme....99
4.4.1.1 Methods of Training Fuzzy Models....100
4.4.1.2 SR Model Training Using Table-Look-up Scheme....102
4.4.2 Implementation of Training Scheme....109
4.4.3 Experimental Data used for the Training System....111
4.4.4 Results of Training with Static Curves and Real Time Operating Data....112
4.5 CONCLUSION....116

Chapter 5:

5. THE NEW ROTOR POSITION ESTIMATION SCHEME: OPERATION AND PERFORMANCE ENHANCEMENT....119

5.1 INTRODUCTION....119
5.2 POSITION ESTIMATION AND IMPLEMENTATION IN C....121
5.3 PERFORMANCE ENHANCEMENT FEATURES....126
5.3.1 Prediction of Flux Linkage and Position....129
5.3.2 Weighting of Predicted and Estimated Values for Error Correction....135
5.3.3 Optimal Phase Selection....141
5.4 SIMULATION OF THE POSITION ESTIMATOR....145
5.5 CONCLUSION....159

Chapter 6:

6. THE NEW SENSORLESS POSITION DETECTION SCHEME - EXPERIMENTAL RESULTS: VERIFICATION....161

6.1 INTRODUCTION....161
6.2 HARDWARE DESIGN....162
6.3 EXPERIMENTAL ISSUES....166
6.4 EXPERIMENTAL RESULTS....168
6.4.1 Chopping Mode Steady State Experimental Results....169
6.4.1.1 Low Speed Chopping Mode Test - 162 rpm....170
6.4.1.2 Mid-Speed Chopping Mode Speed Test - 326 rpm....179
6.4.1.3 High Speed Chopping Mode Test - 606 rpm....184
6.4.2 Single Pulse Mode Steady State Experimental Results....189
6.4.3 Transient Operation Experimental Results....195
6.4.3.1 Transient Operation Test - Start-up....195
6.4.3.2 Transient Operation Test - Change in Load....200
6.5 CONCLUSION....206

Chapter 7:

7. THE NEW SENSORLESS POSITION ESTIMATION SCHEME- EXPERIMENTAL RESULTS: THE STUDY OF HIGH ROBUSTNESS AND RELIABILITY

7.1 INTRODUCTION....209
7.2 OPERATIONAL RELIABILITY AND ROBUSTNESS OF THE SENSORLESS SCHEME....210
7.3 MEASUREMENT NOISE....213
7.3.1 Measurement Noise Tests - Single Pulse Mode....213
7.3.2 Measurement Noise Test - Chopping Mode....221

7.4 THE EFFECT OF LOW SAMPLING RATE 227
7.4.1 Low Sampling Rates Test: Chopping Mode. 228
7.4.2 Low Sampling Rates Test: Single Pulse Mode 234
7.5 FLUX LINKAGE OFFSET TESTS 243
7.6 PERFORMANCE TEST FOR FUZZY PREDICTORS 247
7.7 ERROR ANALYSIS 250
7.7.1 Analytical Analysis of Position Estimation Errors 251
7.7.2 Effect of Flux Estimation Error 255
7.7.3 Effect of Current Measurement Error 257
7.7.4 Error Minimisation by use of Fuzzy Logic 258
7.8 CONCLUSION 259

Chapter 8:

8. CONCLUSIONS AND SUGGESTIONS FOR FURTHER RESEARCH 261

Appendix A:

A MEASUREMENT OF STATIC SR MOTOR MAGNETISATION CHARACTERISTICS 265

A.1 INTRODUCTION 265
A.2 METHODS OF MAGNETIC CHARACTERISTIC DETERMINATION 266
A.3 MAGNETISATION CHARACTERISTICS MEASUREMENT USING LABVIEW 268
A.4 MEASUREMENT HARDWARE 270
A.5 LABVIEW SOFTWARE FOR THE MEASUREMENT TEST 273
A.6 TEST RESULTS 277

Appendix B:

B. SWITCHED RELUCTANCE DRIVE SIMULATION 279

B.1 INTRODUCTION 279
B.2 PREVIOUS SIMULATION METHODS 280
B.3 DEVELOPED SIMULATION METHOD 283
B.3.1 Features of the SystemBuild Based Simulation Software Package 283
B.3.2 SR Motor and Drive Model for Simulation 285
B.3.3 Simulation Algorithm 291
B.3.4 Simulation Algorithm Initialisation 294

Appendix C:

C. DETAILS OF THE DSP BASED CONTROL SYSTEM DESIGN 297

C.1 ADVANTAGES FOR SENSORLESS SR DRIVE OF ADSP-21020 PROCESSOR 297
C.1.1 DSP Circuit Design 299
C.1.2 DSP Programming 300
C.2 ANALOG TO DIGITAL CONVERTERS 301
C.3 INTERFACE AND MEASURING CIRCUITS 302
C.3.1 Current Measurement 302
C.3.2 Voltage Measurement 303
C.3.3 Encoder Interface 304
C.4 POWER CIRCUITS 305
C.4.1 Diode Rectifier 305
C.4.2 Inverter 307
C.4.3 IGBT Gate Control Circuitry 310

Appendix D:

D. PREDICTION ALGORITHM OPERATION IN INITIAL STARTUP REGION 313

Appendix E:

E. FURTHER DETAILS ON RANDOM ANGLE ESTIMATION ERROR 319

REFERENCES 321

PUBLICATIONS 335

UNIVERSITY OF ADELAIDE LIBRARY

Chapter 1: Introduction

1.1 Overview and Background

Early switched reluctance (SR) motors were first designed in the early 19th century and were named "electromagnetic machines" [1]. Indeed the first switched reluctance motor to have been built has been attributed to Robert Davidson, a manufacturing chemist in Aberdeen, in 1837 [2]. He used the motor for driving a battery powered railway vehicle at only four miles per hour.

The early machines used the pull of sequentially excited dc electromagnets to produce continuous torque and rotation. In an early book, [3] Noad described the problems of the motor. It was noted that there was large structural problems due to the out of balance forces imposed by the electromagnets. Also the contact erosion was severe, and we now know that the solid rotor iron circuit would have lead to very large eddy current loss. There was no means of recovering the stored magnetic energy at turn off, which led to arcing flashes at commutation. The motor was a quite a failure, and not viable at this stage.

The idea of a switched reluctance motor lay relatively dormant until the 1960's when the thyristor was invented. This provided for the first time a suitable power switch which made the SR motor viable for the first time. In fact the term "switched reluctance motor" was first coined in 1969 in a paper by Nasar [2]. Work on the machine around this time was rare but included a variable speed axial airgap reluctance motor built by Unnewehr and Koch [3] in 1973. At the time of the above work, thyristors were the only power semiconductors readily available for high current, high voltage control. Since then the development of power transistors, GTOs, Power MOSFETs and most recently, IGBTs and IGCTs, have led to SR motor drives becoming more compact and inexpensive. In addition, the advent of modern advanced microprocessors, microelectronics, and control theory have greatly improved the performance and sophistication of the SR motor drive.

Hence, recently there has been a large volume of research in the control, operation, and design of SR motors and drives. There has been an interest in applications of the SR drive due to the fact that it has a number of inherent advantages such as a wide speed range, simple motor construction, high efficiency, and a high robustness and reliability.

1.2 The Position Estimation Problem

However, in order to control the SR motor satisfactorily, the motor controller requires rotor position feedback. The position measurement needs to be accurate because the performance of the motor drive in terms of efficiency and torque output is decreased by errors in the rotor angle measurement.

The conventional method of measuring rotor position is by using sensors that are mechanically mounted on the motor shaft and physically measure the angle of the rotor. However, in practice the use of these sensors leads to disadvantages in the SR drive system. This is because the sensors can lead to a lower system reliability, higher system expense, greater maintenance and installation costs, a larger amount of connections between the motor and controller, and the need for sensor mounting space.

Therefore, it is advantageous to eliminate the position sensing device and instead estimating the rotor position using analysis of the motors electrical waveforms, such as voltage and current. These methods are commonly termed *sensorless* position estimation schemes, and a large number of such angle estimation methods have been previously developed. These can be classified into two major groups. In one group low amplitude test signals are inserted into the motor phase windings to derive rotor position information, whilst in the other group the actual motor excitation waveforms are monitored without the use of additional signals in the motor. Mathematical model based schemes are also classified under the latter group.

However, the problem of sensorless position estimation has not generally been solved in the methods developed up to this date. This is due to the fact that each of the methods, which use test signals or monitor the motor excitation waveforms, have some limitations and problems in providing accurate rotor position measurements in all operating speeds and conditions found in SR motor drives. Therefore, the methods can not be confidently used under the wide range of speeds and operating modes found in practical motor drives.

Also, the most sophisticated of the previously developed estimation schemes, which are the model based methods, involve complex mathematical computations and use simplified linear motor models, or require large look-up tables. This makes the schemes practically unfeasible due to the fact that the motor normally operate under magnetic saturation and thus can only be described by a nonlinear model. Moreover, complex mathematical computations are detrimental because they increase the delay between the motor waveform measurement and angle estimation, or demand a fast real time processor, which may not be available in all motor drives. Numerical look-up tables are also not desirable, because they have the disadvantage of a large memory requirement, and require accurately measured inputs, which brings about a sensitivity to noise and error.

In practical motor drive applications there are many factors which can lead to error or failure of sensorless rotor position estimation based on measurement of the motor electrical waveforms. These lead from non-ideal practical effects such as measurement errors, low bandwidth measurements, offset errors, noise, and change in the motor parameters. However, no previous research had specifically addressed the problem of the robustness and reliability of the SR motor drive operation with sensorless position

estimation. This is an important problem because the SR motor is often used in a certain application because of it's inherent robustness. Therefore, if the reliability of the sensorless position detection scheme is low, then this cancels any advantages of replacing the mechanical position sensor in the motor drive.

1.3 Summary of Contributions

In order to address the above problems, a new rotor position estimator was developed and is the subject of this thesis. The sensorless estimation method developed in this research does not have restrictions seen in previous schemes, because it can be used under all operating speeds and conditions, including speed and torque transients, standstill, and start-up. In addition, no external testing circuitry or test signals are placed on the motor phase windings.

Moreover, the position estimating scheme does not require complex calculations to be carried out during real time operation, and is thus well suited for practical motor drive controller microprocessors. This is because no complex mathematical model of the SR motor is required in this scheme. Nevertheless, the non-linear characteristics of the machine are not ignored and no simplifying assumptions about the motor saturation or behaviour are made. Additionally, the scheme takes into account not only saturation effects, but other dynamic operation non ideal effects such as mutual inductance, eddy currents, temperature effects, and skin effects. Furthermore, the method does not require a look-up table, and thus the memory requirement is not large.

In this research a major consideration was the robustness and reliability of the new sensorless scheme. This is because motor drives are usually electrically noisy environments with noise often being induced on any measurement circuitry. In addition, practical measurement circuits are subject to error and inaccuracy. Therefore, fuzzy logic theory was utilised in order to satisfy the requirement that the algorithm is not affected significantly by deviations and error in the input data. This is because it has been demonstrated that modelling and estimation using fuzzy set theory is tolerant to noise and errors. Therefore, fuzzy logic was applied in a novel manner in order to allow more reliable operation of the scheme in practical SR drives.

In addition, this method offers the first application in which intelligent knowledge based techniques are utilised in the application of sensorless SR motor position estimation. Using fuzzy logic, human intuition was utilised in the algorithm to provide extra reliability against noise and error on the position estimation. Knowledge based techniques were implemented in an error correction algorithm that uses a linguistic fuzzy logic rule base to determine if a measured signal is corrupted. If a corrupted measurement is detected then a predicted value can be used by the algorithm instead of the measured value.

Another knowledge based system that was developed for the sensorless position detecting scheme used linguistic rules, based on expert knowledge, to give the optimal motor phase for position sensing the most weighting. In this manner, all excited motor phases may be used for position estimation, but the phase in the most optimum region for sensing will be given the most weighting.

In the following chapters of this thesis, the theory and operation of the new fuzzy logic based sensorless position estimation algorithm for SR motor drives is detailed. In Chapter 2 the theory of the SR motor is detailed in order to provide a theoretical basis for the research work presented in the thesis. The applications of the SR motor will be discussed, as well as the advantages and disadvantages of the SR drive in practical applications. The operating principles and control methods will be detailed, where it will be seen that excitation of the SR motor needs to be synchronised with the position of the rotor, and thus some form of position feedback is required.

In Chapter 3 the sensorless position estimation methods that have been developed to date will be detailed. It is shown that each of the previously developed methods have some limitations in estimating rotor position under all motor speeds and conditions. Therefore, these problems are addressed by the new position estimation scheme, which provides accurate and robust rotor position estimation over a wide operating region.

In Chapter 4 the novel fuzzy logic based angle estimation scheme is introduced. To provide a theoretical basis for the scheme, the ideas and issues of fuzzy logic are discussed. It is shown that the sensorless algorithm has two phases: the training phase and the operational phase. In Chapter 4 only the training phase of the algorithm is detailed. It is shown that both static and dynamic motor measurement data is used by the training scheme to develop a fuzzy rule based SR motor model.

Chapter 5 continues the discussion of the new sensorless algorithm by detailing the actual operation phase of the scheme. It will be seen that after the fuzzy rule based motor model has been developed, the position is estimated by the input of the measured voltage and current waveforms to the position estimation algorithm. The two sub-systems, which were developed to enhance the robustness and reliability of the scheme, are also detailed in this chapter. These two sub-systems are the fuzzy logic based predictors of flux linkage and position, as well as the knowledge based optimal motor phase selector. To verify the new sensorless position estimation scheme, simulation results are also given in this chapter. The simulation results use a SR motor simulation package which was also developed for this thesis. The results given demonstrate the sensorless algorithms ability under a wide range of transient conditions.

In practice, simulation results are not adequate because they do not fully capture highly nonlinear and difficult to model effects that are found in practical systems. Therefore, in Chapter 6 a wide range of experimental results are given. The experimental hardware that was developed and constructed for these tests is also discussed. The experimental results demonstrate the ability of the new sensorless angle estimation algorithm for practical SR motor drives. The sensorless algorithms ability is shown not only in the steady state mode of operation, but also during transient operation with wide ranging speeds, mechanical load, and modes of operation.

In Chapter 7 the successful operation of the sensorless scheme with real experimental motor waveforms is extended, to demonstrate that the fuzzy logic based position estimation scheme has a high level of robustness and reliability. Operation of the scheme is detailed for when the motor drive is operating under non-ideal conditions, where the sensorless rotor position detection algorithm must cope with erroneous and noisy signals. It will be seen that due to the error handling ability of fuzzy logic reasoning, the sensorless scheme has a demonstrated robust ability in coping with high levels of error and noise. Results are presented for the algorithm's operation with high levels of noise, very low analog to digital converter sampling frequencies at both low and high motor speeds, erroneous flux linkage estimates, and with short pulses of high amplitude noise.

Chapter 8 provides a conclusion of the research presented in this thesis, and a summary of the new contributions made in this work. Recommendations for future research based on the results shown in the previous chapters are also given.

Appendices are also given to supplement the work found in the chapters. The measurement of the motor's magnetisation characteristics was important for the research work of this thesis. This was because the motor magnetisation data was required for the developed simulation package, as well as for use as training data in the training phase of the sensorless position estimation algorithm. Hence, in Appendix A a fully automated scheme of measuring the motor magnetisation curves of the SR motor, which was developed for this work, is detailed. In Appendix B a simulation method that was developed to model the dynamic characteristics of the SR motor is detailed. The main reason for the development of the motor simulation was to provide simulated transient waveforms of the SR motor for use in the initial testing of the rotor position estimation scheme. In Appendix C the complete SR motor drive system which was designed and constructed to provide experimental verification of the sensorless algorithm is described. It is seen that two major system components were constructed: the DSP based control unit, and the power electronic motor drive unit.

Chapter 2: Switched Reluctance Motor Principles and Control

2.1 Introduction

The switched reluctance (SR) motor has become the subject of a large body of research in the field of electric motor drives. This is partly because the motor has an intrinsic simplicity and inexpensiveness that makes it well suited to many applications. Additionally SR motor drives have a wide speed range, high system efficiencies, and a high reliability and robustness [4]. This advocates the motor to applications where these features are important.

The SR motor is fundamentally simple in its construction. However, this simplicity does not extend to its operation and design. Due to the non-linear characteristics of the machine, coupled with a non-sinusoidal and variable frequency supply, these must be considered from basic electromagnetic principles.

This chapter introduces the theory and operation of the SR motor, in order to provide a theoretical basis for the research work presented in this thesis. In addition the mathematical model of the SR motor developed in this chapter is required for the development of a simulation algorithm which is used in later parts of this thesis. In Section 2.2 the applications of the SR motor will be examined, where it will be seen that the motor has many industrial uses in applications where variable speed drives are required. The advantages and disadvantages of applying the SR motor to practical applications will also be examined in Section 2.3. In addition the industrial applications of the SR motor will be discussed in Section 2.4. In Section 2.5 the various criteria that must be examined when designing an SR drive system will be shown, and the importance of designing all components of the motor drive system in an integrated manner will be discussed.

An examination of the electromagnetic operating principles of the SR motor will also be given in this chapter. Both the simple linear motor model theory in Section 2.6, as well as the non-linear model in Section 2.7 (which takes into account the effects of magnetic saturation) will be detailed. It will be seen that the accurate calculation of the SR motor torque requires the knowledge of the non-linear magnetisation characteristics of the motor. Therefore, a method for measuring these characteristics, that was developed for the thesis work, is discussed in Section 2.8.

In Section 2.9, the various parameters that must be considered in order to control the SR motor will be discussed. The two major types of current control in the SR motor will also be detailed in Section 2.10.

It will be seen in this chapter that the excitation of the SR motor needs to be accurately synchronised with the angular position of the rotor for effective operation. Therefore,

measurement of the rotor position is necessary to operate the machine. In Section 2.11 direct position sensors, which are commonly employed to measure the rotor angle and output electronic signals to the motor controller are briefly discussed. It will be seen that position sensors or encoders have various disadvantages, and thus some form of indirect position sensing is often desirable. These indirect position sensing methods in the SR motor will be further detailed in the next chapter, where it will be seen that there is a need for a robust and reliable indirect position sensing method that can be used under all speeds and conditions.

2.2 Switched Reluctance Motors: an Introduction

The switched reluctance motor is a doubly salient electric machine. The name of the motor describes its two principal features;

(a) Switched: The machine is operated by switching current pulses to each phase on and off in a continuous switching sequence.

(b) Reluctance: The motor is a reluctance type electric machine because of the presence of salient poles on both the stator and rotor. Thus, both of the stator and rotor have a variable reluctance magnetic circuit.

Figure 2.1 shows the physical topology of a typical SR motor. The diagram illustrates a motor with eight salient stator poles (numbered A1 to D2) and six salient rotor poles (numbered 1 to 6). Although many combinations of the number of stator and rotor poles are possible, this particular type has found widespread use.

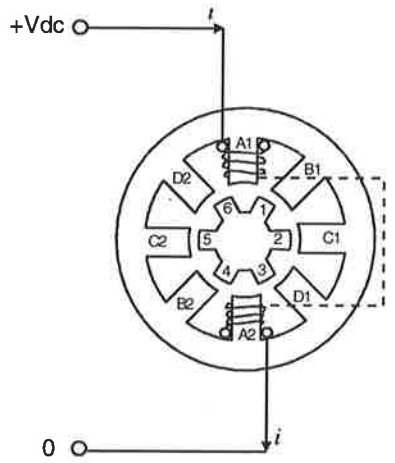


Figure 2.1 Four Phase SR motor topology.

The phase windings on the stator of the SR motor consist of concentrated windings wrapped around each stator pole. In the conventional arrangement each stator pole winding is connected with that of the diametrically opposite pole to form a stator phase. In the diagram below, the connected stator pole pairs are indicated by the same prefix letter.

However other winding arrangements have been proposed, such as the fully pitched motor in which each stator coil is wound around several stator teeth [5].

In the SR motor, there are no brushes or windings of any form attached to the rotor, which entails that there is no electrical circuit constructed on the rotor. This has led to the motor being described as a *brushless* (due to lack of brushes) *unexcited* (due to lack of electrical circuit on the rotor) *dc machine* (due to the dc supply of the motor) [24].

As with other types of motors, it is typical for the stator and rotor to be constructed with laminated material in order to minimise iron losses due to eddy currents. However the current commutation frequency in the switched reluctance motor is normally higher than in an ac motor of equal speed and power rating [6]. In addition the flux density waveform is non-sinusoidal and contains multiple harmonic frequencies [7]. The current waveform is also non-sinusoidal and contains high frequency harmonics, which are dependent on the motor operation. Therefore, high frequency eddy current components are found in the motor core structure, which entails that thinner laminations should be used in an SR motor compared to a similarly rated ac motor. Silicon steel laminations are suitable for general SR motor applications, however for high efficiency and quality aerospace-type applications, materials such as vandium-iron-cobolt alloy are used due to their high magnetic saturation and stress capability [8].

The general principle of operation of the SR motor is the same as all types of reluctance machine. In reluctance machines, one makes use of the fact that a piece of magnetically permeable iron will tend to align itself with the direction of a magnetic field being applied to it. Hence, when current flows in an SR motor stator phase and produces a magnetic field, the nearest rotor pole will tend to position itself with the direction of the developed magnetic field. This position, which is termed the *aligned position*, is reached when the rotor pole center axis is aligned with the stator pole center axis (assuming symmetrical poles). The aligned position also corresponds to the position of minimum reluctance, and hence the position of maximum inductance.

It should be noted that the *unaligned position* is defined as the position when the *inter-pole axis*, or the axis of the center of the inter-polar space in the rotor, is aligned with a stator pole axis. This position corresponds to the position of minimum inductance. These rotor axis positions are illustrated in Figure 2.2

It can therefore be seen from the above general principle, that the rotor will experience a torque attracting it to the minimum reluctance aligned position, when current is applied to the stator winding. Hence, the torque production in the SR motor can be viewed as resulting from the change of the magnetic reluctance seen by a motor phase with the change in rotor position.

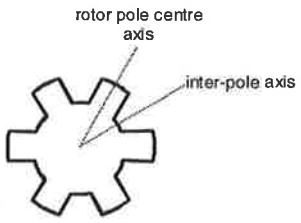


Figure 2.2 Rotor Pole Axis Positions

To achieve continuous rotation, the stator phase currents are switched on and off in each phase in a sequence according to the position of the rotor. Consider the motor schematic that was illustrated in Figure 2.1. If coils A1 and A2 of phase A are excited and produce a magnetic field in a vertical direction, then poles 1 and 4 on the rotor will align themselves with the stator poles of phase A. If the coils of phase A now have their current switched off, and coils B1 and B2 of phase B are now excited, then in a similar fashion the rotor will move so that poles 2 and 5 are aligned with stator poles B1 and B2. Hence, one can deduce that exciting phases A, B, C, and D in sequence will produce rotor rotation in the counterclockwise direction. In other words, a switching sequence that produces a switched magnetic field rotating in one direction will produce a rotation of the rotor in the opposite direction.

From the above discussion, one may see that the switching on and off of excitation current to the motor phases is related to the rotor pole positions. This means that some form of position sensor is essential for the effective operation of the SR motor.

In addition to this, it will be seen below that the motor has a wide range of different output characteristics, depending on what strategy is used to switch the stator excitation currents. However, in general, for motoring operation the stator phases are excited in such a way that the stator phase nearest to a pair of rotor poles is magnetised, in order that the rotor poles are attracted into alignment with the magnetised stator poles. Once the aligned position is reached, the stator is de-energised, so that rotation of the motor occurs in one direction only.

2.3 Advantages and Disadvantages of Switched Reluctance Motors

The SR motor has a number of inherent advantages that makes it favourable to use in certain variable speed drive applications. Nevertheless, the motor also has some inherent disadvantages that must be considered before choosing the motor for a particular application. In Table 2.1, the main advantages and disadvantages of the SR motor drive are summarised, and these will be discussed in more detail below.

It has been reported in reference [9] that the most likely applications where the advantages of the SR drive will have the most benefit over other variable speed drive types, such as

induction or permanent magnet brushless dc motor drives, are those where a very high robustness, high efficiency, and wide speed range brushless drive is required.

Table 2.1 Advantages and Disadvantages of SR drives

Advantages	*Disadvantages*
a) Low cost motor. b) Robust motor construction. c) Absence of brushes. d) No motor short circuit fault. e) No shoot-through faults. f) Ability to operate with faulted phase. g) High torque to inertia ratio. h) Unidirectional currents. i) High efficiency.	a) Need for position measurement. b) Higher torque ripple than other machine types. c) Higher noise than other machine types. d) Non-linear and complex characteristics.

i) Advantages

To some degree, the motor provides a combination of many of the desirable characteristics of induction motor drives, dc machines, and brushless permanent magnet (PM) dc machines. These benefits and advantages, which derive from characteristics peculiar to the SR drive and motor topology, will be detailed below:

a) Low Cost Motor

One of the advantages of the SR motor is that it has an inherent low cost. This is due to the very simple motor construction and low material cost. The stator windings consist of straightforward concentrated coils whilst the rotor contains no windings. This leads to low cost winding production. In addition, the rotor is very simple, and is relatively easy to manufacture. The absence of magnets on the motor, which are found in PM machines, and aluminium, which is found in the rotor cage winding of induction machines, leads to an economic material requirement (except for very high efficiency SR motors which contain specialised alloy materials). There is also a lower material use due to the large interpolar spaces of the rotor, which lowers the material requirements. In addition, a study has found that manufacturing costs of SR motors are approximately 16-25 % less expensive than equivalent induction motor manufacturing costs [10].

b) Robust Rotor.

The absence of any windings on the rotor of the SR motor leads it to be very robust, even at sustained high speed. In addition, since the rotor does not contain magnets, the maximum permissible rotor temperature is usually higher than for PM machines, where demagnetisation may arise if expensive high temperature magnets are not used.

c) Absence of Brushes.

The absence of brushes, such as those found in dc motors, is also an inherent advantage for maintenance and reliability considerations. In the SR motor the periodical maintenance and inspection of commutators and brushes is unnecessary, and flashover problems are eliminated.

d) No Motor Short Circuit Faults.

Another benefit found in the motor is the absence of sustained induced stator phase current in a stator winding short circuit fault [9]. If the controller fails and imposes a short circuit onto a motor phase, there would be no or very little short circuit current due to rotor induced voltages. This is in contrast with machines that have permanently excited rotors such as synchronous and PM motors. In these machines, the rotating flux due to rotor excitation can cause damage by inducing very high currents into shorted windings on the stator.

e) No Shoot-through Faults.

In nearly all types of SR inverter circuits, a shoot-through fault cannot occur if all power devices in a motor phase are simultaneously turned on. This is because the motor phase is connected in series between the power devices in an inverter leg. Therefore, there is no short circuit path even if all the power switches in an inverter leg are switched on (except if the motor phase itself is short circuited at the time of the shoot through fault). In ac inverter bridges for induction motors or brushless dc drives there is the possibility of a shoot-through fault if all devices in an inverter leg are simultaneously turned on. However, modern ac drive inverter circuits are relatively immune to this problem due to commonly available power device protection circuits and rugged power devices.

f) Ability to Operate with Faulted Phase.

With SR motor inverter circuits containing one or two switches per phase, each phase operates independently from the others. Thus, if one of the phases fails due to an inverter or phase winding fault, the remaining phases can continue operation and the motor can continue to operate at reduced power. In addition, starting of the motor is also possible with a disabled phase [11]. This robust feature is an important consideration in critical applications such as in the aerospace field, where maintaining motor operation even under fault conditions is of great advantage [8], [28].

g) High Torque to Inertia Ratio.

Another advantage of the SR motor derives from its low rotor inertia and high torque to inertia ratio. The low rotor inertia derives from the lack of metal in the interpolar spaces

which removes a large amount of weight from the outer parts of the rotor diameter. The low rotor inertia allows the motor to have good acceleration and deceleration characteristics.

h) Unidirectional Currents.

As will be detailed below in Section 2.6, the SR motor can operate with unidirectional currents. Due to this ability, it is possible to drive the SR motor with a simple one switch per phase inverter [11] and still maintain independence between phases.

i) High efficiency

Another advantage of the SR drive system is that it has been shown to have a high efficiency. In reference [12], the experimental results indicate that the SR motor drive system is second in maximum efficiency to the PM motor drive system and higher than other types. However, other studies have found that the SR drive's maximum efficiency is less than or equal to that of a similarly rated induction motor drive [10], [4]. However, perhaps more importantly, the SR motor maintains a high efficiency over a large range of its operating speeds [13].

There have also been statements made in the literature that the SR machine has a higher power density than all other machines. However, it seems when careful analysis is done that the SR motor has either less or no greater power per unit volume than an equivalent induction motor [9].

ii) Disadvantages

To properly evaluate the SR motor, one must also consider its shortcomings or disadvantages. These disadvantages will be discussed below, where it will be seen that the motor topology, which produces some of the benefits discussed above, also leads to some disadvantages.

a) Need for Position Measurement

A disadvantage of the SR motor drive is the requirement for position sensing feedback for phase commutation. This can be provided with a direct sensor attached to the motor shaft. However this can lead to problems in reliability, and increase the system cost, maintenance, and number of electrical connections. The subject of position sensing in the SR motor will further detailed in Section 2.11, and in further chapters of the thesis.

b) Higher Torque Ripple than other Machine Types.

A major disadvantage that is found in the SR drive is the inherent torque ripple developed by the motor, which normally has a higher value than that seen in other ac or dc machines [14]. The torque ripple arises from the non-linear pulses of torque that are produced by each motor phase [15]. Oscillation is thus seen on the total torque waveform (which is the addition of the torque pulses from all the phases), as shown in an example set of waveforms in Figure 2.3 for a four-phase SR motor.

The torque ripple may not be a problem at higher speeds when the commutation frequency is high. In this case, the torque ripple frequency will also high and therefore it may have a minimal effect on the mechanical load if the rotational inertia of the load is relatively large (and thus has a relatively large time constant as compared to the torque ripple).

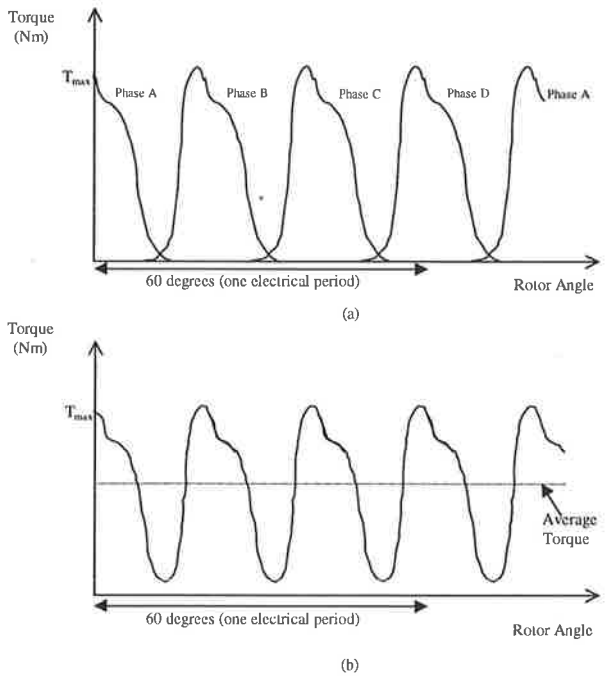


Figure 2.3 (a) Example of instantaneous phase torque of a four phase SR motor (electrical period is 60 mechanical degrees). (b) Total instantaneous torque and average torque.

The torque ripple may be substantially overcome with certain control techniques, however these control schemes require substantial controller computation as well as very precise shaft position feedback [16]. Hence, it seems that a higher controller complexity is required to reduce the torque oscillation.

Furthermore, the motor torque ripple can lead to a high ripple current being supplied by the dc link that supplies the inverter [17]. Therefore, a large and expensive dc filter capacitor that is rated for high ripple current may be required. In addition, if the dc supply is produced by rectifying the ac mains, then this may in turn increase the harmonics presented to the ac supply.

c) Higher Audible Noise than other Machine Types.

Another problem with the SR motor is that it can have a higher audible noise compared to other ac or dc machines [18]. This noise is due to the ovalising deformation of the stator that arises from the radial magnetic attraction to the rotor [18]. The emitted noise reaches a peak when the frequency of the deformation coincides with the natural mechanical resonant frequency of the stator. The noise may be reduced by appropriate control techniques [19], however, as with the torque ripple minimisation schemes, the complexity of the control method is higher. Recently the noise problem associated with SR motors seems to have been reduced, as modern SR motors are mechanically designed to minimise noise.

d) Non-linear and Complex Characteristics

The SR motor also has the disadvantage of highly non-linear characteristics. These are due three main factors: the double saliency structure, the substantial saturation that occurs in the magnetic circuit during normal operation, and the non-sinusoidal current, flux linkage, and voltage waveforms.

This leads to problems for the designer because classical dc or ac motor design methods cannot be applied to the motor, and one normally needs to refer to fundamental electromagnetic principles. In addition, due to the non-sinusoidal nature of the flux linkage and current, classical methods of calculating core losses in the motor (such as Steinmetz's equation) cannot be used [7]. The non-linear nature of the motor also leads to non-linear speed versus torque characteristics, which makes performance of the motor harder to predict.

2.4 Switched Reluctance Motor Variable Speed Drive Applications

The main application for SR motor is in variable speed drive systems. For constant speed applications it seems that no motor can overcome the overwhelming advantages in this application of ac single or three phase induction motors [20].

Other motors are commonly used in variable speed drives. The traditional solution was to use dc machines such as brush type dc motors. These have the advantage of being very easily controlled using appropriate schemes. In fact for controlled speed applications, the dc machine has set the standard in which other drives can be judged against [21].

However, a disadvantage with brush type dc machines is that they must be mechanically commutated, which leads to maintenance difficulties and upper speed limitations. This has led to the widespread use of brushless motor variable speed drives, and in particular, the inverter driven three phase induction motor [22]. These have been made feasible with the

advent of reliable and inexpensive power electronic devices, and microprocessor control technology. In addition to induction motors, brushless permanent magnet ac motors are also widely used for brushless variable speed drives [23].

However, there has also been an interest shown in the use of SR motors for variable speed drive applications. As with other brushless variable speed drive systems it can provide the same control and mechanical output characteristics as a fully controlled brush dc machine. However it also offers other advantages such as a high robustness, low cost, high efficiency, and fault tolerance, as was discussed in the previous section.

Various variable speed applications of the SR motor drive have been developed. One application area has been general-purpose industrial drives, which may be used in industrial applications where speed, acceleration, and torque control is desired. SR motor based industrial drives provide the advantages of a very wide range of operating speeds as well as a high efficiency and robustness [24].

Another industrial application has been in a constant speed drive, where SR motors were used to guarantee a very low speed variation of less than 1.5 rpm at 3000 rpm, independent of load or voltage supply variation [25]. This is of particular interest to plants where the final result of a process depends on the constancy of some preset speed. Plants such as plastic film manufacturers, and fabric plants are of this type. The SR drive was found to have a higher efficiency than other variable speed drives in this application for very low speeds.

Other applications of the SR drive include automotive applications, where the SR motor has advantages of robustness and fault tolerance [26]. The SR motor in this application can also be easily controlled for acceleration, steady speed, and regenerative braking.

The SR motor is also well suited to aerospace applications where the ability to operate under faulted conditions and its suitability for operation under harsh environments are critical [27]. Additionally, the motors very high speed capability and high power density also make the motor well suited in the aerospace field [28].

There are many additional applications where the motor can be successfully applied [29]. These include domestic appliances where cost is of primary concern. In these products, the SR motor can provide a low cost solutions for a brushless fully controllable motor drive [30]. In addition, the motor can be used in battery powered applications, where the motors high efficiency and ability to use a dc supply are important. There has also been some interest in using the SR motor in robotics [31], where the SR motor can provide the high torque and low speed required in this field.

2.5 SR Motor and Drive Design Options

The design of an SR motor drive system is a relatively complex task as there are a wide array of design factors that need to be considered. A diagram of the main components of the drive system is shown in Figure 2.4. It is important to design the motor and drive together in an integrated manner. This means that for optimum performance, the motor, power electronic circuits, control circuits, and measuring circuits should be considered together, and not in isolation.

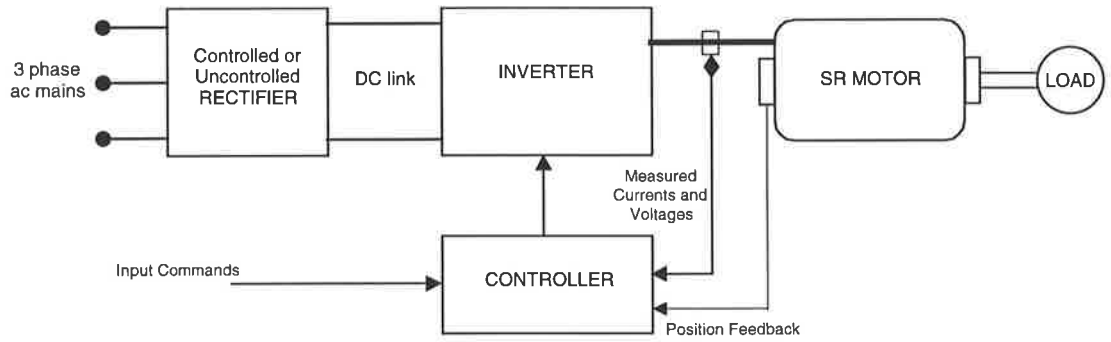


Figure 2.4 Main components of SR drive.

The main criteria that need to be considered in designing the components of the SR drive system will be discussed below. Although some of these criteria can influence the designing of any electrical machine drive, here they will specifically be discussed for SR motor drive systems. It will be seen below that certain design choices, which may be advantageous for one component of the drive system, may bring about disadvantages in another component. This highlights the need for a careful integrated system approach to be taken when designing the drive system.

a) Number of Motor Phases

There are many possibilities in choosing the number of stator phases and rotor poles in SR motors. The simplest SR motor consists of only one phase [32], however unless special methods are used, the motor will have a starting problem, because there is zero torque when the rotor pole is aligned with the stator pole [33]. In fact, to operate the motor in four quadrants (motoring or generating in both forward or reverse directions) at least three phases are required. The most common configuration to date has been the four-phase SR motor, which has eight rotor poles and six stator poles as was shown in Figure 2.1.

An almost unlimited combination of poles is theoretically possible, however there are practical design procedures for determining the optimum number of poles and phases for a particular application, such as that described in reference [34]. A consideration that should be noted is that as the number of phases increases, the complexity and cost of the drive rapidly increases. However, the torque ripple will reduce for a greater number of

phases. These conflicting design parameters exemplify the fact that the motor and drive cannot be optimised in isolation.

b) SR Motor Size

As with other electrical machines, the size of the motor will be proportional to the amount of torque required. It has been shown [35] that the motor running torque T_r is proportional to the active rotor volume V_r, or:

$$T_r = KV_r \tag{2.1}$$

Where:
K is the constant of proportionality dependent on motor parameters.

c) Maximum Speed

The SR motor is capable of operating at very high speeds due to its robust rotor construction, and in most applications the maximum speed is limited by the inverter switching speed and not limited by the motor itself. The maximum speed of the SR motor is itself normally greater than 15000 rpm for a standard SR motor [4].

However, to determine the maximum drive speed, the controller and motor must be considered together. This is because the power electronic device switching speed is directly proportional to the commutation frequency, which is in turn proportional to the motor speed. The maximum switching frequency of the power devices must therefore be taken into account in the SR drive design.

The iron losses due to eddy currents must also be taken into account when the motor is run at higher speeds. The eddy current losses increase in proportion to ω^2, where ω is the motor speed in rad/s, but at extremely high speeds this rate increases even higher due to the laminations having less effect at very high frequencies [36].

At extremely high speeds, the strength of the rotor steel must be taken into account due to the high tensile stress. Additionally the bearing failure rate should be considered under these conditions [36].

d) Number of Power Devices

In general, the number of switches per phase in SR motor drives will vary according to the inverter topology. A wide range of different SR drive inverter types has been developed for the SR drive, and these are detailed below. Circuits with only one switch per phase are possible, however these have various disadvantages such as control restrictions, a need for extra windings, or higher switch voltages. However, with two switches per phase the

motor is fully controllable in four quadrants and has completely independent motor phase control. Therefore, the maximum number of power switches required for the motor operation is *2q*, where *q* is the number of phases.

Another design decision that must be made is the type of power electronic switch that will be used in the inverter. In the past thyristors, GTO's, power BJT's, and power MOSFETs have all been used. In modern SR drives IGBTs are used almost exclusively, and currently is the optimum choice for almost all SR drives. This is because IGBTs offer the output characteristics of a BJT (high current, high voltage) with the input characteristics of power MOSFET (simple voltage gate control). However a recently developed device, the IGCT (Integrated Gate Commutated Thyristor) is expected to overtake the IGBT in medium to high power motor drives in the near future. This is because it offers high voltage and current switching at high frequency, and has faster switching and lower losses than either the IGBT or the GTO. It is also immune to catastrophic failure and does not require any snubber circuits [37].

e) Inverter Topology Types for SR Motors

As it was mentioned, the torque produced in the SR motor is independent of the direction of current flow in each motor phase. This means the inverter is only required to supply unidirectional currents into the stator windings. The three major circuit topology types that have been used for SR motor drives are shown in Figure 2.5. As is indicated in the figure these are commonly termed the *bifilar*, *split dc supply*, and *two switch* type inverter circuits.

For each circuit type in the figure, only the circuit for one motor phase is shown. This is because the circuits for other phases have exactly the same configuration. In addition each phase circuit contains no shared components with other phases, and can thus be considered as independent of the other phases. It should also be noted that the positive and negative dc voltage supply bus shown in the circuits of Figure 2.5, are un-referenced (or floating) voltages. In fact, the negative dc voltage level can be referenced to ground or 0V in actual circuits.

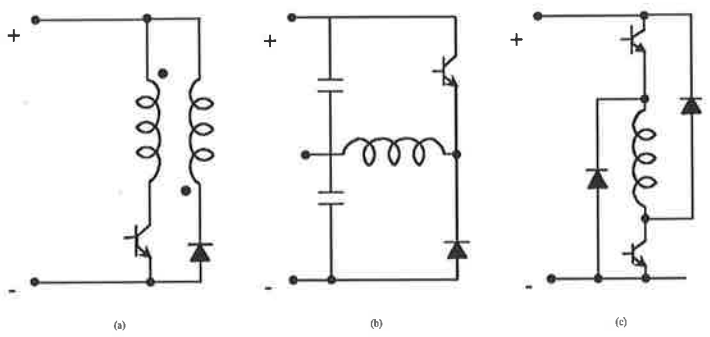


Figure 2.5 Major SR Inverter Topology types: (a) Bifilar Type. (b) Split dc Supply Type. (c) Two Switch Type.

In the circuits shown in Figure 2.5 only one or two switching components per phase are required. Other circuit topology types that require less than one switch per phase have been described [38]. However because these configurations use shared components between the motor phases, they can have limitations in control flexibility, and no longer have the advantages of independent phases.

a) Bifilar Type Inverter Circuit

In Figure 2.5 (a) the bifilar type circuit that may be used on SR motors built with bifilar windings is shown. The bifilar windings are closely coupled, with one winding being connected to a switching device, whilst the other is connected to a free-wheeling diode. Current is increased in the winding when the switching device closes. At turn off, the current transfers to the secondary winding through transformer action, and the inductive energy flows back into the supply via the free-wheel diode. If perfect unity coupling is assumed, then the voltage across the switching device will rise to twice the dc supply voltage during turn off. However, in practice this would be greater. This is because there will be some uncoupled inductance in the primary which will cause high induced voltages when the current in the winding collapses to zero. Thus snubbing circuits would almost certainly be required to protect the switching components from over voltage.

The advantage of the bifilar circuit is that it requires only one switching device per phase. This was the main reason for the circuit topology's use in early research work [39], [40]. However, with the advent of modern power electronic devices, which have both low cost and low losses, this advantage would now tend to be overweighed by the disadvantages of the circuit configuration. These disadvantages arise because the power switch voltage rating must be at least double that of the dc voltage supply, and the circuit has double the number of motor connections as compared to other circuits. There is also a poor utilisation of copper because only one of the windings in the bifilar pair carries the phase current at a given instant of time.

b) Split dc Supply Inverter Circuit

The split dc supply type inverter circuit shown is shown in Figure 2.5 (b). As in the bifilar circuit, this configuration also uses only one switching device and one diode per phase. However, in this configuration a center tapped dc voltage is required. When the switching device is turned on, current increases in the phase winding due to the positive capacitor voltage being applied. At turn off, the current is forced to flow through the diode and thus decays to zero due to the connection to the negative voltage. It is usual for the dc center tap to be implemented using a split capacitor in the dc link. The voltages across each capacitor must remain balanced, which means that there can be no significant power flow difference between the two capacitors.

Upon examination of the circuit, it can be seen that the switching device and the diode must be rated to withstand the dc supply voltage as well any transient switching over voltages. At first hand, the device ratings seem to be half the rating that is needed in the bifilar circuit. This is because the diode and switching device are both connected in series across the dc supply voltage with the split capacitor bank, and thus only half of the dc supply voltage appears across each device. However, in this configuration only half the available dc voltage can be switched across the phase winding. Thus, for the same voltage across the motor phases that is supplied by the bifilar circuit described above, the dc supply voltage must be doubled with respect to the bifilar circuit supply. This entails that the voltage rating of the devices would effectively be the same as in the bifilar circuit.

The circuit thus has the disadvantage of requiring double the supply voltage for the same component ratings and applied phase voltage as the bifilar circuit. This is inherently inefficient. The configuration also has the need for balanced split capacitive components. In addition, it will be seen that the *soft chopping* form of control described below in a later Section 2.9 is not available in this drive. This is because the circuit configuration can not supply a zero voltage level.

c) Two Switch Inverter Circuit

The two switch inverter type circuit, which is shown in Figure 2.5 (c), uses two switching devices and two diodes per phase. Unlike the previous two circuits, three modes of operation are possible which are described below:

i) Mode 1 - Positive Phase Voltage.

A positive phase voltage can be applied by turning both switching devices on. This will cause current to increase in the phase winding.

ii) Mode 2 – Zero Phase Voltage.

A zero voltage loop can be imposed on the motor phases when either of the switches is turned off whilst current is flowing through the phase winding. This results in current flow through a freewheeling loop consisting of one switching device and one diode, with no energy being supplied by, or returned to the dc supply. The current will decay slowly due to the small resistance of the semiconductors and connections, which leads to small conduction losses. This mode of operation is used in soft chopping control, as described below in Section 2.9.

iii) Mode 3 – Negative Phase Voltage.

When both switching devices in a motor phase leg are turned off, the third mode of operation occurs. In this mode, the motor phase current will transfer to both of the

freewheeling diodes and return energy to the supply. When both of the diodes in the phase circuit are conducting, a negative voltage with amplitude equal to the dc supply voltage level is imposed on the phase windings.

In this circuit the switching devices and diodes must be able to block the dc supply voltage amplitude when they are turned off, in addition to any switching transient voltages. However, because the circuit contains two devices in series, the blocking voltage is essentially half the value seen in the previous two circuit types for the same applied motor phase voltage amplitude. This configuration also does not suffer from some of the disadvantages mentioned in relation to the previous two circuits (such as the need for a bifilar winding, or balanced split dc supply). Another advantage of the two switch inverter circuit is that it offers a greater control flexibility with its three modes of voltage control.

A disadvantage of this inverter type, as compared to the bifilar and split dc supply types, is that it contains twice as many switching components per phase. However, with the current wide availability and economy of power semiconductors, in most applications the advantages of the two switch circuit outweighs the cost of an extra switching device per phase. Hence, as is described in Chapter 6, the SR inverter constructed for the experimental work in thesis used this circuit configuration

f) DC Power Supply

The SR drive inverter requires some form of dc supply. Usually, apart from electric vehicle applications, this will be supplied by a rectifier operating off the single or three phase ac mains. For powers above a few kilowatts a three phase rectifier would be recommended, because of the lower waveform ripple content and higher power handling capability compared to single phase rectifiers [4].

2.6 Operating Theory of the Switched Reluctance Motor (I): Linear Model

To provide a basis for the concepts described in the later sections of this thesis, the electromagnetic principles behind the SR motor operation will be examined below. Initially, a simple linear model will be considered, which will give a basic representation of the motors operating characteristics.

Following an examination of the linear SR model and the corresponding operating characteristics, the model will be refined to consider the effects of magnetic saturation. As the practical SR motor normally operates under magnetic saturation, the non-linear magnetic effects should be considered for practical SR designs.

In the linear magnetic model of the motor, the flux linkage versus current relationship is assumed to be linear for any rotor position θ. This means that for any rotor position θ the

flux linkage is linearly related to current. This is demonstrated in Figure 2.6 where the magnetisation curves for the linear SR motor model are shown. In this linear case, the magnetisation curves for each rotor position are straight lines. Hence, the inductance L at any position θ, which is the slope of these curves, is *constant* and independent of current.

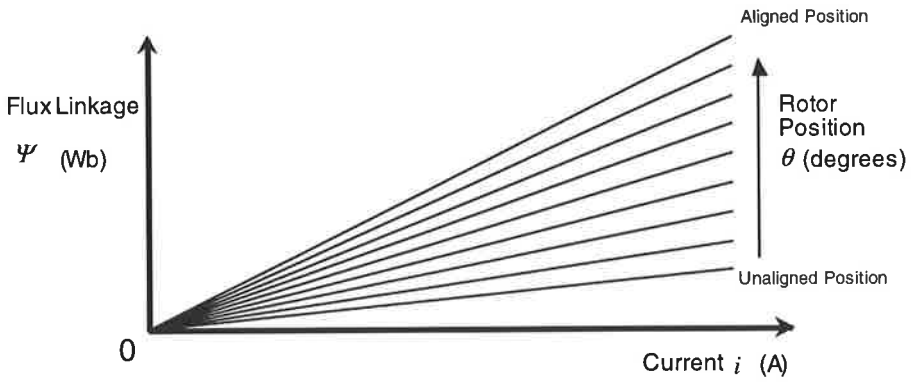


Figure 2.6 Magnetisation Characteristics of Linear SR motor.

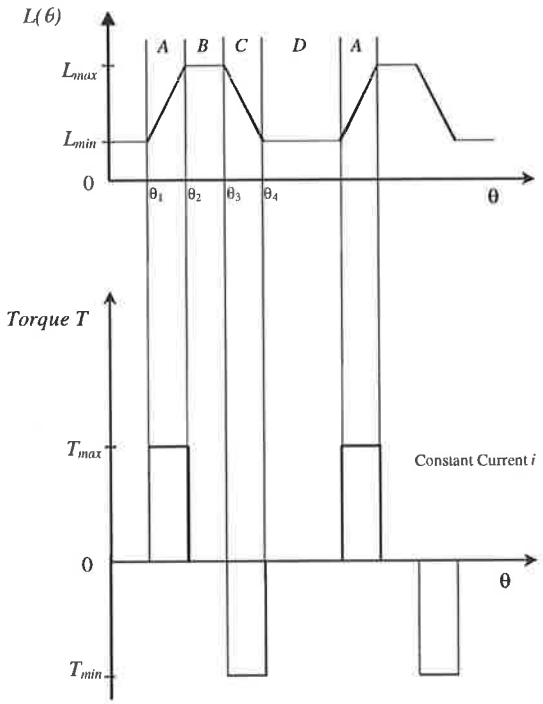


Figure 2.7 Typical Linear Inductance Variations and Corresponding Torque Variations for Constant Phase Current.

As rotation of the rotor in the SR motor occurs, each stator phase undergoes a cyclic variation of inductance. As can be seen in Figure 2.6, in the fully aligned position (when a rotor pole axis is directly aligned with the stator pole axis) the reluctance of the magnetic circuit through the stator and rotor poles will be at a minimum, and thus the inductance of the stator winding will be at a maximum. The opposite will occur in the fully unaligned position (when the rotor inter-pole axis is aligned with the stator pole). If it is assumed that no saturation occurs, then the inductance becomes a function of position only and is not related to the current level. If it is also assumed that mutual inductance between the phases

is zero, then a typical inductance variation $L(\theta)$ with respect to rotor position similar to that shown in Figure 2.7 arises.

Although this is an idealised inductance variation, it is expedient in the understanding of key operating principles of the machine. One should note that in the idealised inductance variation there are sharp corners, which can only arise if flux fringing is completely ignored.

Four distinct regions can be identified in the plot of the linear inductance variation shown in Figure 2.7. These distinct regions correspond to a range of rotor pole positions relative to the stator pole, which will be described below:

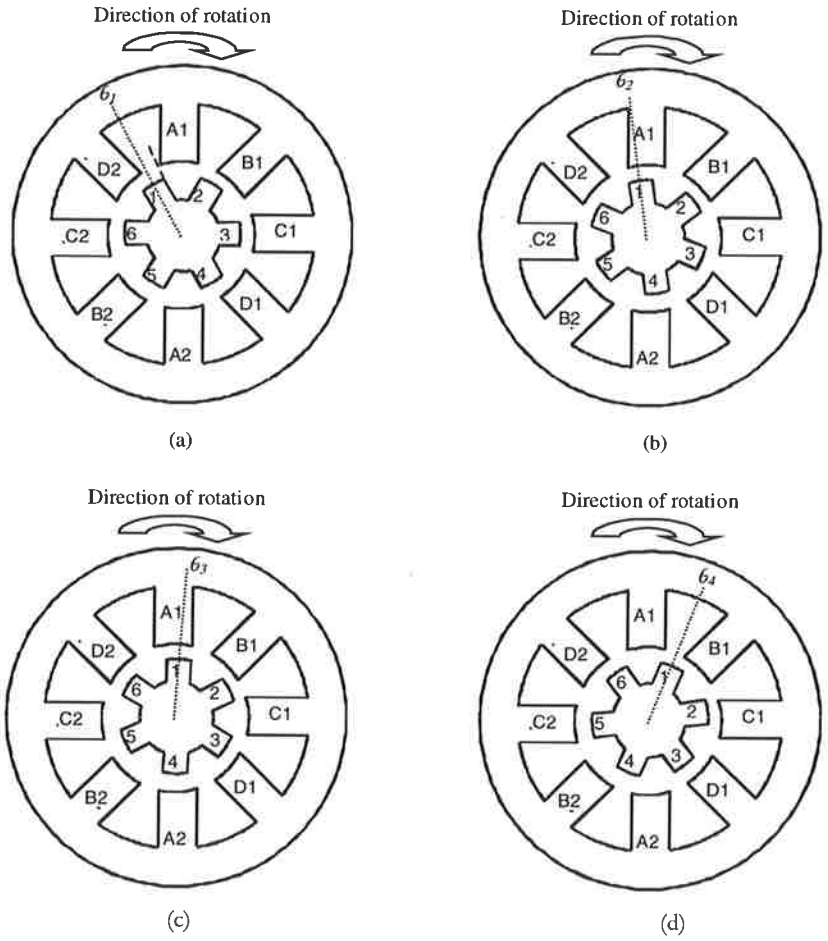


Figure 2.8 Rotor Pole 1 Positions (a) Meeting edge of stator pole A. (b) Overlapped by stator pole A. (c) Edge of rotor pole leaving overlap region. (d) Rotor pole completely leaving overlap region (Note: Airgap space is exaggerated for clarity).

a) Region A:

This region begins at rotor angle θ_1, where the first edge of the rotor, with respect to the direction of rotation, just meets the first edge of the stator pole. The inductance will then rise in a linear fashion until the poles of the stator and rotor are completely overlapped at angle θ_2. At this point, the magnetic reluctance is at a minimum and the phase inductance

is at a maximum. These rotor positions are illustrated in Figure 2.8 for an example four phase motor with rotor pole 1 approaching the stator pole of phase A.

b) Region B:

This region spans from rotor positions θ_2 to θ_3. In this region, the inductance remains constant because the rotor pole is completely overlapped by the stator pole (ie. the overlap area of the poles remains constant). At rotor angle θ_3 the edge of the rotor pole leaves the stator pole overlap region and thus the area of overlap will again begin to decrease. The position at which this occurs is illustrated in Figure 2.8 (c).

c) Region C:

When the rotor moves past θ_3, the rotor pole leading edge begins to leave the pole overlap region, and region C begins. At this point, the inductance begins to linearly decrease, until at θ_4, the rotor pole has completely left the stator pole face overlap region. At this point the inductance is at its minimum once more. The rotor position at which the rotor pole has completely left the overlap is indicated in Figure 2.8 (d).

d) Region D:

In this region the rotor and stator have no overlap and thus the inductance remains constant, at the minimum level, until region A is reached once again.

It was mentioned above that when a stator phase is excited and produces a magnetic field, the closest rotor pole tends to move into alignment with that stator pole. This means that the rotor pole will tend to move towards the maximum inductance region. Thus a motoring torque is produced when a stator phase is provided with a current pulse during the angles when the inductance is rising (assuming motoring rotation is in the direction of increasing θ in Figure 2.7). This means that if positive torque is desired, then excitation should be arranged such that current flows between the appropriate rotor angles when the inductance is rising.

Conversely, if current flows during the decreasing inductance region, a negative torque would result. This is because the rotor will be attracted to the stator pole in such a way that it rotates in the opposite direction to the motoring rotation or in other words, a torque opposite to the direction of rotation is experienced by the rotor.

It should be noted that this reluctance machine torque always acts to decrease the reluctance. The direction of current flowing into the stator winding is irrelevant. This signifies that unidirectional current excitation is possible in the SR motor drive.

The variation of torque with rotor angle for a constant phase winding current is as shown in Figure 2.7. It can be seen that the torque is constant in the increasing and decreasing inductance regions, and is zero when the inductance is constant. One can derive this torque variation by firstly examining the circuit equation of an SR motor phase winding which is given by:

$$v = Ri + \frac{d\psi(\theta,\ i)}{dt} \tag{2.2}$$

Where:

$\psi(\theta,i)$ = the flux linkage through the stator phase winding.

i = the instantaneous phase current.

R = the phase winding resistance.

v = the instantaneous voltage across the stator winding.

As linear SR motor characteristics are assumed, the phase inductance is not related the phase current and thus can be written as $L(\theta,\ i) = L(\theta)$. This means that $\psi(\theta,\ i) = iL(\theta,\ i) = iL(\theta)$ which by substitution into equation (2.2) gives:

$$v = Ri + L(\theta)\frac{di}{dt} + i\frac{dL(\theta)}{d\theta}\omega \tag{2.3}$$

Where: $\omega = d\theta/dt$ is the speed of rotation.

Note that the mutually induced voltage due to mutual magnetic coupling between phases has been ignored. This can be justified because the mutually induced voltages are usually relatively small in value in the motoring phases of the SR motor, compared to the applied motor phase excitation voltage that is supplied from the inverter.

The last term in equation (2.3) is the back emf of the motor whereas the second term is the inductive voltage drop across the phase winding. If both sides are multiplied by the current, the instantaneous electrical power input will be given by:

$$vi = i^2R + \frac{d}{dt}\left[\frac{1}{2}i^2L(\theta)\right] + \frac{1}{2}i^2\frac{dL(\theta)}{d\theta}\omega \tag{2.4}$$

By considering the conservation of energy principle, it can be shown that the first term on the right hand side of the above equation represents the power lost through dissipation in the phase winding resistance. The second term is the rate of change of energy stored in the magnetic field, whereas the final term is the gross mechanical output power.

We can thus write from the last term of equation (2.4) that:

$$P_{mech} = T\omega = \frac{1}{2} i^2 \frac{dL(\theta)}{d\theta} \omega \tag{2.5}$$

Hence, the instantaneous torque developed by the motor using the linear motor model can be defined as follows: however

$$T = \frac{1}{2} i^2 \frac{dL(\theta)}{d\theta} \tag{2.6}$$

Therefore, the magnitude of the instantaneous torque developed in the SR motor is proportional to both i^2 and $dL/d\theta$. If the inductance is increasing with respect to the angle, and current is flowing in the phase winding, then the torque will be positive and the machine will operate in motoring mode. Hence from equation (2.4) it can be seen that when the motor phase is excited during a rising inductance region, part of the energy from the supply is converted to mechanical energy to produce the torque, and another part is stored in the magnetic field. If the supply is turned off during this region then any stored magnetic energy is partly converted to mechanical energy and partly returned to the supply.

However a negative, or braking torque will be developed by the motor if the inductance is decreasing with respect to the rotor angle and current flows in the phase winding. In this case energy flows back to the supply from both the stored magnetic energy and the mechanical load which acts as a generator.

To calculate the mean torque in the SR motor the instantaneous torque produced over one electrical cycle must be integrated. This depends on knowledge of i, as seen in equation (2.6). However, for the linear SR model the analytical solutions for the current waveforms, which allows the mean torque to be calculated analytically also, were derived in reference [39]. Although these linear model waveforms are only a rough approximation of the true current, they are useful in the comparison and design of the motor drive and its various control strategies.

It can also be seen from equation (2.6) that the sign (or direction) of the torque is independent of the direction of the current, and is only dependent on the sign of $dL/d\theta$. This explains the torque waveforms that were seen in Figure 2.7, where for constant current (and constant $dL/d\theta$ magnitude), the magnitude of the torque was constant in the rising or decreasing inductance regions. However, it was seen that the torque changes from positive to negative according to the sign of $dL/d\theta$.

Hence, the ideal waveform for the production of motoring torque would be a square wave pulse of current (with magnitude equal to the maximum possible supply current) flowing only during the increasing inductance period. This current waveform is illustrated in Figure 2.9 (b). However, in practice this type of current waveform is difficult to produce in a motor phase. This is because the motor phase current is supplied from a finite dc voltage source and thus inductance of the stator phase winding would delay the rise and fall of current at the pulse edges. Instead, a more practical current waveform is normally used as is illustrated in Figure 2.9 (c). It can be seen that in this waveform the ideal square waveform is closely approximated by using hysteresis current control. At higher speeds hysteresis current control can no longer be used and a current waveform similar to that shown in Figure 2.10 (b) is seen in the phase winding. These two types of practical current waveforms, which approximate the ideal square pulse waveform at *a) low to medium speeds* and at *b) high speeds*, will be discussed below:

a) Low to Medium Speed Approximation to Square Pulse Current Waveform

At low to medium motor speeds the ideal square pulse current waveform is approximated in the practical motor drive using hysteresis current control, as is shown in Figure 2.9 (c). The hysteresis method of controlling the current is named the *chopping mode control* method in SR motor drives. During the time of conduction (between the turn on and turn off angles), the current is maintained within the hysteresis band by the switching off and on of the phase voltage by the inverter when the phase current reaches the maximum and minimum hysteresis band. An example of the voltage waveform used for the hysteresis current control is shown in Figure 2.9 (d), where a constant inverter dc supply voltage of magnitude V_s is used. It can be seen that the switching frequency of the voltage waveform decreases as the angle increases. This is due to the fact that the phase inductance (Figure 2.9 (a)) is linearly increasing with angle, which has the effect of increasing the current rise and fall time within the hysteresis band.

In the chopping mode control method, the *turn on region* is defined as the angle between the *turn on angle* θ_{on} and the *turn off angle* θ_{off}, and is chosen to occur during the rising inductance region for motoring torque. In the practical chopping current waveform, the current turn on angle θ_{on} is placed somewhat before the rising inductance region. This is to ensure the current can quickly rise to the maximum level in the minimum inductance region before the rising inductance, or torque producing, region. Similarly the turn off angle θ_{off} is placed a little before the maximum inductance region so that the current has time to decay before the negative torque, or decreasing inductance, region. The angle at which the current decays to zero after turn off is labelled as θ_q in Figure 2.9 (c).

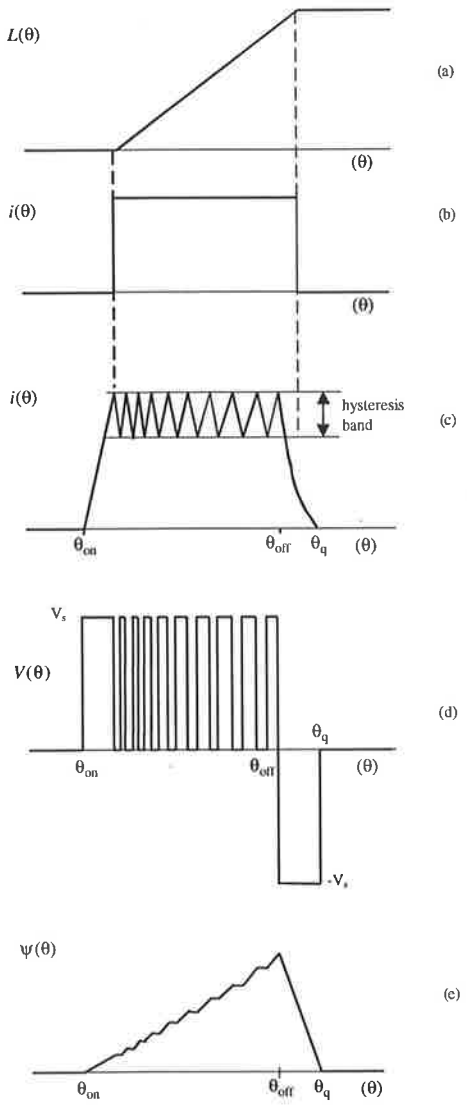


Figure 2.9 (a) Linear Phase Inductance Variation. (b) Ideal Square Wave Phase Current. (c) Chopping Mode Phase Current. (d) Chopping Mode Phase Voltage. (e) Flux Linkage Waveform Corresponding to Chopping Mode Current.

b) High Speed Approximation to Square Pulse Current Waveform

The chopping mode of operation cannot be used at higher speeds, as at these speeds the hysteresis band current level will not be reached. This is because at high speeds the back emf of the motor becomes equal to or larger than the voltage supply in the rising inductance region, which limits the increase of the motor phase current. In addition, the rise time of the current will correspond to an ever-increasing angle as the speed is increased. Eventually at high speeds, the rise time angle will be so large that the turn off angle θ_{off} will be reached before the hysteresis current level has been exceeded. Thus at high speeds the current is switched on and off only once per cycle. In SR motor drive control, this is called the *single pulse mode* of operation. An example of the single pulse mode current is illustrated in Figure 2.10 (b).

In the single pulse mode of operation, the inverter power switches turn on at rotor angle θ_{on}, which places the dc voltage supply V_s across the phase winding, as is shown for the example single pulse voltage waveform in Figure 2.10 (c).

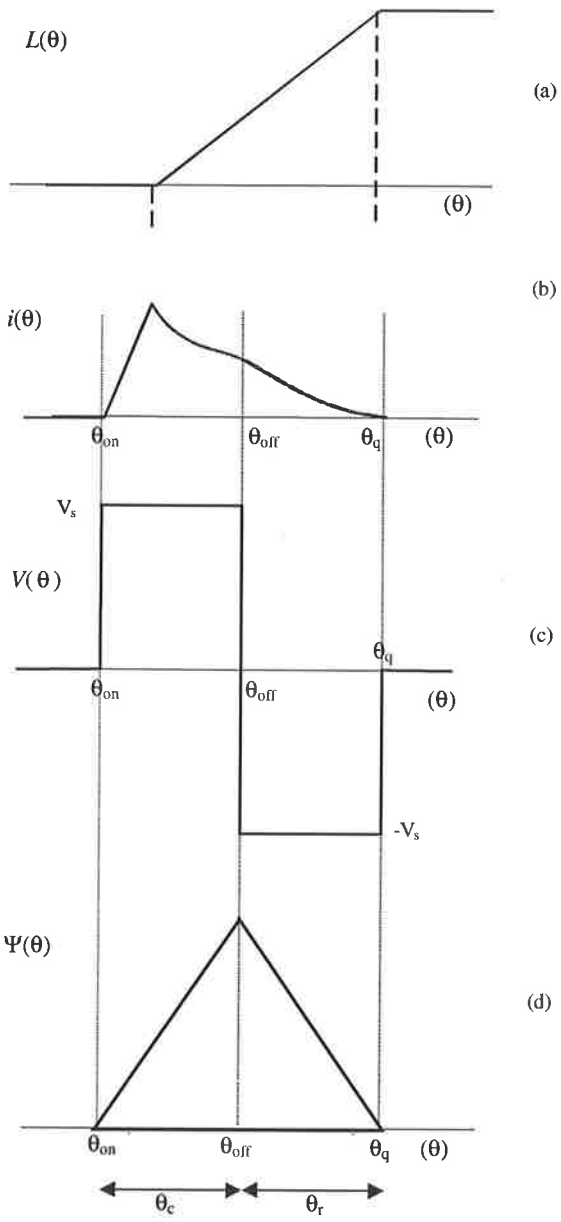


Figure 2.10 (a) Linear Phase Inductance Variation. (b) Single Pulse Mode Phase Current. (c) Single Pulse Mode Phase Voltage. (d) Flux Linkage Waveform Corresponding to Single Pulse Mode Current.

As for the chopping mode case, in order to maximise torque θ_{on} must usually be located prior to the rising inductance region. This is so that, while the inductance is low, the current has a chance to rise rapidly to a substantial value before the torque producing region begins and the motor back emf increases. At rotor angle θ_{off}, the power switches are turned off, and the phase will have a negative voltage (typically $-V_s$) thrown across it. The current will then decay until it becomes zero at rotor angle θ_q.

Similarly to the chopping mode control, it is usual for the turn off angle in the single pulse mode to occur before the maximum inductance point occurs. This is to prevent current flow in the decreasing inductance region where negative torque results. However, in the region of constant maximum inductance, when the rotor pole face is completely covered by the stator pole face, current flow is not detrimental to torque production. Instead one can see from equation (2.4) that, neglecting resistance, the supply power is converted only to magnetic field energy $(\frac{1}{2})i^2 L(\theta)$.

The current and voltage waveforms that were detailed above for the single pulse and chopping mode of operation, produce a corresponding flux linkage waveform in the motor which will be discussed below. As it will be seen, the flux linkage waveform in the single pulse mode of operation is more simplistic, and thus it will be discussed first.

a) Single Pulse Mode Flux Linkage Waveform

In order to predict the flux linkage in the motor phase, the phase voltage equation (2.2) is used. It can be assumed to a good accuracy that the resistive drop Ri in equation (2.3) is negligible compared to the back emf $i.\omega.dL(\theta)/d\theta$ and the reactive drop $L(\theta).di/dt$. This means that in equation (2.2), the Ri term can also be ignored. Therefore, from equation (2.2) it can be derived that the flux linkage will increase at a constant rate during the conduction angle $\theta_c = \theta_{off} - \theta_{on}$, if a constant positive voltage V is applied. In this case, the flux linkage will rise with a constant rate given by:

$$\psi(\theta, i) = \int V.dt = V.t \tag{2.7}$$

Similar analysis shows that the flux decreases at the same constant decreasing rate when a negative voltage is applied that is equal in magnitude to the positive applied voltage. Therefore, for negligible resistive and iron losses, and for equal magnitude but opposite sign turn on and turn off voltages $+V_s$ and $-V_s$, the conduction angle θ_c must equal the energy return angle $\theta_r = \theta_q - \theta_{off}$, where these angles are defined in Figure 2.10 (d). In addition, this implies that the maximum flux always occurs at the turn off angle θ_{off} when the negative turn off voltage is initially applied.

b) Chopping Mode Flux Linkage Waveform

It was seen in Figure 2.9 (d) that the chopping mode voltage consists of a switched voltage waveform with varying switching frequency. To determine the resultant flux linkage in the chopping mode, equation (2.7) can again be used to integrate the switched voltage waveform. From equation (2.7) it can be seen that during the positive voltage pulses the flux linkage will increase, whereas the flux linkage will remain constant when the phase

voltage is turned off (in fact the flux linkage will decrease slightly due to the iR voltage drop which is ignored in equation (2.7)). Therefore, the flux linkage will increase in a step like manner. In addition, during the conduction period the average chopping mode phase current is approximately constant, whereas the phase inductance is linearly rising. Therefore, the flux linkage which is equal to $L(\theta)i$ must also rise in a linear manner during the conduction region. Hence, a flux linkage waveform such as that shown in Figure 2.9 (e) is seen during the chopping mode motor operation.

The linear SR motor model that was discussed above is often used for SR motor control schemes due to the simplicity of the model [40]. However, although the linear equations are simple to analyse and use to predict behaviour, they can be inaccurate when dealing with real SR machines. This is because nearly all practical SR machines are designed to experience magnetic saturation during normal operating conditions. If an SR motor is built so that the magnetic circuit does not normally saturate, the air gap would need to be large, and the magnetic sections thick. However, the corresponding performance of the machine would be low. This is because the torque per unit volume would be lower than an SR motor which is designed to operate with magnetic saturation, and the controller device ratings would need to be higher [41]. This is due to the advantageous property of magnetic saturation in reluctance type machines. As shown in reference [42], if a reluctance machine is operated in the linear region then the theoretical maximum amount of mechanical power that can be produced by the motor can only be half the input power. The rest is stored in the magnetic circuit and must be returned to the supply or dissipated. However with saturation the amount of mechanical energy can reach theoretically up to 100% of the input energy, and practically up to approximately 70% [43].

Therefore, in order to predict the performance of practical SR motors, which operate with magnetic saturation, the non-linear characteristics should be considered, as will be detailed below.

2.7 Operating Theory of the SR Motor (II): Magnetic Saturation and Non-Linear Model

In the linear model described above, it was assumed that the inductance of a phase winding is independent of current. However, in a real SR motor significant saturation of the magnetic circuit normally occurs as the phase current increases, and thus the phase inductance is related to both the phase current level and position. Due to the magnetic saturation effect, the actual phase inductances at a given rotor position can be reduced significantly compared to the inductance given by linear magnetisation characteristics. In addition, the effect of magnetic saturation becomes larger as the motor current level increases.

The effects of saturation in a SR motor can be observed in a plot of its magnetisation curves. This shows the relationship of flux linkage versus current, at rotor positions varying between the fully aligned and unaligned angles. A typical set of SR motor magnetisation curves is shown in Figure 2.11, where it can be seen that there is a non-linear relationship between the flux linkage and current for each curve.

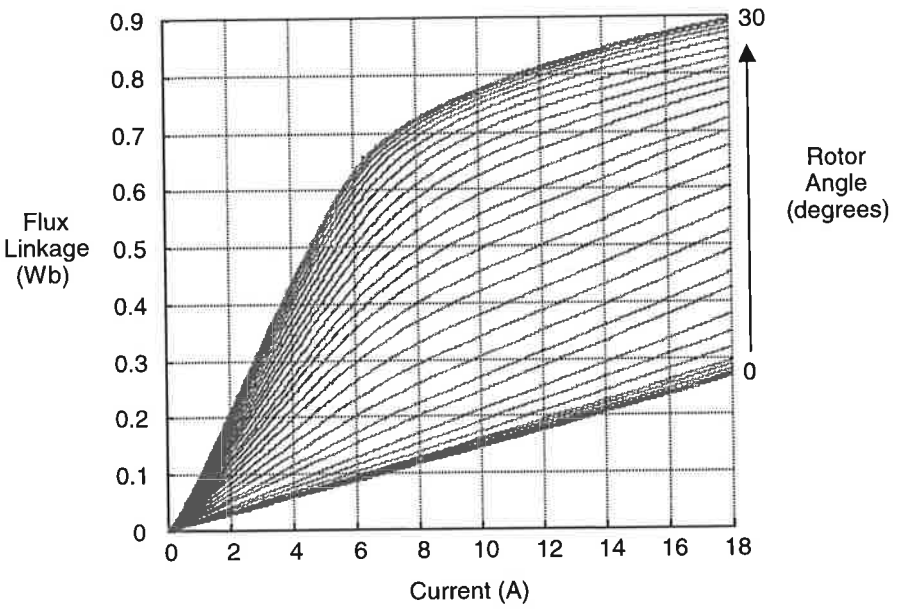


Figure 2.11 SR Motor Magnetisation Characteristics (each curve represents a constant rotor position).

From the magnetisation curves, the plot of inductance versus position and current can be determined. This is because inductance is defined as the ratio of flux linkage to current:

$$L(\theta,\ i) = \frac{\psi(\theta,\ i)}{i} \tag{2.8}$$

Therefore using the above equation, the inductance as a function of rotor position and current can be found from each point in the flux linkage versus current and angle characteristics. It should be noted that the inductance defined in equation (2.8) is related to the slope of the flux linkage curves (Figure 2.11). The flux linkage curve slopes decrease due to the effect of saturation, and thus it can be observed that the inductance also will decrease due to the effects of saturation.

A typical set of non-linear inductance curves for the SR motor shown in Figure 2.12. It should be observed that there is a very significant variation in these characteristics from those predicted in the linear model (see Figure 2.7). This is because as the phase current increases, the saturation in the magnetic circuit increases, which will lead to a decrease in the slope of the flux linkage curves (Figure 2.11) and a corresponding decrease in phase

inductance. Only at low current levels, when the saturation is low, would the inductance curves approach those predicted by the linear approximation.

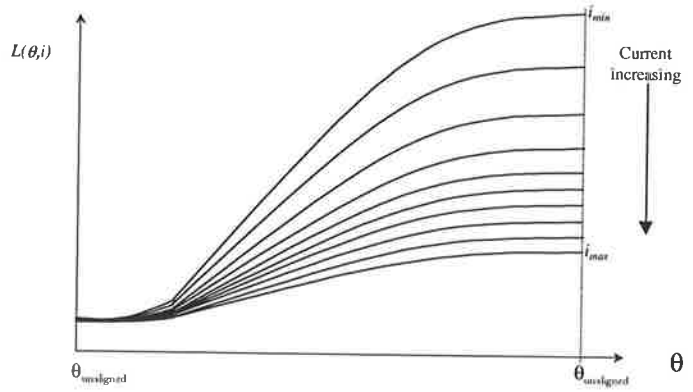


Figure 2.12 Inductance Curves for SR Motor with Saturation (each curve represents inductance variation at constant current).

The magnetic saturation in the steel structure of the motor, which leads to the decrease in phase inductance at higher currents, arises from different effects. Moreover, depending on the position of the motor, different magnetic effects become more significant [36]. These various magnetic effects will be discussed below:

a) Aligned position

When a rotor pole is directly in line with a stator pole axis then that rotor pole is said to be in the aligned position, as illustrated in Figure 2.13 (a). As it has been mentioned above, this position corresponds to the position of maximum inductance. This is because the magnetic reluctance of the flux path is at its lowest when the airgap is smallest.

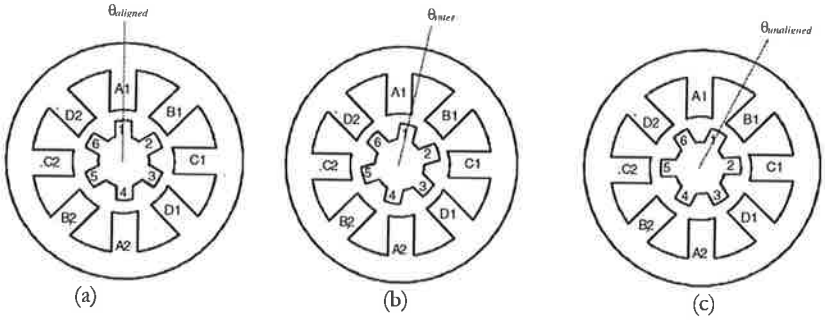


Figure 2.13 (a) Aligned Position (Rotor pole 1 aligned with stator pole A1). (b) Rotor pole 1 in intermediate position with respect to stator pole A1. (c) Rotor pole 1 in unaligned position with respect to stator pole A1.

In the aligned position, the magnetic circuit is susceptible to saturation because the low reluctance allows a large amount of flux to be set up easily. At this position, the principal effect on the magnetic circuit as current rises is that of *bulk* saturation, where the saturation acts on the magnetic circuit as a whole. The bulk saturation leads, in general, to a large decrease in inductance at high current when the rotor is at or near the aligned position.

b) Intermediate position

When the rotor is at some intermediate angle between the fully aligned and fully unaligned positions (Figure 2.13 (b)), the effect of local saturation occurs. Local saturation happens in the pole tips of the stator and rotor when they are only partially overlapped. The flux that flows through the magnetic stator and rotor yoke is concentrated at the partially overlapped pole tips. This leads to the effectual pole area being smaller during partial overlap and means the flux density will be higher.

As the flux density is higher in the pole tips than in the rest of the magnetic circuit, it is easier for the saturation flux density of the pole material to be reached. It follows that, when the overlap area is small, local saturation can be particularly intense. Note that in this region of partial overlap, the saturation region spreads as current is increased. This happens until bulk saturation effects, as described above, also become significant.

c) Unaligned position

In the fully unaligned position, shown in Figure 2.13 (c), no overlap of poles occurs, and the airgap is large. In this position, the reluctance of the magnetic path is at its maximum and thus the inductance is at the minimum. At this angle, the reluctance of the airgap is many times greater than that of the steel sections. This means that saturation is only observed at current levels exceedingly higher than those used during normal operation [14]. Consequently, the magnetisation curve is basically linear in this rotor position.

Note that, unlike the linear model prediction given previously in Section 2.6, there is no constant minimum inductance region when the rotor pole leaves the stator pole face. This is due to the effect of flux fringing between the stator pole and rotor pole [20]. At high current levels, the flux fringing effect can be considerable, leading to some torque component even before any overlap occurs.

Due to the magnetic saturation effect discussed above, the instantaneous torque equation (2.6) which was derived assuming linear conditions will not be generally valid for calculating the torque in SR motors. Therefore, for accurate calculations, the torque must take into account the dependence of phase inductance with current and position.

If one considers the phase inductance saturation, the expression for instantaneous torque production of an SR motor phase can be written as:

$$T = \left[\frac{\partial W'}{\partial \theta}\right]_{i=cons\tan t} \tag{2.9}$$

Where coenergy W' is defined as:

$$W' = \int_0^i \Psi di \tag{2.10}$$

This equation defines a general expression for the instantaneous torque developed in an SR motor.

Therefore, the instantaneous torque produced by the SR motor can be expressed as the derivative of coenergy with respect to the position θ, at constant current i. It should be noted that the relation (2.9) holds only for constant phase current. However, it can be readily shown that for calculating the instantaneous torque (where infinitesimally small differential rotor angles apply), this assumption can be made without affecting the calculated value.

By solving the motor's electrical equation (2.2) and mechanical equation (2.9), together with the differential equation representing the mechanical load and the magnetisation characteristics $\Psi(\theta,i)$, one can describe the behaviour of the SR motor system. However, it should be noted that mutual inductances and effects such as iron losses and change of phase resistance with temperature are all ignored in the derived model. To fully describe the motor accurately these must be taken into account.

Furthermore, another difficulty arises from the fact that no exact analytical solution is possible for this group of differential equations, due to the fact of high non-linearity in the magnetisation characteristics $\Psi(\theta,i)$. An analytical solution to the equations can only be found if the magnetisation curves of $\Psi(\theta,i)$ are approximated by polynomial or sinusoidal functions [44]. If this is done then one can derive analytical solutions for torque and current. However, the errors can be large, due to the difficulty in accurately approximating the magnetisation curves in this manner.

Instead, numerical look-up methods [45] can be used to calculate the motor torque using the non-linear differential equations. Numerical look-up methods use measured values of flux linkage at discrete values of current and rotor angle. These flux linkage values are measured experimentally on the motor, and are stored as a numerical look-up table. Using the measured curves of $\Psi(\theta,i)$, instantaneous values of torque and current can be numerically simulated using the motor equations ((2.9) and (2.21)). In each step of the simulation, the value of flux linkage is found from the look-up table and is used to solve for the current and torque. Hence, the torque output of the motor for given turn on and turn off angles can be found for both chopping mode and single pulse mode control. Conversely, using simulation, the control angles of the motor, to satisfy a given load torque requirement, can also be determined.

2.8 Magnetisation Characteristic Measurement

In order to calculate the SR motor instantaneous torque using numerical look-up simulation method, the SR motor magnetisation characteristics (flux linkage as a function of current and rotor position) should be measured. The magnetisation characteristics vary widely with different SR motor types and thus this measurement should be carried out for the particular motor that is being simulated. In addition to allowing numerical simulation of the motor, the measured SR flux linkage curves were used in this thesis as learning data for creating a fuzzy logic based non-linear SR motor model. Therefore, a method for measuring the flux linkage characteristics of the SR motor was developed for this thesis. The method used data acquisition software with a high speed data acquisition card and motor measurement and control hardware. The method has novel features as it provides a fully automated test system with a user friendly graphical interface that allows simple operation and presentation of measured data.

The details of the SR motor magnetisation curve measurement system developed for this thesis are given in Appendix A. The new measurement scheme was developed using the LabVIEW® data acquisition package. The LabVIEW environment is based on the concept of *virtual instruments,* or *VIs,* which is a term describing the combination of personal computers with software based programmable instrumentation.

a) An outline of the developed LabVIEW based measurement method is given in Figure 2.14. The test system used to measure the switched reluctance motor flux linkage curves consisted of the following hardware:

b) Four phase, 4kW SR test motor.

c) Position setting and rotor clamping device to hold the rotor at a set angle whilst measuring the flux linkage as a function of current

d) Power switching device to control the current in the motor phase that is being measured.

e) Sensors to measure the phase current and voltage.

f) Data acquisition board installed on a personal computer to input the measured data and allow signal processing by the software algorithm.

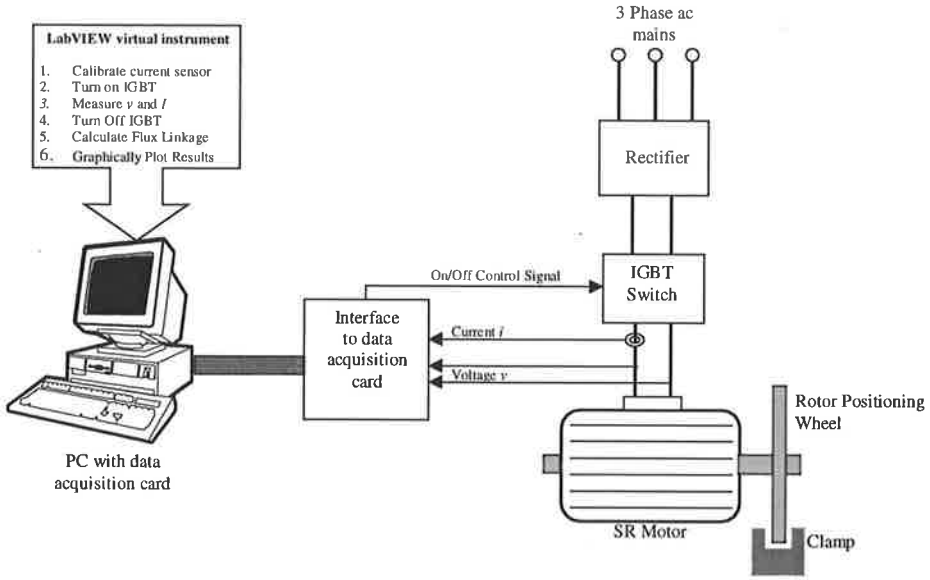


Figure 2.14 Magnetisation Characteristics Measurement Test System.

The software developed in LabVIEW performs calibration of the sensor, switching on and off the motor phase voltage, data acquisition, and calculation and graphical presentation of the flux linkage curve for each angle. The developed software is easy to use and only requires the user to set and clamp the rotor. A simplified flow-chart of the flux linkage curve measurement test is given in Figure 2.15.

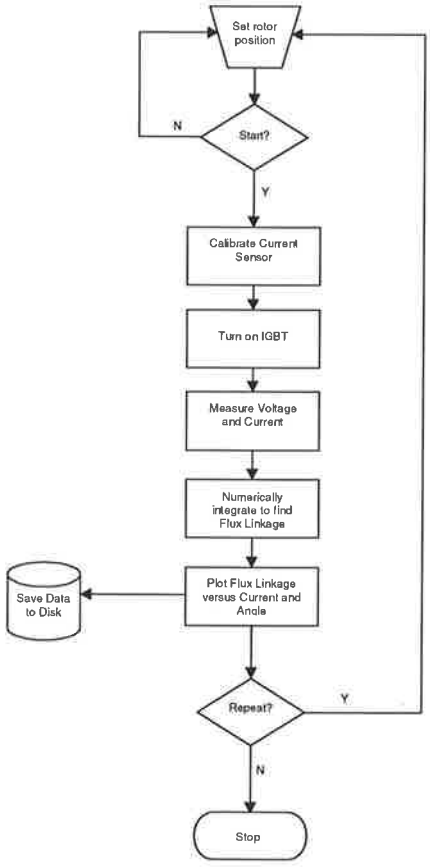


Figure 2.15 Simplified Flow-chart of Flux Linkage Curve Measurement Algorithm

2.9 Control Parameters of the SR motor

A variety of performance characteristics can be obtained in the SR motor by controlling various parameters. These parameters include the chopping mode control hysteresis level at low to medium speeds, and the turn on and turn off angles θ_{on} and θ_{off} at all motor speeds. By controlling these parameters it is possible to produce any desired characteristic such as constant torque, constant power, or some other particular characteristic in between [46].

The control of the SR motor is relatively complex for any high performance operation because of the motors high non-linearity. This means that linear control models cannot be used as in other machines, unless a restriction is placed on the motors current level. Normally numerical simulation of the non linear motor model must be carried out to obtain the optimum control parameters for a particular mode of operation.

As it was discussed in Section 2.6, two distinct modes of operation apply in the SR motor depending on the nature of the current waveform. These modes were the chopping mode control, which can be used at low to medium motor speeds, and single pulse mode of control, which is used at high speeds. Both of these modes of operation will be further detailed below, with an explanation of the corresponding inverter switching operation:

a) Chopping mode control

In the chopping mode control region the turn on and turn off angles are controlled together with the current level. As it was described in Section 2.6, the turn on angle and turn off angle are controlled so that current flows during the rising inductance, or positive torque producing region. This normally entails that the turn on angle is placed shortly before the place where the rising inductance angle begins, and the turn off angle is placed shortly before this region ends.

In the chopping mode, the current level must be controlled because at low speeds the back emf of the motor is less than the applied voltage. Therefore, the current will continually increase when a phase has voltage applied across it during the turn on region. Therefore, if uncontrolled, the current will rise above the limit determined by either the power semiconductor ratings or thermal considerations during the turn on period. Thus, the current must be controlled in this region to remain below the maximum allowable level. This involves switching the voltage across the phase on and off in such a manner that the current is maintained between some chosen upper and lower hysteresis current levels. An example of this form of current chopping control was shown in Figure 2.9 (c).

The actual torque production of the motor in the chopping mode is set by the control turn on and turn off angles and the current hysteresis level. As described in Section 2.7, the control angles to provide a required load torque at a given speed can be determined by simulation of the non-linear equations.

Within the chopping mode of operation, two current hysteresis control schemes can be used. These are termed *soft* and *hard* chopping. Soft chopping can only be used in some circuit configurations, such as that shown in Figure 2.16. For soft chopping control one switching device remains on during the entire conduction period whilst the other is switched on and off to maintain the desired current level. This can be seen in Figure 2.16 (a) and (b) where the two conduction modes during chopping are shown. When both switches are on, the phase winding views the full positive supply, whereas when only one switching device is on the phase experiences a zero voltage freewheeling loop which will decrease the current.

In the hard chopping scheme both devices are switched simultaneously, and have the same switching state at all times. If both switching devices are turned on, the phase winding sees the full positive supply. To decrease the current, the full negative supply is applied by turning both devices off as shown in Figure 2.17. In circuit configurations with less than two switches per phase, only hard chopping can be used.

Soft chopping is more advantageous than hard chopping. This is because of a smaller dc ripple current in the supply, which can substantially minimise the ripple current rating of the dc link capacitor, as well as lower the hysteresis loss in the motor. It has also been found that soft chopping lowers acoustic noise and electro magnetic radiation [36].

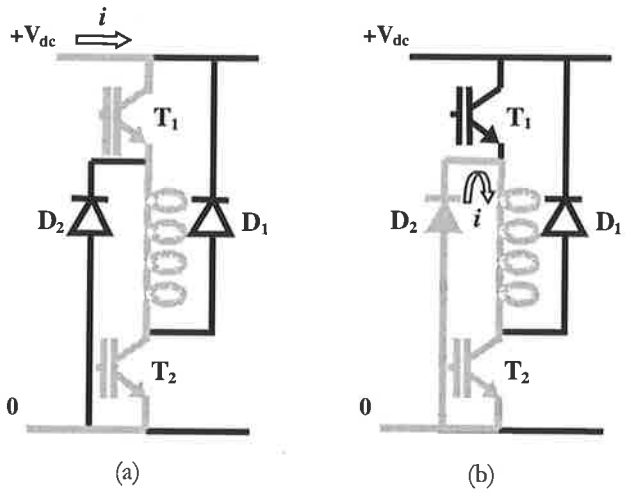


Figure 2.16 Soft Chopping Mode Conduction Paths: (a) Both devices on - positive voltage applied to motor phase (b) T1 turned off - zero voltage freewheeling loop applied to motor phase.

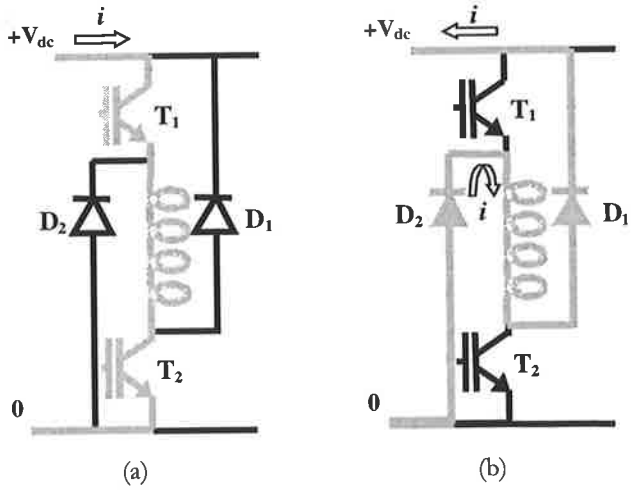


Figure 2.17 Hard Chopping Mode Conduction Paths: (a) Both devices on - positive voltage applied to motor phase. (b) T1 and T2 turned off – negative voltage applied to motor phase.

b) Single Pulse Mode Control

At higher speeds, the back emf of the SR motor eventually becomes greater than or equal to the supply voltage during the rising inductance region. This means that even if a phase is excited the current in the motor phase will not increase in the rising inductance region. Therefore, at higher speeds the turn on angle must be placed before the beginning of the increasing inductance region, in order that the phase current has an adequate time to increase before the back emf becomes high.

In addition, the time available for the current to rise after turn on becomes less and less as the speed of the motor increases. This is due to the fact that the available conduction time is lower for constant switching angles as the speed of rotation increases. This can be seen by considering that speed is the time rate of change of angle. If the conduction angle range is kept constant, then the time it takes for the rotor to rotate through that range will decrease when the speed increases.

Thus, as the speed increases, there will be a point when the current level never rises to the chopping level. At this point, the single pulse mode of operation will come into effect and the current will decrease or remain constant throughout the increasing inductance zone. An example of a single pulse mode current waveform was seen in Figure 2.10 (b).

As the current is not commutated in the single pulse mode, the control in this mode consists only of controlling the on and off angle. The turn on angle θ_{on} can be placed at some point in advance of the rising inductance region where the phase inductance is low, so that current can increase at a faster rate before the increasing inductance region. The angle can be advanced up until maximum allowable current occurs at the peak of the waveform (this may even mean switching on in the previous decreasing inductance zone). The actual control turn on and turn off angles for the single pulse mode, for a given load

torque and speed, can once again be determined by simulating the non linear equations as described in Section 2.7.

The speed at which changeover between single pulse and chopping mode occurs is called the *base speed.* Base speed is defined as the highest speed at which chopping mode can be maintained at the rated voltage and with fixed on and off angles. Below the base speed, the current increases during the rising inductance region, unless it is maintained at the maximum or a lower level by chopping.

Therefore it can be seen that at lower speeds that are below the base speed, the motor is controlled using chopping mode control, whilst at speeds above the base speed the single pulse mode of control is used. In both control modes the control turn on and turn off angles are chosen so that the motor provides the required load torque. The various methods of determining these control angles are discussed in the following subsections:

2.10 Control Methods

a) Linear Model Based Control

Some previous control methods that have been developed [39] assumed that the SR model was linear. These schemes set a constant torque region for speeds below the base speed, where chopping mode can be used. In this region, fixed switching angles are set such that current turn on occurs at the start of the rising inductance region and turn off occurs at the end of that region. As chopping mode is used below base speed, the current can be approximated to be essentially constant at all times in all the phase conduction periods (Figure 2.18). This means that an experimental plot of *average* torque versus constant current level and speed can be determined for these *constant* switching angles. Example plots of torque versus current and speed for these conditions can be seen in Figure 2.19. From this figure, it can be seen that for constant switching angles in the chopping mode the average motor torque is varied by changing the chopping mode current level.

Above base speed, a constant power characteristic is maintained by increasing the conduction angle. However, if a linear motor model is used to calculate the required conduction angle to maintain constant power, the scheme would not be very accurate in most SR motors.

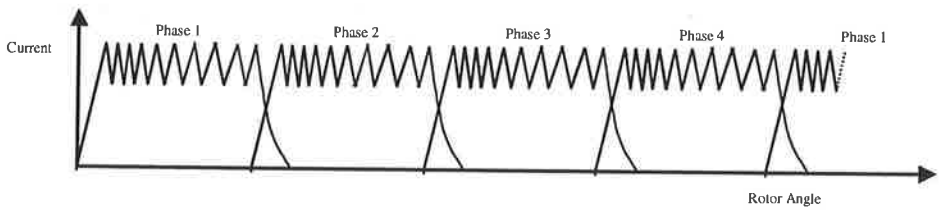


Figure 2.18 Chopping mode current waveforms for 4 phase motor with constant switching angles (approximately equal current at all conduction angles)

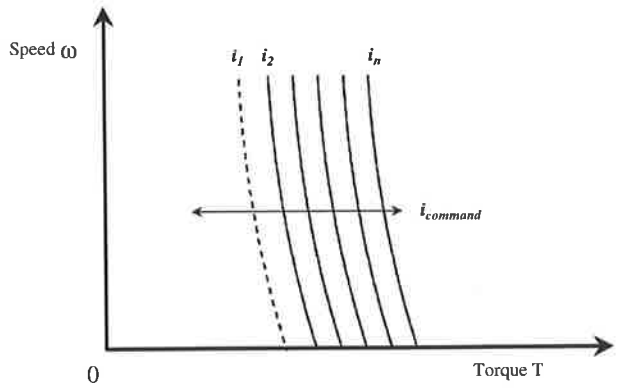


Figure 2.19 Variation of torque with speed and reference current level for constant switching angles.

b) Non-linear Control

Although the linear model can be used for simple control schemes, to accurately control the motor, the non-linear motor model should be used to determine the control angles and hysteresis levels that provide the required motor torque at a given speed. The control angles can be predetermined using simulations of the non-linear motor model. These predetermined angles are then programmed into a motor controller. A more sophisticated technique is to use the non-linear model directly in a control scheme. The controller then calculates the control angles and hysteresis levels on-line during real time motor operation.

Apart from satisfying the load torque, a control scheme must usually take into account other parameters such as minimising the torque ripple, peak current or rms current. There will thus be a set of optimum control angles for a given torque [47] [48]. Due to the non-linear characteristics of the motor, the finding of these optimum control angles is complicated. Furthermore, these have to be found for each torque-speed condition, because the optimum conduction angles vary for the same torque at different speeds. The magnetic saturation effects of the SR motor mean that an analytical expression may not be possible for the optimum control angles. Hence, to find the optimum switching angles to a high accuracy, either a series of experimental tests, or accurate simulations using the non-linear magnetisation curves, must be done.

The control of the SR motor using non-linear control schemes with the non-linear SR motor model, has been of recent interest amongst the control community. Sophisticated non-linear control is needed to have accurate control over the torque and speed of the motor, as well as optimising factors such as overshoot, settling time, torque or speed ripple, and peak current or rms current. Note that it usually impossible to optimise all of the factors as optimising one factor will normally affect the other.

Normally in the control schemes, some non-linear model of the motor is derived, which in itself involves some approximation. This is because some approximate mathematical

function of the magnetisation curves must be found, and these are usually assumed not to vary with time. Examples include a scheme that uses the feedback linearisation control technique [49]. Although theoretically feasible, the developed model is highly complex, and thus the control algorithm is not currently practical for real time operation. A reduced-order SR model was developed for a feedback linearisation scheme which was more practical [50]. However, both of these schemes assume that only one phase is excited at a time.

Another non-linear model scheme makes the approximation that the magnetisation curves can be modelled as straight line regions of *linear, low inductance*, and *high inductance* zones [51]. Although this makes the control equations simpler, operation with a real motor would not be ideal due to this approximation.

A non-linear *Sliding Mode* control scheme has been developed which optimises torque performance in the motor. In addition, the scheme allows two phases to be excited at a time in a four-phase machine. This means higher output power and faster transient responses are possible [52]. Results show that this scheme has very low torque ripple, and a fast response.

A promising form of SR motor control seems to be those making use of fuzzy logic for real time control and neural networks for off line learning of the optimum control angles. These schemes can cope with the high non-linearity of the motor, and changes in the motor parameters over time. One approach has been to use neural networks to calculate the optimum excitation current for minimisation of torque ripple [53], [54]. This information is then used to control the motor. Another neural network method has been developed that determines the turn on and turn off angles, as well as chopping current level, for optimal drive efficiency at any given torque and speed [55].

Fuzzy logic based schemes include a fuzzy logic PID speed controller which has a very fast response and has a high robustness to load torque perturbations [56]. Similar results have been reported in reference [57] where a highly robust fuzzy logic based SR motor controller is reported. Another fuzzy logic based scheme uses a fuzzy adaptive system to learn non-linear current profiles that will minimise torque ripple. The scheme operates on line while the motor is running. A novel part of this scheme is that no knowledge of the machine model is needed, but linguistic information, which is known by experts, is incorporated [58].

2.11 Position Sensing

It can be seen from the above discussion that to control the SR motor satisfactorily, the motor phases are excited at the rotor angles determined by the control method. It is therefore essential to have knowledge of the rotor position. Furthermore, the rotor angle

information must be accurate and have high resolution to be able to implement the more sophisticated non-linear control schemes that can minimise torque ripple and optimise the motor performance.

This means that the performance of an SR drive depends on accurate position sensing. The efficiency of the drive and its torque output can be greatly decreased by inaccurate position sensing, and corresponding inaccurate excitation angles. It has been demonstrated that at high motor speeds an error on only one degree may decrease the torque production by almost 8% of the maximum torque output [59].

Traditionally, rotor position information has been measured using some form of mechanical angle transducer or encoder. The position sensing requirements are in fact similar to that needed for brushless PM motors. However, although position sensing is required for the motor operation, position measurement sensors are often undesirable. This may be due to problems with their reliability, size, or cost [59].

Specifically, the reliability of position sensors becomes a problem when the motor is operated in harsh operating environments. The SR motor is inherently reliable due to its simple structure. However, when the motor is operated in dusty, high temperature, or high vibration environments, the position sensor reliability can be much lower than the motor. For example in optical encoders, the built-in semiconductors that are used to provide the encoder output signals are affected by changes in temperature, and the optical devices can have changing characteristics over time [60]. In addition, a position sensor is undesirable for aerospace applications, where an extremely low failure rate and very high mean time before failure is critical [28].

There are also applications where allocating a space for the position sensor in the drive system becomes undesirable. This may be in cases where the SR motor is used in robotics or computer peripherals. In addition, in many applications the length of the encoder shaft may make it impractical for use [60].

In addition, the cost of the sensor may be a significant portion of the system cost. For example if high performance control were required, an high resolution absolute encoder usually needs to be used. These have a high expense because absolute encoders are complex and expensive to manufacture [60]. In addition, the cost of the system also increases because consideration must be given in the construction and maintenance of the motor due to the mechanical mounting of the sensors.

Another disadvantage is that the sensors entail extra electrical connections to the motor. For example, an 8-bit absolute encoder requires eight signal lines, which must be connected to the controller for the motor shaft. As this cabling runs from the motor to the

low power control side, the cabling and signal drivers must be carefully selected to prevent signal loss and noise [61].

2.12 Conclusion

In this chapter, the SR motor was introduced, and the advantages of using the SR drive were discussed. It was seen that there are many advantages that make the SR drive suitable for many applications such as a simple topology, high motor drive system efficiency over a wide speed range, robust motor construction, and the ability to continue operating with one or more faulted motor phases. It was also seen that the motor can be used in a wide variety of industrial variable speed drive applications.

The motor drive design options were also discussed, and it was shown that a system approach should be taken in order to optimise the drive design. The major parts of the SR drive system that are considered in the design process include the motor, power electronic circuits, control circuitry, and measuring circuits. The drive design procedure normally includes the consideration of the number of motor phases, the motor size and maximum speed, the power devices and inverter topology type, and dc power supply source.

In order to provide a basis for the developed work in later sections of this thesis, a detailed theoretical examination of the operating principles of the SR motor was also given in this chapter. In addition the operating theory is required to develop a simulation of the SR motor drive in order to provide initial testing of the rotor position estimation scheme.

Initially a simple linear model of the motor was shown, which gave a simple description of the general motor operation and torque production. It was seen that for torque production in the practical SR motor two current control methods are used: the chopping mode hysteresis current control at low to medium speeds and the single pulse mode control at higher motor speeds. The corresponding flux linkage waveforms were illustrated, and it was observed that the flux linkage waveform in the single pulse mode has a much simpler waveform than that of the chopping mode.

It was discussed that in the linear model of the SR motor it is assumed that the flux linkage is linearly related to current for any position θ, but significant magnetic saturation normally occurs in the practical SR motor during operation. Hence, for normal operation, the flux linkage of the motor is a non-linear function of both rotor position and current. Therefore, to accurately predict the operating torque and current waveforms of the motor a non-linear motor model was developed. To use the non-linear equations the magnetisation characteristics of the motor must be known, and thus an experimental method developed for this thesis to find the magnetic characteristics was discussed (which is further detailed in Appendix A).

Using the non-linear model of the motor a general expression for the instantaneous torque produced in the SR motor was derived. The importance of this expression is that it can be used to calculate the torque for all SR motor operating conditions, regardless of the level of magnetic saturation.

In this chapter, it was shown that the control of the SR motor is relatively complex due to the non-linear magnetic characteristics of the motor. The control variables of the motor are the hysteresis commutation level in the low to mid speed chopping mode, and the turn on and turn off angles in both the chopping mode and the high speed single pulse mode. Simple linear model based control schemes were also discussed to control the motor torque. However, for high performance operation, more sophisticated non-linear control schemes should be used. These include feedback linearisation, sliding mode, fuzzy logic, and neural network based methods.

It was also seen that rotor position measurement is important to provide satisfactory control of the SR motor. This position feedback must have a relatively high resolution and accuracy for a good motor performance. The rotor angle may be measured by some kind of position sensor that is attached to the motor shaft. However, these sensors can be unattractive because they can lower the drive reliability, and add to the cost, size and maintenance. Hence, it is advantageous to dispense the position sensor from the drive system using an alternative method of position measurement. Therefore, researchers have developed a number of methods to estimate position information without a sensor. All these methods use some form of processing on electrical waveforms passing through the motor windings.

In the next chapter, the various methods of estimating the rotor position without the need for a sensor are detailed. However it will be shown that previously developed methods have some disadvantages and cannot be used to control the motor under all operating conditions. Therefore, a new position estimation method has been developed in this thesis, which overcomes the disadvantages of both position sensors and the limitations of previous angle estimation schemes. This new method will be detailed in subsequent chapters of this thesis.

Chapter 3: A Survey of Position Estimation Techniques in SR Motors

3.1 Introduction

It has been seen from the previous discussion that rotor position feedback is essential for the control of the SR motor. To obtain good performance from the motor drive, the motor phases must be accurately excited at some predetermined rotor angle, in order that the phase current pulses are accurately placed relative to the machine rotor position. As the accuracy of the position feedback decreases, the torque production and efficiency of the motor can be significantly affected.

At low speeds, there may be a tolerance of a few degrees in the rotor position feedback before a noticeable difference in the average torque arises. However at medium and high speeds, the phase switching angles become critical because the torque production of the motor varies widely for a small change in excitation angles [62]. This is because at higher speeds the back emf of the motor is high, and the current pulse length in time is shorter due to the faster change in rotor angle. Due to the high back emf, when the stator and rotor poles begin to overlap, a small delay in placement of the turn on angle may lead to a significant reduction of current level and thus torque. It is therefore essential to have an accurate knowledge of rotor position when operating the SR motor.

In order to obtain the rotor position, shaft based rotor position sensors may be used. These sensors are discussed in Section 3.2, where it is discussed that the sensors are mechanically mounted onto the motor shaft and physically measure the angle of the rotor. The measurement of angle by the position sensors is usually based on optical or electromagnetic sensors. However, the use of position sensors attached to the motor shaft can lead to some disadvantages in practical SR motor drives. These can include lower drive system reliability, higher system expense, additional installation and maintenance costs, an increase in the number of electrical connections, and the need for sensor mounting space.

Therefore, a number of methods have been developed to estimate the position without the use of mechanically mounted position sensors. In this chapter a comprehensive review of the operation of these previously developed position estimation methods will be detailed. In addition, the advantages and disadvantages of each method will be discussed, with particular reference to the application of the schemes to practical SR motor drives.

It will be seen that the previously developed angle estimation methods can be placed into two main groups. These are the *test signal method* group and the *passive waveform monitoring* group. The test signal method group is detailed in Section 3.3.1, where it is seen that low amplitude test signals of various types are used to estimate the rotor position. In Section

3.3.2 the passive waveform monitoring group are also detailed, and it is seen that in these methods only the waveforms associated with the motor excitation are used.

The importance of detailing these angle estimation schemes, is that it is shown that each of these methods have some limitations in providing accurate rotor position measurements over the wide ranging operating speeds and conditions found in SR motor systems. Hence, there is a need for a new sensorless method that does not have any restrictions on operating conditions or control methods, and can be used at all speeds and transient conditions, with a high reliability. Therefore, the following sections provide a background to the development of a new position estimation scheme, which overcomes these problems and provides robust and accurate rotor position measurements over a wide operating region. The new rotor position estimation scheme will be further detailed in subsequent chapters.

3.2 Electro-Mechanical Position Sensors

The need for rotor angle information has been traditionally satisfied by the use of rotor position sensors, which are sometimes called *angle transducers* or *position encoders*. These sensors are attached to the motor shaft and measure the mechanical rotation of the rotor. They provide an electrical signal as an output that provides information about the rotor position. Hence, they are termed here as electro-mechanical position sensors. This measurement of angle by the position sensors is usually based on optical or electromagnetic sensors, or synchros and resolvers, as will now be discussed:

a) Optical Position Sensors

Optical type sensors normally consist of a light emitting diode (LED) which acts as a light transmitter, and a phototransistor to detect light. The sensors are used in combination with a slotted wheel that is placed on the motor shaft. The slotted wheel will either block or pass the emitted light to the phototransistor depending on the shaft position. In this manner the phototransistor will turn on or off depending on the rotor angle. The resolution of optical sensors varies according to the application, however high resolution position sensors are normally expensive.

There are two main types of optical position sensors or encoders. These are termed *incremental* and *absolute* encoders:

Incremental encoders normally use a slotted wheel that contains a number of equally spaced radial lines. The position information is obtained by counting the slots that move past the light detector as the shaft rotates. However these encoders have the problem of the need for a reference position, and unreliability due to missed counts.

Absolute encoders provide a series of uniquely coded positions to overcome the problems of incremental encoders, however they are more expensive. The absolute encoder has a number of different slot patterns on the slotted wheel which are arranged concentrically. For each circular slot pattern there is a light emitter and corresponding sensor, which will output a high or a low electrical signal according to the position of the wheel. For instance, an eight-bit encoder will have eight different slot patterns and eight sensors which are arranged in such a way as to provide a unique pattern at 256 (2^8) equally spaced positions. The pattern of the encoder is usually arranged so that the output from the array of sensors is in Gray Code, Natural Binary, or Binary Coded Decimal. In this way, the output of the sensors can be directly interfaced to a computer controller. Note that as the resolution of the encoder (or number of slot patterns) increases, the expense of the sensor also increases.

b) Electromagnetic Position Sensors

Electromagnetic position sensors operate in a similar manner to optical sensors, except that in these types of sensor the slotted wheel attached to the shaft is usually replaced by a metal toothed wheel, and the light emitter is replaced with an electromagnetic signal emitter. Instead of detecting the variation of light, the sensors detect the change in electromagnetic permeability as the metal teeth pass in front of the sensor. Electromagnetic type sensors have been previously used in commercially developed SR drives (Oulton type). In these developed SR drives, a shaft mounted aluminum slotted toothed wheel was used in conjunction with Radio Frequency (R.F). sensors to provide position feedback. The sensors were encapsulated in a glass filled plastic molding.

c) Synchros and Resolvers

Synchros and resolvers are rotor angle measuring sensors that are attached to the motor shaft, and resemble small ac motors themselves. They use the principle of a rotating transformer to determine position. Synchros have a rotor that contains either one or three windings, and a stator with three star connected windings that are 120 degrees apart. The windings of the rotor are connected to terminals via slip rings and brushes. The rotor position can be determined by applying an ac voltage to the rotor winding. This is because the corresponding voltage induced on any of the stator windings will be proportional to the cosine of the angle between the rotor coil axis and the stator coil axis. Resolvers are a form of synchro in which the stator windings are displaced by 90 degrees to each other instead of 120 degrees. In resolvers also there is a sinusoidal relationship between the stator winding voltages and the rotor angle.

The use of the above mentioned position sensors in SR motor drives has a number of disadvantages. These disadvantages will be discussed below, and are also summarised in Table 3.1.

Table 3.1 Electro-Mechanical Sensor Disadvantages

Electro-Mechanical Shaft Position Sensor Disadvantages
Reliability problems
Expense increases as resolution increases
Additional installation and maintenance costs
Number of electrical connections increase
Size increases

The disadvantages of the electro-mechanical sensors include the following [63]:

a) The position sensors have a tendency to be unreliable due to environmental factors such as dust, high temperature, humidity and vibration.

b) The expense of the sensors rises with the position resolution. Hence if high performance control is required, an expensive high-resolution encoder needs to be employed.

c) There is an additional manufacturing expense and inconvenience due to the sensor installation on the motor shaft. In addition consideration must be given to maintenance of the motor because of the mechanical mounting of the sensors, which also adds to the design time and cost.

d) Mechanical position sensors entail extra electrical connections to the motor. This increases the quantity of electrical wiring between the motor and the motor drive. This wire normally needs to be shielded from electromagnetic noise and thus further adds to the expense of the drive system.

e) The allocation of space for the mounting of the position sensor may be a problem for small sized applications (such as for motors used in consumer products)

Hence, to overcome the problems induced by rotor position transducers, researchers have recently developed a number of methods to eliminate the electro-mechanical sensor for deriving position information. This is achieved by indirectly determining the rotor position. Such methods are commonly termed *sensorless* rotor position estimation methods. The term sensorless seems to imply there are no sensors at all. However there must be some form of sensor used to measure the rotor position. In fact the term sensorless position estimation in reality implies that there are no *additional* sensors required to determine position apart from those which measure the motor electrical parameters to control the motor. These are normally current or voltage measuring circuits.

Hence all sensorless position estimation methods for the SR motor and other electrical machines [64] use some form of processing on electrical waveforms of the motor windings. In essence, the major difference between sensorless position detection, and the electro-mechanical sensors mentioned above, is that there is no mechanical connection of the sensor to the motor shaft. Therefore the sensorless position detection involves electrical measurements only.

3.3 Previous Sensorless Position Estimation Methods

As mentioned in Chapter 2, in the switched reluctance motor, the flux linkage $\psi(\theta,i)$, or inductance $L(\theta,i)$, is a non-linear function of both the stator phase current i, and rotor position θ. Thus, the general principle behind previous sensorless position estimation schemes for the SR motor is that, if one can measure flux linkage or inductance, together with current, then the rotor position may be determined from the magnetisation characteristics. As the switched reluctance motor has a relatively large variation of phase inductance with position, and the mutual inductance between phases is relatively low, the motor lends itself well to these position estimation schemes.

The sensorless position estimation methods that have been proposed are quite diverse, but it is possible for one to divide them into two general groups: Test signals methods and passive waveform monitoring. In the first group, low amplitude test signals of various types are injected into a phase winding when it is unexcited by the power circuit. In the second group, the monitoring of the motor excitation waveforms (such as current, voltage, or flux linkage) occurs, without the use of additional signals in the motor.

In this section, a survey of these previously developed sensorless rotor position detection methods for switched reluctance motors will be discussed. In particular, the advantages and disadvantages of each of the methods will be detailed, with an emphasis on the analysis of the actual use of the developed methods in practical SR motor drives. A summary of the previously proposed methods that will be detailed below, and their various advantages and disadvantages, is shown in Table 3.2.

3.3.1 Test Signal Methods

The position estimation techniques in this first group are those which apply small test signals to the motor phases. These methods operate with phases that are not being used for torque production. This is because when a phase is not being used for torque production, there is no excitation current flowing in that phase. Hence, test signal currents may be used in those phases at that time. Position estimation takes place by analyzing these test signals to determine the phase inductance, which is a function of rotor position.

Table 3.2 A summary of previous sensorless methods

GROUP	METHOD	TASK	BENEFITS	LIMITATIONS
Test Signal	Inject small current pulses, and measure rate of change in current with time.	Determination of incremental inductance from which rotor position is derived.	Good position accuracy, no additional hardware requirements, low negative torque production from test signal.	Interference due to mutual inductance of phases, cannot be used at higher speeds, low position resolution, errors due to finite pulse time.
	Apply small voltage pulse and integrate signal.	Find instantaneous inductance and thus rotor position.	Good position accuracy.	Cannot be used at higher speeds, mutual inductance interference, integration error.
	Measure frequency, phase, or amplitude of small amplitude sinusoidal test signals.	Find inductance of motor phase, and from this, rotor position.	Good position accuracy.	Cannot be used at higher speeds, mutual inductance errors, significant analog circuitry, limited resolution and angle sensitivity.
Passive Waveform	Measure chopping mode current rise or fall time.	Determine incremental inductance from which rotor position is derived.	No additional signal injection circuitry required, immune to mutual inductance errors.	Can only be used to detect small range of angles, restricted to low speeds and chopping mode of control.
	Measure mutually induced voltages.	Rotor position can be found, as it is a function of mutually induced voltage.	No additional signal injection circuitry required.	Controller flexibility limited, only chopping mode current may be used, errors due to magnetic saturation.
	Integrate phase voltage and measure currents.	Flux linkage and thus rotor position is found.	Saturation of motor is modeled, no additional signal injection circuitry required, ability to account for mutual inductance effects.	Large look-up table required.
	Use speed and flux linkage estimation.	Compare predicted and expected flux linkage. The difference will give a value of rotor angle from the stored $\partial\Psi/\partial\theta$ characteristics.	Only one rotor angle magnetisation characteristic is stored.	Only one angle measurement per cycle is available, potentially unstable, errors due to assumptions, need for test signal circuitry at lower speeds.
	Use state observer with measured phase voltages and currents.	State space model of the motor estimates rotor position.	High accuracy and resolution of rotor position.	Restricted to low current levels where motor is unsaturated, computationally expensive.

A common problem with test waveform methods is that there can be significant interference on the small test signals due to magnetic coupling with the torque producing phases. The current flowing in an excited phase may cause significant mutually induced voltages on the other phases, which will corrupt the test signals. However, if the test signal is made larger to overcome this, then significant negative torque production may result (as there will be current flowing in a motor phase in the decreasing inductance region). Another problem is that test pulses have a finite pulse time. This leads to quantisation errors in the rotor position and a limited position resolution.

However the major disadvantage is that these methods can not be used at high speeds. This is because at high speeds current flows over most or all of the electrical cycle in a motor phase and therefore the available testing time is very small or non existent.

In the following sections, the various test signal methods that have been proposed will be discussed in detail, and their benefits as well as disadvantages will be shown:

3.3.1.1 Test Signals with Current Pulses

a) Monitoring Rate of Change of a Commutated Test Current Pulse

The first major work on sensorless position detection for SR motors was carried out by Acarnley et al [65] in a paper where three techniques were proposed. Two of these used test signals on an unexcited winding. These methods are based on the monitoring of the rate of change in current with time of the injected test signals. The basic principle of position detection in these methods involves the fact that the rate of current change is a function of the incremental inductance $l(\theta, i)$ of the phase winding. Thus monitoring the rate of current change of the test signals will provide an estimate of the incremental inductance. This in turn will provide information on the rotor position, in the manner that will be shown below.

The relationship of incremental inductance with rotor position and current can be seen from the following equation, where the incremental inductance is defined as the partial differential of flux linkage with current.

$$l(\theta, i) = \frac{\partial \Psi(\theta, i)}{\partial i} \tag{3.1}$$

The relationship between rate of current change and incremental inductance can be seen by considering the voltage equation for one phase. It was assumed in [65], that the mutual inductances between phases were negligible. Thus, recalling the voltage equation for each SR motor phase (equation 2.2), and ignoring mutual inductance in the motor, the following relationship may be derived:

$$v = Ri + l(\theta, i)\frac{di}{dt} + i\frac{\partial L(\theta, i)}{\partial \theta}\omega \tag{3.2}$$

Rearranging this expression gives the relationship;

$$\frac{di}{dt} = \frac{v - Ri - i\dfrac{\partial L(\theta, i)}{\partial \theta}\omega}{l(\theta, i)} \tag{3.3}$$

The test signal methods in reference [65] are based on this equation with some simplifications. The first test signal method injected a small amplitude chopping mode current waveform in a phase which was not being used for torque production. The test signal current was driven by the main power inverter, with the commutation of the current waveform occurring at a low amplitude in order that the mean test current was a small fraction of the rated current. The current is controlled in such a way that each current

pulse is increased from zero to some low amplitude set level, whereupon it is commutated or chopped, and made to decay to zero again.

Due to the fact that the current peak amplitude was small, the resistive voltage drop Ri and back emf $i.\partial L(\theta,i)/\partial\theta.\omega$ were assumed to be negligible. These assumptions lead equation (3.3) to reduce to:

$$\frac{di}{dt}=\frac{v}{l(\theta,i)} \tag{3.4}$$

The scheme operates by measuring the time that the test current takes to increase from zero to the set maximum test current value. When the rise time of the current is measured, the incremental inductance can be found from the following equation, which follows from equation (3.4)

$$l(\theta,i)=\frac{\Delta t.v}{\Delta i} \tag{3.5}$$

Once $l(\theta,i)$ is found, the rotor position may be found from stored look-up values of incremental inductance versus position. Due to the fact that the magnetisation curves are linear at low current levels in which the test signals operate, the curves can be assumed to be dependent on position only. However this is only true for very low levels of current. If the current is not low then saturation effects occur which causes the incremental inductance to be a function of both current and rotor position.

It should be noted that the test currents are inserted in phases that are not excited. However in SR motors, a phase is normally not excited because it is in the region of inductance variation that would produce negative torque. Therefore, any current that flows into a phase in this region will produce some negative torque component. Hence, the test signals described above will produce a negative torque Nevertheless, the test current level can be set to be small enough that the negative torque resulting is small.

An advantage of this scheme is that no extra hardware is required to produce the test currents. The same circuits used to commutate and control the torque producing current can be used to commutate the low level test current signals also. In addition, due to the low mean level of probing signals, the negative torque resulting is relatively small in this method.

However, this method suffers from difficulties in actual implementation. These practical difficulties are mainly due to the low resolution of angle measurements (due to the limited number of pulses per electrical period), averaging effect (due to finite pulse width), the effect of mutually induced voltages (which corrupts the small level test signals), and the

inability to use the scheme at high speeds (where there is little or no time for testing in each electrical period). These problems will be discussed in detail below. The difficulties due to mutual inductance effects, and the inability to work at high speeds also apply to the other test signal schemes which will be detailed later, and so the discussion of these common difficulties will only be briefly mentioned again in those later sections.

1) Limitation in Sampling Frequency

A disadvantage of the above mentioned scheme, is that the test current pulses must decay to zero before the next sensing current pulse can occur. However, due to the phase inductance, it takes a finite time for the current in the previous pulse to decay. The next rise interval cannot occur until the decaying current has fallen to zero, and hence a physical limitation is placed on the frequency of rotor position estimation (which occurs once per test current pulse in this method). However the problem cannot be solved by using very short test pulses. This is because eddy currents in the motor bring about non linearity in the phase inductance for the first few microseconds following the injection of current [69], which sets a minimum time in which the current must be turned on. The test current pulses should be significantly longer that this time, otherwise the measurements may be invalid. Due to this effect, the sampling resolution of rotor position in this scheme is thus relatively low. At higher speeds this limitation is particularly severe because the change in rotor angle over the pulse width becomes large, and this greatly restricts the number of test pulses per electrical cycle.

2) Averaging Effect

It should also be noted that the finite current pulse, in the commutated current pulse test signal technique, produces an averaging effect. This is because it is assumed that the angle, and thus incremental inductance, is constant over the sampling instant Δt in equation (3.5). However what is really being measured is the average incremental inductance over the sample time. Especially at higher speeds, when there is a larger angle change per unit time, this will lead to an inherent inductance and thus position uncertainty.

3) Magnetic Coupling Between Phases

The test signal methods also have difficulties arising from the fact that the magnetic coupling between the motor phases is ignored. Although it was mentioned previously that mutual inductance effects are normally negligible, this only applies when a phase is used for motoring. In this case the voltages and currents in the motoring phase are normally much higher that the effects produced by mutually induced voltages. However, if a phase is used for angle sensing, with very low amplitude signals, the voltage produced by magnetic coupling between phases becomes significant.

This can be seen by taking the simple case of two phases, where one is carrying torque producing current, and the other is carrying the test current. The voltage equation for the test phase where mutual coupling is considered would be;

$$v_t = \frac{d}{dt}\left(L_t(\theta,\ i_t).i_t + M_{te}(\theta,\ i_e).i_e\right) \tag{3.6}$$

Where:
v_t, = Test phase voltage.
L_t, = Test phase inductance.
i_t = Current of the test phase.
M_{te} = Mutual inductance between the test phase and the torque producing phase. (This is a function of both position and current.)
i_e = Excitation Current of Powering Phase.

Although M_{te} is small compared to L_t, the excitation current in the powering phase i_e is much greater than i_t. Thus, the second mutual inductance term in the above equation can be significant with comparison to the first term (which is the test signal that must be measured). Ignoring the mutual inductance term produces an error in the original equation (3.2), which assumed that the voltages induced by other phases carrying powering current were negligible.

In equation (3.6) it is assumed that only one other phase is conducting current. However if there is more than one powering phase at a given time, then each phase that is carrying current will produce a mutually induced voltage in the phase used for testing. For example, in the case of a four phase SR motor, two phases may simultaneously conduct powering current. Consequently each phase that is conducting current will add another mutually induced voltage term to the above equation.

It has been verified experimentally in reference [66] that the test current waveforms are significantly affected by mutual inductance with driving phases, and that this made absolute rotor position detection difficult. A method for the reduction of the mutual inductance effect has been proposed in reference [67]. It involves using different switching frequencies for both the test signals and the current in the torque producing phase. However this adds a complex switching control scheme to the system and requires sophisticated demodulation techniques [68].

4) Limitations at High Speeds

A major problem with test signal methods is that there must be a *sensing window* (when no excitation current flows) in each electrical cycle, in order that test signals can be injected and position estimation can occur. However, at high speeds, the current waveform of an

energised phase occupies most or all of the phase period. The test signals cannot be applied until the phase is de-energised. This means that the time available for sensing using the test signal method is very restricted or not available at high speeds [59]. This is the major problem with all test signal methods, and limits them to only low speeds in the SR motor.

Improvements to the test signal with commutated current pulses scheme that was described above, were given in reference [69]. The fundamental limitations of the scheme were examined, such as the mutual inductance between phases, eddy currents in the motor laminations, and inverter switching noise. The implementation of the position detection scheme in this reference attempted to minimise the inaccuracies due to those effects. However this imposed limitations on the frequency of the test pulses, and the positions at which testing was possible. Also relatively large test current pulses were used, which generated a relatively significant retarding torque.

b) Monitoring Current Gradient

A similar test pulse current method to that described above is based on the initial gradient of the test current pulses [65]. If we assume that the current is initially zero (before the test current pulse is applied), then the voltage drop across the phase resistance and the back emf may be ignored. This leads to equation (3.3) reducing to a simplified expression for the initial rate of current rise shown below;

$$\left.\frac{di}{dt}\right|_{i=0} = \frac{v}{l(\theta,i)} \tag{3.7}$$

Hence, this method involves turning on the phase that is next in the excitation sequence, and determining the *initial* rate of increase in current (ie when current can be approximated to equal zero as assumed in the above equation). Each current rise gradient will be related to a corresponding incremental inductance and thus rotor position. Thus, if the measured current rise gradient matches the gradient at the position at which switching is desired, then the next phase is excited. However, if the switching position has not been reached, the current rise gradient will not equal that which is desired, and the test voltage is turned off to allow the current to reduce to zero again. The process is repeated until the current gradient reaches the desired value. Note that the actual position is not measured in this method. Only the current gradient is measured and compared with the gradient value at the desired commutation point.

The period of each current pulse is kept small so that the current level is always low, and thus the assumptions of the equation (3.7) will hold. It also means that undesirable torque is minimised, and magnetic saturation is limited which gives a good resolution of

incremental inductance. However the disadvantages of the previous test pulse method that were detailed above, also cause problems with this scheme.

In reference [70] a scheme is proposed which is essentially the same as the method described above. However refinements were made by sampling two phases simultaneously, so that errors due to mutual inductances or switching noise could be detected. However, in this method, the need for two phases to be unexcited at all times placed restrictions on both the speed range and controller flexibility.

3.3.1.2 Calculating Instantaneous Inductance

A test signal scheme was developed in reference [71], in which the position error due to the above mentioned averaging effect of inductance measurement with finite length pulses, is avoided. Instead of determining the inductance as an average value over a timed current pulse period, this scheme calculates the instantaneous inductance at a discrete point in time. This is achieved by applying a voltage pulse to an unexcited phase and then integrating to give the flux linkage. When a prescribed test current level is reached, the flux linkage is sampled at that instant in time. The motor flux linkage and current versus rotor angle characteristic for the prescribed current level is stored, so that the rotor position at the instant the prescribed current is reached can be determined using the sampled flux linkage. Once a measurement takes place the test voltage is removed so that the current decays to zero, upon which the test is repeated.

The pre-set test current level is very small and hence magnetic saturation and unwanted negative torque is minimised. As the current is low, the flux linkage curves will be in the linear region. This means that the variation of flux with angle and current will be relatively high over most angles, except for angles close to the aligned or unaligned positions (Figure 3.1).

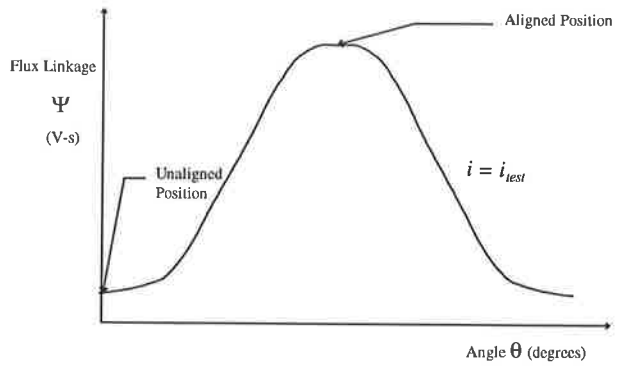


Figure 3.1 Flux linkage for one test current in the linear region

Compensation for errors in this method due to mutual inductance and eddy currents has been reported in [72]. However, offset and measurement errors inherent to the estimation

of flux linkage by the integration of voltage would need to be accounted for. In addition, the method suffers from the same high speed restrictions as the previous test signal techniques, due to injected pulses only being allowed when a phase is unexcited. As the speed increases, the excitation waveform occupies more of the electrical period, and the test pulses occupy a greater angle range. Thus position measurement resolution progressively worsens as the speed increases. It was seen in reference [71] that at medium speeds this method experienced difficulties, and at high speeds the scheme could not be implemented experimentally.

3.3.1.3 Frequency Injection

In the above methods, discrete pulses of current or voltage were used in an unexcited phase winding to determine the inductance value, and thus the rotor position. Other test signal methods have been developed which also determine the inductance of an unexcited motor phase, but. instead of using pulses of current and voltage, they use higher frequency oscillatory signals. These methods make use of the change in amplitude and phase of a high frequency signal that is output from an oscillator connected to an unexcited phase winding, due to the change in inductance of the winding. These frequency injection methods will now be discussed below:

a) Frequency Modulated (FM) Test Signal

In this method, an oscillator is connected to a phase which is not carrying current, in such a way that the oscillator generates a small level signal whose frequency is proportional to the instantaneous inductance of the motor phase [73]. In the scheme, an analog oscillator was implemented using a unity gain differential amplifier. When this circuit was connected to an unexcited phase, it generated a square wave signal with a frequency proportional to the instantaneous inductance of the phase (the proportionality factor is dependant on the circuit parameters). The output signal has frequency $f=k_fL$ where k_f is a factor that is dependent on the chosen circuit resistances.

A frequency to voltage converter was then used to obtain a voltage proportional to frequency, and hence inductance. Since the inductance is related to position, this voltage signal provides rotor position information.

An advantage of this scheme is that only small signal bipolar voltages are applied in order that the saturation effects on the inductance are very low. Thus the inductance is essentially linear and will offer good resolution with variation of rotor position for most angles.

In the previously described test signal methods, mutual inductances are again a problem in this method. The small level test signals are susceptible to corruption from mutually

induced voltages in the unexcited phases that are used for measurement. In reference [73], the FM converter was only used around the minimum inductance region, where it was found that the mutual inductance effects were lowest. However this region has the *least* inductance variation with rotor position. This means that there will be the lowest change in the frequency of the oscillator with position. Therefore, the scheme effectively operates well only in the region of low sensitivity to changes in rotor position, which is a significant disadvantage of the scheme.

In this method, there is also a disadvantage because of the need for significant analog circuitry to implement the FM inductance to frequency encoder, and the FM frequency to voltage decoder. Each phase needs separate analog oscillator and frequency to voltage conversion circuits. In addition, each of these analog circuits introduce their own errors in the position estimation [74]. To obtain accurate results the analog circuitry must have a high bandwidth and very good stability, which further adds to the cost of the system.

As in the other test signal methods, the small window of time available for testing at higher speeds is also a problem. At medium to high speeds, the scheme cannot be used due to little, or no testing time being available, when a phase is not conducting current. However, because of the higher frequency FM test waveform, the resolution of position estimation, when testing can be done, is higher than the current pulse methods previously described above.

b) Phase modulated (PhM) and amplitude modulated (AM) test signals

Other methods of estimating the position using frequency injection methods are the phase modulation (PhM) and amplitude modulation (AM) schemes developed in reference [75]. Essentially these methods are based on the phase or amplitude variation of a sinusoidal small signal test current, due to a change of the motor phase inductance. In these methods, a small signal sinusoidal voltage generator is connected to a phase winding when it is unexcited. This generates a sinusoidal current in the phase winding. As the position of the motor changes, the inductance of the phase winding also changes, which causes the current in the phase winding to change in amplitude and phase (assuming that the voltage from the oscillator is a constant sinusoid). Therefore, the signal changes, due to the varying phase inductance, can be measured, which in turn provides information on the rotor position.

In the PhM scheme, the instantaneous phase angle of the sinusoidal test signal current is measured on a continual basis, whilst the AM scheme measures the peak of the current signal. The phase and amplitude information, of the PhM and AM schemes respectively, are then used to generate the rotor position.

A demodulator is used to convert the phase or amplitude signals to a corresponding inductance value. The demodulation operates correctly when the phase variation and the amplitude of the test current is a one to one function of the motor phase inductance. However, this follows from the required conditions of this scheme, which are:

1. *Constant amplitude sinusoidal voltage test signal:* This is in order that amplitude variations of the current are only due to inductance variation.

2. *Constant frequency of the voltage signal:* This is for two main reasons; firstly the instantaneous phase variation between the voltage and current should not be due to frequency changes. Secondly, the phase inductance itself is a function of frequency also, and only the change in inductance with rotor position is desired.

3. *Low amplitude test signals:* This is in order that the test signal amplitude is small enough that saturation of the phase inductance does not occur.

The demodulated signal, which represents the inductance, is then used to estimate the position using a look-up table.

The reliability of these frequency injection schemes depends on the variation in the phase or amplitude of the current signal with change in phase inductance. If the variation is small (ie. sensitivity to changes is low), then the scheme will be susceptible to errors. It was found in [76] that the PhM scheme was more sensitive for lower values of inductance, whilst the AM scheme was most sensitive for higher inductance values. Therefore, a combination of the two methods was developed and was termed the modified PhM scheme.

However, it has been shown in Reference [77] that the above method, which measures the inductance of the phase from frequency injection, is prone to either low sensitivity to rotor position, or low position resolution, or both. This is because it was found, using experimental investigation, that the variation in the inductance between the maximum and minimum in the SR motor varies with the frequency of the applied test signals. In addition, the inductance variation amplitude (the difference between the maximum and the minimum) was found to decrease with increasing frequency. This occurs due to the effect of the parasitic capacitance of the motor winding at high frequencies. It was found for a typical SR motor that at about 100 kHz there was no variation in the inductance between the maximum and minimum inductance points, and the phase winding behaved as a capacitor. The decreasing inductance effect in fact places a physical limit on the signal frequency of the PhM and AM methods.

Therefore this implies that low frequencies should be used in the PhM or AM schemes. However the resolution of the position estimation also depends on the frequency of the

test signal. This is because the frequency of the test signal determines the rotor position resolution, due to the fact that only one estimate is made per test signal period. Therefore when setting the test signal frequency the angle resolution should be considered. In particular the conditions for the maximum speed of the motor must be considered as this represents the worst case angle resolution for a given test signal frequency. At the maximum speed, the resolution, or the angle between each position estimate, of the position estimation can be found from:

$$\Delta\theta = N \times 6 \times \frac{1}{f} \tag{3.8}$$

Where:

$\Delta\theta$ = angle variation between position samples (degrees)

N = speed of motor (rpm)

f = frequency of test signal (Hz)

Therefore to minimise $\Delta\theta$, the highest possible frequency test signal should be used. However, it was seen in the above discussion that a low test signal frequency should be used to increase the sensitivity of the sensing method. Consequently, it can be seen that that there is a contradiction between position resolution and inductance variation in these frequency injection schemes.

In reference [77] it was found that the PM and AM schemes had both a small inductance variation and relatively low position resolution. In the PM and AM methods described in reference [75], a 5 kHz test signal was used. It was found that this would only result in an inductance amplitude variation of approximately 2.9 to 1 (where 1 represents the minimum inductance amplitude). In addition, the position resolution is approximately 1.8 degrees at 1500 rpm, and 3.6 degrees at 3000 rpm. It would not be possible to increase the position resolution due to the fact that the inductance variation is already low. Therefore high speed operation would not be entirely suitable.

An improved test signal injection method has been described in [77] to overcome the low sensitivity of the PM and AM schemes. This involves adding a capacitor in the oscillator circuit in order to form an R-L-C resonant circuit. The effect of the resonant circuit is to increase the variation in amplitude of the test signal with rotor position, which would increases the accuracy in the measurement of rotor position.

In the method, a 30 kHz test signal was used, which gives a much higher position resolution than the previously mentioned PhM and AM schemes (which used 5 kHz). However, due to the resonance of the R-L-C circuit the variation of the signal is also

higher than the previous scheme. For a 30 kHz signal the signal variation from minimum to maximum was 6.8 as compared to 2.3 if no resonant capacitor circuit is used.

As in the previous test signal methods, the main disadvantage of this scheme is the limitations at higher speeds. At high speeds there will be only a very small, or no time when a phase is not conducting current. Therefore these methods will become difficult to use. Another problem is large errors in the small amplitude injected test signals due to mutual inductance effects, in addition to the need for significant analog circuitry.

3.3.2 Passive Waveform Monitoring

The second main group of sensorless position detection methods are defined as the non-intrusive types, due to the fact that they do not inject any additional signals to the motor. They instead perform calculations on the phase current and voltage waveforms already applied to the motor for torque production. As no test signals are injected in these methods, they do not require additional test signal circuitry. They are also immune to the mutual inductance effects, and limitations at higher speeds of the small test signal methods.

However, some methods in the second group suffer from errors due to the motor back emf and saturation, as well as placing restrictions on the motor control method. Others place limitations on operating conditions, or have restricted application, due to assumptions made in formulating the scheme. The details of the various passive waveform monitoring methods and their advantages and disadvantages will be described below.

3.3.2.1 Monitoring Chopping Mode Current Waveform

In reference [65], a passive waveform technique was described, which monitored the torque producing current during chopping mode operation. In this method the motor phase current was controlled in the chopping mode such that it had a mean value of current I_{mean} and a hysteresis band around the mean of $I_{mean} \pm \Delta i/2$ (ie. a total current variation of Δi in the chopping mode).

If it is assumed that v is much greater than the resistive voltage drop Ri, and also much greater than the back emf, then the time between two commutation switching points of the phase current can be derived as:

$$\Delta t = \frac{l(\theta, i)\Delta i}{v} \tag{3.9}$$

This simplified equation is used in this position detection scheme. It operates by measuring the time Δt in which the chopping current waveform takes to rise or fall by the

hysteresis level Δi, as can be seen in the diagram of Figure 3.2. The incremental inductance can then be deduced from equation (3.9) using the measured time variation between commutations Δt and the known hysteresis current variation Δi.

Once the incremental inductance is found, the rotor position can be determined from the stored characteristics of inductance for the chopping current level I_{mean}. Note that this will lead to some error because in the current is not constant at the value I_{mean} nor is the angle constant over the interval Δt. However the angle found from the stored inductance characteristics assumes both of these are constant during the measuring interval.

To use this method, either the chopping rise time Δt_{rise} or the decay time Δt_{decay} could be monitored.

A disadvantage in this scheme is that the current being monitored is high enough for saturation to occur. The incremental inductance characteristic will thus show a double peaked characteristic around the misaligned position as shown in Figure 3.3. This is due to the lowering flux versus current gradient close to the aligned position when saturation occurs. Therefore, around the unaligned angle there will be four rotor positions corresponding to each value of incremental inductance, and position estimation using the incremental inductance becomes very difficult. Due to this effect, the method was not recommended for continuous rotor position sensing. Instead only the fully aligned position is detected, when the saturation is at a minimum.

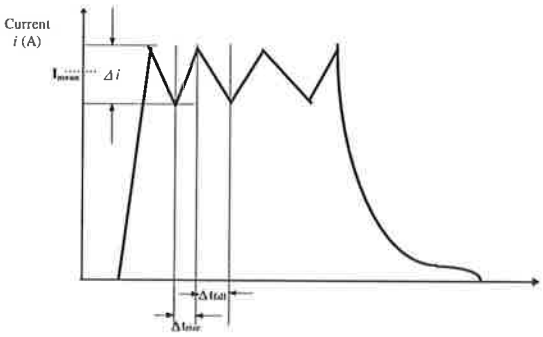


Figure 3.2 Measuring rise and fall time of chopping mode current

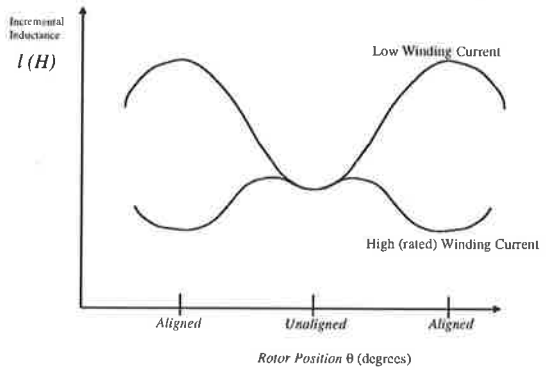


Figure 3.3 Double peaked incremental inductance for high phase current

Another problem with the method is that it is restricted to low speeds. This is because of two main reasons. Firstly, at medium to high speeds the back emf increases in value, and at high speeds can even equal the dc supply value. This causes inaccuracy in the position detection, due to the assumption in equation (3.9) that the back emf is zero. Secondly, at high speeds the chopping mode is unavailable, and thus at these speeds the scheme cannot be implemented, due to the fact that it depends on chopping mode current control.

This method was analyzed in detail theoretically and experimentally in references [78], [79] and [80], where the effect of back EMF and saturation was closely examined. It was found that due to these effects the rotor position could only be found a few degrees around the aligned position. This means that serious restrictions are placed on the control scheme if one uses the above method.

3.3.2.2 Measurement of Mutually Induced Voltages

Another proposed method of rotor position sensing is based on the measurement of the mutually induced voltage in an unexcited phase, due to currents in any torque producing phases. As stated above, in any SR motor there is some mutually induced voltages in an unexcited phase because of the mutual magnetic coupling between the phases.

If there are q motor phases, then the general expression for voltage v_m in a given phase m which takes into account mutual inductance is given by:

$$v_m = \sum_{n=1}^{k} \frac{d\psi_{mn}(\theta,\ i_n)}{dt} \tag{3.10}$$

Where:

ψ_{mn} is the flux linking the phase m with phase n due to current in the $n'th$ phase.

The mutually induced voltage contains rotor position information because it varies with change in rotor angle. Its' variation is due to the fact that both self and mutual inductances are functions of rotor position. As a result, detection of mutually induced voltages can provide rotor angle measurements.

In reference [81] a position detection scheme which measures mutually induced voltages was implemented for a 1hp four phase SR motor running off a 14V supply. However, it was assumed in the scheme that only one phase is conducting current at any one time. The scheme operates by measuring the mutually induced voltage in a non-conducting phase. In the non-conducting phase, the mutually induced voltage v_{m1} due to current i_2 in a torque producing phase which is conducting current will be given by:

$$v_m = \frac{d\psi_m}{dt} \tag{3.11}$$

Where

ψ_m = Mutual flux linkage

In reference [81] it is assumed that the mutually induced flux linkage can be described as a function of mutual inductance and current, and the mutual inductance is only a function of rotor position:

$$\psi_m = M(\theta) i_2 \tag{3.12}$$

Where:

$M(\theta)$ = Mutual inductance.

i_2 = Current in torque producing phase.

It is also assumed in this method that the current in the torque producing phase is kept constant using chopping mode control. Therefore it is assumed that the current i_2 in the above equation is equal to a constant current level, I_0. This constant current level is set to the center of the chopping mode current hysteresis band of the torque producing phase current, i_2.

Assuming that the instantaneous current in the torque producing phase is constant and also that the phase inductance is linear and only a function of position, the mutually induced voltage can be derived as

$$v_m = \frac{M(\theta)}{L(\theta)} V_2 - \frac{M(\theta)}{L(\theta)} \cdot \frac{dL(\theta)}{d\theta} \cdot \omega - I_0 R \frac{M(\theta)}{L(\theta)} + I_0 \frac{dM(\theta)}{d\theta} \cdot \omega \tag{3.13}$$

It can be seen from equation (3.13) that the mutually induced voltage is a function of the mutual inductance, which is in turn a function of position, and thus it can provide position information. Hence, to determine the rotor position in this scheme, the mutually induced voltage in an unexcited phase is measured during the motor operation. This voltage is then used to determine the position from a look-up table of values, where the rotor angle versus mutually induced voltages at constant current is stored. However, in constructing the look-up table it is assumed in this scheme that the speed dependent terms of equation (3.13) are negligible.

This scheme has many limitations which limit its implementation in actual SR motors. These limitations derive from the following reasons:

a) It is assumed in this scheme that the current in the torque producing phase is constant. Therefore the current must be maintained in a hysteresis band using chopping mode control. Consequently the scheme cannot be used at medium or high speeds when chopping mode current control is not available.

b) The scheme assumes that the inductances in the motor are linear (ie. no magnetic saturation occurs) and therefore only depend on rotor position. As it has been discussed, the phase inductance of SR motors is highly non-linear, and a function of both current and position. In addition, it has been demonstrated that the mutual inductance is also non-linear and is a function of current [82], [83]. The mutual inductance in particular suffers from saturation in the iron core of the motor. Therefore the assumption that self and mutual inductances are non-saturable and only a function of position may lead to flawed position estimates in actual SR motors.

c) It is assumed in this scheme that the mutually induced voltage has no dependence on speed (the speed dependent terms in equation (3.13) are assumed to be zero). However this would only be roughly true at low speeds. At medium and high speeds the speed dependent terms will be significant and thus this method is impractical at medium and higher speeds.

3.3.2.3 Using Flux Linkage

a) Using the Non-Linear Flux Linkage versus Current and Angle Characteristics

Sensorless position detection methods have been developed which measure the phase currents and voltages, and estimate the flux linkage of the motor phases from these measurements. The rotor position may be determined from the estimate of flux linkage $\psi(\theta,i)$ if, at the same time, current is known.

A technique that uses the relationship between flux linkage and current to estimate rotor position is described in reference [84]. When a motor phase is energised, the current and voltage is continuously sampled. The flux linkage is then estimated by integration of the phase voltage as shown in the equation below:

$$\Psi = \int (v - iR)dt \tag{3.14}$$

The estimation of flux linkage using this method is particularly effective in the SR motor. This is because the flux returns to zero at the end of each electrical cycle, and hence the integrator can be reset to zero once per cycle. This prevents the accumulation of integration errors and offset.

In this scheme, the estimated flux linkage and corresponding current are utilised to find the rotor position by using the measured magnetisation characteristics of the motor. As was described in Chapter 2, these curves describe the relationship between flux linkage, current, and position. Therefore, angle can be found by looking up the magnetisation curves using the values of flux linkage and current.

The magnetisation curves are stored in the form of a look-up table, and thus a disadvantage of this method is that a large amount of data must be stored. If there are not enough points of data then interpolation must be used. Additionally the magnetisation curves are measured for one phase, and assume that there is no mutual magnetisation effects between phases.

However in reference [84] the mutual inductance effects were also considered, and methods for their correction were suggested. One method made use of a multi-dimensional look-up table with constant mutual inductance coefficients. Also suggested was a lumped parameter reluctance network model of the motor. In this model, the variations of mutual inductance with rotor angle is taken into account. However this model is very complex, and needs finite element modelling or extensive measurements and tests performed on the motor. Due to its very high complexity the corresponding position estimator is computationally expensive.

This flux linkage based method of sensorless position estimation has been implemented in a practical system, however due to the high complexity in these methods the mutual inductance effects were ignored (ie the correction methods were not implemented). The flux linkage based sensorless scheme has been reported for use in a 270 V fuel lube motor drive which provides adjustable speed control of a hydromechanical pump module that is mounted on a gas turbine [85]. Another application reported that uses this flux linkage based sensorless method is for a high speed generator driven by a gas turbine. In this application the motor speed is between 27000 and 46000 rpm and the power output is 30 kW [86].

Therefore, it seems that this scheme can be used in high speed industrial applications. However a number of improvements should be made to this scheme. A major item that must be considered is the robustness and performance of the scheme under the influence of noise and errors. This is because the system depends on the accuracy of the measurements of current and voltage. Inaccurate measurements affect the accuracy of the flux linkage estimate found from equation (3.14), as well as the accuracy of the current value, both of which are used as look-up values in the look-up table. The look-up table will produce an erroneous value if the look-up values are in error, and therefore accurate measurements must be taken. However, most practical motor drive systems are affected by electromagnetic noise, which leads to measurement noise and error.

Another improvement of the scheme would be to take into account the mutual inductances of the motor without the highly complex model proposed in reference [84], which is not practical for real time position sensorless operation. A further improvement would be to reduce the size of memory required by the sensorless scheme's numerical look-up table, whilst still retaining the non linear characteristics of the motor.

b) Using Flux Linkage and Speed Prediction

Another flux linkage based method uses integration to obtain flux linkage, but only attempts to measure a single reference rotor position θ_{ref} [87]. Therefore this can only be used with simple control schemes. In addition, the scheme does not take into account the mutual inductances.

The method predicts an instant in time from speed estimates (derived from previous angle estimates), when the rotor will reach the reference position θ_{ref}. The current is then measured at this predicted instant of time, and the flux linkage is estimated by integration. A stored table of $\partial\Psi/\partial\theta$ versus current measured at the reference rotor position θ_{ref} is utilised to estimate the actual rotor position, from the difference between the measured flux linkage and the expected flux linkage (ie the flux linkage if the predicted time was correct and the actual rotor angle was equal to θ_{ref}). In effect, the error in flux linkage between that expected and that measured is used to estimate the difference in the angle between the expected angle θ_{ref} and the actual measured angle, by using the $\partial\Psi/\partial\theta$ curve.

However the table of $\partial\Psi/\partial\theta$ values is only valid for small variations about θ_{ref}. Therefore if the actual measured rotor angle is outside of a small band of values around the expected value θ_{ref}, then the system will become highly unstable. In addition, the speed estimate is derived from the estimated position. Therefore if the system becomes unstable then any errors in the position can rapidly increase every cycle.

In addition, this method assumes that the flux linkage error is solely due to the difference between the actual angle and θ_{ref}. However from the above discussion it is known that the flux linkage estimation can suffer from measurement and offset errors.

Errors may also result because the method ignores the Ri drop in the flux linkage equation (3.14), and assumes that the phase voltage is equal to the dc supply voltage. Due to these errors, the authors use an injected diagnostic single pulse current in an unexcited phase during the chopping mode. However this results in the problems associated with small test signals already described.

3.3.2.4 Observer Based Methods

Various sensorless position detection schemes have been introduced which are based on mathematical *observer* techniques. In these techniques, which are based on state space control theory, a mathematical model of the SR motor is used. The term *observer* is normally used to describe a state space mathematical model, or *state estimator*, of a physical system which estimates the physical systems output using the system's inputs [88], [89].

Feedback control is used to correct the error between the estimator and actual system's outputs (ie. to improve estimation accuracy), and to define the error correction dynamics.

In the previously developed observer based SR motor position estimation schemes, the software based estimator model is run parallel with the physical motor. The motor voltage is used as an input to the estimator model, and the motor model is used to estimate the currents and rotor position of the actual motor. If the estimator model currents are the same as the actual motor currents then it is assumed that the model of the estimator is correct. Therefore, if the model is correct, the rotor angle estimated by the model should be equal to the real rotor angle.

In these methods, the rotor angle is set up as an estimated state variable of the observer. The observer will contain internal feedback adjustable gains. These are normally adjusted according to the error between the estimated phase current, and the actual current which is measured.

A sophisticated method of continuous rotor position estimation has been developed in reference [90] using the state observer method. In this scheme, a mathematical state space model estimator of the motor was used, where voltage was considered to be the input to the state space model, and current the output. The model had the same voltage inputs as the physical motor. The difference between the model output currents and the physical motor measured output currents were used to force the estimated state variables to converge. This was achieved by using the error to adjust the feedback or *innovation gains*. The gains are adjusted in such a way that the errors between the modeled motor and the physical motor are minimised. The observer was also mathematically proven to be stable under certain conditions. A block diagram describing the topology of the state space observer is shown in Figure 3.4.

Reference [90] provides experimental results using the method with a 68000 microprocessor based processing unit for the calculations. The experiment was based on the assumptions of constant velocity, a load of constant inertia, linear magnetic characteristics, no variations in motor resistance, and no mutual inductance effects.

The assumption of constant velocity was justified in the scheme by the use of a very large rotor inertia. However under normal operating conditions of the motor this would not be realistic. It essentially means that the model would not be able to cope with speed changes during normal transient operation of an SR motor.

In addition, the assumption of magnetic linearity is a major disadvantage in this scheme. The SR motor normally operates under saturation of the magnetic circuit to maintain high efficiency. This means that errors in the model, and thus position estimation, occur during normal motor operation. This is the major constraint in present model based schemes. The

model must be kept linear to make the computations feasible, however this means that the model is inaccurate for most SR motor drives.

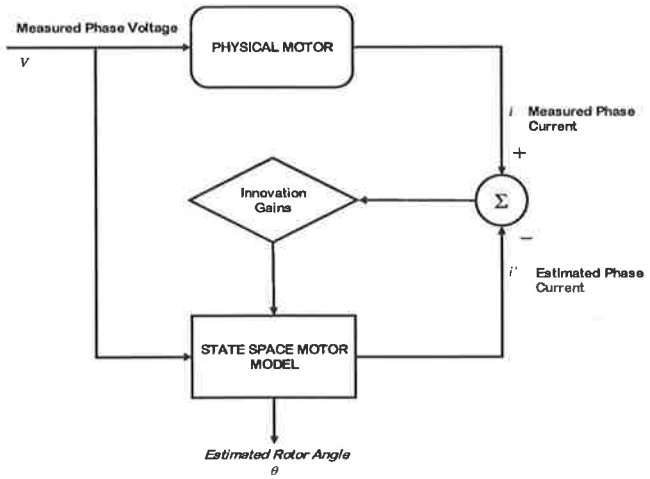


Figure 3.4 State Space Model Observer for SR motor

Improvements in the observer were suggested in [90] to take into account the non-linear magnetic characteristics of the SR motor, and also to adaptively follow alterations in resistance and load. However, due to a high complexity these were not implemented. It can be stated that the addition of these extensions would require a great increase in computation to the method, which in its present state already requires a fast powerful processor to do a large amount of complex real time computations.

An improvement of the discussed observer method was developed in reference [91]. In this method, the observer was extended to operate under transient changes in load and speed. To achieve this, a Reduced-Order Extended Luenberger non-linear observer for joint state and parameter estimation was used. Accurate results were given for experimental conditions where a 32 bit DSP implements the observer. The drive performed well under step changes in load torque.

However, this method ignored magnetic saturation effects, and stated that the motor needed to be operated only in the linear region. As stated above, under normal operating conditions the SR motor will be in the saturation region. Therefore this method implies a high restriction on current levels and performance conditions for most SR motor drives.

An alternative observer based sensorless position detection method which uses *sliding mode observers* has also been presented [92]. Sliding mode observers are based on sliding mode control theory [93]. The basic principle of sliding mode control is to force the state of a plant to "slide" on a chosen surface in the state space that is known as a sliding surface. In sliding mode control the sliding surface is defined so that the tracking error between the desired and actual state variable is zero. However, when designing sliding mode observers, rather than controllers, the problem changes due to the fact that not all states are

measurable. Sliding mode observers are designed instead by defining the *sliding surface* to be that when the state estimation goes to zero.

Simulation results were shown for this sliding mode observer where the observer estimated the rotor position and speed. In actual practical operation however, the operation of this scheme may be difficult. This is because a problem with the scheme is the simplifying assumptions made in formulating the model. The sliding mode method presented assumes that the inductance variation of the motor is linear. In particular, the sliding mode observer error convergence conditions (for the rotor position estimate error to converge to zero) assume that before alignment the inductance will *constantly increase*, and after alignment will *constantly decrease*. However, as has been stated, the SR motor normally operates in saturation. Under saturation, the inductance may rise or fall at any position depending on the phase current, as illustrated in Figure 3.5. This will mean that the error convergence conditions will not be correct for all SR motor conditions.

Therefore, the assumptions in this scheme will restrict the motor to low current levels when little saturation of the inductance occurs. Only if there is no saturation does the assumption of constantly increasing inductance before the aligned position, and constantly decreasing inductance after the aligned position, generally hold. This means that the scheme can only be guaranteed to operate under relatively limited conditions.

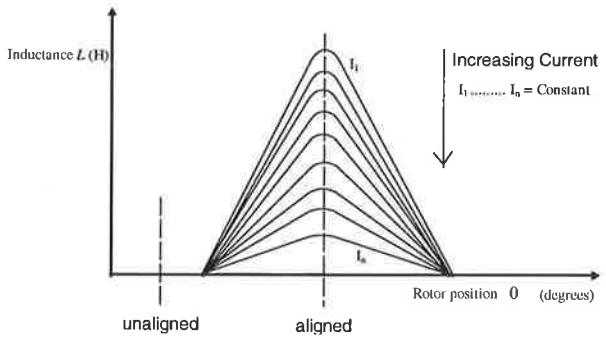


Figure 3.5 Inductance versus rotor position illustrating saturation effect as current increases

Hence although this and the other observer schemes discussed above use sophisticated techniques, they suffer from the high complexity of classical state space methods. Due to the high complexity of the models, the methods above ignore the non linear saturation of the motor inductance. This is in order to make the schemes less complex and more practical to implement. This entails that the schemes can not be used under normal motor conditions when saturation of the magnetic circuit occurs.

3.4 Conclusion.

It can be seen from the above discussion that research into techniques for the sensorless detection of rotor position in the switched reluctance motor is active and widespread. A comprehensive review of existing methods was discussed in this chapter. It was emphasised that accurate knowledge of the rotor position is required for good performance of the motor. Observations were also made about the disadvantages in the use of direct position sensors. Following this, an exposition of various sensorless position measurement methods were given.

It was seen that test waveform methods used low amplitude test signals in unexcited phases to determine the phase inductance, and thus position. A problem with these methods was that they suffered from interference caused by mutual magnetic coupling with excited phases. The mutual coupling between phases produces mutually induced voltages that can corrupt the small amplitude test signals. Test pulses also have inherent averaging errors due to the finite pulse time. However the main disadvantage with the test signal methods is that they can not be used at higher speeds. This is because there is little or no time at high speeds when the motor phases are unexcited, and thus the available testing time is very small at these speeds.

Another major group of position detection schemes were those which passively monitored the motor waveforms. It was seen that passive waveform monitoring techniques do not inject any extra signals into the motor, and thus do not suffer from the problems of the test signal methods. One method was described which monitored the chopping mode waveform. Another method was detailed in which position estimation was extracted from mutually induced voltages. Other schemes were discussed in which the flux linkage was estimated using the measured values of voltage and current. This estimated flux linkage could then be used to determine position. Observer based methods were also described, and it was seen that these methods used a motor model or estimation scheme to determine rotor position.

However the passive waveform methods have various drawbacks for actual SR motor drive applications. The method which monitored chopping mode waveforms suffered from errors due to inductance saturation and motor back emf. It could only be used in the chopping mode operation at low speed. The method which measures mutual inductance had errors due to motor inductance saturation, and restricted the motor to low speeds, and chopping mode control with only one phase conducting at a time. The flux linkage based methods do not impose restrictions on the motor control or assume magnetic linearity of the motor, and are therefore the most practical of the methods. However the flux linkage methods have a high dependence on the accuracy of the measured voltage and current, and require a large look-up table for good accuracy. The observer based methods were

impractical for most applications due to their requirement of magnetic linearity in the SR motor.

In order to address the problems found in the previously developed angle estimation schemes, a new rotor position estimator was developed. The novel sensorless estimation method developed in this research does not have restrictions seen in previous schemes, as it can be used under all operating speeds and conditions, including speed and torque transients, standstill, and start-up. In the new method, no external testing circuitry or test signals are placed on the motor phase windings. The new scheme also addresses the issue of robustness and reliability in practical SR drive operation. In the following chapters, the novel sensorless rotor position estimation scheme will be introduced, and the means by which it overcomes the problems found in previous schemes will be detailed.

Chapter 4: A New Rotor Position Estimation Scheme: Introduction and Training Phase

4.1 Introduction

The SR motor drive was discussed in previous chapters, and it was seen that the drive controller switches the current to a motor phase on and off in synchronism with certain rotor positions. It is therefore essential for the controller to have rotor position feedback from the motor. In Chapter 3, methods of obtaining rotor position feedback were discussed. Position sensors attached to the motor shaft, were seen to be one method of obtaining rotor position. However, it was seen that in many systems rotor position sensors attached to the shaft have disadvantages, and are thus undesirable.

Therefore, a number of sensorless rotor position estimation methods, which have been proposed by researchers to overcome the disadvantages induced by position sensors, were also discussed. However, these methods had limitations, such as inability to operate at medium to high speeds, interference on test signals, or restrictions on the motor operating conditions and control.

In addition, no previous sensorless scheme has been specifically formulated to have a high robustness and reliability against non ideal noise and errors which are commonly found in practical drives.

In this chapter, a new fuzzy logic based rotor position detection technique for SR motor drives is introduced which addresses the problems of the previous sensorless schemes. The scheme may be used under all motor operating conditions including transients, standstill, and start-up. An important feature is that the motor's inherent saturation effects and real time non-ideal characteristics are not ignored. However, at the same time no mathematical model is required. The system also incorporates techniques to overcome measurement errors and inaccuracies and has a high robustness and reliability in practical SR drives.

To provide a theoretical basis for the new rotor position estimation scheme, the basic ideas and issues of fuzzy logic will discussed, beginning with the general introduction to fuzzy logic in Section 4.2. In this section, the features of using fuzzy logic will be explained, such as an ability to model and control indeterminate and non-linear systems without complex or elaborate calculations. The concept of *fuzzy sets* will be discussed, and the differences between classical set theory and fuzzy set theory will be detailed. In addition, the mathematical operators that are used with fuzzy sets will be explained.

The use of these fuzzy sets in *fuzzy relations*, which map an input to an output, will also be explained. Initially, the concept of *fuzzy implication functions* and their interpretation will be

detailed. Then, methods of solving *fuzzy relational equations* using these implication functions will be given. In particular, the two main solution methods that can be used in the new position detection scheme will be defined. These are the *Max-Min* and *Max-Product* methods. In the new position detection scheme that will be described, the inputs are numeric measured values. Hence, the method of using numeric, or crisp, values in the fuzzy relational equations will also be detailed in this section.

The discussion of fuzzy logic theory provides basis for the introduction of the new rotor position detection scheme in Section 4.3. In this section, details of the algorithm will be given and it will be seen that there are two phases for the algorithm. These are the training phase, and the operational phase. In this chapter, the training phase of the new sensorless position detection scheme will be detailed, and the following chapter will detail the operational phase of the scheme.

In Section 4.4, the training phase of the sensorless position detection algorithm is discussed, where it is shown that this phase involves the development of a fuzzy logic based SR motor model. The details of the training algorithm are detailed, and it is seen that training takes place with the input of measured motor flux linkage, current, and rotor position data from the motor. This data is used to create a fuzzy rule base that models the non-linear SR motor. Details of how the model is formed will be given, and the *table look-up scheme* of creating a fuzzy rule base will be explained. It will be seen that two sets of data are used by the training scheme: Firstly, data from the *static* flux linkage curves are used, followed by measurement data of the motor waveforms from *dynamic* real time motor operation tests.

The software implementation details of the training algorithm used to develop the fuzzy logic based motor model will also be given. The training algorithm is implemented in C, and the main subroutines of the program are described. The results of the motor model which is developed by the training algorithm using the static motor data and the dynamic real time test data will also be shown. It will be seen that there is a difference in the motor model generated using the dynamic real time operation test data.

4.2 Introduction to Fuzzy Logic Systems

The concept of *fuzzy sets* was first introduced in a paper by Zadeh over thirty years ago [94]. Since then, after great academic debate [95], *fuzzy logic* has emerged as a serious field of its own and in addition, in the past few years, a large number of research papers have dealt with the topic of fuzzy systems applied to the fields of power electronics and motor drives [96]. Fuzzy logic has the capability to identify, model, and control non-linear or uncertain systems, even in the case where no mathematical model is known. The subject's vitality has been seen in the high amount of research and development in the field.

A unique feature of fuzzy logic is that it provides a systematic framework for incorporating linguistic information [97], [98]. In fact, it has been stated by Zadeh that the main contribution of fuzzy logic is a methodology for computing with words [99]. This allows the ability to use linguistic information about a system provided by human experts. Conventional engineering approaches cannot make use of this knowledge. However, a great deal of human knowledge is linguistic and thus it is very important to incorporate this knowledge into any machine system in a systematic manner. Language is also very important when the available information about a system is too imprecise to justify the use of numbers. In these cases, linguistic information may be the only information, and fuzzy logic can use this in an engineering manner.

Applications of fuzzy set theory, and in particular fuzzy control, have also accelerated rapidly over the past few years. The fields that fuzzy logic has been successfully applied in are wide ranging. A few of these areas have included power electronics, electric drives, industrial process control, automotive engineering, transportation, aerospace, bioengineering, and consumer products. Table 1 illustrates a sample of the range of applications of fuzzy logic that have entered the market from industry [100]. Although the areas of application of fuzzy logic seem to be very diverse, the applications have one common factor in which fuzzy logic provides a role. The common factor is that these are all processes that are non-linear, time varying, complex, or model free in nature. Fuzzy logic is well placed to handle these types of systems. It is often used in systems when classical methods, although theoretically possible, are practically impossible, due to the fact that a mathematical model for the system cannot be found, or is too difficult to be found due to time or cost constraints.

Table 4.1 Some Applications of Fuzzy Logic

Automotive and Power Generation	**Industrial Process Control**	**Robotics and Manufacturing**	**Consumer Products**
Power train and transmission control (General Motors, Honda, Mazda)	Cement Kiln, incineration plant (K. L. Smith, Denmark)	Electric discharge machine (Mitsubishi)	Air Conditioner (Mitsubishi Electric)
Automatic Train Control (Hitachi)	Refining, distillation, and other chemical processes	DASA (German Aerospace Corporation) – POLIS robot system	Cameras and Camcorders (Canon, Minolta, Richoh, Sanyo)
Engine Control (Nissan)	Industrial Sensors, (Endress & Hauser, Germany)	Microcontroller (Motorola)	Television (Mitsubishi Electric)

A particular interest has been shown recently in using fuzzy logic for the control of electric machines. This is partly because of the wide use of variable speed drives in motion control systems. To successfully control these drives using conventional methods, one needs knowledge of some of the motor parameters. However, the motor parameters usually vary

during operation, and therefore it is difficult to predict them accurately. In addition, the motor may behave non linearly, and changes in load torque, friction and inertia may affect the system behavior. Therefore, these systems can be complex and non-linear and time varying, and therefore fuzzy logic can be employed as a control methodology. Hence, recently, there has been a large number of fuzzy logic based research projects on the control of dc machines [101], [102], inverter fed induction motors [103], [104], [105], permanent magnet brushless dc drives [106], and the high performance control of switched reluctance motors [107], [108], [109].

The capability of fuzzy logic to handle non linear and model free systems as seen in the applications discussed above, is also made use of in the developed sensorless rotor position estimation scheme of the SR motor. It will be seen below that fuzzy logic allows the non-linear motor characteristics to be modeled without requiring a complex mathematical description of the motor. This is because fuzzy models are universal approximators of any continuous function. As a complex mathematical model is not used, the developed motor model is well suited for practical real time applications of rotor position estimation, because only simple computations are required. In addition it will be shown that fuzzy logic based methods provide a high level of robustness and reliability and thus are well suited to SR motor drive environments. To provide a detailed explanation of the novel fuzzy logic based rotor position estimation scheme, the concept of fuzzy sets is firstly discussed below.

4.2.1 Fuzzy Sets and Classical Sets

As it was stated previously, in fuzzy logic, variables have values that are based on linguistic expressions. These linguistic expressions are characterised by *fuzzy sets*. These differ from traditional or *crisp* sets in one important manner: A crisp set only allows full membership, or no membership at all. In other words if one asks the question whether an object belongs to a certain set, the answer can only be *true* or *false*. However, membership of a fuzzy set can be partial. In fact the transition between membership and non-membership is gradual and varies between 0 and 100 per cent. This means that an object can partially belong to a fuzzy set, and membership in a fuzzy set can be *true* and *false* at the same time.

To define a fuzzy set firstly let U be a collection of objects where $U = R^n$ is called the universe of discourse. A fuzzy set F in U is defined by some membership function $\mu_F : U \rightarrow [0,1]$. That is, the fuzzy set is a mapping from the domain of definition onto the interval [0,1]. This mapping is called the *membership* function $\mu_F(u)$ and represents the grade of membership for some $u \in U$ in the fuzzy set F.

It should be noted here that the fuzzy set F is different from a classical set. A classical (crisp) set has a membership function that only has two values [0,1]. However, the fuzzy set has a membership function that takes on the value of zero for no membership and one for full membership, but can take on any value in between the range [0,1]. Another difference between fuzzy sets and classical sets is that a variable may be a member of a set and its complement at the same time. For example u may be in the set A and $\overline{A}$ simultaneously, which is impossible under classical set theory

As an example of the above definitions, consider three fuzzy sets which describe an SR motor's phase current as shown in Figure 4.1. These fuzzy sets are *low*, *medium*, and *high*. In this case, the universe of discourse is all possible motor currents. Note that each set is defined via its corresponding membership function μ_i. At a motor current of 18 amperes, for example, the fuzzy set low has a membership of 0.2, whilst the fuzzy set medium has a membership function of 0.6.

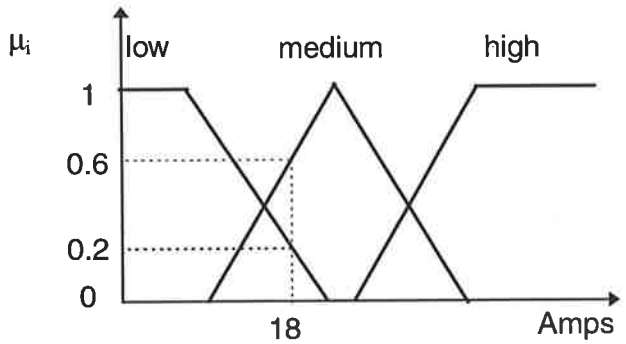


Figure 4.1 Membership functions of three fuzzy sets.

The *intersection*, *union*, and *complement* of a fuzzy set are all important operations which will be used extensively in the development and implementation of the rotor position estimation scheme, and therefore require more detailed explanations.

Let A and B be two fuzzy sets in U, with membership functions μ_A and μ_B respectively. The above operations can then be described as:

Union: The membership function $\mu_{A\cup B}$ of the union $(A \cup B)$ of sets A and B, is given by a fuzzy set in U that has membership function:

$$\mu_{A\cup B} = \max\{\mu_A(u), \mu_B(u)\} \tag{4.1}$$

Where:

$\mu_{A\cup B}$ = the membership function of the union $(A \cup B)$ of sets A and B in domain U
$\mu_A(u)$ = the membership function of the fuzzy set A domain U
$\mu_B(u)$ = the membership function of the fuzzy set B in domain U
max = the maximum function which is the maximum of the fuzzy sets A and B

Intersection: The intersection A∩B of sets A and B is a fuzzy set in U that has membership defined as:

$$\mu_{A\cap B} = \min\{\mu_A(u), \mu_B(u)\} \tag{4.2}$$

Where:

$\mu_{A\cap B}$ = the membership function of the intersection $(A\cap B)$ of sets A and B in domain U
min = the minimum function which is the minimum of the fuzzy sets A and B

Complement: The complement $\overline{A}$ of set A is a fuzzy set in U that has membership function defined as:

$$\mu_{\overline{A}}(u) = 1 - \mu_A(u) \tag{4.3}$$

A major use of the fuzzy sets and operations described above, is to carry out the mathematical procedure for what is generally termed *fuzzy logic reasoning* which processes input data using fuzzy logic to produce a logical output. This reasoning methodology is used extensively in the position detection scheme that will be detailed in later sections. In addition, due to their importance in the position estimation scheme, other concepts required in the fuzzy logic reasoning will be discussed. These concepts include *fuzzy relations*, *fuzzy implication functions*, *compositions of fuzzy relations*, *aggregation of rules*, and *defuzzification.*

4.2.2 Fuzzy Logic Reasoning Concepts

(i) Fuzzy Relation

If U and V are two universes of discourse, then a fuzzy relation R can be defined which maps from U to V. This fuzzy relation is defined by the function $\mu_R(u,v)$ which is a fuzzy set in the space $U\times V$ that is characterised by the membership function:

$$\mu_R : U \times V \rightarrow [0,1] \tag{4.4}$$

(ii) Fuzzy Implication Functions

The fuzzy relation described above, which maps one universes of discourse to another, is used in fuzzy implication functions to infer a logical output from input data using fuzzy reasoning. In this case the two universes are the input space and the output space. In other

words, the fuzzy relation maps the premise space to the consequence space. In fuzzy logic reasoning, there are two important fuzzy implication inference rules. These are the generalised modus ponens (GMP) and the generalised modus tollens (GMT). These are summarised in the table below, where x and y are fuzzy sets characterised by *linguistic* variables, and A, B, A', and B' are fuzzy sets:

Table 4.2 Fuzzy Implications

	Generalised Modus Ponens (GMP)	***Generalised Modus Tollens (GMT)***
Premise 1	If x is A then y is B	If x is A then y is B
Premise 2	x is A'	y is B'
Consequence	y is B'	x is A'

As an example of fuzzy reasoning using GMP, consider the premise:

If current is low then the voltage is low

If the second example premise is;

The current is very low

Then the consequent will be:

The voltage is very low.

A fuzzy implication is in fact simply a special type of fuzzy relation R. This can be seen by considering fuzzy sets A' and B' which are fuzzy subsets in universes U and V respectively. Then, a fuzzy relation R in the product space $U \times V$ could represent the GMP fuzzy implication, or inference rule *If* x *is* A *then* y *is* B in the form of a fuzzy relation equation given by:

$$B' = A' \circ R \tag{4.5}$$

In other words, given a fuzzy subset of U which is A', and given a fuzzy relation R from U to V, then the fuzzy subset of B' of V that is induced by A' is given by the composition of A' and R. In the above equation, the $\circ$ symbol represents a general method for the composition of a fuzzy relation, which will be further discussed below.

There are many methods of defining the fuzzy implication and these correspond to different interpretations of the fuzzy relation equation.

However, there are two main methods for defining the membership values $\mu_R(u,v)$ of the fuzzy implication function R which are the most intuitive, and fit in well with GMP and GMT [97]. These are defined as:

a) Mandani's Minimum Fuzzy Implication:

$$\mu_R(u,v) = \min[\mu_A(u), \mu_B(v)] \tag{4.6}$$

Where: min[ ] = the minimum function, which has a result that is the minimum of the fuzzy sets contained within the square brackets.

b) Larsen's Product Rule of Fuzzy Implication

$$\mu_R(u,v) = \mu_A(u).\mu_B(v) \tag{4.7}$$

(iii) Composition of Fuzzy Relations

A method of solving the fuzzy relational equation needs to be found once the fuzzy implication R is determined. If we have a fuzzy relation such as $B' = A' \circ R$, then the solution to this equation B' for a fuzzy input A' is said to be the solution of the fuzzy relational equation, or the consequence of the compositional rule of inference.

There are two main methods of solving the fuzzy relational equation in the literature. These two methods are most widely used because they use the least computation and normally lead to better results [104], and the selection of the method depends on the type of problem.

These main solution methods are the *Max-Min* and the *Max-Product* composition of fuzzy relations [110]. The *Max-Min* method is the one used by Zadeh [94] in using compositional rules of inference for approximate reasoning based on linguistic rules. The definitions of these methods of solving the fuzzy relational equation will be explained in detail below.

As an example, if x is a fuzzy subset of U and R is a fuzzy relation from U to V, then using the *Max-Min* composition, the fuzzy subset y in V will have a membership function $\mu_V(y)$ defined as:

a) Max-Min composition:

$$y = x \circ R \tag{4.8}$$

$$\mu_V(y) = \max_{x \in U} \{\min[\mu_U(x), \mu_R(x,y)]\} \tag{4.9}$$

Thus an example of approximate reasoning that can be solved using the above compositional rule of inference could be the following two statements:

1. If x is small then y is large
2. x is very small

Using the *Max-Min* composition *y* can be found as a fuzzy subset in space *V*. The consequent fuzzy set could be *y is very large.*

The other major method is called the *Max-Product* composition. This defines the output fuzzy set to have a membership function $\mu_V(y)$ defined as:

b) Max-Product Composition:

$$y = x * R \tag{4.10}$$

$$\mu_V(y) = \max_{x \in U} \{\mu_U(x).\mu_R(x,y)\} \tag{4.11}$$

The computational operator is sometimes expressed in general form as the *sup-star* composition, where *star* represents an operation such as *min* or *product.* The *star* operator can be chosen to fit the application. As mentioned above, other operators exist, such as *sup-bounded-product* and *sup-drastic-product* [98].

The composition of fuzzy relations for both methods can be seen graphically. Firstly, consider a two input - single output style *Max-Min* fuzzy relation defined as:

$$\mu_{B'}(y) = \max_{x_1,x_2} \{\min[(\mu_{A_1'}(x_1), \mu_{A_2'}(x_2)), \mu_R(x_1, x_2, y)]\} \tag{4.12}$$

Where:

$\mu_R(x_1, x_2, y)$ = the membership function of the fuzzy relation from spaces A_1 and A_2 to B

$\mu_{B'}(y)$ = the membership function of the output fuzzy set B'

$\mu_{A_1'}(x_1)$ = the membership function of the input fuzzy set A_1'

$\mu_{A_2'}(x_2)$ = the membership function of the input fuzzy set A_2'

The rule expressed in this statement is: *If x_1 is A_1' and x_2 is A_2' then y is B'.* Here we have two inputs to the relation where A_1, and A_2, are two input universes, and B is the output universe. The inputs are A_1' and A_2', whilst the output is B'. If we use Mandani's rule of fuzzy implication (equation (4.6)) then it can be shown (see reference [97]) that the equation can be rewritten as;

$$\mu_{B'}(y)=\max_{x_1,x_2}\{\min[\mu_{A_1'}(x_1),\mu_{A_2'}(x_2),\mu_{A_1}(x_1),\mu_{A_2}(x_2),\mu_B(y)]\} \tag{4.13}$$

A graphical interpretation of the *Max-Min* Composition can be seen in Figure 4.2. We can see that firstly the maximum of the intersection of A_1 and A_1' as well as A_2 and A_2' is taken. Then, the minimum of these values and the output set B determines the resultant fuzzy set.

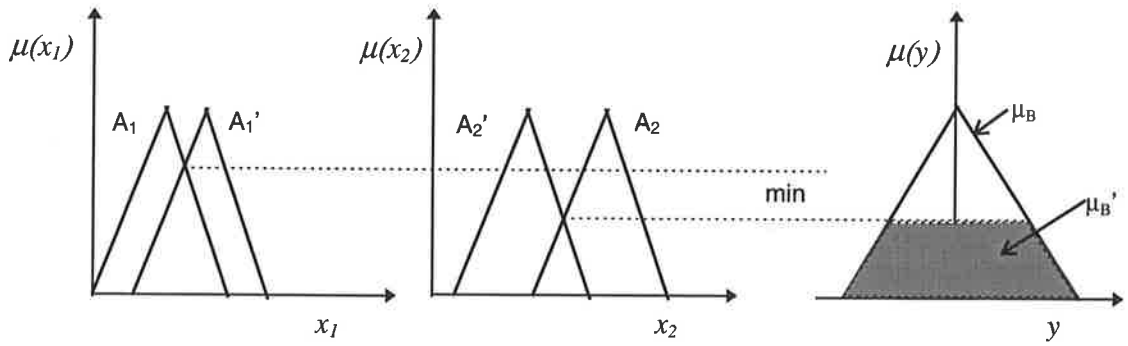


Figure 4.2 Max-Min Composition

The treatment of the *Max-Product* composition is similar to that for the *Max-Min* composition. If we consider the same rule as for the *Max-Min* case for two antecedents A_1 and A_2 that both belong to different universes, then the *Max-Product* composition can be written as:

$$\mu_{B'}(y)=\max_{x_1,x_2}\{\mu_{A_1'}(x_1).\mu_{A_2'}(x_2).\mu_R(x_1,x_2,y)\} \tag{4.14}$$

The *Cartesian Product* of fuzzy sets is defined as [98]:

$$\mu_{A_1'}(x_1).\mu_{A_2'}(x_2)=\min\{\mu_{A_1'}(x_1),\mu_{A_2'}(x_2)\} \tag{4.15}$$

This *Cartesian Product* is often used to rewrite equation (5.14) as:

$$\mu_{B'}(y)=\max_{x_1,x_2}\{\min[\mu_{A_1'}(x_1),\mu_{A_2'}(x_2)].\mu_r(x_1,x_2,y)\} \tag{4.16}$$

If Mandani's rule (4.6) is used for $\mu_r(x_1,x_2,y)$ then this equation can be rewritten as:

$$\mu_{B'}(y)=\max_{x_1,x_2}\{\min\left[\mu_{A_1'}(x_1),\mu_{A_2'}(x_2),\mu_{A_1}(x_1),\mu_{A_2}(x_2)\right]\mu_B(y)\} \tag{4.17}$$

A graphical interpretation of the *Max-Product* composition can now be seen in Figure 4.3.

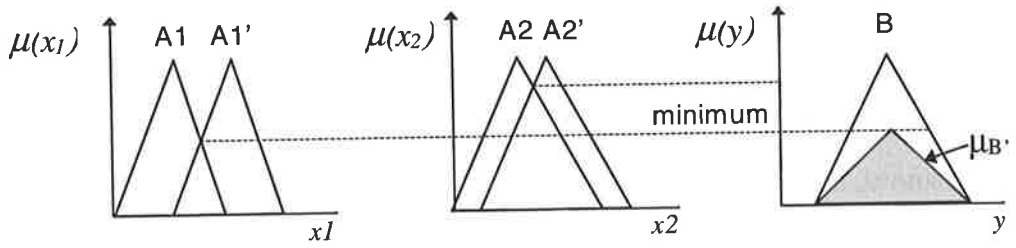


Figure 4.3 Max-Product Composition

Once again the maximum of the intersection of A_1 and A_1' as well as A_2 and A_2' is taken in their respective universes. The minimum of these values is then multiplied with the output set B, and this determines the resultant output fuzzy set.

(iv) Fuzzy Compositions with Crisp Input Values

Normally in engineering systems the input will be a crisp numeric value. The crisp value can be *fuzzified* by mapping the input as a *fuzzy singleton.* A fuzzy singleton has membership value 1 at the crisp input value and 0 at all others. The crisp value is called the *support* of the fuzzy singleton. Therefore, if we want to map a crisp value x onto the universe U then a fuzzy set A' is created that has the properties $\mu_{A'}(x')=1$ for $x'=x$ and $\mu_{A'}(x')=0$ for all other values of $x' \neq x$ in the universe U.

As one can see, there is only one non-zero value for crisp inputs. Therefore, when the inputs are crisp values or fuzzy singletons, the composition of fuzzy relations becomes simpler. For instance the *Max-Min* composition (4.13) becomes:

$$\mu_{B'}(y) = \min\{\mu_{A_1}(x_1'),\mu_{A_2}(x_2'),\mu_B(y)\} \tag{4.18}$$

when there are two crisp input values x_1 and x_2. This is because the maximum of the input fuzzy set and A_1 and A_2 must be at the supports of the input fuzzy singletons x_1 and x_2 respectively.

The equation can be rewritten in the simpler form:

$$\mu_{B'}(y)=\hat{\alpha}\wedge\mu_B(y)$$

$$\wedge \equiv \text{ minimum function} \tag{4.19}$$

where $\hat{\alpha}=\mu_{A1}(x_1')\wedge\mu_2(x_2')$ can be viewed as a weighting or *firing* function. The value of this firing function determines the level of the output fuzzy set.

The *Max-Min* composition for crisp input values can be seen graphically in Figure 4.4. This figure illustrates the implementation of the rule *If x is small (S) and y is large (L) then u is medium (M).* In this figure the crisp input value x is mapped to the input space X as a fuzzy singleton. As mentioned above, the maximum intersection point of this fuzzy singleton and the input fuzzy set (which in this case is S), is at the support of the fuzzy singleton. In a similar manner, the crisp input y is mapped to the input space Y in fuzzy set M as a fuzzy singleton. The maximum intersection point between the input set M and the fuzzy singleton is once again at the fuzzy singleton's support. Using equation (4.19), the firing value is determined as the minimum of the two maximum intersection values in input spaces X and Y corresponding to the input values x and y. In Figure 4.4 this corresponds to the intersection value of set S and x in the input space X. The membership function for the resultant set in the output space is then determined by the minimum of the firing value of the inputs and the output set *medium (M).*

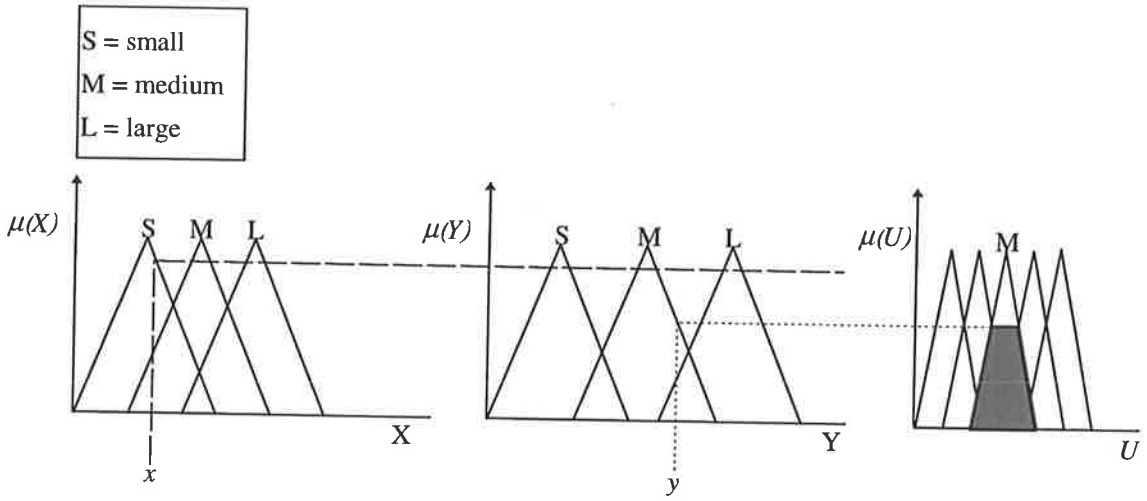


Figure 4.4 Fuzzy Composition with Crisp Inputs

Using similar reasoning, it can be seen that the membership function of the output for the same input values and rule, but using *Max-Product* composition is a simplification of equation (4.17):

$$\mu_{B'}(y) = \left\{ min\left[\mu_{A_1}(x_1'), \mu_{A_{21}}(x_2') \right] . \mu_B(y) \right\} \tag{4.20}$$

This can also be written in the form:

$$\mu_{B'}(y) = \hat{\alpha} . \mu_B(y) \tag{4.21}$$

where once again $\hat{\alpha} = \mu_{A1}(x_1') \wedge \mu_2(x_2')$. This value can also be viewed as a weighting or the firing function on the output membership value.

The use of the *Max-Product* composition with crisp input values, for the same situation as the case discussed above can be graphically seen in Figure 4.5. It can be seen that the only difference in this case is in the formation of the resultant output set in the output space *U*. By using the *Max-Product* composition, the resultant fuzzy set is formed by multiplying the firing value of the inputs with the output space fuzzy set *M*.

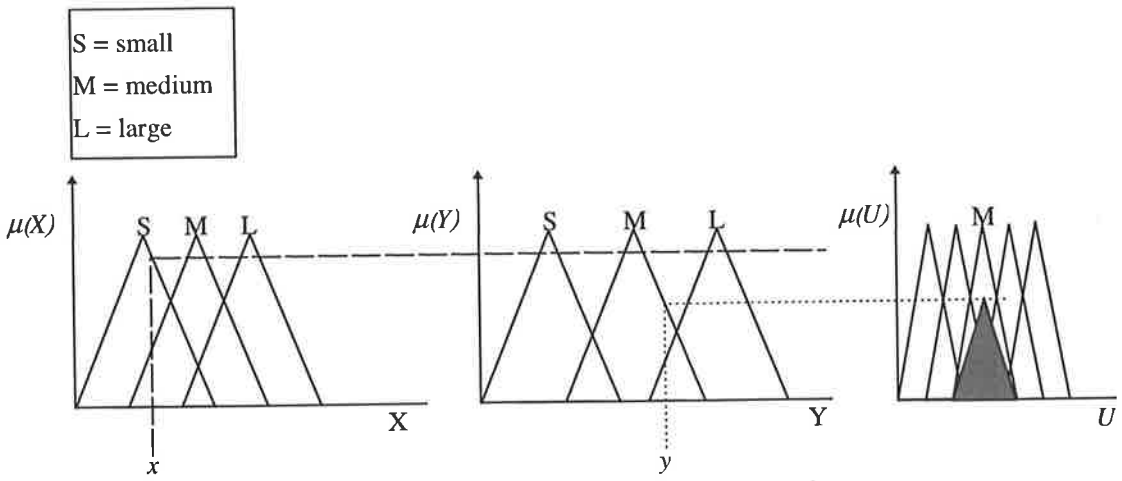


Figure 4.5 Max-Product Composition with Crisp Input

(v) Aggregation of Rules

In normal situations there is more than one rule that is activated at any one time for a given set of inputs. Let us consider again a two input single output system, but with multiple rules. The inputs are x_1 is A_1', x_2 is A_2' and there are k rules which are:

$$\begin{aligned} &R^1\text{: if } x_1 \text{ is } A_1^1 \text{ and } x_2 \text{ is } A_2^1 \text{ then } y \text{ is } B^1 \\ &R^2\text{: if } x_1 \text{ is } A_1^2 \text{ and } x_2 \text{ is } A_2^2 \text{ then } y \text{ is } B^2 \\ &\cdots \\ &R^k\text{: if } x_1 \text{ is } A_1^k \text{ and } x_2 \text{ is } A_2^k \text{ then } y \text{ is } B^k \end{aligned} \tag{4.22}$$

The output of these rules will be the single output set y is B_s'. The connection between the rules is also, or in other words the rules read as follows: *Rule 1 also Rule 2, ..., also Rule k.*

Two extreme cases exist for connecting the rules. These are:

1. All connectives are *ANDs*, which means a conjunctive set of rules

2. All connectives are *ORs*, which means a disjunctive set of rules.

One method of deducing the consequence B_s' is to take the aggregated result of the individual control rules. When the connection between the rules is *OR* then the outcome of the aggregation of the individual rules is the union of the outcome of all the individual rules. The outcome of each individual rules follows the same composition methods described above, and thus the output fuzzy set B_s' is the union of the individual rule fuzzy sets:

$$\mu_{B_S'}(y) = \max_i \mu_{B_S'^i}(y) = \mu_{B_S'^1}(y) \vee \mu_{B_S'^2}(y) \vee \ldots\ldots\ldots \vee \mu_{B_S'^k}(y) \tag{4.23}$$

An important case is the aggregation of rules when there are crisp inputs. In the novel rotor position detection scheme that will be described later, there will be two crisp input values (flux linkage and current) to the fuzzy system. It is thus important to consider the case when rules are aggregated for crisp inputs. In this case, the input values may be treated as fuzzy singletons. As an example, assume that there are only two rules which are:

$$\begin{aligned} &R^1\text{: If } x_1 \text{ is } A_1^1 \text{ and } x_2 \text{ is } A_2^1 \text{ then } y \text{ is } B^1 \\ &R^2\text{: If } x_1 \text{ is } A_1^2 \text{ and } x_2 \text{ is } A_2^2 \text{ then } y \text{ is } B^2 \end{aligned} \tag{4.24}$$

Note that the superscripts in the above equation refer to the rule number, whereas the subscripts refer to the fuzzy set and input labels. If the crisp input values to the system are $\bar{x}_1$ and $\bar{x}_2$ then using equation (4.19) the weighting factor for each rule will be:

$$\begin{aligned} \hat{\alpha}^1 &= \mu_{A_1^1}(\bar{x}_1) \wedge \mu_{A_2^1}(\bar{x}_2) \\ \hat{\alpha}^2 &= \mu_{A_1^2}(\bar{x}_1) \wedge \mu_{A_2^2}(\bar{x}_2) \end{aligned} \tag{4.25}$$

Once again to implement the fuzzy reasoning for the rules, we can use either the *Max-Min* rule or the *Max-Product* rule as the fuzzy implication function. If we consider the *Max-Product* rule for the above two rules, the membership function $\mu_{B_S'}$ of the inferred consequence B_S' is given by:

$$\mu_{B_S'}(y) = \hat{\alpha}^1 . \mu_{B^1}(y) \vee \hat{\alpha}^2 . \mu_{B^2}(y) \tag{4.26}$$

This is graphically illustrated in Figure 4.6 where, as a simplified example, two rules labeled rules 5 and 6 are invoked for crisp inputs of flux linkage (Ψ) and current (i). In this example the rules invoked are defined as:

$$R^5: \text{If } \Psi \text{ is S and } i \text{ is L then } \theta \text{ is S}$$
$$R^6: \text{If } \Psi \text{ is S and } i \text{ is L then } \theta \text{ is S1} \tag{4.27}$$

In Figure 4.6, the consequence in the rotor position output space $\mu_{\Theta_S'}(\theta)$ for each rule is found by using the *Max-Product* implication. The rules are aggregated by taking the union of the output of each fuzzy rule. Therefore, in the bottom of the figure, the output fuzzy set can be seen to be the union of the two fuzzy sets that are the output of each individual rule.

The output fuzzy membership function must be somehow translated into a crisp value of rotor position. This procedure is called defuzzification and will be the subject of discussion below.

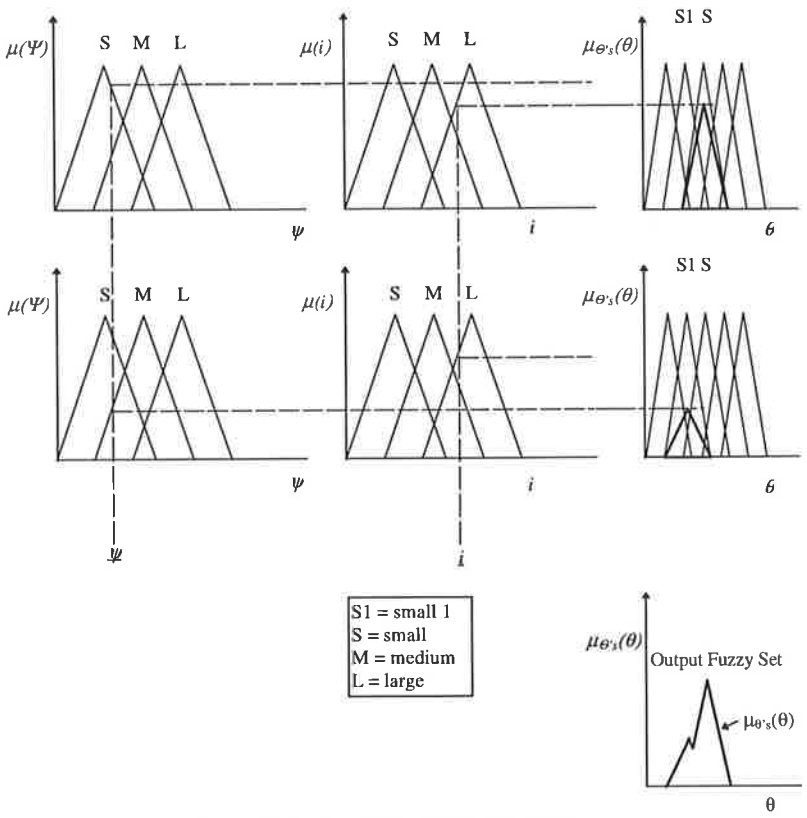


Figure 4.6 Aggregation of rules for crisp inputs

(vi) Defuzzification

Defuzzification is the process of converting the output of fuzzy rules, which is a fuzzy set, to an equivalent crisp output value. This process is required in most engineering applications where a crisp numeric output is normally necessary. For instance, in the position detection algorithm which will be described below, a numeric value of rotor angle is the output. Therefore, a defuzzifier is necessary to provide the crisp value of rotor position from the output of the fuzzy rules.

The defuzzifier performs a mapping from the fuzzy sets in the output space B to a crisp point y which realises the output inferred by the output set B_s'. There are many different choices for this mapping [111], however the most commonly used strategies are the maximum, center average, and center of area methods as will be discussed below:

a) Maximum Method:

The crisp value is taken to correspond to the peak of the output membership function. This method would normally require that a unique peak exists.

b) Center Average Defuzzifier

The crisp output is defined as:

$$\bar{y} = \frac{\sum_{i=1}^{n} \mu_{B'^i}(\bar{y}^i).\bar{y}^i}{\sum_{i=1}^{n} \mu_{B'^i}(\bar{y}^i)} \tag{4.28}$$

where $\bar{y}^i$ is the point in which each fuzzy output set B'^i reaches its peak. Therefore for the output fuzzy set considered in the previous example, the crisp result would be a weighted value of two peaks which is illustrated below in Figure 4.7.

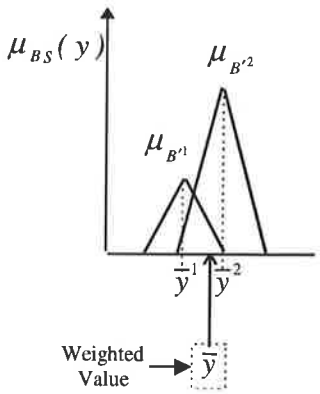


Figure 4.7 Center Average Defuzzification

C: Center of Gravity Method

In this method the crisp value is assumed to be the value of the output y at the center of area of the shape which is made by the region bounded by the output membership function. Mathematically, this is expressed as:

$$y = \frac{\int \mu_{B_S'}(y).y.dy}{\int \mu_{B_S'}(y).dy} \tag{4.29}$$

It can therefore be seen from the above discussions that a fuzzy reasoning system allows a wide amount of interpretation of the fuzzy *If - Then* rules. With this wide array of choices, it is important to choose a fuzzy system that is most suitable for a particular problem. For example, there are different possible compositions of fuzzy relations that may used in a fuzzy reasoning system [100]. However, in practical applications it is often more important to satisfy practical considerations rather to choose the theoretically optimum system. Thus for practical applications the *Max-Min* or *Max-Product* compositions are widely used because they are computationally simple and thus are suitable for real time microprocessor calculation.

There are also many methods for defuzzifying an output of a set of fuzzy rules to obtain a crisp value. Although the maximum method of defuzzification is very simple, it is not often used due to the fact that it provides quite rough results, and needs a unique peak in the output membership function. The center average defuzzifier is also a simple system, but it outperforms the maximum defuzzifier in practical applications [112]. In addition, it is simpler than the center of gravity defuzzifier. Therefore, systems which use the center average defuzzifier have faster computation times, although they may have a lower performance than the more complex defuzzifiers [102]. In the rotor position estimation system, real time speed was important and therefore the center average defuzzifier was used in the system.

In addition the fuzzy membership functions do not have to be triangular shaped or symmetrical as were shown above, and are often represented by trapezoidal or exponential functions [113]. This allows much freedom in the design of a fuzzy system, and it allows the fuzzy system to be able to uniformly approximate any non-linear function [114]. However, triangular functions are beneficial for real time systems because they are simple functions that offer computational simplicity when calculating memberships. Thus, these triangular fuzzy sets were used in the rotor position estimation scheme that will be detailed in the following sections.

4.3 A New Fuzzy Logic Based Rotor Position Estimation Algorithm: Introduction

In the following sections, a new rotor position estimator for the SR motor is described. Commonly this type of scheme is termed a *sensorless* rotor position detection scheme, as opposed to methods that require a physical shaft based position sensor. It will be seen below that fuzzy logic reasoning is used throughout the new position detection scheme. A major consideration in developing the theory of the novel position estimation algorithm was that the final implementation in the SR motor drive should be feasible for currently available microprocessor systems and that the sensorless system should have a very high robustness and reliability. Thus in choosing the fuzzy logic methods to be utilised, computationally efficient rule processing methods should be chosen, which still produce

accurate results. In the new method, these included the *Max-Product* rule implication, a center average defuzzifier, and triangular membership functions. Although these would not necessarily produce the optimum result, they take into account the need for fast learning and fast real time operation. In addition, as will be detailed in later sections, the novel algorithm was specifically developed to utilise fuzzy logic techniques in order to bring about a very high sensorless system robustness and reliability.

The position estimator implemented in this research does not have restrictions seen in other schemes, as it can be used under all operating speeds and conditions, including transients, standstill, and start-up. It also does not require any external testing circuitry or test signals. Moreover, the position estimating scheme has unique improvements over previous methods. No complex mathematical model of the SR motor is required in this scheme, but nevertheless, the non-linear characteristics of the machine are not ignored and no simplifying assumptions about the motor saturation or behavior are made. The scheme models not only saturation effects, but other real time operating non ideal effects, such as mutual inductance, eddy currents, temperature effects, and skin effects.

In later sections, the improvements and advantages of the fuzzy logic based sensorless position estimation scheme will be shown in detail. However, the advantages made available by the scheme are also summarised in Table 4.3 below. As a comparison, the table compares the new scheme with the most sophisticated methods to date: the model based schemes described in the in Chapter 3.

Table 4.3 Improvements of new scheme

Parameter	New Fuzzy Logic Based Scheme	Model Based Schemes
Speeds	All including stall and start-up	Not demonstrated for stall and start-up
High Robustness and Reliability	Demonstrated	Not demonstrated
Mathematical model	None required	Accurate state space model required
Includes non-linear saturation	Yes	No
Includes all real time operating effects	Yes	No
Requires test signals	No	No
Can be used under all current control conditions	Yes	No

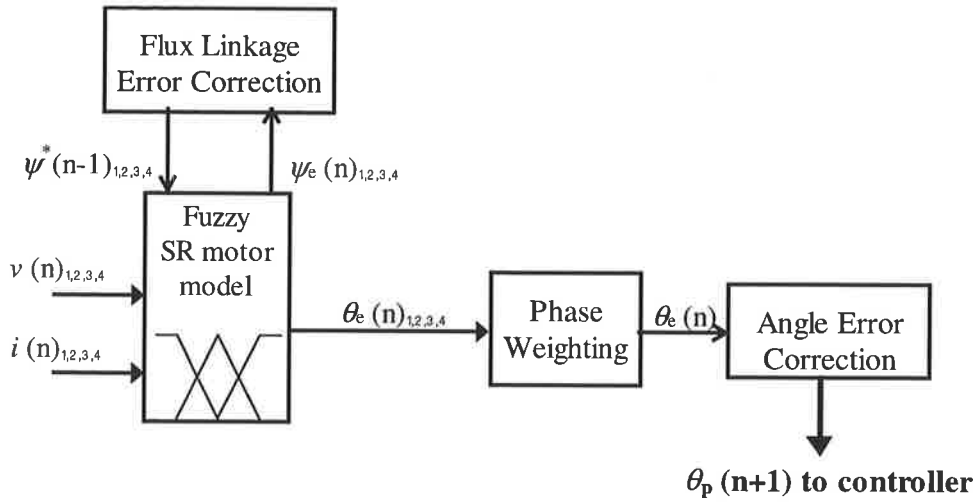
Motor drives are usually electrically noisy environments, which means that noise is often induced on any measurement circuitry. In addition, practical measurement systems are normally subject to error and inaccuracy. Therefore, a major reason for the choice of using a fuzzy logic based estimation scheme was to satisfy the requirement that the algorithm is not affected significantly by deviations and error in the input data. It has been shown (see references [115], [116], [117], [118], [119]) that modelling and estimation using fuzzy set theory is more tolerant to noise and errors in the input measurements than crisp methods.

Hence, as it will be demonstrated in later sections, it was found that the use of a fuzzy motor model in the estimation algorithm provided robustness and resistance to the effects of input noise.

To provide extra reliability against noise and error on the position estimation, two error correction routines are used on the input signals in conjunction. The first error correction system uses a fuzzy logic rule base to determine if a signal is corrupted. The second error correction system uses a fuzzy logic predictor to predict values of flux linkage and angle at the next sample instant. The two systems are used in conjunction to minimise noise on the estimated angle.

In the SR motor, there is normally more than one motor phase operating with excitation current at any one time. All phases that are excited at any given time should be used for position sensing. Nevertheless, there are certain angle positions at which each phase is more accurate than at other angles, and more weighting should be given on the phase that will be more accurate. However, the angle position ranges in which the phases provide more accurate sensing do not have a well defined cut off point, and the weighting which should be given to a phase at any certain position is difficult to define analytically. Nevertheless, these regions and their weighting can be easily described by an expert in linguistic terms. In the developed sensorless position detecting scheme, linguistic rules based on expert knowledge were used to give the optimal phase for position sensing the most weighting. In this manner, all excited phases may be used, but the phase in the most optimum region for sensing will be given the most weighting.

In Figure 4.8, the salient features of the new sensorless position estimation scheme are shown in a simplified block diagram. During operation, measured values of voltage and current are required as inputs to the estimator to determine the rotor position. As mentioned above, the position detection scheme contains error correction blocks, as well as giving greater weight to phases that are most suitable for position sensing. The details of the each of the blocks seen in the figure will be discussed in the following sections. The first step in the development of the rotor position estimation scheme is the creation of a fuzzy logic based motor model using a fuzzy logic training algorithm. Therefore, this is the first component of the new estimation scheme that will be discussed below:



$v(n)_{1,2,3,4}$ = the four phase voltages of the SR motor

$i(n)_{1,2,3,4}$ = the four phase currents

$\psi_e(n)_{1,2,3,4}$ = the estimated four phase flux linkages (from integration)

$\psi^*(n-1)_{1,2,3,4}$ = the corrected flux of step (n - 1) used as integration constant

$\theta_e(n)_{1,2,3,4}$ = the estimated position from the fuzzy model from all excited phases

$\theta_e(n)$ = the single weighted value of position after the the phase weighting

$\theta_p(n+1)$ = next step prediction of angle

Figure 4.8 Simplified Block Diagram of Rotor Position Estimation Scheme

4.4 Training Phase: Development of an SR Motor Fuzzy Logic Based Model

One of the major components of the new rotor position estimation algorithm is a fuzzy logic based motor model. A training scheme is used to create a fuzzy motor model that is termed a *fuzzy rule base*. As it will be described in further sections, this rule base is used to provide a value of rotor position from the inputs of the position estimation algorithm.

The fuzzy rule base which models the motor is used in a similar manner to a fuzzy rule base in a *fuzzy logic controller* [120] (Figure 4.9) which contains a fuzzifier for the input of crisp signals, a *fuzzy reasoning mechanism* which uses the fuzzy rule base, and a defuzzification unit to output a crisp output value. The purpose of the fuzzy reasoning mechanism and rule base is to process the inputs by using the fuzzy rules stored in the fuzzy rule base, together with composition methods such as those described previously in Section 4.2.2. Therefore, in the rotor position estimation scheme, the fuzzy rule base is used by the fuzzy reasoning mechanism to estimate the rotor position from the input values of current and flux linkage.

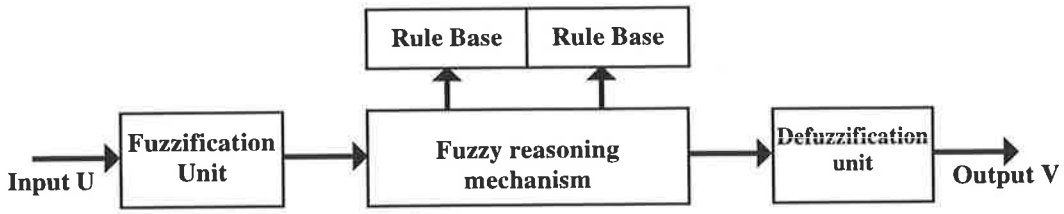


Figure 4.9 Fuzzy Logic Controller

The main advantages of developing a fuzzy logic based model of the SR motor, rather than a conventional mathematical model are:

i) No mathematical model is required.
ii) Fuzzy models are universal approximators.
iii) No requirements for large look-up table.
iv) Fuzzy models allow fast computation.

These advantages will be discussed below:

(i) No Mathematical Model Required

Fuzzy logic system identification and modelling does not require an accurate mathematical model. It therefore provides a mathematical *model free* estimation and modelling approach. Hence, fuzzy logic well suited to systems that are unknown, ill defined, or are structurally difficult to model due to naturally existing non-linearities and other modelling difficulties. As it is stated in reference [121], the switched reluctance motor is very difficult to define in a precise and accurate manner with a conventional mathematical model. This is because the motor has non-linear magnetisation characteristics and complex magnetic coupling interactions between the motor phases. Hence, fuzzy techniques are well qualified in providing a model of the switched reluctance motor.

Neural networks [122] can also be used to model the switched reluctance motor using a mathematical model free approach, but they often have a long learning time, and do not allow the examining of the internal structure of the model as with fuzzy logic linguistic rules [123]. Therefore, fuzzy models are favorable due to the fact that their behavior can be explained using linguistic rules and thus they can be easily adjusted by altering the rules [124].

(ii) Fuzzy Models are Universal Approximators

Although fuzzy modelling does not require any mathematical model, it has been well proven that fuzzy models are universal approximators [125], [126], [127], [128]. Therefore,

a fuzzy model can approximate any continuous function to any degree of accuracy using arbitrary fuzzy sets (e.g. triangles, trapezoids, exponential curves, and other types of fuzzy sets). In other words, for any continuous function $f(x_1, x_2, \ldots\ldots, x_n)$ and for every error bound $\varepsilon > 0$, there exists a fuzzy model $F(x_1, x_2, \ldots\ldots, x_n)$ which uniformly approximates $f(x_1, x_2, \ldots\ldots, x_n)$ and is always ε close to f. The switched reluctance motor model is a non linear continuous function, and therefore, it is possible to model this function using fuzzy sets without the requirement for mathematical based modelling.

(iii) No Requirement for Large Look-up Table.

In some previous SR motor position estimation schemes discussed in Section 3.3.2.3, a table of measured static motor characteristics is used to describe the motor. The measured motor data provides a numerical model of the static angle versus flux linkage and current characteristics. Methods that use a numerical table are commonly called table look-up methods, and although they have the advantage of being fast, they have the disadvantage of needing a large memory to store the table. The size of the table must be very large for accurate position estimation, otherwise some sort of interpolation needs to be used.

However, in this application, and in others where numerical data is learnt by a fuzzy system, it is found that the memory requirement of the stored fuzzy model is much lower than that required by the equivalent look-up table [129]. For example, in reference [130] it is shown that for an 8-bit temperature controller the memory requirement is reduced from 64kB RAM to less than 0.5kB when a fuzzy rule based model is used instead of a look-up table. This represents a reduction in memory requirement of over 99%, which would allow a cheaper hardware implementation.

In addition, the numerical table look-up methods require accurate measured inputs for the table look-up operation, and are thus sensitive to noise and error. However, it will be seen in later sections that fuzzy methods have a high noise and error handling ability, which also makes them more favorable than the numerical table look-up methods.

(iv)Fuzzy Models Allow Fast Computation

As it has been mentioned above, an important criterion in the development of the new angle estimation scheme, was the practical implementation in real SR motor drives. One of the major practical considerations is the complexity of computation of the angle estimation algorithm. This is because a computationally demanding algorithm will have detrimental effects on the system performance, because during the actual operation of the angle estimation, the angle estimates should be produced as quickly as possible after the motor measurements. If the estimates are not calculated fast enough then the correlation between the angle estimates and the actual rotor angle may not be high. This is because

during the delay time of the angle estimate calculation, the actual physical rotor position will change. Hence, the calculation time must be as low as possible, particularly for high-quality motor control. In addition computationally demanding algorithms will demand a fast real time microprocessor, which may not be available in all motor drives.

Approximate mathematical models (such as polynomials, splines or any other traditional approach) of the non-linear SR motor model could be used in principle to provide position estimation. However, the mathematical model will increase in complexity in proportion to its accuracy in modelling the non-linear motor, and the fully accurate model will be in practice unavailable. As in other non-linear mathematical models of power electronic systems and motor drives, their complexity will lead the model being computationally expensive with a relatively slow response [131]. Hence it was seen in Chapter 3 that previously developed model based sensorless schemes assumed that the SR model was linear and time invariant, in order for real time operation to be viable with a simplified model.

However, fuzzy logic does not need a complex mathematical model, and thus has the advantage of a fast response due to relatively simple mathematical calculations used in fuzzy rule processing [132]. They are often used in motor drives ahead of mathematical model based techniques precisely for this reason [133]. In addition, it has been mathematically proven that the *fastest* possible universal computation scheme corresponds exactly to fuzzy logic methods using Max-Min composition [134]. Therefore, in terms of real time sensorless SR motor operation it can be said that fuzzy logic techniques represent (in some reasonable sense) the best choice.

4.4.1 SR Motor Model Training Scheme

To create a fuzzy model of the motor, a training scheme is used which trains a fuzzy logic model based on numerical information about the SR motor. In this sense, the motor model is created by using an *adaptive* fuzzy system. During the learning process, the training scheme creates a fuzzy logic based model that takes into account the motor's magnetic saturation, mutual inductances, and other ill defined real time operating effects.

To model the motor, the training system derives information from two main sources: The static flux linkage curves of the motor, and the dynamic real time operating waveforms of the motor. From the static flux linkage curves of the motor, the training method develops a static motor model, and then, using the dynamic real time test results it develops a more realistic motor model by modifying the static model to account for the non ideal real time operating effects.

The static flux linkage curves of flux linkage versus current and angle are readily available for SR motors by measurement. The measurement technique of static flux linkage curves has been detailed earlier in Chapter 2 and Appendix A, and it was seen that the technique entails measuring flux linkage and current at fixed rotor positions. The static flux linkage curves provide important information about the electromagnetic characteristics of the SR motor phases, and thus are used as training data for the developed training algorithm in order to model the SR motor

However, for the training system to model the motors dynamic real time operating effects (which can include mutual coupling between phases, temperature variations, eddy currents, and skin effects), measurements of voltage, current, and position, while the motor is running under actual working conditions are required for training data. It is proposed that this could be performed typically on a single test motor with an encoder attached to the shaft. The motor could be run under this test and then the results used for all other motors of that model. If manufacturing irregularities need to be taken into for highly accurate control, then each selected motor could be run under test once before starting their service life.

Although the fuzzy training scheme described here learns the motor model from the two sources of information, it should be noted that either the static flux linkage curves, or the operating test results individually are sufficient for the training scheme to operate. If only the flux linkage curves are used, then the real time effects that affect flux linkage and current (mutual inductance, eddy currents, temperature effects, skin effects) will not be modeled. However, if only the dynamic real time operating test points of flux linkage, current, and angle are used, then there is a possibility that some points on the static flux linkage versus current and angle plane will not have been covered during the test. This is because there may be some angles where current does not flow under normal operation, or very high currents may not be allowed by the controller. However, these points of current and angle could be stored in the static magnetisation curves. Thus, the static motor data from the magnetisation curves are used in conjunction with the real time operating test.

Before discussing the implemented training scheme of the position estimation scheme in detail, various training procedures of fuzzy models will be discussed. The various advantages and disadvantages of the methods will be seen and the reasons for choosing the selected method will be given.

4.4.1.1 Methods of Training Fuzzy Models

Various methods have been described for the training of fuzzy models. One method has been to use feedforward neural networks [135], [136]. Based on these networks, back

propagation training algorithms are used to adjust the parameters of the fuzzy logic model, when numerical training data is fed to the neural network. The advantage of using neural networks to tune the fuzzy model rather than using neural networks alone, is that the resultant fuzzy model is open to the user in the form of transparent *If - Then* rules, whereas a neural network acts as a non-linear *black box* which is inaccessible to the user. In addition, linguistic information can only be incorporated in the fuzzy model either before or after training, which can not be done using neural networks alone.

Another method of training fuzzy models is to use genetic algorithms [137]. Genetic algorithms are adaptive methods which can be used to solve many search and optimisation problems based on the biological process of evolution. In this method the parameters of the fuzzy model are represented by bit strings. These bit strings are called *populations of individuals*, which undergo operations named after their biological counterparts, such as reproduction, crossover, and mutation. When a given bit string reaches a certain level of *fitness* which represents some system objective, then that is used in the final system.

Other training procedures have been developed which use adaptive techniques from classical adaptive control to adjust the parameters of a fuzzy model [138]. In this training procedure, both the rules and the membership function shapes are adapted according to the input data.

The above training methods are well proven and can provide very accurate modelling of non-linear systems. However, these training procedures have a disadvantage in that their computational requirement is very high. The genetic algorithm needs iterative computations, whilst the neural network training algorithm implements a non-linear optimisation and search procedure. This means the training algorithm may be slow to converge and may be trapped in its search in local minima [139]. The training procedure using classical adaptive methods can model a system with identification errors converging to zero in certain systems. However, the speed of convergence can be slow, as there are complex mathematical equations that need to be solved during the fuzzy model adaptation.

Due to the requirement of intensive computations in the above mentioned training algorithm, the above described methods may not be suitable for applications where real time computational speed is an important parameter. For these applications a fast, simple, and effective technique would be more suitable, and the *table look-up scheme* of training fuzzy models [140] is one of these. This method provides the requirements of simplicity as well as speed and accuracy. The main advantage of this method is that it performs only a one pass operation on the numerical input-output data pairs to generate the fuzzy *If - Then* rules which describe the motor. Although the optimum fuzzy model will not normally be

generated using the table look-up scheme, the method's accuracy is nearly as high as the others [140].

Due to its suitability to practical applications, the table-look-up scheme was used for the training phase of the rotor position estimation system in order to derive a fuzzy logic based SR motor model in the form of a fuzzy rule base. As mentioned above, the static flux linkage curves, which contains measured points of flux, current, and angle at various measured positions, as well as dynamic real-time measurement data are used in the first step to generate a set of fuzzy logic rules. The details of the procedure for the generation of fuzzy rules using the table-look-up scheme will now be discussed.

4.4.1.2 SR Model Training Using Table-Look-up Scheme

In the training of the fuzzy logic model using the training scheme, the basic objective is to learn and model the motor characteristics from the numerical data measured from the motor. The motor characteristics are defined as a two input – one output function that relates flux linkage and current (the inputs of the function) to rotor angle (the output of the function). The training task involves creating a fuzzy model of this function from the training data.

In both the first stage of learning from the static flux linkage curves and the second stage of learning from the dynamic operation measurement tests, the training data is the same. This data is defined as a two-input one-output *input-output pair* (where the word "pair" in this term refers to the fact that there is a set of input values paired with a set of output values, and not a pair of two values). Each point of measured data presented to the training system is given as:

$$(\Psi^{(n)}, i^{(n)}; \theta^{(n)}) \tag{4.30}$$

where:

$\Psi^{(n)}$ = the flux linkage input data point of the nth data pair.
$i^{(n)}$ = the current input data point of the nth data pair.
$\theta^{(n)}$ = the angle output data point of the nth data pair.

As it was mentioned previously, the training phase produces a fuzzy logic rule base from the data and this rule base is used in the rotor position estimation scheme to map input flux linkage and current input values to output values of angle. Hence, this fuzzy rule base identifies and models the non-linear characteristic function of the SR motor relating flux linkage and current to rotor position:

$$\{f: (\Psi, i) \rightarrow \theta\} \tag{4.31}$$

As it will be detailed below, the training phase consisted of the following steps:

Step A: Dividing the Input and Output Spaces into Fuzzy Regions
Step B: Generating Fuzzy Rules from Input Data of Flux, Current, and Angle
Step C: Assigning rule degrees
Step D: Create the Fuzzy Knowledge base

a) Dividing the Input and Output Spaces into Fuzzy Regions

The first step in creating the fuzzy knowledge base is to divide the input and output domains into fuzzy regions, where a fuzzy region is defined as some range of values in a variables domain over which a fuzzy membership function is defined. For example the fuzzy region for the fuzzy set *HIGH* in the current domain may range from 8A to 9A. However, in the first instance, the *domain interval* of each variable must first be chosen, where the domain interval is defined as the region between the minimum and maximum values of the variable in its universe of discourse that the variable will most probably take. (note that the values of the variables are still permitted to lie outside this domain interval). The domain intervals for each of the variables were defined as $[\psi^-,\psi^+]$ for the flux linkage, $[i^-,i^+]$ for the current, and $[\theta^-,\theta^+]$ for the angle, where the first variable in each of the brackets is the lowest value in the respective domain interval, and the second variable is the highest value.

In this application, the domain intervals of each of the variables are easily chosen. This is because the flux and current are determined by the rating of the machine and the angle domain is defined by the electrical cycle of the machine. The actual domain range can be extended or contracted to suit any SR machine.

In this thesis, the rated current of the SR machine used was 9A and therefore a domain of 0 to 20A was used for current (i). Note that the extended domain above 9A was chosen so that all transients or irregularities in control could be handled by the system. Similarly, the domain for flux linkage (ψ) was chosen to be 0 to 1 Wb, since the flux linkage is always below this value in the SR test machine. Moreover, since the electrical cycle of each phase of the test motor was 60 degrees, the domain of angle (θ) could be chosen to range from 0 to 60 degrees. However, as it was mentioned before in Section 2.7, the inductance characteristics of the SR motor are almost symmetrical around the alignment point, and thus the motor magnetisation characteristic curves are normally given only from the unaligned to aligned angles. Hence, in the four phase motor (such as that used in this thesis), a domain of 0 to 30 degrees (unalignment to alignment) can be used. The benefit of this is that the number of fuzzy sets required is reduced by half, which saves memory

and the number of rules. However, there will be a reduction in accuracy due to the small asymmetry of the SR motor.

Once the domain intervals for each variable are chosen, each domain is then divided up into fuzzy regions. In the table-look-up training method, great deal of flexibility is available in this process. This is because the number of regions per domain may be different for each variable. Also the length of the fuzzy regions may be equal or of different within each domain. The shapes of the membership functions for the fuzzy regions may be any of the possibilities discussed in Section 4.2.2. It should be noted that the process of choosing the fuzzy regions is largely automated in many of the other training methods such as the neural network or genetic algorithm training schemes. Hence some intuition is required in the table look-up training method.

To determine the fuzzy regions in the rotor position estimation method, the variable spaces of ψ, i, and θ were divided into N_1, N_2, and N_3 regions respectively and number of regions was chosen to be:

$$\boldsymbol{N_1 = 37,\ N_2 = 39,\ N_3 = 30} \tag{4.32}$$

To have a symmetrical number of fuzzy sets around the center fuzzy set in the flux and current domains, an odd number of sets was chosen, whereas 30 sets were chosen in the angle domain, in order to have one set per degree in the electrical cycle. This choice of sets was found to provide sufficient accuracy in this work (as will be detailed in the results shown in later sections). Although more regions would provide greater accuracy in such systems, this also leads to more memory requirement due to the greater number of fuzzy sets and rules. It should be noted that the choice of the number of input-output fuzzy regions in this method is arbitrary, and subject to trial and error. The number of sets chosen in this work was found after experimentation of the algorithm. Many automated methods have been developed in order to optimise the number of fuzzy sets [141], and any one of these could be used for this application. However, using trial and error, it was found that the number of sets chosen above provided a good performance without requiring an overly large rule base.

During the development of this work, the following values for the number of fuzzy regions were also used: $\{N_1 = 20, N_2 = 20, N_3 = 30\}$, and $\{N_1 = 63, N_2 = 53, N_3 = 30\}$. However, it was found that although the rule base with $N_1 = 20$ and $N_2 = 20$ performed well for the simulation results, the performance was not as high in the experimental results. However, the higher number of regions $N_1 = 63$ and $N_2 = 53$ did not offer much greater accuracy than the number of regions defined in equation (4.32), and thus a lower number of sets was chosen to decrease the storage requirement for the number of fuzzy

sets and rules. In all the results which are shown below, the number of regions shown in equation (4.32) are used.

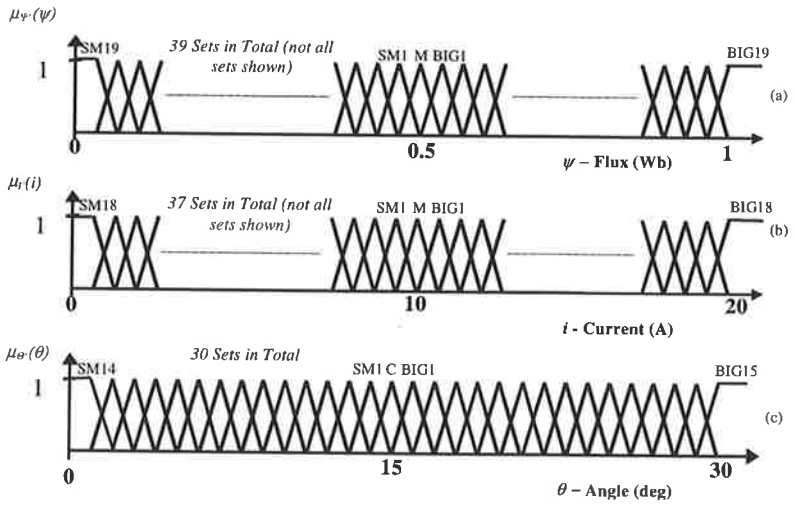
In the next stage, each region was then assigned a fuzzy membership function. In this thesis, all fuzzy sets were chosen to have the same shape, and thus all the membership functions were chosen to be isosceles triangular shapes. The maximum point of each triangle was chosen to lie at the center of the fuzzy region and is given a membership value of 1. The other two vertices were chosen to lie at the centers of the two neighboring fuzzy regions and at these two points the membership values were made zero. Defining the membership functions in this relatively simple manner made the calculation of membership values of a fuzzy set very fast, and therefore very fast to implement on a microprocessor in real time, as will be detailed in Chapter 6. However, it should be kept in mind that these sets would not normally be the optimum in terms of accuracy compared to the more complex schemes. Nevertheless, the speed of calculations would be much faster, which is an important consideration for real time operation.

A graphical representation of the membership functions which were chosen to partition each of the variable domains can be seen below in Figure 4.10. The value of the membership function for each fuzzy set varies from 0 to 1 and it can be seen that there is a 50% overlap between adjacent functions. It can also be seen in the figure that each fuzzy set is denoted by a fuzzy linguistic term ranging from *SMn* (*Small n*) to *SM1* (*Small 1*) to *Med* (*Medium*) and then from *BIG1* to *BIGn*. Here n is an integer and varies between 0 and $N_1/2$, $N_2/2$, and $N_3/2$ (where N_1, N_2, and N_3 are defined by equation (4.32)) for ψ, i, and θ respectively.

b) Generating Fuzzy Rules from Input Data of Flux, Current, and Angle

After the fuzzy membership functions in each of the input and output domains are defined, measured training data can be used to generate fuzzy rules in order to create the fuzzy rule base model. During the training phase, each input-output data pair, which consists of a crisp numerical value of measured flux linkage, current, and angle, is used to generate the fuzzy rules which model the system.

To determine a fuzzy rule from each input-output data pair, the first step is to find the degree of each data value (flux, current, angle) in every membership region of its corresponding fuzzy domain. The variable is then assigned to the region with the maximum degree. As an example consider the current i variable for an input-output data pair consisting of $\psi^{(i)}$, $i^{(i)}$, and $\theta^{(i)}$. The degree of the data value $i^{(i)}$ is found in the different fuzzy regions. This is illustrated for the input domain of current as shown in Figure 4.11, where only five of the membership functions are shown for simplicity. For an input of 12.2 A, $i^{(i)}$ has membership degree 0.75 in BIG2, 0.25 in BIG3 and zero in all others.



$\mu_{\Psi'}(\psi)$ = membership value in fuzzy set Ψ of input flux value ψ
$\mu_{I'}(i)$ = membership value in fuzzy set I' of input current value i
$\mu_{\Theta'}(\theta)$ = membership value in fuzzy set Θ' of input angle value θ

Where:
Ψ' ranges from set *SM19* to *BIG19*
I' ranges from set *SM18* to *BIG18*
Θ' ranges from set *SM14* to *BIG15*

Figure 4.10 Fuzzy domain regions for each variable: (a) Flux Linkage, (b) Current, (c) Rotor Position

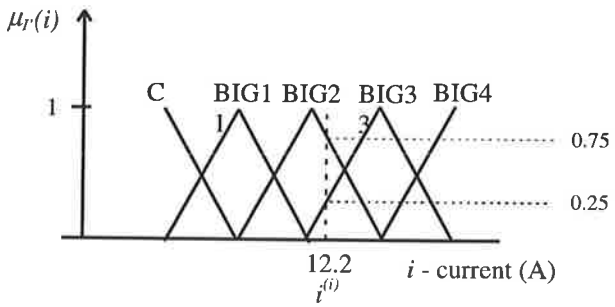


Figure 4.11 Finding Membership Function

This variable is thus assigned to the set *BIG2* because this is the region in which the variable has the maximum degree. If the same procedure produced a result for the remaining variables that assigned $\psi^{(i)}$ to the fuzzy set *BIG5* and $\theta^{(i)}$ to the fuzzy set *SM6* (where *BIG5* and *SM6* are fuzzy sets in the flux and angle domain respectively) then the resultant rule based on the training data would be:

$$\text{Rule } (i) : \textit{If } i \text{ is BIG2 and } \Psi \text{ is BIG5 } \textit{Then } \theta \text{ is SM6} \tag{4.33}$$

Another input-output data set such as $([\psi^{(i+1)}, i^{(i+1)}], \theta^{(i+1)})$ could produce another rule such as:

$$\text{Rule } (i+1) : \textit{If } i \text{ is BIG1 and } \Psi \text{ is BIG5 } \textit{Then } \theta \text{ is SM4} \tag{4.34}$$

Hence, each training data set produces a corresponding fuzzy rule, which is stored in the fuzzy rule base. However, it can be seen that with a large amount of measured training data there will normally be rules produced by different training data which are identical, and therefore the number of stored rules does not necessarily correspond to the number of training data sets. In addition there may be rules generated by different data sets that are contradictory, and the method for dealing with this case will be explained below:

c) Assigning rule degrees

When each new rule is generated from the input-output data pairs, a *rule degree* or *truth* is assigned to that rule, where this rule degree is defined as the degree of confidence that the rule does in fact correlate to the function relating flux linkages and current to angle. Any feasible technique can be used for determining the degree or truth of a generated rule. In the developed method a degree is assigned which is the *product* of the membership function degree of each variable in its respective region. For example, the rule given in equation (4.34) would have degree:

$$Degree\ (Rule\ i) = \mu_{BIG2}(i).\ \mu_{BIG5}(\Psi).\ \mu_{SM6}(\theta) \tag{4.35}$$

Where:
$\mu_{BIG2}(i)$ is the membership degree of current in region *BIG2*.
$\mu_{BIG5}(\psi)$ is the membership degree of flux in region *BIG5*.
$\mu_{SM6}(\theta)$ is the membership degree of angle in the region *SM6*.

The purpose of this assignment is to choose between data sets that produce the same antecedents but different consequents. This would arise because when there is a large amount of measured data, some data pairs will produce rules that have the same antecedent but a different consequent (due to errors or noise in the measured data). This would mean that there are conflicting rules in the system. Conflicting rules are resolved by choosing the conflicting rule that has the highest degree. This rule is the one that is placed in the fuzzy rule base.

As an example consider two input-output data pairs *n* and *m*, which produced the rules:

Rule (*n*) : *If i* is BIG2 and Ψ is BIG4 *Then* θ is SM7 (4.36)
Rule (*m*) : *If i* is BIG2 and Ψ is BIG4 *Then* θ is SM9 (4.37)

Thus for this example, there would be two rules with the same precedent but different consequent. If the membership functions for each of the variables was as follows:

(i) Data Set n:

(a) $\mu_{BIG2}(i^{(n)}) = 0.41$
(b) $\mu_{BIG4}(\Psi^{(n)}) = 0.73$
(c) $\mu_{SM7}(\theta^{(n)}) = 0.79$

(ii) Data Set m:

(a) $\mu_{BIG2}(i^{(m)}) = 0.92$
(b) $\mu_{BIG4}(\Psi^{(m)}) = 0.76$
(c) $\mu_{SM9}(\theta^{(m)}) = 0.80$

Then by multiplying the membership function degrees of each variable, the rule *n* will have degree 0.41x0.73x0.79 = 0.236, whilst rule *m* will have degree 0.92x0.76x0.80 = 0.559. Therefore, only the rule with the highest degree (*m*) will be placed into the fuzzy rule base.

d) Create the Fuzzy Rule Base

As it can be seen from the above, every training data set produces a corresponding fuzzy rule which is stored in the fuzzy rule base (except if an identical rule exists on the rule base already, or the generated rule is eliminated due to a lower degree of truth than an existing rule with the same antecedent but different consequent). Therefore, as each input-output data pair is processed, and the rules are generated, a fuzzy rule or knowledge base is created.

The rule base that is created is in the form of a table that can be looked up by the fuzzy reasoning mechanism. This look-up table representation of the rules is formatted so that the fuzzy sets of the input variables (or the antecedents of the rule) are the axes of the table, and the output variable fuzzy sets (the consequent of the rules) are the stored table values. Thus, in this case, the current and flux linkage fuzzy sets, which are the antecedents, are the axes of a two dimensional look-up table, and the stored table values are the rotor position output sets.

	Current i	
Table Values: Angle θ	**SMALL2**	**SMALL1**
Flux Ψ **SMALL2**	**CENTER**	**SMALL3**
SMALL3	**SMALL3**	**SMALL5**

Figure 4.12 Example two by two fuzzy rule base look-up table.

As an example, a simplified example of a two by two fuzzy rule base table is seen in Figure 4.12 (the complete fuzzy rule base generated by the training scheme will be seen in Section 4.4.2.2. From examining the antecedents and consequents in the table, it can be seen that the *If-Then* rules represented in this table are:

If i is SMALL2 and Ψ is SMALL2 *Then* θ is CENTER (4.38)
If i is SMALL1 and Ψ is SMALL3 *Then* θ is SMALL3 (4.39)
If i is SMALL2 and Ψ is SMALL3 *Then* θ is SMALL3 (4.40)
If i is SMALL1 and Ψ is SMALL3 *Then* θ is SMALL5 (4.41)

4.4.2 Implementation of Training Scheme

The training phase of the fuzzy system which was described above was implemented in C, and can be executed on any system that has a C compiler by simply cross compiling to the particular target system. This training procedure is the same for both phases of training (using the static training data and the dynamic real time training data). A flow-chart showing the logical flow of the software routine is given in Figure 4.13. It can be seen that the computer algorithm consists of the following main subroutines:

1. Initialization
2. Read data
3. Find fuzzy regions
4. Calculate membership values
5. Make rule
6. Place rule on rule base

The *Initialization* subroutine resets the fuzzy rule base, which in this software implementation is stored as a two-dimensional C language *array* type, with each element of the array being a *structure* type. The structure type consists of two variables: The first is the linguistic label which represents the consequent of the rule stored in this point of the array, whilst the second variable is the degree of the rule being stored on this point of the array. If the training algorithm is being run for the first time then the fuzzy rule base is completely initialised. This is achieved by setting the degrees to zero and rule labels to *XX* in all elements of the array. The label *XX* is arbitrarily chosen to represent a point on the array that does not have any rule stored. If the training algorithm is not being run for the first time, but instead is going through a further training phase, then the rule table is loaded from a stored file.

The *Read Data* subroutine reads the input-output data of flux, current, and angle. In the program, the flux linkage and current is labeled as input data *x1* and *x2* respectively, whilst the angle is labeled as the output data *y*.

The *Find Fuzzy Regions* subroutine determines which fuzzy regions *x1*, *x2*, and *y* are within according to the fuzzy set regions defined for each of the variables domain. This is simply achieved by seeing if the value of the variable is contained within any fuzzy region, in other words, if it has non-zero membership in any fuzzy set. The fuzzy regions are stored in the C program as arrays.

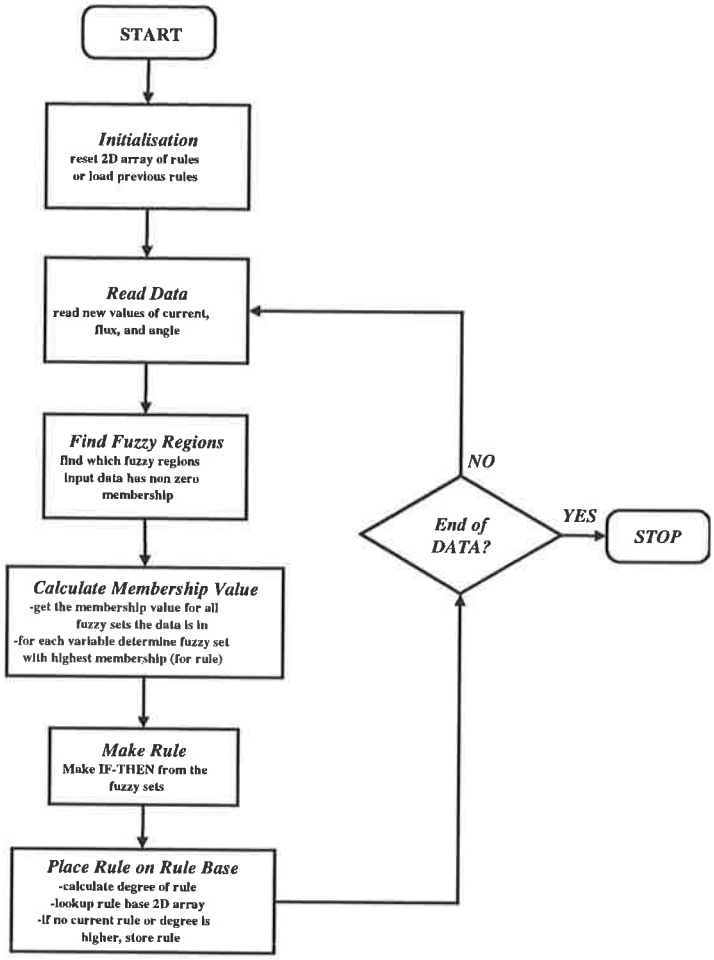


Figure 4.13 Training Algorithm

The *Calculate Membership Values* routine determines the membership value of all the fuzzy regions that each variable is a member of, as found from the previous subroutine. As the regions are simple triangular functions, this is easily calculated from the value of the variable, as was shown in Figure 4.11. This subroutine then determines which region each variable has its highest membership, and passes the label of this region, and the membership value to the next subroutine.

The *Make Rule* routine takes the labels of the fuzzy sets determined in the previous function and creates the fuzzy *If - Then* rule from these sets. It determines the degree of this rule by multiplying together the membership value of each variable in these fuzzy sets (as shown in equation 4.35).

The *Place Rule on Rule Base* subroutine stores the rule determined in the previous routine in the two-dimensional rule array. Firstly, it looks up the point on the array referenced by the two input labels. If there is no rule stored at this point already then the output fuzzy set label is stored at this point as well as the rule degree. If there is already a rule stored at this

point then the output label already stored on the table and the new label is compared. If these are the same, then an identical rule has been generated and the new rule does not need to be stored. If the output labels are different then the degrees between the new rule and the stored rule are compared. If the new rule has higher degree, then the new fuzzy set label and rule degree replaces the present one in the array.

4.4.3 Experimental Data used for the Training System

Before the training phase can begin, the two sources of training data are required. The data for the first training step, which used the static flux linkage curves was gained experimentally, as was detailed in Section 2.8 and Appendix A. The data for the second training set needed an experimental test bed that could provide measurements of current, voltage, and the angle of the SR motor under wide ranging speeds and loads. The experimental set up to achieve this is the same hardware system that will be described in detail in Appendix C. In this system, the four phase SR motor is controlled using a DSP based controller board, and isolated current and voltage transducers are to measure the current and voltage in each phase of the motor. To measure the real time rotor angle during the dynamic operation an 8 bit, 256 point absolute encoder was attached to the motor shaft.

A dc generator was also connected to the SR motor shaft to provide a variable load in order to take measurements at wide ranging dynamic speed and load conditions. The desired load that is placed on the motor is adjusted by varying the load resistance value connected to the dc generators armature. In this set up, the load can be rapidly switched during the test by opening or closing a mechanical switch that is connected between the load and the dc generator.

To run the dynamic measurement tests, the speed of the motor was varied by adjusting the speed reference signal of the DSP controller and adjusting the load via the dc machine. Measurements of voltage, current, and angle were taken while the motor was running, which are then down loaded to a PC. LabView software (which was described in Section 2.8 and Appendix A) was used to automatically convert the raw measured signals from the sensors into actual voltages in volts, currents in amperes, and rotor angle in mechanical degrees. LabView was also used to find the flux linkage of the motor from the measured voltage and current, by numerical integration of the motor phase voltage equation (in the same manner as for the static flux linkage curve measurements described in Section 2.8 and Appendix A).

The experimental set up was used to measure real time operational points of the SR motor under a wide range of operating conditions. These included transient and steady state speeds, step changes in load, and chopping and single pulse mode. Each test provided a

set of measured input-output data points of flux linkage, current, and rotor position to be used in the second training phase. In total over 30000 data points were used for the training.

Extensive experimental waveforms from the SR motor will be shown and discussed in depth in Chapter 6. Therefore, to avoid repetition here, sample sets of experimental data can be viewed in Chapter 6.

The amount of data that is required to be measured in the dynamic tests and used for training data can not be exactly specified. However, it can be said that the accuracy of the model, up to a point, will increase with an increase in the data processed during the training phase. It is important that data that is measured during the training phase should be measured from as many motor operating conditions as possible including wide ranges of currents, speeds, and loads. This will ensure that the model developed from the dynamic measurement training phase will include real time operating effects seen in a wide range of motor operating conditions. This is important because if data from a wide range of *real time* conditions is used for training, then the developed motor model will be able to predict the rotor position more accurately from real time measurements of current and flux.

4.4.4 Results of Training with Static Curves and Real Time Operating Data

As it was stated previously, the first step in generating the fuzzy knowledge base is to use the static magnetisation data from the measured static flux linkage versus current and angle characteristics of the motor phases. Each point on the motor's magnetisation curve represents an input-output data pair that can be used in the training phase. This is because each point on the curve represents an *input* set of flux linkage and current and an *output* value of angle.

The measured magnetisation characteristics which were measured from the motor were previously detailed in Figure 2.11 Every point in the characteristics was saved to one data file as an numerical array with a three column width, and with each row representing one input-output data pair (with one column representing flux linkage, current, and angle respectively). This data file was then read by the training algorithm as detailed in Section 4.4.2 to generate the fuzzy rule base from the data pairs.

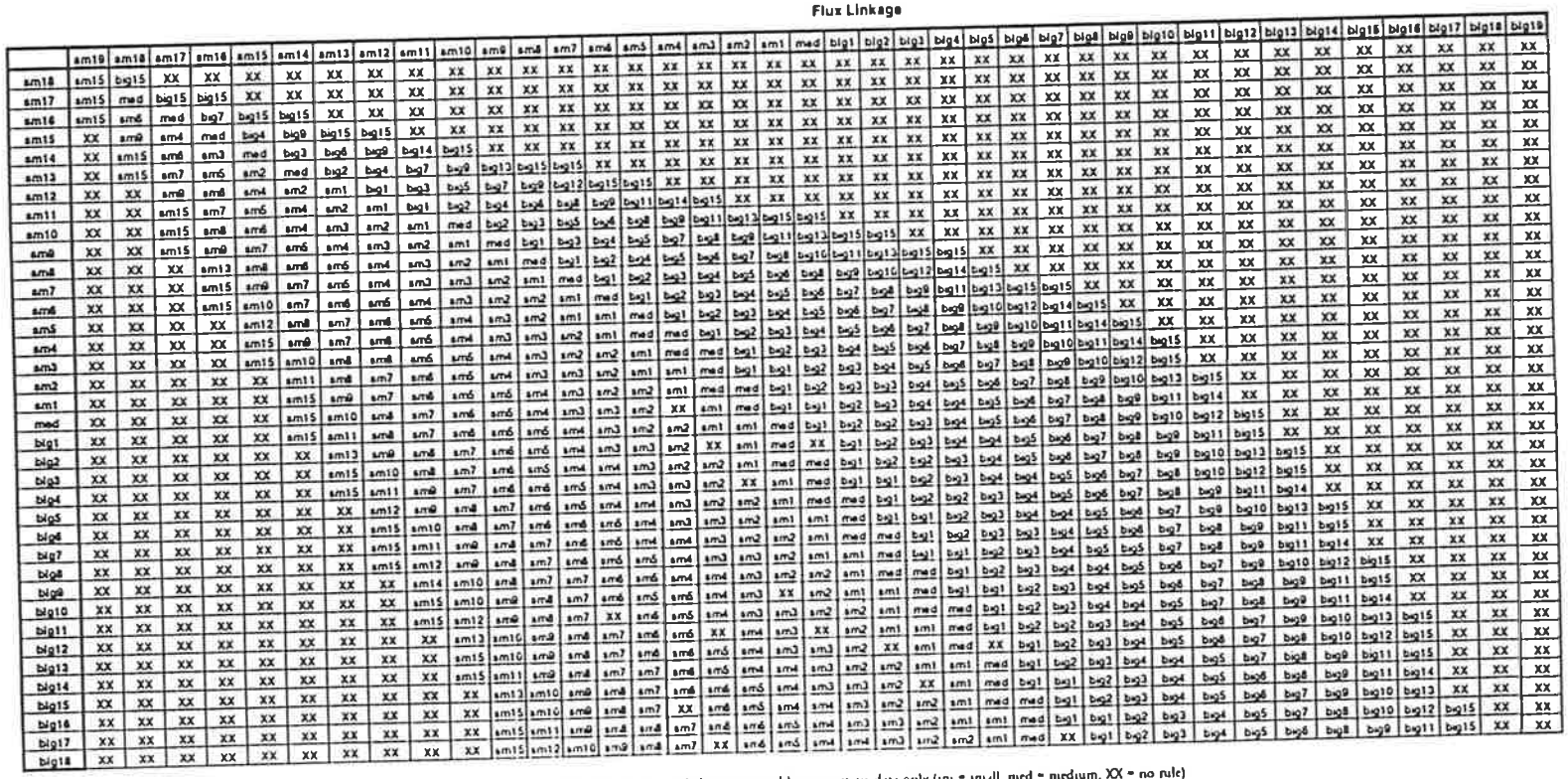


Figure 4.14 Fuzzy rule base generated by using static data only (sm = small, med = medium, XX = no rule)

Flux Linkage

Current

	sm19	sm18	sm17	sm16	sm15	sm14	sm13	sm12	sm11	sm10	sm9	sm8	sm7	sm6	sm5	sm4	sm3	sm2	sm1	med	big1	big2	big3	big4	big5	big6	big7	big8	big9	big10	big11	big12	big13	big14	big15	big16	big17	big18	big19
sm18	sm12	big15	XX	XX	XX	XX	XX	XX	XX	XX	XX	XX	XX	XX	XX	XX	XX	XX	XX	XX	XX	XX	XX	XX	XX	XX	XX	XX	XX	XX	XX	XX	XX	XX	XX	XX	XX	XX	XX
sm17	sm15	med	big15	big15	XX	XX	XX	XX	XX	XX	XX	XX	XX	XX	XX	XX	XX	XX	XX	XX	XX	XX	XX	XX	XX	XX	XX	XX	XX	XX	XX	XX	XX	XX	XX	XX	XX	XX	XX	XX
sm16	sm15	sm6	med	big7	big15	big15	XX	XX	XX	XX	XX	XX	XX	XX	XX	XX	XX	XX	XX	XX	XX	XX	XX	XX	XX	XX	XX	XX	XX	XX	XX	XX	XX	XX	XX	XX	XX	XX	XX	XX
sm15	sm15	sm9	sm4	med	big4	big9	big15	big15	big13	XX	XX	XX	XX	XX	XX	XX	XX	XX	XX	XX	XX	XX	XX	XX	XX	XX	XX	XX	XX	XX	XX	XX	XX	XX	XX	XX	XX	XX	XX
sm14	XX	sm12	sm6	sm3	med	big3	big6	big9	big14	big15	big15	XX	XX	XX	XX	XX	XX	XX	XX	XX	XX	XX	XX	XX	XX	XX	XX	XX	XX	XX	XX	XX	XX	XX	XX	XX	XX	XX	XX
sm13	XX	sm14	sm7	sm4	sm2	med	big2	big4	big7	big9	big13	big15	big15	XX	XX	XX	XX	XX	XX	XX	XX	XX	XX	XX	XX	XX	XX	XX	XX	XX	XX	XX	XX	XX	XX	XX	XX	XX	XX
sm12	XX	sm15	sm9	sm6	sm4	sm2	med	big1	big3	big6	big7	big9	big12	big15	big15	XX	XX	XX	XX	XX	XX	XX	XX	XX	XX	XX	XX	XX	XX	XX	XX	XX	XX	XX	XX	XX	XX	XX	XX
sm11	XX	XX	sm13	sm7	sm5	sm4	sm2	mod	big1	big2	big4	big6	big9	big9	big11	big14	big15	XX	XX	XX	XX	XX	XX	XX	XX	XX	XX	XX	XX	XX	XX	XX	XX	XX	XX	XX	XX	XX	XX
sm10	XX	XX	sm14	sm8	sm6	sm4	sm3	sm2	med	mod	big2	big3	big5	big8	big9	big11	big13	big15	XX	XX	XX	XX	XX	XX	XX	XX	XX	XX	XX	XX	XX	XX	XX	XX	XX	XX	XX	XX	XX	XX
sm9	XX	XX	sm15	sm9	sm7	sm5	sm4	sm3	sm2	sm1	mod	big1	big3	big6	big8	big9	big11	big13	big15	XX	XX	XX	XX	XX	XX	XX	XX	XX	XX	XX	XX	XX	XX	XX	XX	XX	XX	XX	XX	XX
sm8	XX	XX	XX	sm13	sm8	sm6	sm6	sm4	sm3	sm2	sm1	mod	big1	big2	big4	big4	big5	big7	big9	big11	big15	XX	XX	XX	XX	XX	XX	XX	XX	XX	XX	XX	XX	XX	XX	XX	XX	XX	XX	XX
sm7	XX	XX	XX	sm14	sm9	sm7	sm6	sm4	sm3	sm3	sm2	sm1	mod	big1	big2	big3	big4	big5	big6	big8	big9	big10	big12	big14	big15	XX	XX	XX	XX	XX	XX	XX	XX	XX	XX	XX	XX	XX	XX	XX
sm6	XX	XX	XX	sm15	sm10	sm7	sm6	sm5	sm4	sm3	sm2	sm2	sm1	mod	big1	big2	big3	big4	big5	big6	big7	big8	big9	big11	big13	big15	XX	XX	XX	XX	XX	XX	XX	XX	XX	XX	XX	XX	XX	XX
sm5	XX	XX	XX	XX	sm12	sm8	sm7	sm5	sm5	sm4	sm3	sm2	sm1	sm1	mod	big1	big2	big3	big4	big5	big6	big7	big8	big9	big11	big12	big15	XX	XX	XX	XX	XX	XX	XX	XX	XX	XX	XX	XX	XX
sm4	XX	XX	XX	XX	sm14	sm9	sm7	sm6	sm5	sm4	sm3	sm3	sm2	sm1	mod	mod	big1	big2	big3	big4	big5	big6	big7	big8	big9	big10	big11	big14	big15	XX	XX	XX	XX	XX	XX	XX	XX	XX	XX	XX
sm3	XX	XX	XX	XX	sm15	sm10	sm8	sm6	sm6	sm5	sm4	sm3	sm3	sm2	sm1	mod	mod	big1	big2	big3	big4	big5	big6	big7	big8	big9	big10	big11	big14	big15	XX	XX	XX	XX	XX	XX	XX	XX	XX	XX
sm2	XX	XX	XX	XX	XX	sm11	sm8	sm7	sm6	sm5	sm4	sm3	sm3	sm2	sm1	sm1	mod	big1	big2	big3	big4	big5	big6	big7	big8	big9	big10	big12	big13	XX	XX	XX	XX	XX	XX	XX	XX	XX	XX	XX
sm1	XX	XX	XX	XX	XX	sm14	sm9	sm7	sm6	sm6	sm5	sm4	sm3	sm2	sm2	sm1	mod	mod	big1	big2	big3	big3	big4	big5	big6	big7	big8	big9	big10	big13	big15	XX	XX	XX	XX	XX	XX	XX	XX	XX	XX
med	XX	XX	XX	XX	XX	sm14	sm10	sm8	sm7	sm6	sm6	sm4	sm3	sm3	sm2	sm2	sm1	mod	big1	big1	big2	big3	big4	big4	big5	big6	big7	big8	big9	big11	big14	big15	XX	XX	XX	XX	XX	XX	XX	XX	XX
big1	XX	XX	XX	XX	XX	sm15	sm11	sm8	sm7	sm6	sm6	sm5	sm4	sm3	sm2	sm2	sm1	mod	big1	big2	big3	big4	big5	big6	big7	big8	big9	big10	big12	big15	XX	XX	XX	XX	XX	XX	XX	XX	XX	XX
big2	XX	XX	XX	XX	XX	XX	sm13	sm9	sm8	sm7	sm6	sm6	sm4	sm3	sm3	sm2	sm1	sm1	mod	mod	big1	big2	big3	big4	big4	big5	big6	big7	big8	big9	big11	big13	XX	XX	XX	XX	XX	XX	XX	XX	XX
big3	XX	XX	XX	XX	XX	XX	sm14	sm10	sm8	sm7	sm6	sm5	sm4	sm4	sm3	sm3	sm2	sm1	mod	mod	big1	big2	big2	big3	big4	big5	big6	big6	big7	big8	big10	big12	big15	XX	XX	XX	XX	XX	XX	XX	XX
big4	XX	XX	XX	XX	XX	XX	sm15	sm11	sm9	sm7	sm6	sm6	sm5	sm4	sm3	sm3	sm3	sm2	sm2	sm1	mod	mod	big1	big1	big2	big3	big4	big5	big5	big6	big7	big9	big10	big12	big15	XX	XX	XX	XX	XX	XX
big5	XX	XX	XX	XX	XX	XX	XX	sm12	sm9	sm8	sm7	sm6	sm6	sm4	sm4	sm3	sm3	sm2	sm2	sm1	mod	mod	big1	big2	big2	big3	big4	big5	big5	big7	big7	big9	big10	big14	XX	XX	XX	XX	XX	XX
big6	XX	XX	XX	XX	XX	XX	XX	sm15	sm10	sm8	sm7	sm6	sm5	sm4	sm4	sm3	sm3	sm2	sm1	sm1	mod	big1	big1	big2	big3	big4	big4	big5	big5	big7	big8	big10	big13	big15	XX	XX	XX	XX	XX	XX
big7	XX	XX	XX	XX	XX	XX	XX	sm15	sm11	sm9	sm8	sm7	sm6	sm5	sm4	sm4	sm3	sm2	sm1	sm1	mod	big1	big2	big3	big4	big4	big5	big5	big7	big8	big9	big11	big15	XX	XX	XX	XX	XX	XX	XX
big8	XX	XX	XX	XX	XX	XX	XX	sm15	sm12	sm9	sm8	sm7	sm6	sm6	sm4	sm4	sm3	sm2	sm1	sm1	mod	big1	big1	big2	big3	big4	big5	big5	big7	big7	big9	big11	big14	XX	XX	XX	XX	XX	XX	XX
big9	XX	XX	XX	XX	XX	XX	XX	XX	sm14	sm10	sm8	sm7	sm6	sm6	sm4	sm4	sm3	sm2	sm2	sm1	mod	mod	big1	big2	big3	big4	big4	big5	big6	big7	big8	big10	big12	big15	XX	XX	XX	XX	XX	XX
big10	XX	XX	XX	XX	XX	XX	XX	XX	sm15	sm10	sm9	sm8	sm7	sm6	sm6	sm4	sm4	sm3	sm3	sm2	sm1	mod	mod	big1	big2	big3	big4	big4	big5	big6	big7	big8	big10	big12	big15	XX	XX	XX	XX	XX
big11	XX	XX	XX	XX	XX	XX	XX	XX	sm15	sm12	sm9	sm8	sm7	sm7	sm6	sm5	sm4	sm3	sm3	sm2	sm2	sm1	mod	mod	big1	big2	big3	big4	big4	big5	big6	big7	big9	big11	big14	XX	XX	XX	XX	XX
big12	XX	XX	XX	XX	XX	XX	XX	XX	XX	sm13	sm10	sm9	sm8	sm7	sm6	sm5	sm5	sm4	sm3	sm3	sm2	sm1	sm1	mod	mod	big1	big2	big2	big3	big4	big5	big6	big7	big9	big10	big13	big15	XX	XX	XX
big13	XX	XX	XX	XX	XX	XX	XX	XX	XX	sm15	sm10	sm9	sm8	sm7	sm6	sm6	sm5	sm4	sm4	sm3	sm3	sm2	sm2	sm1	mod	mod	big1	big2	big3	big4	big4	big6	big7	big8	big10	big13	big15	XX	XX	XX
big14	XX	XX	XX	XX	XX	XX	XX	XX	XX	sm15	sm11	sm9	sm8	sm8	sm7	sm6	sm6	sm5	sm4	sm4	sm3	sm2	sm2	sm1	sm1	mod	big1	big2	big3	big4	big4	big5	big7	big8	big9	big13	big14	XX	XX	XX
big15	XX	XX	XX	XX	XX	XX	XX	XX	XX	XX	sm13	sm10	sm9	sm8	sm7	sm6	sm6	sm5	sm4	sm3	sm3	sm2	sm2	sm1	sm1	mod	big1	big2	big3	big4	big5	big6	big7	big9	big12	big13	big15	XX	XX	XX
big16	XX	XX	XX	XX	XX	XX	XX	XX	XX	XX	sm15	sm10	sm9	sm9	sm7	sm7	sm6	sm5	sm4	sm4	sm3	sm3	sm2	sm2	sm1	mod	mod	big1	big2	big3	big3	big6	big7	big9	big11	big12	big15	XX	XX	XX
big17	XX	XX	XX	XX	XX	XX	XX	XX	XX	XX	sm15	sm11	sm9	sm9	sm8	sm7	sm6	sm6	sm5	sm4	sm4	sm3	sm3	sm2	sm1	sm1	mod	big1	big1	big2	big3	big4	big5	big7	big8	big10	big11	big14	XX	XX	XX
big18	XX	XX	XX	XX	XX	XX	XX	XX	XX	XX	sm15	sm12	sm10	sm9	sm8	sm7	sm7	sm6	sm6	sm5	sm4	sm4	sm3	sm2	sm2	sm1	sm1	mod	big1	big1	big2	big2	big3	big5	big6	big9	big10	big13	XX	XX	XX

Figure 4.15 Fuzzy rule base generated by using static data only (sm = small, med = medium, XX = no rule)

After training the system with all the points on the static flux linkage curves, the rule table shown in Figure 4.14 was generated. As it has been mentioned, in the rule base table, the labels XX represent the combinations of inputs for which there is no rule. For example, there is no rule for the inputs *Current is SMALL16* ***AND*** *Flux is BIG10*. The rule consequent for these inputs would be stored in the bottom left hand corner of the table. The reason for the large area that has no rules, can be easily seen if one compares this result with the magnetisation curves of the motor (Figure 2.11). The areas on the rule table with no rules correspond to the empty areas on this graph where the curves do not lie, and where the current and flux linkage data pairs cannot generate rules.

However, there are some empty rule areas which cannot be explained by this as they lie in the region of flux and current in which the curves lie. At these points, there would not have been data sets measured in the static test to produce a rule in these regions. However, this is resolved in this thesis by the real time data tests, in which there is measured data in these regions that generates corresponding rules.

The static flux linkage curves will characterise the motor to a good degree. However, as it was mentioned, real time operating effects such as mutual inductances between phases, eddy currents, temperature effects and skin effects may be significant. Therefore, as it was detailed above, the next step of the training phase involved using the measured real time operating data of current, flux linkage, and angle of the motor phases. The training algorithm for the dynamic measurement data was executed in exactly the same manner as the previous training phase with the static curves. However, in this case the training algorithm begins with the rule table already generated from the static data. Therefore, as described in Section 4.4.1.2, rules will only be added to the rule base in the second training phase if a completely new rule is produced from an input-output data pair of the dynamic tests, or if a conflicting rule is generated that has a higher rule degree than the rule already in the rule base.

After this second learning task is performed, the generated fuzzy *If - Then* rules in the fuzzy rule base determine a fuzzy logic system mapping inputs flux and current to angle according to the modeled non-linear function. After the two tests are carried out, the fuzzy system will model the non-linearity of the motor under real time conditions to a good degree.

The generated fuzzy rule base for the test motor after the second training phase is given in Figure 4.15. The modifications made to the rule base from the static data training phase are highlighted. It can be seen from this result that the real time test does make differences to the non-linear mapping of the motor model, to that created by using the static flux linkage curves alone. This difference would account for the differences in the waveforms

due to the real time operational effects that are not captured by the static magnetisation curves.

It can be seen that although there is a relatively large amount of rules stored on the look-up table fuzzy rule base, the storage requirement is not great compared to the large amount of training data which is used to generate the model, and the large number of data points which would be required for an equivalent numerical look-up table. The economy of storage essentially derives from the fact that the fuzzy sets span over a range of values and also overlap by 50% with adjacent fuzzy sets (as was shown in Figure 4.10). Therefore, any input pair of flux linkage and current will normally be members of two fuzzy sets each (as seen in Figure 4.11).

4.5 Conclusion

It was explained in previous chapters that SR motor drives need position feedback for phase commutation. Mechanical sensors attached to the motor shaft are usually used for this purpose. However, due to various disadvantages involved with mechanical sensors, a method of estimating the position without the shaft sensor may be desirable, and there have been many techniques developed which can detect the rotor position in the SR motor.

The application areas of the previous techniques, however, are limited to certain conditions. Therefore, in this chapter a new fuzzy logic based rotor position detection technique was introduced together with some background information required for the scheme.

As it has been shown in this chapter, fuzzy logic is used extensively in the new sensorless position detection scheme. Thus, an introduction to fuzzy logic was given in Section 4.2 to provide a theoretical basis for the concepts of the scheme. In the section, fuzzy sets were also introduced, as well as the fuzzy implication functions needed for fuzzy reasoning. The various compositions of fuzzy relations were described, and the compositions with crisp inputs were highlighted. Defuzzification of the consequence of the fuzzy relation is needed in the rotor position estimation scheme, and various methods of defuzzification were given.

The benefits of using fuzzy logic for the rotor position estimation scheme were given in Section 4.4. It was seen that the benefits include the ability to model and control non-linear and complex systems, without complex mathematical models. The SR motor has non-linear magnetisation characteristics and complex magnetic coupling interactions between the motor phases. Therefore, fuzzy logic methods are well suited to modelling the switched reluctance motor. It was also discussed that fuzzy models act as universal approximators, and thus it is possible to provide a mathematical model free method of

describing any SR motor. In addition it was discussed that fuzzy models offer an economy of storage space compared to position estimation methods which use numerical look-up tables to describe the motor. An important consideration which also favored the use of fuzzy logic methods was the computational complexity. It was seen that traditional mathematical model based methods are computationally expensive and thus often unpractical, which has lead to linear models being used in previous model based angle estimation schemes. However, fuzzy logic methods do not require a complex mathematical model and offer simple computations, and thus have the advantage of a fast computation time.

Another reason for the choice of fuzzy logic based methods was to provide a high level of robustness and reliability of the angle estimation scheme. As it will be detailed in Chapter 7 that, fuzzy logic methods are tolerant to a high degree of noise and errors in the input signals, and thus are well suited to motor drive environments.

In this chapter, it was shown how fuzzy logic was used in the development of a fuzzy logic based model, which is a major component of the new sensorless position detection scheme that was introduced in Section 4.3. This fuzzy model is developed by a training algorithm, which learns the motor model from measured motor data. The details of this learning system were explained in Section 4.4, where the implementation of the training scheme in the C programming language was also discussed. It was seen that there was two possible training phases for the system to learn the motor model. This included using the static magnetisation curves, and real time dynamic operation data.

The following chapter will detail the operation of the scheme after the training phase, when the fuzzy system estimates the rotor position from measurements of current and voltage. In addition, it will be seen how performance enhancement features were added to minimise the effects of noise in the measurements.

Chapter 5: The New Rotor Position Estimation Scheme: Operation and Performance Enhancement

5.1 Introduction

The main purpose of Chapter 4 was to describe in detail the background theory of the new fuzzy logic based position estimation scheme, and to detail the initial training stage of the algorithm. The method in which a non-linear fuzzy logic rule based model of the motor is developed was explained. It was seen that there were two training phases for the motor model, one which used the static data of the non-linear magnetisation curves of the motor, and the other which used dynamic real time measurement data. The training method of the fuzzy logic model provided a nonlinear model of the motor without any complex mathematical description, and therefore the developed system is commonly termed mathematically model free [142].

In this chapter, the actual operation of the rotor position estimation will be detailed. It will be seen that after the fuzzy rule based SR motor model has been generated from training, the system is available for position sensing by applying the measured voltage and current waveforms of the motor to the sensorless rotor position estimation algorithm. Details of the operation of the sensorless algorithm will be given in Section 5.2, where it is shown that that the fuzzy logic motor model acts as a nonlinear mapping of flux linkage and current to the rotor position. The steps that the algorithm performs to estimate the rotor position also will be detailed in this section. In addition, the software implementation of the position detection technique in C will also be explained.

As it was mentioned previously, a major consideration in the development of the new sensorless algorithm was the actual application in real SR motor drives. Therefore, the reliability and robustness of the algorithm was highly important. In practice, drive environments are electromagnetically noisy, due to the proximity of power electronic devices, which have high amplitude voltage and current switching transient waveforms, with low power computation circuits. Moreover, leakage inductances and coupling capacitances, which are always finite in such systems, can lead to noise voltages being induced in measurement circuits.

It will be detailed in Chapter 7 that fuzzy methods provide an inherent high level of robustness against input signal error and noise. However, to provide an extra level of robustness against the above mentioned noise and errors, two further sub-systems were developed to further enhance the performance of the developed sensorless method. These two features are the fuzzy logic based predictors of flux linkage and position, and the knowledge based optimum phase selector, which will be discussed in the following sections.

The flux linkage and rotor angle predictors are described in detail in Section 5.3. The purpose of the developed predictors is to forecast future values of flux linkage and rotor position during the operation of the sensorless algorithm. The developed predictors are implemented using a fuzzy logic rule based system, with the rules of the fuzzy prediction system being adapted during run time. The predictors are used to minimise errors by using a combination of the estimated and predicted rotor position and flux

The knowledge based optimal phase selector is also explained in Section 5.3. This sub-system is used because in the SR motor there may be more than one phase that conducts excitation current at any instant of time. For example, in a four-phase motor, normally two, and up to three phases may have some current flow, depending on the motor speed and the actual control method. If three phases were conducting current at a given instant in time, this would normally consist of two phases being turned on, with one previously excited phase having a decaying current component. Any of these current carrying phases may be used for rotor position estimation.

Theoretically, each of these phases should produce the same rotor position estimate. However, as will be explained below, in practice each phase has regions of optimal sensing, and the rotor position in the optimum sensing region will most likely be the most accurate. Nevertheless, a mathematical description describing the optimum sensing regions of a motor phase is difficult to define accurately, and would vary from motor to motor. In addition, a precise mathematical function describing the expected accuracy of a phase would also be difficult to define. However, general linguistic rules can be easily formed by a human expert, and thus in the developed scheme, the optimum phase is chosen using human intuition that is encapsulated by linguistic rules. Fuzzy logic techniques are well suited to linguistic knowledge based rules and therefore, as will be described below, a fuzzy rule based system was developed to select the optimum phase for position sensing.

In Section 5.4, the new sensorless position estimation scheme is verified using simulation waveforms of the motor. These waveforms are derived from the SR motor simulation package which was developed for this thesis, and is outlined in Appendix B. The simulation results that are given illustrate the algorithms ability under a wide range of operating conditions. These include motor startup from standstill, low and high motor speeds, low and high acceleration, chopping mode and single pulse mode currents, low and high currents, and high speed stalling of the motor. The simulation tests allowed the algorithm to be tested with motor operating conditions that were not possible to physically perform on the actual test motor. For example, very high acceleration and rotor stall at high speeds were tests which could easily be simulated, but could not be achieved safely in the test motor.

In the results that will be shown, the motor currents, voltages, and actual rotor position are detailed. The resultant estimated angle which is output by the sensorless position detection algorithm is also presented, and it will be seen that the algorithm has a high accuracy under all the simulated motor conditions.

In Chapters 6 and 7, the verification of the new sensorless algorithm is continued by detailing extensive operation details of the new scheme with actual experimental motor waveforms, with an emphasis on the high robustness and reliability of the method in real SR motor drives.

5.2 Position Estimation and Implementation in C

In the previous chapter, the training phase was described in which a fuzzy logic rule based model of the SR motor is developed using training data from both static and dynamic motor measurement data. After the learning phase is complete, the fuzzy model encapsulates the nonlinear function relating the SR motor rotor position to the flux linkage and current. The model is then utilised during the operation of the sensorless rotor position estimation scheme to calculate the rotor position from measured values of flux linkage and current. In this mode of operation, the fuzzy model is essentially used as a nonlinear mapping of flux linkage and current to angle, based on the fuzzy rule base created previously in the training phase.

The sensorless system essentially operates as follows: While the motor is running, the phase currents and voltages in each of the four phases are measured and the flux linkages are estimated by integration using the motor voltage equation (2.2). In the actual implementation of the algorithm in C, numerical, trapezoidal integration is used to calculate the flux linkage. Trapezoidal integration was used due to its relatively high accuracy and simple calculations [142], which made it well suited for real time implementation. The trapezoidal integration method used in this work is given by:

$$\psi(n) = \psi(n) + \Delta T[v(n) - Ri(n) + v(n-1) - Ri(n-1)]/2,$$
$$\psi(0) = 0 \qquad (5.1)$$

Where:

$\psi(n)$ = flux linkage at digital sample n
n = sample number
ΔT = sampling period
t = $n\Delta T$
= integration time

It should be noted that the initial flux linkage value at $t = 0$ equals zero. This is due to the fact that it is known from the motor flux linkage characteristics that when no current flows

in a motor phase that the flux linkage will also be zero. Therefore, at the end of each electrical cycle for each phase the flux linkage can be reset to zero in the integrator. As it will be discussed in Chapter 7, this feature of SR drive flux linkage estimation provides a means of reducing the effect of flux linkage offset errors, because the accumulation of these errors in each phase will not normally continue for more than one electrical cycle.

The crisp numeric flux linkage and current values from each phase are then input to the fuzzy logic rule base. These inputs will trigger the *If - Then* rules in the rule base, which have previously been created from the training phase. As it was described in the previous chapter, there is a 50% overlap between adjacent fuzzy sets, and this means that the crisp values of current and flux linkage will normally be members of two fuzzy sets. Therefore, as it will be detailed below, four rules will normally be triggered per phase measurement. Therefore, composition of multiple fuzzy rules is required, using the *Aggregation of Rules* procedure that was detailed in the previous chapter.

Note however, that when the aggregation of the rules occurs, that the measurements from each separate phase are considered separately. This means that if the current and flux measurement from one phase triggers four rules, and the measurements from another phase also triggers four rules, that these rules are not aggregated as eight rules together. Instead the four rules from each phase are aggregated separately, which will in fact produce two values of rotor position output. The reason for this is that each phase has different optimal sensing regions, and thus the accuracy of one phase is normally higher than another phase. Therefore the use of the estimated rotor angles from more than one phase requires some intelligent form of combination, and the procedure for this is described in Section 5.3.3.

In the developed method, the *If - Then* rules were composed using the Max-Product composition of the fuzzy rules, and the rules are aggregated using the union of the output of each of the individual rules (as was previously described in Section 4.2).

The aggregate of the fuzzy rules triggered by the inputs of each phase will produce an output fuzzy set in the *rotor position* fuzzy domain. This represents the estimated rotor angle that is determined by the fuzzy rule base from the measured inputs of the motor phase. A single crisp numeric value of estimated rotor position is required and thus the output fuzzy set is then converted into a single crisp value of angle using defuzzification. In this method the center average defuzzification formula (4.28) was used to determine the crisp output of angle.

Note that in practice, any method of rule composition and defuzzification may be used, but the overall procedure described above remains the same. However, in choosing the Max-Product and center average defuzzification methods, the computation speed due to

the simple calculations of these methods [140] was primarily considered. This is because the speed of computation has a direct relationship to the time needed to estimate the rotor position. As was described previously, a high computation speed is advantageous, because during the computation time, the rotor position will change from the position at the time at which the current and voltage measurements were taken for the calculation. Hence, due to the calculation time, there will be some inherent error between the estimated angle from the measurements and the actual angle at the time at which the rotor position estimate is made. Therefore, a minimisation of the calculation delay time, and the corresponding rotor position change during the calculation time is required. In addition, a short time in producing estimates is beneficial, because this means that a motor controller, which uses rotor position, would have a greater frequency of rotor position updates. This normally leads to a more accurate motor position and speed control.

Similarly, in the fuzzy logic training algorithm that was discussed in Chapter 4, the position sensing procedure was also written in the C programming language. Some of the subroutines from the learning algorithm were used again, as there were only a few minor differences. The algorithm had the following steps, which are shown in the flow-chart of Figure 5.1:

i) Initialisation
ii) Read Data
iii) Find Fuzzy Regions
iv) Calculate Membership Values
v) Determine Rule Outputs
vi) Defuzzify

The first four procedures are almost the same as explained in Section 4.4.1.2, and so will not be detailed again here. The only difference was in the *Initialisation* routine. In this case a new empty rule base was not initialised as in the training phase, but instead the two dimensional rule base array created in the training phase was loaded into memory from storage.

During each iteration, the *Read Data, Find Fuzzy Regions,* and *Calculate Membership Values* subroutines will perform the following functions: The *Read Data* subroutine will receive the numeric input values of current (from measurement) and flux linkage (found from the numerical integration of the measured voltage and current). Then the *Find Fuzzy Regions* routine will then find *every* fuzzy set in the current and flux fuzzy domain, in which the crisp numeric input values of current and flux have a non zero membership. These are then classified as the *Input Fuzzy Sets.* The *Calculate Membership Value* subroutine will then calculate the membership values of the crisp input data in all of these Input Fuzzy Sets.

Then, the Input Fuzzy Sets and their corresponding membership values are passed onto the next subroutine, which is the *Determine Rule Outputs* routine.

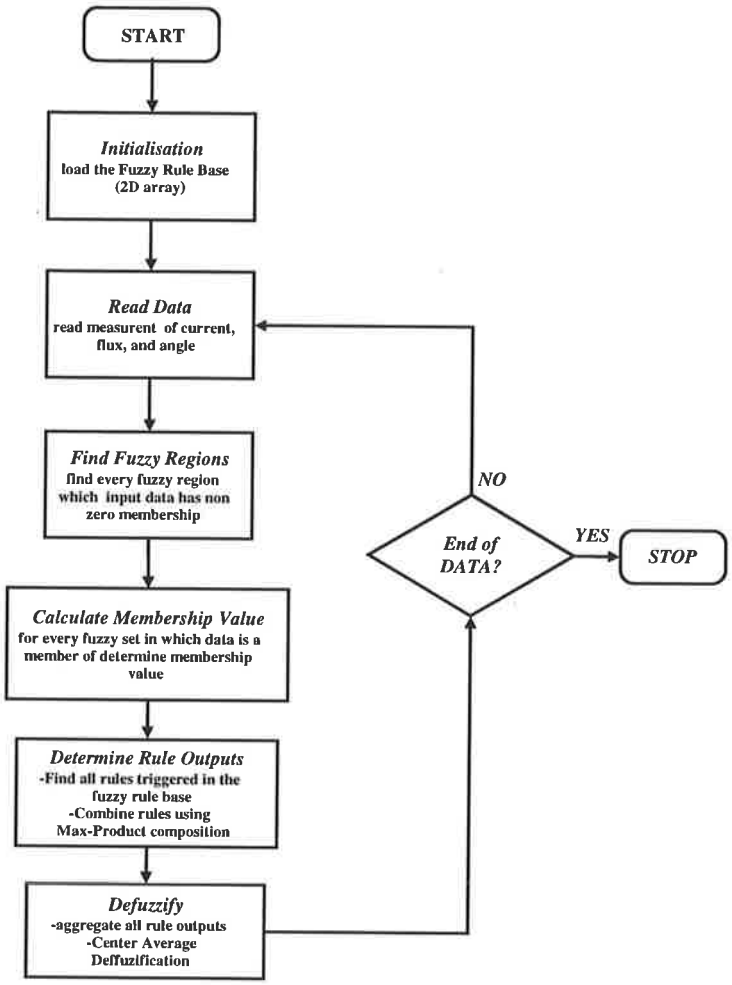


Figure 5.1 Position Sensing Routine Flow-chart.

In the *Determine Rule Outputs* Routine, all the rules that are triggered by the inputs are found. This is achieved by looking up the two dimensional rule array for every combination of the Input Fuzzy Sets, and seeing if a rule has been stored in that location. As it was shown in Chapter 4, there is a 50% overlap between adjacent fuzzy sets in each of the variables fuzzy domains. Therefore there will normally be two Input Fuzzy Sets in which each crisp value of current and flux linkage is a member of, and thus there will normally be four triggered rules per motor phase measurement.

As mentioned in Chapter 4, in the C language implementation each rule is stored on a two-dimensional array as a C language structure type that consists of the rule label and its rule degree. In this C implementation, if there is no rule stored in a given rule location on the array then the label will be XX. Thus, if the label is not XX then there is a stored rule at that location, and thus this can become a triggered rule.

As an example, if flux was found to be in sets *BIG2* and *BIG3*, and current was found to be in sets *BIG1* and *BIG2*, then four possible *If - Then* rules could be triggered with the *If* parts shown in the rules below:

If flux is *BIG2* and current is *BIG1 Then* angle is *BIG1* (5.2)

If flux is *BIG2* and current is *BIG2 Then* angle is *BIG2* (5.3)

If flux is *BIG3* and current is *BIG1 Then* angle is *BIG1* (5.4)

If flux is *BIG3* and current is *BIG2 Then* angle is *BIG2* (5.5)

The consequence (or *Then* part) of the rules are found by looking up the output fuzzy set stored in the two dimensional rule base array. If there is no rule stored at that location then the rule is not triggered.

The output of every rule that is triggered by the inputs will then be determined using the Max-Product composition (as previously detailed in Section 4.2.2). By using this method, for each rule the routine compares the two membership values of the inputs (found from the previous routine) and determines the minimum. This minimum value is then multiplied to give the *height* of the output fuzzy set that is stored in the rule array.

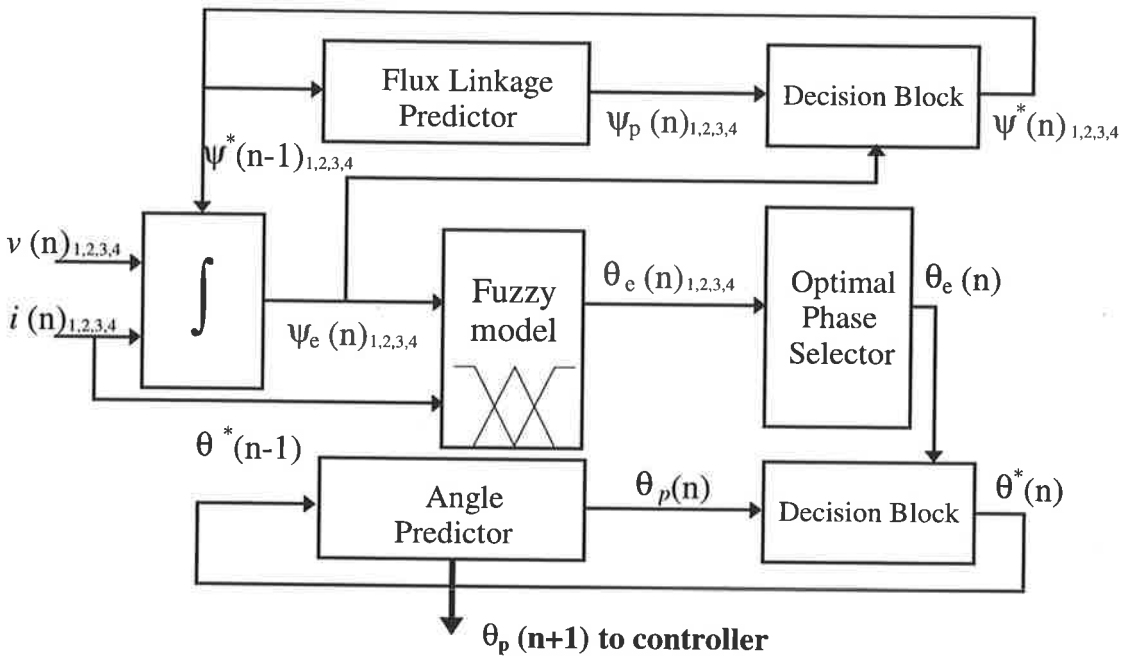
The *Defuzzify* routine aggregates all the triggered rule outputs and produces a crisp output value of angle. As it was described in Chapter 4, the center average defuzzification calculation uses the height of all the output fuzzy sets, which are found in the previous Determine Rule Outputs routine.

As it was mentioned above, all phases which are conducting current are used for position sensing, and thus there will be a crisp rotor position value found for each conducting phase using the above routine. The method of combination of these rotor position estimates from each of the phases, in a way which takes into account the change in accuracy of the phases at different rotor angles, is described in Section 5.3.3.

The above routine essentially encapsulates the algorithm used to estimate the rotor position from the fuzzy logic motor model using measurements of current and voltage only. However, additional performance enhancement features have been added so that the sensorless angle estimation algorithm copes better with measurement errors and inaccuracies found in real motor drives. These performance enhancement features use human linguistic knowledge to increase the accuracy under measurement uncertainties. One of the performance enhancement schemes uses a fuzzy logic based predictor of flux linkage and rotor angle. The other uses human intuition to pick the most desirable phase for estimating angle in order to maximize accuracy. The details of these performance enhancement features will be discussed in the following subsections:

5.3 Performance Enhancement Features

In this section, details will be shown of the two performance enhancement algorithms which were added to the angle estimation algorithm to increase the robustness against measurement error and noise. These two performance enhancement algorithms, together with the algorithms previously described above constitute the complete fuzzy logic based position estimator. A block diagram of the complete algorithm is shown in Figure 5.2. This estimator directly replaces the mechanical position sensor required by the conventional SR motor controller.



$v(n)_{1,2,3,4}$ = the four phase voltages of the SR motor

$i(n)_{1,2,3,4}$ = the four phase currents

$\psi_e(n)_{1,2,3,4}$ = the estimated four phase flux linkages (from integration)

$\psi^*(n-1)_{1,2,3,4}$ = the weighted flux of step (n - 1) used as integration constant

$\psi_p(n)_{1,2,3,4}$ = the predicted flux linkage

$\psi^*(n)_{1,2,3,4}$ = the weighted value of estimated and predicted flux linkage

$\theta_e(n)_{1,2,3,4}$ = the estimated position from the fuzzy model from all excited phases

$\theta_e(n)$ = the single weighted value of position after the phase selector

$\theta_p(n)$ = the predicted value of fuzzy position

$\theta^*(n)$ = the weighted value of estimated and predicted position

$\theta^*(n-1)$ = previous value of weighted position used for prediction

$\theta_p(n+1)$ = next step prediction of angle

Figure 5.2 The complete block diagram of the Fuzzy Logic Based Position Estimation Algorithm

As it has been mentioned previously, the sensorless position estimation algorithm was designed to have performance enhancement features, which would make it more robust to

the noise, measurement errors, and calculation errors that occur in a real motor operating environments.

Modern electric motor drives are electrically noisy environments due to the proximity of high current power circuits with small signal electronic circuits. The motor current and voltage in motor drives can be switched at high frequencies (in the low to high kHz range) with advanced power electronic switching devices. Due to leakage inductances and finite coupling capacitances, this can cause noise on any low voltage current and voltage measurement circuits and associated analog to digital converters. This noise will cause errors in the reading of the currents and voltages that are input to the sensorless algorithm ($i(n)_{1,2,3,4}$ and $v(n)_{1,2,3,4}$ in Figure 5.2). Any error in the measurement of currents and voltages will correspondingly lead to an error in the flux linkage found from integration ($\psi_e(n)_{1,2,3,4}$ in Figure 5.2), and consequently the estimated position ($\theta_e(n)_{1,2,3,4}$ in Figure 5.2).

Other flux linkage error effects that may arise in the position estimation algorithm could be due to calculation errors. These arise from any offset errors in the flux linkage integration, or errors due to the numerical integration. The accuracy of the numerical trapezoidal integration algorithm which was used in the flux estimation (equation 5.1), depends on the frequency of sampling of the signal being integrated. This is because in the trapezoidal method of integration the area of the trapezoids that approximate the integral may be significantly different according to the sample rates.

To observe this, consider the two examples shown in Figure 5.3. The area of all the strips with width Δt are added up to estimate the integral of a function $x(t)$ (where the integral in the sensorless algorithm is the flux linkage). One can see that in the case shown in case Figure 5.3 (b) where the sampling frequency has been halved, the integration is less accurate as because the trapezoids have a less accurate approximation to the area under the curve. In a similar manner, the accuracy of the flux linkage value used in the sensorless position detection algorithm, which is found from trapezoidal integration, degrades as the sample time increases.

The general analytical expression for the degradation in the accuracy of the trapezoidal integration due to larger sampling times can be found as follows [143].

If we consider the integration of a continuous function $y = x(t)$ from time $t = m$ to time $t = n$, and the sampling period is P, then there will be $N = (n-m)/P$ intervals in which there will be a trapezoidal approximation to the area beneath the curve. Each of the trapezoids will have a width P, and the area of each trapezoid will be (with reference to Figure 5.3 (a));

$$\frac{1}{2}\left[x(m)+x(k_1)\right]P, \qquad \frac{1}{2}\left[x(k_1)+x(k_2)\right]P, \ldots\ldots\ldots, \frac{1}{2}\left[x(k_{n-1})+x(n)\right]P \tag{5.6}$$

The sum of all the trapezoidal areas will equal the numerical integration of the function from time *m to n*, and it can be shown that this sum *J* is equal to:

$$J = \int_m^n x(t) \approx P\left[\frac{1}{2}x(m) + x(k_1) + x(k_2) + ... + x(k_{n-1}) + \frac{1}{2}x(n)\right] \tag{5.7}$$

In the angle estimation scheme, the estimated flux linkage waveform corresponds to integral *J*. Now if the *actual* continuous integral of the function *x(t)* between time *m* and *n* is defined as J^* (which in the sensorless estimation scheme corresponds to the *actual* motor flux waveform), then the error between the estimated integral using numerical integration and the actual integral is given by:

$$\varepsilon = J^* - J \tag{5.8}$$

It can be shown [144] for a general function *x(t)* having continuous second derivatives (which is satisfied by any real flux linkage waveform derivative), that the above error is bounded by the values:

$$\frac{(n-m).P^2}{12}M_2^* \le \varepsilon \le \frac{(n-m).P^2}{12}M_2 \tag{5.9}$$

Where:

M_2^* = Smallest value of the second derivative of *x(k)*.

M_2 = Largest value of the second derivative of *x(k)*.

The important point to note from equation (5.9) is that, in general, the integration error is directly proportional to the square of the sampling period P^2. Therefore, to minimise the integration error the sampling period should be as small as practically possible. This means that the accuracy of the flux linkage integration of the sensorless algorithm will be dependant on the sampling frequency of the current and voltage waveforms at a minimum. However, normally in an actual implemented system, the minimum period of integration is higher than the possible sampling period of the currents and voltages, and is in fact set by the minimum possible calculation time of the algorithm by the microprocessor. Therefore, the integration period *P* is equal to the sampling period of the integration signals, or the minimum integration frequency, whichever is higher.

It should also be noted from the above equation that the maximum integration error is also proportional to the highest value of the second derivative of the integrated function *x(k)*. This means that when trapezoidal integration is applied to the flux linkage estimation, the maximum error is dependent on the second derivative of the integrated current and voltage waveforms. It can be recalled that at high motor speeds when the motor operates in the single pulse mode, the current and voltage waveform are simple functions. However

due to the commutation seen in the chopping mode, the current and voltage waveforms are more complex and non-linear. It can be expected that in the single pulse mode that there are wider integration intervals in which the second derivative is lower than for the chopping mode waveform. Therefore, for the same conditions, it can be expected that the error in the integration of flux linkage in the chopping mode may be higher than in the single pulse mode.

In general, for the same waveforms, the accuracy of the flux estimation will increase with the decrease of the integration period *P*. Nevertheless, normally there will always be some error in the numerical integration, and therefore, the angle estimation algorithm should have a good *tolerance* to the flux estimation integration error at all times. This is because the scheme must be able to operate with practical systems where the sampling rate or computation rate is low due to hardware or software limitations, and thus numerical integration errors will always arise.

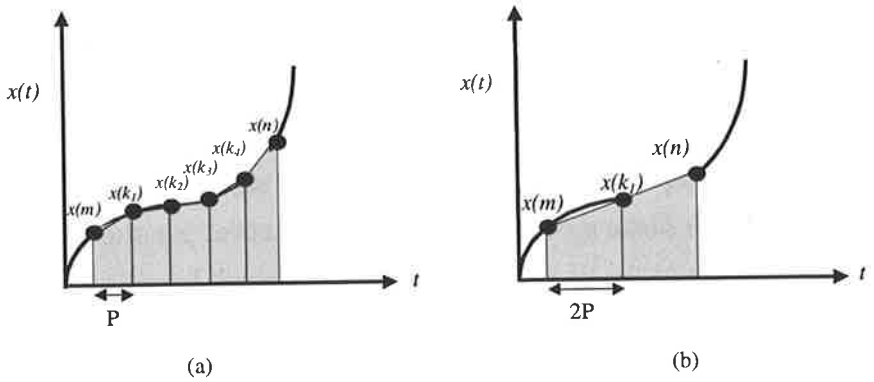


Figure 5.3 Trapezoidal integration example: (a) Sampling Period = P. (b) Sampling Period = 2P.

5.3.1 Prediction of Flux Linkage and Position

As it was mentioned previously, the robustness and reliability of the new sensorless algorithm was a highly important consideration, in order that the system would be compatible with practical SR motor drives. It will be detailed in Chapter 7, that the use of fuzzy logic based systems provides an inherent high fault tolerance against noise and errors. In addition, to provide an extra fault tolerance function to the scheme, prediction algorithms are used to forecast future values of flux linkage and rotor position, as was shown in the outline block diagram of Figure 5.2.

The prediction algorithms are implemented using fuzzy logic, and their purpose is to predict future values, so that if a measurement inaccuracy occurs, the predicted value may be used to lower the error. To achieve this, a comparison between estimated and predicted rotor position and flux values are made during each iteration. Then some combination of these is chosen in order to lessen the effect of errors.

The purpose of the predictor can be better understood if the ideal case is taken in the first instance. In the ideal case, the estimated values of flux linkage (from integration) and position (from the output of the fuzzy motor model) can be predicted accurately using the prediction algorithm. Now consider the case where for a short instant of time, the measured values of flux linkage and position are erroneous. At this time the values of the predicted values (which are predicted from the previous *correct* values of flux linkage and position) will be a good approximation to the actual values of flux and position in the machine, if the prediction algorithm is accurate. In this case the estimated values can be ignored, and instead the predicted values are used.

Of course this does not offer an ideal solution. The first question that arises is:

"If the estimated and predicted value are different, which is actually the more correct value?"

Human intuition is required to try to answer this problem, and this will be discussed below in Section 5.3.2.

An important fact about this prediction scheme is that it will be of usefulness only for *short instants of noise.* The scheme assumes that the steady state error of the measured signals is low. This is because the system will *learn* the noisy signal if it is sustained, and will thereafter not be able to make a correct prediction. However for short noise instances the noise can be very high and the predicted values can be used, based on the previous values with small error.

Potentially any form of predictor, such as neural networks, can be used in this error minimisation method. Fuzzy logic was chosen for this problem because, as mentioned previously, fuzzy methods provide the benefit of a fast execution time, due to the simple calculations used [144]. This is an advantage for real time implementation of the algorithm in an actual SR drive system.

There are also a wide array of fuzzy logic based prediction algorithms which have been developed (examples can be seen in references [145], [146], and [147]). However in this work, the *table look-up learning scheme* (as detailed in Chapter 4) was used again for these prediction methods, because fast learning and simple computations are a feature of the table look-up scheme. In addition, simple triangular fuzzy sets were again used which allowed fast computation of membership functions in real time operation.

The problem of predicting the flux linkage and angle in future steps of time is a problem of *time series* prediction. It has been demonstrated that fuzzy logic systems are excellent solutions for time-series prediction [148], [149]. This derives from the fact that a fuzzy logic system is a non-linear mapping of an input data to its output, and also that fuzzy logic controllers are universal approximators of any non-linear function [150].

The fuzzy logic predictor operates by generating fuzzy rules from the numerical input-output data pairs of previous data points, each separated by a constant step of time, and creating an adaptive *predicting fuzzy rule base.* The rules on this predicting fuzzy rule base define the relationship between the present value of data and past values of data. The fuzzy predictor can then make a prediction from this predicting fuzzy rule base.

For example, if $x(k)$, $(k = 1,2,3, ...)$ is a time series of previous rotor position values (or previous flux linkage values) each separated with a constant time interval (which is equal to the rotor position computation period of the sensorless algorithm), and the future value of $x(k+l)$, at time step $k+l$ in the future, is to be determined from a window of n previous measurements $x(k-n+1)$, $x(k-n+2)$,....., $x(k)$, then $k-n$ input-output pairs ($[x^1, x^2, ..., x^n]$,$[y^1]$) can be formed, where $x^1, x^2, ..., x^n$ are the inputs and y^1 is the output. These input-output pairs will be:

$$\begin{aligned} &[x(k-n),...., x(k-1)] && \rightarrow [x(k)] \\ &[x(k-n-1),...., x(k-2)] && \rightarrow [x(k-1)] \\ &..... \\ &[x(1),...., x(n)] && \rightarrow [x(n+1)] \end{aligned} \qquad (5.10)$$

In the above equation, the symbol $\rightarrow$ indicates some function relating a future value (eg. $x(n+1)$) with previous values (eg $x(1),...., x(n)$).

Every time a new measurement is made, a new input-output pair consisting of the previous values $[x(k-n),...., x(k-1)]$, and the present value $[x(k)]$ is made, and thus a new rule can be formed relating previous values to future values. In this manner, the predicting fuzzy rule base is adaptive in nature, and will change during the actual operation according to the system input values.

The input-output data pairs described above are used to create rules in the predicting fuzzy rule base in exactly the same procedure as in Steps A to D in Section 4.4.1.2. The adaptive fuzzy predicting rule base can then be used to predict a future data value $x(k+l)$, from the previous n data points. Here the value l is a chosen integer which represents the value of $x(k)$ at the data point $k+l$ in the future (where each data point is separated in time by one computation period of the sensorless algorithm). Essentially, the predicting fuzzy rule base is used as the non-linear mapping between the previous n data points and $x(k+l)$.

To make a prediction, the previous values $x(k-n+1)$, $x(k-n+2)$,....., $x(k)$, are used as the crisp input to the fuzzy predictor. The inputs will trigger rules in the fuzzy predicting rule base and this will give an aggregated fuzzy output. This output is then defuzzified to give the crisp prediction of $x(k+l)$. The operation of the fuzzy predictors with the predicting fuzzy rule base, uses the same methods of rule composition and deffuzification as described previously in Section 5.2, and so the details are not described again at this point.

In the case of the fuzzy predictors of angle and flux linkage, all the input and output fuzzy regions needed to create the rules (as described in Step A of Section 4.4.1.2) are exactly the same because both the output and inputs are all the *same* variable. For example, in the rotor angle predictor all the inputs are previous values of rotor angle and the output is a future value of rotor angle. This means that all the inputs and outputs would have the same fuzzy domain, namely the fuzzy domain of rotor position

The input and output domains used for creating the rules and prediction were the same fuzzy partitions shown in Figure 4.10 of the previous chapter. Therefore, the fuzzy domain region for all the inputs and outputs of the rotor angle predictor ranges from 0 to 30 degrees as shown in Figure 4.10 (c). Correspondingly, the fuzzy domain for all the inputs and outputs of the flux linkage predictor are also seen in Figure 4.10 (a). The flux predictor and angle predictor are separate, in that they have different input-output fuzzy domains and rule bases, but they use the same procedure of creating the prediction rule bases, and predicting future values.

It should be noted that in this fuzzy predictor, both learning and prediction occurs simultaneously, unlike the previously described training method in Chapter 4. Specifically, at every iteration, the values of flux linkage and angle are used to modify the fuzzy rule base by creating a new rule that maps past to present values. Then the updated rule base is used to predict the future value of flux linkage and angle. Hence this scheme can be classified as an adaptive fuzzy system.

In this application values of l=1 and n=4 were used for the flux linkage predictor, and l=*1* and *2* and n=*4* are chosen for the angle predictor (where l and n are the parameters defined above). Therefore for any iteration k, the four previous and present values of flux linkage: $[\psi_p(k-n+1),\ \psi_p(k-n+2),\ \psi_p(k-n+3),\ \psi_p(k)] = [\psi_p(k-3), \psi_p(k-2),\ \psi_p(k-1),\ \psi_p(k)]$, are used to predict the next iteration's value of flux linkage $\psi_p(k+l) = \psi_p(k+1)$.

Similarly, the previous four values of angle are used to predict the next two values in time of angle $\theta_p(k+1)$ and $\theta_p(k+2)$. Two values are predicted because the next value of angle $\theta_p(k+1)$ can be used to compare the predicted and estimated value, and the next value in time after this angle $\theta_p(k+2)$ can also be used by the motor controller.

A flow-chart of the prediction algorithm for the flux linkage can be seen in Figure 5.4. The operations shown in this block diagram were written in the C programming language. Although the flux and angle prediction operates separately, the same algorithm is used, and therefore in the figure the values of $x(k)$ represent either flux linkage or rotor position. However, for the rotor position predictor the value $x(k-5)$ is also used in the rule learning block, and $x(k+2)$ is predicted by the prediction block.

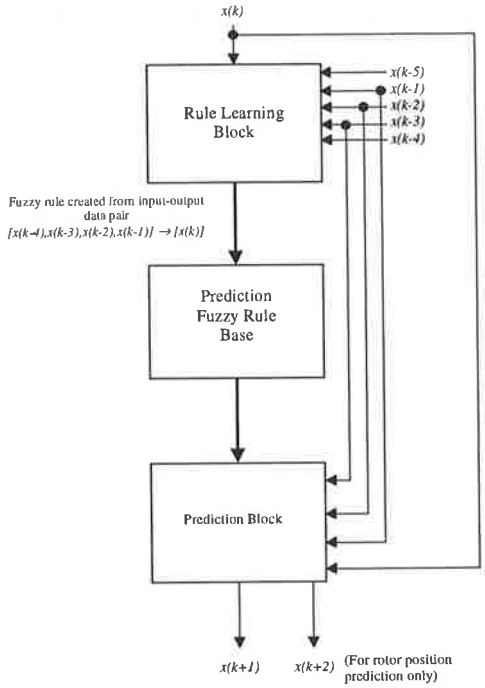


Figure 5.4 Flow-chart of the Prediction Algorithm

As it can be seen, in each iteration both training of the fuzzy rule base and prediction from the rule base occurs. Specifically, when a new value of flux linkage or rotor position is estimated by the integrator or fuzzy model respectively (as outlined in Figure 5.2), it is first passed into the rule learning block, together with previous iteration values. For the flux linkage prediction, the rule learning block creates a new rule and modifies the rule table in the manner described above, from the new input-output data pair consisting of the present value *x(k)* and the previous four values x(*k-1*), *x(k-2), x(k-3),* and *x(k-4).* As the fuzzy rules of the rotor predictor have four previous inputs and two output predicted values, *x(k)* and *x(k-1)* are used as the output values, and *x(k-2), x(k-3), x(k-4),* and *x(k-5)* are used as the input values of the input-output data pair.

Hence for the flux prediction, these values form an input-output data pair which is used to define a fuzzy rule relating the previous four values to the present value *x(k).* The input-output data pair can be written as:

$$[x(k\text{-}4),\ x(k\text{-}3),\ x(k\text{-}2),\ x(k\text{-}1)],\ \rightarrow [x(k)] \tag{5.11}$$

For the rotor position prediction, the input output data pair relates four previous values to the present value and the value of the previous step

$$[x(k\text{-}5),\ x(k\text{-}4),\ x(k\text{-}3),\ x(k\text{-}2)],\ \rightarrow [x(k\text{-}1),\ x(k)] \tag{5.12}$$

This rule can then modify the fuzzy rule base so that the fuzzy rules which predict the next values from the previous four values is continuously adapted with each new measurement.

After this learning block, the prediction routine is executed, which estimates the next iteration value *x(k+1)* (and *x(k+2)* for the angle prediction), from the values of *x(k)*, *x(k-1)*, *x(k-2)*, and *x(k-3)*. In this case the inputs presented to the fuzzy rule base are:

$$[x(k-3),\ x(k-2),\ x(k-1),\ x(k)] \tag{5.13}$$

As it was described above, the prediction is made by using the rules in the adaptive fuzzy rule base by fuzzifying the crisp input values, performing rule composition, and defuzzifying the output of the rules to produce a crisp predicted value. Note that in this routine, the present measured value *x(k)* is used as both an *output* value of the input-output data pair during the rule adaptation stage, and an *input* value to the fuzzy rule base in the prediction stage.

It should also be noted that the same C level routines for operations such as fuzzifying, rule composition, and defuzzifying could be commonly used in this prediction algorithm as well as the previously described angle prediction and training algorithms. This allows a modular function approach to the programming of the complete sensorless algorithm.

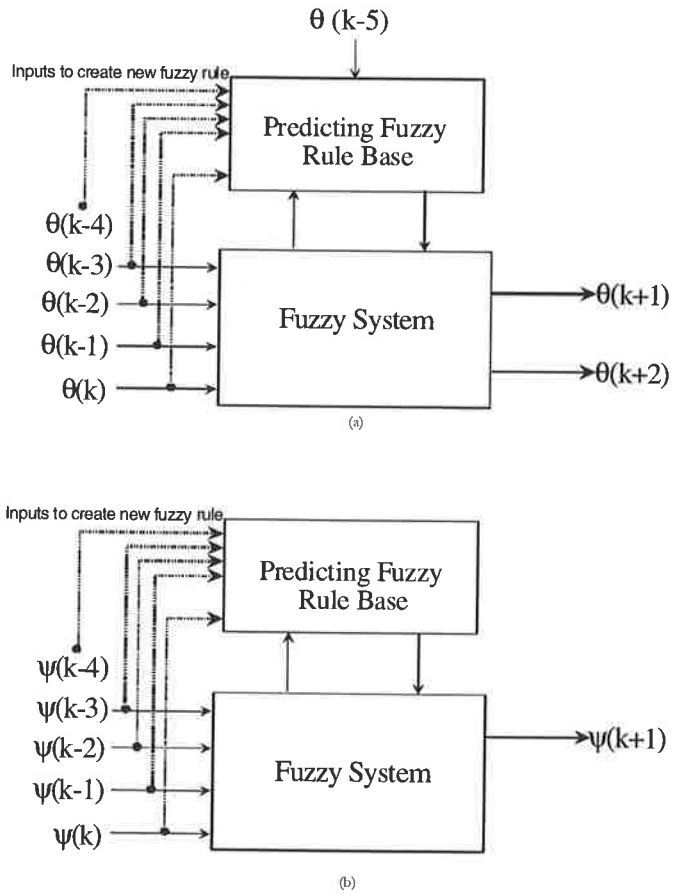


Figure 5.5 Fuzzy Angle (a) and (b) Flux Linkage Predictor.

It can be deduced that initially there will be no previous values in which the predictor can either make a rule or predict a value. As the prediction is made from the previous four inputs, it will take four iterations of the algorithm before there are enough previous values for the predictors to create a rule and make a prediction. However, although theoretically the predictor could start to make predictions after the fourth iteration (when the first rule is created), it can be expected that there may be some lagging time before the predictor will have enough rules stored on the rule base to make a prediction.

As mentioned above, the fuzzy angle predictor and fuzzy flux linkage predictors are used in the sensorless algorithm as a performance enhancement technique to overcome errors. The block diagram of the predictors shown above in Figure 5.5 are thus a detail of the predictors shown in the complete sensorless algorithm diagram shown above in Figure 5.2. However, it should be noted that the predicted value of flux linkage $\psi(k+1)$ used in Figure 5.5 (b) is re-labeled as $\psi_p(n)$ in Figure 5.2. The two labels are used to differentiate between the general explanatory case shown in Figure 5.5 and the specific case of the rotor position detection scheme shown in Figure 5.2. In addition, the predicted values of rotor angle $\theta(k+1)$ and $\theta(k+2)$ in Figure 5.5 (a) are re-labeled as $\theta_p(n)$, and $\theta_p(n+1)$ respectively in Figure 5.2. The labels given in Figure 5.2 will be used to refer to the predicted values in the following sections.

5.3.2 Weighting of Predicted and Estimated Values for Error Correction

As can be seen in the block diagram of Figure 5.2, the predicted values of rotor position $\theta_p(n)$ (from the angle predictor), and flux linkage $\psi_p(n)$ (from the flux linkage predictor), are used in conjunction with the estimated values of flux linkage $\psi_e(n)$ (from integration) and rotor position $\theta_e(n)$ (from the fuzzy model output). In the ideal case, the predicted and estimated values should be exactly the same. However, as mentioned above these may differ due to errors. In this case either the predicted values or the estimated values may be used, and a decision must be made as to which value should be chosen.

In this system a knowledge based, heuristic decision maker was implemented, which places a weighting on both the predicted and estimated values. It then usually uses some combination of the two values. This decision making algorithm was termed a *Decision Block*. From Figure 5.2, it can be seen that the decision blocks of the flux linkage and angle produce a final weighted value $\psi^*(n)$ and $\theta^*(n)$ respectively.

The principal purpose of these decision blocks is to implement human intuition in selecting a good weighting between the estimated and predicted values of flux linkage and angle. For instance, it can be said that under steady state speeds, the rotor position and flux linkage trajectories will be regular and periodic functions. Under this condition the fuzzy

predictors will be able to forecast with good accuracy (as will be demonstrated in the results below, and is also shown for similar fuzzy logic based predictors in references [138], [139]). Therefore, if the predicted and estimated values differ under steady speeds, when the waveforms are regular and periodic, then this would more likely be from calculation or integration errors in the estimated values. Hence more weighting can be placed on the predicted value.

However, during transients the fuzzy predictors may not perform as well, due to the learning period always required with new events. In this case, if there is a difference between the estimated and predicted values then the predicted value would more likely be in error, and thus more weighting will be placed on the estimated value.

Thus under *steady* speeds and conditions, it can be intuitively said that the confidence in predicted values will be *high*, whereas under transient speeds and conditions, confidence will be *low*. In addition, it can be said that the confidence in the predicted values will be *higher* for *low* acceleration values than for *high* acceleration values.

In the above discussion, *high*, *low* and *steady* are linguistic terms that contain a certain amount of fuzziness. Therefore choosing from the predicted and estimated values of flux and position can be efficiently achieved using a fuzzy system. The developed fuzzy system determines the weighting (or confidence) of the predicted value from 0 to 100 percent, with the estimated value consisting of the remaining weight. In this way the fuzzy system, which is called the Decision Block, attempts to make the best choice of weighting to derive the correct value.

An example illustration of the Decision Blocks for the rotor position and flux linkage values is shown in Figure 5.6. As one can see in the Figure, the inputs to the Decision Block are the estimated and predicted values, as well as an acceleration factor (which is defined below). This outputs a weighted value of the estimated and predicted values, using the linguistic knowledge described above.

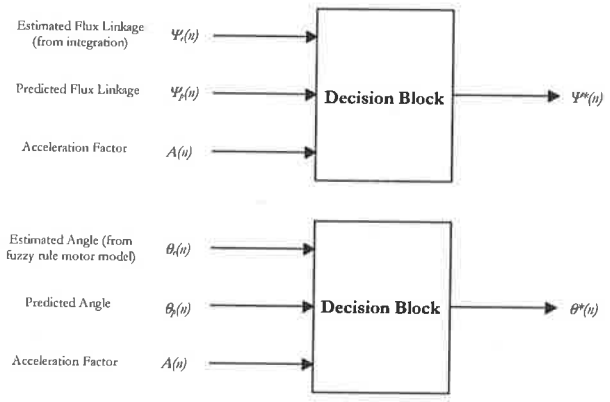


Figure 5.6 Decision blocks

As the acceleration input shown in Figure 5.6 can not be directly measured in this application, an approximation is made based on a block of previous angle measurements. Instead of acceleration, an *acceleration factor* is used which gives an approximation of the actual acceleration. This approximation can be used in this application because only the *relative* acceleration is important (eg. *High* or *Low)*, and not the actual numeric value. Therefore an acceleration factor A_n is defined as:

$$A_n = \frac{\theta_n - \theta_{n-k}}{k\Delta T} - \frac{\theta_{n-1} - \theta_{n-1-k}}{k\Delta T} \tag{5.14}$$

Here, $\theta_{(n)}$ is the rotor angle at step n and ΔT is the time between each iteration, and k and l were chosen to both equal 5. Therefore, in essence, this equation estimates the average speed over the last six iterations (ie. over iteration n to n-5 where n is the last estimated position value), and compares it to a previous estimated average speed measured over n-5 to n-10). The difference of these two values provides an estimate of the relative motor speed transient magnitude.

In the simulation results which will be shown in a later section of this chapter, the above equation (5.13) is used for the Decision Block. However in the experimental results which are detailed in the next chapters the acceleration factor was modified to use the average of the previous 3 estimated acceleration factors given by (5.14). Therefore, if the present estimated acceleration factor is labeled A_n, then the acceleration factor used by the decision block is given by:

$$(A_n + A_{n-1} + A_{n-2}) / 3 \tag{5.15}$$

The reason for this alternate method for the actual experimental system, is that in the actual system, noise, measurement, and calculation errors have some effect that is not seen in the simulations. Therefore, filtering of the acceleration factor estimates by averaging the previous values (which are calculated from motor position estimates) lessens the effect of angle estimate noise on the calculation of the acceleration factor presented to the decision block. Note that more sophisticated filtering methods are possible, however as it was stated above, the scheme was optimised for the actual real time implementation in SR drives, and thus where possible simple calculations were desired, to minimise the real time computation requirement.

The Decision Block was designed for a practical motor drive system where transients in the motor load, motor current, or flux linkage are associated with a transient change in speed. In this case, to detect a transient condition it was only necessary to monitor the speed of the motor. However, advanced SR drives may have a very high bandwidth speed control loop [151], and thus even under conditions of fast changing motor loads there may be very little speed change. Furthermore, there may still be a change in the motor current

level (due to a change in motor output power at constant speed) and thus a change in the flux linkage waveform magnitudes. If this is the case then the predictor of flux linkage may have a lower accuracy during the occurrence of the flux waveform transient, but may still be given a high weighting by the Decision Block because the constant speed will indicate steady state conditions (even though the flux linkage has changed). It should be noted that the rotor position value decision block will not be affected by this condition at any time, because the rotor position prediction is affected by speed transients only, which are detected by the acceleration factor defined above.

Therefore, to allow the flux linkage value Decision Block to detect all transient conditions (ie. changes in motor speeds, as well as changes in the flux linkage waveforms at constant speed), an additional information signal which detects changes in the motor current is required to be added to the developed Decision Block. The monitoring of current is adequate in order to detect both current and flux linkage transients, due to the fact that current is directly related to the flux linkage through the motor magnetisation characteristics. In addition, similarly to the detection of acceleration, only relative signals describing the change in current are required by the decision block. Therefore, as an example, the change in rms current could be used to detect transient changes in the motor waveforms.

However, a more sophisticated technique is to monitor the instantaneous dc bus link voltage and current in order to continuously calculate the motor real output power. The calculation of instantaneous real motor power would allow the detection of changes in the motor load, and therefore transients in the flux and current waveforms. This would therefore allow information about transient conditions to be fed to the Decision Block.

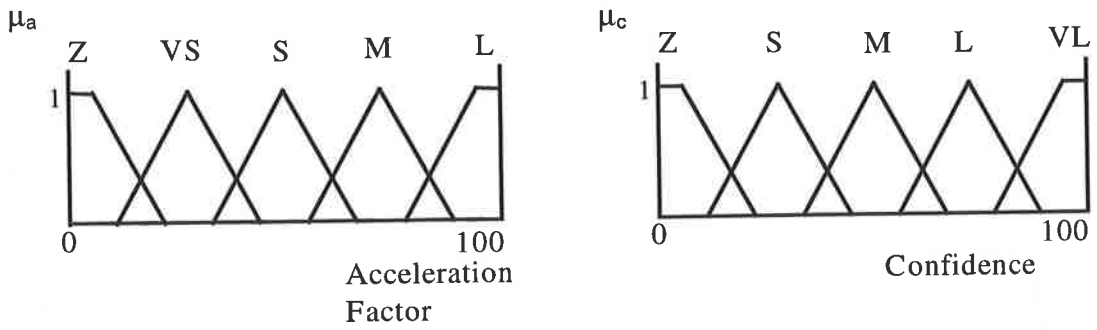
Although detection of the rms current or instantaneous real motor power would have a good accuracy in detecting changing motor waveforms, there are disadvantages in requiring these measurements. This is because the detection of the rms phase currents is relatively computationally complex for the SR motor [152], due to the fact that the waveforms are non-sinusoidal. Therefore, the calculation is undesirable for real time computations. In addition, the calculation of real time power from the dc link will require current and voltage sensors on the dc link bus, which may not be available in all SR drive systems.

Hence, a proposed simpler method in detecting transient changes in the motor waveforms is to monitor the control signals of the SR motor controller. Whether there is a torque, speed, or position control loop implemented in the motor controller, there will always be some control signal that will change when there is a change in the motor load in order to maintain the desired control function. Instead of monitoring the actual current or power waveforms in order to detect transients, as discussed above, the command signals can be

more easily monitored in practical motor drives. The level of the command signal is input to the fuzzy logic decision block that was shown in Figure 5.6 (in addition to the acceleration factor), to decide the weight of the flux linkage prediction value. However, this additional input will only be required for very highly speed regulated systems, where there is almost no change in the speed of the motor even for large changes in the motor electrical waveforms.

For many practical SR drives there will be some transient change in the rotor speed during all changes in the motor load. This change in speed will be detected by the change in acceleration factor defined in equation (5.13) and hence detection of the current changes will not be required to signal a transient condition to the Decision Block. Therefore, for the developed system, only the acceleration factor was used to select the weighting of the predicted flux linkage values. Nevertheless, as mentioned above, the addition of another input, such as a control signal, can be easily added. For many practical systems this additional input is not required, and thus the computation requirement of the real time system can be lowered by omitting this input to the decision block.

Therefore, the developed fuzzy system which gives the predicted values of flux linkage $\psi_p(n)$, and position $\theta_p(n)$, a weighting or confidence value is a single input - single output fuzzy system. The input fuzzy domain is the *acceleration factor,* whilst the output domain is the *confidence.* The membership functions of the variables acceleration μ_a and confidence μ_c for this decision block are shown in Figure 5.7. For simplicity, both fuzzy domains have been normalised to vary from 0 to 100.



Where:
Z = set *ZERO*
VS = set *VERY SMALL*
S = set *SMALL*
M = set *MEDIUM*
L = set *LARGE*
VL = set *VERY LARGE*

Figure 5.7 Membership functions for decision block

Once again the Max-Product rule composition, and center average defuzzification are used for this system as described in Chapter 4. In addition, the rule processing uses the same *C* language routines discussed previously and therefore the details will not be repeated here.

The fuzzy rule base that was used is shown in Table 5.1. The rules on this table are created using simple intuition using the general heuristic rules describing the predicted value accuracy, as was discussed above. This demonstrates the ease in which fuzzy logic can encapsulate human intuition expressed in linguistic terms, to easily create a knowledge based algorithm [153]. In addition, as the rules are represented in an easily understandable and transparent linguistic form, they can easily be modified to optimise the system operation [154].

Table 5.1 Fuzzy rule base for confidence of predicted values

Acceleration	***Confidence***
Zero (Z)	*Very Large (VL)*
Very Small (VS)	*Large (L)*
Small (S)	*Medium (M)*
Medium (M)	*Small (S)*
Large (L)	*Zero (Z)*
Very Large (VL)	*Zero (Z)*

The fuzzy rule table shows the rules that would be triggered for any input value of *acceleration factor*. For example if this factor was equal to 65 (after being normalised) then from Figure 5.7 one can see that the input would be in the fuzzy region small (S) and medium (M). Therefore, using these inputs, the rules that would be triggered from Table 5.1 are:

If acceleration is *small* (S) *Then* confidence is *medium* (M) (5.16)

If acceleration is *medium* (M) *Then* confidence is *small* (S) (5.17)

These rules are aggregated as described in Section 4.2.2, and the outputs of these rules are then defuzzified to give a crisp value of confidence. The confidence is essentially the weighting given to the predicted values of flux linkage and angle. For example, if the confidence was 37, then the algorithm would multiply the predicted value of flux linkage $\Psi_p(n)$, by 0.37, and the estimated value $\Psi_e(n)$, by 0.63. This means that at all times that a combination of the estimated and predicted values of flux linkage and rotor angle are used. Thus the system can emulate simple intuitive behaviour and use both sources of relevant information, without making an abrupt decision between one or the other.

As it was seen in Figure 5.2, where the complete sensorless algorithm outline is shown, the weighted rotor angle from the estimated and predicted value is used as an input to the rotor position predictor, in order that further predictions are corrected. In addition, the flux linkage value output from the decision block is used as the next integration constant for the flux linkage integrator. In this manner, the corrected values are used to not only correct the present values of flux linkage and position, but also to correct future values of flux linkage and position.

5.3.3 Optimal Phase Selection

In normal operation of the SR motor, the excitation region for each phase may overlap, as was seen in Chapter 2. Therefore, there will often be current flowing in two or more motor phase windings at a given time. Hence, if more than one phase is simultaneously conducting current, every excited phase can be used for estimating rotor position. During the operation of the position estimation algorithm every motor phase will have its current and voltage measured and each phase flux linkage will be estimated through the integrator. If a motor phase is excited, then the current and flux linkage are input to the fuzzy model.

Theoretically, the same position should be output by each of the excited phase rotor position estimations. However, in practice when the scheme is operated on a real SR motor drive noise, measurement, and calculation error will have some effect, and therefore each phase may produce a slightly different estimated angle result. In addition, it is important to note that each phase has rotor angle regions of optimal sensing. In some rotor angle regions the rotor position estimation will be more affected by errors than at other rotor angle regions (as will be mathematically detailed in Section 7.4).

The reason that each phase will be operating in a different phase region at any point in time is that at every physical rotor position, the rotor to stator phase angle will lie in a different region in each motor phase. For example, as was seen in Chapter 2, in a four phase SR motor the rotor angle relative to each phase is separated by 15 mechanical degrees. Hence every motor phase will be in a different region of rotor angle. Therefore, for implementation in a practical drive, the estimated rotor position from the phase in the rotor angle that lies in the optimal region should be given the most weighting.

The optimal sensing region can be found from an analysis of the flux linkage curves, as is discussed in further detail in Section 7.4 and also in reference [155]. The optimal sensing region is illustrated in Figure 5.8 for the magnetisation curves of the four phase motors. Note that the region shown is only approximate, as it is difficult to exactly define in an exact manner, as will be discussed below.

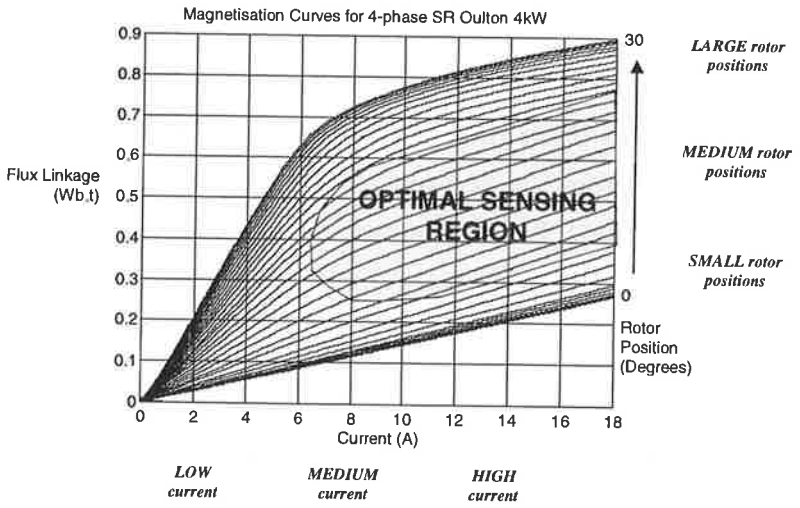


Figure 5.8 Approximate optimal sensing region of the magnetisation curves

It can generally be said from the magnetisation curves, that when the angle is near the unaligned position (ie. for *small* relative angles) and the current is *low*, that the curves are very tightly bunched up. Therefore under this condition, small errors in the flux linkage estimation or current measurement will result in large errors in the position estimate. Additionally, when the angle is close to alignment (ie. *large* relative angles) the curves are also tightly bunched up, and therefore a small error in current measurement can produce large errors in rotor angle. Therefore, the optimal sensing positions, where the best resolution is offered, is for *medium* angles between alignment and unalignment.

However, the optimal sensing region in fact does not stop or start abruptly but has a transition region, or in other words it contains smooth edges. In addition, the terms *small, low, medium,* and *large* used above to describe the regions, are also linguistic terms which can once again be naturally represented again by a fuzzy system. Therefore, to decide whether a motor phase measurement is in the optimal sensing region, a Decision Block similar to the one described above is placed after the Fuzzy Model seen in Figure 5.2. The decision block can encapsulate the general heuristic rules that were mentioned above, which describe the optimal sensing regions of the motor phases. Based on the heuristic rules, it places a weight or confidence on the angle estimates when more than one phase is excited ($\theta_e(n)_{1,2,3,4}$), and outputs one final weighted value ($\theta_e(n)$).

This final weighted value is based on the weighting or confidence of each of the rotor position estimates corresponding to which region the estimated rotor position lies in each phase. In essence, the decision block decides the optimum phase for angle measurements, and gives this phase the greatest weighting if more than one phase is used in producing a rotor position estimate. It is thus called a *Optimal Phase Selector*, as was seen in the block diagram of Figure 5.2.

To perform the weighting of each of the position estimations from each phase, based on the heuristic rules described above, the Decision Block used in the Optimal Phase Selector uses a two input - single output fuzzy system. The input fuzzy domain is *current* and *angle* and the output is *confidence*. It gives a weighting or confidence value ranging from 0 to 100 percent of each phase's rotor position estimate. The membership functions on each of the input and output fuzzy domains used in the Decision Block are shown below in Figure 5.9.

The Optimum Phase Selector uses the same Max-Product rule composition and center average defuzzification techniques as used by the Decision Block described above in Section 5.3.2. These techniques are implemented using the same *C* algorithms as previously described in Chapter 4, and thus the details will not be repeated here.

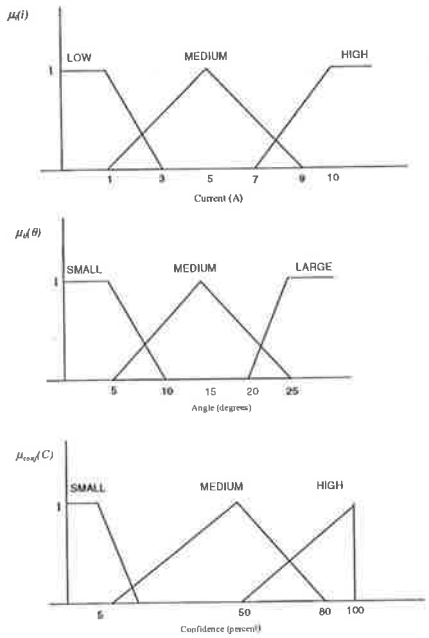


Figure 5.9 Fuzzy phase selector domains. ($\mu_i(i)$ = fuzzy membership functions of current. $\mu_\theta(\theta)$ = fuzzy membership functions of rotor angle. $\mu_{conf}(C)$ = fuzzy membership functions of confidence.)

The fuzzy rule base that defines the linguistic rules which are used by the Optimal Phase Selector is shown below in two-dimensional array of rules relating the inputs of current and angle to the output confidence value. It can be seen from the rule table that an example rule in this system is:

If current is *SMALL* (S) and angle is *SMALL* (S) *Then* confidence is *SMALL* (S) (5.18)

As it was discussed above, these rules are based on heuristic knowledge about the optimal sensing regions in the flux linkage curves. The ability of fuzzy logic to model this heuristic knowledge allowed a simple and easy to understand linguistic based system to be easily developed. This is achieved without the requirement of analytically defining the optimal regions of position sensing.

Another advantage of using the fuzzy system is that the fuzzy linguistic rules of the Optimal Phase Selector can remain unchanged even when a different motor is used. This is because only the definitions of the fuzzy membership functions in the input domains of current and angle are required to be changed if there is a change in the motor with different optimal phase sensing regions. For example, the membership function of *LOW* current seen in Figure 5.9 could be modified to lie over a different range of the current domain. However, the fuzzy rule base does not need to be changed, and this allows the modification of the Optimal Phase Selector Block for another motor to be very simple.

As it was mentioned above, each of the four motor phases produces an estimated value of position, and each of them will be given a confidence weighting by the fuzzy phase selector, based on the estimated position and the phase current. To determine the final angle value $\theta_e(n)$, each estimated phase angle is multiplied by its respective confidence value found from the Optimal Phase Selector, and the total is divided by the addition of all the confidence factors. Thus if there were two phases which produced an angle estimate, then the algorithm would compute the equation:

$$\theta_e = \frac{\theta_1 . C_1 + \theta_2 . C_2}{C_1 + C_2} \tag{5.19}$$

Where:
θ_e = the final angle estimate
θ_1 , θ_2 = the phase angle estimates of phase 1 and phase 2 respectively.
C_1 , C_2 = confidence values of phase 1 and phase 2 respectively.

This weighted value is the final aggregate *estimated rotor position* derived from each excited phase. As it was described above, to help minimise errors, this aggregate estimated rotor position is combined with the predicted value of rotor position in the Decision Block to produce a final rotor position.

Table 5.2 Fuzzy Rule Base for Optimum Phase Decision Block

Current	Small (S)	**S**	**S**	**S**
	Medium (M)	**M**	**H**	**S**
	Large (L)	**M**	**H**	**S**
		Small (S)	Medium (M)	Large (L)
		Angle		

5.4 Simulation of the Position Estimator

In the previous sections, the complete system of the new fuzzy logic based sensorless rotor position detection was detailed. To show the effectiveness of the scheme, results will be shown below of the actual position estimation performance. Firstly, in this section, the position estimation is tested with simulated SR motor current and voltage waveforms. These motor waveforms were generated using the simulation algorithm of the four-phase SR motor, as is detailed in Appendix B. This simulation algorithm can generate the motor electrical waveforms for any transient speed profile of the SR motor by using the non-linear model of the motor.

The simulation tests carried out in this section allowed the sensorless position estimation method to be tested under any operating conditions that could not be safely achieved using the real laboratory motor. For example, very high acceleration and rotor stall from high speeds were two tests which could be simulated easily, but would have been unsafe on the actual experimental motor. However, the system can only be finally proven with actual experimental results, due to the fact that actual real time effects such as measurement error, noise, calculation error, non ideal devices, electromagnetic coupling, controller delays, and quantisation error are difficult to fully model using drive simulations. Therefore in Chapters 6 and 7 an extensive analysis of actual experimental results will be given, with a wide range of motor speeds and conditions being tested. In addition, particular attention will be given to the experimental robustness and reliability of the new sensorless algorithm.

In this section, simulation results will be illustrated and discussed which will highlight the ability of the sensorless algorithm to operate with the following motor characteristics:

i) Transient motor starting from standstill.
ii) Low motor speed and standstill (zero speed).
iii) Low acceleration.
iv) High acceleration.
v) High speed.
vi) High speed stalling of the motor.
vii) Chopping mode currents.
viii) Single pulse mode currents.
ix) High and low phase currents.

In the following results, the motor currents, voltages, and actual rotor position are detailed. In addition, the output estimated and predicted angle, as well as the estimated and predicted flux linkages for each phase which are output by the sensorless position detection algorithm, are also presented.

a) *Chopping Mode Current 0-1000rpm Transient Test:*

In this simulation test the motor is simulated to accelerate from 0 to 1000 rpm in 300 ms and then the rotor is brought to a sudden standstill. As it was mentioned above, the simulated motor waveforms are generated with the simulator of the four phase motor that is detailed in Appendix B. For this test, the simulated rotor angle, phase voltage, phase current, and the integrated phase flux linkage waveforms for phase A of the motor are shown in Figure 5.10. The waveforms of the other three phases are identical, except for being phase separated by 15 degrees relative to the previous phase.

In the waveform of the actual rotor position given in Figure 5.10 (a) it can be seen that the rotor position accelerates from standstill, until at $t = 0.3s$ when the speed is 1000 rpm, it is instantaneously stalled. The rotor speed is then zero until $t = 3.5s$ at which time the motor accelerates slightly. Therefore these simulation results test the performance of the sensorless algorithm under conditions of acceleration from start-up, sudden stall, zero speed, and low acceleration and speed.

The simulated voltage in this test, which can be seen in Figure 5.10 (b), was set to turn on at a fixed rotor position (in this case 15 degrees) and off at another fixed rotor position (40 degrees). During the on period, the phase voltage is switched on and off between the positive rail of 250V and 0V. This is because the current reaches the chopping mode level, and in this case soft chopping control is simulated. When the phase is switched off at 40 degrees, the full negative supply of -250V is placed across the phase until the phase current decays to zero.

In Figure 5.10 (c), the corresponding phase current of the motor is detailed. It can be observed that in this test the motor is operating in chopping mode during the entire startup period. In this simulation, the chopping hysteresis band was set to have a high value of 16A and a low value of 14A. However it can be seen that at times the phase current falls outside these bands during the chopping period. This is due to the fact that the simulated motor current controller has a minimum commutation frequency in order to more closely simulate a practical motor controller. Thus, during very fast current rise periods or fall times, the chopping controller may not act until the current has left the hysteresis band.

As the graph is plotted with time as an axis, the phase current pulses become progressively shorter from 0 to 0.3s, because the switching angles are constant and the speed is constantly increasing. After 0.3s when the motor is stalled, one can see that the rotor angle remains constant, but that voltage and current are still applied to the phase. This is because the motor has stalled at an angle of 18 degrees, which means that the phase shown is still in its turn-on region. Therefore, the controller will apply current to the phase, which is maintained in the current hysteresis band by soft chopping.

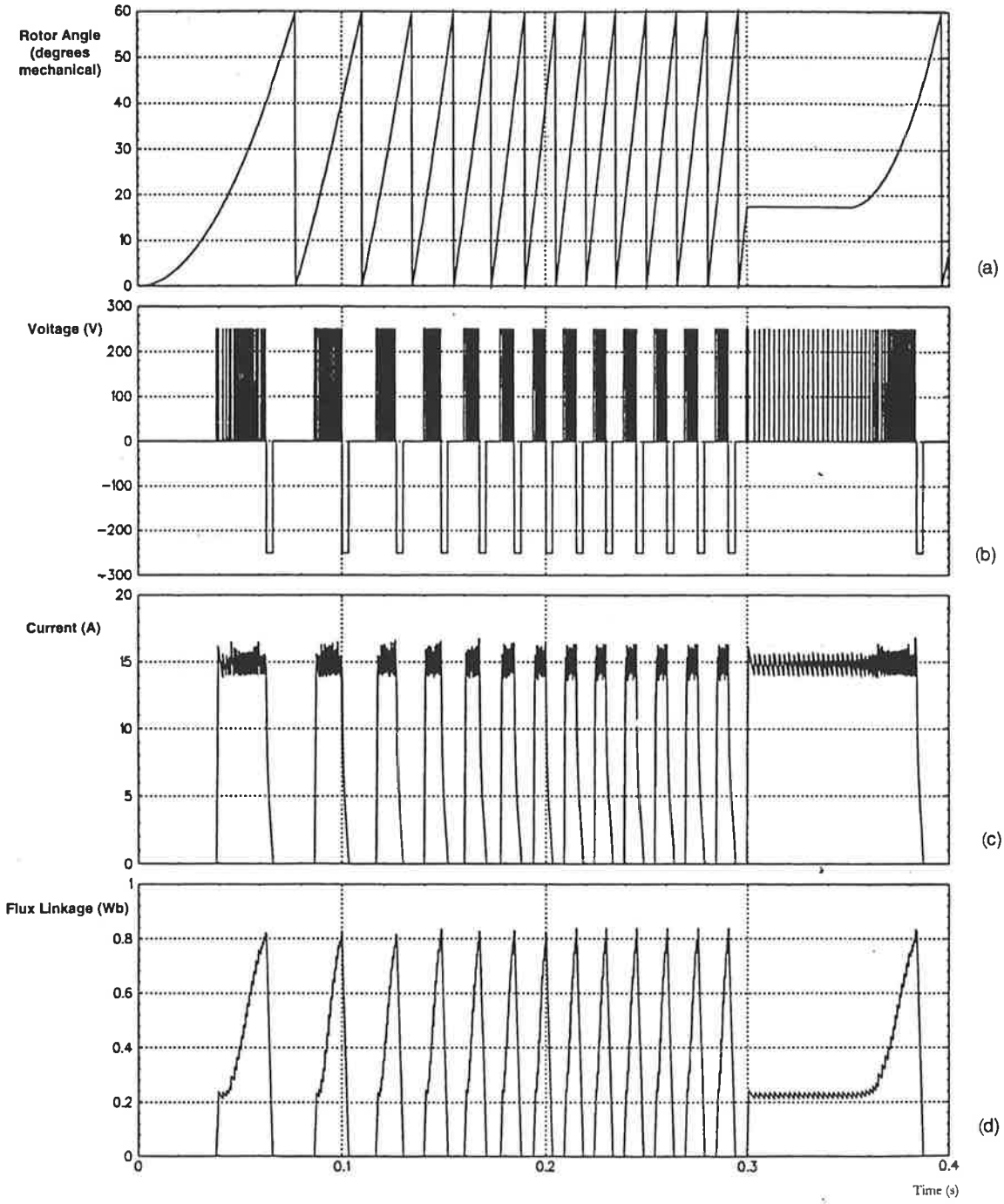


Figure 5.10 Waveforms for 0-1000rpm transient test (a) Actual rotor position. (b) Phase A Voltage. (c) Phase A current. (d) Phase A flux linkage.

The phase flux linkage waveform is found from the numerical integration of the phase voltage and current, as detailed in equation (5.1). Figure 5.10 (d) plots the flux linkage waveform corresponding to the currents and voltages of this test. It can be seen that the flux linkage pulses have a non-linear variation due to the commutation of the currents. In addition it is interesting to note that when the motor is stalled between $t=0.3s$ and $t=0.35s$ that the flux linkage remains relatively constant. This is because when the rotor is stalled, the rotor position is constant and the motor acts essentially as a constant inductance. Therefore for constant current, the flux linkage must also be constant (there is a small variation due to the small variation of the current in the hysteresis band).

To estimate the rotor position $\theta^*(n)$, the motor phase currents from each of the four phases $i(n)_{1,2,3,4}$, as well as the four phase voltages $v(n)_{1,2,3,4}$, are input into the estimation algorithm system, as was shown in the outline in Figure 5.2. As it was detailed above, the estimated flux linkage and current is input to the fuzzy rule based SR motor model to generate an output estimated rotor position. It was also mentioned above that predictors of both flux linkage and rotor position are used to help detect and reduce errors in the estimated values of flux and angle. In addition a decision block is used to choose the phase which is most likely to generate an accurate position estimate.

To show the sensorless systems accuracy in determining rotor position, the actual rotor angle and the estimated rotor angle is shown together in Figure 5.11. This figure also plots the values of the predicted angle $\theta_p(n)$ and next step predicted angle $\theta_p(n+1)$ from the fuzzy predictor. As mentioned above, these are used to enhance the performance of the estimator, and predict the next step angle for the controller.

One can see from the graphs that the output angle from the fuzzy system is very close to the actual rotor position at all times of the test, including the acceleration and stall period (in the first few iterations the position varies between 0 and 59.7 degrees, however this does not represent a large error due to the fact that 0 and 60 degrees are in fact the same angle). The average angle error between actual and estimated angle is about 0.4 degrees, as can be seen in Figure 5.12. It can be seen that in the rotor position estimation error there are regular peaks seen throughout the test, and the estimation error is rarely zero. As the simulation waveforms are noise free in this test (although there will be some error due to the numerical integration of flux linkage), these errors would be due to slightly erroneous outputs from the fuzzy rule based SR motor model (due to a not completely accurate model), or erroneous output of the fuzzy predictors (due to non perfect predictive rules). However, it can be said from the angle error plot, that these effects are very low, due to the low amplitude of the angle error peaks.

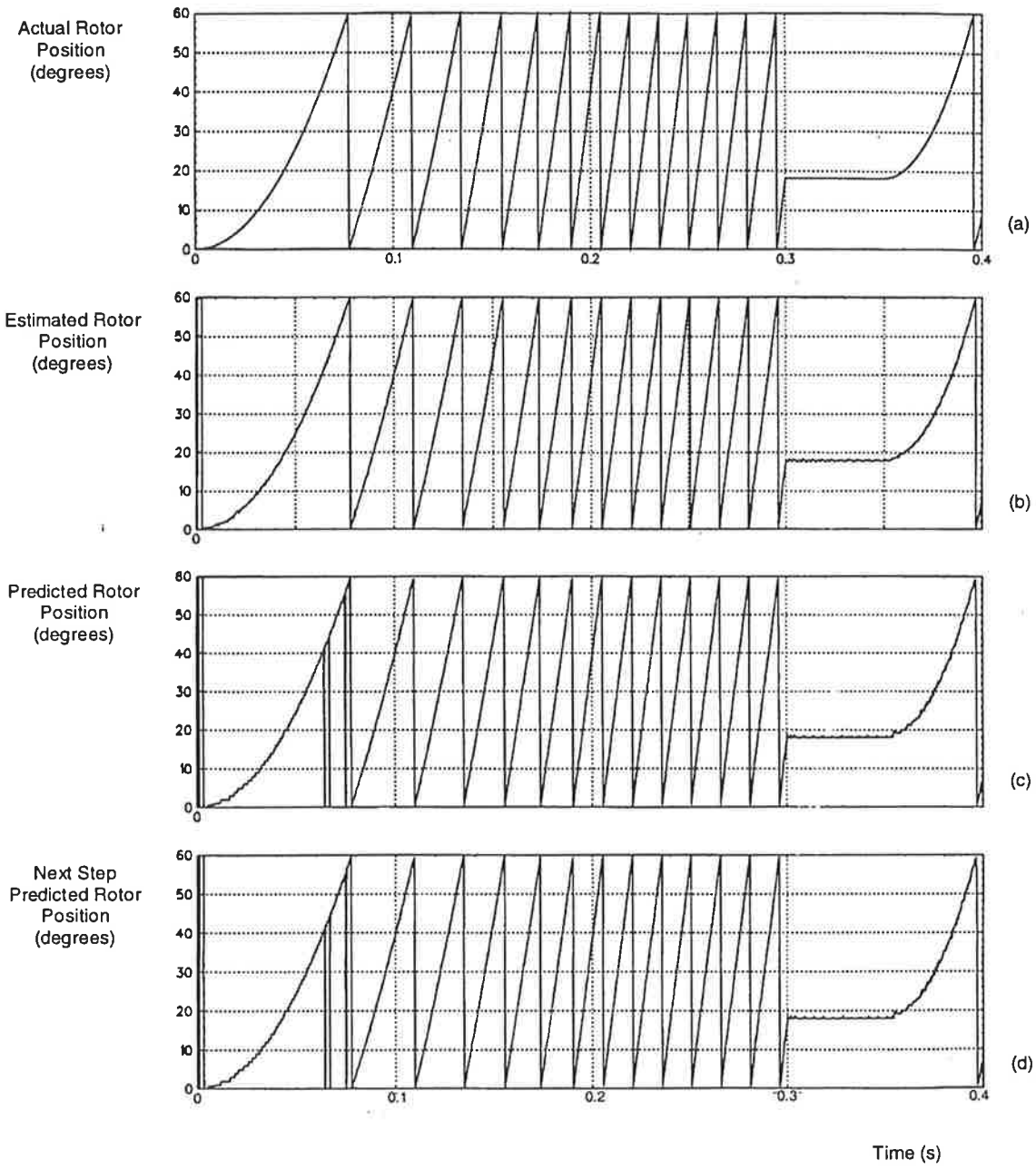


Figure 5.11 Angle Waveforms for 0-1000rpm transient test. (a) Actual rotor angle. (b) Estimated rotor angle. (c) Predicted rotor angle. (d) Next step ahead predicted angle.

The average error (about 0.4 degrees) due to erroneous outputs from the fuzzy rule based model is explained by the finite resolution possible from the finite number of fuzzy sets that were chosen to divide the fuzzy output domain of rotor angle, and the fuzzy input domain of current and flux linkage. A rough calculation of the expected error can be determined by the number of fuzzy sets per rotor degree in the output domain. In this case 30 fuzzy sets were chosen to cover a range of 30 degrees of rotor angle. Hence, one would expect to a first approximation (without considering the overlap between the fuzzy sets, and the combination of the fuzzy rules when more than one rule is triggered by the inputs) that the minimum resolution would be roughly 1 degree. In the result of this test, where the average angle error is approximately ±0.4 degrees corresponds well with this rough calculation.

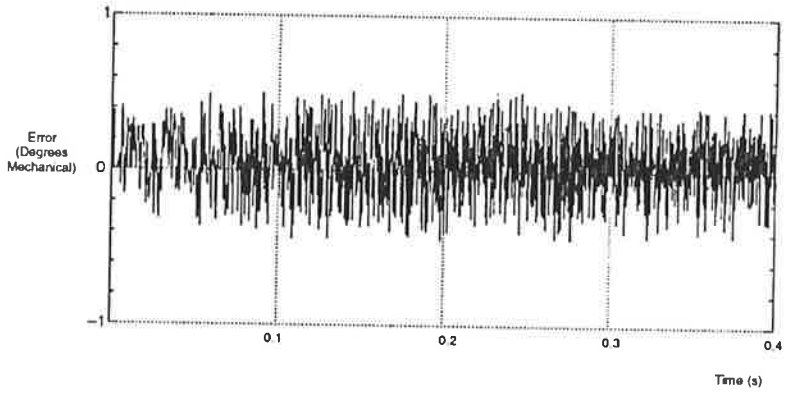


Figure 5.12 Angle error for 0-1000rpm transient test.

The position error could thus be reduced by increasing the amount of fuzzy sets in the variables domain, but an increase in the number of fuzzy sets would lead to more rules being required, and a corresponding increase in memory or storage requirements. For real time systems memory may be a resource that needs to be minimised due to increased system cost, although this is rapidly becoming less of a problem due to less expensive memory integrated circuits. The developed system was designed to be optimised for practical motor drives, and therefore a compromise was made between the memory requirement and the resolution of the position estimation. Nevertheless, for applications where higher resolution is required, the basic sensorless system remains unchanged, and only the number of fuzzy sets in the variable domains need to be increased.

The predicted angles from the fuzzy predictor are also shown in Figure 5.11(c). In this particular test where there is no noise and the acceleration is smooth, and it can be seen that the predictors have a very fast learning time, and the predictions are very accurate. There are also very few points where no predictions can be made due to a lack of predictive rules. It can thus be said that, under ideal conditions, the fuzzy predictors are very fast and accurate. However, it can also be seen from the figure that in the initial learning period there are 4 points where a prediction cannot be made. This would occur

due to a particular combination of previous points that had no corresponding learnt rules in the predictor's fuzzy rule base.

It should be noted that when the predictor cannot make a prediction due to lack of rules, that the fuzzy predictor output defaults to zero, and thus the predicted value is not used in determining the final position estimation $\theta^*(n)$. As it was mentioned before, there will be some finite time before the predictors build up enough rules to make accurate predictions of angle. One would expect to see instances where there are erroneous or no predictions during the start-up of the motor, because initially there are no stored rules.

The operation of the flux linkage fuzzy predictors is illustrated in Figure 5.13, where the actual phase flux linkage and the predicted flux linkage are shown for each motor phase (it can be recalled from the above discussion that the flux linkage prediction makes a prediction for each motor phase). As in the angle prediction, if no prediction can be made then the fuzzy prediction defaults to zero, as is highlighted in the figure. It can be seen that even with the highly non linear chopping mode waveforms of the chopping mode flux during acceleration, that the fuzzy predictor learns the motor behaviour rapidly, with only a few points in the initial learning period where predictions cannot be made. It can also be seen by comparing the actual values of flux for each phase (Figure 5.13 (a), (c), (e) and (g)) with the corresponding predicted values of flux (Figure 5.13 (b), (d), (f) and (h)), that the predicted values of flux linkage compare accurately with the actual values.

By comparing the performance of the flux linkage prediction with the angle prediction seen previously in Figure 5.11, it can be said that the angle prediction has a higher performance. This is because there are a larger number of points where a prediction cannot be made in the flux linkage prediction. The reason for this can be understood if one compares the waveforms of the angle trajectory in Figure 5.11 (a) with the flux linkage waveforms seen in Figure 5.13. The flux linkage waveforms can be seen to have a more non-linear trajectory than the relatively smooth curve of the rotor trajectory. Therefore, the prediction of the rotor position will be simpler than the prediction of the flux linkage waveform. This is because, in general, the complexity of the waveform increases the modelling and prediction difficulty [142].

It should be noted that these simulation tests provide ideal noise and error free input data to the sensorless position estimation algorithm. Hence, the ability of the predictors of flux linkage and angle to minimise the effect of short, high amplitude pulses of noise is not discussed in this section. The ability of the predictors to increase the robustness against noise pulses will be detailed in Chapter 7, where the high robustness and reliability of the sensorless system in practical SR drives will be shown.

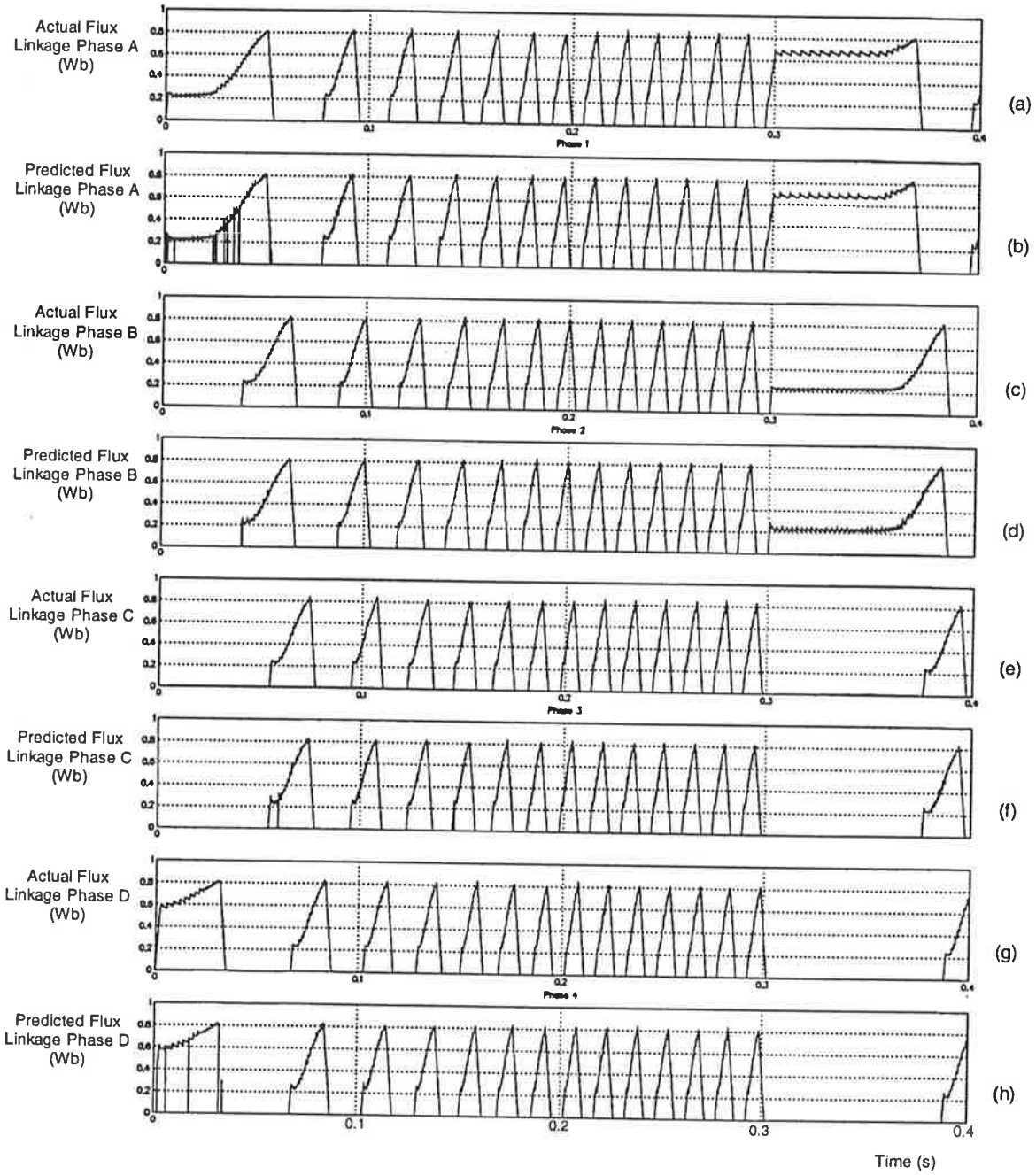


Figure 5.13 Flux linkage waveforms for 0-1000rpm transient test. (a) Estimated Flux Phase A. (b) Predicted Flux Phase A. (c) Estimated Flux Phase B. (d) Predicted Flux Phase C. (e) Estimated Flux Phase C. (f) Predicted Flux Phase C. (g) Estimated Flux Phase D. (h) Predicted Flux Phase D.

b) Single Pulse Mode Current 0-3000 rpm Transient Test

The above transient operation simulation test was extended to an even harsher motor run. In the test the simulated motor experiences a rapid acceleration from 0 to 3000 rpm in 200 ms, is then stalled instantaneously from 3000 rpm to 0 rpm, and after is again slowly accelerated. The conditions of this test allow the sensorless position estimation algorithm to be tested for a number of important conditions. This includes a high acceleration (seen from $t=0$ to $t=0.2s$ in Figure 5.14), motor stalling from high speed (seen at $t=0.3s$), zero speed operation (seen from $t=0.3s$ to $t=0.35s$), slow acceleration and low speed (seen from $t=0.35s$ onwards), as well as both chopping mode and single pulse mode currents. In addition, the test allows the sensorless scheme to be tested when there are relatively high motor currents in the chopping mode, and relatively low peak motor currents in the high speed single pulse mode.

The plot of the rotor position, phase current, phase voltage, and phase flux linkage are shown together for the motor phase A in Figure 5.14. As in the previous results, soft chopping mode was specified for the chopping mode of control and a dc rail of 250V was used. As this test is at a higher speed than the previous set of results, the waveform pulses at high speed have a smaller width in time.

In Figure 5.14 (a) the actual rotor position during the running of this test is shown. Initially the speed is zero, after which the motor experiences a rapid acceleration up to 3000 rpm at $t=0.2s$. It can therefore be seen that during the acceleration, the rotor electrical cycle period (the time between 0 and 60 mechanical degrees) is continuously decreasing. Between $t=0.2s$ and $t=0.3s$ the motor speed is kept constant at a speed of 3000 rpm, and thus the rotor electrical cycle period is constant. At $t=3.5s$ the rotor is suddenly stalled, and it can thus be seen that the rotor angle remains constant. It should be noted that this type of condition would be very difficult to measure in practice due to the high forces that would be required to instantaneously stop the rotor from a speed of 3000 rpm. For testing this type of condition, simulation of the motor offers an alternative when experimental equipment does not allow the test to be carried out in practice. At $t=3.5s$ the rotor is again accelerated with a low acceleration rate, and the rotor position again gradually increases.

It can be seen in the phase current and voltage waveforms of Figure 5.14 (b) and (c) that, when the motor accelerates initially from zero speed, the motor operates in chopping mode. As the motor speeds up, the chopping current level is no longer reached due to the increasing back emf of the motor, and thus the motor begins to operate in the single pulse mode. This happens after only a four electrical cycles for the motor phase which is shown. This is because the speed quickly becomes high due to the large acceleration, and thus the back emf of the motor also quickly becomes high enough to limit the rise of the phase

current. During the high speed region, the current is limited in the single pulse mode to a low level of approximately 5A by the back emf of the motor.

The flux waveforms for motor phase A are also seen in Figure 5.14 (d). Initially in the single pulse mode of operation the flux waveform is non-linear due to the chopping mode operation. During the single pulse mode, however, the flux linkage waveform becomes a simple triangular function, with a linear rising and falling flux variation during each pulse.

As it was discussed above, this test presents the sensorless algorithm with very fast transients, a wide range of speeds including standstill, and also low currents during the single pulse mode. This combination provides a good test of the algorithms capabilities.

The resultant estimated angle from the angle estimation algorithm for this test can be seen in Figure 5.15. In Figure 5.15 (a) the actual rotor angle is again shown, and Figure 5.15 (b) plots the final estimated angle from the algorithm. It can be seen that, even with these fast transients, the estimated angle tracks the actual angle at all times with a high accuracy. As it can be seen in Figure 5.16, the error between the actual and the estimated angle is always small, and has an average amplitude of approximately 0.4 degrees.

In Figure 5.15 (c) and (d), the predicted and next step ahead predicted rotor angle waveforms are detailed. It can be seen that there are only four points during the initial learning period during which no prediction can be made due to a lack of rules (when the prediction output is set to zero). After this initial period, a prediction can always be made by the predictive algorithm, and these predictions follow the actual rotor trajectory closely.

It can also be seen that the angle predictions are accurate even though there is acceleration of the rotor up until $t=0.2s$. Hence, under ideal noise free conditions (such as that seen in the simulation) the fuzzy prediction algorithm has a high performance, even under motor high transients. In this case, the weighting of the predicted value by the Decision Block, as was discussed in Section 5.3.2, could be made less conservative so that even under medium or high acceleration the predicted values had a higher confidence. Nevertheless, it will be seen in Chapters 6 and 7 that with real experimental results which contain noise and errors the prediction performance is not as high. Therefore, the weighting of the prediction value should be conservative for practical systems.

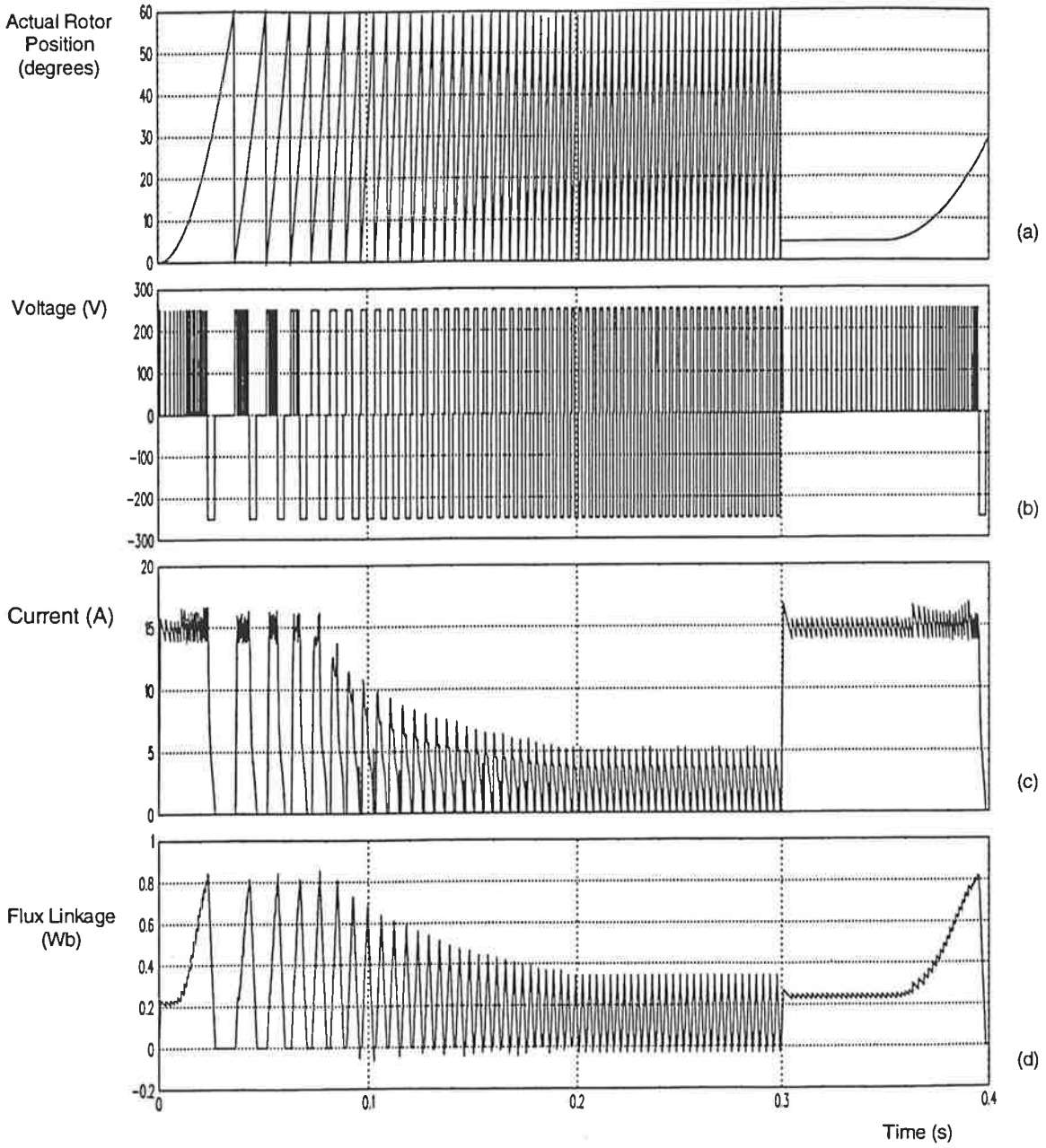


Figure 5.14 Waveforms for 0-3000rpm transient test (a) Actual rotor position. (b) Phase A Voltage. (c) Phase A current. (d) Phase A flux linkage.

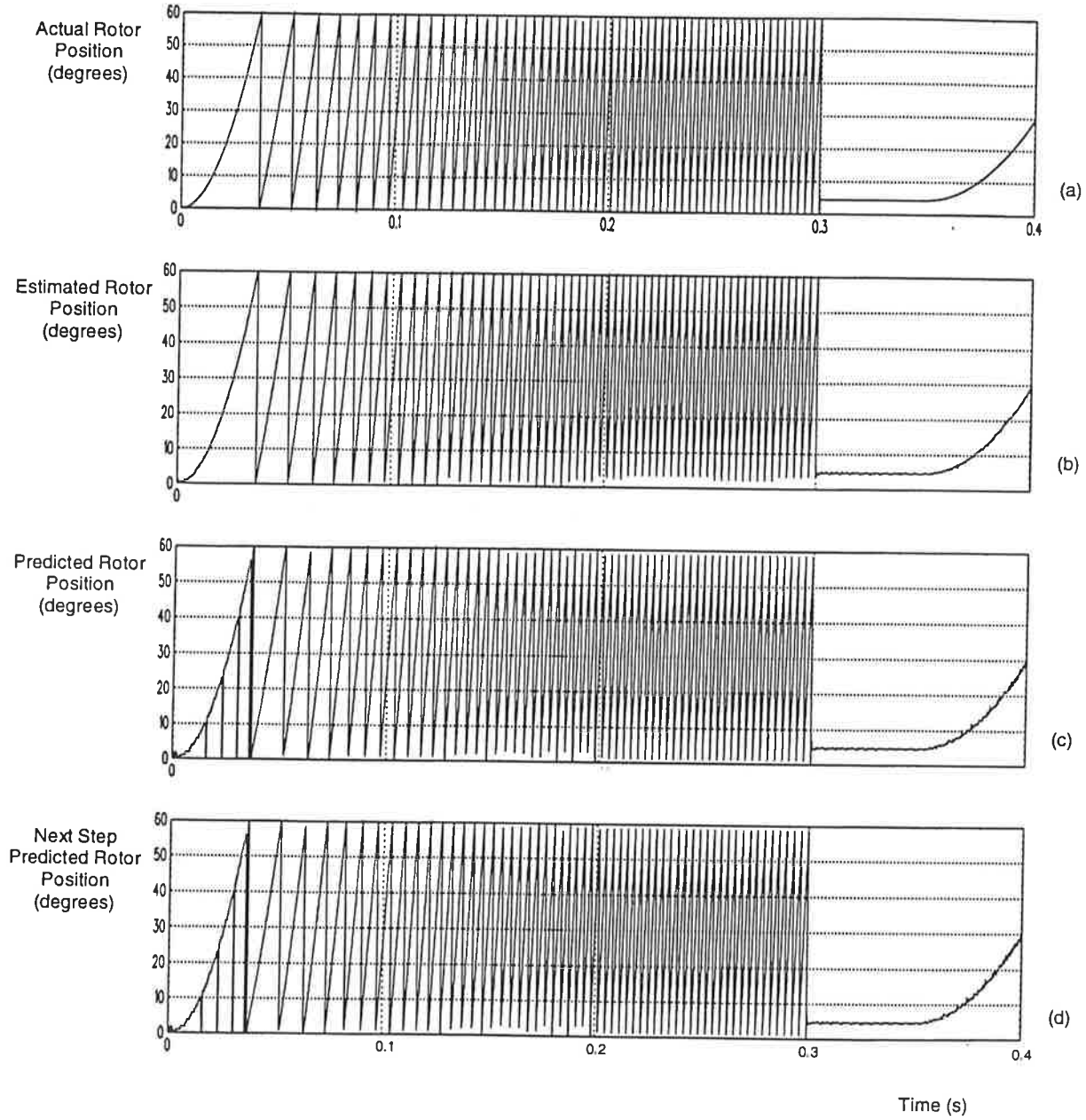


Figure 5.15 Angle Waveforms for 0-3000rpm transient test. (a) Actual rotor angle. (b) Estimated rotor angle. (c) Predicted rotor angle. (d) Next step ahead predicted angle.

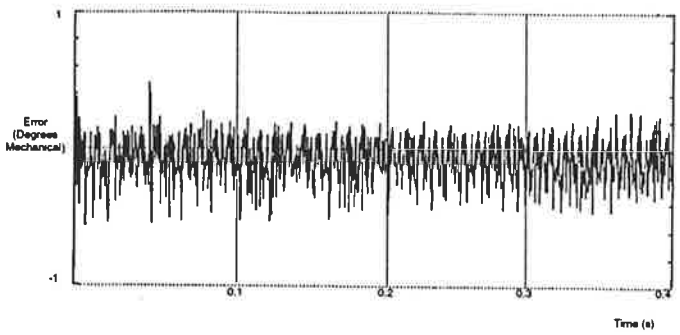


Figure 5.16 Angle error for 0-3000rpm transient test.

The flux linkage predictors are also examined in detail for each of the four phases in Figure 5.17. It can be seen that the fuzzy predictors also work very well, even under transient conditions. However, as explained previously, due to the higher complexity of the flux waveform in the chopping mode, there will normally be more iterations where predictions cannot be made. This can be observed in the predicted phase A flux value seen in Figure 5.17 (a). Unlike the small total number of points where predictions could not be made in the angle prediction, there are nine points in the initial phase A flux pulse where a prediction cannot be made. However, after this initial period, accurate predictions are always made by the flux linkage predictor.

Nevertheless, it should be noted that these simulation results represent ideal conditions for the flux linkage predictor, and that with actual experimental measurements, the prediction of flux linkage does not operate as effectively during transient operation. Due to the ideal conditions, the flux linkage predictor in this case essentially simply tracks the actual flux signal during the transient operation before $t = 0.2s$ (with at least a one sample learning delay). In Chapters 6 and 7, more realistic results will be seen for the flux prediction, where it will be shown that there is always some learning period during transient operation where predictions cannot be made. The effect of noise on the system will also be explored further in the next chapters. It will be seen that even with actual experimental motor waveforms, the system can cope well with significant noise.

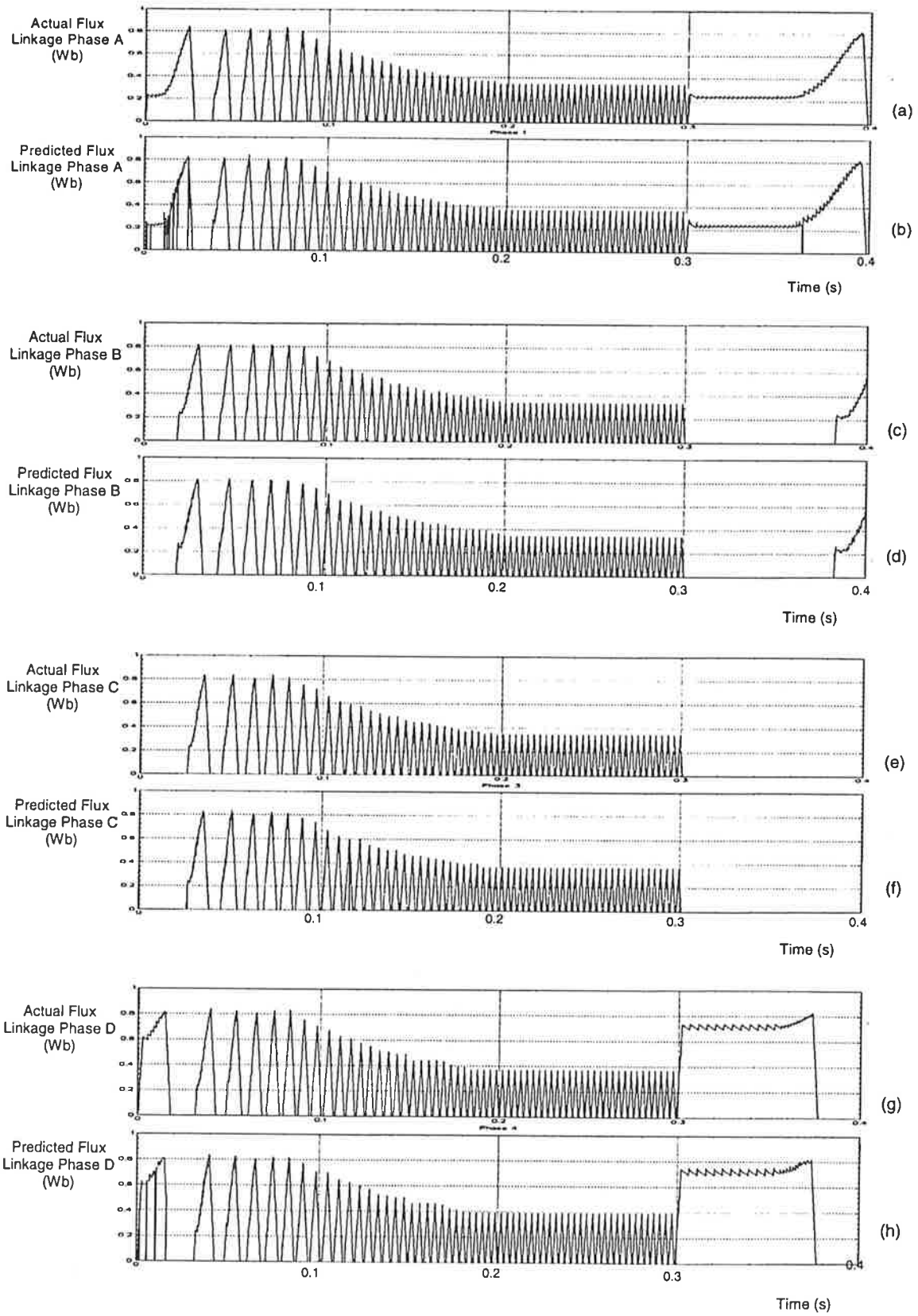


Figure 5.17 Flux linkage waveforms for 0-3000rpm transient test. (a) Estimated Flux Phase A. (b) Predicted Flux Phase A. (c) Estimated Flux Phase B. (d) Predicted Flux Phase C. (e) Estimated Flux Phase C. (f) Predicted Flux Phase C. (g) Estimated Flux Phase D. (h) Predicted Flux Phase D.

5.5 Conclusion

This chapter completed the discussion of the theory that was applied to a new fuzzy logic based sensorless rotor position detection scheme for the SR motor. In Chapter 4, the development of a training scheme for a fuzzy logic rule based SR motor model was explained. This fuzzy rule based model learnt the nonlinear characteristics of the SR motor using training data from static and dynamic real time tests. In this chapter, the use of the fuzzy model to estimate rotor position was shown.

In Section 5.2, the details of sensorless position estimation using the fuzzy logic rule based model were given. It was seen that the position sensing routine was implemented in *C*, and the algorithm determined position by using the fuzzy logic rule base that was learnt during the training phase. This fuzzy logic model provided a non-linear mapping of the input values of flux linkage and current to the output value of estimated rotor position. At each iteration the measured values of voltage and current were used to determine rotor position. Firstly, the flux linkage is estimated by trapezoidal integration, and then the current and flux values are used as inputs to trigger the fuzzy rules in the rule base. This leads to a fuzzy output of rotor position, which was defuzzified to produce a crisp output value of rotor angle.

It was explained that real motor drives are electrically noisy environments. Thus, to make the sensorless scheme more robust to measurement errors due to noise, various performance enhancement features were introduced in Section 5.3 These two added features were the fuzzy logic based predictors of flux linkage and position, and the optimal phase selectors.

The flux linkage and angle predictors were described in detail in Section 5.3.1 The predictors operated by predicting future values of flux linkage and rotor position from the previous values. The prediction algorithm is implemented using a fuzzy logic rule base which is adapted during operation. This fuzzy rule base contained rules which predicted future values of flux and position from previously measured ones.

The predicted values were made use of in conjunction with a fuzzy logic based Decision Block, as was detailed in Section 5.3.2. This used knowledge based heuristic rules to determine whether the predicted values of flux and position from the fuzzy predictors, or the estimated values, were more likely to be correct. As linguistic knowledge can be used to estimate the confidence to be placed on the predicted value, the fuzzy system provided an efficient method of implementing this knowledge in order to determine a weighting for the predicted values. The developed fuzzy system determines the weighting (or confidence) of the predicted value from 0 to 100 percent, with the estimated value consisting of the remaining weight.

The other performance enhancement feature was the Optimal Phase Selector, and this was detailed in Section 5.3.3. The phase selector is used because more than one phase can conduct at any one time in the SR motor. There are optimum regions for position sensing, and therefore the optimum phase should be given the highest confidence. It was seen that the optimum regions of position sensing are difficult to describe analytically, and a mathematical function describing the weighting that should be given in each region is difficult to define. However, general linguistic rules can easily be defined and can be implemented using fuzzy logic. Hence, rules for the optimal phase selector can be determined by intuition, and encapsulated as heuristic rules in a fuzzy system.

Hence, a fuzzy logic based decision block was developed which performed a weighting of the position estimations from each phase. This Optimal Phase Selector used a two input - single output fuzzy system where the input domain was current and angle and the output was confidence. It gives a weighting or confidence value ranging from 0 to 100 percent of each phase's rotor position estimate, and places a higher weighting on the motor phase in the optimum position sensing region.

The chapter provided verification of the sensorless scheme using simulated results. These results were shown in Section 5.4 where a wide range of conditions were tested, including; motor starting from standstill, zero speed, low and high motor speeds, low and high acceleration, stalling of the motor from high speed, chopping and single pulse mode, and high and low phase currents. It was seen in the results that in all these simulated conditions, the estimated rotor position from the sensorless estimation algorithm had a high accuracy. In addition, it was seen that the flux linkage and angle prediction showed a high accuracy and fast learning time. Hence, these simulation results gave confidence that the sensorless technique could be used under operation with real SR motor waveforms.

However, the final verification of the sensorless algorithm could only come when real motor waveforms were actually used. The next two chapters detail the successful results of the sensorless scheme with experimentally measured motor waveforms, with an emphasis on the high reliability and robustness of the scheme, and suitability for practical motor drives.

Chapter 6: The New Sensorless Position Detection Scheme - Experimental Results: Verification

6.1 Introduction

In the previous chapter, the new sensorless position detection scheme, which can be applied under any type of motor operating condition, was verified using simulated waveforms of the motor. A wide range of simulated conditions was used to test the sensorless scheme. These included transient and steady state motor speeds, start up and stall, chopping and single pulse mode, and also operation of the motor with low and high speed acceleration. The results of the tests verified that the position sensorless scheme has the ability to successfully predict the rotor position of the motor under wide ranging operating conditions and speeds, and with motor waveforms corrupted by noise.

Although these simulation results were successful, further tests were performed using real experimental waveforms of the SR motor. This is because in practice, actual experimental waveforms include highly non-linear and difficult to predict effects that are usually not possible to accurately simulate.

The actual operating effects of the SR motor include:

a) Mutual inductance between motor phases.

b) Parameter variation of motor inductances and resistances, due to saturation and temperature rise respectively.

c) Asymmetrical inductance variation in the motor phases:

   As it was mentioned in Chapter 2, it is normally assumed that the inductance of the motor phase is identical for identical angles on each side of the aligned position. However, there may be some asymmetry in the inductance characteristics around the alignment point in a real SR motor.

d) Variation in the magnetisation curves in each of the phases of a practical SR motor:

   As was discussed in Chapter 2, it is normally assumed that in an SR motor each phase has exactly the same magnetisation characteristics. However, in an actual motor each phase may have slightly varying magnetisation characteristics.

e) Effects on the motor waveforms of eddy currents:

   Experimental studies of the SR motor have shown that eddy currents in the motor laminations can distort the phase current, especially during current transients. As it is shown in reference [156] eddy currents lead to exponentially decaying terms in the phase

current when a change in phase voltage occurs.

Therefore, experimental waveforms, which will be affected by all the above effects, are used to verify the ability of the sensorless scheme to operate with a real SR motor. When compared to using tests using simulation results, this provides a more vigorous evaluation of the effectiveness of the scheme.

In this chapter, results of executing the sensorless position detection scheme using real experimental SR motor waveforms are given. The real motor waveforms are captured with a data acquisition system, and the hardware developed and constructed for these experimental tests is explained.

a) A wide range of experimental results will be shown which demonstrate the effectiveness of the fuzzy logic based sensorless method. These experimental results include a wide range of operating conditions, such as: chopping mode, single pulse mode, steady state and transient speeds, steady and transient mechanical loads, and start up.

In Section 6.2, the components that were developed for the sensorless switched reluctance motor drive will be discussed. The drive is made up of several sub systems which include the motor, power electronic inverter, interface, measuring devices, and a DSP board.

In Section 6.3, a wide range of experimental results are shown, which demonstrate the ability of the new sensorless angle estimation algorithm for practical SR motor drives. In Section 6.3.1, the experimental results are shown for the motor operating in the chopping mode. Results are presented for various speeds and loads in this mode of operation. Furthermore in Section 6.3.2, the angle estimation is shown for when the motor operates at the higher speed single pulse mode of operation. The sensorless scheme's ability is shown not only in the steady state mode of operation, but also during transient operation. In Section 6.3.3, the results are presented for the motor operating with both transient changes in speed and transient changes in load. These results demonstrate the ability of the sensorless scheme to operate with real experimental motor waveforms, and with wide ranging speeds, mechanical load, and modes of operation.

6.2 Hardware Design

A switched reluctance motor drive system was designed and constructed with a controller that was based on the ADSP-21020 digital signal processor. The drive consists of the components illustrated in Figure 6.1. As one can see from the figure, the drive is made up of several distinct sub systems that include:

I) Control and Measurement Circuits

a) DSP board with ADSP21020 processor: The DSP features a 30 ns single cycle instruction speed, 48 bit program memory bus, and 40 bit data memory bus.

b) Analog to Digital (A/D) converters: 12 bit MAX122ACNG devices were used with a conversion time of 2.8 μs.

c) Interfaces for signal input and output from the DSP board to external circuitry. This includes: Opto-isolated IGBT gate driver interfaces, buffers, isolation amplifiers and programmable gain amplifiers between the voltage and current signal measurement circuits, and the DSP.

d) Encoder interface circuit between the shaft encoder, used for checking of estimated position, and the DSP data bus.

e) Measuring circuits for the measuring of current (using Hall Effect transducers) and voltage (using resistor bridge and isolation buffers).

II) Power Circuits

a) Three phase diode rectifier: to supply dc voltage to the motor drive inverter

b) Power electronic inverter: The constructed inverter was a two switch per phase type, which used IRGPC40U 40A, 500V rated IGBT switches. The IGBT gate driver circuits used the IR2110 high and low side gate driver chip with opto-isolated interfaces.

c) Switched reluctance motor (as detailed in Appendix A).

As has been mentioned previously, the motor used in this thesis is a four phase switched reluctance motor. The power electronic inverter is connected to the motor phases, and has dc voltage supplied to it from the rectifier. The voltage and current of each phase are measured using fully isolated sensors, and after sampling by the A/D converters, the measurements are transferred to the controller digitally through high speed analog to digital converters. The controller consists of a high speed DSP chip with on board memory. It can perform the fuzzy logic based rotor position estimation using the measurements of current and voltage only. In addition it provides control of the motor via control of the power inverter switches. These drive sub systems will discussed in more detail in Appendix C.

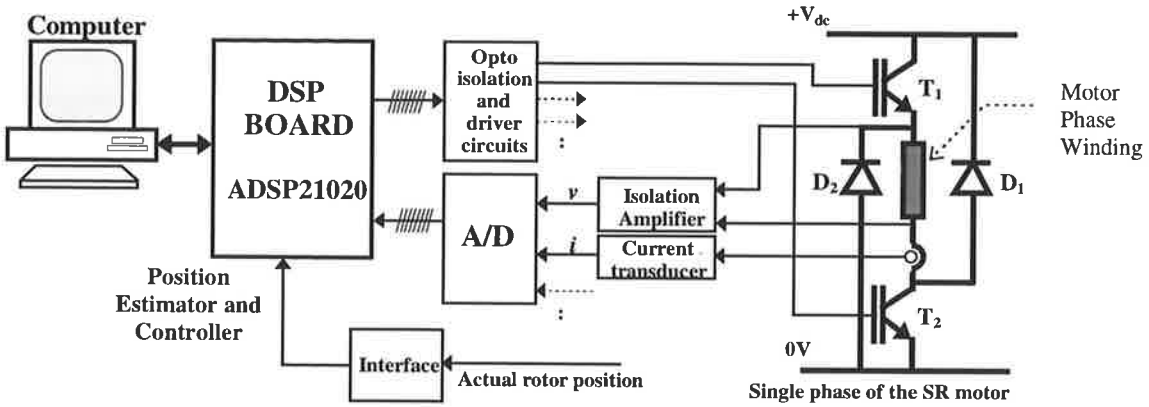


Figure 6.1: Developed Sensorless SR Motor Drive Hardware System

The control and measurement circuits listed above were designed and constructed on a multiple printed circuit board system, to form the DSP based control and measurement system of the SR motor drive. The data signals of the various boards were connected together using a 96 pin connector bus system, and all the boards were mounted into a single case. For the input of the motor current and voltage to the measuring circuits, high voltage insulated connectors were used. In addition, the layout of the circuit boards was carefully designed to isolate the high voltage and current motor phase signals from the controller low voltage circuitry. The constructed unit can be seen in the photograph of Figure 6.2.

The power circuits listed above were also designed and constructed, and with the control and measurement unit previously described above, formed a complete SR motor drive system. In Figure 6.3 the completed power electronic four phase SR motor inverter circuit is shown. In the developed circuit, all of the IGBTs of the inverter unit are mounted on the same heatsink. In addition, the connections between the power switches are formed with copper bus bars in order to provide a low inductance path between the devices and the dc bus. The dc link filter capacitance is also connected to this copper bus bar, and is mounted on the back side of the heat sink.

This power circuit also includes the IR2120 based IGBT gate control circuitry. The gate control circuits are placed on a printed circuit board which is mounted close to the IGBT switches in order that the stray inductance and capacitance of the connection between the gate driver circuit and the IGBT gate can be minimised. To decrease the stray impedance further, and to minimise interference, twisted shielded cable pairs were used in the connections between the IGBTs and the driver board. However, for minimum stray impedance and interference optic cable should be used in all of the gate driver unit interconnections.

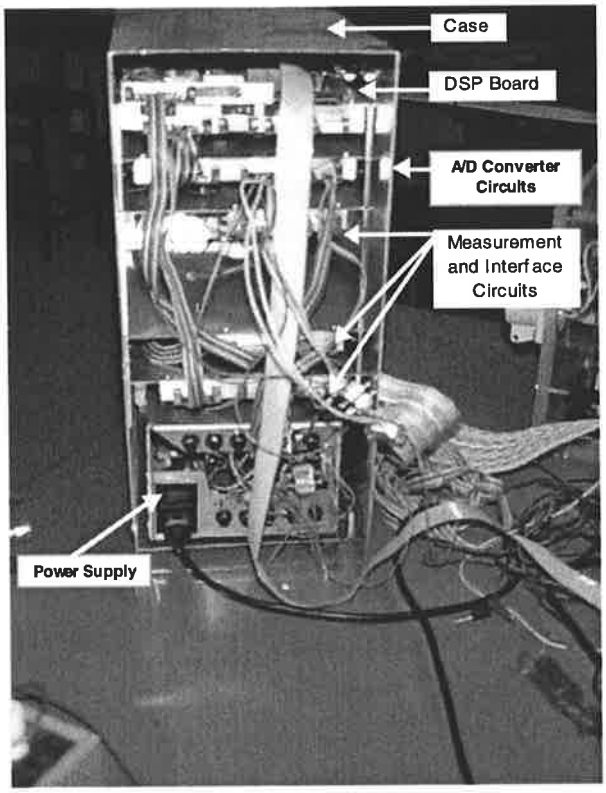


Figure 6.2 Developed DSP Based Complete Control Unit.

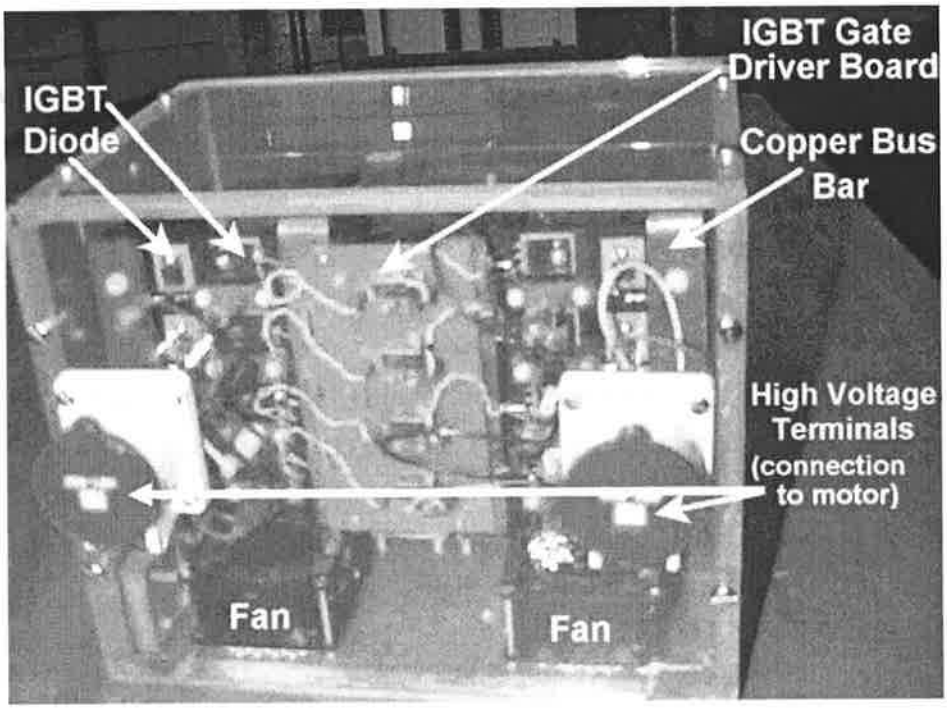
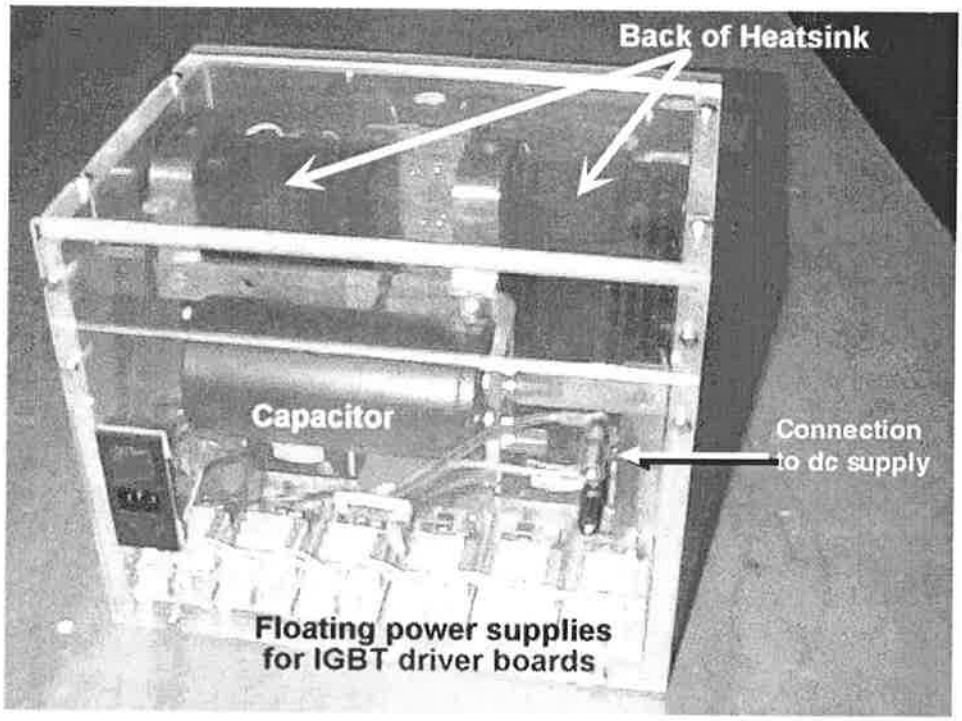


Figure 6.3 (a)



(b)

Figure 6.3 (a) Front of Power Inverter Unit. (b) Back of power Inverter Unit.

6.3 Experimental Issues

In the following experimental results that are shown below, there are some practical application points which apply in all cases, and will therefore be discussed together in this section. This includes issues such as the starting procedure in the sensorless motor drive, the initialisation of the fuzzy predictors in each test, and the use of predicted angle when the fuzzy logic based predictors do not output a predicted angle due to lack of rules in the learning period.

a) Start-up Procedure

As it has been discussed previously, the rotor angle is a non-linear function of flux linkage and current. It was also mentioned that the magnetic characteristics of a SR motor phase are essentially symmetrical around the rotor - stator pole tip alignment point. Therefore, in essence there are two possible values of absolute rotor position for each point of flux linkage and current, that is, one on each side of the aligned position.

Hence during the start up of the sensorless motor drive, there are two problems. Firstly, the position is not known and therefore, the controller does not have knowledge of the required initial phase control strategy. Secondly, if only one phase is used initially, there will be two solutions to the estimate of rotor position for each flux linkage and current data pair.

This problem is well documented [157], [158], and is easily solved using a simple method. In the initial starting instant, two phases of the motor are excited using a short pulse of current,

to produce two sets of flux linkage and current pairs. This will produce four possible values of absolute position (two from each motor phase). Only one angle estimate of one phase will agree with one angle estimate of the other phase. This is the actual absolute rotor position. After this step is performed, the absolute value of rotor position has been found, and there will be no ambiguity in further measurements. This is because knowledge of the last rotor position, and the direction of rotation, allows the controller to decide which of the two possible angles found from a flux linkage and current pair is in fact the correct position.

b) Initialisation of Fuzzy Predictors in Each Experimental Test

In each of the experimental tests below, the fuzzy predictors of flux linkage and rotor position are *initialised* at the beginning of each of the tests. Therefore, in each of the graphs that are plotted, at time $t=0$ there are zero rules in the fuzzy prediction rule base and learning begins with the first iteration. This is performed so that every test shown below has a fair comparison, regardless of whether the motor starts at $t=0$ (as in the start up tests) or not (as in the steady state speed tests).

It should be remembered that in all of the tests, this *arbitrarily* places a learning period at the initial stages of each test, regardless of the motor operating conditions. In normal operation the learning period normally takes place at the motor start-up, and when there is a change in speed or motor conditions. Therefore, under normal steady state conditions this learning period will have been essentially completed, and thus the fuzzy predictors will be constantly tracking and predicting rotor position and flux linkage.

In addition to this, when the predictors cannot make a predicted value, due to a lack of developed rules in the learning system, the output is set to zero, which signifies that no prediction can be made at that particular iteration (in addition there was a software flag output implemented in the software to differentiate between no output, and an actual predicted value of zero degrees). If no prediction can be made for the current angle and flux linkage, then it is not of high consequence, as these predicted values are used only for the error minimisation, in the manner explained previously in Section 5.3. However, if no prediction can be made for the next step angle, then this creates a problem for the controller, which uses the next step for control purposes. Therefore, a backup system is used for the prediction of the next angle value, as will be explained below

c) Use of Next Step Predicted Angle in Fuzzy Predictor Learning Period

In the tests shown below, when the predictors can not make a prediction, the output is set to zero. However, although the fuzzy predictor of flux linkage and rotor position is only required for error minimisation, the next step angle is used by the controller. Therefore, in the case when the output of the next step angle is zero, the prediction reverts to a simpler prediction scheme which is independent and running in parallel to the predicted value.

The independent next step angle prediction acts essentially as a backup, and normally is not used by the controller, except when the predictor cannot make any prediction. This independent next step angle predictor performs a linear extrapolation of the previous two iteration's angle rotor position values [159].

The value of the predicted angle can be found from the simple relation:

$$\theta_{n+1} = \theta_{n-1} + 2\Delta T \frac{(\theta_n - \theta_{n-1})}{\Delta T} \tag{6.1}$$

Where:
θ_{n+1} = predicted angle of the next iteration step.
θ_n = predicted angle of the present iteration step.
θ_{n-1} = predicted angle of the previous iteration step.
ΔT = iteration period

An example of the predicted angle using this method is shown in Figure 6.4, in which the linear interpolation method can be seen. The predicted angle using this method is also normalised to one electrical cycle (60 degrees). This is achieved using the following method: if the predicted angle is greater than 60 degrees, then 60 degrees is subtracted from both the predicted angle and the previous angle. These new angles are then used for prediction in the next iteration.

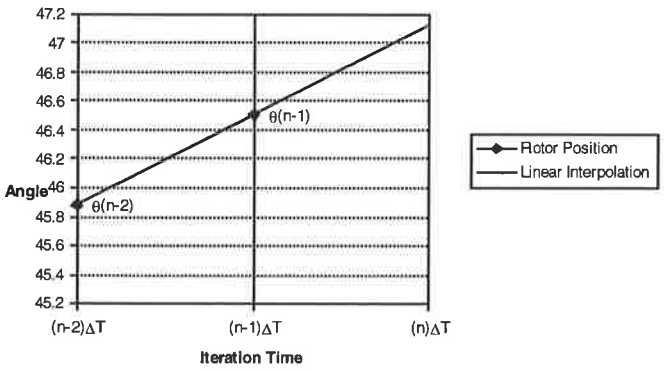


Figure 6.4 Linear Interpolation of Rotor Angle

The extrapolated value will not normally be exact in the above prediction. Nevertheless, the extrapolation equation is very simple and suitable for fast processing, and therefore, guarantees a next step position value for the controller during any learning period of the fuzzy predictors.

6.4 Experimental Results

The hardware developed to control the SR motor and measure the motor waveforms was used to obtain experimental results of the developed fuzzy logic based sensorless position detection scheme. Using the experimental hardware, a wide range of operating modes and

conditions were applied to this motor, including transient and steady loads, transient and steady speeds, acceleration from zero speed, chopping mode current control, and single pulse current control.

The mechanical torque load on the SR motor could be varied using the DC generator attached to the SR motor with a common shaft. Varying the speed reference of the motor controller produces a change in the speed of the motor at any load torque (for average output power less than the rated value of 4kW).

The waveforms of current and voltage were measured during all of the tests using the current and voltage measuring circuits and the analog to digital converters discussed previously. These measured waveforms of current and voltage were then input to the sensorless position detection algorithm to produce the estimated angle.

In addition to the current and voltage, the actual rotor angle was measured during all of the tests using the encoder attached to the motor shaft. This was used to compare the estimated angle from the position detection scheme with the angle measured by the encoder. The angle measured by the encoder had an 8-bit output, which meant that 256 discrete positions per revolution could be measured. Therefore, the encoder measurement will normally have some quantisation error, and thus does not provide an exact reference. Nevertheless, it was taken to be the true rotor angle when comparisons were made between the estimated and measured angle.

A large amount of experimental tests were performed on the motor to vigorously prove the performance and reliability of the fuzzy logic sensorless rotor position detection scheme under all conditions. In this section, the results are given for the estimated rotor position, which is obtained by processing the measured motor waveform data using the new fuzzy logic based sensorless estimation algorithm. In addition, the predicted values of the flux linkage and angle that are output from the fuzzy logic predictors are shown. As it has been discussed, the predicted values of flux linkage and rotor position are used to filter out errors in the estimated flux linkage and rotor position. The performance of the predictors will be examined under experimental conditions, to determine their value during actual motor operation.

6.4.1 Chopping Mode Steady State Experimental Results

The first set of experimental results is an examination of the performance of the scheme in low speed chopping mode motor operation. As it has been discussed previously, chopping mode is used in the SR motor at low to medium speeds. At high speeds the back emf of the motor becomes higher than the dc supply voltage during pole overlap. This means the current can no longer rise to the chopping mode commutation level and thus chopping mode does not occur. Thus, the chopping mode operation of control will be examined for low to medium speeds, and the single pulse mode will be examined later for higher speeds.

In the experimental SR drive that was used, the chopping mode of operation was used from start up until approximately 650 rpm, upon which the operation changed from the chopping mode to single pulse mode. To examine the performance of the scheme under varied motor conditions, results will be shown below for different motor speeds and power output in the chopping mode control region. Variations in motor speed entail a different motor back emf, whilst the change in output power brings about a change in the phase currents. Hence these variations have the effect of changing both the current levels and flux linkage waveforms of the motor, and therefore, they test the scheme at different regions of the motor's non-linear magnetisation characteristics (ie flux linkage versus current and position).

6.4.1.1 Low Speed Chopping Mode Test - 162 rpm

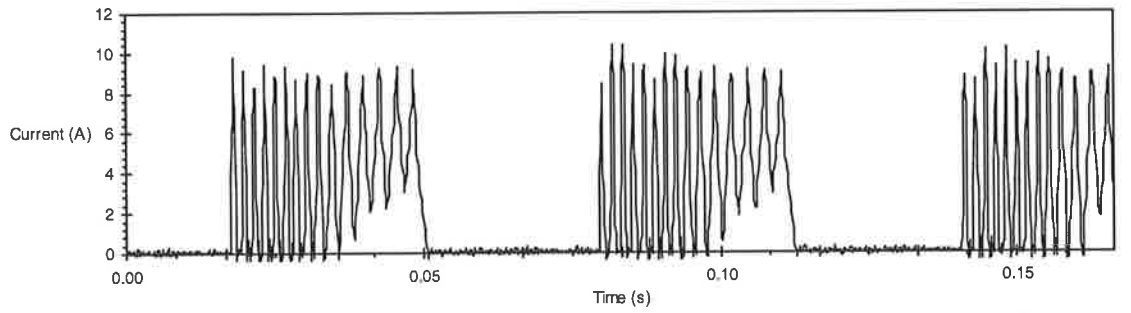
In this test the low speed chopping mode is examined, for the case when the speed and currents are relatively low. The speed in this particular test is kept constant at 162 rpm, and the motor lightly loaded at 5Nm. The motor voltages and currents are sampled by the analog to digital converters at a frequency of 6000 Hz. It will be seen in the measurements that the chopping mode currents, voltages and flux linkages have a non-linear and fast varying nature. Hence, this test examines the ability of the sensorless scheme to operate under actual experimental conditions with these waveforms.

As was discussed in Section 5.3, the fast time varying waveforms in the chopping mode of operation lead the flux linkage to be susceptible to numerical integration errors. This is further detailed mathematically in Chapter 7. However, it can be generally said that with fast varying waveforms, the higher frequency dynamics will not be fully captured in the measurement by the A/D converters. This will reduce the accuracy of the current and voltage waveforms used for the flux linkage integration, which in turn will affect the angle estimation, because the flux linkage is an input to the estimator.

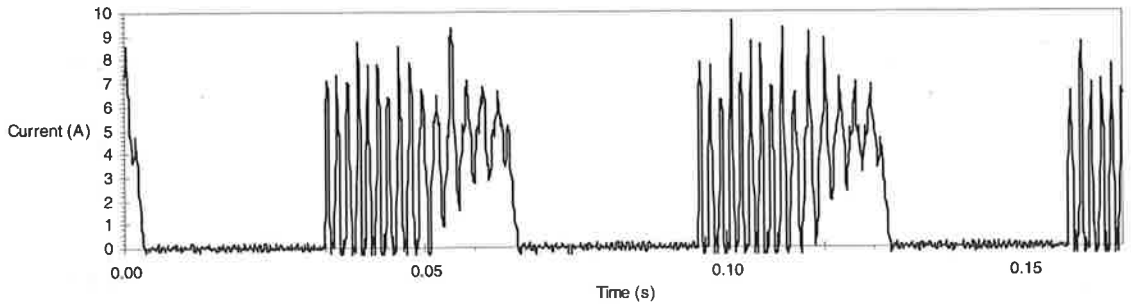
Additionally, the non-linear fast varying flux linkage waveforms present a more difficult problem for the fuzzy predictors of flux linkage than linear waveforms. This is because simple linear waveforms can be described with a lower quantity of fuzzy rules, which means the learning period is increased for complex and non-linear waveforms.

The set of current waveforms that were measured in this test can be seen in Figure 6.5. The controller commutates the current at a command level of 8A, and then turns on the phase again when the current reaches 4A. However, in the current waveforms shown in the below figures, one can see that the current is not always commutated at a level of 8A or turned on again when the level decreases to 4A. The reason for the current not always being commutated at the level of 8A is because the controller implements a minimum switching interval (ie. maximum switching frequency), in order to minimise the switching losses of the power devices. Hence, the current is uncontrolled for some time after turn on or after commutation during the minimum switching interval. If the current increase or decrease is

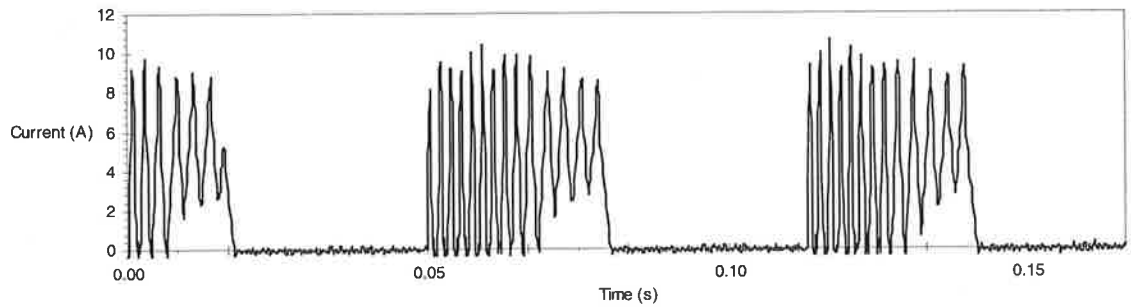
fast enough, it may increase above 8A or decrease to zero before the phase voltage is switched. An overriding over-current control routine is implemented in the DSP controller, so that if the current sensors measure an over-current, a software interrupt is triggered which implements a shut down subroutine.



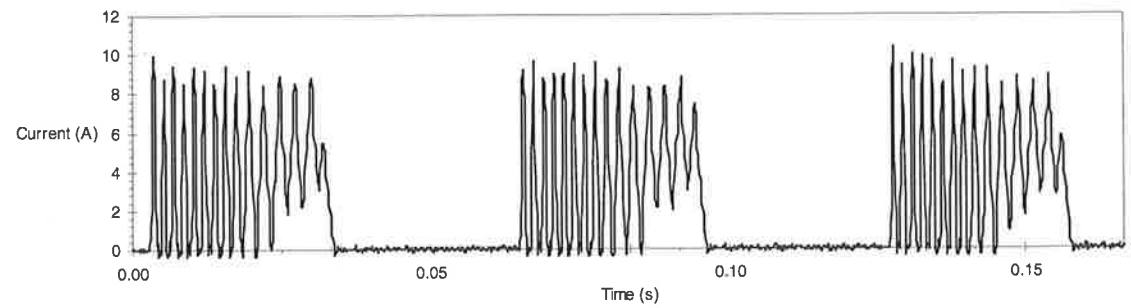
(a)



(b)



(c)



(d)

Figure 6.5 Chopping Mode Phase Currents of the SR Motor - 162 rpm. (a) Phase A, (b) Phase B, (c) Phase C, (d) Phase D.

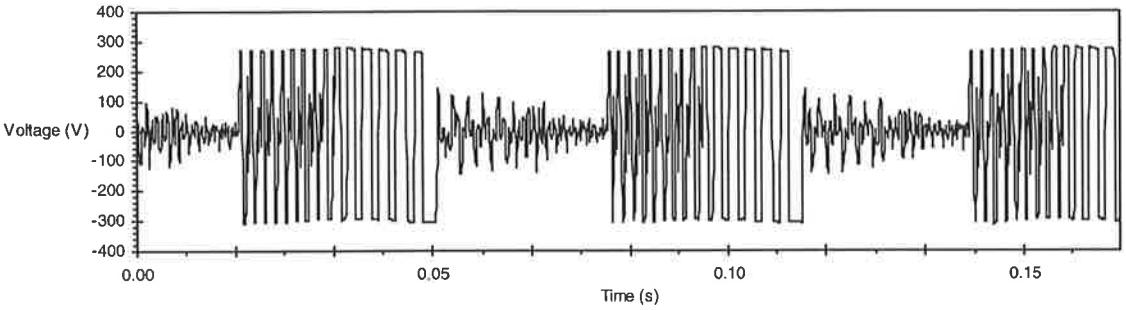
It can also be seen in these results that the current level in a phase falls slightly below zero after the voltage is turned off. This is because when the voltage to a phase is turned off, the phase current conducts through the inverter freewheel diodes. If the voltage is turned off for long enough that the phase current decays to zero, then the current in the diode will extinguish. However, before the diode turns off a negative current will be imposed due to the reverse recovery effect of diodes.

In addition, there is the effect of the capacitance in the circuit, (mainly due to the snubber capacitance as shown in Figure C.6) which produce this negative current. This results from the voltage change across the motor phase inductance and the snubber capacitors, which occurs when the current decays to zero in the motor phase. This voltage change in the snubber capacitance produces an oscillatory current, which has a waveform that depends on the interaction between the snubber capacitance, the motor phase inductance and resistance, and stray inductance and resistances.

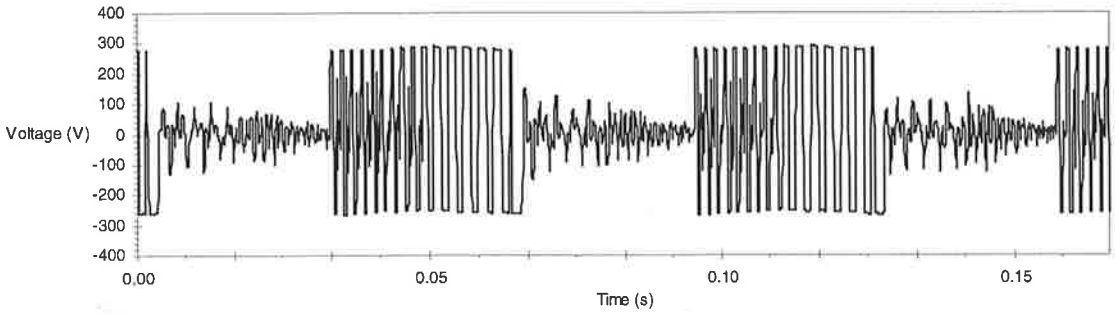
The voltage waveforms of the four motor phases can also be seen in Figure 6.6. The rise and fall of each phase current shown in Figure 6.5 corresponds to the switching of the motor phase voltages. It can also be seen that when the motor voltage is in its off region (ie. the phase current is zero), that the motor phase voltage does not stay constantly zero. In fact, high frequency and complex voltage oscillations can be observed in the phase voltage during off periods. This is primarily due to mutually induced voltages in non-conducting phases due to currents in the conducting phases. As has been stated above, in a real SR motor, inter-phase magnetic coupling always exists, primarily due to stator pole to pole flux leakage. In addition, in the voltage waveforms there are voltage oscillations due to snubber capacitors, which cause oscillations when the power semiconductor devices turn off.

Moreover, measurement errors can occur in the voltage measuring circuit, due to induced switching noise and magnetic coupling with the power circuits, when there are transients in the voltages and the currents in the motor. The effect of switching noise on the measurement circuits is most prominent when the current in a motor phase is being commutated, due to the high magnetic field changes that correspondingly occur.

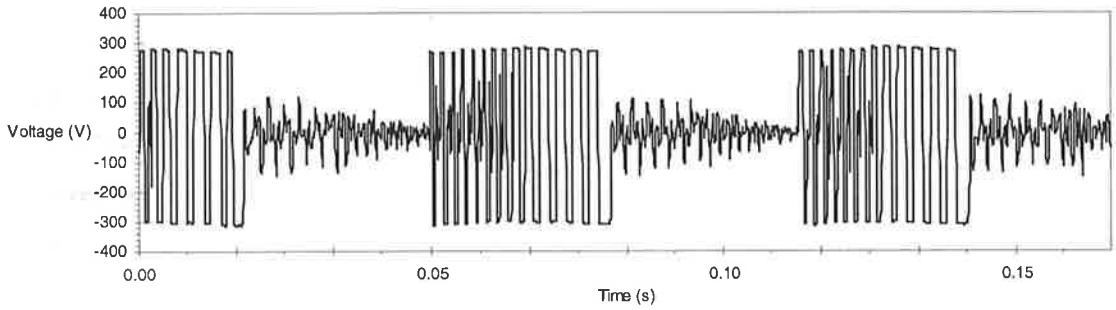
The voltage measurements show a low frequency oscillation in the dc voltage level of the inverter voltage pulses, which has the effect of a sinusoidal ripple on the voltage applied by the inverter. This is a characteristic phenomenon found in inverter drives that have a dc supply that is sourced from an ac mains rectifier. The output of the ac to dc voltage rectifier has harmonic components at multiples of the ac input supply frequency, with the main harmonic being at frequency 2ω (where ω is the ac mains frequency) [160]. However, an exact analysis of the harmonic ripple must take into account the line inductances, filter capacitance, filter reactance, and dc link current. These low frequency harmonic ripples on the dc link are transmitted onto the inverter output as sideband harmonics, which are a function of the dc link ripple and the inverter frequency, as detailed in reference [161].



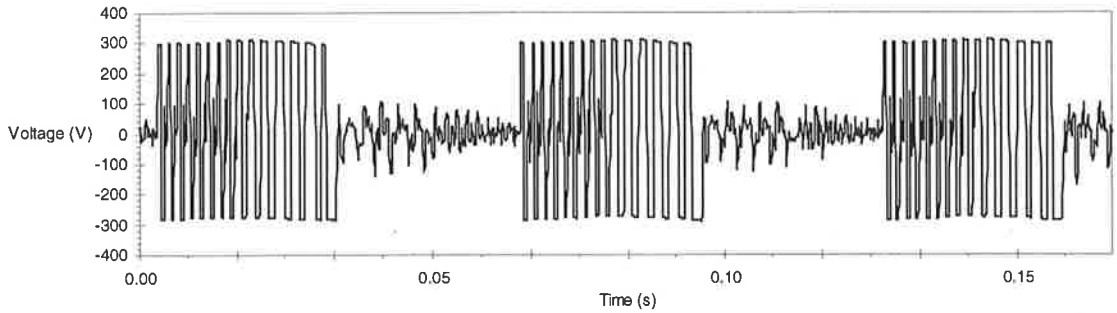
(a)



(b)



(c)



(d)

Figure 6.6 Phase Voltages of SR Motor - 162 rpm. (a) Phase A, (b) Phase B, (c) Phase C, (d) Phase D.

It can be seen that as expected, the current and voltage of the motor in this test are more complex in nature compared with those obtained in Chapter 5 from simulation, due to the complex and difficult to model real operational effects found in the actual SR motor drive. Therefore, the experimental waveforms presented here provide a more vigorous evaluation of the ability of the sensorless scheme.

In Figure 6.7, the estimated flux linkages found from integration of the actual voltages and currents are shown for all motor phases. It can be seen from the figure that in this mode of operation, the flux linkage waveform is highly complex and non-linear. During the chopping of the phase current, the flux linkage rises and falls in synchronism with the applied voltage. The general trend in the waveform is that the flux linkage increases in the *on* region of the phase, when the average voltage is positive. When the average voltage becomes zero or negative the flux linkage will decay to zero, and the regions when a motor phase does not conduct current, there are still some small amplitude flux linkage waveforms. This is due to the inter-phase coupling that was described above. In addition, measurement errors due to noise, integration errors, and dc offset will also produce errors in the flux linkage waveform.

As it has been discussed, the flux linkage predictor takes inputs of the previous values of the estimated flux linkage to produce a prediction of the flux linkage of the next iteration. The predicted values of flux linkage that are output from the algorithm's fuzzy predictors of flux linkage are given in Figure 6.8. Initially there are no rules stored in the fuzzy predictor's rule base, and the predictor has no knowledge or predicting ability about the flux linkage waveform. Thus, the prediction ability will be poor in the initial stages. However, with each iteration, rules will be generated describing the flux linkage waveform, and thus the fuzzy rule knowledge base will continually increase.

It can be seen in the figure that there are a number of points where the fuzzy predictors cannot make a prediction (ie. the output is made to be zero) in the initial stage of learning, due to lack of stored rules in the fuzzy learning rule base. However, after approximately 66.5 ms (400 iterations), or 18% of one revolution, the fuzzy predictors have effectively learnt the flux linkage waveforms. This demonstrates the fast learning ability of the predictors, even with the complex experimental waveforms.

As it has been mentioned previously, the fuzzy predictor of flux linkage helps to enhance the performance of the sensorless system, by helping to overcome transient errors and noise in the estimated value of flux linkage. If there is an error in the estimated value, then the predicted value can be used to smooth out the error. A more detailed discussion of the use of the fuzzy predictor to overcome errors in the practical motor drive will be discussed in the next chapter.

In Figure 6.9, the actual angle measured from the shaft encoder is shown together with the estimated angle from the sensorless algorithm. One can see from the results that the output angle from the fuzzy system accurately estimates the actual rotor angle at all times during this experimental test.

It was discussed in Chapter 4 that the resolution of the output estimated rotor position is dependent on the number of membership regions in which the output fuzzy domain is divided into. For a practical implementation, the minimum amount of membership regions

that will still provide the desired accuracy of results is used. This is because using a lower number of fuzzy sets decreases the required number of fuzzy rules in the fuzzy system and thus increases the efficiency of memory usage, as well as the speed of operation. In this thesis the output region was divided into regions such that there was one membership function per mechanical degree. Therefore, the output resolution of the estimated angle should be approximately 1 degree.

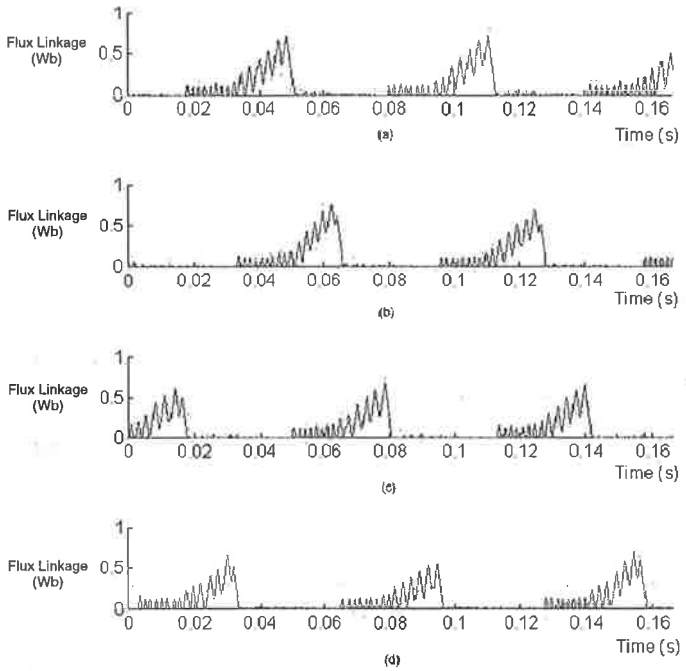


Figure 6.7 Phase Flux Linkages -162 rpm

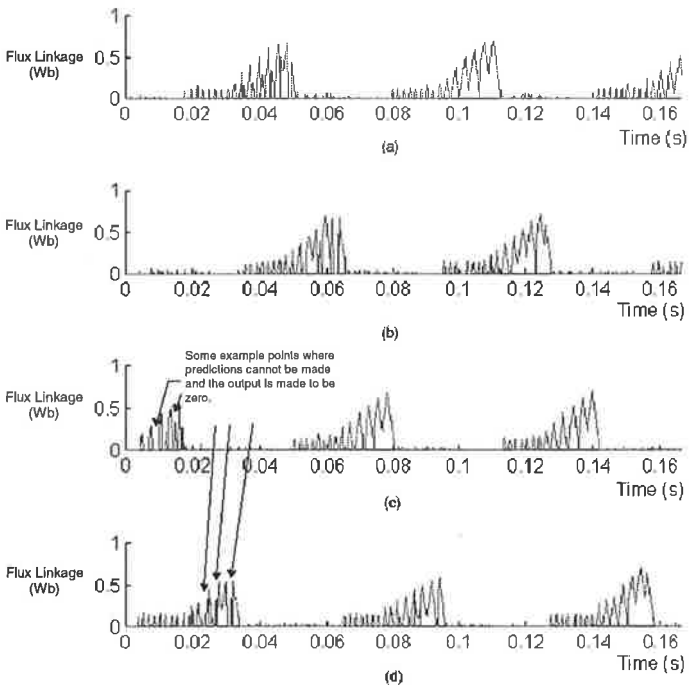
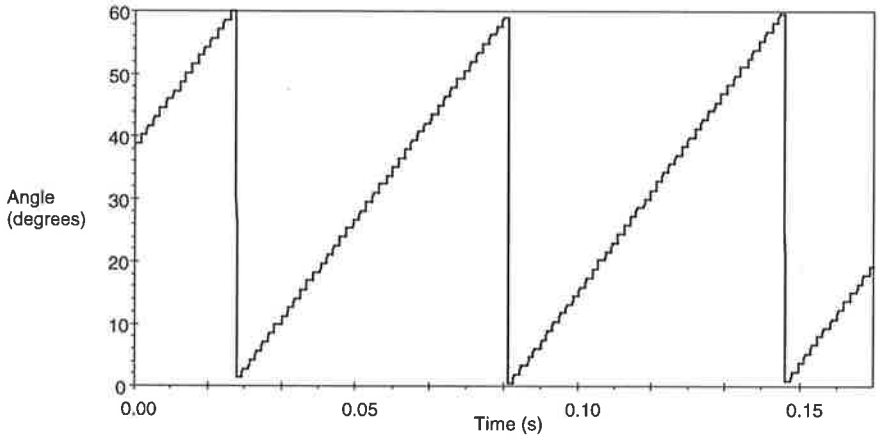
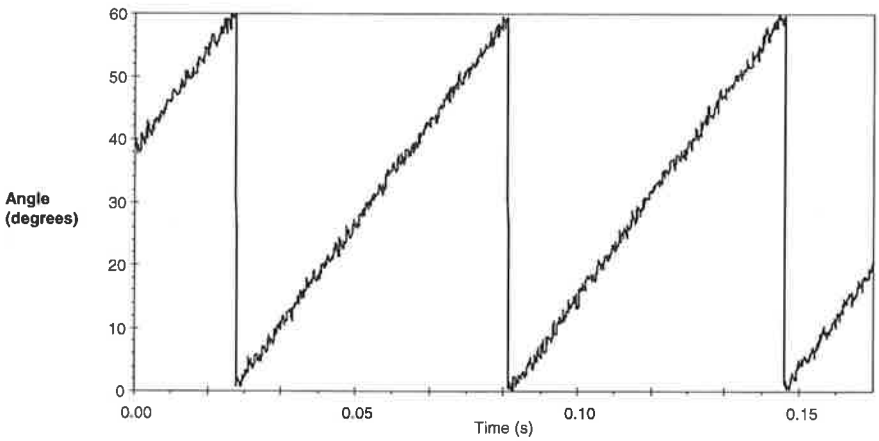


Figure 6.8 Predicted Flux Linkage - 162 rpm (Selected points where predictions cannot be made are highlighted).

However, the actual accuracy of each particular angle estimate at a given instant of time will vary according to the particular set of inputs of that iteration. This is due to the variations in accuracy of the fuzzy model and the fuzzy rules at various points on the input - output plane (where the current and flux linkage data are the inputs and rotor position is the output). The output accuracy will also be affected by the behaviour of the fuzzy predictors, because at some iterations the prediction accuracy may be higher than at other iterations, for example if the learning period has been longer and more accurate rules have been developed. In addition the particular value of error in the angle estimator inputs will vary at each iteration due the fluctuating value of switching noise, measurement error, integration error, and dc offset at any given instant of time. Hence, the actual estimation error at any given instant of time will in general be highly variable. Nevertheless, in this test the total angle error between the angle measured from the encoder has an average value of 0.48 degrees, and a maximum error of 1.55 degrees.



(a)



(b)

Figure 6.9 (a) Measured Rotor Position - 162 rpm. (b) Estimated Angle from Sensorless Scheme - 162 rpm

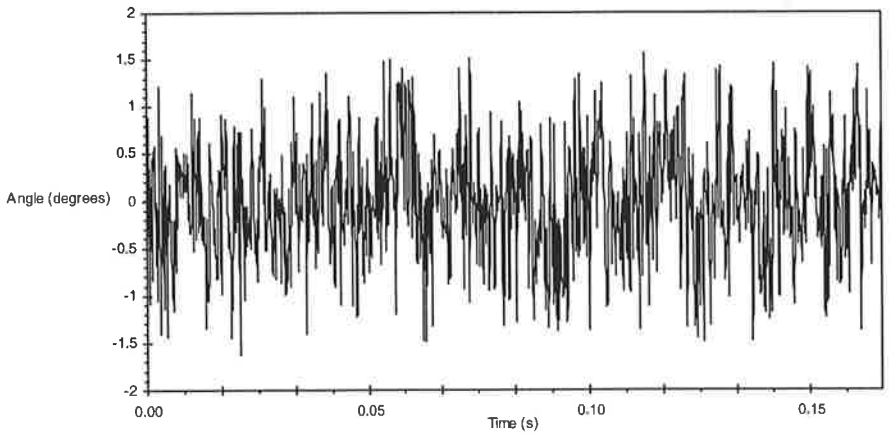


Figure 6.10 Error between Estimated and Measured Angle - 162 rpm

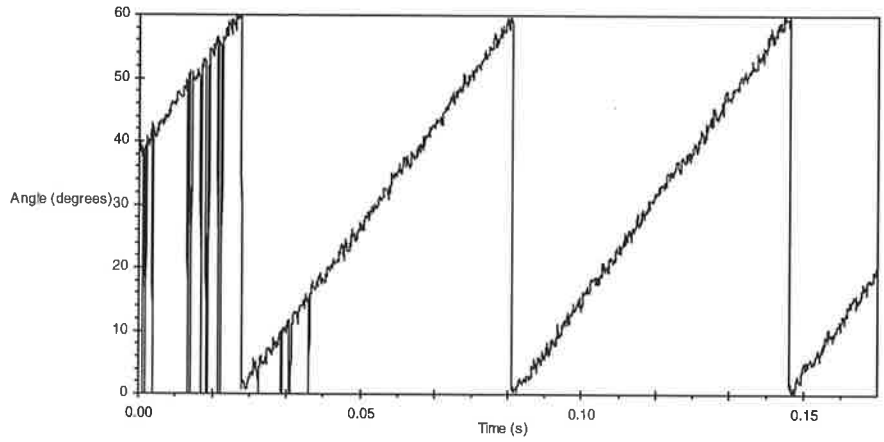
The plot of the angle estimation error of this test is shown Figure 6.10. It should be noted that the plot of the angle estimation error is a comparison between the estimated value and that measured with a 8 bit encoder, which in itself has some quantising error, as it divides one revolution into 256 steps. Therefore, the actual error between the estimated angle and the true physical rotor angle may at some points be less or more than that shown in the results.

In Figure 6.11 the plots of the predicted angle and next step predicted angle from the fuzzy angle predictors are also shown. As it has been discussed in Chapter 5, the predicted value of rotor position is used to reduce the effect of a transient error in the estimated value of the position. As it can be seen in these waveforms, before approximately 200 samples, or 9% of one revolution of the rotor, there are some points when the fuzzy predictors cannot make any prediction due to the initial learning period (as in the above flux linkage case, there are no prediction rules initially). However, after this time, the predictors learn the angle trajectory waveform, and can provide predictions of the angle for almost all samples.

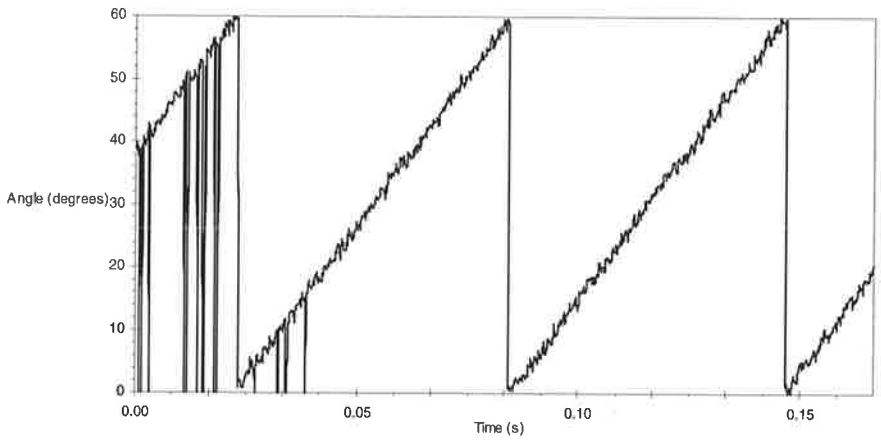
As it can be recalled, in the prediction of flux linkage that was shown above, the learning period was approximately 400 iterations, or double the amount for the angle prediction. The shorter learning time in this angle prediction case is due to the fact that the angle waveform has a linear characteristic within each electrical period. Therefore, the fuzzy angle predictors have a shorter learning period than the predictors of flux linkage, as the flux linkage predictors have a much more complex waveform to learn. As it was previously stated, simple linear waveforms will not require as many rules to be created in the fuzzy rule base due to the simpler trajectory of the waveform. This means that the flux linkage prediction algorithm will require a greater amount of created fuzzy rules, and a longer learning period, to describe the flux waveform.

It was detailed in Chapter 4 that the only inputs to the angle predictors are the previous values of the estimated position. No attempt is made to filter the previous position data, to reduce the variations of the estimated angle due to errors, or to use function approximations

of the previous input data to reduce the effects of errors. This is due to the primary reason that the scheme was developed to run in high speed real time operation. Hence, any complex calculations were avoided where possible. Fuzzy logic based prediction methods which use input error minimisation techniques usually involve iteration techniques [162],thus would not be suitable for real time operation.



(a)



(b)

Figure 6.11 (a) Predicted Angle - 162 rpm. (b) Next Step Ahead Predicted Angle - 162 rpm

Hence the accuracy of the predicted angle is expected to be equal or greater to the error of the estimated angle, as this is the only input information to the prediction algorithm. This is confirmed in Figure 6.12, where the difference between the predicted angle from the angle prediction algorithm, and the measured angle is shown. After the initial learning period, the error is comparable to the estimated angle error that was given Figure 6.10. Although the average error of the predicted and estimated angles is approximately the same, it should be recalled that the primary purpose of the predicted angle is to detect high amplitude transient error spikes in the estimated angle that may be caused by switching noise or other error producing effects. Thus the predicted angle can be used for removing high amplitude error spikes in the angle estimation, as will be examined in detail in Chapter 7.

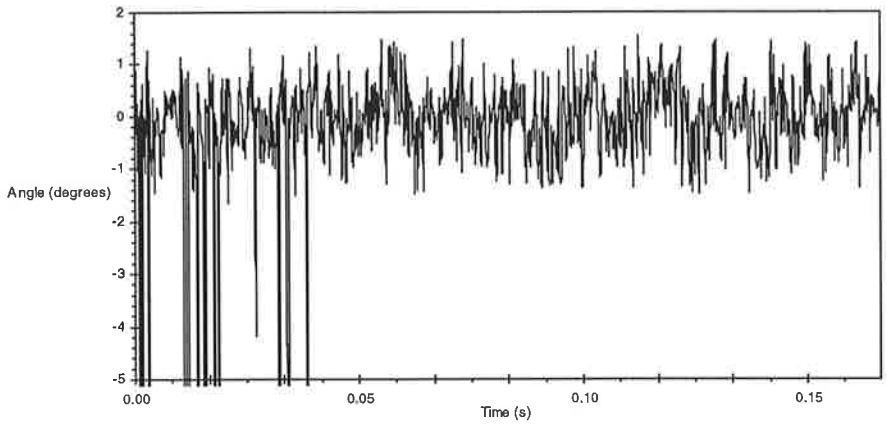


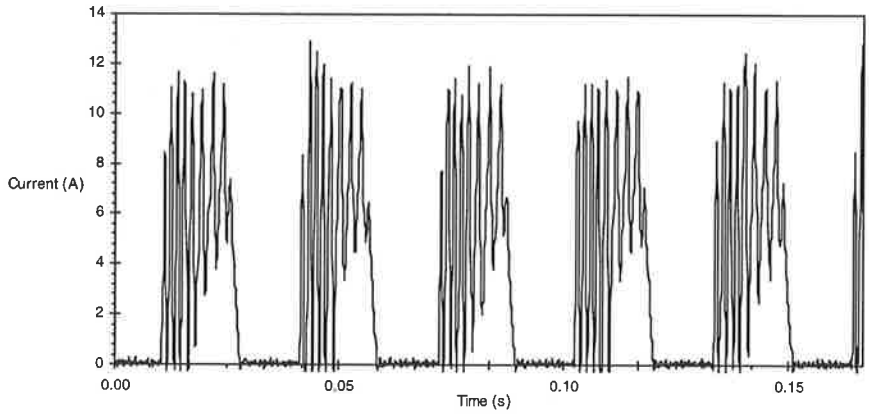
Figure 6.12 Error between Predicted and Measured Angle (The points heading off the graph are the times at which no prediction is made in the learning period).

6.4.1.2 Mid-Speed Chopping Mode Speed Test - 326 rpm

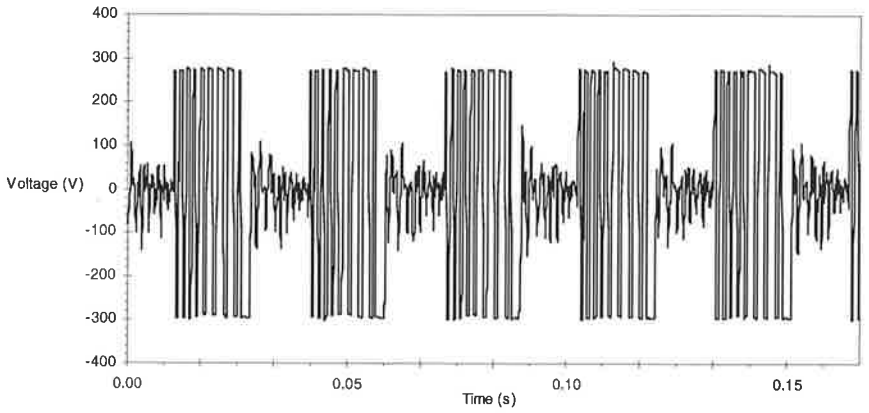
As it has been discussed, the sensorless algorithm should be tested thoroughly with a wide range of input data. The algorithm should be tested with the motor operating at varying levels of current chopping level and torque, because this in turn varies the motor current and flux linkage waveforms. The different current and flux linkage levels in the motor will lead to different input data in the both the sensorless position detection scheme and the waveform predictors. In addition, the algorithm should be tested at different motor speeds because the back emf of the motor is proportional to the motor speed. If the back emf of the motor changes, it also affects the current and flux linkage of the motor, which in turn entails different inputs into the position estimator.

Therefore, a second set of experimental waveforms of voltage and current were measured in which the speed and torque output of the motor, and the phase current levels were increased over the previous test at 162 rpm, to observe the performance of the scheme in mid speed chopping mode operation. The speed of the motor in these tests was set to a steady state speed of 326 rpm, so that it is approximately in the middle speed of the chopping mode (in the drive used in this thesis the chopping mode was set to run from start-up until approximately 650 rpm). In this case the motor is running with a mechanical load of 10 Nm being placed onto the motor.

The measured waveforms of voltage and current are shown in Figure 6.13. For simplicity, only the motor waveforms of phase A are plotted. As in the previous test, the motor is in chopping mode and thus similar waveforms of current and voltage can be seen. The current waveform in this case can be seen to have a higher average component during the turn on period than the previous case. This is because the maximum reference current has been raised to 10 A by the controller, to supply the added power output at this higher speed.



(a)



(b)

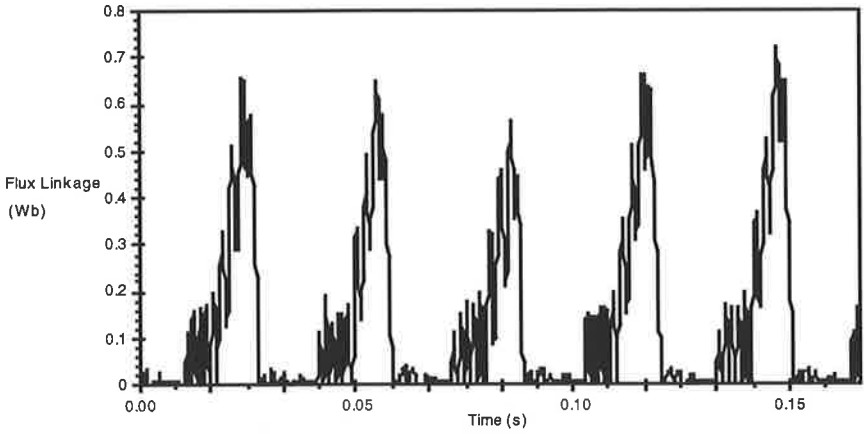
Figure 6.13 (a) SR Motor Phase A Current -326 rpm. (b) SR Motor Phase A Voltage 326 rpm

It can be seen in Figure 6.13 (a) that the current level increases up until approximately 12 A in some of the current pulses. This is due to the same effect that was discussed in the previous test, which is that the controller implements a maximum switching frequency. This means that the current may rise above the maximum hysteresis level due to fast current changes, before it is commutated.

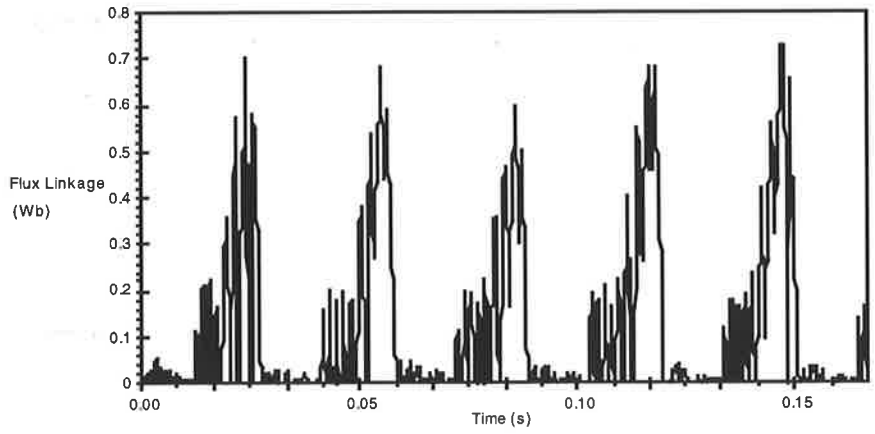
One can also see that, similarly to the previous test at 162 rpm that there are mutually induced voltages superimposed on the measured phase voltage waveforms. In addition, as in the previous test, the effects of switching noise, offset errors, and measurement errors will again produce errors in the measured motor waveforms.

The plot of the estimated flux linkage of each phase, found from the measured values of current and voltage, can be seen in Figure 6.14 (a). Additionally, the predicted values from the fuzzy logic predictors can be seen in the Figure 6.14 (b). Although the flux linkage waveforms are complex and highly non-linear, the fuzzy predictors can provide accurate predictions in almost all cases after the initial learning period (where the initial learning period is defined as the initial region where prediction points can not be made). In these results, the initial learning period that is when there are some points where no prediction can

be made, lasts for less than 400 iterations or 36% of a revolution. After this point, the predicted flux linkage curves follow the estimated flux linkage closely, and there are only a few points where there are no predictions (ie. the predictor output is set to zero).



(a)

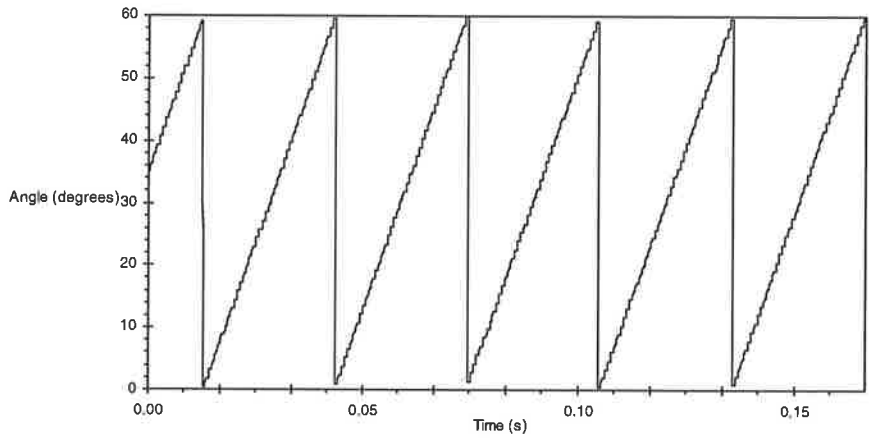


(b)

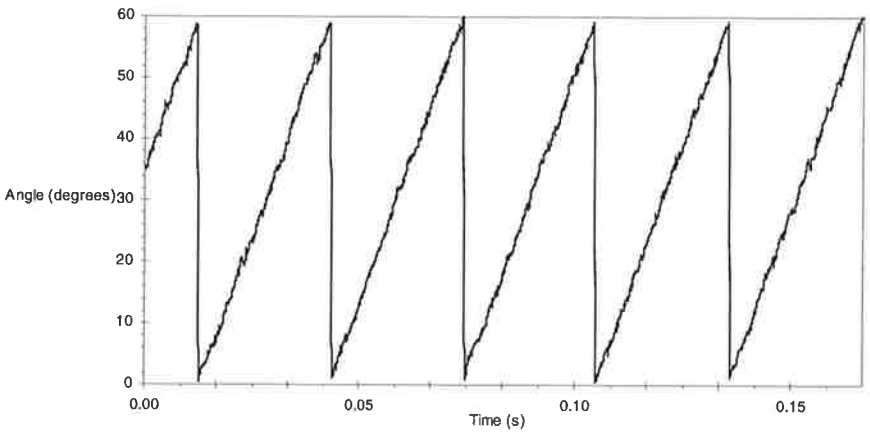
Figure 6.14 (a) Phase Flux Linkage - 326 rpm. (b) Predicted Flux Linkage - 326 rpm

If one compares the learning period of the flux linkage predictor in this test (in terms of the number of iterations required in the learning period), and the learning period of the flux predictor in the previous set of results of Section 6.4.1.1, then it can be perceived that they are very similar. This is expected because the form of the waveform in both cases is very similar, and thus one can expect approximately the same amount of learning data for both cases. Although the same amount of data is required for this case, this entails that the amount of rotor revolution in the learning period is greater because of the higher motor speed. If one required that the rotor movement during the learning period remained constant then the sampling frequency of the measured data must be increased. However, if one has a constant data throughput frequency (as is normally the case for practical A/D converters), then in general it can be said that the rotor movement for a learning period will increase with the speed of the motor. This may be a disadvantage at higher speeds, but could be solved by using high speed A/D converters for very high speed SR motor drives.

The measured rotor angle from the shaft encoder and the estimated angle from the position detection algorithm are shown in Figure 6.15. The average error (calculated as the average of the absolute value of error in all the samples) in this test result is 0.36 degrees, whilst the maximum error is 2.64 degrees. This is comparable to the previous angle error result for the previous test results in Section 6.4.1.1. The instantaneous angle error can vary according to the actual measurement error and noise value at each iteration time, and so the error in this case is slightly different than that seen in the previous test.



(a)



(b)

Figure 6.15 (a) Measured Rotor Position - 326 rpm. (b) Estimated Angle from Sensorless Scheme - 326 rpm.

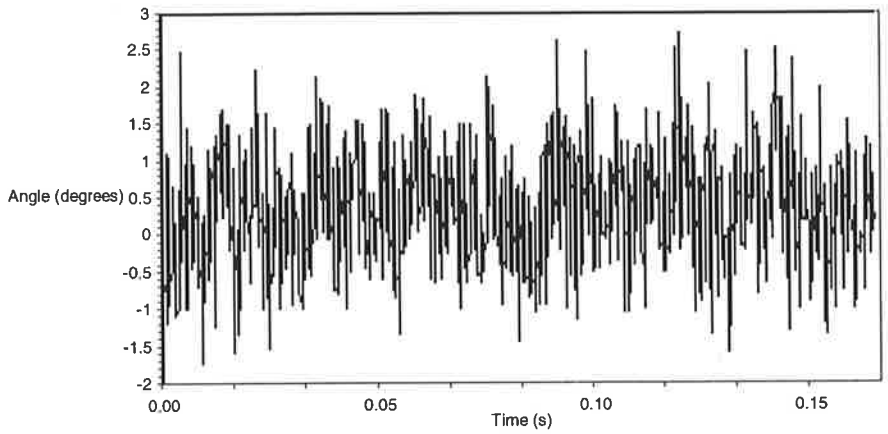
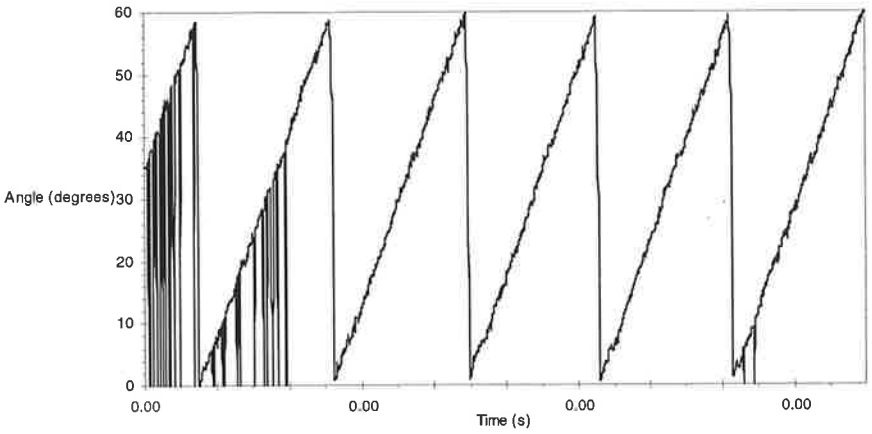
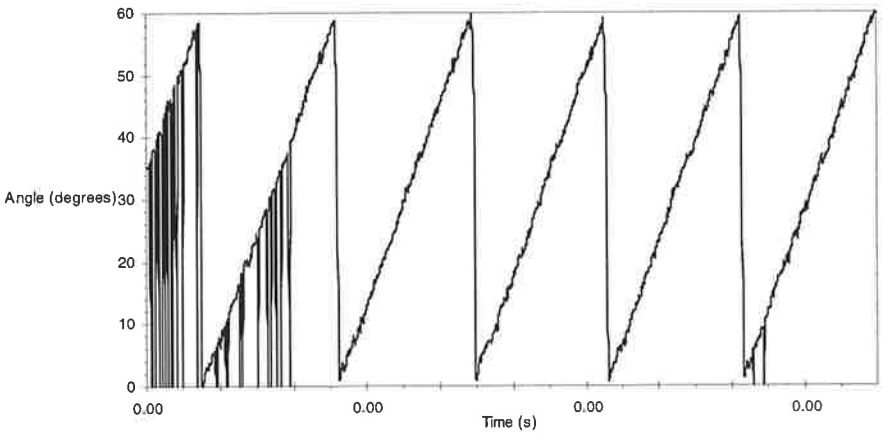


Figure 6.16 Error between Estimated and Measured Angle - 326 rpm



(a)



(b)

Figure 6.17 (a) Predicted Angle - 326 rpm. (b) Next Step Ahead Predicted Angle - 326 rpm.

The instantaneous error is plotted in Figure 6.16. Once again the error is calculated reference to the measured position of the shaft encoder, which in itself has some error due to quantisation.

Figure 6.17 plots the values of the predicted angle and predicted next step angle from the fuzzy logic based predictor. The angle predictor once again demonstrates a fast and accurate learning ability. After approximately 200 iterations or 18% of one rotor revolution at steady

speed, the angle waveform has been effectively learnt. The amount of iterations in the learning period for the angle prediction is comparable with the learning period of the angle in the previous test at 162 rpm, which was shown in Section 6.4.1.1. This is because the form of the angle variation is linear in both cases, and hence approximately the same number of input data is required in both of the test cases to learn the angle waveform.

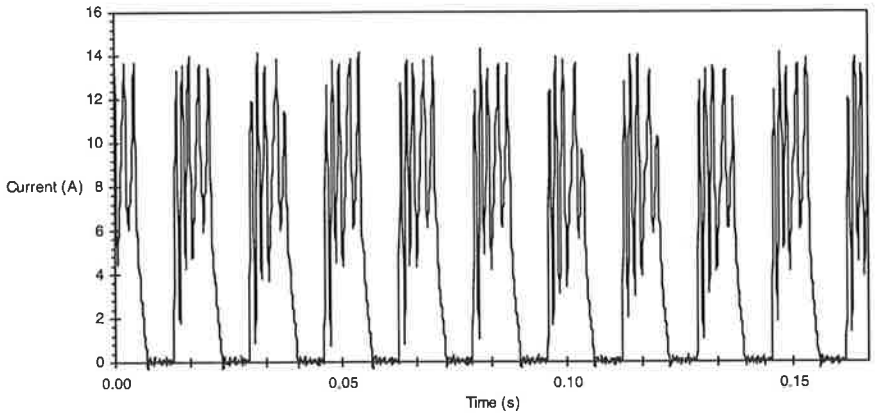
As it was discussed previously, the angle waveform is much simpler to learn than the non-linear flux linkage waveform. Thus, the learning period for the rotor angle predictor is considerably less than the 400 iterations required for the flux linkage predictor in this test.

6.4.1.3 High Speed Chopping Mode Test - 606 rpm

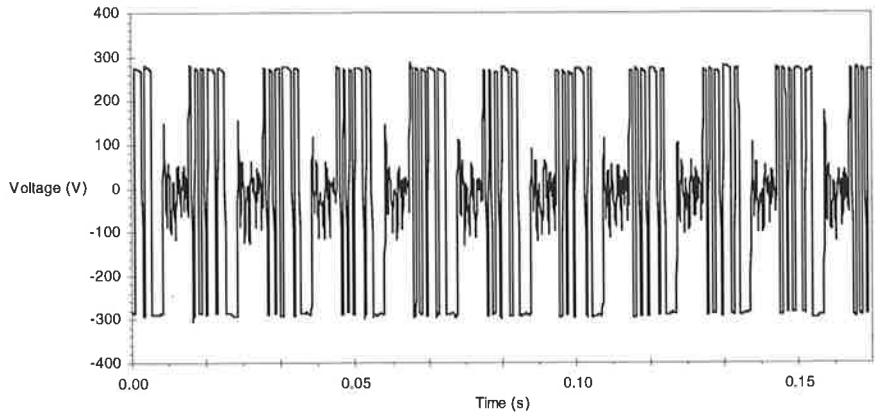
As it was stated previously, in the experimental drive changeover from the chopping mode of operation to the single pulse mode of operation occurred at 650 rpm. Hence, the higher speed chopping mode occurred just before this speed. It should be noted that hysteresis was added to the motor controller, in order that unwanted oscillations between the two modes was prevented. If no hysteresis is added, then the two modes may continually alternate if the motor speed remains close to 650 rpm. Therefore, in the experimental system, the chopping mode control was switched to single pulse mode control at 650 rpm, but re-switching into the chopping mode only occurred when the speed decreased to 620 rpm.

In this section, experimental results are given for the case of the motor being mechanically loaded at higher speeds of the chopping mode. In addition the maximum current in this test is increased to 14 A (as opposed to 12A in the previous test). The current levels and the back emf of the motor are greater in this higher speed chopping mode condition. In addition the back emf is higher for this higher speed, and this also affects the current waveform, and thus the flux linkage waveform. In this case the back emf will be approximately 85% higher than the previous chopping mode test at 326 rpm, due to the fact that the back emf is approximately proportional to speed. Therefore, the different current and flux levels of this test provides different data points which test the algorithm with different input values.

The speed for this test is a steady state speed of 606 rpm, and the motor in this experiment is supplying an external load of 14 Nm. The current and voltage waveforms of Phase A are shown below. As it can be seen in the figure, the current waveform has higher average component during the turn on period than the previous case in Section 6.4.1.2, as the load demands a greater power output at this higher speed.



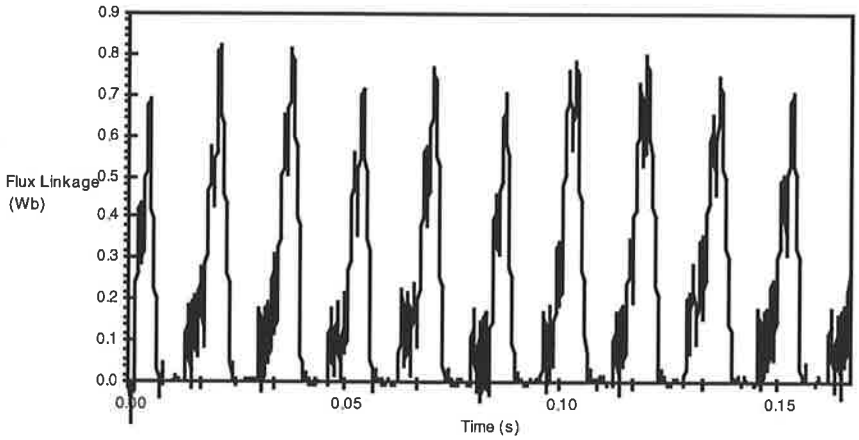
(a)



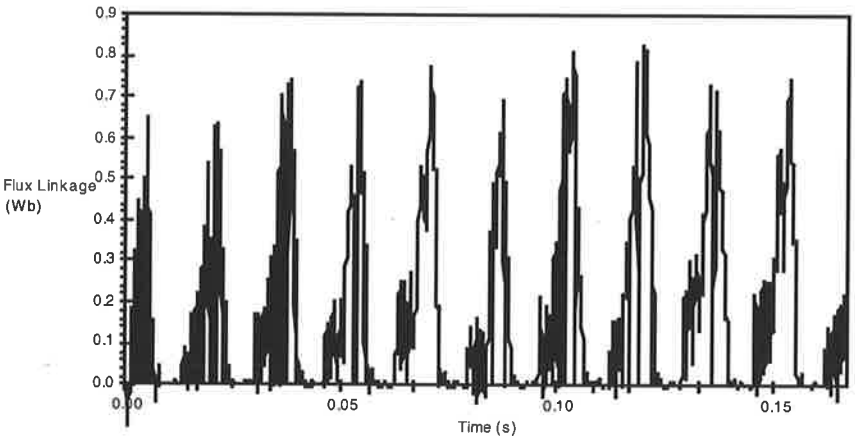
(b)

Figure 6.18 (a) SR Motor Phase A Current - 606 rpm . (b) SR Motor Phase A Voltage - 606 rpm.

In Figure 6.19, the results of the estimated flux linkage for this test is shown. It can be seen that the estimated flux linkage waveforms found from the measured phase voltages and currents are again highly complex and non-linear, and the peak values of the flux vary slightly between each pulse. This is due to the fact that the hysteresis current controller does not always commutate the current at the hysteresis level (due to the previously mentioned minimum control bandwidth). Due to the complex waveform, the prediction of the complex waveform can be difficult. Nevertheless, as can be seen in Figure 6.19 (b), the predicted values from the fuzzy predictors are relatively accurate, and after the initial learning period, predictions can nearly always be made. Due to the complex waveform it was found that the learning period was again relatively long. It was found in this test that the learning period lasted for approximately 420 iterations, during which time there are many points where no predictions can be made. This amount is approximately equal with the results given for the chopping mode results of Section 6.4.1.1 and 6.4.1.2. This was expected because the form of the flux linkage waveforms is similar in each of these tests.



(a)



(b)

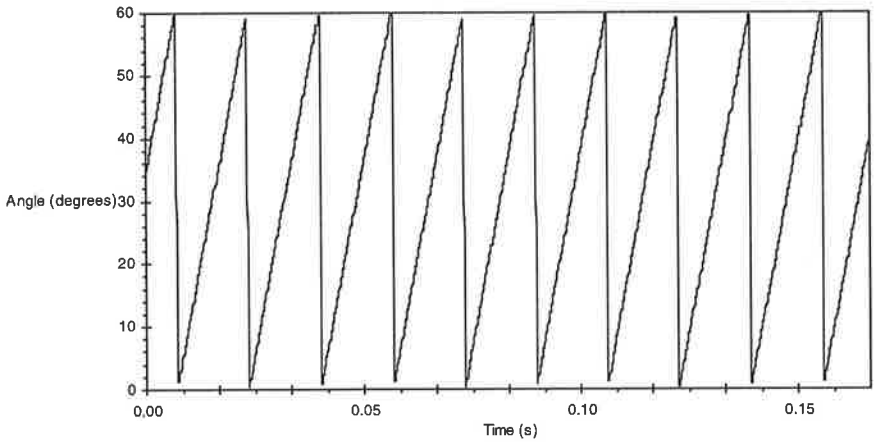
Figure 6.19 (a) Phase Flux Linkage - 606 rpm. (b) Predicted Flux Linkage - 606 rpm.

The actual angle measured from the shaft encoder, and the output estimated angles from the sensorless algorithm are given in Figure 6.20. As one can see from these figures the estimated angle accuracy is good throughout this chopping mode test.

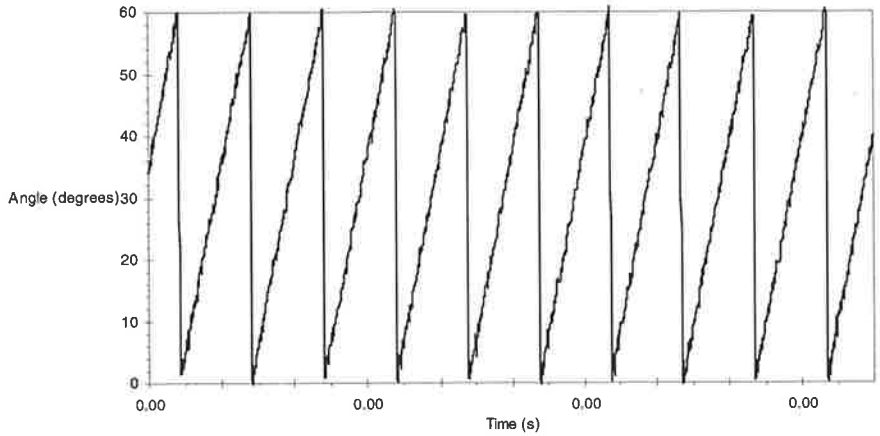
To examine the performance of the angle estimation, the error between the output estimated angle and the measured angle is detailed in Figure 6.21. The error amplitude has an average value of 0.79 degrees, and a maximum value of 2.8 degrees relative to the encoder measured position.

It can be seen that the error is larger in this particular case, as compared to the previous two tests. Although a detailed analysis of errors will be given in Chapter 7, a brief explanation will be given at this point. The main reason for the increase in the error in this particular result is that the speed of the motor has increased, which means that the period in time of the electrical cycle has decreased. Due to the fact that the sampling time is constant, this entails that the number of sampling instants per electrical cycle has decreased in this test. This lowers the effective bandwidth of the measurement of voltage and current, and thus a lower amount of high frequency variations of the chopping mode waveforms will be captured. Hence the flux linkage estimation which integrates the measured waveforms will have higher

errors due to this low effective measurement bandwidth effect (as will be detailed in the next chapter), and thus the position estimation will also have higher errors.



(a)



(b)

Figure 6.20 (a) Measured Rotor Position - 606 rpm. (b) Estimated Angle from Sensorless Scheme - 606 rpm.

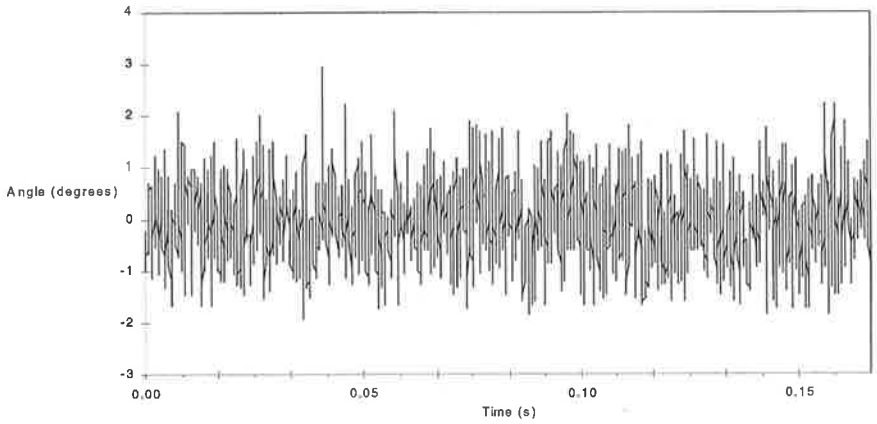


Figure 6.21 Error between Estimated and Measured Angle - 606 rpm

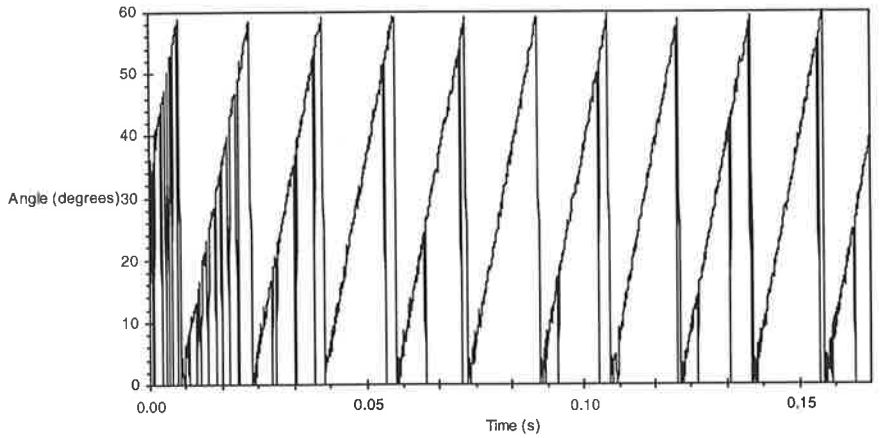
The decrease in the effective bandwidth at this higher speed chopping mode test is further compounded by the fact that the chopping mode motor waveforms are highly non-linear and have fast variations. This means the accuracy of flux linkage estimation is further reduced

than if the waveforms had simpler dynamics. It will be seen in the next section, that in the single pulse mode of operation the current and flux linkage waveforms of the motor have much lower non-linearity and fast varying components than in the single pulse mode. As the high frequency components in the single pulse mode are less significant, the waveform measurements can have a lower measuring bandwidth. This means that one of the most difficult operation regions of the motor as far as angle estimation is concerned is in the high speed chopping mode region, because of the dual effects of low effective measurement bandwidth, and highly non-linear and fast varying waveforms. The combination of these effects will lead to low bandwidth measurements of the voltage and current, which leads to higher errors in the flux linkage estimation of the sensorless angle estimation algorithm, and thus a corresponding higher error in the output estimated angle.

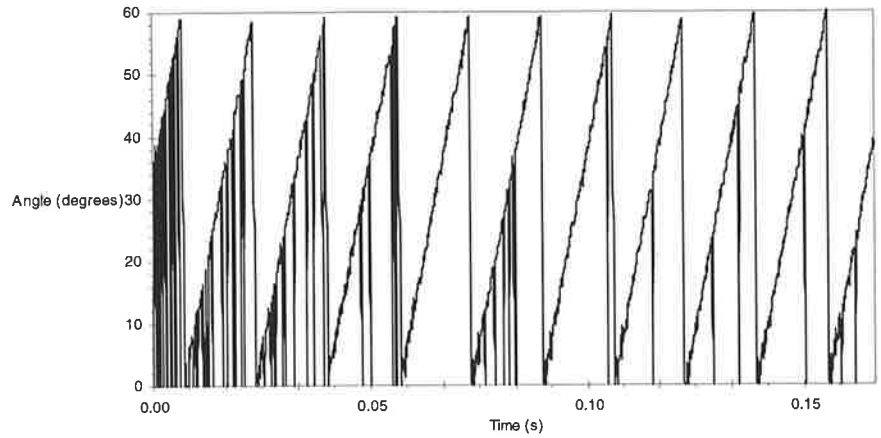
It should be noted that at any particular instant the error may be higher or lower compared to the average error. This is due to the fact that the error in flux linkage and current will vary according to the instantaneous effect of the various error producing effects. This will vary according to the particular value of measurement noise, error in flux linkage due to the above mentioned low effective bandwidth effect, and integration and offset errors at each particular sampling instant. Therefore, the instantaneous position estimation error (as shown in Figure 6.21) varies with each sample.

Nevertheless, even with the higher error results in this test, these results show that that the sensorless scheme has a good performance in the higher speed chopping mode. This is despite the lower samples per electrical cycle of the non-linear and fast varying waveforms.

The predicted values of rotor position from the predictor algorithms are given in Figure 6.22. In this case the predicted angles have achieved a good accuracy in following the rotor position trajectory. The initial learning period, when there are a lack of predictions, is approximately 260 iterations, which in this test is 43% of one revolution. This is slightly higher than the lower speed chopping mode tests, and is related to the fact that the estimated angle error is also higher in this test, because of the effects explained above. If the estimated angle error is higher, then there may be higher random noise variations of the estimated angle. Thus the prediction of the noisier estimated angle will be more difficult, than the case when the error is lower. This will lead to a longer learning period, as more rules in the predictors knowledge base must be created to learn the angle trajectory with higher errors.



(a)



(b)

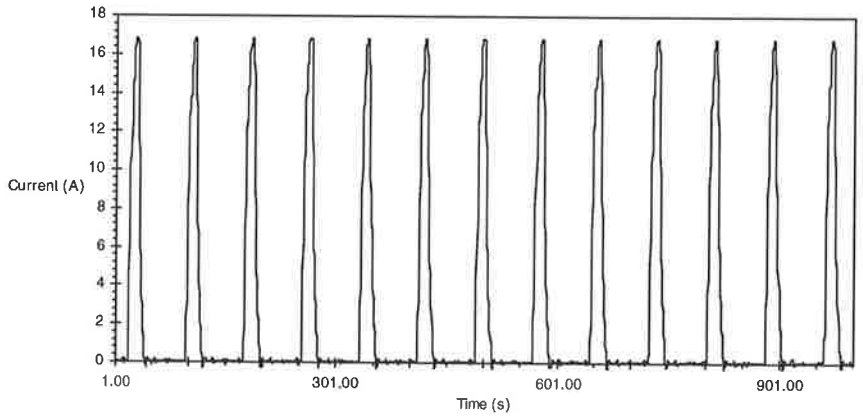
Figure 6.22 (a) Predicted Angle - 606 rpm. (b) Next Step Ahead Predicted Angle - 606 rpm.

The above experimental results show that the sensorless rotor position estimation scheme can be used effectively in an actual SR motor system operating in the high speed ranges of the chopping control region. It was mentioned that this particular mode of operation is one of the most difficult for the position estimation algorithm. This is because of two main reasons: Firstly, the effective bandwidth of the measurements decrease (assuming a constant A/D converter sampling frequency) due to a lower amount of measurements per electrical cycle for higher speed operation. Secondly, the chopping mode motor waveforms are highly non-linear and fast varying. Therefore, these two dual effects will mean that the accuracy of the flux linkage estimation by integration will be lower and this will impact on the accuracy of the angle estimates. It will be seen in the next section that the higher speed single pulse mode waveforms have lower fast varying dynamics, and thus are less sensitive to lower measurement samples per electrical cycle.

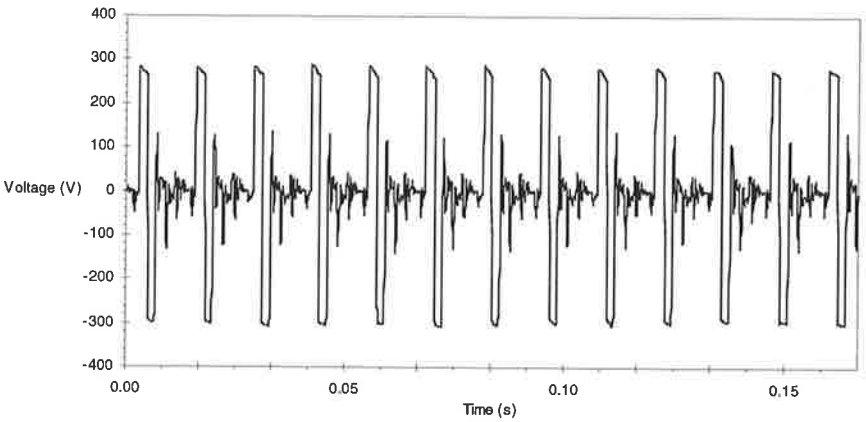
6.4.2 Single Pulse Mode Steady State Experimental Results

It was discussed in Chapter 2 that at high motor speeds the chopping mode commutation of current is not used, and the current is only controlled with the turn on and turn off angles. This is due to the fact that as the speed of the motor rises the back emf of the motor increases, and at high speeds the back emf during pole overlap can be higher than the dc

supply voltage. If this is the case, then the current will not reach the chopping mode current level during the phase conduction period. The motor drive is thus in the single pulse mode, where the voltage applied to the phase in each cycle is turned on and off only once, and the current is only controlled using the on and off angles only. As it was mentioned previously, in the motor drive system used in these experiments, the chopping mode ended at a speed of approximately 650 rpm. In order to show the operation of the position estimation in various motor conditions, the following results show the performance of the fuzzy logic based sensorless scheme in the higher speed range single pulse mode.



(a)



(b)

Figure 6.23 (a) SR Motor Phase A Current 810 rpm. (b) SR Motor Phase A Voltage -810 rpm

In the results described below, the speed of the motor is increased into the high speed region where the control method has changed for the chopping mode to the single pulse mode. In Figure 6.23, the current and voltage waveforms of Phase A are shown for the single pulse mode of the motor with a steady state speed of 810 rpm. In this particular test, the motor was mechanically loaded with a 7 Nm torque.

The current waveform for each phase can be seen to be a single pulse in each electrical cycle. Correspondingly, the voltage has a single turn on and single turn off period. During the turn on period of the voltage the current increases from zero, whilst at turn off the current is

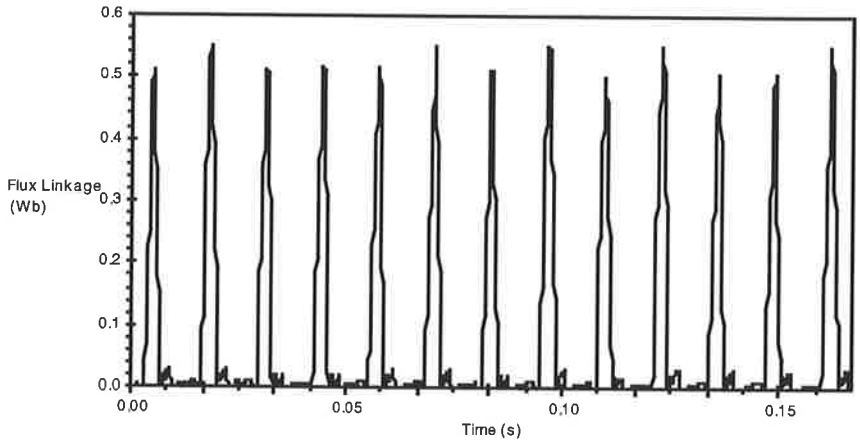
commutated so that it decays back to zero. In this test the current waveform can be seen to be regular in all the electrical periods, and each pulse has the same waveform and also approximately the same peak value of 17 A. The higher current levels in this test allow the angle estimation algorithm to be tested with different data inputs than the previous tests. The regularity of the waveforms is due to the constant speed and torque in this test, which means that the turn on and turn off angles are kept constant.

It can be seen that, as previously mentioned, the current waveforms have a much more simple wave-shape than the highly non-linear waveforms in the chopping mode. The high frequency components of the current in the single pulse mode are less significant, and thus the number of samples per electrical cycle, or the measurement bandwidth, can be reduced relative to the chopping mode. However, at very high speeds, when the electrical cycle time is very short, the actual single pulse motor phase current waveform itself will be at a high frequency. At these speeds, the A/D must sample at a high enough frequency to capture the fundamental dynamics of the single pulse mode currents. This applies to all sensorless position detection schemes that measure the phase current. Nevertheless, another advantage of the fuzzy logic based algorithm is that it can cope with a very low number of samples per electrical cycle, as will be examined in Chapter 7. Hence, by using fuzzy logic techniques, the cost of the A/D converters can be lowered, due to the fact that only a relatively low number of sampled per electrical cycle are required in the fuzzy logic based estimation algorithm.

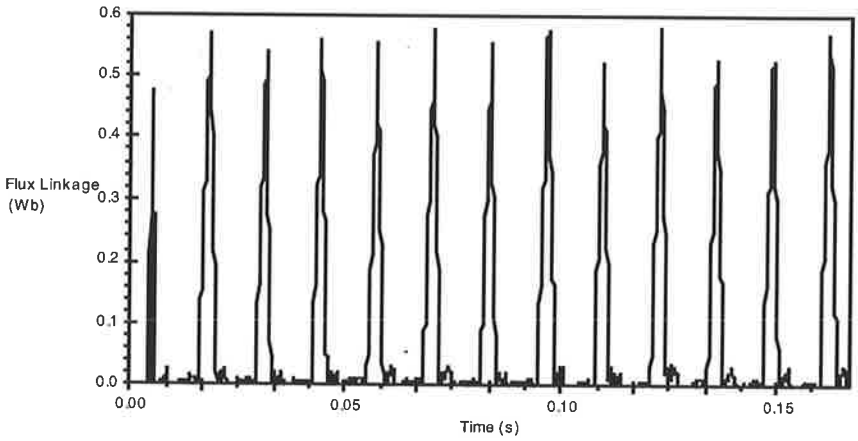
In Figure 6.24 (a) the estimated flux linkage found from the measured waveforms of voltage and current is shown. There are variations in the maximum amplitudes of each pulse due to small variations in the on and off control angles and the dc supply voltage ripple and variation. It can be seen that in the single pulse mode the flux linkage in the single pulse mode has a triangular wave-shape. It can be recalled from Chapter 2, that in the idealised single pulse waveforms, the flux linkage has a perfect triangular wave shape. This is due to the fact that it is assumed that during turn on the voltage is a constant positive dc level, and during turn off it is a constant negative dc level. However, in the practical case voltage source inverters can not usually maintain a constant dc voltage when current flows. During the duration of the positive voltage pulse, the level of voltage drops as energy is removed from the power supply. In addition to this, the dc voltage bus ripple component is superimposed on the voltage waveform which varies the waveform of each voltage pulse. Therefore, the flux waveform will not be perfectly triangular in the single pulse mode. However, in general, the effect of the non ideal voltage source has only a small effect, and the single pulse mode flux has a linear and simple variation, in contrast to the flux linkage that is found in chopping mode operation.

The flux linkage characteristic is simpler than the flux linkages seen above in the chopping mode experimental results. Therefore, it can be expected that the fuzzy predictors of flux linkage should have a shorter learning period in this case. This is confirmed in Figure 6.24,

where the learning period is less than 200 iterations, corresponding to 46% of one revolution, compared with the learning period of approximately 400 - 450 iterations that was found in the chopping mode experiments.



(a)



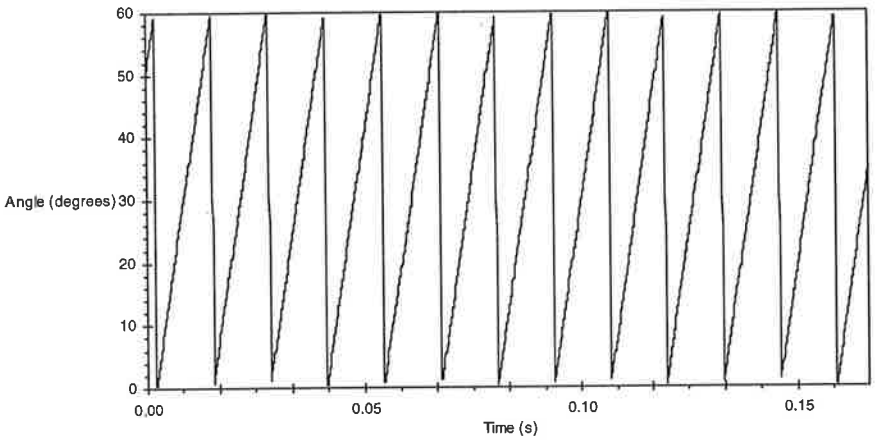
(b)

Figure 6.24 (a) Phase Flux Linkage - 810 rpm. (b) Predicted Flux Linkage - 810 rpm.

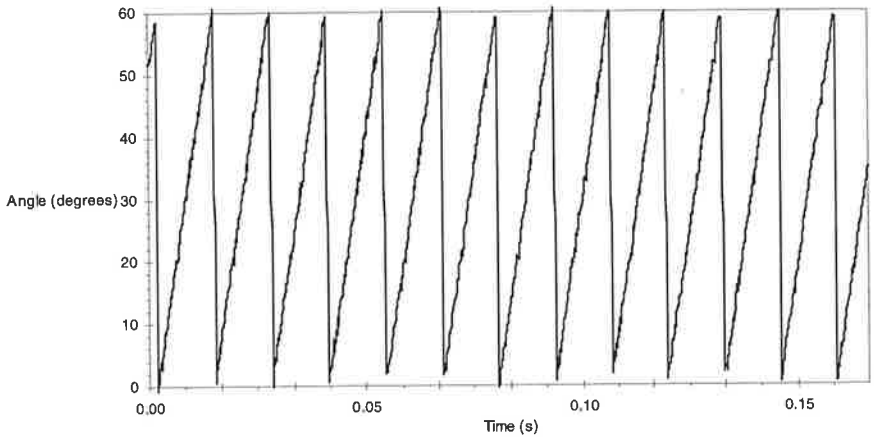
The estimated and measured rotor positions for this test are shown in Figure 6.25. It should be noted that there are some points where the measured rotor position, and correspondingly the estimated rotor position does not reach zero degrees. This is because only the sampled points are shown. Although the A/D converters in the constructed system have a very high sampling frequency capability, the experimental results are demonstrated with the purpose of showing the performance with a low sampling frequency of 6000 Hz. This is in order to demonstrate the ability to perform with slower, low cost components (in terms of sampling frequency and iteration or calculation speed) which are more compatible with practical economical systems. Therefore, at this higher motor speed, the actual zero degree point of the rotor may fall in between two sample points. As the angle estimation algorithm uses the currents and voltages at the sampling points, the corresponding estimated angle will also not be exactly zero, if the rotor angle of zero falls in between the sample times.

It can be seen that in this test the estimation rotor angle has a good accuracy. In this test, the

average amplitude of error in this test was 0.52 degrees, whilst the maximum error in this test was 1.92 degrees.



(a)



(b)

Figure 6.25 (a) Measured Rotor Position - 810 rpm. (b) Estimated Angle from Sensorless Scheme - 810 rpm.

The actual angle error is detailed in Figure 6.26. It is interesting to note that the error in this test is less than the previous high chopping mode speed test that was described in Section 6.3.1.3. In that section, it was said that because the A/D converter sampling frequency was maintained at the relatively low frequency of 6000 Hz, the bandwidth of the measurements were low, relative to the higher speed motor waveforms. Therefore, the error in the flux linkage estimation, which uses integration of these waveforms, increased and resulted in a higher angle estimation error. In this particular test, the bandwidth of the measurements are even less than that of the previous chopping mode test. Hence, the flux linkage for the same conditions should have an even greater error, leading to a higher error of the rotor position. However, in this test the single pulse mode region of control has been entered, and hence the waveforms of voltage and current have a reduced higher frequency component, due to the lack of the hysteresis commutation of current found in the chopping mode. Thus, relative to the bandwidth of the current and voltage signals, the bandwidth of the A/D conversion is still adequate, and thus flux linkage estimation errors are lower than for the previous high

chopping mode speed test. This entails a lower angle estimation error, as observed in these results.

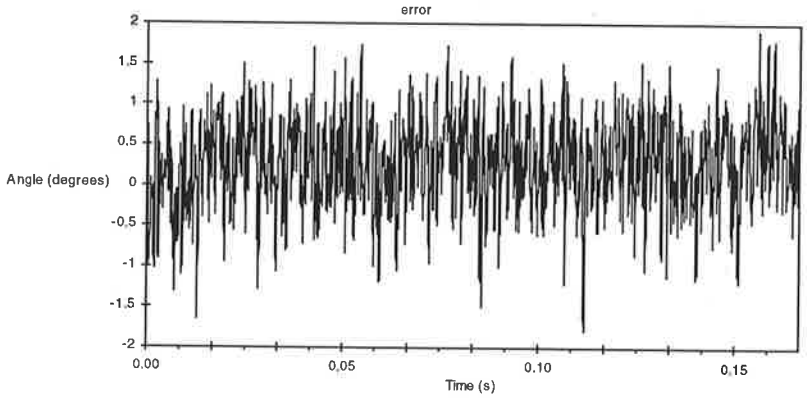


Figure 6.26 Error between Estimated and Measured Angle - 810 rpm

The results of the prediction of rotor angle is shown in Figure 6.27, and it is shown that the initial angle waveform learning period approximately the same as the previous tests.

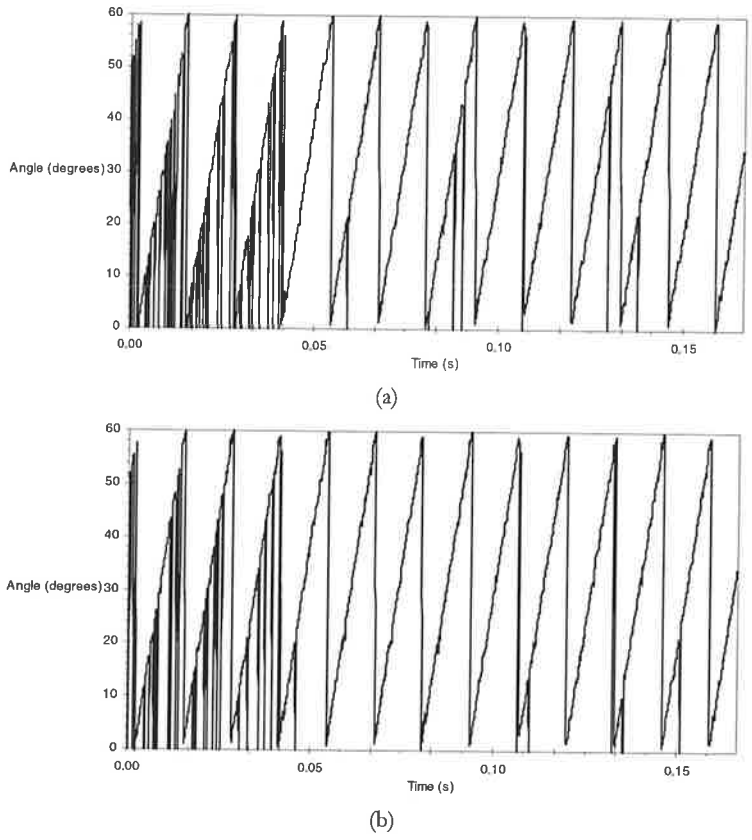


Figure 6.27 (a) Predicted Angle - 810 rpm. (b) Next Step Ahead Predicted Angle - 810 rpm.

It was found that approximately the first 240 iterations were needed for the initial learning period. This was equivalent to 52% of the one revolution of the rotor at constant speed. In comparison with the flux linkage prediction of this test, it is seen that the learning period is slightly longer. Unlike the previous chopping mode tests, the flux linkage waveform in this case is also more linear and simple in nature, and thus has approximately the same learning period as the rotor angle predictor. Hence, it can be concluded that in general, for the

developed fuzzy logic based prediction algorithm, approximately 200 - 250 iterations are required for the approximating of simpler waveforms, whilst a higher learning period is needed for highly non-linear, fast varying waveforms such as the flux linkage in the chopping mode of operation.

6.4.3 Transient Operation Experimental Results

For the sensorless position detection scheme to be viable, it must be able to accurately estimate the rotor position during all modes of operation and speeds. This entails that the sensorless scheme must accurately determine the rotor position not only in steady-state operation, but also during all transition times between different torque outputs and speeds, and hence during all times when transient motor operation occurs. In addition the sensorless scheme must operate during the start up from zero speed.

6.4.3.1 Transient Operation Test - Start-up

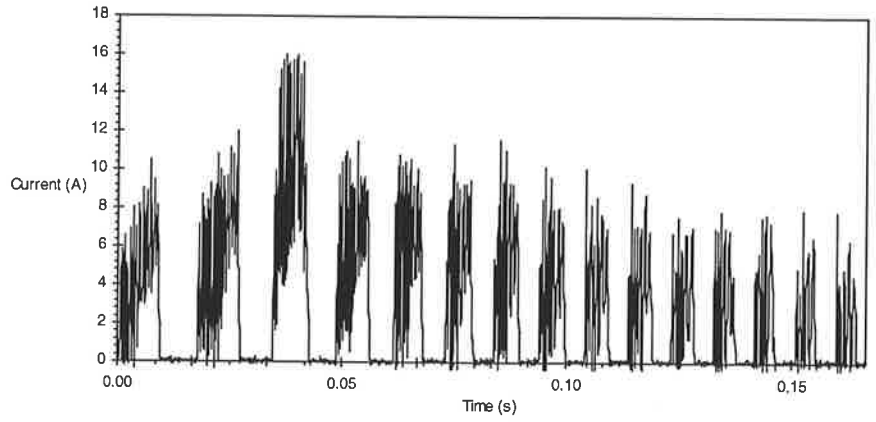
To verify the operation of the sensorless algorithm during transient operation, a set of experimental results are given for the motor waveforms during a transient start-up from zero speed to 346 rpm. The Phase A current for this test and the corresponding Phase A voltage is shown in Figure 6.28. At the commencement of the test the phase currents are high due to the initial motor acceleration of the rotor and load inertia. However, when the motor approaches the steady state speed of 346 rpm the currents become significantly lower due to the increase in back emf. In addition, it can be seen that as the motor speed of the motor increases from zero speed, the phase current conducting time becomes shorter. This is due to the fact that the controller maintains a constant phase conduction angle (on and off angles remain constant), and varies the output torque of the motor by varying the current commutation level.

In Figure 6.29, an expanded view is shown of the first current pulse after the initial start up of the motor. One can see clearly that the initial transient current waveform is highly non-linear in nature. Non-linear current waveforms are typical during transients or for continual acceleration in the SR motor. Thus, this operation will present a more difficult problem for the position estimation due to two main reasons:

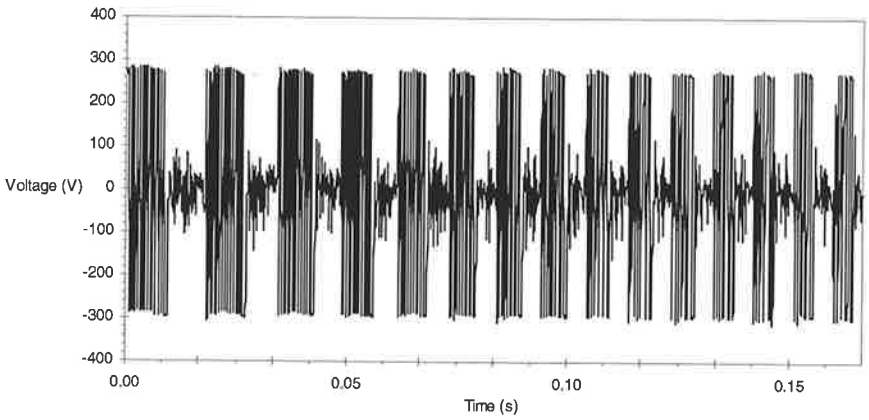
I. The transient motor waveforms have a wide frequency bandwidth, which means that not all the components of the waveforms will be captured by the A/D converter measurement system. This will lead to an increase in errors in the flux linkage estimation, which integrates the measured waveforms of voltage and current.

II. The predictors of flux linkage and rotor position, which are used to lessen errors in the flux linkage and position estimation, are not as effective during transient modes of operation. This is because of the learning period always required when the motor waveforms vary. Therefore, the confidence in the predicted values will not be as high in

the transient mode of operation, which means the predicted values may not be as useful for lessening the effect of error deviations in the estimated flux linkage or rotor angle.



(a)



(b)

Figure 6.28 (a) SR Motor Phase A Current - Transient Start Up. (b) SR Motor Phase A Voltage - Transient Start Up.

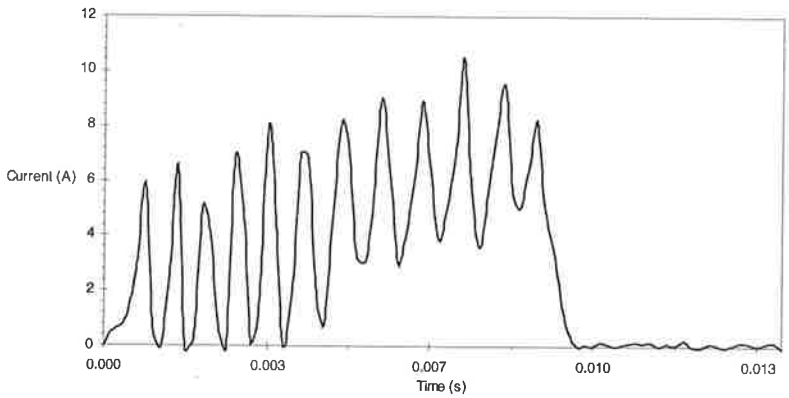


Figure 6.29 Expanded SR Motor Phase Current - Transient Start Up.

Apart from these two main problems due to transient operation, the effects of measurement errors and switching noise will also have some effect on the position estimation. Hence, transient operation poses a difficult tests for the rotor position estimation algorithm.

The flux linkage estimated from the phase current and voltage is shown in Figure 6.30 (a). In addition, a more detailed view of the flux linkage pulse immediately after start up is shown in Figure 6.31. It can clearly be seen that the waveforms of the phase flux linkage are complex and non-linear for this transient start-up test. As stated above, these waveforms result in a more difficult examination of the fuzzy predictors' capability.

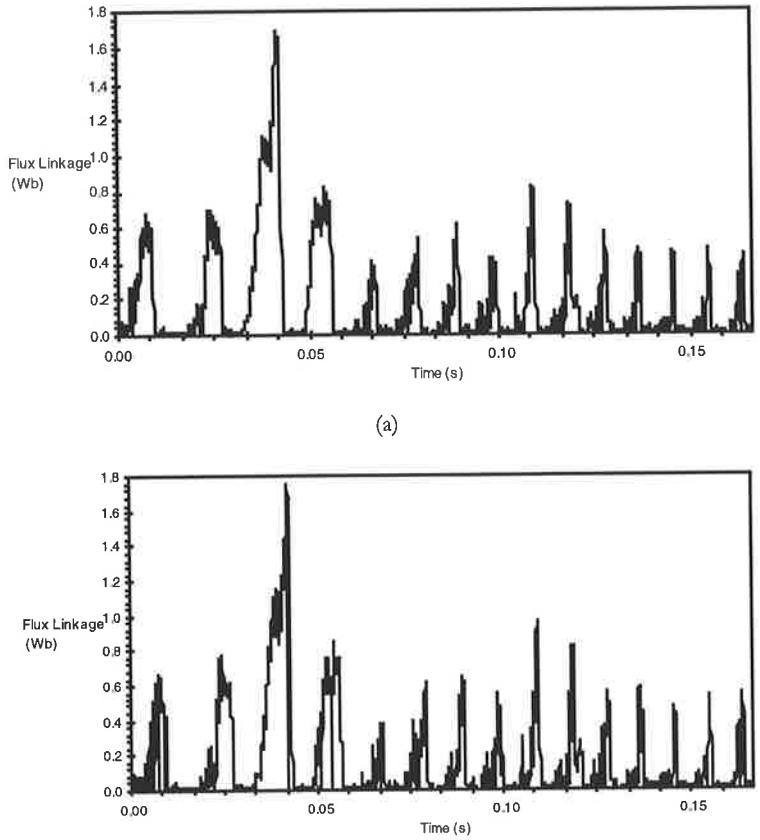


Figure 6.30 Transient Start Up (a) Phase Flux Linkage. (b) Predicted Flux Linkage.

The analysis in Section 5.3.1 of the fuzzy predictors showed that the prediction might not be as accurate for fast varying waveforms. Thus it is expected that the prediction of flux linkage would not be as accurate in this case. In Figure 6.30 (b) the result is shown for the prediction of the flux linkage waveform. It is confirmed that there are points throughout this transient test when a prediction cannot be made, as well as points when the predicted value is erroneous. Therefore, as it was mentioned in the previous chapter, there is a lower confidence in the accuracy of the predicted values during transient operation. The initial learning period that was given for previous tests is not applicable in this case because predictions cannot be made at some iterations throughout the test, which implies that the waveforms are not completely modelled at any time in the transient case.

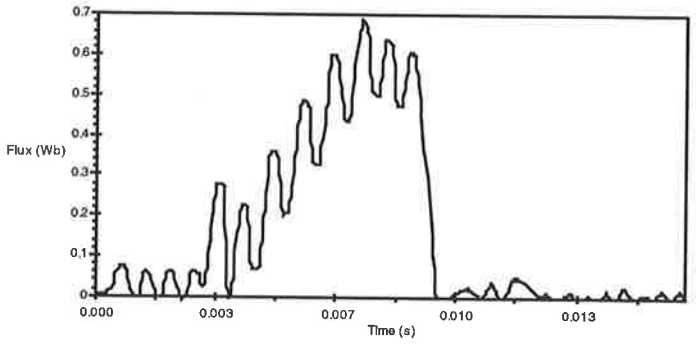
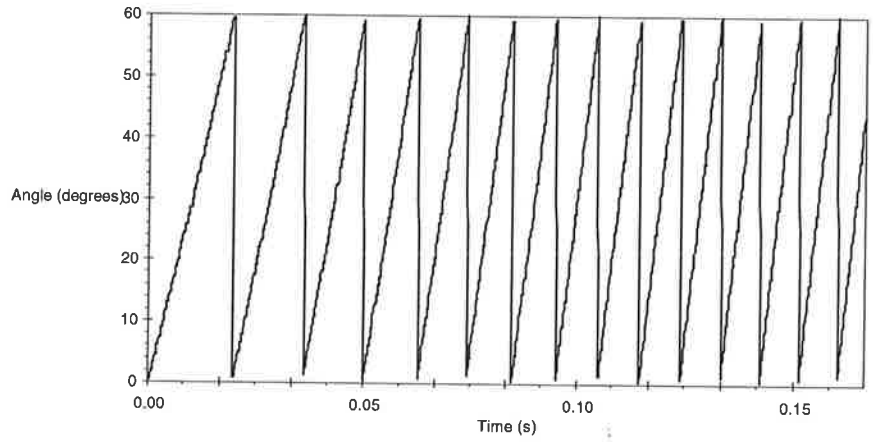
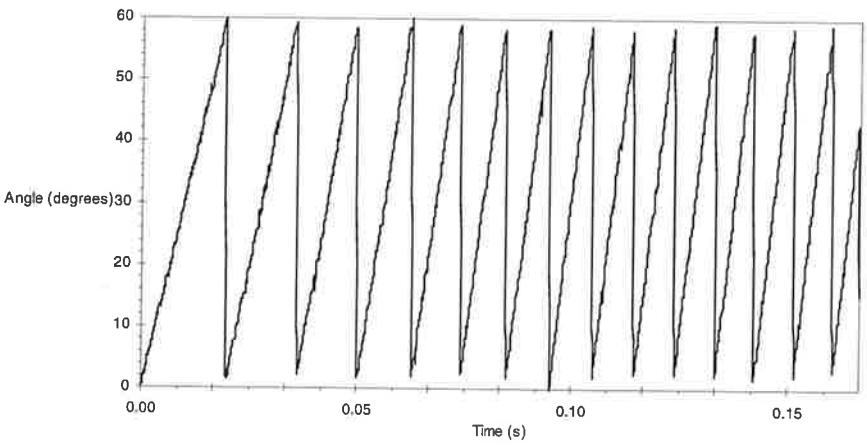


Figure 6.31 Expanded Phase Flux Linkage - Transient Start Up

In Figure 6.32 the measured encoder angle and the estimated rotor angle for this test are illustrated. The estimated angle follows the measured encoder position closely throughout the test. This shows that it is possible to have a good accuracy in the position estimation during start up and transient conditions.



(a)



(b)

Figure 6.32 (a) Measured Rotor Position - Transient Start Up. (b) Estimated Angle from Sensorless Scheme - Transient Start Up.

It can be seen in Figure 6.33 that even in this transient start up case, that the error between the actual and estimated angles is relatively low. The average error in this 0.82 degrees whilst the maximum error is 2.87 degrees. Compared to steady state tests, which were previously shown, the average angle error is somewhat higher and the performance has suffered due to the higher flux linkage estimation errors, and lower performance of the predictors.

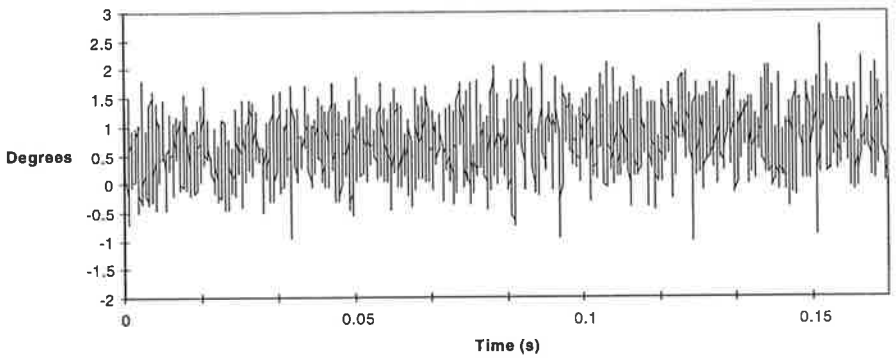
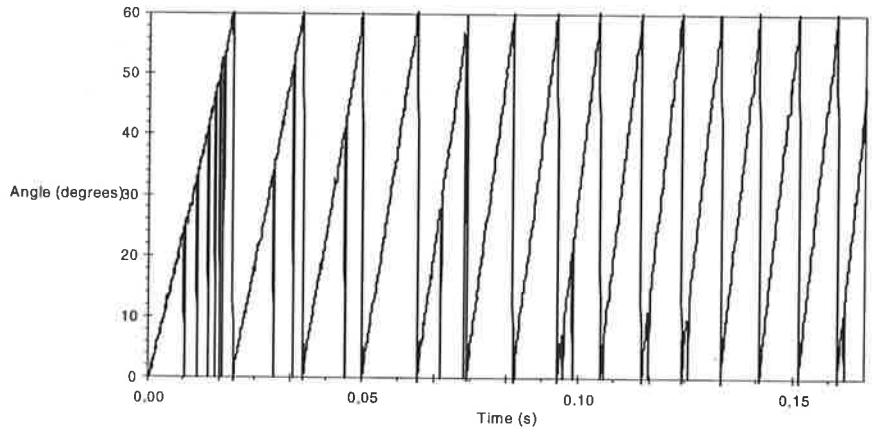


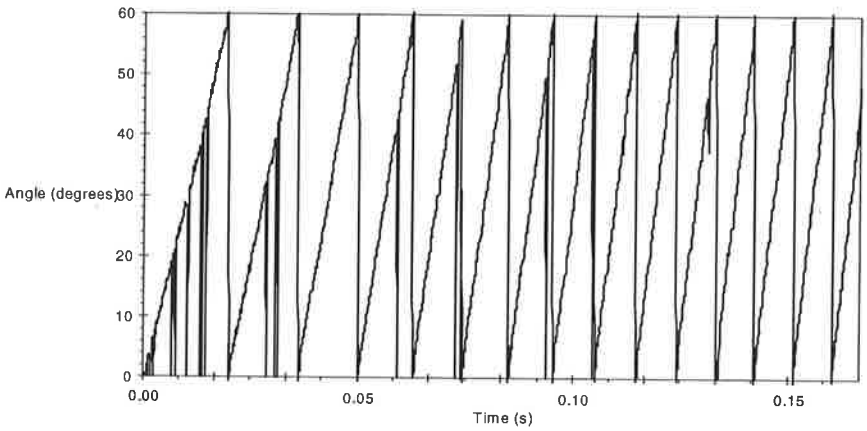
Figure 6.33 Error between Estimated and Measured Angle - Transient Start Up

As it was discussed above, the predictors of angle have a higher accuracy during steady state operation. Hence, in this test the performance of the angle prediction is not as high as for the steady state test. It can be seen in the predicted angle and the next step ahead predicted angle in Figure 6.34 that there are points throughout the transient test where a prediction cannot be made due to lack of rules. In addition some of the predicted values are inaccurate. This was expected in this transient speed test because the trajectory of rotor position is continuously changing in contrast to the linear variation of the previous steady state speed tests. However, the performance of the predictors is still relatively good, and in most instances quite accurate predictions of the motor position are made.

In this test, the angle prediction performed better than the flux linkage prediction even though both the flux and position had transient waveforms. This is due to the fact that the rotor position trajectory is less complex than flux linkage waveform. Therefore, the angle trajectory is easier to learn for the fuzzy predictors, which leads to a shorter learning period, and a greater amount of accurate prediction values.



(a)



(b)

Figure 6.34 (a) Predicted Angle - Transient Start Up. (b) Next Step Ahead Predicted Angle - Transient Start Up.

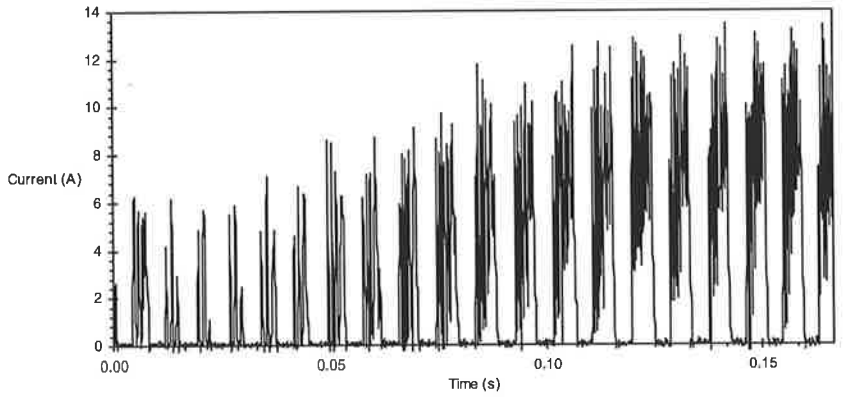
6.4.3.2 Transient Operation Test - Change in Load

Another class of transient operation arises from changes in the mechanical load of the motor while the motor is operating. The Phase A current and voltage waveforms of the motor in response to a change in torque is shown in Figure 6.35. In these experimental results, the motor is running in the chopping mode at 454 rpm with no load, when an equivalent change in torque of 8 Nm is applied to the motor. The change in motor torque is applied by switching the resistive load on the dc generator connected to the SR motor shaft to a lower value. This causes a greater dc generator current and higher power output, which originates from the SR motor output mechanical power. The resistance of the dc generator is lowered at $t = 0.045$ seconds in the motor test. Due to the electrical time constant of the dc generator circuit the torque does not change in a step manner but has an exponential rise. It can be seen that the average current level rises in response to the change in torque at $t = 0.045$ seconds in an exponential manner also.

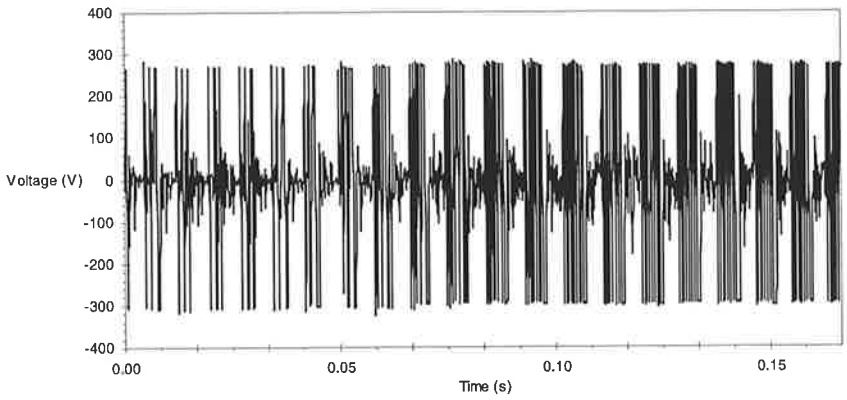
Greater detail of the current waveform after the change in torque is applied at 0.045 seconds can be seen in expanded area of the test results that is shown in Figure 6.36. The results

show that there is a time lag between the change in the dc generator output circuit and the increase in power output of the SR motor. The peak current level of the chopping mode pulses can be seen to exponentially rise after the increase of load at 0.045 seconds. Nevertheless, there is considerable variation in the current chopping amplitude level. This is because the controller has a speed control loop, and during torque changes suffers from oscillations in the current amplitude control and voltage commutation control until the speed settles to a new steady-state. This voltage and current control oscillation also leads to highly non-linear and oscillatory flux linkage.

As in the previous transient test, the waveforms of the current are highly non-linear, and thus this test also examines the ability of the scheme to cope with flux linkage estimation problems when high bandwidth measured motor waveforms are not fully captured by the A/D converter.



(a)

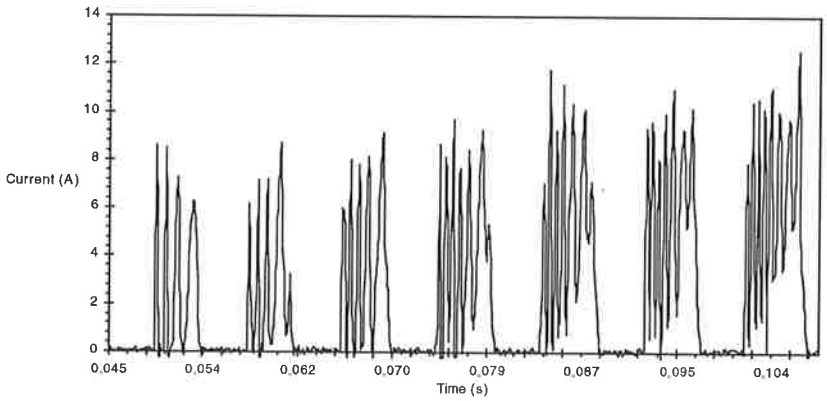


(b)

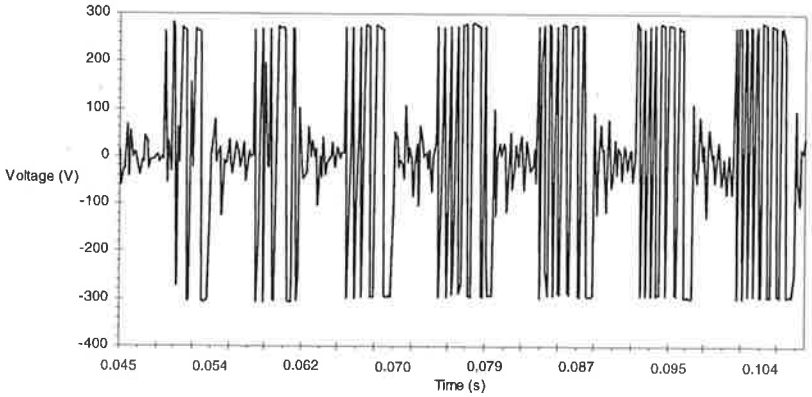
Figure 6.35. Transient Load: (a) SR Motor Phase Current. (b) SR Motor Phase Voltage.

The plot of the estimated flux linkage in Figure 6.37, shows that in synchronism with the currents, the phase flux linkage increases with the rise in motor output torque. An expanded pulse of the flux waveform after the torque increase is placed on the motor, is shown in Figure 6.38. It is clear that the variation of the flux linkage is highly non-linear, and has changes in amplitude between each electrical cycle during the torque transient. The

maximum flux linkage in each electrical cycle in general increases as the torque increases, but there is some oscillation in the amplitudes due to the variation and control oscillations of the applied voltage and current during the transient.



(a)



(b)

Figure 6.36. Expanded SR Motor Phase Waveforms for t = 0.045 s to 0.108 s: (a) Current. (b) Voltage.

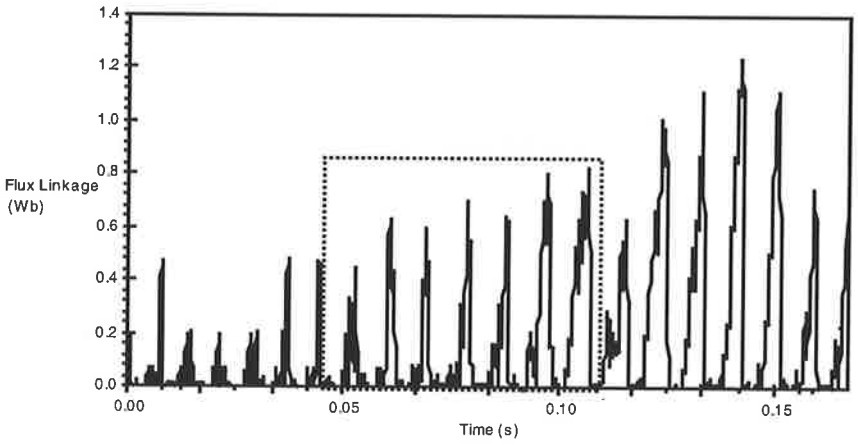


Figure 6.37 Estimated Phase Flux Linkage – Transient Load.

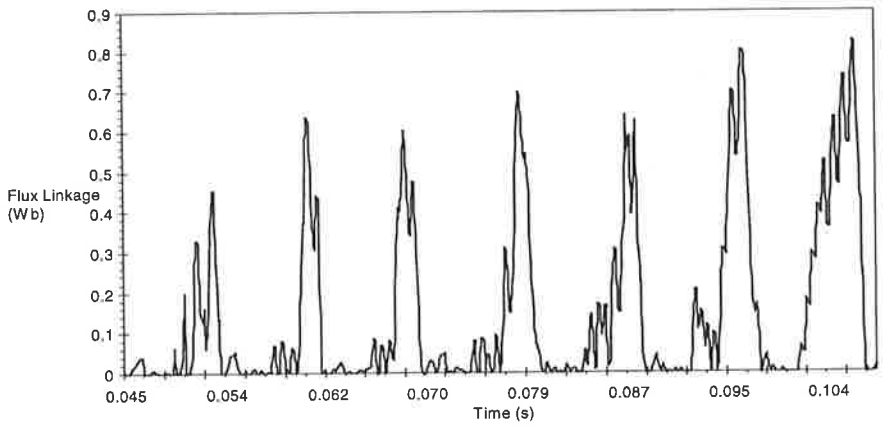


Figure 6.38 Expanded Phase Flux Linkage for t = 0.045 s to 0.108 s.

The predicted values of the flux linkage waveform are shown in Figure 6.39. In this transient test, the predicted values of flux linkage are quite inaccurate. There are points throughout the test when a prediction cannot be made, which implies the waveform is not learnt. This is due to the highly varying and transient nature of the waveforms, which makes them difficult to be learnt by the fuzzy predictors.

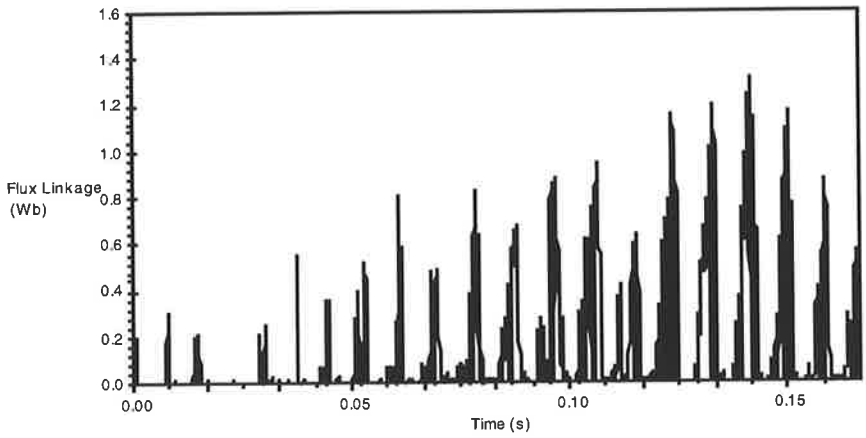


Figure 6.39 Predicted Flux Linkage - Transient Start Up

In Figure 6.40, the measured encoder and estimated rotor position values are shown respectively. Although the transient test leads to flux estimation errors and difficulty of prediction, the sensorless algorithm performs comparatively well in this transient test, with considerably accurate position estimation being provided. The average angle error in this case is 1.11 degrees, whilst the highest error between the measured encoder position and the estimated position was 2.93 degrees. Note that the higher error entails that the 0 and 60 degree points are often not reached in the estimated angle. This is because the 0 and 60 degree point is in fact the same angle, and if there is some error then the estimated angle may be placed on the opposite side of the graphs. For example, if the actual angle is 59.8 degrees and there is an error of +2.2 degrees then the estimated angle will be 2 degrees.

The error has greatly increased in this test from the steady state tests shown previously. This increase is predominantly due to the high non-linearity and fast variation of these waveforms, which leads to greater flux linkage estimation and angle estimation difficulties. Therefore, the error in this case has some offset during the entire test from the measured value. The difference between the estimated and measured angle can be viewed below in Figure 6.41.

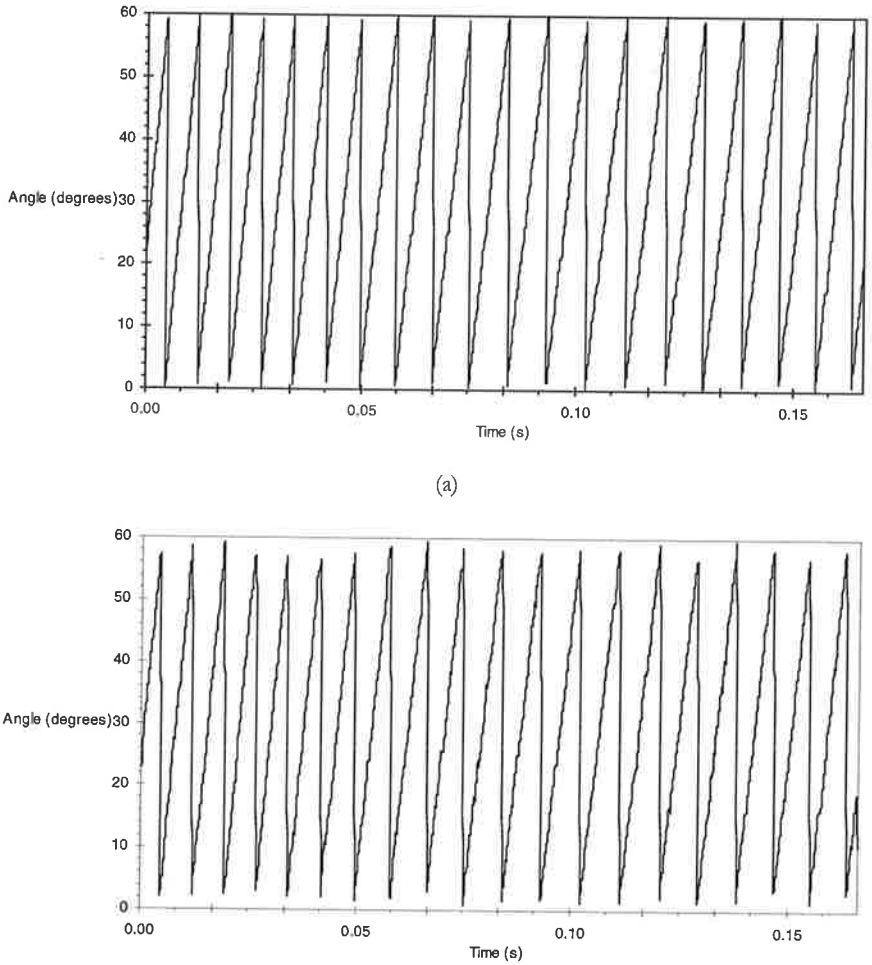


Figure 6.40 Transient Torque: (a) Measured Rotor Position - (b) Estimated Angle from Sensorless Scheme.

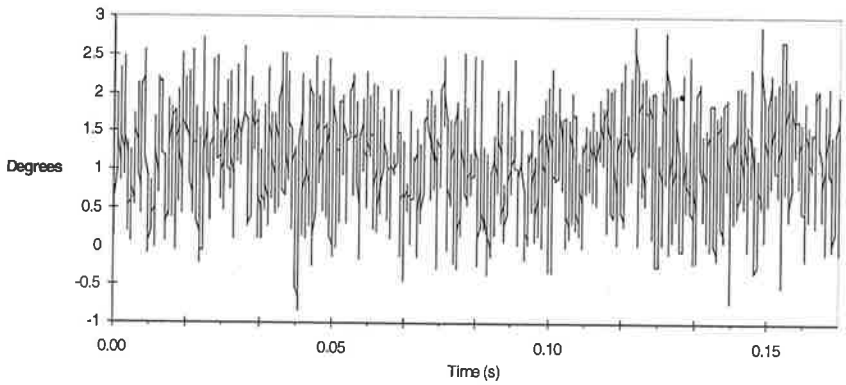
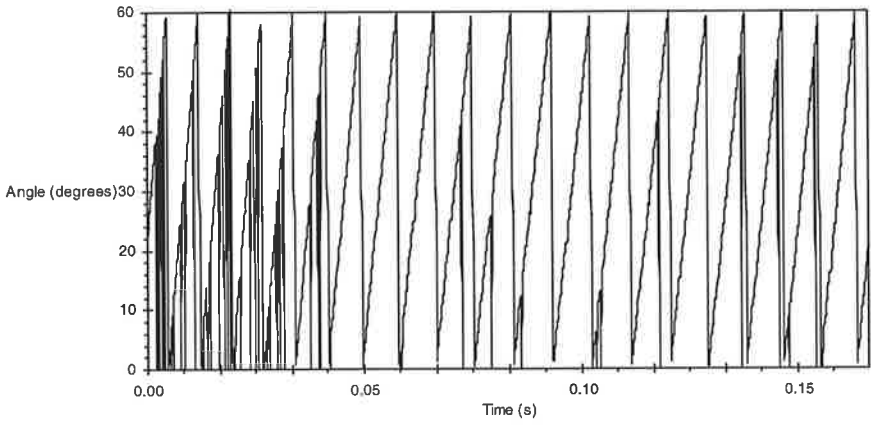


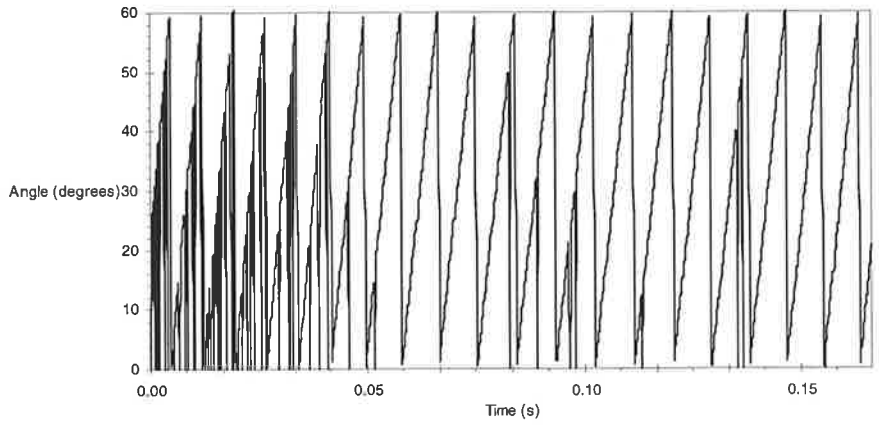
Figure 6.41 Angle Error - Transient Torque

The predicted rotor positions are shown below in Figure 6.42. Throughout the transient test,

the predicted angle curves show a good accuracy of prediction. This is because, as opposed to the current and flux linkage waveforms, the rotor position is a relatively linear and simple waveform. Thus, the predictor has less difficulty with the learning and prediction of this waveform. In this case the initial learning period when the rules are being constructed and there are a lack of predictions, lasts for approximately 280 iterations, or approximately 35% of one revolution (assuming the speed is constant at 454 rpm). However, it can be seen that in the various regions after the initial learning period that there are some points where no predictions are made due to lack of rules. This is due to a slight speed oscillation after the higher load is applied at 0.045 seconds after the beginning of the measurements.



(a)



(b)

Figure 6.42 Transient Torque: (a) Predicted Angle. (b) Next Step Ahead Predicted Angle.

The results of above experimental tests verify that the sensorless angle estimation operates well under transient variations of the speed and load of the motor. It was seen that the angle was estimated to a good accuracy. This was expected as the estimation is based on a non-linear fuzzy logic based SR motor model that included modeling of the motor's static and dynamic characteristics.

As discussed in Chapter 5, the fuzzy predictors of angle and flux linkage do not perform as well under transient conditions. Nevertheless, the fuzzy angle predictors in this test still

performed adequately. The flux predictors had a poorer performance due to the highly complex and non-linear waveforms of flux linkage that were seen in the tests.

One can see from these transient results, that the transient flux linkage waveforms have a much greater complexity than the angle variation waveform, especially in the chopping mode. The predictors of flux linkage and angle operate by making a step ahead prediction based on previous estimated values, and for less complex and time varying waveforms this prediction is easier. Thus it was expected, and observed experimentally, that the angle prediction would have a more accurate output than the flux predictors would.

6.5 Conclusion

The hardware that was developed for the sensorless SR motor drive was discussed in this chapter. The drive consists of various interdependent sub-systems, which incorporate the power, measuring, and computation circuits. The DSP plays an important role in the sensorless scheme as it allows the algorithm to be operated at higher speed, which increases the possible rotor position estimation frequency per rotor revolution. Nevertheless the tests shown were taken with the A/D converter sampling frequency limited to 6000 Hz. This demonstrates the ability of the scheme to work with a relatively long iteration time of 166.7 μs. Therefore, other slower microprocessors can also easily be used, except for applications where the motor is operated at very high speeds and the electrical cycle period is very small. In this case a high sampling frequency must be used.

The experimental results given have demonstrated that the sensorless scheme can be used to obtain position information in a practical environment under different load conditions with real SR motors. The measurements have also shown that the rotor position can be successfully determined in the SR motor by the fuzzy logic based method. Angle estimation was shown for a wide range of speeds and conditions, including transient operation of the motor. It was found in the particular measurements shown of steady-state operation, that the average deviation between the estimated error and the measured encoder position ranged from 0.36 to 0.79 degrees.

It was seen that the scheme performed well with transient motor operation also, even with a low A/D sampling frequency. In the transient start up test from zero speed to 346 rpm the average error was 0.82 degrees, and for the transient torque change at 454 rpm the average error was 1.11 degrees.

In the results shown, the rotor angle was measured with an 8-bit encoder for comparison purposes. The encoder measurement also has errors due to quantisation of the angle, and thus the comparison between the estimated and measured angle is not completely equivalent to a comparison with the actual rotor position. In fact, the actual error between the estimated angle and the actual rotor angle may be slightly lower or higher than that shown due to the

encoder quantisation error. A true analysis of the error would require a higher resolution encoder that would have a closer approximation to the physical rotor position.

The predictors of flux linkage and angle were also shown to be effective. It was shown that in general the fuzzy logic based prediction algorithm had a fast learning period of approximately 200 – 250 iterations for simpler waveforms, such as the rotor angle trajectory and the flux linkage in the single pulse mode. However, the learning period became longer for highly non-linear waveforms, such as the flux linkage in chopping mode. It was also concluded in this chapter, that the performance of the prediction of fuzzy logic based angle and flux linkage predictors is not high during transient motor operation, because of the inherent learning period. Therefore, during transient periods of motor operation, the prediction cannot be used as effectively in reducing error spikes of the estimated flux and position.

In this chapter, it was also concluded that, apart from measurement errors and noise, two major practical effects that influence the position estimation are the bandwidth of the analog to digital converter measurements, and the bandwidth of the current and voltage waveforms. It was found that as the speed of the motor increased that the number of measurements per electrical cycle decreased at a constant A/D sampling frequency, which has the same effect as the bandwidth of the measurement system decreasing. This results in increased errors in the flux linkage estimation, which can lead to higher errors in the angle estimation (the effect of low bandwidth measurements on the flux estimation will be detailed in the next chapter).

A similar effect is caused by high bandwidth current and voltage waveforms. During the chopping mode the current and voltage has fast changing components due to the current commutation and thus has significant higher frequency bandwidth. This means that unless very high frequency A/D converters are used, the full frequency components of the voltage and current will not be captured. This will lead to errors in the flux linkage estimation, which in turn can lead to higher errors in the rotor position estimation.

It was seen that at medium to high speeds the single pulse mode of control is used and that the waveforms in this mode are much simpler in nature. Therefore, the waveforms have lower high frequency harmonic components and thus have a lower sampling frequency requirement from the A/D converters.

From the above analysis, it can be summarised that the performance of the scheme reduces with higher speeds due to the decreasing bandwidth of the constant A/D sampling frequency. However, this is compensated somewhat at higher speeds due to the simple waveforms in the single pulse mode. The accuracy also reduces during the chopping mode due to high frequency waveform components. In addition, the error reducing capability is lowered during transients due to the learning period of the prediction algorithms. Hence, one of the worst condition for the scheme is during higher speeds of the chopping mode of

control during a transient. However, it was shown above in the transient operation experimental results that the sensorless algorithm could cope well even under these conditions.

Therefore, it was shown in this chapter that the scheme performs well under a wide range of conditions, even with a low A/D sampling frequency. The high performance under these conditions derives from the high robustness of the position estimation algorithm to errors in the input flux linkage and current signals. This robustness will be analysed in detail in the next chapter, where it will be shown that the robustness of the algorithm derives from the nature of the fuzzy reasoning implemented. Additionally, the experimental results will be furthered to show operation of the scheme when the motor drive is operating under non ideal conditions and with highly erroneous conditions. It will be seen that due to the error handling ability of the scheme, it has a high robustness and can cope well with high levels of input signal noise.

Chapter 7: The New Sensorless Position Detection Scheme-Experimental Results: The Study of High Robustness and Reliability

7.1 Introduction

In the previous chapter, the experimental implementation and evaluation of the fuzzy logic based sensorless position detection scheme was detailed. The experimental tests verified that the new scheme could successfully predict the rotor position of the practical SR motor under real operating conditions. It was also shown that the rotor position could be estimated under a wide range of speeds and conditions, including low speed chopping mode, and higher speed single pulse mode. The sensorless scheme was found to operate effectively with transients in both the speed and mechanical load of the motor.

However, for any position detection scheme to be used in replacement of a position sensor, its operational reliability and robustness in actual operation must be demonstrated. This is because, if the reliability of a sensorless position detection scheme is low, then this lessens or cancels any advantages of replacing the mechanical sensor.

In this chapter, the successful operation of the sensorless scheme with real experimental motor waveforms will be extended, to demonstrate that the fuzzy logic based position estimation scheme has a high level of robustness. Operation of the scheme will be examined when the motor drive is operating under non-ideal conditions where the sensorless rotor position detection algorithm must cope with erroneous and noisy signals. It will be seen that due to the error handling ability of fuzzy logic reasoning, the sensorless scheme has a demonstrated robust ability in coping with high levels of error and noise.

In a practical application non-ideal conditions that the position estimation must operate with can include:

a) Measurement errors due to noise.

b) Low bandwidth motor waveform measurements (eg. large sampling period of analog to digital converters)

c) Flux Linkage estimation errors, which may be caused by:

i) Offset errors.

ii) Measurement errors.

iii) Noise.

iv) Change in the phase resistance with temperature.

Hence, in this chapter, the reliability of the sensorless scheme is shown by executing the algorithm with erroneous experimentally measured motor waveforms. The effects on the position estimation of the above conditions are then examined in detail.

In Section 7.2, the concept of robustness is defined, and it is explained that by using fuzzy set theory in the sensorless position detection algorithm, the requirements of a robust system can be satisfied. This provides a basis for the later sections of the chapter, which provide a demonstration of the robust capability of the sensorless algorithm.

The robustness and reliability of the new sensorless rotor position detection algorithm is demonstrated with a wide range of experimentally based results. In Section 7.3, the results are presented for the motor operation with high levels of noise, and both results for the single pulse and chopping mode are shown. Section 7.4 details results for when the sensorless scheme must operate with very low analog to digital converter sampling frequencies, at both low and high motor speeds. Furthermore, in Section 7.5, the results are presented for the sensorless scheme operating when the flux linkage measurement is erroneous due to errors or parameter variation.

In Section 7.6 the performance of the real time operation fuzzy predictors of flux linkage and angle is detailed further, to demonstrate their ability in lowering the effects of high amplitude transient noise.

To provide a theoretical basis for some of the results and conclusions that are given in this chapter, Section 7.7 provides a detailed theoretical examination of how the various practical SR motor drive conditions described can act to decrease the accuracy of the position estimation. In addition, a theoretical basis for error production in the sensorless drive is given, in order that these can be understood in an analytical manner.

7.2 Operational Reliability and Robustness of the Sensorless Scheme

In an actual motor drive application, electromagnetic coupling between the high power circuit and the low power measurement and control circuits, can lead to a high level of noise in any measurements taken, particularly during the switching of power devices when transient currents occur. In addition to measurement noise, in an actual drive application the sensorless position detection scheme may need to cope with sensor errors, integrator offset, low sampling times, and parameter variation. In order that rotor position information is not lost or corrupted, and continuous operation of the motor is achieved, the sensorless scheme should be robust to these practical effects.

Thus, it is of very high importance for all practical applications, that the sensorless rotor position detection scheme is demonstrated to have a high level of reliability and robustness. If a high level of robustness is not achieved, then the advantages of implementing a position sensorless system, rather than using a position sensor, may be

diminished. This is particularly true for the SR motor which has an inherent robustness as described in Chapter 2, and thus the reliability of the position sensing should ideally be no less or greater than the reliability of the motor.

To examine the robustness of the sensorless algorithm it is instructive to examine the concept of robustness from the field of robust statistics. It has been defined by Huber [163] that a robust algorithm should have the following features:

i) The algorithm should have a reasonably good accuracy in the assumed model of the underlying system.

ii) Small deviations of the data should decrease the performance of the algorithm by only a small amount.

iii) Large deviations in the data should not cause a catastrophe.

The first of these requirements essentially states that the output of the algorithm should be accurate when the input data is noise free, or the data is *"clean"*. This is achieved by an accurate model of the underlying system in the algorithm. In Chapters 4 and 5, the development of an accurate non-linear fuzzy logic model of the SR motor was described. By using the fuzzy model of the motor, the non-linear characteristics could be captured, without a complex mathematical model or simplifying linearisations of the motor model. Results of estimated angle were shown in both simulation and in practical results in chapters 5 and 6 respectively. It was seen that the accuracy of the algorithm in predicting rotor position was high for relatively clean data in the inputs of current and voltage. Therefore, the sensorless position detection algorithm has already been shown in the previous chapters to satisfy the first requirement of a robust algorithm, as defined above.

To satisfy the second requirement of a robust system, the algorithm must be shown to be resistant to the effects of noise in the input data. This entails that small deviations in the inputs of the sensorless algorithm should not have a significant adverse effect on the output rotor position estimate. Also, in a real SR drive application of the sensorless algorithm, the input data will have noise that can not usually be guaranteed to have a Gaussian distribution model, and thus the algorithm should be robust to both Gaussian and non-Gaussian noise.

A major reason for the choice of using a fuzzy logic based SR motor model and position estimation scheme was to satisfy the requirement that the sensorless algorithm is not affected significantly by deviations in the input data. It has been shown in reference [164] that modeling and estimation using fuzzy set theory is more tolerant to noise and errors in the input measurements than crisp methods. It is also shown in [164] that fuzzy systems are tolerant to both Gaussian and non-Gaussian noise on the inputs. Essentially this is due

to the fact that the width or size of the membership functions in fuzzy systems can be considered as an allowable level of noise.

As it has been seen in previous discussions, fuzzy sets are defined over a range of values, with the membership function of the fuzzy set varying for different values in the range. This means that an input data point with error or noise can still be placed, with lower membership function, in the same set as a point with no error or noise (depending on the amplitude of the error). In other words, by the use of fuzzy sets, input data which is corrupted by noise, can be accepted into the same set as clean data but with a lesser degree of truth [165]. The length of range of the membership function will determine the range of values with noise which will be accepted as a part of the fuzzy set. Therefore, by the fuzzification of the input data, small deviations in the input data do not have significant effect on the output position estimation. Hence, by using fuzzy techniques the second requirement for robust algorithms can be satisfied in the position estimation algorithm.

To satisfy the third requirement of algorithm robustness the notion of a breakdown point should be examined [166], (where the breakdown point is defined as that point where the algorithm fails by producing an unacceptably high output error due to large and abnormal deviations in the input data). Large deviations in the input due to noise can be defined as data points which have abnormally high deviation from the correct value, compared to the mean level of input data noise. For example, in the SR motor drive, there may be high amplitude but short duration periods of electromagnetic noise due to fast turn off of the current in the inverter power devices. In the field of robust statistics these higher deviations in the data are termed outliers, as opposed to inliers which lie closer to the mean level of noise. A scaling factor is used to help differentiate between inliers and outliers in the data. For example, the error in a data point could be normalised to the mean of the absolute errors of a data range [167].

Although these robust statistic concepts are directly applicable to engineering tasks such as modeling and pattern recognition, where the data is analysed off line using iterative methods, the idea of a breakdown point and outlier and inlier data is applied in the sensorless position estimation algorithm. As has been previously discussed, the angle and flux linkage of the motor are predicted in each iteration step using a fuzzy logic based predictor, and a confidence weighting is given to the predicted value according to the acceleration. During steady-state conditions, the predicted value is used with a high weighting, and this effectively rejects any outlier input data due to abnormally high errors in the current or voltage measurements. Therefore, an abnormally high error in the rotor position estimate, or breakdown point, can be avoided using the angle and flux predictors.

In the sections below, results will be shown using experimentally based data, that the second and third requirements of robust algorithms are satisfied by the implemented sensorless position detection algorithm. The experimentally based results will examine the

consequence of input noise and error, which is caused by various real operation effects. In addition, the effect of abnormally large pulses of noise, or outliers, will be examined.

7.3 Measurement Noise

The first sets of results that will be shown in this section examine the effects of noise on the sensorless position detection scheme. In these tests, random noise was added to the experimentally measured waveforms that are the input to the position estimation algorithm. The noise was added using a random Guassian noise generator that is available in the *Xmath* mathematical software package (which is detailed in Appendix B). The noise was increased in stages to observe how robust the sensorless position estimation was to increasing levels of noise.

7.3.1 Measurement Noise Tests - Single Pulse Mode

In Figure 7.1 the waveforms of current and voltage of one phase of the SR motor are shown for the case when the motor is operating in single pulse mode at a steady speed of 660 rpm, and there is an added random noise error of up to 10% of the maximum level of the measured signals. The added noise is Guassian in nature, and therefore, has a finite variance [168], however the problem of non-Guassian noise will be later examined in Section 7.6.

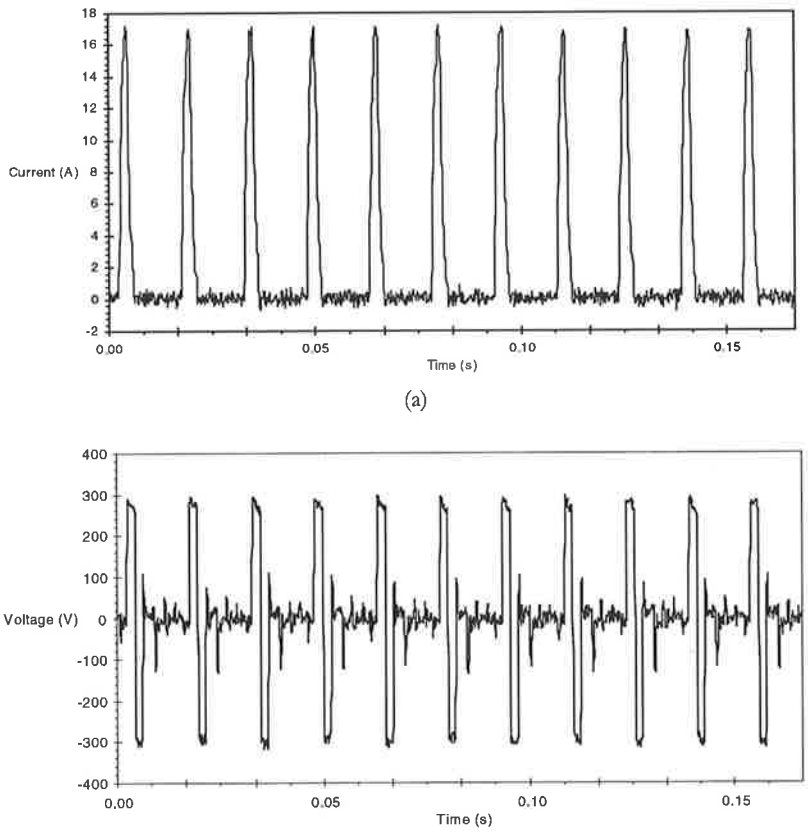
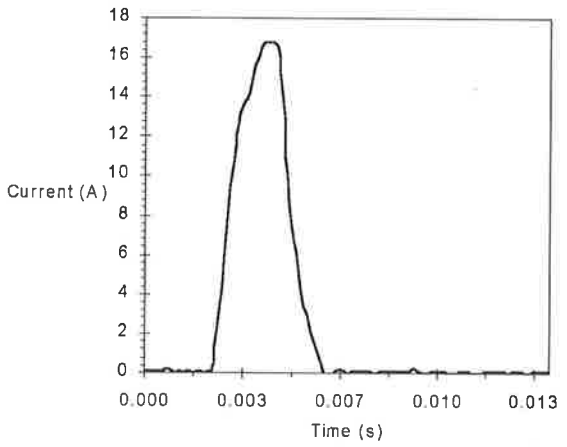


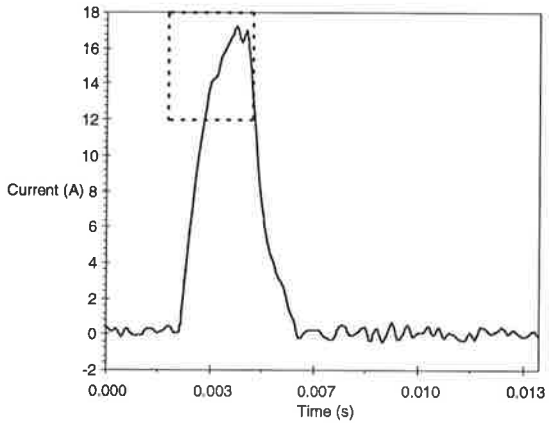
Figure 7.1 10% Noise: (a) SR Motor PhaseA Current. (b) SR Motor PhaseA Voltage.

It should be noted that the original measured signals before the addition of random noise, are not noise or error free. This is because all measured signals contain some inherent measurement inaccuracy and noise. Therefore, in the comparisons that are made below between the signals with and without added error, it should be noted that the original signal always contains some error. Hence, the signal with added error has an error component that consists of both the added noise as well as the original noise component of the measured signal.

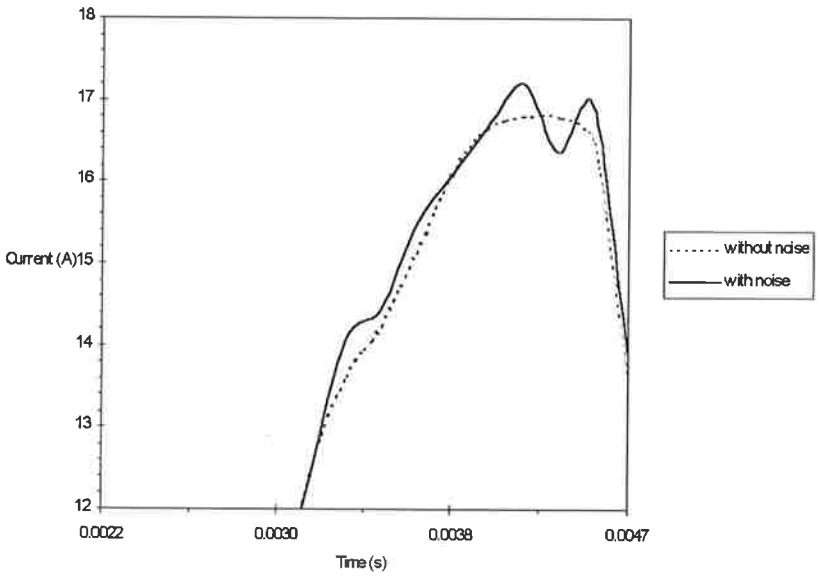
A more detailed examination of the current and voltage waveforms is also shown in Figure 7.2 and Figure 7.3. In Figure 7.2, the waveform of one current pulse is shown for the cases when the current is with and without the added noise. In order to clearly see the effect on the current of the added noise, an expanded view is also shown in Figure 7.2 (c) that compares the current and waveforms both with and without the noise given in Figure 7.2 (a) and Figure 7.2 (b).



(a)



(b)



(c)

Figure 7.2 SR Motor Phase Current: (a) Without Noise. (b) With Added Noise (10% of maximum). (c) Expanded Comparison of Current Waveforms, with and without noise.

In Figure 7.3, similar waveforms are shown for the phase voltage that corresponds to the single pulse of current shown above. The expanded view of the voltage in Figure 7.3 (c) clearly shows that the voltage with noise deviates significantly at various points in time from the measured voltage without added noise.

In order to provide a practical robustness and reliability, the position estimation algorithm must be able to cope with the added noise on the input data of voltage and current. As it was mentioned previously, these deviations in the input signal due to noise must only have a small effect on the estimated position, in order for the algorithm to be classified as robust.

The estimated and measured angle for this test with added input signal noise is shown in Figure 7.4. It can be seen that there is now added noise in the estimated angle signal because of the corruption of the measured voltage and current signals. It was expected that the input signal noise would degrade the estimated position output of the position estimation algorithm. However, it can be seen that operation with input noise of 10% of the input signals maximum amplitude, has only a relatively small effect on the estimated position values. This can be seen in detail in the plot of angle error (Figure 7.5). The average amplitude of the error between the measured and estimated angle in this test is 1.24 degrees, whilst the maximum amplitude of error is 3.97 degrees. The maximum estimation error represents 6.6% of one electrical cycle of 60 degrees. Therefore, the maximum output error (as a percentage of the maximum output angle of 60 degrees), is less than the maximum 10% input error (as a percentage of the maximum input signals in this test).

Hence, although the error in the estimated angle has increased due to the input signal noise, the degree of degradation of the estimates is not high, and operation of the motor is still possible. Therefore, the second requirement of a robust algorithm, as described above, has been satisfied in this case due to the fact that the noise in the input signals decreased the performance of the estimation only by a small amount.

In addition, at no point is there a large or protracted deviation in the estimated rotor angle from the actual rotor angle. The underlying trajectory of the estimated angle always follows that of the actual angle (ie a linear variation from 0 to 60 degrees), and so it would be possible to filter the error component of the estimated angle using a low pass filter.

However, this may not be satisfactory when the actual motor speed has fast transient changes, as in this case the actual rotor trajectory waveform would be filtered also. In addition, the low pass filter can introduce some phase change to the output signal. A suitable filtering method could be to use a moving average of the angle estimation signal, as this has the benefit of simple computation.

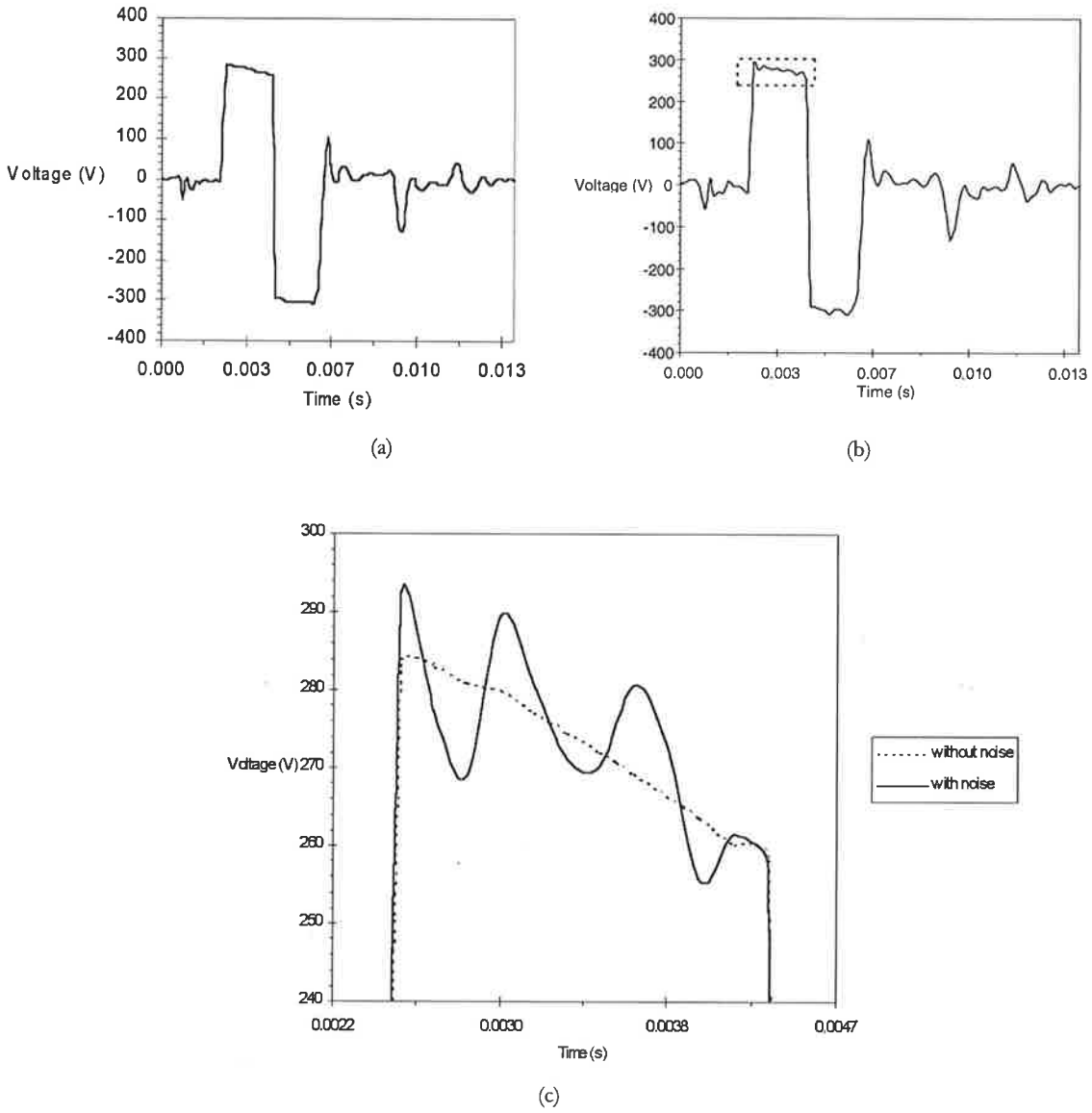


Figure 7.3 SR Motor Phase Voltage: (a) Without Noise. (b) With Added Noise (10% of maximum). (c) Expanded Comparison of Voltage Waveforms, with and without noise.

However, these filtering techniques are not examined in this thesis, as a wide range of filtering techniques are already commonly known [169]. Instead, the emphasis is placed here on observing and examining the actual error and noise effect on the estimated angle, due to input errors, in order to observe the robustness of the novel estimation scheme.

The operation of the flux and angle predictors was detailed in the previous chapter, and will also be examined again in Section 7.6. Therefore, in order to avoid repetition, the predicted values of flux and angle, and the next step predicted values are not shown in these test results.

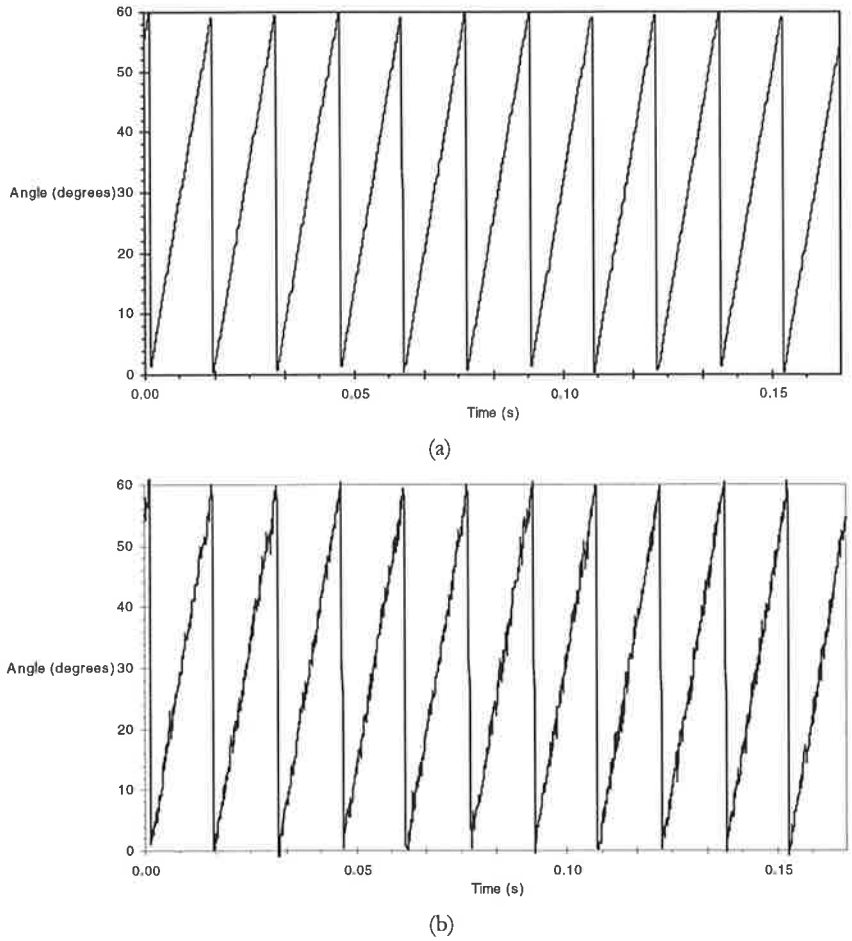


Figure 7.4 (a) Measured Rotor Position. (b) Estimated Angle from Sensorless Scheme with Input Noise.

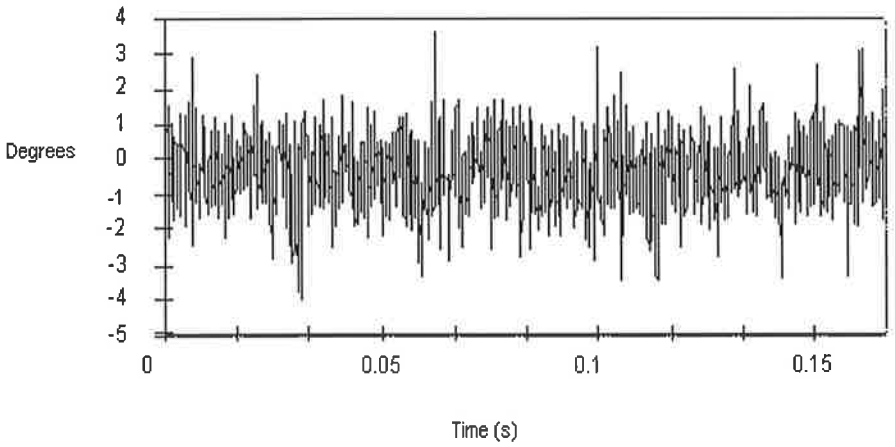
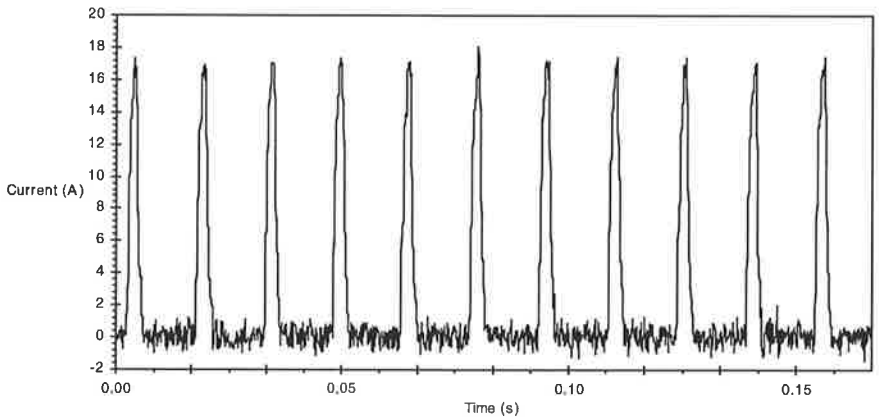


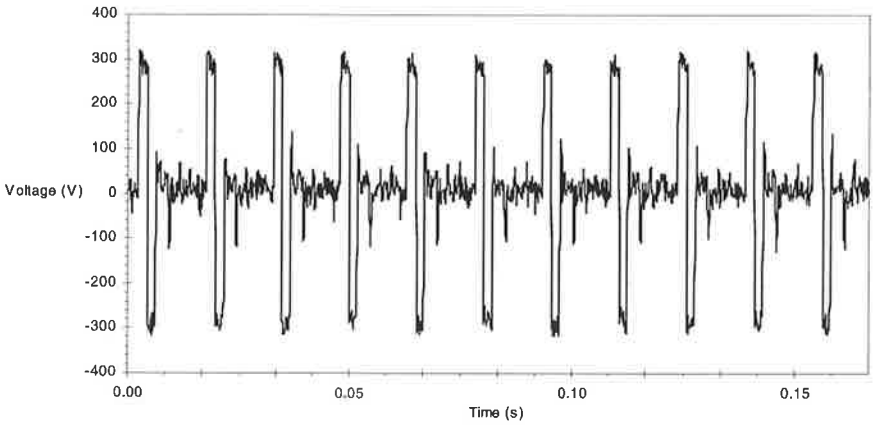
Figure 7.5 Error between Estimated and Measured Angle - 10% of Maximum Amplitude Noise.

As it has been demonstrated in the above result, the sensorless scheme is robust to measurement noise. It can therefore be said that the algorithm shows the characteristics of a robust algorithm as defined above in Section 7.2. It was shown above that deviations in the input data of current and voltage due to measurement noise and error only decreased the performance of the scheme by a small amount. However, further experiments were carried out to test the scheme at higher noise levels, and to see the operational limits of the current system.

Therefore, in Figure 7.6 the motor waveforms of current and voltage are shown for the same motor operation as above, but with a noise level of up to 20% of the input measured signals. In this set of results the noise has a significant component, and provides a difficult test for the sensorless algorithm. The added noise can be clearly seen in the expanded waveforms in Figure 7.7 (a) and Figure 7.8 (a), which provide plots of the noisy single pulse of current and the corresponding noisy phase voltage (the current and voltage without noise were given previously in Figure 7.2 and Figure 7.3). In order to clearly observe the noise amplitude an expanded waveform comparison of the current with and without the added noise is seen in Figure 7.7 (b) and a comparison of the voltage with and without noise is seen in Figure 7.8 (b).

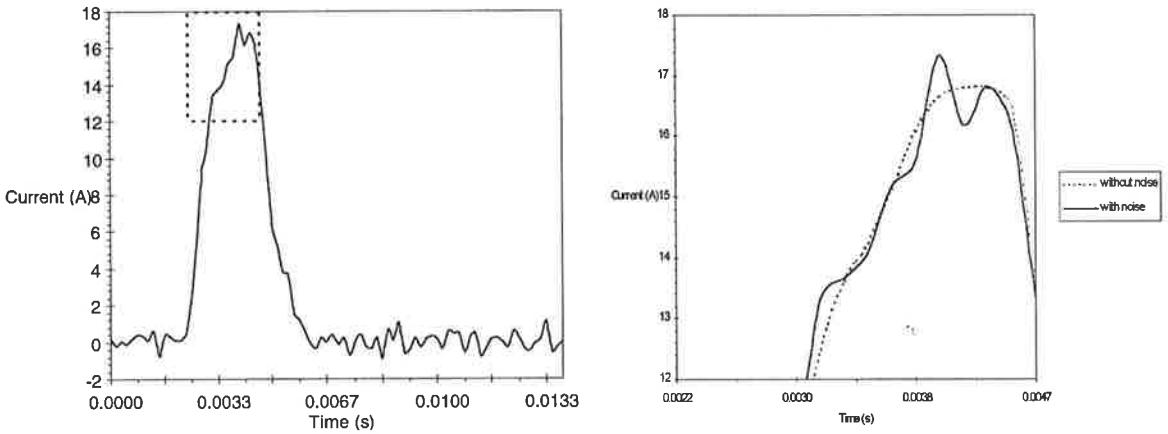


(a)



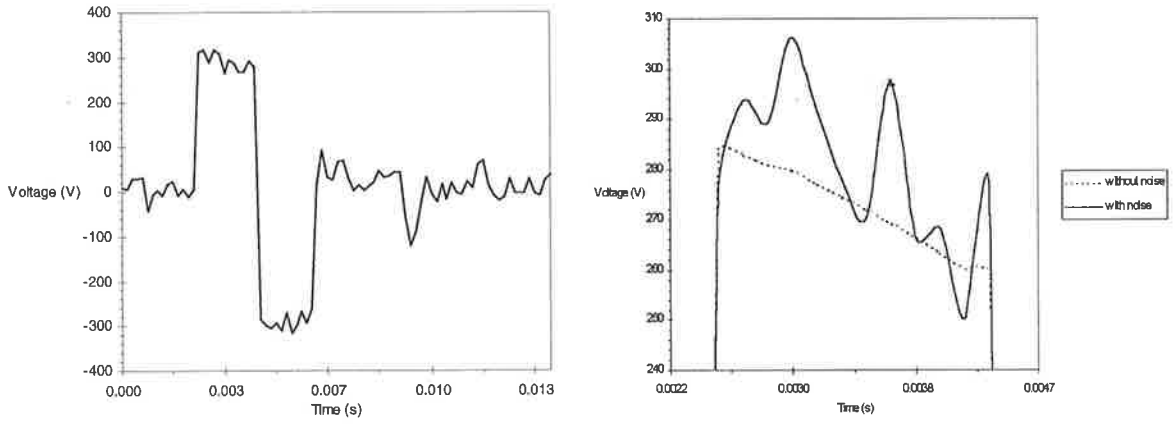
(b)

Figure 7.6 20% of Maximum Level Noise: (a) SR Motor Phase Current. (b) SR Motor Phase Voltage.



(a) (b)

Figure 7.7 20% of Maximum Amplitude Noise: (a)Expanded SR Motor Phase Current. (b) Expanded Comparison of Current Waveforms, with and without noise.



(a) (b)

Figure 7.8 20% of Maximum Amplitude Noise: (a) Expanded SR Motor Phase Voltage. (b) Expanded Comparison of Voltage Waveforms, with and without noise.

In Figure 7.9, the estimated angle from the angle estimation algorithm is shown for this experiment (the measured angle was shown in Figure 7.4). It can be seen that the error in the estimated angle position has correspondingly increased over the previous test, because of the higher level of corruption in the motor input signals of this test. However, it can be seen the general trajectory of the rotor angle has been retained even for this high level of noise. It can be said that due to the high amplitude input noise, that at some points the current or voltage, or both of these signals, has a large error deviation. Nevertheless, at no points in this test has the large deviation of the input current and voltage data caused a catastrophic breakdown of the algorithm. In addition, the error in the estimated angle is not large relative to the level of the input noise. The average angle estimation error is 2.80 degrees, whilst the peak error is 9.92 degrees, as can be seen in the plot of error in Figure 7.10. In this test, the peak value of the input noise is 20% of the input signals maximum amplitude, whereas the peak value of the output noise (in the angle estimation) is 16.5% of the electrical angle cycle of 60 degrees.

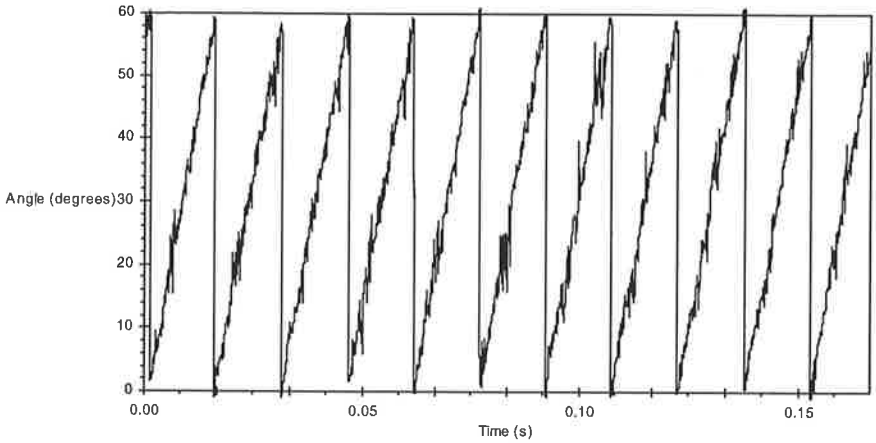


Figure 7.9 Estimated Angle from Sensorless Scheme - 20% of Maximum Amplitude Input Noise.

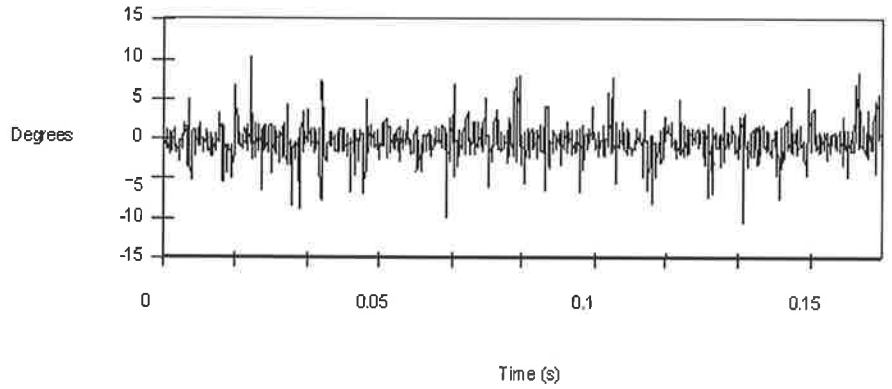


Figure 7.10 Error between Estimated and Measured Angle - 20% of Maximum Amplitude Input Noise

Hence, the requirements of a robust algorithm have again been demonstrated in this test. It has been shown that the large deviations in the input current and voltage do not produce a catastrophic breakdown in the algorithm, and even the peak estimation error has a lower percentage error than the peak input error. In addition, as the average angle estimation error is 2.80 degrees, it entails that the smaller deviations in the noisy inputs produce only small deviations in the output estimated signal. Furthermore, as mentioned above, this signal could be improved for angle commutation in highly noisy systems by using filtering of the estimated signal.

It can be seen in Figure 7.10, that there are often high peaks in the angle error. At any particular point, one or more reasons can cause these error peaks to occur. For example: at a high error peak there may be a high measurement error, flux estimation error, lack of predicted value of flux or position from the predictors (to compensate the error in flux or position), or a combination of more than one of these reasons. A high voltage measurement error has a delayed effect due to the fact that it is always passed through the integrator before input to the angle estimation algorithm.

Note that in this case of highly noisy measurements, a completely accurate rotor position estimate is not possible, as the only information input to the fuzzy sensorless scheme is the

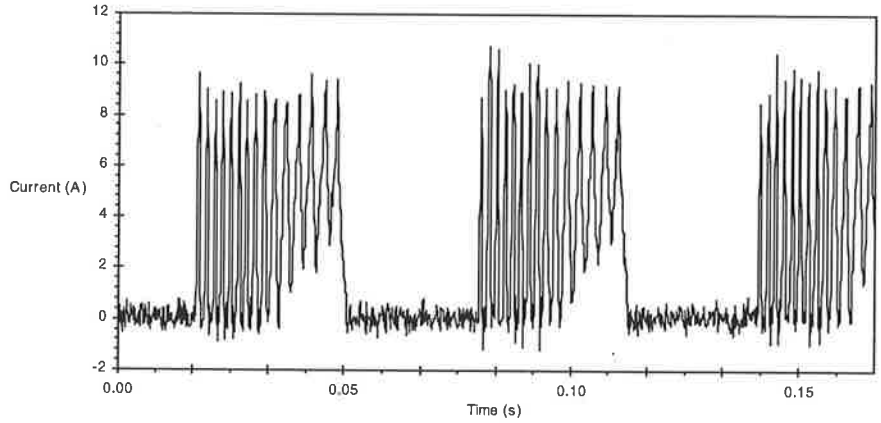
noisy inputs of voltage and current. In addition, the original measured waveforms of voltage and current also have some degree of measurement error, noise, and A/D converter quantisation error. Therefore, in fact the current and voltage waveforms shown with noise have in fact a higher level of noise than that indicated, due to the original waveforms also having some error.

However, even though completely accurate angle estimation is not possible, it is demonstrated here that the *robustness* of the scheme is high. In addition, it is possible to obtain the angles (with less accuracy) to turn on and off the motor phases, by using filtering of the estimated angle. The high level of noise has not led to the situation where the motor cannot be controlled due to loss of tracking of the rotor position. This is because the requirements of a robust algorithm, as explained in Section 7.2, have been satisfied.

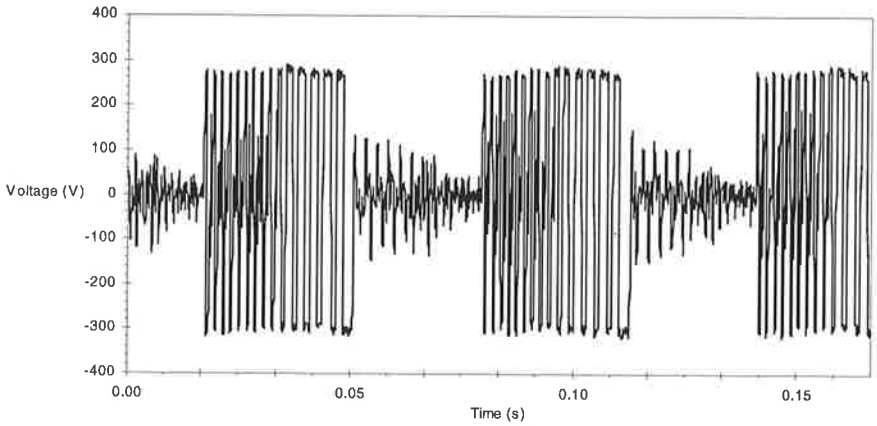
7.3.2 Measurement Noise Test - Chopping Mode

In the previous section, the robustness of the scheme to input data noise was confirmed using waveforms in the single pulse mode operation. However, it is beneficial to test the robustness of the scheme in the chopping mode also, in order to verify the robustness of the sensorless algorithm in bothsingle pulse and chopping modes of motor operation. In Figure 7.11, waveforms are given for the motor operating in the chopping mode and at a speed of 162 rpm, and where the noise component of the input waveforms had an amplitude of up to 10% of the maximum level of the measured signals.

As mentioned above, the measured waveforms have some inherent error due to measuring error and noise, and A/D converter quantisation. Therefore, the added noise is in addition to any errors already on the measured voltage and current waveforms. In Figure 7.12, and expanded view of the waveforms of current with and without added noise are shown. In order to clearly view the effect of the input noise a graph is shown in Figure 7.12 (c) of only the peaks of the currents. In this figure the peak value of the current with noise is plotted as a square point, and it can be seen that in all cases it deviates from the peak of the current waveform without noise. Furthermore an expanded view of the voltage is shown in Figure 7.13 with and without the added noise. In the comparison between the voltage with added noise and that without added noise in Figure 7.13 (c) one can clearly see that the noise produces a significant error in the voltage which is input to the angle estimation algorithm.



(a)



(b)

Figure 7.11 10% of Maximum Amplitude Noise Chopping Mode Waveforms: (a) SR Motor Phase A Current. (b) SR Motor Phase A Voltage.

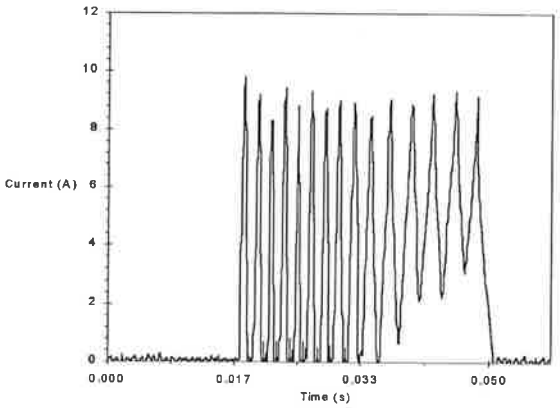


Figure 7.12 (a)

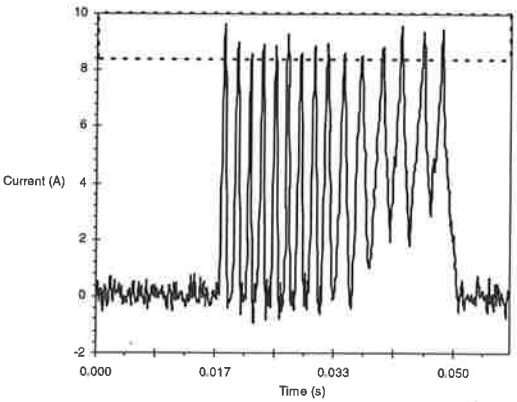
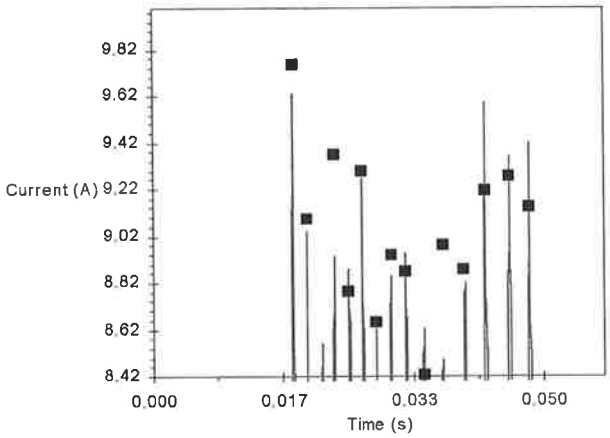


Figure 7.12 (b)



(c)

Figure 7.12 Current Waveforms Amplitude: (a) Phase A Current without added noise. (b) Phase A Current with Noise at 10% of Maximum. (c) Expanded view with comparison of the waveform peaks with and without noise. The squares indicate the peak of the current waveform with noise.

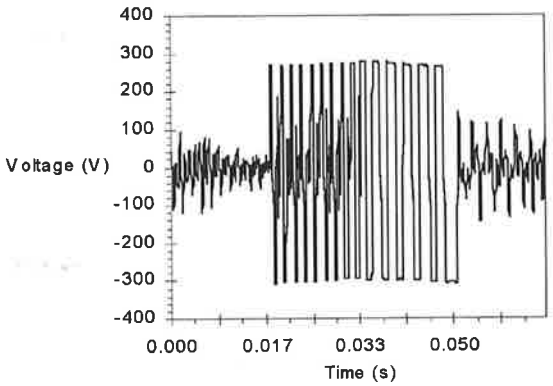


Figure 7.13 (a)

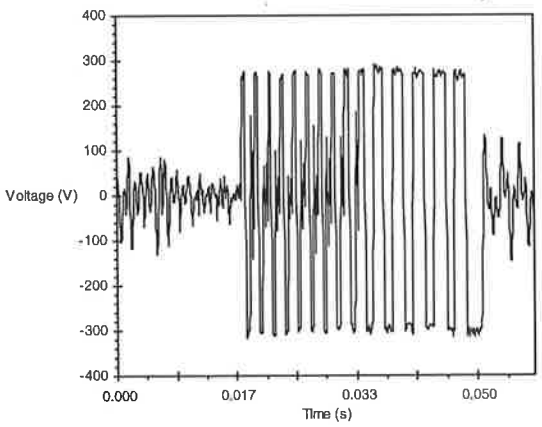
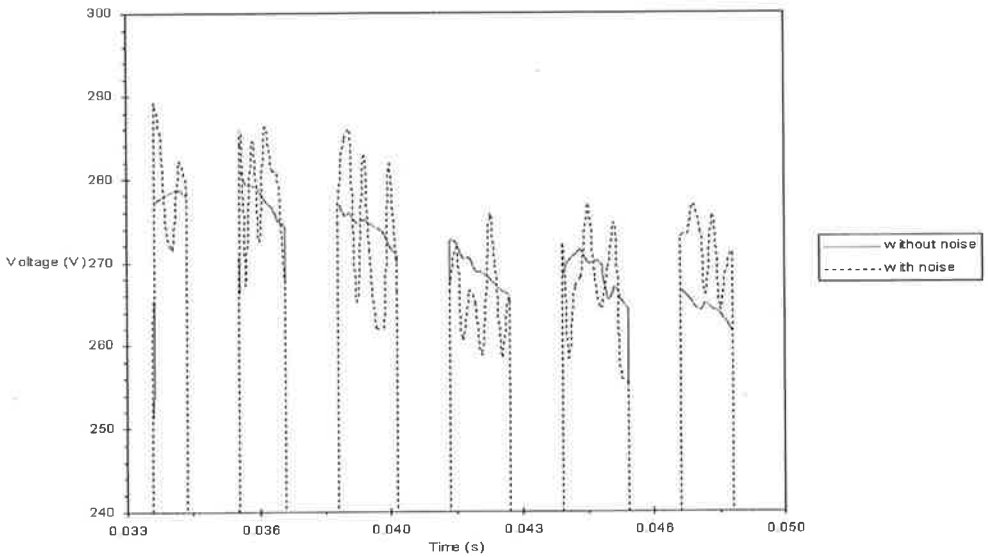


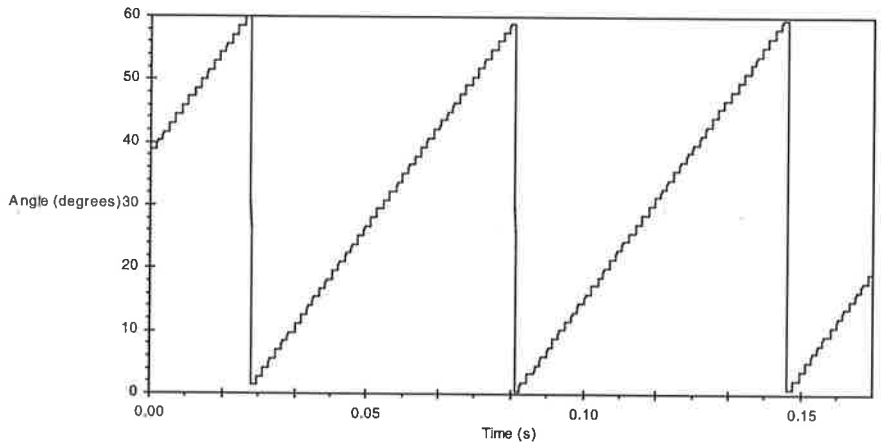
Figure 7.13 (b)



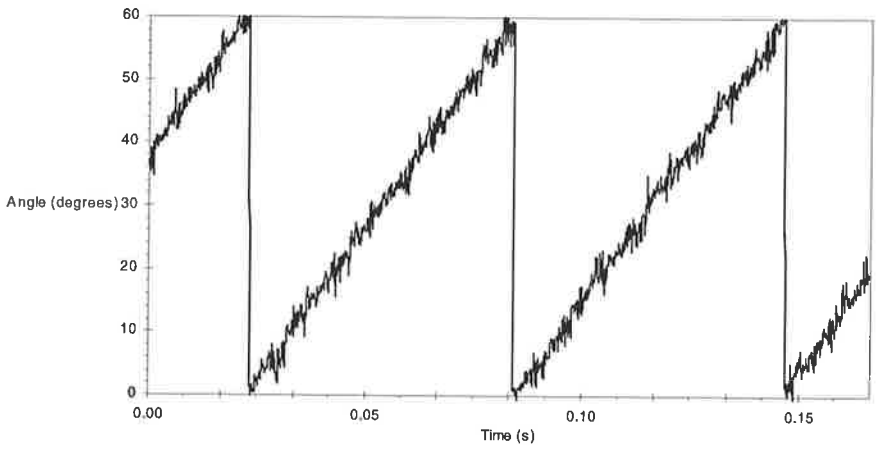
(c)

Figure 7.13. Voltage Waveforms: (a) Phase A Voltage without added noise. (b) Phase A Voltage with Noise at 10% of Maximum. (c) Expanded view with comparison of the waveform peaks with and without noise.

The measured angle from the encoder as well as the estimated angle from the angle estimation algorithm are given in Figure 7.14. It can be seen in these results that the second requirement of a robust algorithm, as defined above, holds once again in this test: There is only a small effect on the output of the algorithm (the estimated angle) due to the noise on the inputs of voltage and current. The average error in this test is 1.79 degrees whilst the peak angle estimation error is 5.24 degrees. Hence, the peak output error is 8.7% of an electrical cycle of 60 degrees, which is less than the peak input error relative to the current and voltage amplitudes. The error amplitude between the estimated angle and measured encoder angle is detailed in Figure 7.15.



(a)



(b)

Figure 7.14. 10% Noise, Chopping Mode Test (a) Measured Rotor Position. (b) Estimated Angle.

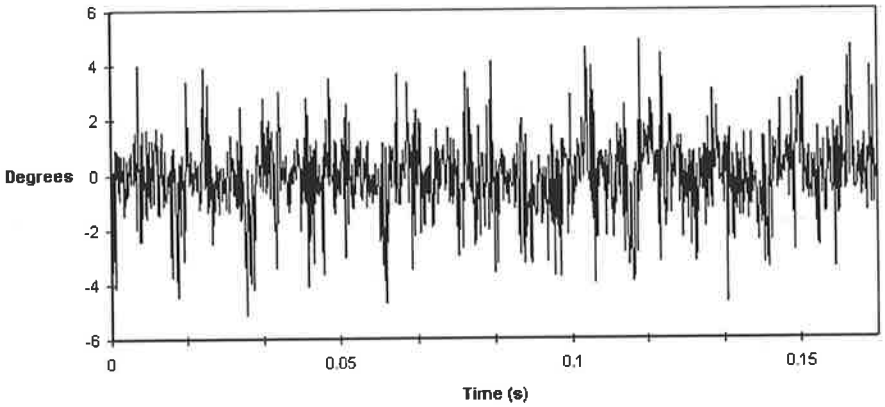
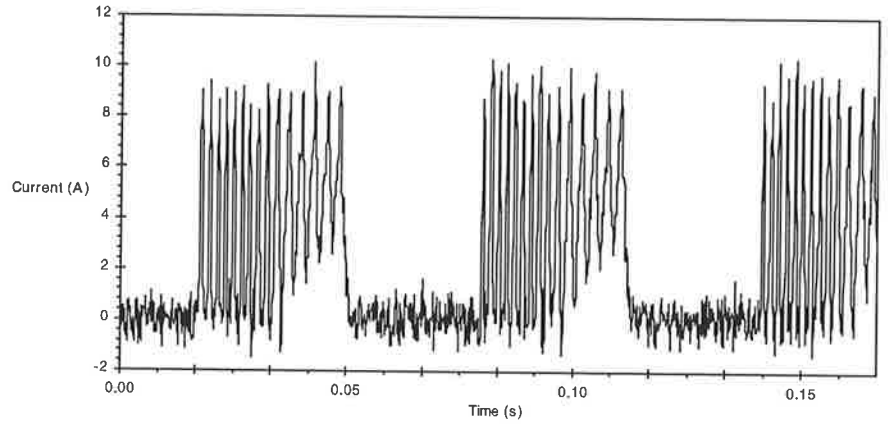


Figure 7.15 Error between Estimated and Measured Angle, 10% Noise, Chopping Mode

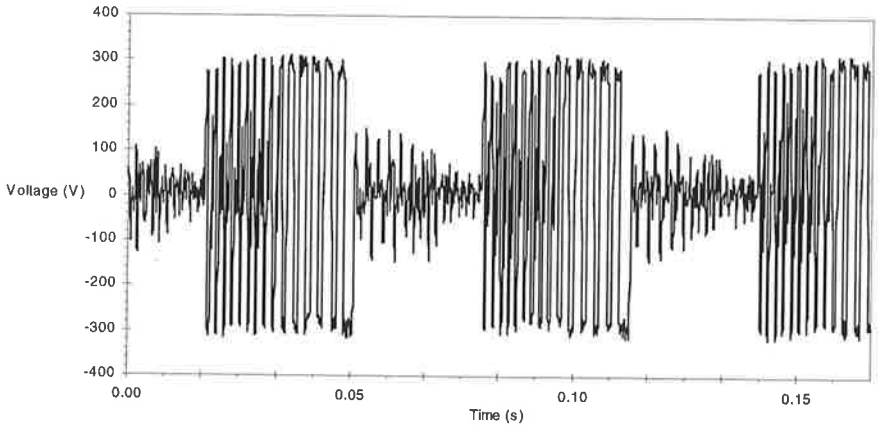
The above results show that the sensorless scheme is robust to measurement noise in the chopping mode also. The deviations in the input data of current and voltage due to measurement noise and error, in the above chopping mode test, only decreased the performance of the scheme by a small amount. Thus, the second requirement for a robust algorithm was satisfied. In order to test the algorithm to higher levels of noise in the chopping mode, the noise component level was increased to 20% of the input signal maximum. At this higher noise level, the scheme is tested to observe if it satisfies both the second and third requirements of robust algorithms. This is because the algorithm must not suffer from a catastrophic breakdown to the higher points of noise in the current and voltage inputs (ie. points where the noise is close to the 20% of the maximum amplitude level), and only be affected by a small amount at points when the noise is smaller.

In Figure 7.16, the waveforms of current and voltage are shown when the current and voltage has an added noise component of 20%. An expanded plot of the waveforms is given in Figure 7.17, and compared to the waveforms without added noise (as given previously in Figure 7.12 and Figure 7.13) it can be seen that there is now a significant noise level.

The estimated angle for this test is plotted in Figure 7.18. As compared to the previous result at a noise level of 10% of the maximum amplitude, the error in the estimated angle has increased in this test. This is expected due to the high input signal corruption of this test. However, the algorithm has still maintained a high robustness to the input noise. At no point is there a catastrophic breakdown in the algorithm, and in fact the underlying trajectory of the rotor angle is always followed in the estimated results. Compared to the input signal error level which has a peak value of 20% of the input signal amplitudes, the output estimation angle error is not overly large. The average error in this test is 3.24 degrees whilst the peak angle estimation error is 10.02 degrees. This peak value represents 16.7% of the electrical cycle of 60 degrees. The plot of the error between the estimated and measured encoder angle is given in Figure 7.19 (the peak value error of amplitude 10.02 degrees is slightly off the chart).

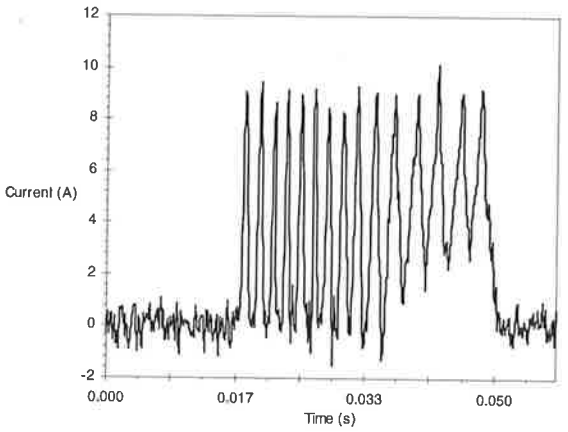


(a)

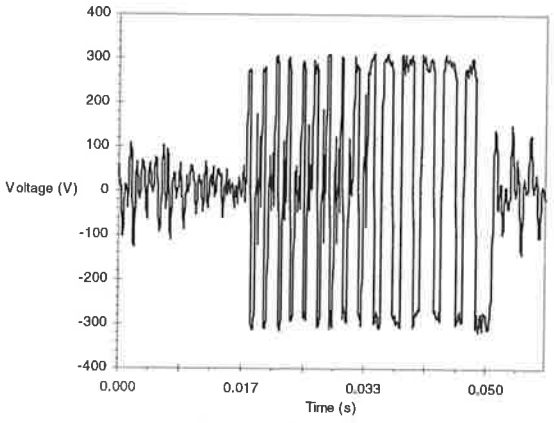


(b)

Figure 7.16 20% of Maximum Amplitude Noise, Chopping Mode: (a) SR Motor Phase Current. (b) SR Motor Phase Voltage.



(a)



(b)

Figure 7.17 20% of Maximum Amplitude Noise, Chopping Mode: (a) Expanded SR Motor Phase Current. (b) Expanded SR Motor Phase Voltage.

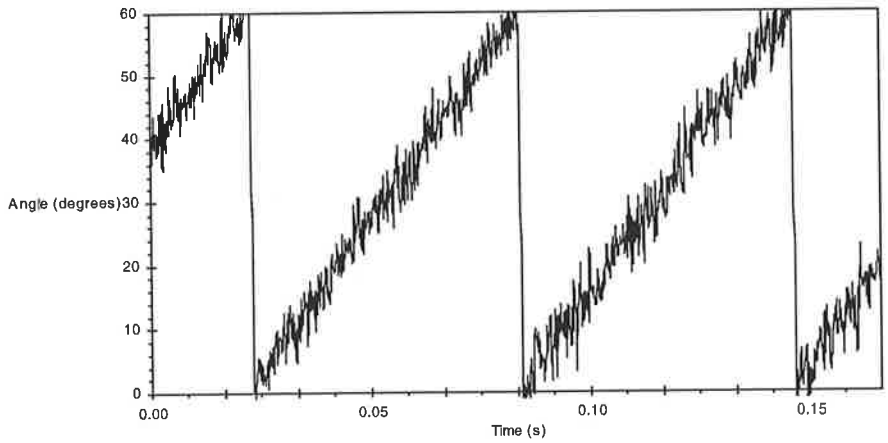


Figure 7.18 Estimated Angle from Sensorless Scheme.

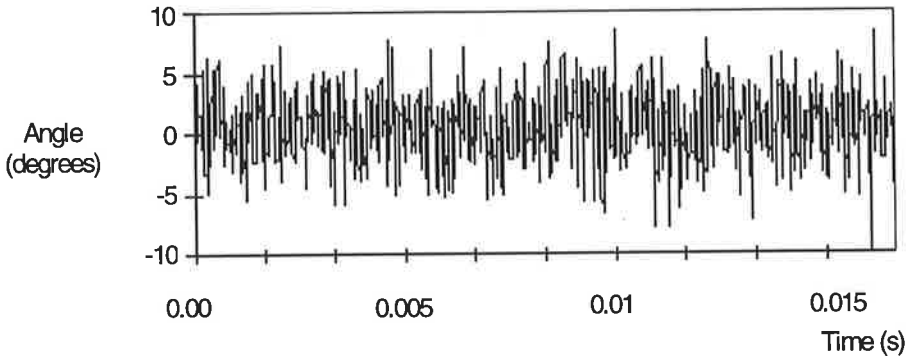


Figure 7.19 Error between Estimated and Measured Angle with 20% noise.

7.4 The Effect of Low Sampling Rate

In this section, another important practical effect for the operation of the angle estimation scheme in real SR motor drives is considered. During operation with a practical SR motor drive, the sampling rate of the analog to digital converters, which convert the measured waveforms into digital data, will have some effect on the accuracy of the position estimation. A system that is only accurate with high sampling rates may not be useful in a practical application. A high sampling rate system may have a high cost and may not suit a particular application in which the total system cost must be kept low.

To prove the wide ranging usefulness of the developed sensorless position detection scheme, various tests were performed using experimental data, to determine the ability of the scheme at low sample rates. In these tests, the results are shown for the case when the sampling frequency is deliberately reduced. This also entails that the theoretical required processing speed of the algorithm also becomes lower, because the rotor angle is estimated only once per sampling period (when new information about the voltage and current magnitudes is entered into the algorithm). Hence, although in this thesis a sophisticated high speed DSP based system was developed, the tests in this section will demonstrate that the scheme is viable also in systems with a low A/D converter sampling speed and low speed microprocessor.

Flux linkage is one of the inputs to the fuzzy model in the sensorless angle estimation algorithm. It can be recalled from Section 5.3 that the numerical flux linkage integration becomes less accurate when the sampling rate is reduced. It was shown that for trapezoidal integration, the error in the integration is approximately inversely proportional to P^2 where P is the number of samples in the integrated waveform. Hence, the integration error is inversely proportional to the $1/f^2$ where f is the sampling frequency. Hence, the accuracy in the flux linkage integration is particularly affected at lower sampling frequencies. This means that the major effect of low sampling rates on the angle estimation algorithm is the decrease in accuracy of the numerical flux linkage integration. As the flux linkage is an input to the fuzzy model, the decrease in the flux linkage estimation accuracy will also affect the accuracy of output position estimates from the fuzzy rule based motor model.

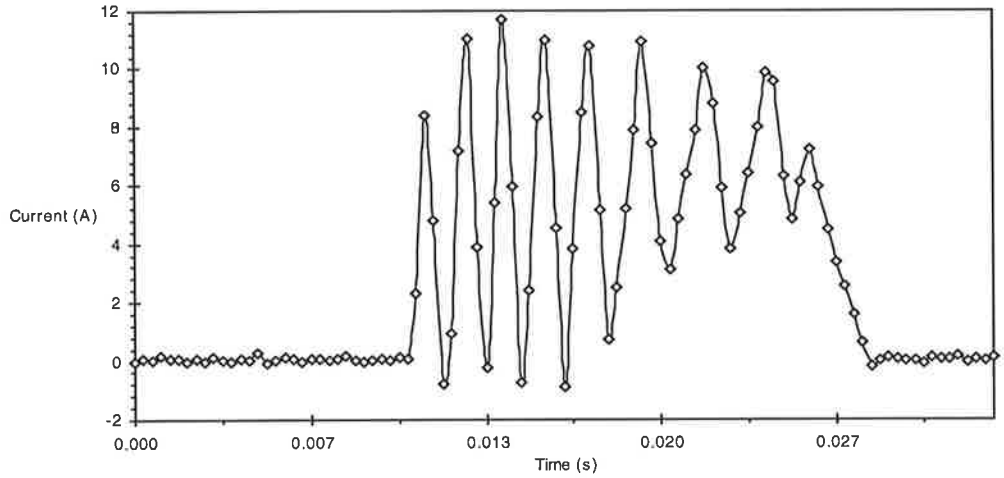
Hence, for a wide applicability, the angle estimation algorithm must have a high robustness to numerical flux linkage error from a low sampling frequency. In the following sub sections the effects of the reduced sampling will be analysed.

7.4.1 Low Sampling Rates Test: Chopping Mode.

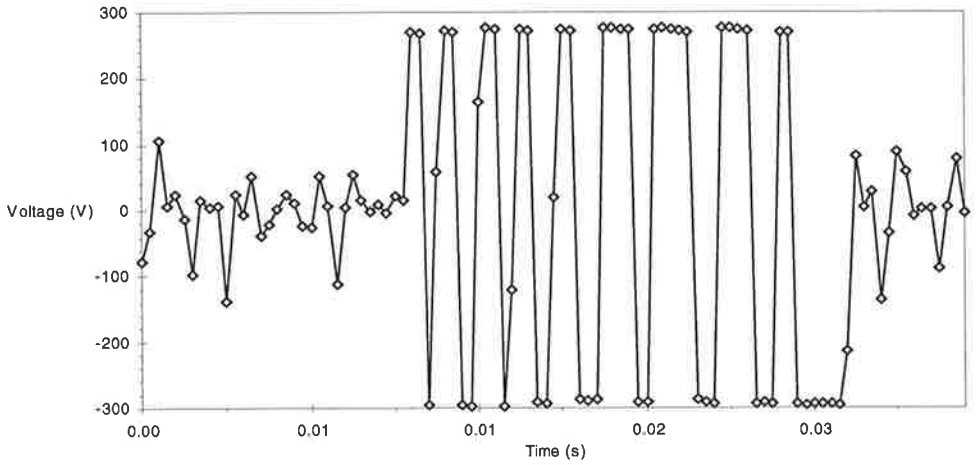
In order to test the robustness of the algorithm to low sampling frequency and the corresponding flux linkage estimation error, the chopping mode operation is firstly analysed. This is due to the fact that the chopping mode waveforms have a much greater complexity and non-linearity than the single pulse waveforms.

Hence, for the same sampling frequency and motor speed (ie. for the number of samples in the integrated waveforms), the chopping mode waveforms will normally produce a higher error in the estimated flux linkage. This is because, as was shown in equation (5.9), the trapezoidal integration error over an integration interval is proportional to the largest value of the second derivative of the measured waveforms. In any given integration interval, the chopping mode currents and voltages will normally have much higher waveform variations than the single pulse mode waveforms. This means that the second derivative of the waveforms in the integration period will be higher, which will lead to a higher flux linkage numerical integration error.

In Figure 7.20, experimental currents and voltages are shown for the motor operating in the chopping mode at a speed of 326 rpm, as was described in Section 7.3. However, in this case the sampling rate has been reduced to 3000 Hz, which is half of that that was shown previously in that section. Therefore, the sampling period is 333 μs, which corresponds to 92 samples per electrical cycle of 60 degrees. For a higher clarity in Figure 7.20, only one electrical pulse is shown and data points are shown in the figures which represents one sample point of the waveforms by the A/D converters.



(a)



(b)

Figure 7.20 Waveforms at motor speed of 326 rpm with a 3000 Hz sampling frequency: (a) SR Motor Current (b) SR Motor Phase A Voltage.

As it was stated above, the most important effect of the decrease in sampling rate, is that the flux linkage found from integration of the motor voltages and currents, will be less accurate. This effect can be seen in Figure 7.21, where the flux linkage is compared from between that estimated with 6000 Hz sampling frequency and that estimated with 3000 Hz sampling frequency. One can see that there is a higher error in the lower sampling frequency case due to the lower accuracy of the numerical integration. The peak error between the flux linkage estimation at 3000 Hz and the flux estimation at 6000 Hz has a value of 13.8%, of the maximum flux linkage amplitude at 6000 Hz.

It should be noted that even for the sampling frequency of 6000 Hz that there will be some flux linkage estimation error. Thus even the results given in Chapter 6, which used a 6000 Hz sampling frequency, also in fact showed the robustness of the scheme to flux linkage estimation errors. Therefore, the results given in this section demonstrate the schemes robustness to an even greater flux linkage estimation error.

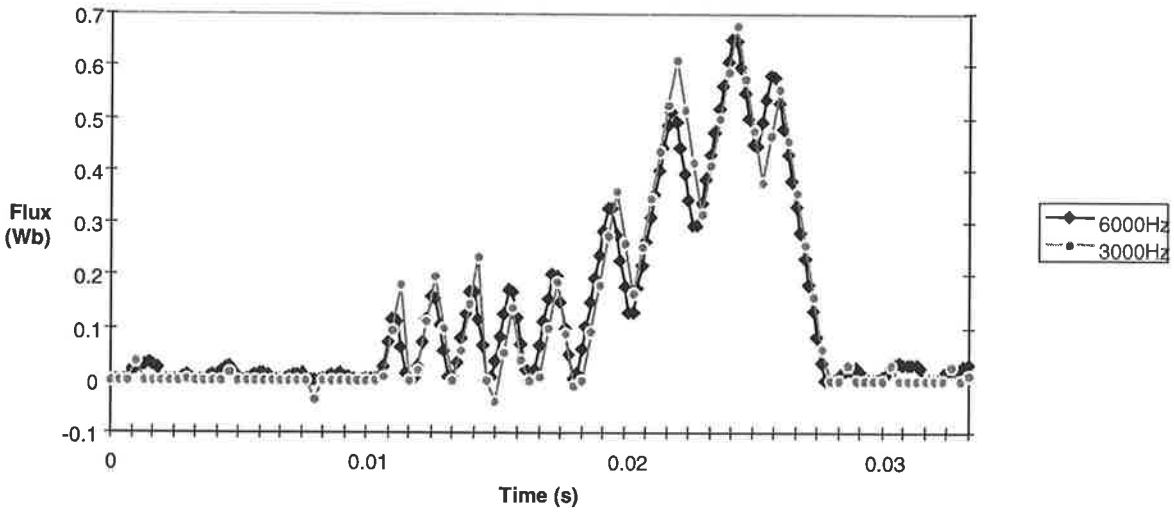


Figure 7.21 Comparison of Flux Linkages, 6000 Hz Sampling Frequency and 3000 Hz Sampling Frequency

The waveforms of estimated and actual rotor position for this test are given in Figure 7.22. It can be seen that the estimated angle has a higher error that for the case with 6000 Hz sampling speed shown previously in Section 6.4.1.2.

The plot of angle error between the estimated and measured value is given in Figure 7.23. The estimated angle has an average error of 2.32 degrees, whereas the peak of the error is 5.61 degrees, or 9.35% of the electrical cycle of 60 degrees.

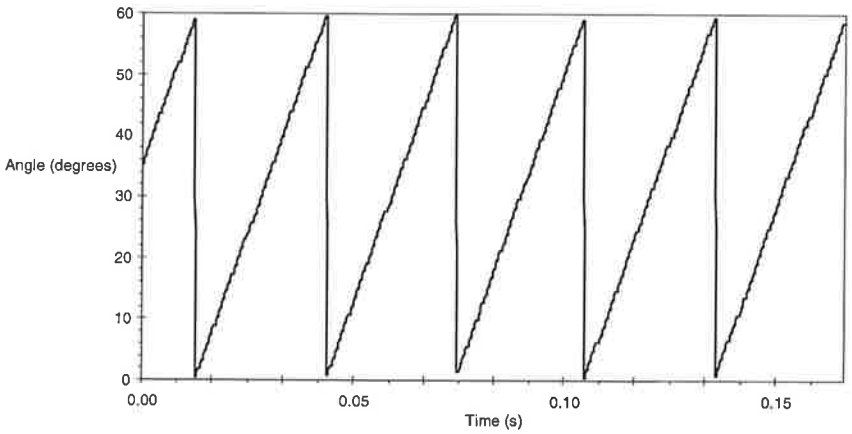
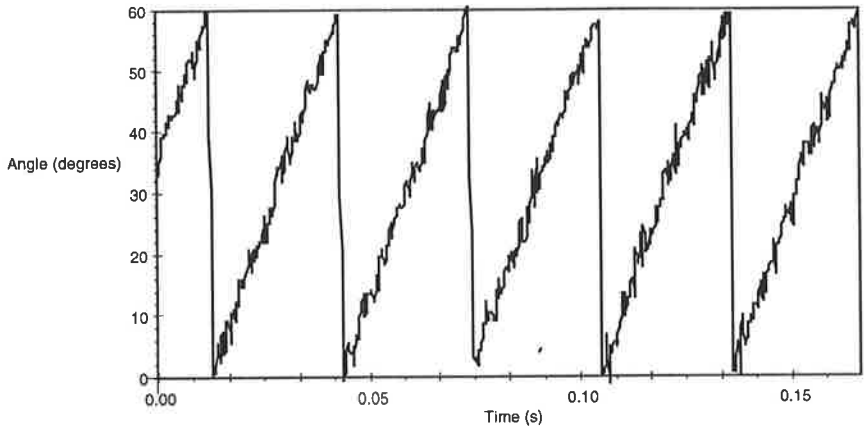


Figure 7.22 (a)



(b)

Figure 7.22 326 rpm 3000 Hz sampling frequency. (a) Measured Rotor Position. (b) Estimated Angle from Sensorless Scheme

Although the error in the angle estimation has increased, the algorithm has demonstrated a robustness against low sampling frequency, and higher flux linkage estimation error. It can be seen that the peak angle error is not overly large, relative to the error in the flux linkage, which has a maximum error of 13.8% relative to the peak flux linkage value at 6000 Hz. In addition, it was mentioned that the flux linkage estimation at 6000 Hz in itself has errors, and therefore the actual flux linkage error was higher than this value.

Therefore, as the value of the peak error in the angle estimation is less than the peak input error of flux linkage, it demonstrates that the larger deviations in the flux linkage do not cause a breakdown in the algorithm. In addition, the average angle estimation error of 2.32 degrees means that the smaller deviations in the flux linkage only produce a smaller deviation in the output estimated angle. Hence, the algorithm satisfies the requirements of a robust algorithm during this flux linkage estimation error test.

It should be noted that in this case, the main error occurs in the flux linkage, which is only one input to the fuzzy model, whereas in the previous section noise was placed on both the current and voltage, which led to an error in both the current and flux linkage inputs of the fuzzy model. Therefore, this test is not exactly equivalent to the tests with input noise in Section 7.3, as in this test the algorithm must only contend with an error in one of the inputs to the fuzzy logic based motor model.

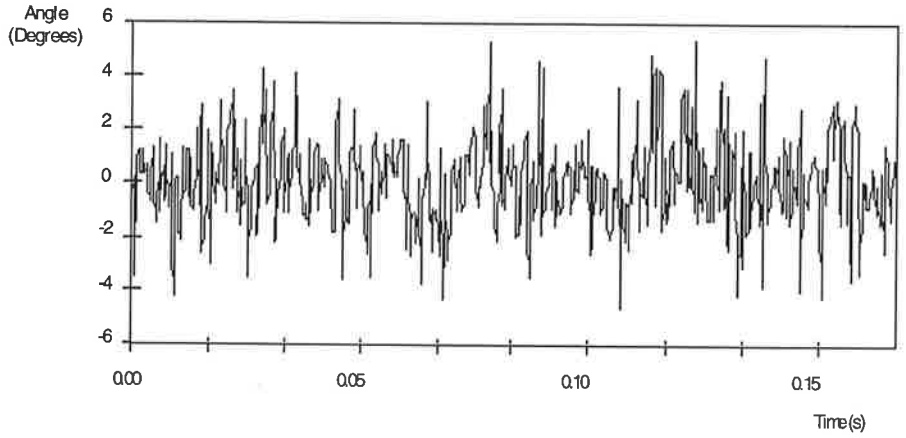


Figure 7.23 Error between Estimated and Measured Angle - 326 rpm 3000 Hz sampling frequency.

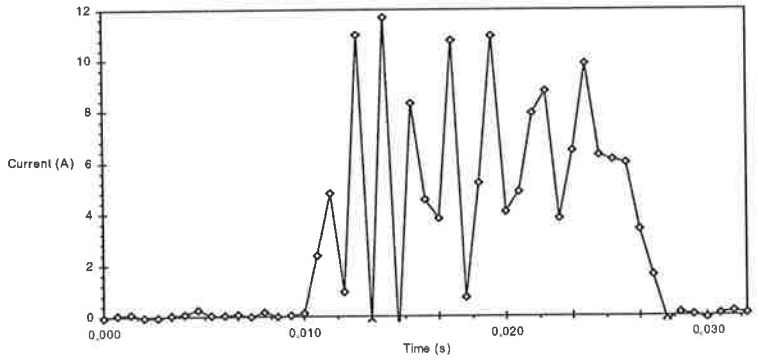
The above results show that the angle estimation algorithm demonstrates robustness against low sampling frequency, and the corresponding flux linkage error. To test the limits of the algorithm, the sampling frequency is further decreased to 1.5 kHz. This represents a difficult test of the algorithm, due to the corresponding high flux estimation errors. In an actual motor drive application, a sampling frequency of 1.5 kHz would normally be lower than the minimum practical sampling frequency. In reference [170], it is stated that a sampling frequency of at least 5 to 10 kHz is required for digital control of electric machines. Therefore, a sampling frequency of 1.5 kHz would not normally be feasible in a practical digital motor control system, and thus this test would be at the lower limit of the possible sampling frequencies.

In Figure 7.24, the experimental results of current and voltage are shown for a sampling frequency of 1500 Hz, which represents a sampling period of 667 μs, or 46 samples per electrical cycle.

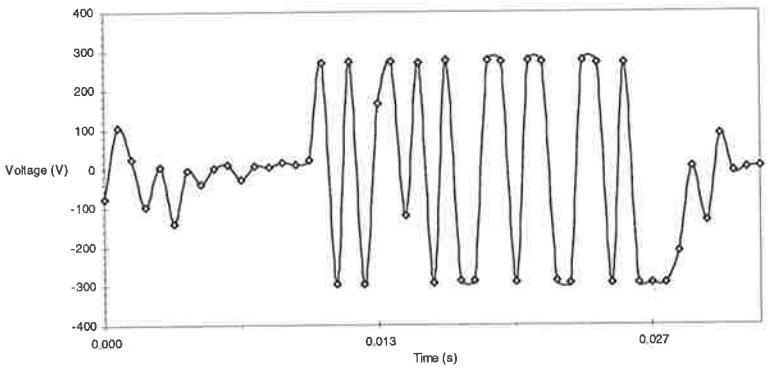
It can be seen from the current waveform, that a significant amount of the dynamic characteristic of the waveform is lost due to the low sampling rate. Therefore the line which has been drawn between the sampled points is not accurate: only the actual sampled points shown are. In itself, the low sampling time of the current does not present any problem to the position estimation, as only the current at the *actual sampling instant* is needed in the position estimation. The main effect of the less sampling rate is to decrease the accuracy of the flux linkage numerical integration.

Therefore, due to the reduction in sampling frequency, the flux estimation has a higher error component. The increase in numerical integration error of the flux linkage can be seen by comparing the estimated flux at 1.5 kHz in Figure 7.25 to the previous flux estimate at 3 kHz in

Figure 7.21. In this test the peak error between the flux estimated at 1.5 kHz sampling frequency, and that measured at 6 kHz, is 29.8% of the peak flux linkage amplitude measured at 6 kHz.



(a)



(b)

Figure 7.24 326 rpm 1500 Hz sampling frequency: (a) SR Motor Phase Current. (b) SR Motor Phase Voltage.

In Figure 7.26, the result of the angle estimation for this low frequency test is shown. One can see that there is now a very high error in the angle estimate. Nevertheless, it can be seen that the general path of the rotor angle is followed throughout the test interval, despite the very low sampling frequency. As mentioned previously, it would be possible to filter the estimated angle trajectory to provide a position signal to the controller.

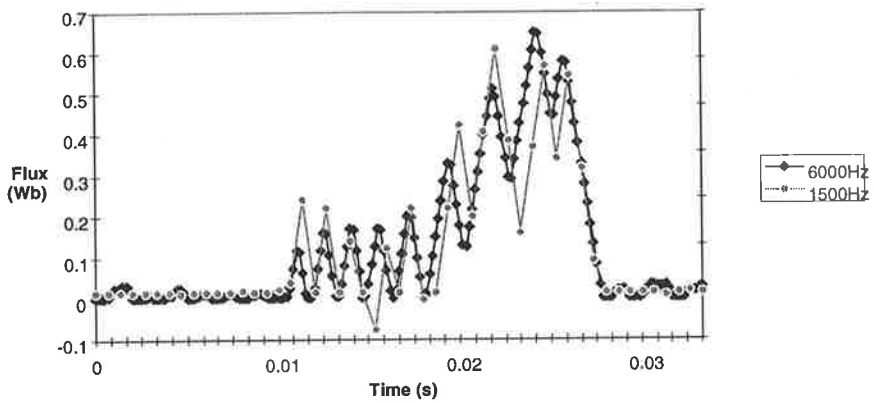


Figure 7.25 Comparison of Flux Linkages 6000 Hz Sampling Frequency and 1500 Hz Sampling Frequency

As expected, in this test the estimation error is higher than that with a sampling frequency of 3 kHz shown previously. The average error in the results was 3.82 degrees, whilst the maximum error was 7.79 degrees, or 13% of one electrical cycle. A plot of the actual error between the estimated and measured angle can be seen in Figure 7.27. These error results

show that even with the very low sampling frequency as well as a high flux estimation error, there is no breakdown of the algorithm. Therefore, the robustness of the algorithm is to low sampling frequencies is again demonstrated in these results.

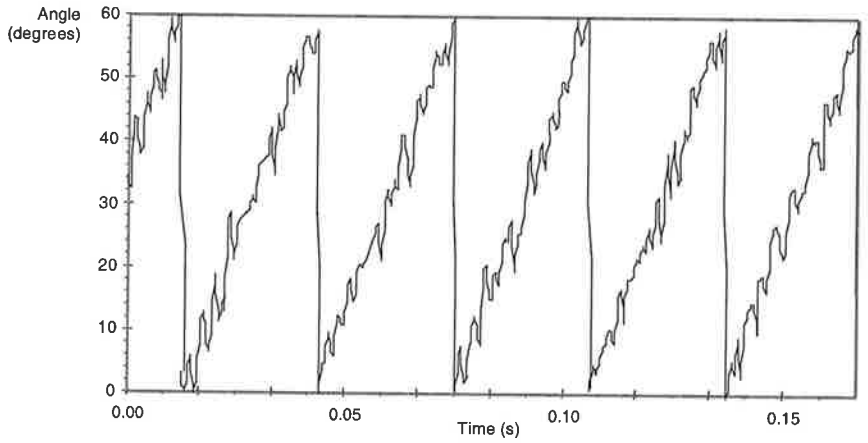


Figure 7.26 Estimated Angle from Sensorless Scheme - 326 rpm 1500 Hz sampling frequency

Although the peak error of the angle estimation error is 13%, which is less than half the flux estimation peak error of 29.8%, it can not be concluded that the position estimation algorithm performed particularly well in this case. This is because, as mentioned above, in this test only *one* of the inputs to the fuzzy logic based motor model is affected by error. The motor current in these tests does not have the high error that is seen in the flux linkage waveform. Hence, only one of the two inputs to the fuzzy rule based SR motor model has a high error. The effect of having only one input in error is not as pronounced as having both inputs to the fuzzy model in error. This subject will be examined in detail in Section 7.7, where a mathematical derivation of the separate effect of flux linkage and current errors on the angle estimation will be given.

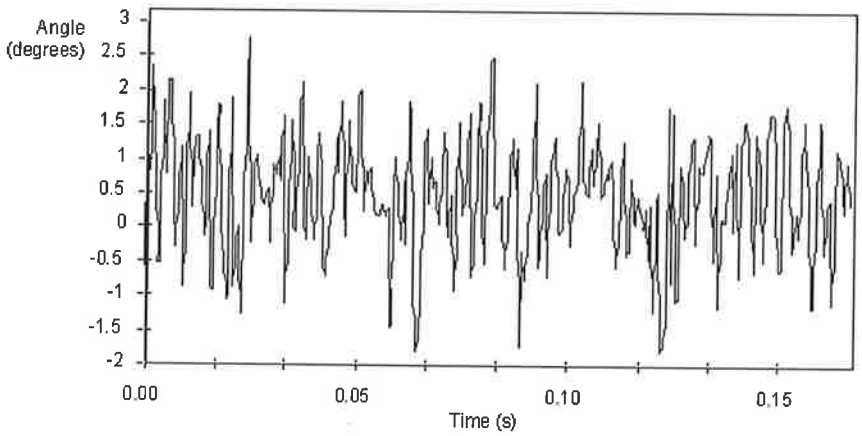


Figure 7.27 Error between Estimated and Measured Angle - 326 rpm 1500 Hz sampling frequency

7.4.2 Low Sampling Rates Test: Single Pulse Mode

In the previous set of results, the effect of low sampling rates was examined for the motor operating in the chopping mode. It was discussed in the previous section that the error of

the flux linkage, for waveforms at the same sampling frequency and motor speed, was normally higher in the chopping mode of operation. This is because the integration error is directly proportional to the highest second derivative of the waveforms in the integration period. Therefore, as the chopping mode currents and voltages have a more complex and higher time varying waveform than the single pulse mode currents and voltages, this will normally lead to a higher integration error.

However, it was also discussed previously in Section 5.3 that the integration error is also proportional to the integration time of the integrated waveform. It is also known that as the motor speed rises, the electrical cycle period in time will decrease. Therefore, at higher speeds when the single pulse mode operates, the integration accuracy will be affected by the smaller period in time of the integrated waveforms (which are the current and voltage pulses). Essentially this is due to the fact that the smaller time period of the electrical cycle leads to a lower number of samples per waveform pulse as the speed increases (for a constant A/D converter frequency).

Hence, in the high speed single pulse mode of the motor there will be two main effects on the flux linkage integration: The simpler waveforms compared to the chopping mode waveforms will act to decrease the error (relative to the chopping mode current at the same sampling frequency), whilst the decrease in number of samples per waveform pulse at higher speeds will act to increase the integration error. It can also be seen that when the motor speed keeps increasing, eventually the number of samples in the integration period decreases to a very low level (for constant A/D converter sampling frequency). When this occurs, the low number of measured samples effect will overwhelm any decrease in error due to the simpler waveforms.

Therefore, it is important to examine the operation of the angle estimation in the higher speed mode of motor operation. In this section, the robustness of the angle estimation to the decrease in the number of samples per waveform in the single pulse mode will be examined. To be classified as robust, the algorithm must not breakdown when there is a large error in the flux linkage in the single pulse mode, due to a low number of samples per waveform pulse. Results are shown in this section of the angle estimation with the motor operating in the single pulse mode at a speed of 810 rpm. The sampling frequency in the following results is set at 3 kHz and 1. 5 kHz. It will be seen that this represents a very low number of samples per electrical cycle, and thus presents a difficult test of the angle estimation algorithm.

In the first set of results in this section, the waveforms of current and voltage are shown for the motor operating in single pulse mode at 810 rpm, with a sampling frequency of 3 kHz. At this sampling frequency there is one sample every 333 μs, which at this motor speed results in only 37 samples per electrical cycle of 60 degrees. However, the actual number of samples over the integrated current and voltage waveform pulses is less,

because the current pulse does not span an entire electrical cycle in this test. Therefore, it can be seen in Figure 7.28 that there are in fact only 12 sampling points in the period of one current pulse. In the waveforms shown, each data point represents one sampling instant of the A/D converter.

The major effect of the low sampling frequency is the corresponding error on the flux linkage integration. In the previous section with chopping mode results, it was seen that there was error in the flux linkage waveform at a sampling frequency of 3 kHz, which had a peak of 13.8%, relative to the flux estimated at a sampling frequency of 6 kHz. In this single pulse mode test, there is the same sampling frequency, but due to the higher speed there are less samples per electrical cycle (37 as opposed to 92 samples per electrical cycle in the previous section). Therefore, it can be expected that this decrease in the number of samples will act to increase the flux linkage integration error. However, the current and voltage waveforms in the single pulse mode have a much lower complexity than the chopping mode waveforms. As discussed above, this decrease in waveform complexity will act to decrease the flux linkage integration error. It was found that in fact this second feature was dominant in this test. This was because, even though there were only 12 samples in the integration of a flux linkage pulse waveform, the error was still relatively low.

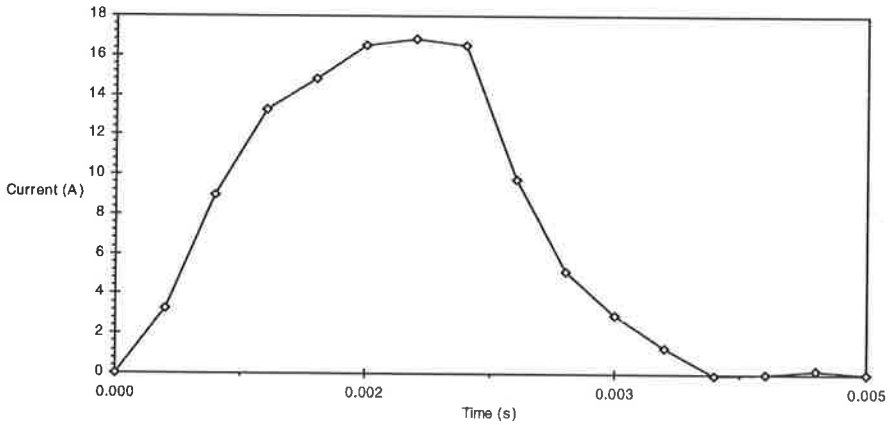
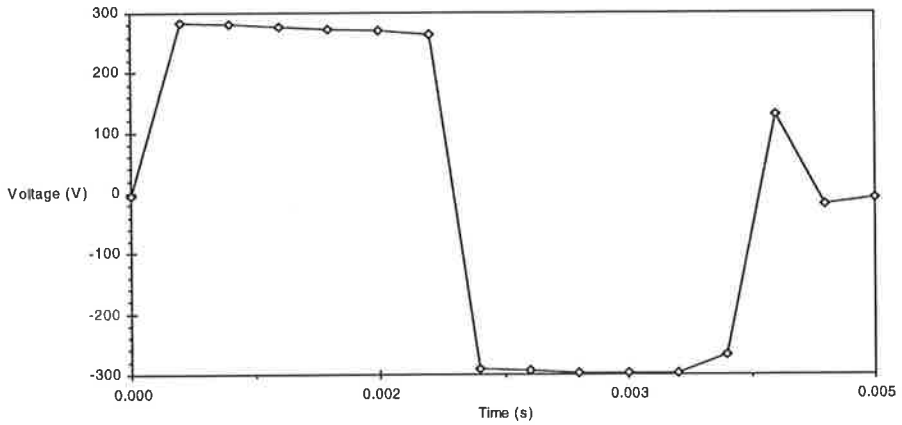


Figure 7.28 (a)



(b)

Figure 7.28 810 rpm, 3000 Hz Sampling Frequency: (a) SR Motor Phase Current. (b) SR Motor Phase Voltage.

In Figure 7.29, the flux linkage measured in this test at a 3000 Hz sampling rate, and that measured at a 6000 Hz sampling rate are shown. It can be seen that the difference in the two waveforms is small. In fact, the peak error of the flux waveform with 3000 Hz sampling rate is only 4.2% relative to the peak flux value at 6000 Hz, which is less than the peak error found in the chopping mode flux waveforms measured at 3000 Hz that were shown above.

The increase in integration error due to the lower number of samples per electrical cycle in this test compared to the chopping mode, was more than compensated by the decrease in integration error due to the lower complexity of the current and voltage waveforms. It can be concluded that the flux integration is less sensitive to low sampling frequencies in the single pulse mode of operation, due to the much simpler current and voltage waveforms.

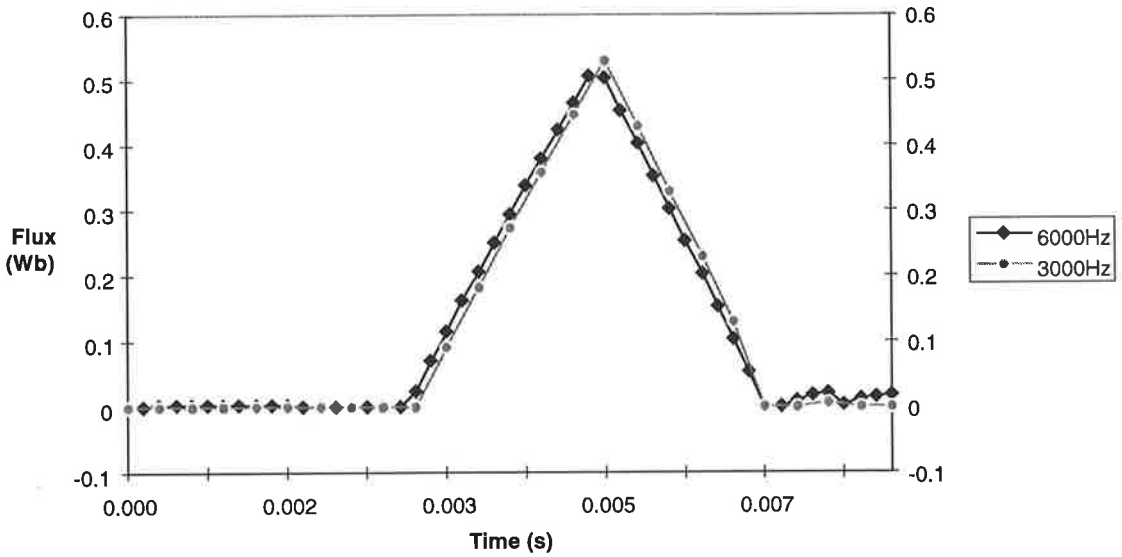


Figure 7.29 Comparison of Flux Linkages 6000 Hz Sampling Frequency and 1500 Hz Sampling Frequency.

The results of the estimated rotor position from the angle estimation algorithm are shown together with the measured encoder angle in Figure 7.30. It was predicted that the error in

the flux linkage would lead to an error in the estimated rotor position. However, the error in the flux linkage is relatively small, and thus from Section 7.2, it was expected that for a robust algorithm that the effect on the estimated angle will also be small. This was confirmed in the results of the resultant estimated angle, where there is an average error of 0.92 degrees and a peak error of 3.2 degrees, or 5.3% of 60 degrees. In Figure 7.31, the plot of the error between the estimated and measured angle is detailed for this test.

In the chopping mode results for a sampling frequency of 3000 Hz, it can be recalled that the peak angle estimation error was 9.35%, due to much the higher flux linkage estimation error. Hence, it can again be seen that this low sampling rate has a greater negative effect on the angle estimation algorithm accuracy in the chopping mode of operation, due to the more complex, nonlinear, and time varying waveforms of the chopping mode.

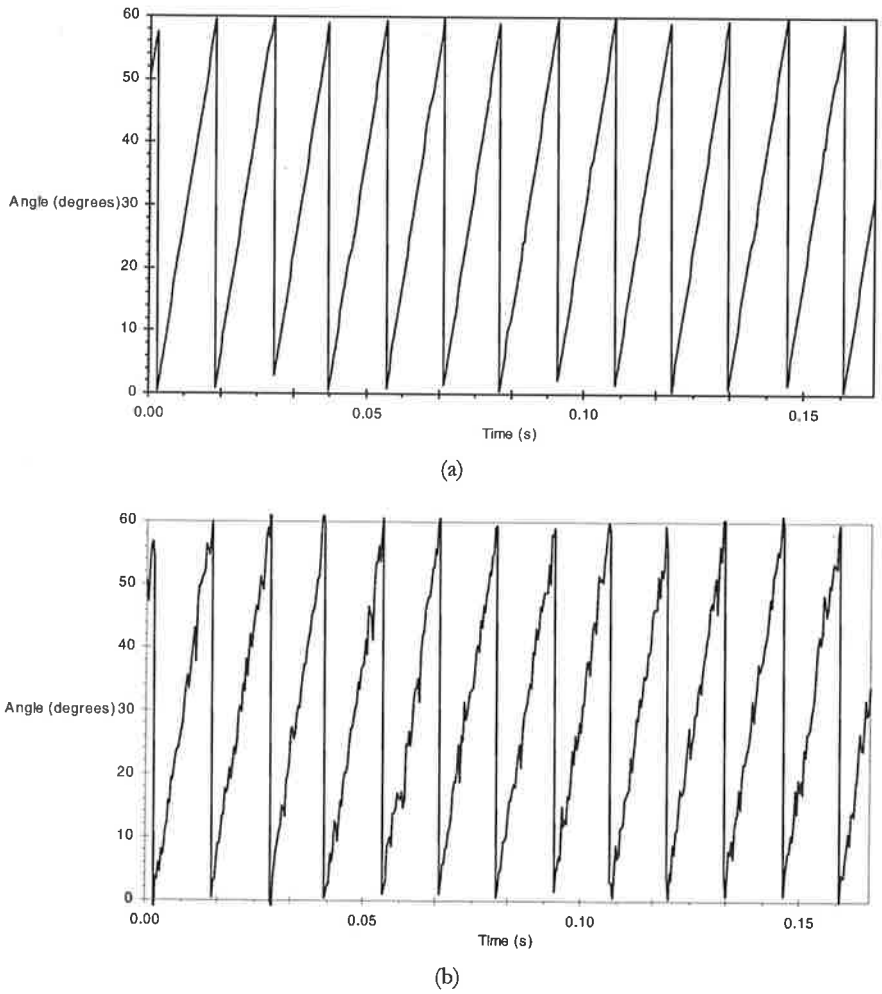


Figure 7.30 810 rpm, 3000 Hz Sampling Frequency: (a) Measured Rotor Position. (b) Estimated Angle from Sensorless Scheme.

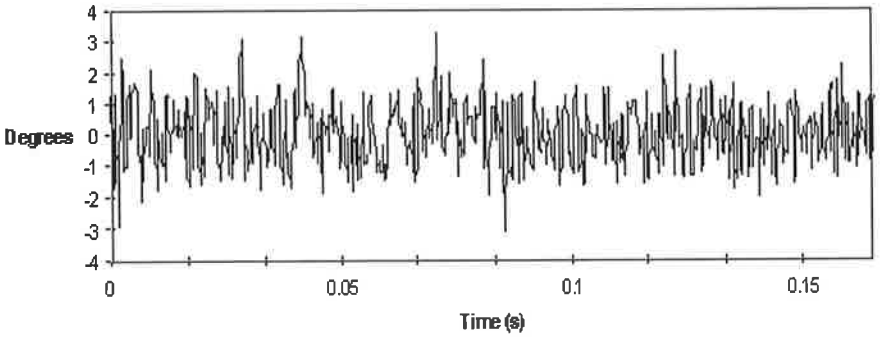


Figure 7.31 Error between Estimated and Measured Angle - 810 rpm 3000 Hz

These results demonstrate that the angle estimation is not affected greatly by the low sampling frequency of 3 kHz. Therefore, the estimation algorithm again satisfied the second requirement of robustness, in that the small flux error only caused a small output error.

In order to test the limits of the algorithm, the sampling frequency is decreased to 1.5 kHz. It was previously mentioned that this frequency would be lower than any practical A/D converter frequency that would be used in a motor drive. Therefore, this represents a lower limit of possible sampling frequencies that would be used with the angle estimation scheme.

The measurements of the single pulse mode current and voltage for a sampling frequency of 1500 Hz and a motor speed of 810 rpm are shown in Figure 7.32. The time between each sample in this case is 667 μs, or 18 samples per electrical cycle. However, as one can see in the Figure 7.32, this represents only 6 samples in the integration period of one current pulse.

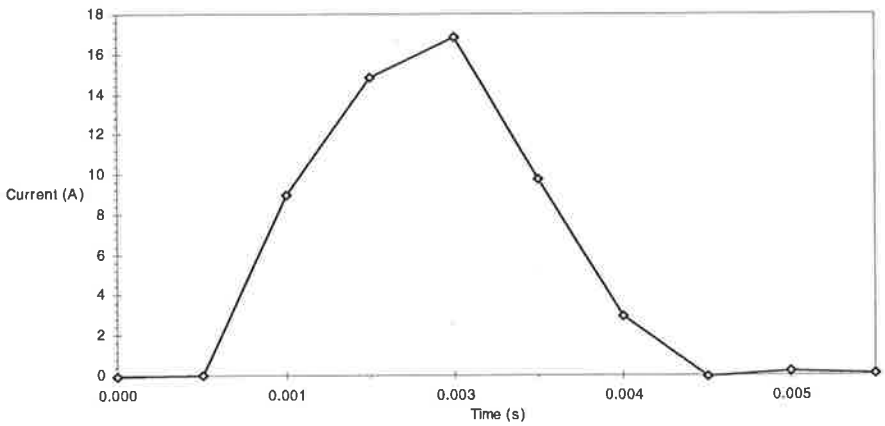
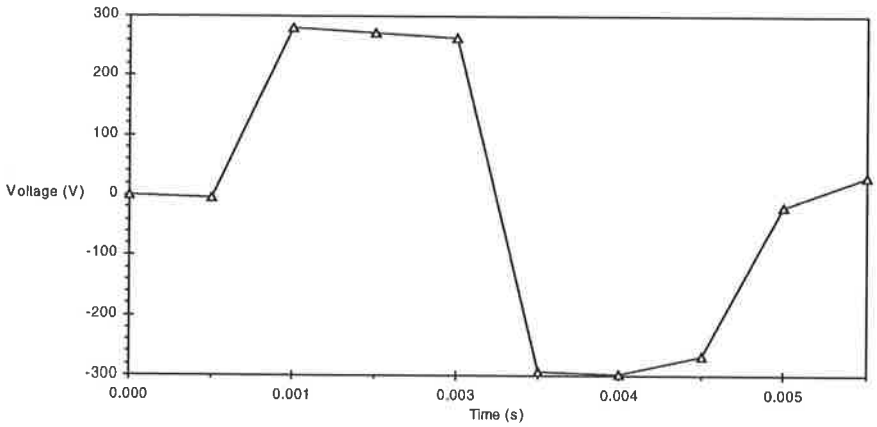


Figure 7.32 (a)



(b)

Figure 7.32 810 rpm 1500 Hz Sampling Frequency. (a) SR Motor Single Phase Current Pulse. (B) SR Motor Single Phase Voltage Pulse.

The low sampling frequency, and very low amount of samples in the integration of the flux waveform leads to a high error in the estimated flux linkage waveform. In Figure 7.33 the flux linkage estimated at 1500 Hz sampling frequency is compared to that with that measured at 6000 Hz. It can be seen that the flux estimation error is now high, due to the very small number of integration intervals. In this test the peak error between the flux estimated at 1500 Hz and that measured at 6000 Hz was 26.4% of the peak value of flux linkage. However, what is most significant in this case is that the error in all the iterations remains approximately constant. This is mainly due to the significant time lag (or phase shift) between the actual and integrated flux values, because of the low number of integration points. Therefore, in this situation, every flux linkage point that is input to the fuzzy model has a high error value of approximately 25%. This is different to the previous low sampling rate results, as in those cases there were many points which had an error much less that the peak error.

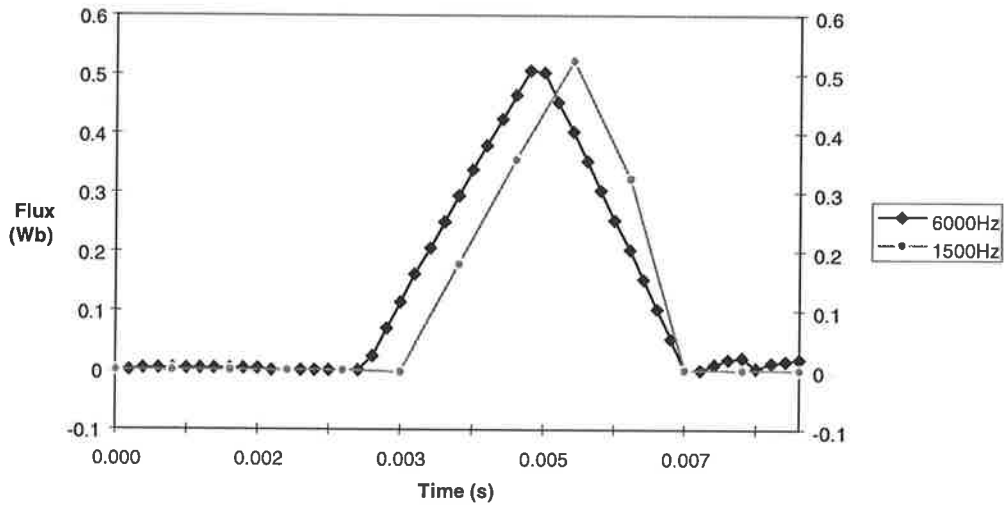


Figure 7.33 Comparison of Flux Linkages 6000 Hz Sampling Frequency and 1500 Hz Sampling Frequency

It can be noted that in the last point of the 1500 Hz estimated flux linkage curve, the flux abnormally returns to zero. This is due to the automatic flux reset feature in the flux integration. When the current is detected to have reached zero after a voltage turn off, then the flux linkage is reset to zero. Therefore, due to the flux linkage reset, the last point of the flux estimate does not have any error relative to the flux measured at 6000 Hz.

The resultant estimated angle is given in Figure 7.34, where it can be seen that there is a large error in the position estimates. Due to the higher flux linkage error, the angle estimation error is higher than that in the previous test at 3000 Hz. In this test the flux linkage error is constantly high, and therefore, this result represents a demonstration of the algorithms ability to cope with large and sustained input error. The resultant estimated angle waveform shows that, although the angle error is large, the underlying trajectory of the rotor position is maintained, and the algorithm does not suffer from a catastrophic breakdown. Therefore, this test again demonstrates that the algorithm conforms to the third requirement of robust algorithms, defined in Section 7.2.

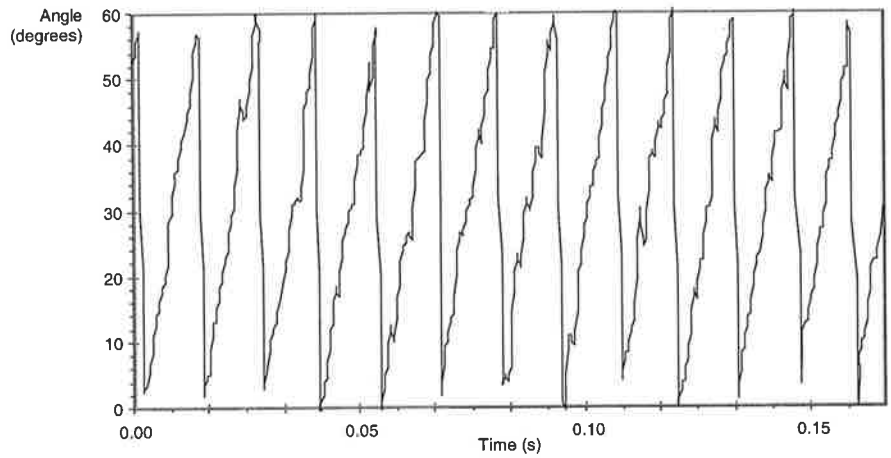


Figure 7.34 Estimated Angle from Sensorless Scheme - 810 rpm 1500 Hz Sampling Frequency.

In Figure 7.35, the error in each sample is shown relative to the measured encoder position given in Figure 7.30. In these results the average error was 4.6 degrees, whilst the peak error was 17.4 degrees, or 29% of one electrical cycle. Therefore, due to the high sustained flux input error to the fuzzy logic based motor model, there is a very large average and peak output error of the algorithm.

It should be noted that although the flux linkage error is relatively constant, there are points where the flux linkage error may have a greater negative effect on the output angle error. Therefore, the instantaneous angle error will vary according to the flux levels in each of the four motor phases. In Section 7.7, the various regions of flux linkage and rotor position where the effect of flux error is higher will be explained. In addition to the flux linkage error, the measurement error and noise on the current and voltage will also produce angle estimation errors. It will be shown in Section 7.7 that the angle estimation error is also determined by the phase current level in each of the motor phases. Hence, at

any particular iteration the actual angle error is hard to predict, and is highly varying due to a combination of one or more of the above mentioned variable error producing effects.

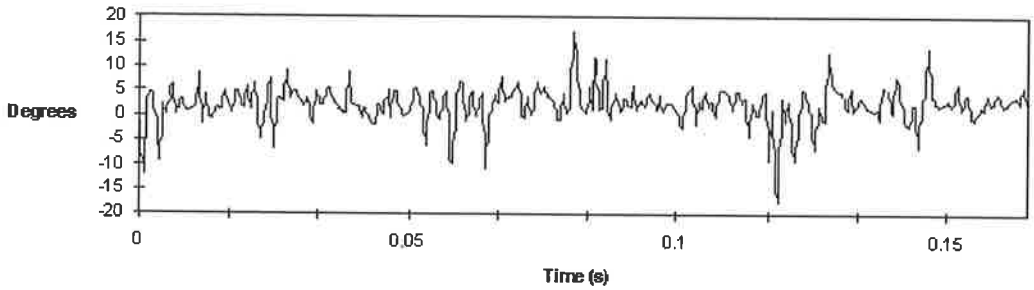


Figure 7.35 Error between Estimated and Measured Angle - 810 rpm 1500 Hz Sampling Frequency.

Hence, from the above results it can be concluded that the number of samples per electrical period was adequate in the 3000 Hz test, but too low in the test at 1500 Hz. For the sampling frequency of 3000 Hz, there were 37 samples per electrical cycle. If it is assumed that the flux error in single pulse mode is only dependant on the number of samples per electrical cycle, then at least 37 samples per cycle should be used at all speeds. This can provide an approximate guide to the minimum sampling frequency required to operate the algorithm at the top speed of the motor.

For example, if the motor is required to operate at a maximum speed of 3000 rpm, then one electrical cycle of 60 degrees for a four phase motor would have a period of 3.33 ms. Hence if one requires 37 samples per electrical cycle, an A/D converter frequency of 11 kHz is required.

Although this is a simple approximation, it provides a first order figure of the sampling frequency which would be adequate at the highest motor speed. It should be noted that for motor speeds that are less that the highest speed, the number of samples per electrical period would correspondingly increase. Therefore, the accuracy would also continuously increase at lower speeds in the single pulse mode. When the speed has reached chopping mode, then the number of samples per electrical cycle will be much greater than that at higher speeds. For example, in the previous section, results were shown for the chopping mode waveforms at a motor speed of 326 rpm. At this speed, for a sampling frequency of 11 kHz, there will be 337 samples per electrical period. This is almost double the number of samples per electrical cycle in the chopping mode results shown in the previous chapter (Section 6.4.1.2), in which the sampling frequency was 6 kHZ.

As it was mentioned previously, the error in the flux linkage trapezoidal integration is approximately inversely proportional to f^2. Hence, for a relatively modest sampling frequency of 11 kHz, a higher performance can be expected than the already accurate results shown in the above results.

7.5 Flux Linkage Offset Tests

In the sensorless position estimation scheme, the flux linkage of each motor phase is continuously estimated using the measured phase voltages and phase currents. As it has been detailed previously (see equation 2.2), the flux linkage is estimated using integration of the phase electrical equation *(v-Ri)*. In some other types of motor drives, where the same integration equation is performed to find motor flux linkage, critical problems can be found, particularly at low speeds. For example in the direct torque control of induction motor drives [171] [172], the flux linkage must be estimated using exactly the same equation (2.2). However, in the operation of the induction motor drive the flux estimation can have substantial errors due to uncertainty and noise in the measurements of voltage and current, and variation of the resistance due to temperature [173] [174]. There is also the effect of dc offset which may be present on the current and voltage measurements. These effects will lead to dc offset and errors on the flux linkage waveform, and due to continuous performing of the integration, these errors will accumulate over time. This flux linkage offset problem is also found in the indirect vector control of induction motors [175], and the control of permanent magnet motor drives [176].

The SR motor drive is generally immune to such problems, as explained in reference [84]. This is because in the SR motor, the flux always returns to zero at the end of each current conduction period, which allows the integrator to be reset to zero in *every* electrical cycle. This prevents any large accumulation of errors over time due to the above effects of current and voltage dc offset, measurement errors, and resistance variation. Reference [84] provides results that state that even a 50% variation in the stator resistance values used in the flux integration equation leads to negligible error in flux estimation. For this reason, the flux estimation technique is very effective for the sensorless rotor position estimation of the SR motor.

Even though the flux linkage integration is reset to zero in each electrical cycle, and is thus generally immune to offset problems in the SR motor, to test the robustness of the angle estimation algorithm, results will be shown below for operation with flux linkage waveforms with offset. In these tests, a constant flux linkage dc offset error was introduced into the flux linkage waveform to examine the effects of dc offset errors of the measured signals, measurement errors, and stator resistance estimation error in the flux estimation. This would have the outcome of modelling the above effects, in the fact that the flux linkage presented to the angle estimation algorithm would be constantly in error. However the results presented here should be considered as an exaggeration of any errors in the flux linkage waveforms that would normally occur practically, due to the fact that normally the flux linkage would be reset to zero after each electrical cycle.

a) Flux Linkage Offset Test: Positive Offset

Figure 7.36 shows the flux linkage for the case when the motor is operating in the chopping mode in the same conditions as was given in the previous chapter in Section 6.4.1.1. This test was chosen because, as it has been detailed above, the chopping mode normally is more susceptible to a greater level of integration errors in flux estimation, due to the fast time varying waveforms. Hence, adding offset to the flux linkage, in addition to the inherent error of the flux estimation in the chopping mode will present a more difficult test than for the single pulse mode. In this test, a flux linkage error is added such that the flux linkage has a constant positive offset of 0.025 Wb, or 4% of the peak flux linkage value without error. Although this is not an overly large error value, due to the fact that is has a constant value, it means that the *relative* effect at the lower flux values is higher than for the peak flux values

It can be seen in Figure 7.36 that no flux linkage reset takes place after each cycle as normally occurs in the flux linkage estimation. Hence, the flux linkage has an offset value of +0.025 Wb at all times, including the regions when there is no actual flux linkage in the motor.

This constant offset is a simple but inexact simulation of the flux linkage that would occur due to change in the phase resistance or measurement errors and noise. In addition, this test assumes the worst case condition when no flux linkage reset is made at the end of each electrical period.

The estimated rotor position is shown together with the actual angle Figure 7.37. It can be seen that the error in the flux linkage leads to some errors in the estimated angle. As mentioned in previous results, the actual angle estimation error in each iteration can vary, because the sensitivity of the algorithm to the error in the flux linkage varies according to the actual value of flux linkage, rotor position, and current (as will be detailed in the Section 7.7).

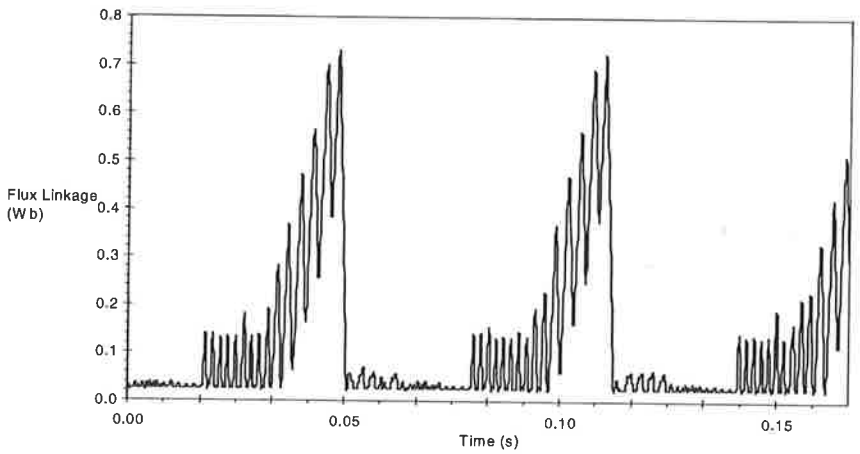


Figure 7.36 Flux Linkage of Phase A with Offset of 0.025 Wb.

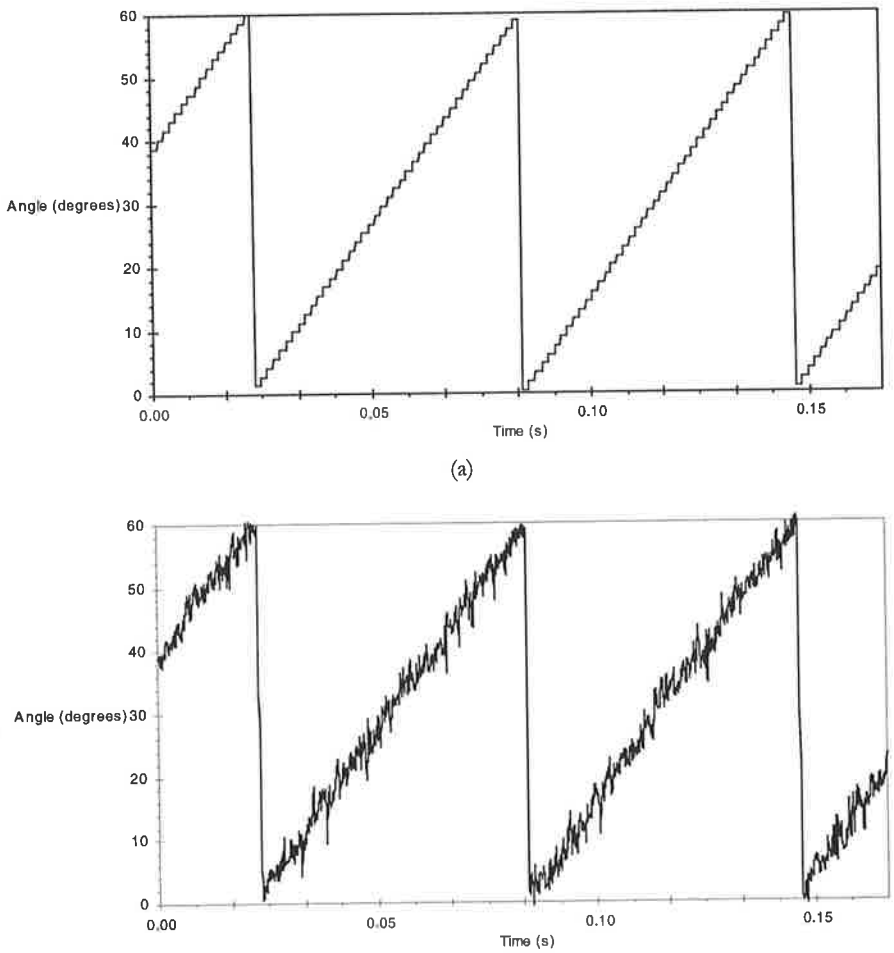


Figure 7.37 Flux Linkage Offset of 0.025 Wb: (a) Measured Angle. (b) Estimated Angle from Sensorless Scheme

Furthermore, it has been discussed that the flux linkage has inherent integration errors in the chopping mode due to the high time variation of the currents and voltages. Hence the actual angle estimation error will be highly variable, and depend on the complex interaction between the actual error of all the inputs to the algorithm, the flux linkage integration error, in addition to the sensitivity of the algorithm at different values of flux linkage and current.

It can be seen in Figure 7.38 that even thought there is a constant flux linkage error, the angle estimation error not exceedingly large. The average error in this test is 1.47 degrees, whilst the peak error is 6.0 degrees, or 10% of one electrical cycle. Although this error is relatively high, it highlights the ability of the scheme to operate with a lesser performance with corrupted flux linkage signals. The robustness of the scheme is maintained, as even in this case the control of the motor will not be lost.

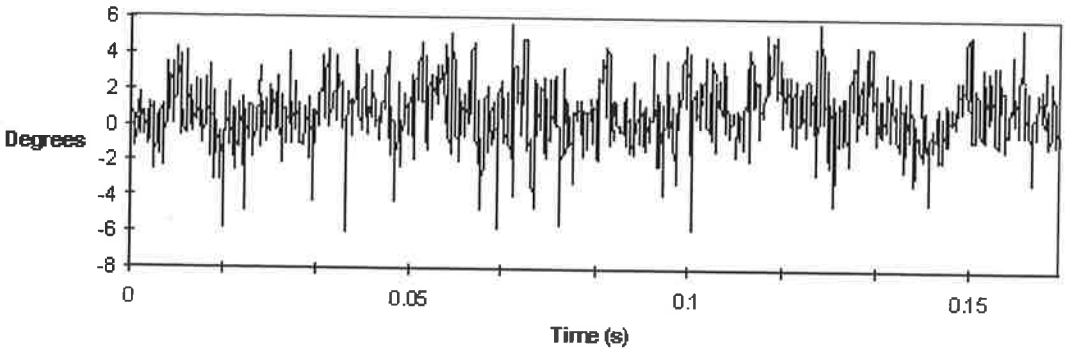


Figure 7.38 Error between Estimated and Measured Angle - Flux Linkage Offset of 0.025 Wb.

b) Flux Linkage Offset Test: Negative Offset

In Figure 7.39, the flux linkage is shown for the same motor speed as in the previous test. In this test however, a constant negative flux linkage offset is added to the estimated waveform. One reason for performing this test was to observe the algorithms performance when the estimated flux linkage is always lower than the true value. It will be detailed in Section 7.7 below, that the algorithms sensitivity to flux linkage error is highest when the flux linkage is low. Therefore, this test deliberately places the flux linkage constantly lower than the actual flux to test the robustness of the algorithm to more periods with lower flux linkages in all of the phases. In addition, the constant offset of the flux linkage is increased in amplitude such that it is -0.05 Wb, which represents a error which is 7.5% of the peak value. Therefore, the effect of increase error in the flux linkage will also be seen.

In Figure 7.40, the estimated angle is shown for this test, which can be compared with the measured encoder angle in Figure 7.37. As the actual angle was previously shown above, it is not plotted again here. The error in the rotor position estimates for this test is plotted in Figure 7.41.

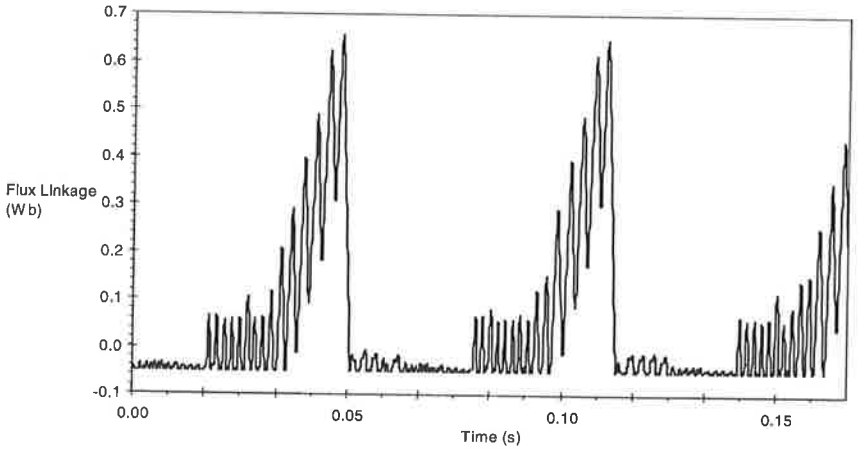


Figure 7.39 Flux Linkage with Offset of -0.05 Wb -162 rpm.

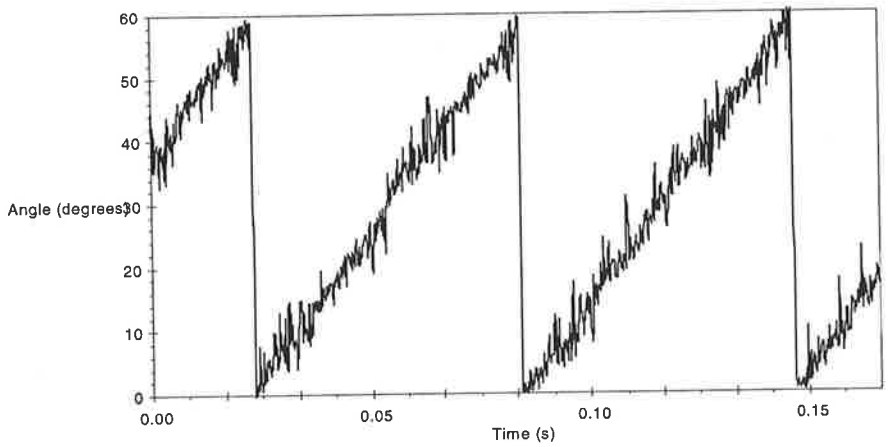


Figure 7.40 Estimated Angle from Sensorless Scheme - Flux Linkage Offset of -0.05 Wb -162 rpm

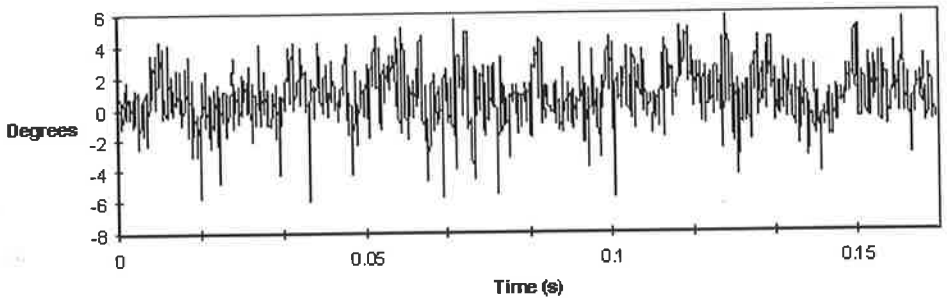


Figure 7.41 Error between Estimated and Measured Angle - Flux Linkage Offset of -0.05 Wb -162 rpm

A comparison with the previous test, which had a smaller and positive flux linkage offset shows that the error in the estimated angle has correspondingly increased with the increased flux linkage error. In fact the average error in this test is 1.83 degrees, whilst the peak error is 8.34 degrees or 13.9% of an electrical cycle. Therefore, the peak error in this test is relatively high, compared to the peak value of the input error. However, as explained previously, the estimated flux linkage also has error due to integration of the fast time-varying waveforms, before the additional offset error is included. Therefore, the actual flux linkage error is higher than simply the error of the offset value.

Hence, with these results also, the algorithm can be said to show robustness. This is because the error in the flux linkage due to offset, as well as the inherent integration error, decreased the performance of the scheme, but not by an undue amount.

7.6 Performance Test for Fuzzy Predictors

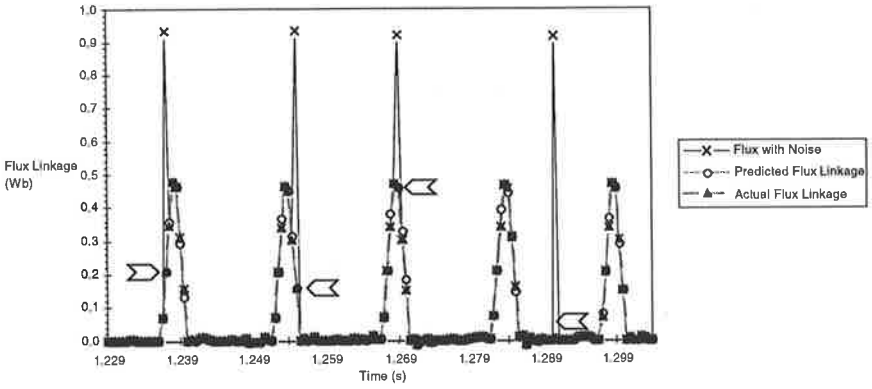
It was discussed previously that the predictors of flux linkage and position are used to lower the effect of high amplitude impulse type noise. This type of noise can often be found in the practical SR motor drive because of electromagnetic noise which is generated by the inverter. The generation of this noise is due to the switching or commutation of high amplitude currents in the inverter circuit. The commutated current waveforms have relatively short rise and fall times, and hence these waveforms contain significant amounts of energy at high frequencies (such as radio frequency or RF region). This radiated energy

can be transmitted through parasitic stray capacitances to the control, interface, and measurement circuitry and cause noise. Some parasitic capacitances will always exist between the high power inverter circuits, the high and low voltage side of the opto-isolation circuits, the low and high voltage side of the current and voltage measuring circuits, and the low voltage control and A/D converter circuits [177].

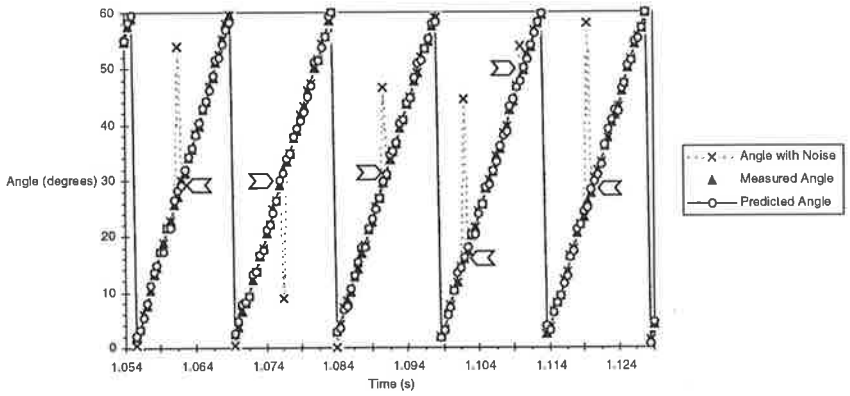
The characteristic feature of this generated electromagnetic noise is that it can have a high amplitude during the switching of a power device in the inverter circuit, which causes a rapid change in voltage or current. However this noise is only seen during the switching instant, which is normally less than 0.5 μs in IGBT inverter circuits [178]. Therefore, the coupled noise in the control and current and voltage measurement circuits may have a high amplitude, but be transient in nature. This type of high amplitude impulse type noise is defined as *non-Guassian* noise, and presents problems for practical systems because it is difficult to mathematically model and define. It was reported in [143] that currently there is active research in using fuzzy logic techniques to filter non-Guassian noise in practical systems.

Hence, in this work a method was developed to lower the effect of *non-Guassian* noise for the practical operation of the sensorless position estimation scheme. To do this, fuzzy logic based predictors of flux linkage and angle were implemented to predict the angle and flux linkage of future iterations, in order that high amplitude transient noise could be detected and discarded during operation of the angle estimation algorithm in practical SR drives. As detailed in Chapter 5, the fuzzy predictors can forecast with very good accuracy at steady motor speeds, and the forecasting algorithm is based on creating fuzzy logic based rules from the previous estimations of flux linkage and angle. However, as has been mentioned in the previous sections, the predictors main task is to reduce the effect of impulsive noise, and can not operate with constant levels of noise or error in the input measurements of current and voltage.

In Figure 7.42, a demonstration of the fuzzy predictor's ability is shown. These results show the estimated flux linkage and angle, for the case when the motor is rotating at a steady state speed of 670 rpm. The results show an expanded area of the waveforms, after the fuzzy predictors have learnt the waveforms. The learning period in this case was set to 1s (after the motor had settled to a steady state speed), which represents approximately 12 revolutions of the rotor at the above constant speed and the power. In order to observe the ability of the predictor at low sampling speeds, the iteration time of the algorithm was fixed at 500 μs.



(a)



(b)

Figure 7.42 Error Elimination Ability of Fuzzy Logic Based Predictors: (a) Flux Linkage. (b) Rotor Position. The points with arrows highlight the iterations where the predicted value can be used instead of the estimated angle to lessen the effect of switching noise.

In order to model the effect of switching noise, it can be seen in Figure 7.42 that a regular error of high amplitude (compared to the waveform's maximum amplitude) is placed at regular spacings, in both the estimated flux linkage waveform and the estimated rotor position waveform.

A large and short error pulse in the flux linkage waveform could occur from a large error in the current or voltage measurement due to switching noise. It would normally result in a large error in the estimated angle. This is because the high flux linkage error would normally cause a high error output from the fuzzy logic based motor model. In addition, the large error pulses in the estimated angle from the fuzzy model, could result from either a high error in the current measurement, or flux estimation error due to switching noise, or both of these effects.

In Figure 7.42 (a), the waveform of the actual flux linkage estimated from the measured current and voltages are shown, with a triangle representing each point where the flux is estimated from the current and voltage measurements. It can be seen that the estimates of the flux linkage are regular and periodic. In each triangular flux linkage pulse, there are 9 samples, and the results show that the amplitude of these samples is approximately equal every electrical cycle of 60 degrees. In the figure, a flux linkage waveform with error can also be seen. The added high error pulses model the effect of very high switching noise.

In this test, the estimated flux linkage waveform with error is input to the flux linkage predictor instead of the actual estimated flux. When this waveform is input to the flux predictor it can be seen that the points with high level noise have effectively been removed by the predicted value.

In Figure 7.42 (b), the waveforms are shown of the measured encoder angle, and the estimated angle with added error pulses (at different test times, but with the same conditions as the flux linkage test). In the results, the measured encoder positions are shown by a triangular point at each sample time. In this test, the estimated angle that has been corrupted with high amplitude noise pulses, is input to the angle predictor. It can be seen that the noise in the estimated angle is effectively removed in the predicted angle value. The predicted value can thus be used instead of the estimated value to reduce the effect of switching noise, as explained in chapter 6.

The very high error pulses shown in Figure 7.42 would normally lead to a controller error every time the error pulse occurred (due to a high rotor position error). This could cause the controller to change the switching patterns of the motor phases and thus change the switching state of the inverter power switches. Hence, this would lead to erroneous switching of the motor voltage that may cause greater harmonics in the motor waveforms, increased torque ripple, and audible noise [179], [180]. In addition there would be higher losses due to the motor phases being unnecessarily commutated, due to inverter losses and heating from the power devices being switched in error.

The results above have shown that when the fuzzy logic based predictors of flux linkage and angle are used, that the high error pulses from sources such as switching noise are effectively eliminated, which leads to a more robust and stable motor drive operation. When the high error spikes occur, they can be effectively discarded by using the predicted value from the fuzzy predictors, as was detailed in Chapter 6.

7.7 Error Analysis

There are various sources of error that are inherent in the sensorless position estimation in SR motors. Reference [181] and [182] provide error analysis for the test signal methods of sensorless position estimation and error analysis for sensorless SR motor drives in general respectively. In this section, sources of position estimation error of the method described in this research will be identified and their effect on the position estimation accuracy will be analysed.

Fundamentally, the sensorless rotor position estimation algorithm operates by processing the input signals, which are the motor flux linkage and the current, and producing the output estimated rotor position. Therefore, in general, the accuracy of the scheme depends on the accuracy of the input values of flux linkage and current. The current is directly measured, whilst the flux linkage in this scheme is estimated by integration from the

measured voltage and current, and the motor phase resistance value. Both the current and flux linkage measurement are affected by measurement errors, whilst the flux linkage is also affected by integration errors and variation of the phase winding resistance, which is primarily due to variation of the resistance with temperature [183].

The various sources of position estimation errors are identified and classified under two groups: Measurement Errors and Parameter Variation. These sources include the following:

I. Measurement Errors.

a) Integration offset error.

b) Amplitude quantisation errors due to digital implementation.

c) Time quantisation due to digital implementation.

d) Measurement noise, which may include;

   i) Switching noise, due to coupling of measuring circuit with the switching power semiconductor circuit.

   ii) Radiated electromagnetic interference from motor and power circuit on the measuring circuits.

   iii) Noise in measuring circuits (including analog to digital (A/D) converter circuits) due to non ideal circuit layout and grounding.

   iv) Errors due to non ideal measuring devices and components which may introduce an offset or amplitude error.

   v) Noise in analog to digital converter circuits due to noise generated from any connected computer bus lines.

II. Parameter Variation

a) Variation of motor phase winding resistance value, which is primarily due to temperature variation.

7.7.1 Analytical Analysis of Position Estimation Errors

As it was mentioned above, the only inputs to the sensorless position estimation algorithm are the flux linkage (estimated from the measured voltage and current) and measured current of the motor phases. The position estimation errors due to errors in these inputs will now be analysed.

From previous sections, it is known that the flux linkage ψ of each motor phase can be estimated by integrating the flux linkage producing voltage v-iR. Then this flux linkage value is used together with the current i, measured at the same instant of time, to form an input data pair for the sensorless position estimation algorithm.

In the fuzzy logic based position estimation scheme algorithm, the integration of the flux linkage equation was performed by using digital real time integration as was shown in equation (5.1), which is rewritten here for convenience:

$$\begin{aligned} &\psi(n) = \psi(n) + \Delta T[v(n) - Ri(n) + v(n-1) - Ri(n-1)]/2, \\ &\psi(0) = 0 \end{aligned} \tag{7.1}$$

Analog integrators can also be used to estimate the flux linkages of the motor but these often have the problem of drift in the output signal, and the need for compensation [184], particularly for long integration periods, which as will be discussed below, corresponds to the low speed operation in the SR motor.

As can be seen in the above equation, the flux linkage is set to zero at the beginning of each integration period of the flux linkage wave form. This normally will correspond to the beginning of the flux linkage pulse in each electrical cycle. Therefore, as was explained above, the problem of integration offset in the flux linkage is not great in the SR motor, because of the ability to reset the flux linkage to zero in each electrical cycle.

The sampling period ΔT in the above equation is determined by the actual implementation of the measurement hardware. The smallest practical limit is the conversion time of the analog to digital converters which sample the voltages and currents. Hence, the practical value of ΔT is finite and this means that there is a quantisation of time. Due to this time quantisation, there will be some finite error, as the digital integration (equation (5.1)) only equals the actual flux linkage (given by equation (2.2)) exactly when ΔT tends to zero.

Normally the sampling time ΔT used in a practical system is low enough that the digital integration of the flux linkage can be assumed to be accurate, although it can be said that a faster sampling speed will always lead to less errors from time quantisation. From the results shown previously, it was found that the fuzzy logic based angle estimation scheme had the ability to cope well with high values of ΔT, and as was stated in Section 7.4, a sampling period of 0.33 ms (ie. 3 kHz) was adequate for position estimation. This sampling period is large compared to the capability of most analog to digital converter currently available. In most practical applications the sampling period, and thus the time quantisation error, will be significantly less. Thus, the error of flux linkage due to time quantisation should present no problem in practical operation for the fuzzy logic based angle estimation scheme.

Even if the digital integration can be assumed to be exact due to a small sampling period (and thus a low time quantisation error), errors exist in the flux linkage if there are errors in the measured values of voltage and current. If it is assumed that the measured quantities have some finite errors, then the values can be defined as:

$$\begin{aligned} \tilde{v} &= v + \Delta v \\ \tilde{i} &= i + \Delta i \\ \tilde{\psi} &= \psi + \Delta \psi \end{aligned} \tag{7.2}$$

Where:

$\tilde{v}, \tilde{i}, \tilde{\psi}$ = values of voltage, current, and flux used by the algorithm

v, i, ψ = actual values of voltage, current, and flux in the motor

$\Delta v, \Delta i, \Delta \psi$ = errors in the values of voltage, current, and flux

Now, for one sampling instant, the corresponding error in the flux linkage is given by:

$$\Delta\psi\,(n+1) = \Delta T(\Delta v(n) - R\Delta i(n) + \Delta v(n-1) - R\Delta i(n-1))/2 \tag{7.3}$$

Therefore, for k samples times after the initial sample, the corresponding accumulated error in the flux linkage estimate will be [182]

$$\Delta\psi(k) = \sum_{n=0}^{k-1} \Delta T(\Delta v(n) - R\Delta i(n) + \Delta v(n-1) - R\Delta i(n-1))/2 \tag{7.4}$$

Note that the value of the flux error in the initial sample $\Delta\psi(0)$ will be zero due to the flux initialisation.

As mentioned above, one source of measurement error is amplitude quantisation due to digital implementation. If n bit A/D converters are used, then the maximum amplitude quantisation error of the current and voltage at a given sample n; is equal to:

$$\begin{aligned} \Delta v(n) &= \frac{2V_{\max}}{2^n - 1} \\ \Delta i(n) &= \frac{2I_{\max}}{2^n - 1} \end{aligned} \tag{7.5}$$

Where V_{max} and I_{max} are equal to the maximum voltage and current respectively which are measured by the A/D converters.

In the worst case the quantisation error will always be constant at the maximum value. Therefore, in this case, the error in the flux linkage at the *kth* sample instant will be given by:

$$\begin{aligned}\Delta\psi(k) &= \sum_{n=0}^{k-1} \Delta T\left(\frac{2V_{\max}}{2^n-1} - R\frac{2I_{\max}}{2^n-1} + \frac{2V_{\max}}{2^n-1} - R\frac{2I_{\max}}{2^n-1}\right)/2 \\ &= k\Delta T\left(\frac{2V_{\max}}{2^n-1} - R\frac{2I_{\max}}{2^n-1}\right)\end{aligned} \tag{7.6}$$

and the worst case flux error at sample k will be bounded by

$$-k\Delta T\left(R\frac{2I_{\max}}{2^n-1}\right) \le \Delta\psi(k) \le k\Delta T\left(\frac{2V_{\max}}{2^n-1}\right) \tag{7.7}$$

From the above equation, it can be seen that the error in the flux linkage increases directly proportionally to the value of k. Therefore, the error increases in direct proportion to the integration period. This is because k reaches higher values for longer integration intervals.

It can be seen that the ability of resetting of the flux linkage to zero in the SR motor (ie. k becomes zero) after each flux linkage pulse, minimises the effect of increasing error due to the growing sample number k in Equation (7.7). At low speeds, the flux pulses, and thus the integration interval, will be longer in time than at high speeds. Therefore, this quantisation error becomes lower as the motor speed increases.

As described above, another source of measurement error may be due to measurement noise. This type of noise can be categorised into Guassian and non-Guassian type noise. As it has been discussed earlier in the chapter, non-Guassian type noise consists of impulsive high amplitude type noise, and is difficult to mathematically model. Recent research on this type of noise can be found in reference [143], and it currently constitutes an active area of research. However, for simplicity, it will be assumed that the measurement noise can be approximated by a normal distribution and is thus Guassian type noise in this discussion. Hence, one can define the mean of the current and voltage errors as μ_i and μ_v and the variance of the error as σ_i^2 and σ_v^2 respectively. This means that the mean of the flux linkage error due to measurement noise will be:

$$\mu_{\psi(k)} = k\Delta T(\mu_v - R\mu_i) \tag{7.8}$$

whilst the variance of the flux linkage error will be:

$$\sigma^2_{\psi(k)} = k^2\Delta T^2(\sigma_v^2 + R^2\sigma_i^2) \tag{7.9}$$

It can be seen from equation (7.8) that the mean error is proportional to k. Hence, once again, it can be seen for the case of measurement noise, that the probability of high noise

in the flux linkage estimation increases in proportion with the integration interval k. As mentioned above, the integration is reset after each flux pulse, which limits the value of the number of samples k to within the flux integration period. Additionally, as the motor speed increases and the flux interval becomes shorter, the effect of measurement noise on the flux linkage correspondingly decreases. Nevertheless, the integration period in each electrical cycle will be highest at low speeds, and thus the measurement noise will be more problematic at low speeds. However, if the measurement noise has a high mean value, then the flux linkage noise will also have a high mean value, even for small integration periods.

Another possible source of error in the estimation of the phase flux linkage is the variation of the phase winding resistance used in the integration equation. During operation of the machine the value of the resistance changes due to the change in temperature of the machine. If we assume that the resistance changes by a value ΔR then the flux linkage integration equation will become

$$\begin{aligned}&\psi(n) = \psi(n-1) + \Delta T[v(n) - (R+\Delta R)i(n) + v(n-1) - (R+\Delta R)i(n-1)]/2 \\ &\psi(0) = 0\end{aligned} \tag{7.10}$$

However, the estimation algorithm uses the value R for the resistance, and so there will be an error in the flux estimate in each integration step of

$$\Delta\psi(n+1) = \Delta T(\Delta R(i(n) + i(n-1)))/2 \tag{7.11}$$

Therefore, the error in the flux estimate in the k*th* sampling instant will be given by

$$\begin{aligned}\Delta\psi(k) &= \sum_{n=0}^{k-1} \Delta T(\Delta R(i(n) + i(n-1)))/2 \\ &= k.\Delta T(\Delta R(i(n) + i(n-1)))/2\end{aligned} \tag{7.12}$$

Again, it can be seen that the error increases in proportion to the value of k, or the integration interval, and any resistance change will cause an error in the flux linkage waveform. However, due to the fact that the integration interval, and thus k is reset at the end of each flux integration in the SR motor, it places a limit on the maximum value of this error to that which occurs during one flux pulse integration interval.

7.7.2 Effect of Flux Estimation Error

If there are flux linkage estimation errors due to one or more of the above explained effects, there will be a corresponding error in the rotor position estimation. It should be noted that even if the flux linkage is not obtained by the integration of the motor waveforms, but is directly measured using a flux sensing coil, there may still be measurement errors which lead to position estimation errors. It is therefore of interest to analyse the effect of flux linkage estimation errors on the estimate of rotor position.

In this analysis, the methods used by the fuzzy logic based sensorless angle estimation algorithm to minimise errors in the flux linkage (such as the fuzzy learner/predictor of flux linkage) are taken to have no added beneficial effect, in order to consider the worst case. Thus, the actual effect of flux linkage error on the rotor position estimate may in general be less in the fuzzy logic based angle estimation scheme.

Consider firstly the SR motor magnetisation characteristics shown again in Figure 7.43, which are assumed for this analysis to represent the true motor characteristics (ie. secondary effects such as mutual inductances are ignored).

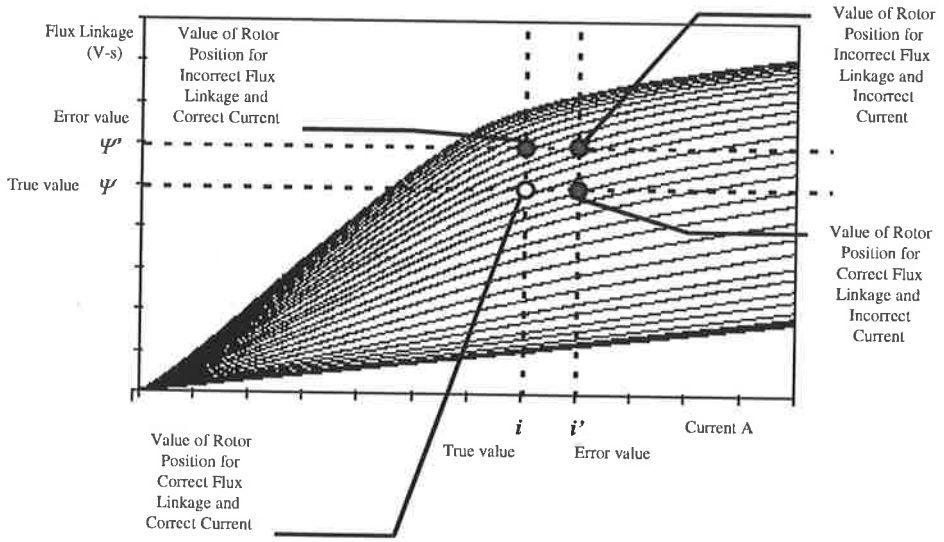


Figure 7.43. Examination of Error of Flux Linkage and Angle in Flux Linkage Characteristics.

Figure 7.43 shows the effect of errors in both the flux linkage and current measurement. The measurement of flux and current provides a point on the magnetisation curves that corresponds to a certain rotor position. The true values will correspond to the correct point of rotor position, whereas the erroneous values will lead to different points on the curves and thus an erroneous rotor position. This figure also exemplifies the difficulty of using simple numerical table look-up techniques (described previously in Section 3.3.2.3) to derive the angle. The table look-up method depends on high accuracy of measured inputs, as otherwise the wrong point in the flux linkage versus current plane will be given. In the fuzzy logic based estimation scheme however, the input region in essence is divided into fuzzy domains. Therefore, the input points do not need to be *exact*. An erroneous input point may still be in the same membership *set* that the true value is in.

In order to allow the error analysis in this section to be applied to sensorless position estimation techniques in general, and to consider a worst case error, a simple examination of the error can be considered, which does not take into account the fuzzification of the inputs.

Firstly, to examine the error, a quantity $D_{\theta\psi}$ or *density of angle variation with flux* is defined for a given motor current I such that:

$$D_{\theta\psi}(I) = \frac{\theta_N(I)}{\psi^1(\theta, I) - \psi^2(\theta, I)} \tag{7.13}$$

Where :
θ_N (I) = the number of $\psi(\theta, i)$ curves seperated by one rotor angle degree
in the flux region $\psi^1(\theta, I) \rightarrow \psi^2(\theta, I)$ at constant current $i = I$.

In this case let us assume that the current measurement is exact, so the effect of flux linkage error can be determined separately (the effect of current error will be discussed below).

Now let the actual motor flux linkage be ψ, and the estimated flux linkage be ψ^e. The error in the flux linkage will then be $\Delta\psi=\psi-\psi^e$. In addition, it is assumed that the actual flux ψ produces the actual rotor angle θ, whereas the estimated flux ψ^e produces the erroneous angle θ^e. Hence, the error in the estimated position is $\Delta\theta=\theta-\theta^e$.

In general, the angle error for a given flux error will be given by:

$$\Delta\theta = \Delta\psi . D_{\theta\psi}(I) \tag{7.14}$$

From the above equation it can be seen that, for a given flux linkage estimation error, the corresponding angle error will be highest when the current is low, or the actual rotor position is close to the aligned or unaligned position. This is because the density of angle variation with flux $D_{\theta\psi}$ is highest in these regions.

One can recall that this was precisely the result that was determined by human intuition and used in linguistic form by the fuzzy logic based optimum phase selector of the algorithm that was described in Section 5.3.3 .

7.7.3 Effect of Current Measurement Error

As it was mentioned above, the two inputs to the sensorless position estimator are the currents and flux linkages. In this section, the error in the angle estimation due to error on the current measurement will be examined. The sources of error on the current measurement were explained above, and so are not repeated at this point.

To examine the effect of current measurement error, consider once again the motor characteristic curves of current versus flux linkage and angle shown in Figure 7.43.

Similarly to the above case, for a given flux linkage Ψ a quantity $D_{\theta i}$ or *density of angle variation with current* is defined such that:

$$D_{\theta i}(\Psi) = \frac{\theta_N(\Psi)}{I^1(\theta,\Psi) - I^2(\theta,\Psi)} \tag{7.15}$$

Where :

$\theta_N(\Psi)$ = the number of $i(\theta,\psi)$ curves seperated by one rotor angle degree in the current region $I^1(\theta,\Psi) \rightarrow I^2(\theta,\Psi)$ at constant flux $\psi = \Psi$.

The flux linkage measurement is assumed to be exactly accurate, (although, in fact, it will have some error due to the error in the current measurement), so that the effect of current error can be found separately. Hence, for a given error in the current measurement Δi, the angle error will be given by

$$\Delta\theta = \Delta i . D_{\theta i}(\Psi) \tag{7.16}$$

Therefore, the angle error that results from a given error in the current measurement will be the largest at points where the density of angle variation with current is the highest. This corresponds to the regions when the motor current level is low. Higher level of currents are desirable to increase the position estimation accuracy. Once again this confirms the fuzzy rules used by the fuzzy logic based phase selector described in Section 5.3.3.

7.7.4 Error Minimisation by use of Fuzzy Logic

In actual operation, several of the above sources of error will act simultaneously in an unpredictable and ill defined manner, and will have the effect of corrupting the flux linkage and current measurements. However, as has been described in previous chapters, and detailed in the experimental results shown previously, the fuzzy logic based sensorless algorithm is quite robust to input signal corruption. As has been previously discussed, this is mainly due to the fuzzy logic based structure of the scheme.

Due to the fact that all of the inputs are fuzzified and placed into fuzzy sets which encompass a *range* of values, a small variation in the input signal due to measurement errors will often place the corrupted input signal in the same fuzzy set as the uncorrupted signal. In addition, several other fuzzy systems are incorporated in the scheme to minimise the impact of measurement errors. This includes the fuzzy predictors, which act as non linear filters of noise, and the fuzzy phase selector decision block, which uses expert knowledge to choose the conducting phase which is most robust to measurement errors.

In order to optimise the operation of the fuzzy logic based angle estimation algorithm, there are several motor design alternatives that can be applied. Although the algorithm is

designed to operate with any SR motor type, the physical characteristics of the motor can be improved to allow a high compatibility with the position estimation.

7.8 Conclusion

In most applications where motor drives are used, the reliability of the drive is of utmost concern. This is particularly the case for some applications of the SR motor drive, such as in aerospace type applications [185], [186], [187], where the reliability and robustness are the main reasons for the choice of the motor drive type. The SR motor is in these cases chosen for its high reliability, and in particular its ability to operate when one or more phases fail. However, the mechanical sensor reduces the reliability of the motor. Nevertheless, if the sensorless angle position detection algorithm does not have a very high robustness and reliability, it will not be advantageous over the position sensor, and will in fact degrade the system reliability.

It was shown using vigorous experimentally based results, that the fuzzy logic based sensorless position estimation scheme has a high level of robustness and reliability, and is thus well suited to a wide range of systems. The sensorless scheme was found to cope with the erroneous operating conditions that are found in motor drive environments. It was demonstrated to be robust to high levels of random noise, low sampling rates of the analog to digital converters, flux linkage measurement errors caused by errors and parameter variation, and high amplitude error spikes due to switching noise. It was also found that the sensorless position detection scheme is suitable to control the motor at almost all *practical* analog to digital converter hardware speeds. In addition, prediction of the motor flux linkage and rotor position allowed the effect of short pulses of error from switching noise to be lessened.

The ability to cope with high levels of noise derives from the system's ability of fuzzifying the input signals and then processing with fuzzy linguistic rules. With this system, an input with noise will normally be able to be partially a member of the same membership function that the error free signal would be. This is in fact a unique ability of fuzzy logic, as opposed to crisp logic. Therefore, the same rules can be triggered by noisy and noise free signals, depending on the level of the noise.

A theoretical analysis of the various sources of error that are inherent to sensorless position estimation algorithm was provided. The various sources of error where detailed, and an analytical derivation of the effects of these errors on the position estimates was identified. It was also seen that the ability to reset the integration of the flux linkage estimation in each electrical cycle was beneficial in reducing angle estimation errors. In addition, the analysis of the effect of flux linkage and current errors on the position estimation confirmed the expert knowledge implemented in the fuzzy logic based optimal phase choosers. The error analysis described, can generally be used for all electric motors where the stator flux linkage and current is used in position estimation.

In this chapter, a detailed experimental evaluation of the fuzzy logic based sensorless algorithm was carried out, with the primary aim of demonstrating the high robustness of the scheme. It was found that in the practical SR motor drive system the scheme could be used with a high level of input signal corruption. As previously mentioned in this thesis, this is achieved without requiring any mathematical model of the motor which is being controlled, which would be impractical due to having high complexity and being computationally expensive. In addition, the sensorless method does not require a numerical look-up table, which requires high memory and needs accurate inputs. Therefore, using the benefits of fuzzy reasoning the scheme can successfully estimate the rotor position under high error and noise conditions in practical SR drives.

Chapter 8: Conclusions and Suggestions for Further Research

The switched reluctance motor is a doubly salient reluctance machine which has a number of operational advantages. These include a wide speed range, simple construction, high efficiency, and a high robustness and reliability.

However, the SR motor drive requires rotor position feedback in order to synchronise the switching of the SR motor's current to the rotor position. The position measurement needs to be accurate, as the efficiency and torque output of the motor are decreased by errors in the motor current switching angles.

Conventional SR drives use sensors that are mechanically mounted on the motor shaft to measure the rotor angle. The use of these sensors can lead to disadvantages due to a lower-system reliability, higher system expense, greater maintenance and installation costs, a greater number of connections between the control circuits and the motor, and the requirement for sensor mounting space.

In order to eliminate the requirement for a position sensor, a number of sensorless rotor position estimation methods have previously been proposed. These schemes operate by estimating the rotor position using measurements of electrical waveforms in the motor. The previous methods can be classified into two main groups: the test waveform methods and the passive waveforms monitoring methods.

The test waveform methods use low amplitude test signals of some form, in unexcited phases. A difficulty with these methods is that they suffer from interference caused by magnetic coupling with excited phases. Moreover, the methods cannot be used at higher motor speeds when there is little or no time when the phases are unexcited.

Passive waveform monitoring schemes are those which monitor the actual motor excitation waveforms, without injecting any extra signals into the motor. This group includes methods that monitor the motor current, voltage, or mutually induced voltages. The mathematical model, and table look-up based schemes are also classified in this group of sensorless schemes.

Difficulties are found in the various passive waveform methods, such as limitations in operating speeds and conditions, and the assumption of a simplified linear model, which can lead to high errors due to the magnetic saturation normally found in practical SR drives. In addition, the complex mathematical computations required in mathematical model based schemes are detrimental because they increase the delay time between the motor waveform measurement and the corresponding angle estimation. A fast real time microprocessor would also be required, which may not be available or economical for all SR drives. Numerical look-up tables are also undesirable because they require a large memory and accurately measured inputs.

Moreover, the issue of the robustness and reliability of the SR motor drive operation with a sensorless position estimation scheme has not been specifically addressed in previous research. In practical drives, the sensorless algorithm must be robust against non-ideal effects such as measurement errors, low bandwidth measurements, offset errors, noise, and change in the motor parameters.

To address the difficulties seen in previous sensorless schemes, a new rotor position estimator was developed. The sensorless estimation method developed in this research offers the following features:

- It can be used under all motor operating speeds and conditions.
- It can operate under speed and torque transients, standstill, and start-up.
- No external testing circuitry or test signals are placed on the motor phase windings.
- It does not require complex calculations to be carried out during the real time operation.
- No complex mathematical model of the SR motor is required.
- The non-linear characteristics of the machine are not ignored and no simplifying assumptions about the motor saturation or behaviour are made.
- No numerical look-up table is required, and thus the memory requirement is not large.

Motor drives are usually electrically noisy environments with noise often being induced on any measurement circuitry. Moreover, in most motor drive applications, the reliability of the drive system is of utmost concern. If the sensorless position detection algorithm is not robust against noise and error, then it will not be advantageous over shaft-based position sensors. Therefore, in this research a major consideration was the robustness and reliability of the new sensorless position estimation scheme. It has been demonstrated that modelling and estimation using fuzzy set theory is tolerant to noise and errors, and thus fuzzy logic was applied in a novel manner in order to allow more reliable operation of the scheme in practical SR drives.

This sensorless method is also the first application in which heuristic knowledge based techniques are utilised in the application of sensorless SR motor position estimation. Human intuition, encapsulated as linguistic rules, was used in the algorithm to provide extra reliability against noise and error on the position estimation. A linguistic fuzzy logic rule base was implemented to determine if a measured signal is corrupted by noise or error. A confidence weighting is placed on the measured value based on the linguistic rules, in order that a combination of the measured and a predicted value can be used. Another knowledge based system was developed to give the optimal motor phase for position sensing the most weighting.

In this thesis the new fuzzy logic based sensorless position estimation method for SR drives, which addresses the problems and limitations of previous sensorless schemes, was detailed. Simulation and experimental results were also shown in order to demonstrate the successful operation of the scheme.

In Chapter 2, the background theory of the SR motor was given in order to provide a theoretical basis for the work presented in the thesis. The electromagnetic operating principles of the motor using both a linear and non-linear model were shown, and the control parameters were detailed. It was demonstrated that the excitation of the SR motor needs to be synchronised with the position of the rotor, and thus some form of position sensing is required.

In Chapter 3, previously developed sensorless position estimation methods were shown. Both the test waveform and the passive waveform monitoring groups were detailed, and as discussed above, the methods have some problems in estimating rotor position under all motor speeds and conditions.

A novel fuzzy logic based angle estimation scheme was introduced in Chapter 4, which addressed the problems found in previous sensorless schemes. The training phase of the algorithm was detailed in this chapter. It was shown that both static and dynamic motor measurement data was used in the training method to develop a fuzzy rule based SR motor model.

The operation method of the new sensorless scheme after the training phase, was detailed in Chapter 5. The rotor position was estimated using measurements of the voltage and current waveforms, together with the fuzzy rule based motor model. In addition, the fuzzy logic based predictors of flux linkage and position, as well as the knowledge based optimal motor phase selector were detailed in this chapter. These were used to provide a higher operational reliability and robustness to the new scheme. Simulation results were also given in this chapter, to demonstrate the ability of the new scheme under a wide range of transient conditions such as: motor starting from standstill, zero speed, low and high motor speeds, low and high acceleration, stalling of the motor from high speeds, chopping and single pulse modes, and high and low phase currents.

In Chapter 6, a wide range of experimental results were given to demonstrate the sensorless algorithm's ability in practical SR drives where non-ideal effects are often found. The sensorless algorithm's operation was shown for a wide range of experimental operating conditions such as: chopping mode, single pulse mode, steady and transient speeds, steady and transient mechanical loads, and motor start up.

In Chapter 7 experimental results were shown which demonstrate that the fuzzy logic based sensorless position estimation scheme has a high level of robustness and reliability. The results show that the sensorless scheme can cope with the erroneous operating

conditions that are found in practical SR motor drive environments. The sensorless algorithm was tested with high levels of random noise, low sampling rates, flux linkage errors, and high amplitude error pulses. It was found that the sensorless algorithm could cope with a high level of input signal corruption and thus is well suited to practical motor drives.

Improvements to the developed sensorless method could be the subject of further research. It is suggested that to reduce the rotor position estimation error, a cooperative design in both the hardware and software of the SR motor drive should be made. The error analysis detailed in Chapter 7 leads to considerations that should be taken into account in the motor mechanical design, in order that the sensorless algorithm is most effective. This form of cooperative design falls into the category of mechatronic engineering. Mechatronics emphasises the synergistic integration of mechanical, electronic, and software design. Although it falls outside the scope of this thesis, mechatronic systems are detailed in reference [188].

It was found that in Chapter 7 that the sensorless algorithm is most sensitive to input signal errors when the density of the flux linkage curves is high. Therefore the design of the SR motor should be such that these regions of the magnetisation characteristics are minimised. This is equivalent to making the ratio of the maximum to minimum inductances $\alpha=L_{max}/L_{min}$ as high as possible for a given motor frame and size. If this ratio is high, then there is a greater area between the fully aligned and unaligned curves of the magnetisation characteristics, which reduces the density of curves. However, there is a trade off effect, due to the fact that the back emf also increases when the inductance ratio α is increased. This then decreases the speed at which back emf equals the supply voltage, and thus decreases the maximum power output for a given dc voltage supply.

Further work can also be carried out to implement the algorithm on a high speed microprocessor which would provide real time rotor position estimation of the rotor position, in addition to real time closed loop current control based on the rotor position estimates. The stability of the motor drive system with such a controller should also be examined.

In addition, further research could be carried out to investigate the improvements that could be made to the developed sensorless algorithm using recent developments in fuzzy logic theory. For example, the number of fuzzy sets in the input-output fuzzy domains of flux linkage, current, and rotor position may be optimised using neuro-fuzzy techniques, and the shape of the fuzzy sets themselves can also be optimised [189]. In addition a faster real-time implementation of the sensorless algorithm could be achieved by using hardware based digital fuzzy processors [190]. Furthermore, fundamental research which categorically proves the higher computational efficiency of fuzzy logic based computation methods in real time applications, such as the fuzzy logic position estimator, needs to be further explored.

Appendix A: Measurement of Static SR Motor Magnetisation Characteristics

A.1 Introduction

The static magnetisation characteristics of the SR motor describe the flux linkage as a function of current and fixed rotor position. The measurement of these SR motor magnetisation curves was important for the research work developed in this thesis. Firstly, this was because the flux linkage versus current and angle characteristics were required in the developed SR motor simulation algorithm, which is detailed in Appendix B. These simulation waveforms were subsequently used to provide initial verification of the sensorless angle estimation algorithm. It was seen in Chapter 5 that simulation waveforms were used to test the sensorless algorithm with motor waveforms under motor operating conditions that were difficult to obtain in the experimental tests.

The flux linkage curves were also of importance for the development of the fuzzy rule based SR motor model. As was detailed in Chapter 4, one of the training phases of the fuzzy model used the experimentally obtained flux linkage curves. This fuzzy rule based model subsequently forms an important element of the sensorless position estimation scheme.

It is also possible to calculate the magnetisation curves without experimental measurement of the motor waveforms by using finite element methods [191], [192]. However, these methods are more suited to the design stage. This is because the accuracy of such methods varies according to the choice of the elements used, and in addition, they are computationally complex. Secondary effects such as manufacturing irregularities, three-dimensional fields and non-uniform iron structure are difficult to model. Furthermore, in all cases experimental evaluation is eventually necessary.

Therefore, the acquisition of the magnetisation curves of an SR motor can be achieved more effectively by experimental means. For this reason, an automated scheme of measuring the magnetisation curves was developed. This method used data acquisition software with a data acquisition card and interface hardware. The developed system allowed a fully automated test set-up and rapid development time, and it provided a user friendly interface with all the tools necessary for acquiring, analysing and presenting the measured data. In the sections below, the SR motor magnetisation characteristic measurement method that was developed for the thesis will be explained. The resultant magnetisation characteristics measured were used in both the simulation of the test motor and the learning phase of the fuzzy logic based motor model.

A.2 Methods of Magnetic Characteristic Determination

Although there is a need for the measurement of flux linkage versus current and position in switched reluctance and other motors, there is currently no readily available equipment on the market for this purpose. This has led to various methods being proposed:

a) Measuring Flux Directly

One method of determining magnetic flux is to employ magnetic sensors that measure the flux inside the motor directly [193], [194]. This method is not usually applied, as it is very expensive. It requires sensors to be installed when the motor is assembled, thus complicating the motor design. In addition, the flux sensor may not be able to measure a wide range of the flux variation accurately.

b) Measuring Inductance Directly

Another method for obtaining the motor characteristics is to measure the inductance of the motor directly, for various values of currents. Motor inductance can be determined by ac bridge methods [195]. However, these are limited effectively to low power rated machines since they require additional equipment to superimpose an ac signal on a large dc current that is injected into the motor phase. In addition, the incremental inductance is normally measured at with a sinusoidal signal with about 1kHz frequency. This means the measurement will not be valid for all operating conditions because the motor current normally contains many high and low frequency harmonic components. Another disadvantage of this scheme is that at each angle a number of measurements must be made, which makes the procedure very time consuming.

c) Measuring Flux Linkage Indirectly

The most preferred method of obtaining the motor's magnetisation characteristics is to indirectly measure the stator flux linkage from voltage and current measurements on the phase winding circuit. In these methods, a voltage source is applied to the phase winding, and the terminal voltage and current is measured. If the phase resistance is known, then the flux linkage can be found from integration.

In most integration techniques the general principle is to apply a voltage pulse to the motor winding with the rotor clamped to some fixed position. The current will rise up to some level, and then the voltage is turned off. Throughout this time, integration takes place to determine the instantaneous flux linkage, and in practice, analog and digital integration can be employed.

The integration is based on the electromagnetic circuit equation. The flux linkage is related to the electrical variables by the motor voltage equation defined before as:

$$v(t) = Ri(t) + \frac{d\psi(t)}{dt} \tag{A.1}$$

Where:
$v(t)$ = instantaneous phase voltage
$i(t)$ = instantaneous phase current
$\psi(t)$ = instantaneous flux linkage

Therefore, at any time the flux linkage can be determined as:

$$\psi(t) - \psi(0) = \int_0^t (v(t) - i(t)R)dt \tag{A.2}$$

Where: $\psi(0)$ = flux linkage at time t = 0

Therefore, if a voltage is applied to a motor phase winding and the instantaneous current and voltage is measured, then the flux linkage at any instant can be found. The phase resistance must however be known to a good degree of accuracy.

The integration method is the preferred scheme for measuring the magnetisation curves, as it does not suffer from the disadvantages mentioned above for the other schemes. However, for the integration method accurate integration techniques must be used. As will be discussed below, both analog and digital integration techniques can be implemented.

i) Analog Integration

Analog integration techniques use operational amplifier circuits to integrate the signal. However, the accuracy of the result can be affected by drift in the amplifiers [196], and the need for accurate components. There is also the problem of temperature sensitivity of analog circuits and component imperfections.

An analog integration scheme has been developed in [197] in which a large current pulse is injected into a motor phase with a discharging capacitor and the corresponding flux linkage is measured with a hardware integrator. However in this method, there is the need for a power resistor that exactly matches the motor phase resistance. This would be difficult to obtain to a good accuracy, and a different resistor would be needed for different motors. A small error in the resistance value could produce a significant difference between the actual and measured flux linkage. In addition, the temperature drift of the resistor would rarely match that of the phase winding resistance. This particular test method is also time consuming because a separate test must be done for each point of current and position.

b) Digital Integration Methods

Digital integration involves converting the current and voltage measurements to digital data using analog to digital (A/D) converters. The digital data is then used in the integration.

An advantage of evaluating the flux linkage by digital techniques is that the problem of drift and component imperfections in analog integration can be eliminated. In addition, the digital flux measurements can readily be used in computer based analysis and data graphing programs.

A novel digital integration scheme has been described in [198] that uses two different methods of determining the flux at a given current and angle. In the first method the rotor is kept in a fixed position whilst the winding is excited with a sinusoidal voltage. This will produce a current and flux waveform in the motor that is essentially sinusoidal. Thus, a plot of flux versus current can be produced. The second method uses a dc current, whilst the rotor is rotated at a constant speed. If the current and speed are constant, then the flux linkage versus position at that constant current may be found. This is because for constant current and speed the flux linkage will be a function of time only (which for constant speed will make it a function of angle). Instead of changing position, the current level is changed for each test. A problem with this scheme is the great difficulty in maintaining a constant current and speed during the test.

Some recently introduced digital methods have used a personal computer [199] or digital oscilloscope [200] to acquire the voltage and current waveforms, and then integrate and plot the flux linkage. In these methods a voltage pulse is applied to the phase so that the current rises to at least rated value, upon which it is turned off. The methods offer a great advantage, as the entire operation of data acquisition, integration and presentation of flux linkage can be done in one single step. Only the angle needs to be changed and fixed before running each test. However, there is still a disadvantage with these methods because the phase voltage is manually turned on with a switch.

A.3 Magnetisation Characteristics Measurement using LabVIEW

In this thesis, an improvement on the above digital methods was therefore made by constructing a PC based digital integration system that provides control of both phase voltage turn on and turn off, and voltage and current measuring. In addition, the system constructed was very user friendly and the operator is only required to change and fix the rotor angle. The measurement test is fully automated, and produces a graphical output of the flux linkage curves for viewing and storage.

The new measurement scheme is based on the LabVIEW® data acquisition package, a graphical programming environment developed by National Instruments. The use of LabVIEW enhances the benefits of the digital flux linkage measurement schemes discussed previously. Some advantages of using LabVIEW are that it is user friendly and allows rapid development of versatile instrumentation systems. It also provides features needed for acquiring and analysing data, control, and presentation of results.

The LabVIEW environment is based on the concept of *virtual instruments,* or *VIs,* which describes the combination of personal computers with programmable instrumentation. A virtual instrument (VI) can be defined as layers of software and hardware, added to a personal computer, in such a way that the computer acts as a custom designed electronic instrument. The hardware can include IEEE-488, VXI, or plug in data acquisition (DAQ) boards. In LabVIEW the VIs consist of two main elements which are a *front panel* and a *block diagram*

i) Front Panel:

The front panel is a graphical user interface used for data presentation and control inputs. The front panel is analogous to a traditional electronic instrument that is used to perform test and measurement functions. However, the most obvious benefit of the virtual instrument is that the front panel can be highly customised by the user for their particular application. An example front panel that was implemented for the magnetisation characteristic measurements is shown in Figure A.4. The details of this front panel will be discussed in Section A.5

ii) Block Diagram

The layer behind the front panel is called the block diagram and is essentially the program that implements the users desired analysis, acquisition, and control. In LabVIEW even the block diagram consists of graphical function blocks, which the user connects together in a similar manner to connecting a flow-chart, so that no code needs to be written. In addition, modular programming concepts are encouraged by using VIs as subroutines (or *sub-VIs)* and placing them in higher level VIs. In Figure A.5, the block diagram that was developed for the front panel of Figure A.4 is shown. The functions of this block diagram will also be discussed below in Section A.5.

An outline of the developed LabVIEW based measurement method is given in Figure A.1. The various components of the measurement system will be explained below in Section A.4.

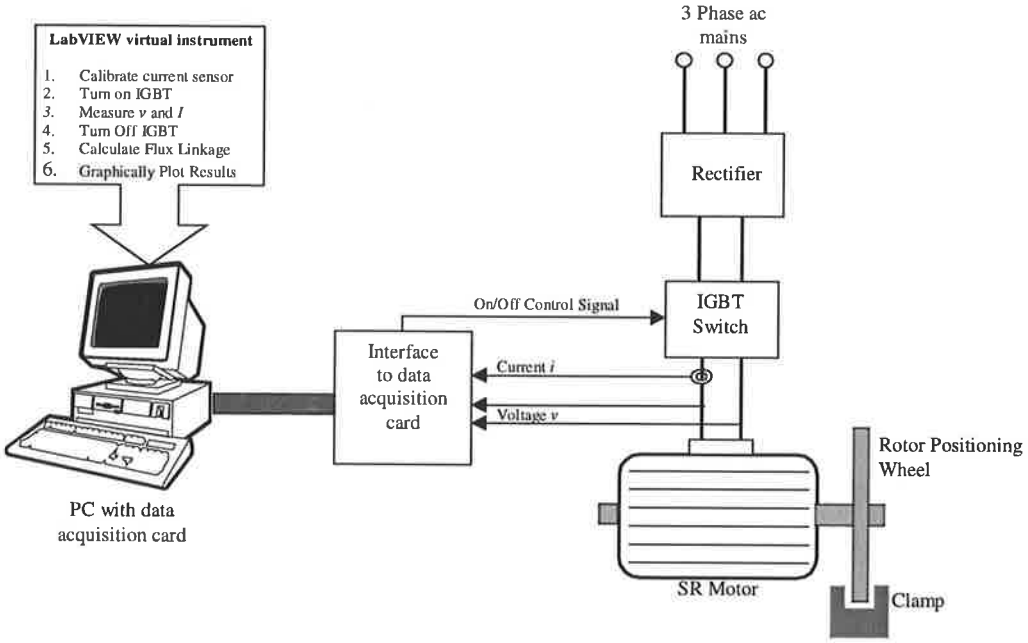


Figure A.1 Magnetisation Characteristics Measurement Test System.

A.4 Measurement Hardware

The test system used to measure the switched reluctance motor flux linkage curves consisted of the following equipment:

a) SR motor

b) Position setting and rotor clamping device.

c) Power switching device

d) Current and voltage sensors

e) Data acquisition board installed on a personal computer.

The equipment used in the measurement system developed for this thesis will be detailed below:

a) SR Motor

The motor that was tested by the measurement system was a TASC drives Oulton PLD112S type SR motor. This motor was used in the experimental work of this thesis. The specifications of the motor are given in Table A.1 below:

Table A.1 Specifications of SR motor used in this research.

Rated Power at 1500 rpm	4.0 kW
Rated Torque	25 Nm
Rated Current per Phase	9 A
Rated Speed	1500 rpm
Motor Starting Torque	150% of full load torque for 5 seconds
Inertia of Rotor	0.0083 kg.m^2

b) Rotor clamping and mechanical measuring devices

In order to carry out the magnetisation curve test, the rotor must be firmly fixed in a known position. Each test is carried out for one rotor position, whereupon the flux linkage versus current is found for this set angle. The rotor clamping device must fulfil two main roles: Firstly, it must provide very firm clamping to hold the rotor into position, even though large torque's will be felt when the phase is excited. Secondly, it must be able to accurately position the rotor to a desired angle.

The clamping device consisted of a large aluminium disc, attached to the motor shaft, with small holes on the outer diameter spaced by one degree. The rotor could be fixed to a given angle by inserting a pin into the given angle pinhole, and locking the disc with an attached clamp. The rotor clamping device was designed and assembled carefully so that the pin holes were accurately spaced in order to minimise positioning errors. In addition, the clamping action was made strong enough to hold the rotor through the impulse torque, attempting to align the rotor pole with the nearest stator pole, when current is initially applied. The rotor clamping device attached to the SR motor shaft is shown in Figure A.2.

As the motor has eight stator poles and six rotor poles, the electrical cycle is 30°. Therefore, assuming that the machine is symmetrical, the characteristics of the motor can be obtained by rotating the angle through only 30°.

c) Power Switching Device

The hardware used in the test facility (Figure A.1) included an IGBT switching device. This was used to switch on the dc supply to the motor phase winding. This applies a step voltage, and corresponding current, from which the flux linkage can be found.

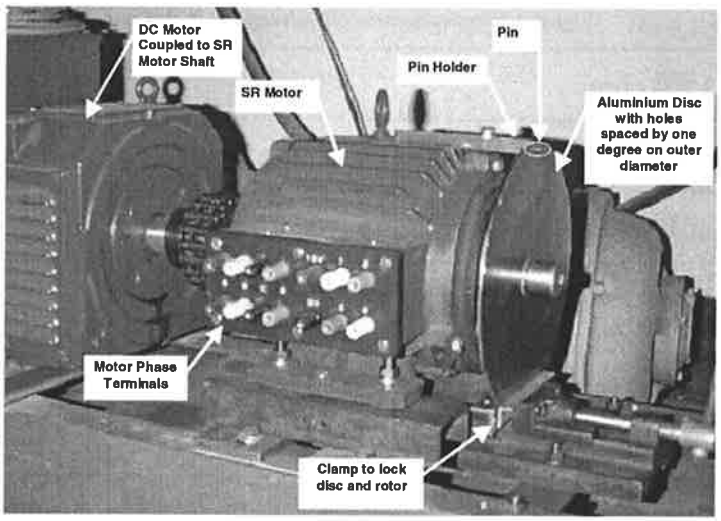


Figure A.2 Rotor clamping device constructed for measurement test.

The power switch was controlled by the LabVIEW VI. The VI provided a control signal via the digital output port of the data acquisition board. However, the IGBT needs a 15V gate signal to operate effectively, and furthermore, the power device must be isolated from the DAQ board for safety. Therefore, an opto-isolating gate drive circuit was used to provide the necessary isolated IGBT gate signal. The digital control signal from the DAQ board is connected to the opto-isolating gate drive circuit that provides the necessary IGBT gate drive.

The dc voltage supply that was switched onto the motor phase consisted of a three phase rectifier supplied by a three phase variac. The variac voltage was adjusted so that the peak current reached during the test (just before the IGBT turns off) did not exceed approximately 22A, which is a higher current level than all operating currents for the motor. It should be noted that the voltage supply is unregulated, and thus the dc level dropped as the current demand increased during each test. However, this can be easily eliminated by using a high power DC voltage regulator.

d) Current and Voltage Sensors

Phase current was measured using a Hall Effect device, which provided non intrusive measurements. The motor phase voltage was measured by means of an opto-isolated simple voltage divider circuit, which presented a small amplitude voltage, in ratio to the phase voltage, to the DAQ board.

e) Data Acquisition Board

A PC bus based plug in data acquisition (DAQ) board fully compatible with the LabVIEW software was used to collect data, as well as to provide digital control signals. The board used had a maximum sampling rate of 100 kS/s, and provided a 16 bit sampling ADC with up to eight differential inputs. The inputs could be software configured for either 0 to

+10V or -10V to +10V operation. In addition, each channel had software programmable gains of 1, 2, 5, 10, 20, 50, and 100. Also provided on the board were 8 digital IO lines and two 16 bit DACs (digital to analog converters). As mentioned above, one of the digital lines was used as a gate control signal for the IGBT. It should be noted that the board could be configured in software with a LabVIEW front panel so that no hardware jumper settings were required.

A.5 LabVIEW Software for the Measurement Test

As stated previously, the virtual instruments (VI) which perform the magnetisation characteristic tests on the switched reluctance motor to calculate the flux linkage curves, were implemented using LabVIEW. The software developed contains functions which perform calibration of the sensor, switching on and off the motor phase voltage, data acquisition, and calculation and presentation of the flux linkage curve. In the flow chart of Figure A.3, the general steps carried out by the algorithm during each measurement test run are shown. The details of the algorithm which performed the measurement test will be discussed below.

The top level VI (main routine) that controls the entire test was named the *Main Test VI*. Normally the operator of the test only views the front panel of this VI. The block diagram (algorithm code) and the *sub-VIs* (subroutines) of this VI are hidden from the view of the operator, and need only be accessed by the programmer. In this way, a very simple to use virtual test instrument is constructed, with the operating details being hidden from the user.

The front panel of this VI (Figure A.4) allows the user to enter the resistance of the motor phase winding, which is previously measured. After the user instructs that a test should be performed, the user is asked to check that the rectified dc power supply is off, in order that calibration of the current sensor can take place.

After the calibration is executed by a subroutine, the user is then instructed to set the rotor position (using the rotor clamping device), turn on the main dc voltage supply to the motor, and press the on screen button to start the measurement test. The voltage and current measurement is then executed, after which the front panel displays a graph of the measured current and voltage. The calculated flux linkage and the flux linkage versus current for the measured rotor position is also graphically plotted in the front panel, and the results are saved to the computer disk drive. Hence, the only task the user must perform is to set the rotor position on the motor, and enter the phase resistance.

The calibration of the Hall-Effect current mentioned above is executed before each test because these sensors normally have some offset error, which should be removed for

higher measurement accuracy. As the offset error can drift over time, the sensor must be calibrated periodically to obtain accurate results.

In this system, the calibration was done by the LabVIEW software in a manner that was free from user effort. The calibration routine operates by reading 50 values from the current sensor when the dc voltage supply to the power switching circuit is off, and the current flowing in the measured motor phase is zero. The measured value from the current sensor should be exactly zero at his time, however normally some positive or negative offset voltage is seen which affects all measured results. The average of the 50 measured voltage readings from the current sensor is taken to determine the offset voltage of the Hall effect current sensor. After each calibration, the data that is measured later is automatically corrected using an offset calibration factor.

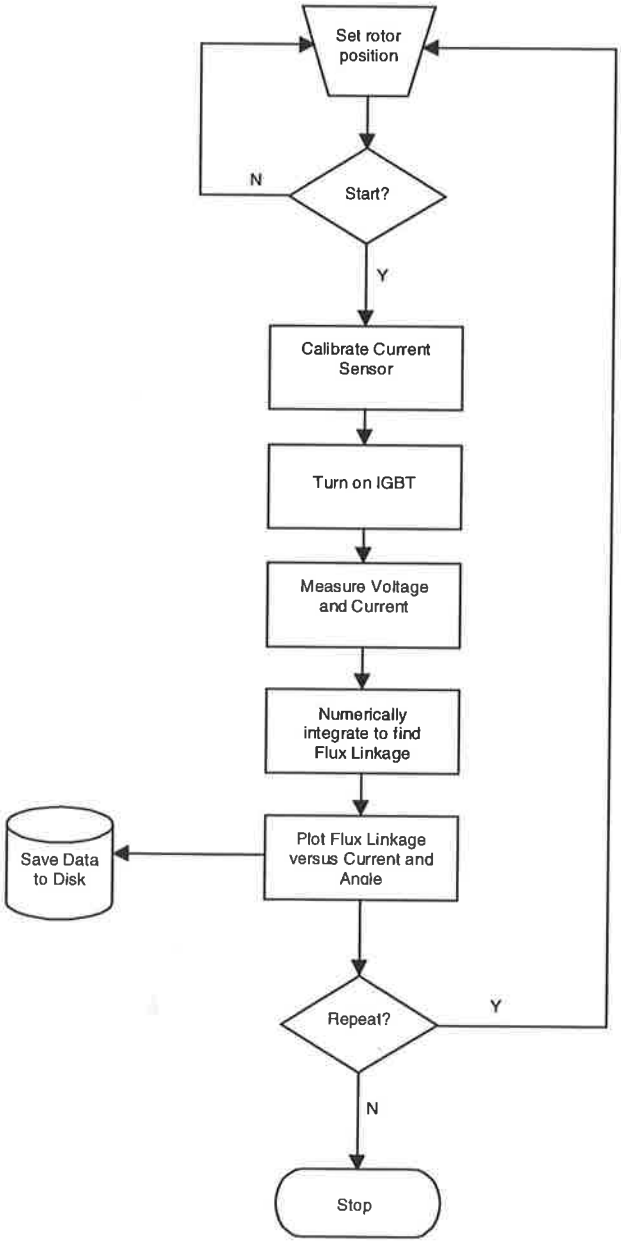
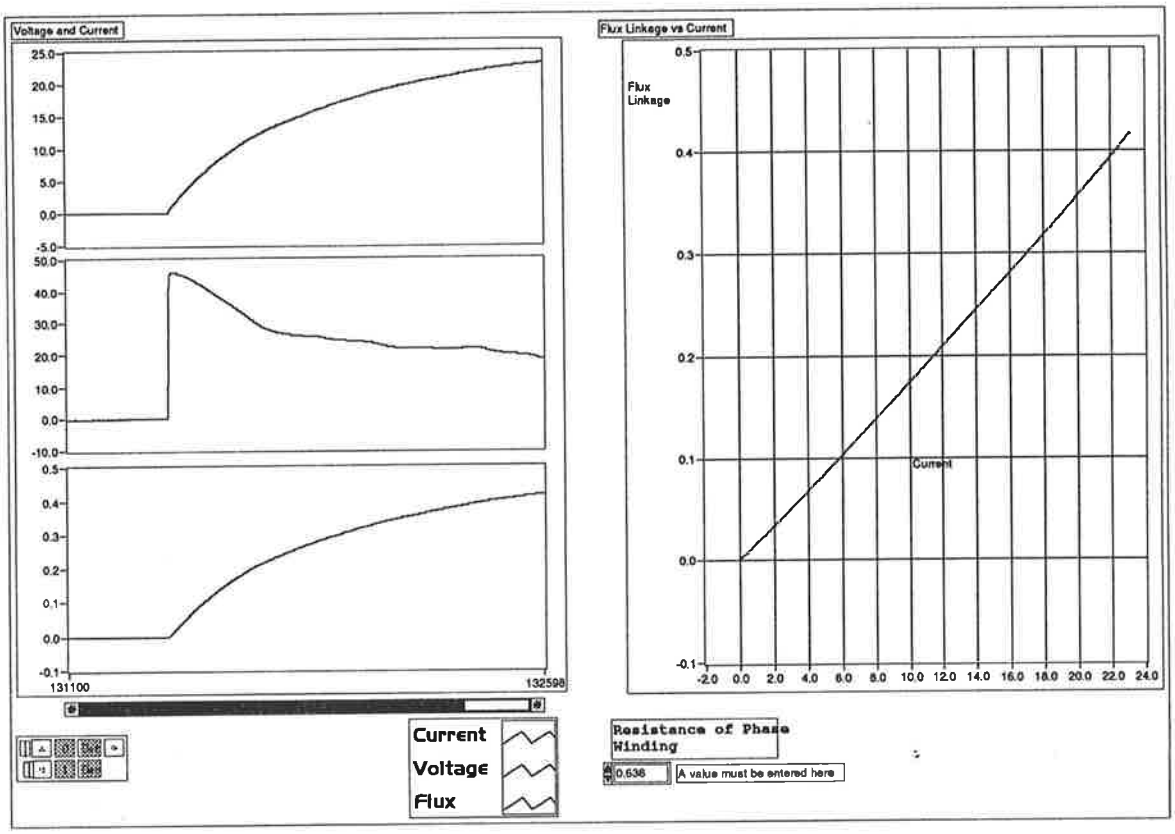
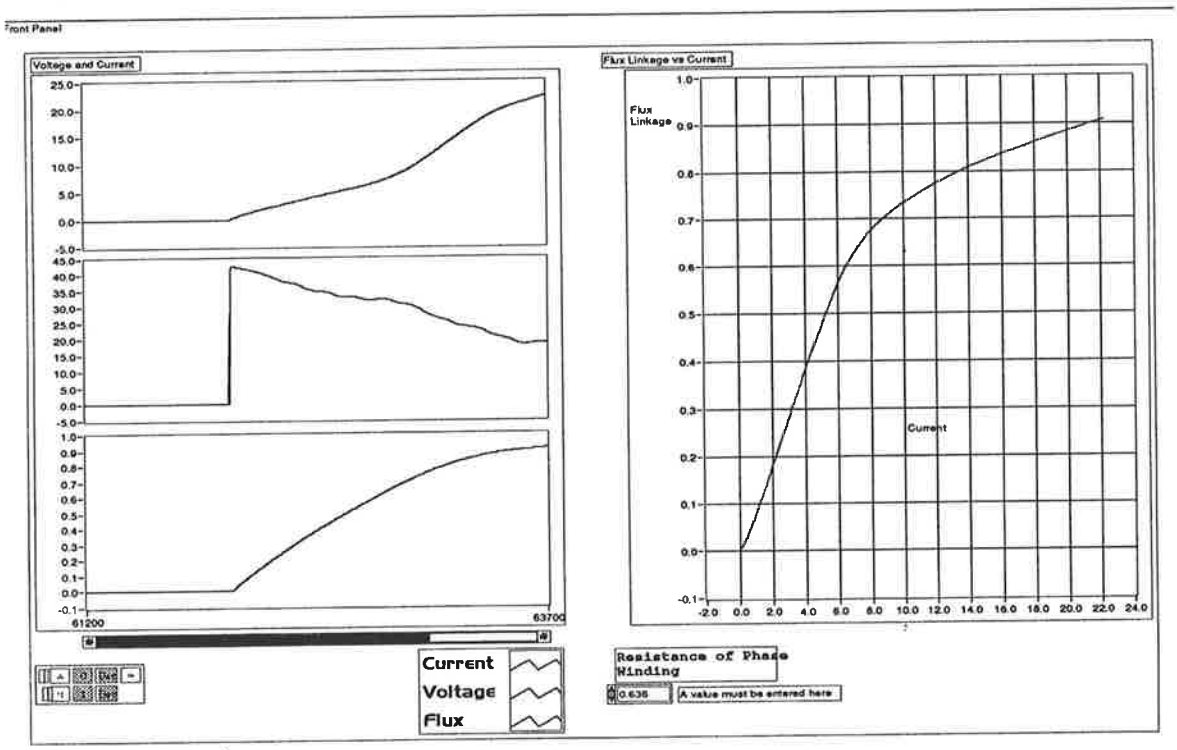


Figure A.3 Simplified Flow-chart of Flux Linkage Curve Measurement Algorithm



(a)



(b)

Figure A.4 Front Panel of Main Test VI. (a) Measuring characteristics with motor phase in linear region. (b) Measuring characteristics with motor phase in saturation region.

The actual block diagram of the *Main Test VI,* which contains the LabVIEW algorithm that performs the measurement test, is shown in. In Figure A.5 (a) the first step of the *Main Test VI* block diagram algorithm is shown. In this step, the user is asked to check that the rectified dc power supply is off, in order that the current sensor can be calibrated. The second step of the block diagram (Figure A.5 (b)) performs the calibration of the current sensor with a calibration sub-Vi (which is seen in the diagram as a single icon) and informs the user when this step is finished. The user is then instructed to set the rotor position (using the rotor clamping device), turn on the main dc voltage supply to the motor, and press the on screen button to start the test. In the third step of the block diagram (Figure A.5 (c)), a sub-VI turns on the IGBT, measures the voltage and current, and then turns off the IGBT. This sub-VI then outputs the measured values of voltage and current, and the sampling period. In the fourth and final step of the block diagram (Figure A.5 (d)) the measured voltage and current is integrated to calculate the flux linkage by a sub-VI which performs the integration (using the measured values and sampling period). From this the user is presented with on-screen plots of current, voltage, flux linkage and flux linkage versus current. These values are also automatically stored numerically onto the computer disk drive.

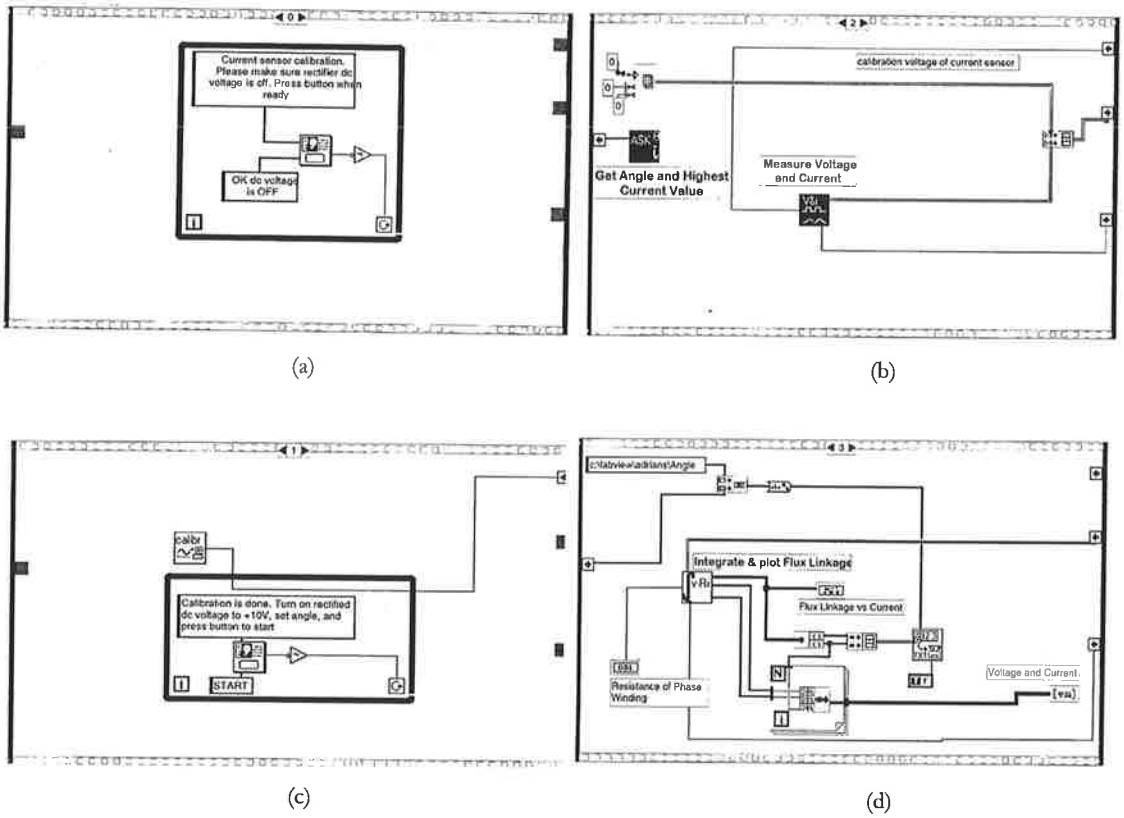


Figure A.5 Block Diagram of *Main Test VI:* (a) Subroutine 1 (b) Subroutine 2 (c) Subroutine 3 (d) Subroutine 4.

Hence, it can be seen in the block diagram of the *Main Test VI* that the algorithm is represented by simple graphical icons or blocks that are connected together. The simple

block diagram and icons makes the algorithm easy to follow and debug, because the details of the operations performed by the icons are hidden. The icons seen in the *Main Test VI* block diagram in themselves represent layers of *sub-VIs*, which are similar to subroutines in text based programming languages. This modular technique of programming also makes the programming easier, due to the fact that low level blocks or algorithms, when successfully debugged, can be treated as *black boxes*, or blocks which can be used without knowing the details.

A.6 Test Results

In the test performed here, the flux linkage versus current curve of a single rotor angle is automatically saved to a spreadsheet file. A number of tests are performed and the final curves are then plotted on the same graph to show the SR motor's magnetisation characteristics. In the four-phase motor that was tested, the electrical cycle is 30 degrees, and hence the magnetisation curves are symmetrical for each rotor angle variation of 30° from alignment to unalignment (assuming motor stator and rotor pole symmetry). Therefore, the motor flux linkage characteristics are plotted over 30 degrees, and in this case 0 degrees is defined as the unaligned position whilst 30 degrees is defined as the aligned position. A plot of the measured flux linkage characteristics taken from the test motor used in this thesis was shown in Figure 2.11. In the results, one can observe the distinct saturation seen on the magnetisation characteristics, when the current is above approximately 6A.

To evaluate the accuracy of the test, a comparison was made with reference [201], where the flux linkage curve for the aligned position only of a 4kW, four-phase Tasc Drives SR motor was presented. Table A.2 shows the comparison made between some of the measured values and values obtained from Figure 8 of reference [201].

Table A.2 Measured Flux linkage at aligned position

Current (Amperes)	Measured results of flux linkage (Wb)	Flux linkage (Wb) in reference [201]
2	0.205	0.207
4	0.435	0.435
6	0.627	0.627
8	0.720	0.722
10	0.773	0.775
12	0.797	0.797

It can be seen from the table above that the values are in very good agreement. The closeness of the values suggests that a high confidence can be placed on the results.

One should also note that no two makes of the even the same model motor can be expected to have exactly the same magnetic characteristics. This is due to small manufacturing irregularities. Therefore, the same test should be performed on every motor that is having its performance evaluated.

Appendix B: Switched Reluctance Drive Simulation

B.1 Introduction

In this appendix, the simulation method that was developed to model the dynamic performance of the switched reluctance motor drive is described. The components of the motor drive system which were simulated included the SR motor, inverter, and the controller. The developed simulation algorithm was designed to simulate these components during transient conditions for all modes of motor operation. In essence, the simulation algorithm operates by determining the control voltage of each motor phase, and numerically solving the SR motor differential equations (which were derived in Chapter 2) to find the corresponding motor current and flux linkage.

The main reason for the development of the simulation algorithm described in this appendix was to provide calculated current and voltage waveforms, which were then used to simulate the performance of the novel rotor position estimation scheme. In the initial stages of development, it was valuable to have calculated motor waveforms before real measured motor waveforms are used. This is because a wide range of motor operating waveforms under various operating conditions could easily be obtained for any feasible test condition using calculations. These were then used as test inputs to the position estimation algorithm to find and correct problems, before the algorithm was developed for operation with actual motor waveforms.

As it was discussed in Chapter 2, the switched reluctance motor operates with a series of current and flux linkage pulses. These pulses are transient in nature, and therefore the motor does not operate in a steady-state mode. This is unlike the dc motor in which normally the flux and current are essentially constant in both time and space. Additionally, in ac motors (such as induction, synchronous, or brushless dc motors) a frame of reference that rotates with the flux can be chosen in which the flux linkage and current are essentially constant also. However, in the SR motor there is no reference frame in which the flux linkage and current of the motor are constant [36], and therefore, simple equations cannot be used to calculate the motor waveforms. Thus, to provide calculated waveforms to test the position estimation algorithm, a numerical simulation of the motor was required.

Another advantage of the motor simulation was that transient waveforms, as a function of speed or acceleration, that would have been difficult to obtain experimentally could be attained. For example, in practice, safety requirements do not allow the stalling the motor suddenly if it was running at high speed. However, the motor waveforms from this type of test could be simulated instead and used to observe how the position detection algorithm performs in this condition. In addition, actual motor drives have some finite current limit, which should not be exceeded, and therefore simulated waveforms can be used for testing

the angle estimation algorithm with currents that are larger than that allowed in the physical drive. However, it should be noted that the simulation results should only be a first step in verifying a drive, and experimentally obtained waveforms must be used to provide final proof of the system.

In Section B.2, previously developed techniques for the simulation of the SR motor drive will be discussed. It will be seen that these methods have been primarily for solving for the torque and current waveforms of the motor simultaneously. Therefore, they also solve the electrical and mechanical equations simultaneously and need information about the motor and load inertia. However, for the testing of the position estimation method, only simulated waveforms of current and voltage are required. Therefore, a computationally fast simulation method was developed that did not require the torque equations to be solved, or mechanical information about the motor, was developed. In Section B.3.1, the graphical software package *SystemBuild* with which the simulation was developed is discussed. In Section B.3.2 the mathematical model used in the simulation was shown, whereas the actual implementation method of the simulation is detailed in Section B.3.2.

B.2 Previous Simulation Methods

A number of different methods of simulating the SR motor have previously been developed, with each have varying degrees of complexity and accuracy. The goal of these simulations is usually to provide a method of solving for the phase currents, flux, and torque in the motor for given supply voltages that are derived from the switching control strategies. The various different methods of achieving the simulation results include:

a) Using linear models of the motor.

There have been simple simulation models developed which use a linear magnetic model of the motor [202], or assume that the inductance variation of the motor can be approximated by sinusoidal functions [203]. By using a linear model of the motor, the motor waveforms can be found using simple functions. However, as was detailed in Chapter 2, the SR motor normally operates with non-linear magnetic characteristics, and hence these assumptions could make the simulation quite inaccurate for most SR motors.

b) Using piece-wise linear magnetic models.

Another previously developed method uses piece-wise linear magnetic models to derive an SR model which can be numerically simulated [204], [205]. In this schemes the magnetic non-linearity of the motor is simplified by assuming that the flux linkage is a piece-wise linear function of rotor position as shown in Figure B.1. In this figure, it can be seen that the magnetic curve has been reduced to two straight lines. An advantage of this is that it simplifies the simulation motor considerably, which in turn reduces the simulation

computation time. However, a disadvantage is that it is difficult to accurately model the magnetisation characteristics of the motor with piece-wise linear models. It has been shown in [206] that the inaccuracies in the current and torque produced using this method are quite high (10 - 25% error).

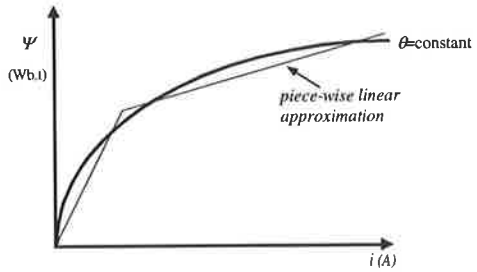


Figure B.1 Piece-wise linear approximation of non-linear magnetisation curve.

c) Analytic equation methods.

Other methods that have been developed provide analytic expressions of the flux linkage versus current and angle in the form of a single analytical equation [207], [208], [209]. As the motor model is encapsulated in analytical equations, this method allows for rapid computer implementation and execution time. However, the approximations made in the deriving the analytical model leads to errors in the generated waveforms (eg. 5 - 10 % error in reference [207]).

d) Least squares and polynomial curve fitting methods.

Other simulation methods have used least square curve fitting method to represent the flux linkage curves [210]. In these methods, the flux linkage curves are each approximated by a sum of three exponentials. In addition, polynomial curve fitting has also been used to approximate the magnetisation curves [211]. However, as will be explained in Section B.3.2, a problem with these methods is that they require the calculation of the *differential* of a function which is only specified by tabulated points. This can lead to significant errors in the differential calculation and thus lead to errors in the simulation results.

e) Using bivariate splines.

A method has been developed which approximates the magnetisation curves of the motor using bivariate splines [212]. The method models the non-linearity of the magnetisation characteristics as well as modeling the mutual effects of the motor. Using the developed model torque and current are computed for given control angles. However, this bivariate spline model is complex and also requires an accurate measurement of the motor mutual and self inductances as a function of rotor angle. This makes the model difficult and time consuming to develop.

f) Using neural networks to model the motor.

A recent method that has been developed is to use artificial neural networks to model the motor using various learning algorithms [213]. Neural networks are well suited in this task as they can readily capture the non-linearity of the motor. The methods use back-propagation training to learn the non-linear function of flux linkage versus angle and current from numerical training data. The input training data to the neural network is the experimentally derived magnetisation characteristic data of the motor. After training, the neural network acts as function that will provide a value of motor current when values of angle and flux are input to the network. Very accurate results were shown for this method in reference [213], but there was a disadvantage of relatively long training times.

g) Finite element field analysis.

The most advanced methods of SR motor simulation use finite element (FEM) analysis to calculate the magnetic fields in the motor using the physical structure of the motor [214]. The instantaneous current and torque waveforms are then calculated from the results of the FEM analysis, together with the numerical solution of the non-linear differential equations describing the drive [215]. However, FEM methods usually have a high computation time and rely on the accuracy of the physical dimensions of the motor.

Except for the linear model simulation methods, in all the above simulation techniques the basic starting point is to have the flux linkage versus current and position characteristics in a form suitable for use by the simulation. The magnetisation characteristics can be found by measurement as was described in Appendix A, or estimated using analytical or numerical calculations [191]. Essentially, it is the difference in the handling of this magnetisation data that separates the different simulation techniques.

The methods discussed above are designed so that the simulation results offer some insight into optimum control and excitation strategies, or to optimise the design of actual physical topology and dimensions of the motor. For this purpose, simulation of both the torque and current waveforms are required and therefore it is necessary to simulate both the electrical and mechanical differential equations simultaneously. The inputs required for the simultaneous simulation of both electrical and mechanical equations are the inertia of the mechanical load and the rotor, and the control parameters. From this, the differential equations describing the motor are solved to calculate the current, flux linkage, and torque of the motor. The speed and rotor angle position can then be determined from simulated torque using the mechanical equations of the motor.

B.3 Developed Simulation Method

In this thesis, an alternative simulation algorithm type to those described above was developed. This was because the simulation was designed for the specific application of calculating the *current* and *voltage* in order to test the position estimation scheme (flux linkage and angle were also simulated for comparison purposes). Therefore, for this application, the output motor torque was not required, and thus the simulation time could be considerably reduced by not solving the differential equations that describe the developed motor torque. In addition, the motor speed is a data input parameter in the developed simulation. Therefore waveforms which are a function of defined speed conditions such as start-up, motor stall, as well as steady or changing speeds could be easily specified.

The developed simulation algorithm was written in the software package *SystemBuild,* which is part of the *MatrixX* software package [216]. This software package is a graphical block diagram modeling tool which can be used to accurately model real time systems. The software provides a user friendly interface for the development of simulations, as it is programmed using predefined or user defined blocks which are placed together. This allows the algorithm to be constructed using graphical building blocks of mathematical functions without any hand written code being required. The features of the software package used for the implementation of this simulation scheme will be discussed below:

B.3.1 Features of the SystemBuild Based Simulation Software Package

The *MatrixX* software package provides a solution for real world design problems such as control design, real time control, digital signal processing, system identification, and optimisation. *SystemBuild* is a major component of the *MatrixX* product, and is used for the development of real time systems and control systems. The most prominent feature of the *SystemBuild* package is that it uses a graphical block diagram editor for developing design models. A short description of the software package will be given in this section, as well as the features that make it well suited to the SR motor simulation.

Due to the graphical block diagram editor in *SystemBuild*, the basic functional unit is called a *block*. The basic block architecture is illustrated in Figure B.2, and the various attributes of a block that can be seen in the figure, include:

a) Name:	A user defined name
b) Type:	The function of the block (eg. integration)
c) Number of Inputs:	The number of signals which are connected to the input of the block

d) Number of Outputs: Represents the number of signals output by the block

e) Number of States: Dynamic blocks have a number of "memory elements" which are referred to as states. The number of states determines the order of the system.

f) Data Types: This can be specified to be either Double-Precision, Floating Point, Integer, or Boolean

A block can perform some mathematical function, depending on how the blocks attributes are defined. In general, every block is defined as an input-output system that can either be *single input/single output* (SISO) or *multi input/multi output* (MIMO). In the constructing of a simulation model, either predefined blocks may be used, or *User Code Blocks* may be built using software code (such *C* programming language).

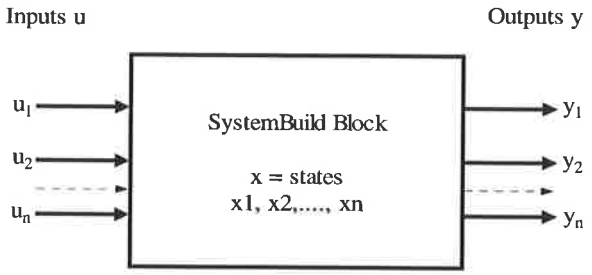


Figure B.2 SystemBuild Block Architecture.

Hence, the SR motor drive was modelled by connecting these function blocks to form a *block diagram* that describes the simulation model. Each connection appears in the block diagram as a line similar to wiring and thus connecting blocks together to form the simulation model is very simple, as is shown in the outline of Figure B.3. The connections originate from the outputs of the blocks, and may be connected as inputs to one or more other blocks. During the actual simulation run, the connections between the blocks form communication channels in which data is transferred. In addition, external connections can be made in order to transfer data to and from the block diagram. In the developed simulation algorithm, an *external input* (which originates from outside the block diagram) was the input data of instantaneous motor speed. In addition, the *external outputs* (which exit the block diagram) of the simulation were the motor current, voltage, and flux linkage. These external outputs are stored as numerical data on the computer hard drive, and can be used later for plotting or analysis purposes.

Another user-friendly feature of *SystemBuild* is that graphical displays can be added onto the simulation to provide a graphical output of any data connection while the simulation is running. Therefore in the simulation, graphical output blocks were placed so that the current, voltage, and flux linkage waveforms could be viewed during the simulation.

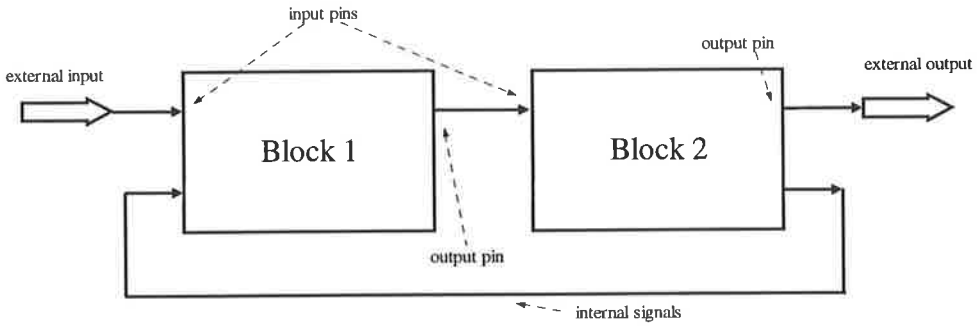


Figure B.3 Block Connections.

Another component of the *MatrixX* package used in the simulation is *Xmath,* which is a graphics and analysis package. It is tightly integrated with *SystemBuild* so that the output from a block diagram can be displayed in *Xmath* graphics. In addition, code can be written in the *Xmath* language called *MathScript.* This is similar to C code, but with an extensive range of mathematical functions. This code can then be used in a *SystemBuild* block as a *user code block.*

The above mentioned features of *SystemBuild* made it very well suited to the modeling of the SR motor. It's principle advantages lay in it's simple and intuitive graphical block diagram editor and it's ability to model real time systems. Therefore, it allowed the simulation to have a fast development time, be simple to use, and provide a high quality graphical output of motor waveforms. The details of the block diagram developed for the simulation and it's output results will be given in Section B.3.3. However, the SR motor drive system that was modelled will first be discussed below.

B.3.2 SR Motor and Drive Model for Simulation

A. Experimental motor

The actual SR motor that was modelled corresponded to the motor that was used in the experimental measurements of the work in this thesis. It should be noted that the simulation algorithm could model other SR motor types simply by changing the parameter data. The values of the parameter data used in the motor simulation are listed in Table B.1.

B. Simulation Model of the SR Motor

To simulate the SR motor the basic task that must be executed is to solve the differential equations describing the motor's circuit. Hence, the differential equations of the motor were detailed in Chapter 2 in order to provide a basis for the simulation algorithm. As was discussed in Chapter 2, the dynamic motor model consists of the voltage equations and the mechanical equations. The inter-phase coupling due to mutual inductances and common magnetic circuit interactions is usually ignored in most of the published literature of SR motor simulations. However an analysis of the effect of mutual inductances for a four

phase SR drive was published by *Moriera* and *Lipo* [217] and for a three phase machine by *Arkadan* and *Kielgas* [218]. It was found that the modeling of the mutual inductances make a relatively small difference on the predicted motor waveforms.

Table B.1 Experimental SR motor ratings and some physical parameters.

Rated Phase Current	9 A
Rated Power	4 kW
Rated Voltage	600 V
Rated Speed	1500 rpm
Rated Torque	25 Nm
Starting Torque	38 Nm
Rotor Pole Arc β_r	17.70 mm
Stator Pole Arc β_s	17.70 mm
Pole Pitch	12.12 mm
Rotor Pole Length	17.52 mm
Airgap	0.40 mm
Rotor Diameter	95.57 mm
Stator Diameter	96.10 mm
Number of Rotor Poles	6
Number of Stator Poles	8
Winding Resistance (25 degrees C)	0.7 Ω

Hence, in the developed simulation, the mutual inductances were neglected in order to reduce the simulation complexity and decrease the computation time. The main justification for this, was that the motor simulation was designed for the purpose of providing simulated waveforms of current and voltage in order to test the position estimation algorithm, and not for providing extremely accurate motor performance predictions. In addition, the position estimation algorithm was tested with waveforms which include mutual coupling effects in the experimental tests with real motor waveforms. Therefore, these effects did not need to be calculated in the initial simulation tests, and this allowed the simulation tests to be computationally faster.

Therefore, as was detailed in Chapter 2, if the mutual effects are ignored in the motor, the differential equation for the voltage of *each* phase is given by the following equation.

$$\pm V_{phase} = Ri_{phase} + \frac{d\psi(\theta,i)}{dt} \tag{B.1}$$

Where:

$\pm V_{phase}$ = the voltage impressed across a motor phase winding (V)
i_{phase} = current flowing in phase winding (A)
ψ = flux linkage (Wb)
θ = rotor displacement (mechanical degrees)

The voltage can be positive, zero, or negative depending on which switching mode the phase is in, and this is emphasised by the ± symbol in front of the voltage given in equation (B.1).

Additionally, it is known from Chapter 2 that the mechanical equations of the motor are as follows:

$$\frac{d\omega}{dt} = \frac{1}{J}\left(T(\theta,i) - T_{mech}\right) \tag{B.2}$$

$$\frac{d\theta}{dt} = \omega \tag{B.3}$$

Where:

ω = angular speed (radians per second)
θ = angle (radians)
$T(\theta, i)$ = electromagnetic torque (Nm)
T_{mech} = load mechanical torque (Nm)
J = inertia of the drive (kg.m^2)

The voltage equation (B.1) can be rewritten in order that the independent variable is the motor phase current as is shown below:

$$\frac{di}{dt} = \frac{1}{\frac{\partial \Psi}{\partial i}(\theta,i)}\left\{\pm V - iR - \omega\frac{\partial \Psi}{\partial \theta}(\theta,i)\right\} \tag{B.4}$$

Hence, using this equation, the current can be calculated using numerical integration. However, it can be seen that this equation contains partial differential coefficients on the right hand side of the equation and thus problems arise in methods where current is calculated from equations written in this form [219]. This is because in all the simulation methods, the flux linkage curves $\Psi(\theta,i)$ are either approximated, or stored as a look-up table. Although the curves of flux $\Psi(\theta,i)$ may be quite accurate using these approximations or look-up tables, the numerical error when one finds the differential of this function $\partial\psi/\partial i$, or $\partial\psi/\partial\theta$ from the approximation or look-up table may be quite large. Therefore, there is a fundamental difficulty in accurately obtaining values for the differential functions

on the right hand side of equation B.4 during a simulation, and thus these methods were not used in this work.

To overcome the problems of solving for the current using equation (B.4) the voltage equation given in equation (B.1) may be rewritten in the form:

$$\Psi_{phase} = \int (V_{phase} - i_{phase} R) dt \tag{B.5}$$

The differential equation form of Equation (B.5) for a four-phase motor can then be given by

$$\begin{aligned} \frac{d\Psi_1(\theta_1, i_1)}{dt} &= \pm V - i_1 R \\ \frac{d\Psi_2(\theta_2, i_2)}{dt} &= \pm V - i_2 R \\ \frac{d\Psi_3(\theta_3, i_3)}{dt} &= \pm V - i_3 R \\ \frac{d\Psi_4(\theta_4, i_4)}{dt} &= \pm V - i_4 R \end{aligned} \tag{B.6}$$

Where the subscripts 1, 2, 3, 4 represent the equation for the corresponding motor phase.

The above form eliminates all the differential functions on the equation's right hand side which were seen in equation (B.4). Hence, using this equation, the flux linkage can be solved for directly using time-stepped integration. This method was first described by *Stephenson* and *Corda* in reference [219]. The flux linkage equation in this form was used to find the flux linkage and current in the developed simulation model.

In the simulation model, equation (B.6) is used to find the flux linkage using numerical integration. The current is found at each time step n by using the flux linkage and rotor angle values to look up a value from the magnetic characteristics of the motor (which are stored in the form of a look-up table). In other words, after each step of integration, the current is found from the look-up table, which is then used in the right hand side of equation (B.6) for the next integration step. Normally, the magnetic characteristics are measured as $\Psi(\theta,i)$ (flux linkage as a function of current and rotor position), as was seen in the measured magnetisation curves of Figure 2.11 in Chapter 2. However, for this method, the look-up table of $i(\Psi,\theta)$ (current as a function of flux linkage and rotor position) is required. Therefore, the look-up table $i(\Psi,\theta)$ is derived from the numerical inversion of the measured curves of $\Psi(\theta,i)$. The visual representation of the inversion is given in Figure B.4, where the aligned, unaligned, and an intermediate position are inverted from a function of $\Psi(\theta,i)$ to $i(\Psi,\theta)$.

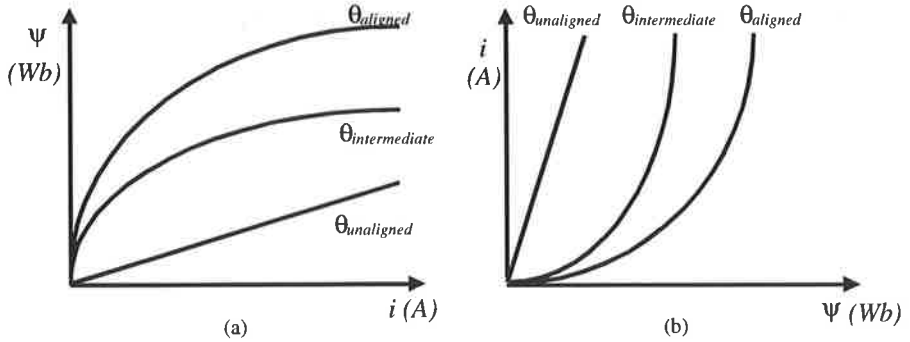


Figure B.4 Inversion of flux linkage curves: (a) Flux Linkage as a function of Current and Rotor Position, (b) Current as a function of Flux Linkage and Rotor Position.

From the right hand side of equation (B.6), it can be seen that the other variables which need to be calculated for the flux linkage to be determined in each integration step are the rotor position θ, and the phase voltage V. In previous simulation schemes, the rotor position is found by solving the mechanical equations (B.2) and (B.3). To achieve this, the torque produced by the motor is calculated, and then the motor speed can be calculated from the integration of equation (B.2). From the motor speed, the rotor position can then be found by the integration of equation (B.3).

However, the primary purpose of the development of the simulation algorithm was to provide simulated current and voltage waveforms for the testing of SR motor angle estimation schemes. For this purpose it is more intuitive to specify the simulation waveforms as a function of a predetermined speed function instead of calculating the speed during the simulation. For example, simulated current and voltage waveforms may be required for various conditions such as motor start-up and acceleration, constant speed, transient acceleration or deceleration, or motor stall. These conditions can be easily specified by a speed function which is specified as a function of time in *XMath,* which is then input to the simulation. Figure B.5 shows example speed versus time curves for the various cases mentioned above. Note that using this simulation technique, it is also possible to input measured speed curves (from speed sensor) directly into the simulation to obtain more realistic operating characteristics.

Hence, in the developed simulation, the speed of the motor is also an input variable to the motor model. This means that equation (B.2) does not need to be solved and therefore computation time can be saved by only solving the electrical equations. The simulation internally generates the instantaneous angle from the speed, by integration of the simple equation (B.3):

$$\theta = \int \omega . dt + \theta_0 \tag{B.7}$$

Where: θ_0 is the rotor angle at $t=0$ (the first simulation step), which determines the starting rotor position, and is set before the simulation begins.

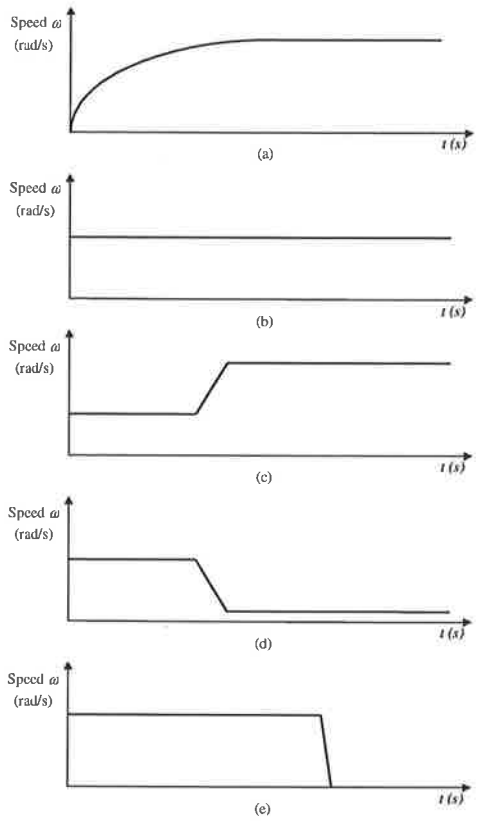


Figure B.5 Example Speed Curves for Input to Simulation: (a) Motor Start-up and Acceleration. (b) Constant Speed. (c) Transient Acceleration. (d) Transient Deceleration. (e) Motor Stall.

B. Simulation of Inverter Voltages

In the simulation, the motor phase voltages V are determined by the simulation of the SR drive inverter. The simulation of the inverter determines the switching state and the voltage applied to each phase. As it was explained in Section 2.9, the inverter output voltage is defined by the turn on and turn off angles, as well as the phase current level in the chopping mode of operation. Hence, in the simulation of the inverter, the simulation algorithm takes the rotor angle and phase current magnitude as the inputs and then outputs a voltage according to the rotor angle and mode of operation. The mode of operation implemented in the simulation is either chopping mode or single pulse mode, as was previously discussed in Chapter 2. The simulated inverter automatically detects which mode of operation it should be operating in, according to the current magnitude. If the simulated phase current does not reach the chopping mode hysteresis level during the phase turn on period, then the single pulse mode is simulated, otherwise, the chopping mode of operation is simulated.

As it was detailed in Chapter 2, the hysteresis current control used in the chopping mode uses two current limit bands. The limits may have their values changed in the simulation so

that they may accurately simulate the physical controller. In addition, both hard and soft chopping modes of operation can be simulated by the algorithm by setting a control parameter.

The voltage drops across the semiconductors (such as the IGBTs and diodes), as well as the circuit wiring are not modelled in the simulation. This is because these voltage drops are relatively small compared to the typical supply voltage. Thus, the voltage drop across both IGBTs in a phase leg would be negligible compared to the normal on state motor phase dc supply voltage (eg. approximately 0.8% of the 500V supply for the 4kW motor used in the experiments). Nevertheless, these voltage drops may be accounted for by adding accurate models of the switching devices in the simulation using their corresponding data sheets, rather than assuming that they are ideal. This would normally increase the computation time because the voltage across the semiconductor devices is a non linear function of the current flowing through it, and this would be required to be calculated in each simulation step.

Additionally the on and off switching times of the IGBTs and the reverse recovery times of the diodes are also neglected. Instead, it is assumed that the devices switch instantaneously. This is because the transient switching times are small and has negligible effect on the output motor phase voltage waveform. For example in a typical industrial IGBT motor drive, the switching frequency of the output motor voltage is typically about 5-10 kHz [220] (in this thesis the designed inverter had a maximum switching frequency of 10 kHz). However, IGBTs used for motor drives have a typical turn off time of approximately 500 ns, and a turn on time of approximately 200 ns. Therefore, for a 10 kHz voltage switching frequency, the turn on and turn off switching time of the IGBTs in each period would consist of approximately 700 ns, or 0.07% of the voltage period time.

B.3.3 Simulation Algorithm

As it was discussed above, the simulation algorithm was implemented in *SystemBuild* using various function blocks connected together to form the motor model. The *SystemBuild* block diagram of the simulator is outlined in Figure B.6 and will be explained here. In the actual simulation, the current, voltage, and flux linkage for all four phases of the motor were calculated, however, for simplicity, only the values for one phase are shown in the block diagram because the procedure is exactly the same for all phases. An outline of the simulation steps that are performed by the block diagram shown in Figure B.6 is given in Figure B.7.

As it can be seen, during the run time simulation, the only external input is the motor speed data. This is input in the form of a column vector of numeric values, with values of

speed for each time step. For example, at iteration *n* of the routine, the input to the simulation will be the *n'th* value of the speed vector.

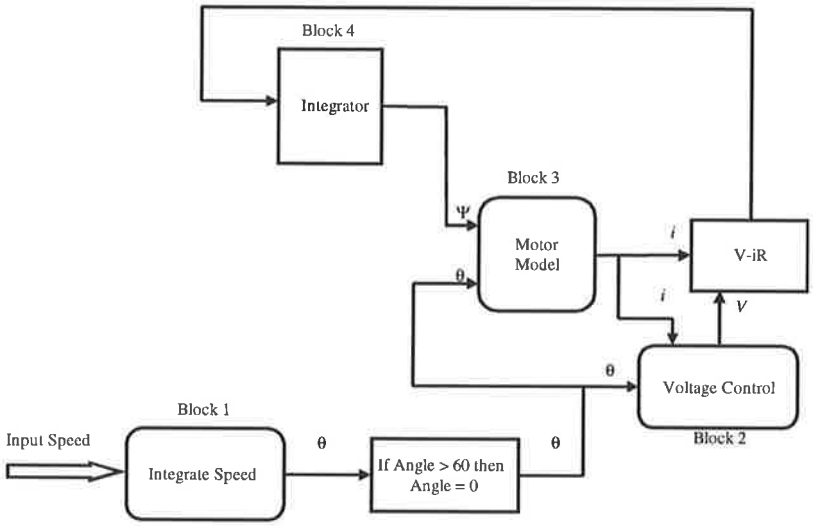


Figure B.6 Simulation block diagram

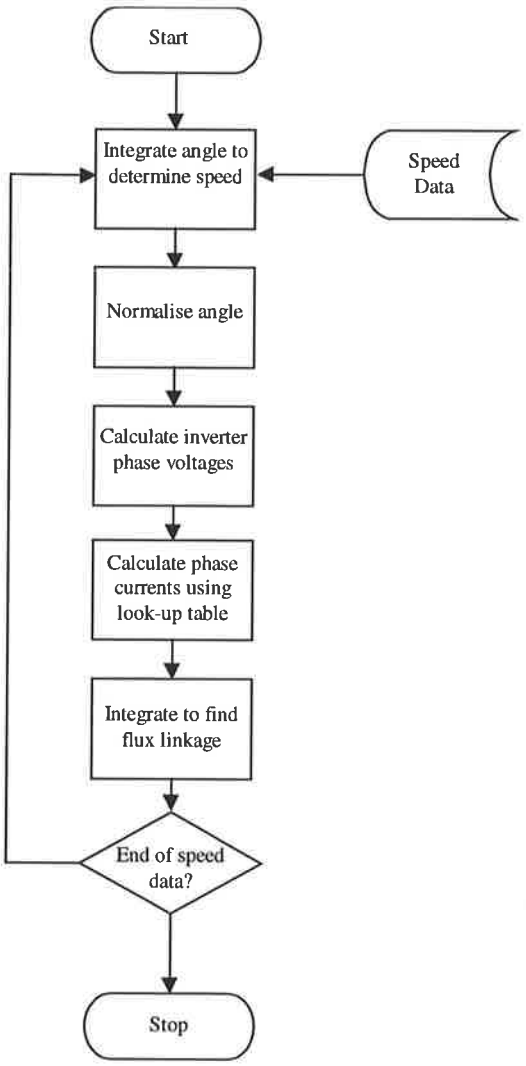


Figure B.7 *SystemBuild* simulation algorithm flow chart.

In Figure B.6 the block *Integrate Speed* (Block 1) takes the speed vector as it's input and integrates to determine the output of the block angle or θ. When the angle is greater than or equal to 60 degrees mechanical the integrator is reset to 0. In this way, the angle only varies between 0 and 60 degrees mechanical which represents one electrical cycle for the four phase SR test motor. The value of angle, or θ, is an input to both the block *Voltage Control* (Block 2) and *Motor Model* (Block 3). The *Voltage Control* block is a *User Code Block*, which in this case, is a *MathScript* function that simulates the inverter output voltages and determines the motor phase voltage. The block calculates the phase voltages according to the input angle θ and phase current level, and the output voltage values of this block are used to calculate the flux linkage. The algorithm that is executed to calculate the phase voltage is illustrated in Figure B.8.

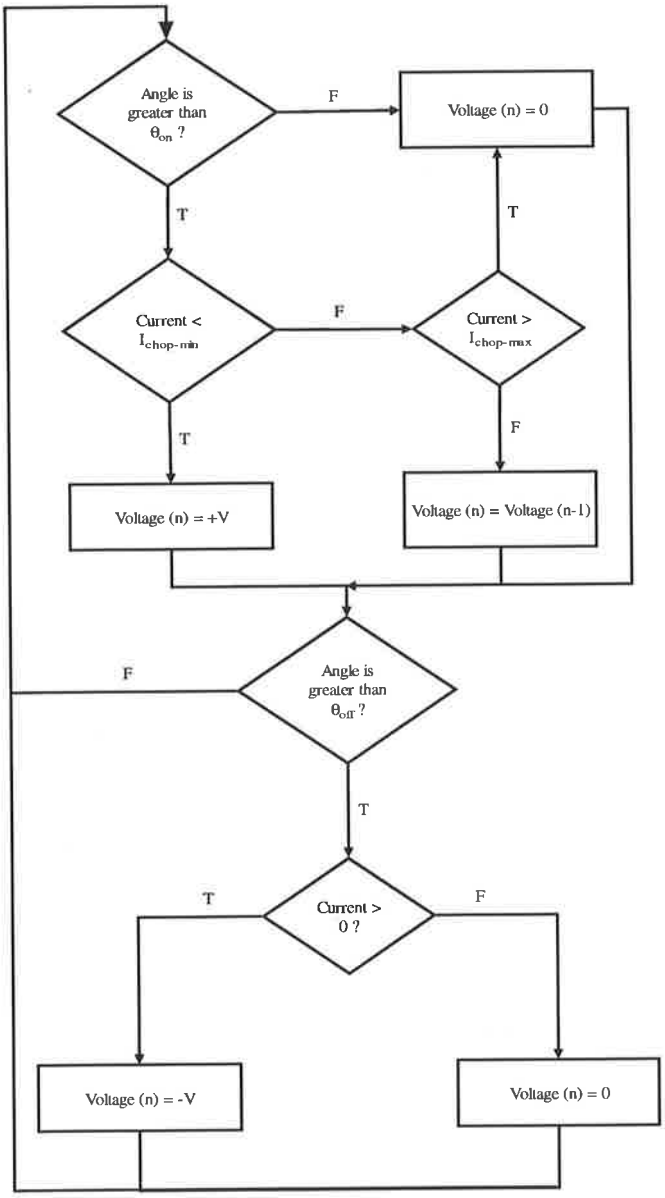


Figure B.8 Block diagram of the voltage controller: θ_{on} = phase turn on angle, θ_{off} = phase turn off angle, $I_{chop-min}$ = minimum value of chopping mode current hysteresis band, $I_{chop-max}$ = minimum value of chopping mode current hysteresis band, T = true, F = false.

The *Motor Model* block (Block 3) contains the three-dimensional matrix of values that contains the measured points of the motor magnetisation characteristics. As it was mentioned above, the measured points are stored in the form of current as a function of flux linkage and angle. During the simulation, the values of the flux linkage ψ and angle θ in each iteration are used to determine the phase current i by looking up the table of values stored in the matrix. If the exact input values of angle and flux are not stored on the look-up table, then three-dimensional interpolation is used between the two closest points of angle and flux to find an output value of current.

The generated voltage from the *Voltage Control* and the current found from the *Motor Model* block is then supplied to the block $V - iR$, in which the current is subtracted from the product of current and phase resistance. This forms the right hand side of the motor equations (B.6) which can then be integrated to find the flux linkage. The integration takes place in the *Integrator* block, which is a predefined function block that can perform integration of the input data signal. In this block, the integration of the motor voltage equation given in equation (B.5) is performed at each iteration step n to determine the flux linkage of the iteration $n+1$.

B.3.4 Simulation Algorithm Initialisation

Before the simulation described above can be run, various data parameters must be stored on the PC that will run the simulation. These include the motor and inverter parameters, the motor magnetisation data, and the simulation run time input data, which will be discussed below:

A. Motor and Inverter Parameter Set-up

The parameters of the simulated motor and inverter drive are entered by the user, and can be easily altered at any time by entering different values. The parameters which must be entered include the dc bus voltage V. This is the voltage that will be used as the motor phase voltage when a phase is turned on. In addition the turn-on (θ_{on}) and turn-off (θ_{off}) angles are specified by the user. These turn on and turn off angles may be set to vary with speed or to remain constant. However, in the developed simulation, the limit of the angle variation was set to be between 0 and 60 degrees mechanical, as this is the electrical cycle of the simulated four phase SR motor.

The mode of current control, can also be specified by the user to simulate the physical controller. In the simulation, soft chopping or hard chopping may also be used, by simply changing a parameter in the algorithm so that the voltage is zero or $-V$ volts respectively, when the phase is turned off during chopping. The chopping mode is automatically determined to begin when a certain current level is reached, as happens in an actual motor

controller. The level of current, at which chopping begins, can be set by the user, and would normally be set to the same level as the physical motor controller. The hysteresis band during chopping mode can also be specified by the user.

The rotor resistance (see Table B.1) is another parameter that is required in the simulation algorithm to solve the motor's phase equations (as shown in equation (B.6)). This is entered in the simulation after measurement from the actual motor. The resistance can be entered either as a constant value, or as a value that varies with the simulation time (in order to simulate heating effects).

B. Motor Magnetisation Characteristic Data

In the simulation, magnetisation data is stored in the form of a look-up table that contains the stored data points of the motor non-linear magnetisation characteristic function relating current to flux linkage and angle (as shown in Figure B.4 (b)). The relationship between flux linkage, angle, and current is experimentally measured and stored as a discrete numerical points in the three-dimensional look-up table. For an accurate simulation the points on the curve must be measured accurately. In this research, the flux linkage curves were measured accurately in the manner described in Appendix A, where the result of this measurement was also detailed. In the *Simulink* simulation algorithm, the measured results are stored as a numerical function block such that flux linkage and angle are the input variables and current is the output variable. Due the fact that the function is stored as discrete points, three-dimensional interpolation is applied on these points during the simulation to approximate the function. Hence, a large amount of points must be measured for a high simulation accuracy.

C. Inputs During Run Time

The parameters mentioned above are set before the simulation begins, however while the simulation is running the only data input requirement that is required is the instantaneous motor speed. As was previously discussed, having the speed as the input allows a fast computation time because the mechanical equations do not need to be solved. As mentioned previously, in the simulation the motor speed is input to the simulation as a numerical vector of instantaneous speed versus time. This vector can be generated easily by specifying any function of time in *Xmath* or obtained from the actual system via a speed transducer.

Since the simulation is designed to generate the voltages and currents of the SR motor, the values of torque are not calculated here. However, a more complex simulation can be developed which calculates the instantaneous torque without having speed as an input. In this case, the mechanical differential equation must be solved, and the inertia of the system must be known which means that the computation time will correspondingly be greater.

Appendix C: Details of the DSP Based Control System Design

The high speed DSP board carries out the control of the SR motor. Inputs to the digital signal processor include the current and voltage of each phase. From these inputs only, the fuzzy logic based sensorless position estimation is carried out, and all the control switching signals of the motor drive can be determined by the DSP. For test purposes an interface to the motor shaft encoder is also provided, in order to compare the estimated angle from the position estimation algorithm with a measured rotor angle.

The DSP performs the following operations during real time motor operation:

a) Reading of encoder data, and conversion of data to rotor angle position in degrees.

b) Generation of variable gain signals for the variable gain amplifiers of the measuring circuits.

c) Generation of A/D converter circuit control signals.

d) Execution of the fuzzy logic based position sensorless algorithm.

e) Determination of motor control commands (such as chopping mode current level, turn on angles, and turn off angles).

f) Generation of the inverter individual IGBT gate drive signals based on motor control commands.

g) Storing of measured data in RAM for access by personal computer via parallel link. In the developed system the up-loading of the stored data could only occur when motor control operation had ceased, and a data transfer routine was executed. (ie. not during motor operation).

The advantages that the DSP has in performing these functions in real time derive from the architecture of these processors that will be discussed below.

C.1 Advantages for Sensorless SR drive of ADSP-21020 processor

For the SR motor drive developed, an Analog Devices ADSP-21020 processor was used which is currently one of the more advanced DSP families available. This DSP is a special type of Reduced Instruction Set Computer (RISC) processor. It has a limited number of basic fixed length instructions, but these can execute at very fast speed and with high processor efficiency. DSPs were originally intended for signal processing applications where Fast Fourier Transforms, Convolutions, and Digital Filters are implemented. Similar mathematical routines are required in advanced motor control applications, and therefore

DSPs are now widely applied in these systems [221]. The features of this particular DSP that make it well suited to the fuzzy logic based sensorless SR drive include:

a) High Speed Mathematical Computation

This DSP has the benefits of a very fast 30 ns instruction rate and all instructions are executed in a single-cycle. It has a wide range of single cycle arithmetic operations, including division, multiplication, max, min, addition, subtraction, and combined addition/subtraction.

The fuzzy logic computations such as fuzzification, rule inference, and defuzzification consist mainly of these simple arithmetic functions. Therefore, this results in a very fast processing of the fuzzy logic based computations in the sensorless scheme.

b) 40 Bit Precision

The ADSP-21020 handles the extended precision 40 bit IEEE floating point format. It also handles 32 bit IEEE floating point format as well as 32-bit integer and fractional formats. This allows highly accurate calculations to be performed.

c) Efficient Data Flow

The ADSP-21020 has a separate program and data memory area and separate program and data memory buses, which is known as the *Harvard Architecture* arrangement. This allows the processor to simultaneously fetch an instruction and two operands in a single cycle. In addition, parallel arithmetic/logic (ALU), multiplier, and shifter units allow single multi function compute instructions with parallel ALU and multiplier operations. The processor can perform data transfer and arithmetic operations in the same instruction cycle. This dramatically increases execution speed, which is important for real time operation.

d) Wide Memory Buses and Input/Output Interface

As mentioned previously, the DSP has two memory areas, the program memory and data memory. The program memory address bus (PMA) is 24 bits wide which allows up to 16 million words of mixed instruction code and data. The data memory address (DMA) bus is 32 bits wide, which allows access to 4G words of data.

The data memory data (DMD) bus is 40 bits wide on the ADSP-21020, whilst the program memory data (PMD) bus (which can hold instruction code together with data) is 48 bits wide.

The very wide PMD bus width was highly useful in the implemented drive system. This is because 12 bit A/D converters were used to sample the voltages and currents. Therefore

after data conversion, the complete set of four phase voltages or four phase currents could be read and stored in a single execution cycle of 30ns.

C.1.1 DSP Circuit Design

The DSP is connected to various components in the developed drive design. These components are listed below

a) On board memory.
b) Address decoders and bus drivers to interface with eight 12-bit A/D converters which input the current and voltage signals.
c) Opto-isolated gate driver circuits of the inverter IGBTs.
d) Programmable amplifier gain logic for the voltage measuring circuits.
e) Shaft encoder input.

These peripheral circuits will be described in more detail below.

In Figure C.1 a simplified circuit diagram is shown of the DSP and its peripheral connections. For clarity, only the major connections that are to the A/D converters and the opto-isolated IGBT gate drive interfaces are shown. Other connections that are not shown include the on board RAM, shaft encoder inputs and logic signals from the DSP to the programmable gain amplifiers located in the voltage measuring circuits.

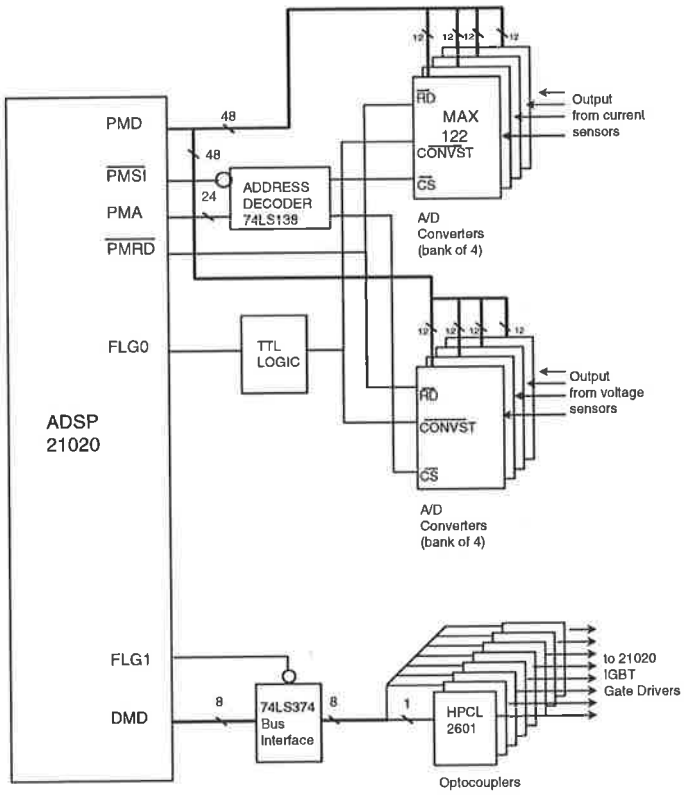


Figure C.1: Digital Signal Processor and Peripheral Components

C.1.2 DSP Programming

The DSP can be programmed with a combination of C and assembler. The exact same C routines that implemented the fuzzy logic based sensorless position scheme (as described in Chapter 4 and 5) could be compiled onto the 21020 DSP, due to the fact that the fuzzy logic sensorless algorithm was written in standard ANSI C code. The 21020 processor has a specific C compiler and runtime C library so that ANSI C code can be complied into ADSP-21020 assembly language files. The compiled assembly code is downloaded onto the DSP board via a parallel link with the personal computer.

In addition low level hardware routines were written as assembly functions. This included routines that performed the following tasks:

Processor reset.
Configuring DSP memory and wait states.
Initialising of registers
Configuring and enabling interrupts
Control of A/D converters (start conversions, read values, store results)
Output of digital control signals to the IGBT gate drivers and voltage measurement gain selection amplifiers.
Reading shaft encoder digital word and conversion to angle in degrees.

The writing of these low level functions in assembler allowed faster real time operation due to more compact and optimised code, than would otherwise be available if C was used.

During each normal execution cycle approximately 1200 instructions are processed before a new estimated rotor position is produced (the cycle time will vary slightly according to which particular subroutines are used in the fuzzy prediction and fuzzy rule processing routines). This means that the processing time is approximately 33 μs. The processing time could be further reduced by optimisation of the code, and full assembly programming of all of the routines of the sensorless position detection scheme.

During operation all the voltages, currents, and angles are stored into memory in each measurement cycle. After operation of the program (and the motor) is stopped, the personal computer can upload the contents of the DSP memory banks and thus upload the measured data. This however limited the length in time of motor waveforms that could be stored, due to the limitation in the DSP on board RAM in the developed system. Therefore, a method that can be used is to store only the measurements from every *nth* iteration, so that the time length of the stored waveforms is extended. In the developed system n was specified to be 5, and thus the period between each measured point was approximately 165 μs. In order for the measured data to be spaced at exactly the same intervals in time, an interrupt was used in

combination with an internal DSP timer to store the measured points at exactly 1/6000 s frequency.

As has been discussed above, the peripheral circuits connected to the DSP allow it to obtain information about the motor waveforms, and control the power electronic inverter drive. These other circuits are essential for the sensorless motor operation, and will be detailed below.

C.2 Analog to Digital Converters

The analog to digital converters (A/Ds) provide the interface from the analog signals that are output from the current and voltage sensors that measure the motor phase waveforms, to the digital data required for manipulation by the DSP. To provide good resolution, 12 bit A/Ds were used (Maxim MAX122-ACNG). These devices provide a high speed conversion time of 2.8μs.

It is highly desirable in this system that all measurements are sampled at the same instant of time. Thus, all voltage and current values must be sampled simultaneously. To achieve this, eight A/D converters were used, one for each of the four phase voltages and currents. The A/D converters are connected to the same *conversion start* (CONVST) control signal which is output by the DSP, in such a way that all the converters begin and complete the data acquisition at the same time. The data acquisition circuit of one of the eight A/D converters is shown in Figure C.2.

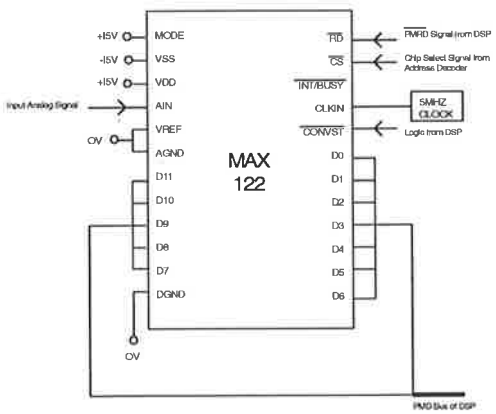


Figure C.2: Analog to Digital Converter

As was mentioned above, the program memory data bus of the DSP has a large 48-bit width. This allows two banks of four A/D converters to be connected together. Only one read operation is required to read four sets of 12 bit data from the A/D converters. This provides a significant saving in processing time. In the circuit developed, one of the A/D banks reads the four phase currents, and the other bank reads the four phase voltages.

Each A/D converter requires a 5MHz clock that was derived using the 25MHz clock of the DSP and a divide by five circuit. Other periphery circuits constructed to interface the A/Ds to the DSP included an address decoder and an interrupt request generator, which outputs an interrupt signal to the DSP when all A/D converters have ended the conversion.

The process of data conversion begins with the DSP outputting a signal requesting conversion to begin. When data conversion has been completed an interrupt is generated. Upon this signal being received, the DSP enters an interrupt service routine. This reads the data in two 48 bit words as described above, with the correct bank of A/D converters (ie. the current or voltage measuring bank) being selected with the address decoder. When a bank of A/Ds is selected via the address decoder, they output their data on the DSP bus, and the DSP then reads the 48-bit word placed on the bus.

C.3 Interface and Measuring Circuits

The implemented measuring circuits provide measurements of voltage and current in a form suitable for processing by the A/D converters. For protection from dangerous voltages and faults in the power side, both the current and voltage measurements circuits must be electrically isolated from the power circuit. Another measurement that is taken is the rotor position, which is measured with a shaft encoder to provide a reference for checking the estimated position.

The interface circuits which were implemented allow the DSP to switch the IGBTs on and off in the desired manner. Once again the low voltage DSP circuitry must be protected from high voltages found in the power circuitry. Therefore, the ground referenced 5V logic signals from the DSP are converted to the IGBT gate drive signals through galvanically isolating opto-couplers and isolated gate driver circuits.

C.3.1 Current Measurement

The current is each phase is measured by LEM 25-NP Hall Effect closed loop compensated current transducers.

A measuring current based on the closed loop Hall effect sensor was developed to measure each of the phase currents. In the developed circuit the output sensor currents are 2mA per Ampere of current being measured. This is converted to a voltage proportional to current by the sensor output resistor. In the circuit built a 162Ω resistor was used, which made the output voltage 320mV per Ampere of current being measured. The current measuring circuit per motor phase is given in Figure C.3.

A buffer (OPA633KP) was used interface between the current sensor and the analog to digital (A/D) converter. The buffer has two main purposes. Firstly it will not allow more

than 5V to pass, therefore ensuring that over-voltages are not transmitted to the analog to digital (A/D) converters, which have a maximum input rating of ±5V. Secondly, the buffer chosen is a good signal line driver, ensuring that the voltage maintains its value over the signal lines to the A/D converter.

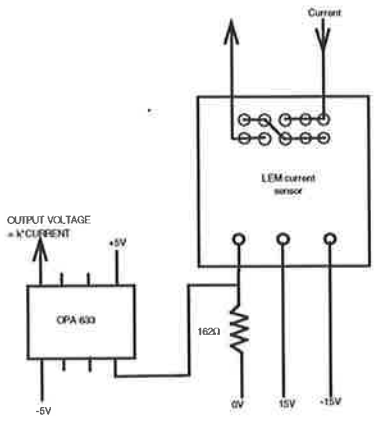


Figure C.3 Current sensing circuit

C.3.2 Voltage Measurement

To measure the voltage across a motor phase, simple resistor voltage dividers are used as shown in Figure C.4. The resistor divider is used to convert the actual phase voltage, which could be up to 500 V dc in the developed system, with a value suitable for input to the A/D converters. The A/D converter inputs must be less than 5V.

The resistors are chosen to be of high value so that the current flowing in the resistor leg is small. Nevertheless, the value must not be overly large because very high resistors tend to be less stable and non-linear with voltage [222]. In the designed circuit a ratio of approximately 1/100 between input and output voltage was desired. Resistance values of R1 = 210 KΩ and R2 = 2.05 KΩ were used for the actual resistive divider (as shown in Figure C.4) which led to an actual ratio of 1/103.44. In order to maintain a high accuracy of this ratio, resistors with highly accurate manufactured resistance values were chosen. These were metal foil type resistors with a small tolerance band of ±0.1%

The voltage across the voltage divider resistance R2 (which is a step down version of the phase voltage) is not referenced to ground, and may in fact be floating at hundreds of volts higher or lower than ground level. Therefore, an isolation amplifier is used to convert the voltage across R2 to a voltage referenced to ground. To achieve this an ISO122P isolation amplifier was used, together with a NMA1215S dc to dc converter, which provided a floating power supply on the high side of the isolation amplifier.

In order to provide greater digital conversion accuracy, a programmable gain amplifier was used to adjust the gain of the voltage signal. When the measured voltage is low, the gain of

the amplifier is increased so that the voltage level is made higher before the A/D converters sample it. This increases the accuracy of the measured voltage, because a low level signal is more susceptible to noise. The gain is controlled by the DSP, and is set according to the real time level of the signal. A PGA204 amplifier was used which allows the gain to be set by a 2-bit word. The control word (which is output by the DSP), the corresponding gain, and the signal levels at which they are set is shown in Table 1.

Table 1 Control Signals for Changing Gain of Programmable Gain Amplifier

Control Word	Gain	Voltages
00	1	2.5 <= V <= 5
01	2	1.25 <= V < 2.5
10	4	0.625 <= V < 1.25
11	8	0 <= V < 0.625

The circuit shown in Figure C.4 was built to implement the voltage measuring functions described above. One circuit was implemented for each motor phase.

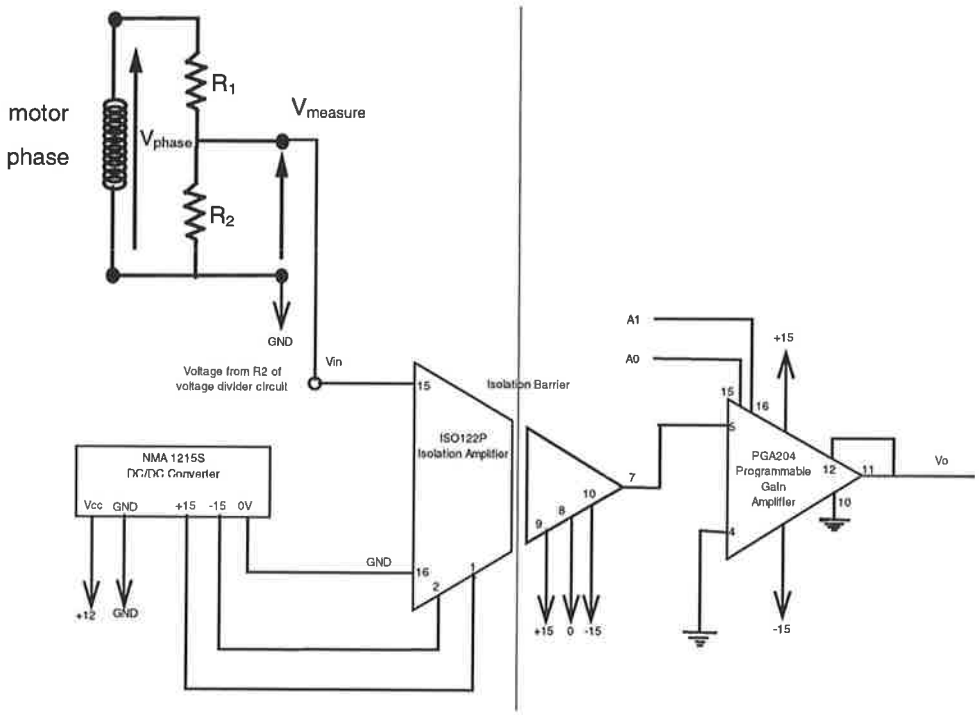


Figure C.4 Isolation circuitry for voltage measuring of one motor phase.

C.3.3 Encoder Interface

To provide an angle reference that would be used to compare the estimated angle value with a measured value, an absolute shaft encoder was attached to the shaft. The encoder provided 256 equal spaced position measurements per revolution with *Gray Code* encoding of the position value.

The encoder was interfaced to the DSP data bus at memory location 0x40000040. An eight bit three-state buffer was used to provide connection of the encoder output to the data bus, as can be seen in Figure C.5. When the DSP provided the control signals to read the encoder, the buffer would turn on its outputs, upon which the DSP would latch onto the 8 bit word provided output by the encoder.

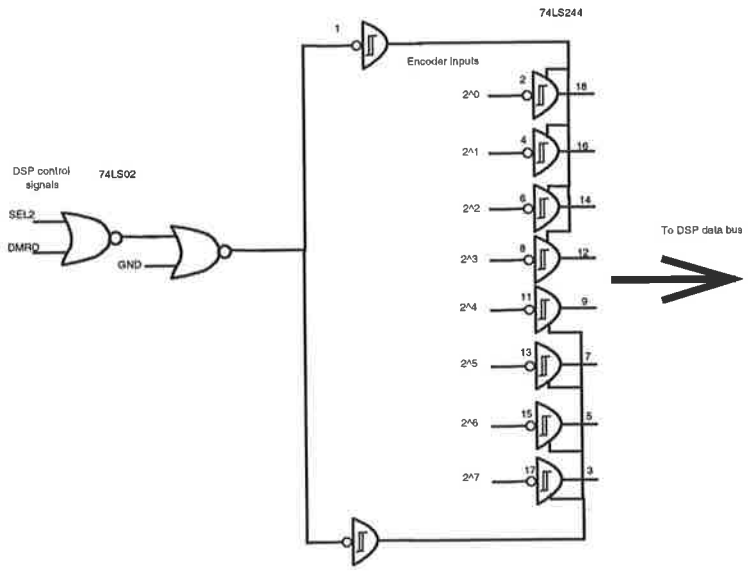


Figure C.5 Encoder to DSP interface Circuit

C.4 Power Circuits

In the above sections, the DSP control and associated circuits were detailed. These circuits act as the *controller* of the motor drive. The other main part of the drive can be termed the *power processing* side, in which the inverter processes the input high power supply voltage to an output motor voltage according to the controller's signals.

The power electronic inverter drive that is used to supply the switched reluctance motor consists of a dc supply followed by an inverter connected to the motor phases. The dc supply may be variable or fixed depending on the control strategy. However in most cases an uncontrolled diode inverter is used to provide a fixed dc supply, and therefore one was used in the developed drive.

C.4.1 Diode Rectifier

In the designed system a diode rectifier was constructed to supply dc voltage to the motor drive inverter, and the input ac voltage of the rectifier was fed from three phase ac mains via a variable step down transformer. The transformer output ac voltage was set such that the output rectified dc voltage had a value of approximately 280 V. The uncontrolled diode rectifier was designed to handle the current requirement of the motor. As more than one phase of the SR motor may be conducting at any one time, one must take this case into account when calculating the power requirements. In the actual motor used for the project,

the rating of each motor phase was 9A, and as it was a four-phase motor normally one or two phases would have positive voltage applied at any one time. Therefore considering the case that two motor phases are conducting the rated current, the rectifier must be able to supply 18A. To allow a safety margin, 30A rms rated diodes were used.

The diodes were also chosen to handle the peak voltage due to the input ac voltage. A safety factor of at least 50% over the maximum ac voltage should normally be imposed in choosing the diode blocking voltage rating.

A filter capacitance was placed between the rectifier and inverter in order to provide a smooth and stable dc voltage to the inverter. In the case of a SR motor load, there will often be a large transient current component, and therefore the capacitance must be able to supply this current without a significant decrease in the dc voltage level. This entails a large capacitance. However the capacitance must also be able to withstand the rated dc supply voltage. This often means the capacitor is an expensive part of the system design, and thus the actual capacitance value is often limited by the component cost.

Electrolytic capacitors offer a large capacitance per unit volume and are therefore most suitable for the rectifier filter. The capacitor chosen must be able to maintain the rms current that must be supplied by the capacitor. The capacitor filter bank placed after the diode rectifier will often result in transient discontinuous currents with high peak value. In order to reduce the transient peak value of the diode currents supplying the filter capacitor, an added inductor can be used together with the filter capacitor on the dc side of the rectifier, to form a low pass LC type filter. The disadvantages of this arrangement is that the filter inductance adds to the cost, size and losses of the rectifier.

Transient voltages and inrush currents can occur during the turn on of the rectifier, unless special procedures are observed. For example, if ac voltage is suddenly switched on to the rectifier using a contactor switch, and the filter capacitor is initially discharged, then a step voltage will occur across the filter capacitor. In the worst case this step voltage will be equal to the maximum line to line voltage, for a three-phase rectifier. This will lead to a large inrush current into the capacitor, which could destroy the diodes. A solution to this problem is to use a current limiting resistor on the dc side of the rectifier, which is placed between the rectifier output and the filter capacitor. This resistor is shorted out after the turn on transient using a mechanical contactor or power semiconductor device, in order to minimise the power loss of the resistor in normal operation. Other rectifier turn on methods are described in reference [223].

C.4.2 Inverter

The inverter designed and built to drive the SR motor in this project was the two switches per phase type SR motor drive. This type of circuit was previously discussed in Chapter 2. The inverter together with the rectifier, which supplies the dc voltage, is shown in Figure C.6.

The power devices used in the implemented inverter were IGBTs (International Rectifier type IRGPC40U), rated at 40A and 500V. Although the motor is only rated for an average current of 9A, the IGBTs are chosen at a higher rating to allow for current peaks which may occur during starting, braking and overloading. It is recommended by semiconductor manufacturers to allow for a 200% overload requirement in determining the peak IGBT current required for inverter drives [224].

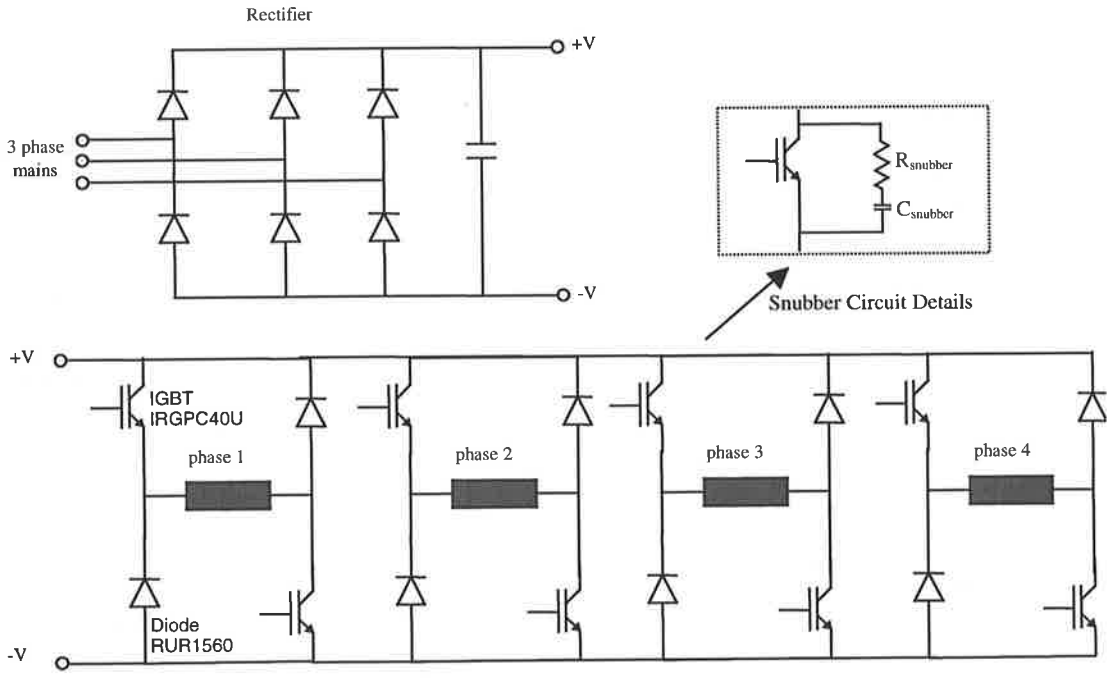


Figure C.6 Inverter and rectifier circuits for the four phase switched reluctance motor drive

IGBTs are used in the inverter due to their advantageous properties [225]. These include high switching frequency, simple voltage gate control, low on state losses, and high short circuit current capability. Therefore they are very suitable for high frequency high-power switching circuits such as in the SR motor drive.

However, due to the very high switching speeds of the IGBT devices, particular care must be taken to minimising stray inductance in the circuit. This is due to the very high di/dt values possible when the current flowing through an IGBT is interrupted when it switches off. Any

stray inductance, in combination with a large di/dt value when the IGBT turns off, will lead to a voltage spike that may be above the IGBT's rated voltage and cause the device to fail.

To examine this, consider one phase of the SR motor as shown in Figure C.7. In addition, let us consider the chopping mode of operation, where the bottom IGBT gate is biased to keep the device on, whilst the top IGBT is turned on and off with a pulsed gate drive. Each time the upper device is turned on, the current in the motor phase (i_L) will increase and will flow from the positive to the negative dc rail. However when the upper device is turned off, the current in the highly inductive motor phase cannot change instantly and thus it must circulate through the free-wheel diode (D2) of the bottom device. When the upper IGBT turns on once again the motor phase current will commutate from the free-wheel diode back to the upper IGBT and the phase current will again begin to increase.

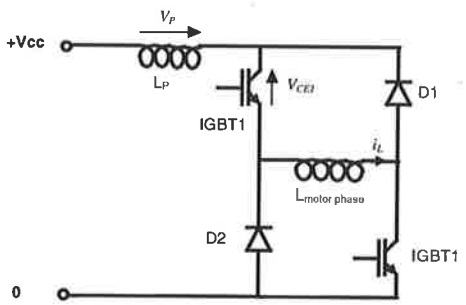


Figure C.7 One Phase of the SR motor with Stray Inductance

In an ideal circuit with no stray inductance, the voltage between the collector and emitter (V_{CE1}) of the upper IGBT when it was turned off, would increase until it had reached a value of $V_{CC}+V_D$, where V_{CC} is the dc bus voltage and V_D is the forward diode drop of the diodes. At this time the anode of D2 will be have a voltage equal to the forward bias voltage above the cathode. At this point the diode will turn on and commutate the current, which would clamp the upper IGBT voltage from increasing any further.

However real power circuits always have some parasitic leakage inductance. In Figure C.7 this is represented by a lumped inductance (L_P) which is placed between the dc supply and the upper IGBT. Although in an actual circuit the parasitic capacitance is in fact distributed throughout the power circuit, the effect is the same as the lumped parasitic inductance model. Now when the upper IGBT turns off, the inductance L_p, will resist the change in current which follows. It will develop a voltage V_P across itself such that

$$V_P = L_P \times \frac{di}{dt} \tag{C.1}$$

This voltage opposes the decrease in current through the bus, and therefore the polarity of this voltage is such that it adds to the dc bus voltage. Therefore the voltage across imposed on the upper IGBT is increased due to the parasitic inductance effect. This surge voltage can often be high enough to exceed the IGBT maximum collector-emitter voltage rating (V_{CEmax}) and cause the device to be destroyed.

Stray inductance occurs in the power supply leads and interconnection between the IGBT's and the freewheeling diodes. Snubber circuits can be used to reduce the destructive effects of the stray inductance in the power circuit. However snubber circuits have a number of significant disadvantages; they add more components that must withstand high voltages, they add to the system cost, add unnecessary complexity to the power circuit, make manufacturing more difficult, and often increase losses significantly. Therefore the priority in IGBT power circuit design should be the reduction of stray circuit inductance as a starting point, and the addition of snubber circuits should only take place when other measures have been exhausted and parasitic inductance continues to causes problems. However in the power inverter circuit developed snubber circuits were used for each power device, as seen in Figure C.6. In this circuit the RC snubber network absorbs the energy stored in the stray inductance during turn-off, and reduces the peak turn-off voltage across the IGBT.

A solution in reducing leakage inductance is to use laminated buses consisting of alternate copper plates and insulating layers [226]. This comprises a transmission line layout with very low inductance. The laminated bus bars are made wide and thin with alternating positive and negative dc rails. This topology results in the largest possible magnetic field cancellation, and thus the minimum bus inductance. The bus inductance decreases as the distance between laminated plates becomes smaller, and as the separation between the surfaces of the bus plates is made more uniform [227]. For the absolute minimum stray inductance the IGBT and dc filter capacitor connections should be bolted directly into the laminated bus structure, and the connection plates for the IGBT collector/emitters to the diode anode/cathodes should be another wide bus on the laminated stack.

In addition to the above inverter design considerations, thermal effects must be considered. During the inverter operation the IGBTs will generate heat due to conduction and switching power losses. This heat, if not removed, will produce a temperature rise in the junction of the IGBTs, which can cause failure. Therefore the inverter IGBTs must be placed on a heatsink, so that most of the generated heat is conducted away from the IGBT junction and to ensure that the junction temperature is not exceeded. To design the heatsink, the IGBT losses must first be estimated, taking into account switching and conduction losses. To calculate these losses analysis of the IGBT characteristics must be used, as well as the circuit currents and voltages [228]. It was calculated using the IRGPC40U data sheets, that the maximum IGBT loss in the inverter that was built, would be approximately 26W. To calculate the heatsink requirement from the estimated power loss one may use the thermal equation [228]:

$$R_{th_{S-A}} = \frac{\Delta T_{j-a}}{P_D} - R_{th_{J-C}} - R_{th_{C-S}} \tag{C.2}$$

where $R_{th_{S-A}}$ = heatsink to ambient thermal resistance.

$R_{th_{J-C}}$ = internal junction to case thermal resistance.

$R_{th_{C-S}}$ = case to heatsink thermal resistance.

$\frac{\Delta T_{j-a}}{P_D} = R_{J-A}$

= junction to ambient thermal resistance.

ΔT_{j-a} = temperature difference between junction and ambient.

P_D = power dissipation of IGBT.

Using the above equation it was found that the estimated heatsink requirement was one which offered a temperature rise 2° per Watt. The thermal resistances in the above equation were based on the TO-218AC package of the IGBTs that were used in the developed drive. In the built drive a higher rated heatsink was used in order to add a thermal safety factor.

C.4.3 IGBT Gate Control Circuitry

To turn the IGBTs of each phase in the developed inverter on, a +15V control signal is applied between the gate and emitter. However, a complication arises for the upper or *high side* IGBTs connected to the positive voltage bus, which are floating relative to ground. The +15V gate voltage must be supplied relative to the emitter, which due to the IGBT rating could be up to 500 volts above ground. However, the gate voltage must be controllable from the microprocessor logic, which is referenced to ground. Therefore, level shifting of the logic control signal is required, from ground level to the voltage of the high side IGBT emitter, which swings between the two dc rails.

There are many different ways of overcoming the above problem. An efficient method is to use a single IC chip high and low side gate driver (such as the International Rectifier IR2110). This IC provides the necessary gate signals for a both a *high* side and *low* side IGBT at its outputs, whilst its inputs are ground referenced logic level signals and so are easily compatible with a microprocessor control system.

With this single chip solution, an external floating supply is needed to provide the voltage for the high side floating output of the IR2110 that drives the upper IGBT. To provide the high side supply, the bootstrap technique may be used. With reference to Figure C.8, a diode and bootstrap capacitor is connected to the ground referenced +15V supply. When the IGBT emitter has been pulled down to the 0V rail (which occurs at any time the freewheeling diode conducts), the bootstrap capacitor is charged via the diode to approximately +15V minus the diode conduction voltage drop.

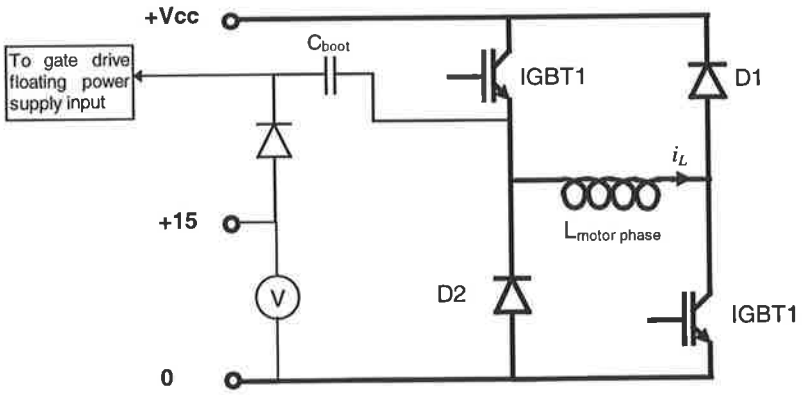


Figure C.8 Bootstrap Method

However, a number of disadvantages lead from the bootstrap floating supply method in inverter applications, such as:

The on time of the high side IGBT is limited by the discharging time of the bootstrap capacitor. This is because the voltage on the capacitor decreases at any time the IGBT gate voltage is high, due to the quiescent current of the high side channel.

There is a minimum time the high side IGBT must be pulled down to ground voltage in each switching cycle. This is due to the finite charging time of the bootstrap capacitor when it is being refreshed via the diode. This problem can be more severe in the switched reluctance motor drive than other motor inverters. This is because the conduction time of the freewheeling diodes (which pulls the high side IGBT to ground level) is highly varying, and dependent on the motor currents at turn off. In the SR drive, the bootstrap capacitor can only be charged when the freewheeling diodes conduct. If this diode conduction time is short for some motor operating conditions, the bootstrap capacitor will not have its voltage refreshed.

Another problem particular to the SR motor drive is that at turn on the high side IGBT is not referenced to ground. Therefore, some external means of pulling the high side device to ground must be found so that the bootstrap capacitor may be charged at turn on.

To overcome these problems a simpler, but more cost and space expensive solution, was used in the developed drive of this thesis. This involved the use of separate floating +15V supplies for each high side IGBT. In this way the above limitations were overcome. The IR2110 based gate driver circuit with separate floating gate drive supplies is shown in Figure C.9. In this circuit the ground referenced IGBT switching logic signals are input to the IR2110 driver, which then provides the necessary IGBT gate signals on the high power side.

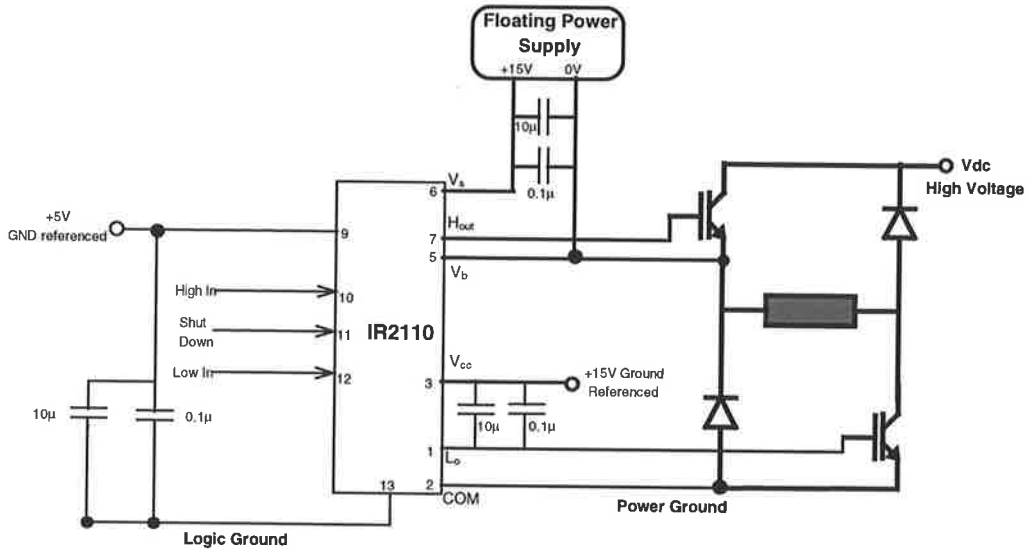


Figure C.9 Gate Drive Circuitry

As explained previously, the control signal for each IGBT is produced by the DSP according to the control algorithm. The eight IGBT gate drive DSP control signals are generated with an eight-bit word that is output onto the DSP data bus. The data bus is buffered with eight tri-state D flip-flops that are controlled by DSP control signals. To provide high galvanic isolation between the power circuit and the DSP circuits, opto-isolators are used on each of the eight digital outputs before being fed to the IR2110 gate driver. This opto-isolation is in addition to the isolation supplied by the gate driver, and thus ensures very high electrical isolation. The interface circuits between the DSP and gate drivers are shown in Figure C.10 for one IGBT gate.

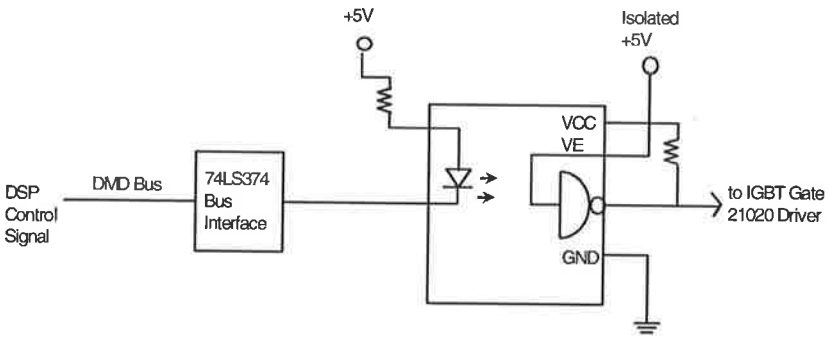


Figure C.10 Isolated IGBT Gate Drive Interface.

Appendix D: Prediction Algorithm Operation in Initial Startup Region

In this Appendix, the operation of the prediction algorithm that was discussed in Chapter 5, will be further examined. In particular, the operation of the algorithm during the initial startup period will be detailed, in order to explain the conditions under which the algorithm can operate without an error occurring during this period. The exceptional conditions in which the algorithm can fail, even for ideal operating conditions and noise free input data, will also be examined.

In Figure 5.11 (c), it can was seen that there were four iterations in the initial start up period when the angle prediction failed, and the output defaulted to zero. However, in all other iterations there was an accurate angle prediction made by the prediction algorithm. The question may arise as to why the angle predictors could not make a prediction at these four iterations, when at all other times the predictions were relatively error free. To answer this question, it is instructive to consider in detail the learning and prediction process in the initial period after startup because this is the period in which the errors occur in the results shown in Figure 5.11 (c). The analysis of the learning and prediction process will give an insight into the ways in which the algorithm can fail.

Immediately after startup, there are no predictive rules, and thus there is no stored knowledge base for the flux linkage and angle predictors. Therefore, in the initial stage it could be reasonably expected that the predictors would have a very poor performance, and not be able to make any prediction for some time after startup. However, it will be shown below that the prediction algorithm can operate in the critical initial startup time, even without any stored rules, due to the following points:

(i) The input data to the predictors, which is the previous and present values of flux linkage and angle, are mapped onto fuzzy set domains. These fuzzy sets are then used to produce a rule relating previous and past values on the fuzzy logic rule base.

(ii) When making a prediction, the input crisp data of previous values is mapped onto the fuzzy domain. Each crisp value will normally be placed onto two fuzzy sets in this process.

(iii) As detailed in Section 5.3.1, each rule has four inputs and therefore the input data will normally trigger 2^4 =16 rules relating previous values with future values. The nonlinear combination using defuzzification will produce a discrete predicted value.

To show why the above three points lead to the prediction algorithm being able to operate in the initial startup time even without any stored rules, consider the following example. The case of the flux linkage and angle prediction has the same principles, and therefore a

general case is considered for the prediction of an arbitrary input signal x when the prediction algorithm has no stored rules. In this example the crisp data input values are:

$x(k-4) = x1$
$x(k-3) = x2$
$x(k-2) = x3$
$x(k-1) = x4$
$x(k) = x5$

Where $x(k-4)....x(k)$ represent the present and previous four iterations values (of flux linkage or angle).

In the first stage of the prediction algorithm, the previous and present values are used to make a predictive fuzzy rule that is placed on the knowledge base of the fuzzy predictor. As it can be recalled from Chapter 5, during the rule making process, the input values of the input/output data pair $(x1,x2,x3,x4)$ and the output value of the data pair $(x5)$ are mapped on to the corresponding fuzzy sets in which the crisp values have the highest membership degree.

Let us assume that the input/output data pair values are mapped onto the following fuzzy sets in the input/output fuzzy domains:

$x1 \rightarrow Fa$
$x2 \rightarrow Fb$
$x3 \rightarrow Fc$
$x4 \rightarrow Fd$
$x5 \rightarrow Fe$

Where $Fa...Fe$ are fuzzy sets in the input/output fuzzy domain.

In this case, the following fuzzy rule will be created and stored on the knowledge base:

$$If\ x(k-3)\ \text{is}\ Fa\ And\ x(k-2)\ \text{is}\ Fb\ And\ x(k-1)\ \text{is}\ Fc\ And\ x(k)\ \text{is}\ Fd\ Then\ x(k+1)\ \text{is}\ Fe \qquad (1)$$

The next step of the process is the prediction phase. In the prediction phase the inputs $x(k-3) = x2$, $x(k-2) = x3$, $x(k-1) = x4$, and $x(k) = x5$ are used to predict $x(k+1)$.

Now, it may be expected that, because during the initial phase there is no rule stored on the rule base that defines a rule from the crisp inputs of $x2$, $x3$, $x4$, $x5$, that the prediction will fail. However, in general, a prediction can be made even if there are no previously

stored rules. This is due to the fact that the crisp values of *x2, x3, x4, x5* will normally belong to two fuzzy sets. (This is because as it can be recalled from Figure 4.10, that there is a 50% overlap in the triangular fuzzy sets which define the fuzzy regions in the planes of flux linkage, angle, and current).

If the case is taken that the rotor is moving in a positive direction, and therefore the angles are increasing with time, then the following will apply:

$$x5 > x4 > x3 > x2 \tag{2}$$

As mentioned previously, each crisp value can be a value of two adjacent sets, for example:

$$\begin{aligned} &x2 \text{ is a member of } Fa \text{ and } Fb \\ &x3 \text{ is a member of } Fb \text{ and } Fc \\ &x4 \text{ is a member of } Fc \text{ and } Fd \\ &x5 \text{ is a member of } Fd \text{ and } Fe \end{aligned} \tag{3}$$

This will trigger 16 rules, one of which will have the precedent:

$$If\ x(k\text{-}3) \text{ is } Fa\ And\ x(k\text{-}2) \text{ is } Fb\ And\ x(k\text{-}1) \text{ is } Fc\ AND\ x(k) \text{ is } Fd \tag{4}$$

Assuming that none of the other 15 rules have a corresponding output stored on the fuzzy rule base, this will be the only rule that produces an output. From (1), the resultant fuzzy output will be

$$x(k+1) = Fe \tag{5}$$

The fuzzy set Fe will then be defuzzified to give a crisp value x_e. Note that as the defuzzification of the single triangular fuzzy set Fe will be at the center value of the set (according to the center average defuzzification rules), the value x_e will not necessarily equal $x5$ even though $x5$ is a member of the fuzzy set Fe.

Thus, in general even in the initial startup case when no rules are stored a prediction can be made from the rule which is immediately stored from the latest measured values in the learning step (the accuracy of this prediction will in general be higher as the iteration number increases when previously stored rules can also be used). However, the following conditions must be satisfied to allow the above conditions to hold in order that a

prediction can be made, and for the predicted value in the initial stage to have a small error:

Condition 1: The change in angle between each iteration must be small. This is in order for the crisp values of each iteration to be a member of one common fuzzy set with the previous iteration's crisp value (as was detailed in (3)).

This condition is generally satisfied if the following holds:

(a) The algorithm iteration period is in general much smaller than the mechanical cycle variation period.

(b) The level of noise and error in the angle and prediction estimates is low.

At very high speeds the condition (a) may not hold. However, during the starting operation period (when the critical condition of no rules being stored occurs), the rotor speed is generally zero, and therefore initially the variations between each iteration will be relatively small. However it was seen in the thesis that starting the algorithm during non-zero speed was also possible.

If there is random noise in the flux linkage and angle estimates, the crisp angle values between iterations may be mapped onto random non-adjacent fuzzy sets. This will mean that no prediction will be able to be made if (b) does not hold.

However, even in the ideal theoretical case, for a smooth running system with no errors in the flux linkage or angle estimates, the following condition must also hold, otherwise there will be a failure in the prediction algorithm (output will be zero),

Condition 2: The present value (e.g. x5 in the above analysis) must not have a membership of 1 in a corresponding fuzzy set, as this will mean that the value is a member of one fuzzy set only.

The reason that this condition must be satisfied can be seen by considering the example given in (3). If in this example $x5$ has a membership of 1 in Fe and thus zero membership in all other fuzzy sets, then the rule seen in (4) will not be triggered. This will mean in that no prediction can be made and the prediction algorithm will fail.

Note that due to round-off errors in the digital implementation of the algorithm, the value of $x5$ does not need to have exactly a membership of 1 for failure of the algorithm to occur. Therefore, even for a seemingly smooth running system, the algorithm may fail, particularly in the start-up region.

Although the above condition explains why there may be an error even in the ideal case of no flux or angle estimation errors, it should be also be noted that (as can be seen in Figure 5.12), even in the ideal simulation case that there are errors in the flux linkage and angle estimates. These are due to:

i) erroneous outputs from the fuzzy model due to errors in the fuzzy model

ii) integration errors in the flux linkage estimation due to time and amplitude quantisation of the voltage and current

iii) erroneous outputs from the fuzzy predictors which correspondingly lead to estimation errors

iv) finite number of sets in the input/output domains of the fuzzy model

Therefore these errors may also at some instances of time lead to the case that two consecutive angle estimates will not have a common adjacent fuzzy set and Condition 1 will not hold.

Appendix E: Further Details on Random Angle Estimation Error

In this Appendix, the appearance of random angle estimation error in the constant flux linkage offset tests in Section 7.5 will be explained. This test is examined in detail in this Appendix, because it may be expected that for a constant input flux error there will be relatively constant output angle estimation error. Although the discussion is aimed at explaining the random angle estimation variations for the constant flux linkage offset tests, the explanations can also be applied in explaining the appearance of seemingly random angle estimation errors in the other results presented in Chapter 6 and 7.

To explain the relatively random angle estimation error in the constant flux linkage offset tests, it should firstly be noted that a constant flux linkage error in each of the phases will have a different effect at each point in time. This is because the *relative* error of the constant flux linkage error is higher in any particular phase when the flux linkage of that phase has lower amplitude, as opposed to when it has higher amplitude.

Therefore the *percentage* error of the input flux linkage value (which is input to the rotor position estimation algorithm fuzzy motor model), is continuously changing in each motor phase relative to the actual flux linkage value. In the test shown in Section 7.5, the chopping mode was deliberately chosen, as it is more susceptible to integration errors. This means that the actual flux linkage amplitude in a given phase will have fast-time varying components. Thus, the relative error of the flux linkage input due to a constant offset will also have fast time variation.

It is also found in Section 7.7 that the actual effect on the rotor position estimate of a flux linkage error is dependant on the instantaneous value of the phase current and rotor position, as well as the flux linkage amplitude value. Hence, as the chopping mode is used in this test, the actual effect of the error in the flux linkage will have fast time varying changes, due to the above mentioned fast time varying changes in flux linkage and current, as well as the slower time varying changes due to the change in the rotor position.

It can also be recalled from Section 5.3.3 that the optimal phase selector gives a confidence weighting to each phase that is conducting current. The current in each phase in the chopping mode is rapidly varying. This means that the confidence given to each phase will also be time-varying. At any two points in time, the combination of current amplitude values will be different and thus the confidence weightings will also be different. Therefore, the final error value will depend on the time changing confidence values, as well as the time changing error in the position estimate in each of the phases.

Additionally, as detailed in this thesis (especially section 6.14), the fuzzy logic predictors will have varying levels of accuracy according to the accuracy of the developed rules, number of iterations, and complexity of the waveforms.

Finally, it can be recalled that before the addition of the flux linkage offset error to the flux linkage waveforms, there are already errors. These are due to errors in the experimentally measured values of current and voltage from noise and measurement error. Also, there are errors in the original estimated flux linkage waveform due to measurement noise and errors in the current and voltage, in addition to time and amplitude quantisation errors, and trapezoidal integration error. Hence at any given instant of time, the inherent estimation error (before the effect of flux offset is taken into account) can be highly variable.

Therefore, considering the above error producing effects, it may be expected that the actual angle estimation error in each of the phases at any given instant of time may have some time-variation. In addition, each of the angle estimates from each of the conducting phases is combined in a non-linear manner (by the phase selector). Hence, the final estimation error will also be time-varying in nature.

The apparent randomness occurs due to the combination of all the above error producing effects. Due to the complexity of the system component's interaction, and the randomness of the inherent measured noise and error, it is difficult to mathematically define the actual noise at any instant of time.

References

1. Byrne J.V., O'Dwyer J.B., McMullin, M.F., 'A High Performance Variable Reluctance Drive: A New Brushless Serve', PCIM, February 1986, pp. 60-66.
2. Byrne J.V., McMullin M.F., 'Design of a Reluctance Motor as a 10kW Spindle Drive', MOTOR-CON Proc., Geneva, September 1982, pp. 10-24.
3. Noad H.M., 'A Manual of Electricity', Lockwood, London, 1859, pp. 674-684.
4. "PWM Inverter Controller methods – current direction of field", Publication no. 635, The Institute of Electrical Engineers Japan, pp. 80, May 1997. (in Japanese)
5. Barrass P. G., Mecrow B. C., Clothier A. C., "The Unipolar Operation of Fully Pitched Winding Switched Reluctance Drives", Int. Conf. Elec. Machines ICEM'94, pp. 71-76, 1994.
6. Miller T. J. E., Jahns T. M., "A Current-Controlled Switched Reluctance Drive for FHP Applications", Conference on Applied Motion and Control, Minneapolis, pp. 109-117, June 1986.
7. Materu, P. Krishnan R., "Estimation of Switched Reluctance Motor Losses", IEEE IAS Proceedings, Pittsburgh, pp. 176-187, October 1988.
8. Ferreira C. A., Richter, E. "Detailed Design of a 250 kW Switched Reluctance Starter/Generator for an Aircraft Engine", SAE 1993 Transaction, vol. 102, Journal of Aerospace, Section 1, pp. 289-300.
9. Miller, T. J., "Switched Reluctance Drives", PCIM Ref. Series – Switched Reluctance Drives, Intertec, Ventura California, pp. 1-71, 1988.
10. PWM Inverter Report, IEE Japan, No. 635, pp. 70-81, May 1997 (in Japanese).
11. Richter E., "Switched Reluctance Machines for High Performance – A Review Paper", Int. Conf. Elec. Machines, pp. 18-24, 1990.
12. Miller T.J., 'Brushless Reluctance Motor Drives', IEE Power Eng. Journal, Vol. 1, No. 1, November 1987, pp. 325-331.
13. Sudgen D.M., Blake R.J., Randall S.P., Stephenson, J.M., Lawrenson, P.J., 'High Performance MOSFET Switched Reluctance Motor Drives', IEEE Industry Applications Society Annual Meeting, Atlanta, October 1987
14. Hsu J. S., Liou S. P., Woodson H. H., "Comparison of the nature of torque production in reluctance and induction machines", IEEE Trans. Energy Conv., vol. 5, no. 2, June 1990, pp. 304-309.
15. Moghbelli H. H., Adams G. E., Hoft R. G., "Prediction of the Instantaneous and Steady State Torque of the Switched Reluctance Motor using the Finite Element Method (FEM)", IEEE IAS Annual Meeting, pp. 59-70, 1988.
16. Steiert U., Spath H., 'Torque Control of the Doubly-Salient Reluctance Motor', ETEP, Vol. 3, No. 4, pp. 265-272, July/August 1993.
17. Jiang, Y., Ekstrom, A., "General Analysis of Harmonic Transfer Through Converter", IEEE Trans. Power Elec., vol. 12, no. 2, pp. 287-293.
18. Camerorn D.E., Lang J.H., Umans S.D., 'The Origin and Reduction of Acoustic Noise in Doubly Salient Variable-Reluctance Motors', IEEE Trans. Ind. Appl., Vol. 28, No. 6, pp. 1250-1255, Nov./Dec., 1992.

19.Wu C., Pollock C., 'Analysis and Reduction of Vibration and Acoustic Noise in the Switched Reluctance Drive', IEEE Trans. Ind. Appl., Vol. 31, No. 1, pp. 91-99, Nov./Dec. 1995.

20.Hendershot J. R., "Application of SR Drives", IEEE IAS Tutorial on Switched Reluctance Drives, pp. 60-90, 1990.

21.Lawrenson P.J., 'Switched Reluctance Drives - A Fast-Growing technology', Electric Drives and Control, April/May 1995.

22.Whiting J. M. W., Taufiq J. A., "Recent Development and future trends in traction propulsion drives", Int. Conf. Elec. Machines, pp. 195-199, 1992.

23.Miller, *Brushless Permanent-Magnet and Reluctance Motor Drives*, Oxford, U.K., 1989.

24.Lawrenson P.J., 'Switched Reluctance Motor Drives', Electronics and Power, pp. 144-147, Feb. 1983.

25.Grondona L., 'SR motors from Italy', PCIM Europe, pp. 18-19, Jan./Feb. 1994.

26.West J.G.W., 'DC, induction, reluctance and PM motors for electric vehicles', Power Engineering Journal, pp. 77-88, April 1994.

27.Richter E., 'Switched reluctance machines for high performance operations in a harsh environment - a review paper', Int. Conf. Electrical machines (ICEM '90), Part 1, , pp. 18-24, Aug. 1990.

28.Ferreira A. C., Jones S. R., Dragner B. T., Heglund W. S., 'Design and implementation of a five-hp switched reluctance, fuel-lube, pump motor drive for a gas turbine engine', IEEE Trans. Power Electronics, Vol 10, No. 1, pp. 55-60, Jan. 1995.

29.Hendershot J. R., 'Application of SR drives', Switched Reluctance Drives Tutorial, IEEE Industry Applications Society Conference, 25th IAS Annual Meeting, Seattle, pp. 60-90, Oct. 1992.

30.Lawrenson P. J., "Switched Reluctance Drives – A Fast Growing Technology", Electric Drives and Controls, April/May 1985.

31.Goel P.K., Cushing I., 'Direct-drive SR motor outperforms geared systems in robotics', Power Conversion and Intelligent motion, pp. 52-55, Feb 1989.

32.Compter J.C., 'Microprocessor-controlled Single Phase Reluctance Motor', Drives/Motors/Controls, Brighton, pp. 64-68, 1994.

33.Chatratana S., Bolton H.R., Pedder D.A.G., 'Investigations into a small single-phase switched reluctance motor', IEE Proc. B, Vol. 131, 1984, pp. 51-60.

34.Lawrenson P.J., Stephenson J.M., Blenkinsop P.T., Corda J., and Fulton N.N.: "Variable-speed switched reluctance motors', Proc. IEE Pt. B, 1980, 127, pp 253-265

35.Finch J.W., Harris M.R., Musoke A., Metwally H.M.B., 'Variable Speed Drives Using Multi-tooth per Pole Switched Reluctance Motors', Incremental Motion Control Systems Society Symposium, University of Illinois, 1994, pp. 293-302.

36.Miller T.J.E., 'Switched Reluctance Motors and Their Control', Clarandon Press, Oxford, 1993.

37."IGCTs – Megawatt power switches for medium voltage applications", ABB Review, pp. 12-17, 3/1997.

38.Pollock C., Williams B.W., 'Power converter circuits for switched reluctance motors with the minimum amount of switched', IEE Proc. Pt B., 1990, 137, (6), pp. 373-384.

39.Ray W.F., Davis R.M., 'Inverter drive for salient reluctance motor; its fundamental behaviour, linear analysis, and cost implications', IEE Proc. Electric power Applications, 1979,2,(6), pp. 185-193.

40.Davis R.M., Ray W.F., Balke R.J., 'Inverter drive for switched reluctance motor: circuits and component ratings', Proc IEE Pt. B, 1981, 128, (2), pp. 126-136.

41.Byrne J.V., Lacy J.G., 'Characteristics of saturable stepper and reluctance motors', Small Electrical Machines IEE Conf. Publ. 136, 1976, pp. 93-96.

42.Byrne J.V., 'Tangential Forces on overlapped pole geometries incorporating ideally saturated materials', IEEE Trans. Mag., Vol. MAG-8, No. 1, March 1972, pp. 2-9.

43.Stephenson J.M., El-Khazendar M.A., 'Saturation in Doubly-Salient Reluctance Motors', Proc. IEE, Vol. 136, Pt. B, No. 1, January 1989, pp. 50-58.

44.Pulle D. W. J., "New data base for switched reluctance drive simulation", IEE Proc. B, vol. 138, no. 6, pp. 331-336, Nov. 1991.

45.Stephenson J. M., Corda J., "Computation of torque and current in doubly salient reluctance motors from nonlinear magnetisation data", Proc. IEE., vol. 126, no. 5, PP. 393-396, May 1979

46.Bose B.K., Miller T.J.E., Szczensny P.M., Bicknell W.H., 'Microcomputer control of switched reluctance motor', IEEE Trans. Industry Applications, 1986, Vol. 22, pp. 708-715.

47.Pulle D. W. J., Petersen I. R., "A generalised approach to torque and current computation in switched reluctance motors", EPE97, pp. 3.547-3.551, 1997

48.Torrey D. A., Lang J. H., "Optimal-efficiency excitation of variable-reluctance motor drives", IEE. Proc. B, vol. 138, no. 1, pp. 1-14, Jan. 1991.

49.Ilic-Spong M., Marino R., Peresada S.M., Taylor, D.G., 'Feedback linearizing control of switched reluctance motors', IEEE Trans. Automatic Control, Vol, AC-32, No. 5, 1987, pp. 371-379.

50.Taylor D.G., 'An Experimental Study on Composite Control of Switched Reluctance Motors', IEEE Control Systems, February 1991, pp. 31-36.

51.Buja G.S., Valla M.I., 'Control Characteristics of the SRM Drives. Part II: Operation in the Saturated Region', IEEE Trans. Industrial Electronics, Vol. 41, No. 3, 1994, pp. 316-325.

52.Haiqing Y., Panda S.K., Chii L.Y., 'Performance Comparison of Sliding Mode Control with PI Control for Four-quadrant Operation of Switched Reluctance Motors', 1996 International Conference on Power Electronics, Drives and Emergy Systems For Industrial Growth, New Delhi , pp. 381-387, Jan 1996.

53.Kavanagh R.C., Murphy J.M.D., Egan M.G., 'Torque ripple Minimisation in Switched Reluctance Drives using Self Learning Techniques', IECON'91, Kobe, Japan, October 28-Nov 1, 1991, pp. 289-294.

54.Ray D.S., Green T.C., Williams B.W., 'Neural networks used for torque ripple minimisation from a switched reluctance motor', IEE fifth Eur. Conf. Power Electronics and Applications, 1993, pp. 1-6.

55.Ismail F., Wahsh S., Mohomed A., Elsimary H., 'Optimal control of variable reluctance motor by neural network', IEEE Int. Symp. Industrial electronics, June 1-3, 1993, pp. 301-4.

56.Sharma V.K., Singh B., Murthy S.S., Chandra A., Al-Haddad K., 'Performance analysis of fuzzy logic based speed controller for switched reluctance motor drive', pp. 373-380, 1996 International Conference on Power Electronics, Drives and Emergy Systems For Industrial Growth, New Delhi , Jan 1996.

57.Bolognani S., Zigliotto M., "Fuzzy Logic Control of a Switched Reluctance Motor Drive", IEEE Trans. Ind. Appl., vol. 32, no. 5, pp. 1063-1068, 1996.

58.Reay D.S., Mirkazemi-Moud M., Green T.C., Williams B.W., 'Switched Reluctance Motor Control Via Fuzzy Adaptive Systems', IEEE Control Systems, Vol. 15, No. 5, 1995, pp. 8-15

59.MacMinn S.R., 'Control of the Switched Reluctance Machine', Switched Reluctance Drives Tutorial, IEEE Industry Applications Society Conference, 25th IAS Annual Meeting, Seattle, October 12, pp. 36-59.

60.Robinson D. T., "Absolute Inductive Position Transducer Offers High-Speed Operation", PCIM magazine, pp. 20- 27, Feb. 1997.

61.Orlosky S., "Design Optical Encoder Interfaces for Optimum Performance", PCIM magazine, pp. 62-68, May 1996.

62. MacMinn S.R., 'Control of the switched reluctance machine', Switched Reluctance Drives Tutorial Course, IEEE Industry Applications Society Annual Meeting, 1990, pp. 44-45.

63. Lee P.W., and Pollock C., 'Rotor position detection techniques for permanent-magnet and reluctance motor drives', Conf. Rec. IEEE Industry Applications Society Annual Meeting, 1992, pp. 448-455.

64. Ertugrul, N. and Acarnley, P.: 'A new algorithm for sensorless operation of permanent magnet motors', IEEE Trans., 1994, IA-1, pp. 126-133

65. Acarnley P.P., Hill R.J., Hooper C.W., 'Detection of rotor position in stepping and switched reluctance motors by monitoring of current waveforms'. IEEE Trans., 1985, IE-32, pp. 215-222.

66. Dunlop G.R., and Marvelly J.D.: 'Evaluation of self commutated switched reluctance motor', Proc. Electrical Energy Conference, Adelaide, 1987, pp. 317-320.

67. Egan M. G., Harrington M. B., Murphy J. M. B. "PWM-based position sensorless control of variable reluctance motor drives", 4th EPE Conf. Proc.., Florence, 1991, Vol. 4, pp. 24-29

68. Ray W. F., Al-Bahadly I.H. "Sensorless methods for determining the rotor position of switched reluctance motors", 5th EPE Conf. Proc., Brighton, 1993, Vol. 6, pp. 7-13.

69. Harris, W.D., and Lang, J.H.: 'A simple motion estimator for variable-reluctance motors', IEEE Trans., 1990, IA-26, pp. 237-243

70. MacMinn, S.R., Rzesos, W.J., Szczesny, P.M., and Jahns, T.M.: 'Application of sensor integration techniques to switched reluctance motor drives', Conf. Rec IEEE Industry Applications Society Annual Meeting, 1988, pp. 584-588

71. Mvungi, N.H., Lahoud, M.A., and Stephenson, J.M.: 'A new sensorless position detector for SR drives', IEE Proc. fourth Int. Conf. Power Electronics and Variable Speed Drives, 1990, pp. 249-252

72. Mvungi N.H., and Stephenson J.M., 'Accurate sensorless rotor position detection in an SR motor', EPE Conf. Proc., 1991, pp. 390-393.

73. Ehsani M., Husain, I., and Kulkarni A.B., 'Elimination of discrete position sensor and current sensor in switched reluctance motor drives', IEEE Trans., 1992, IA-28, pp. 128-135.

74. Ehsani M., Husain I., and Ramani K.R., 'An analysis of the error in indirect rotor position sensing of switched reluctance motors', IEEE Int. Conf. Industrial Electronics, Control and Instrumentation, 1991, pp. 295-300.

75. Ehsani M., Mahajan S., Ramani K.R, and Husain I., 'New modulation encoding techniques for indirect rotor position sensing in switched reluctance motors', Conf. Rec. IEEE Industry Applications Society Annual Meeting, 1992, pp. 430-438.

76. Ehsani M., Mahajan S., Ramani K.R, and Husain I., 'New modulation encoding techniques for indirect rotor position sensing in switched reluctance motors', Conf. Rec. IEEE Industry Applications Society Annual Meeting, 1992, pp. 430-438.

77. Laurent P., Gabsi M., Multon B., "Sensorless rotor position analysis using resonant method for switched reluctance motors", IEEE IAS Annual Meeting, 1993, pp. 687-694.

78. Panda S.K., and Amaratunga G.A.J., 'Waveform detection technique for indirect rotor-position sensing of switched-reluctance motor drives. Part 1: Analysis', IEE Proc. Pt. B., 1993, 141, (1), pp. 80-88.

79. Panda S.K., and Amaratunga G.A.J., 'Waveform detection technique for indirect rotor-position sensing of switched-reluctance motor drives. Part 2: Experimental results', IEE Proc. Pt. B., 1993, 141, (1), pp. 89-96.

80. Panda S.K., and Amaratunga G.A.J., 'Analysis of the waveform detection technique for indirect rotor position sensing of switched-reluctance motor drives', IEEE Trans., 1991, EC-6, pp. 476-483.

81. Ehsani M., and Husain I., 'Rotor position sensing in switched reluctance drives by measuring mutually induced voltages', Conf. Rec. IEEE Industry Applications Society Annual Meeting, 1992, pp. 422-429.

82. Preston M. A., Lyons J. P., "A Switched Reluctance Motor Model with Mutual Coupling and Multi-Phase Excitation", IEEE Trans. Magnetics, Vol. 27, No. 6, Nov. 1991, pp. 5423-5425.

83. Davis R. M., Al-Bahadly I., "Experimental Evaluation of Mutual Inductances in a Switched Reluctance Motor", IEE Conf. No. 324, 1990, pp. 243-248.

84. Lyons J.P., MacMinn S.R., and Preston M.A., 'Flux/current methods for SR MOTOR rotor position information', Conf. Rec. IEEE Industry Applications Society Annual Meeting, 1991, pp. 482-487.

85. Ferreira C. A., Jones S. R., Dragner B. T., Heglund W. S., "Design and Implementation of a Five-hp, Switched Reluctance, Fuel-Lube, Pump Motor Drive for a Gas Turbine", IEEE Trans. Power Elec., Vol. 10, No. 1, Jan. 1995, pp. 55-60.

86. Jones S. R., Dragner B. T., "Performance of a High Speed Switched Reluctance Starter/Generator System Using Electronic Position Sensing", 1995, pp. 246-253.

87. Ray, W.F and Al-Bahadly, I.H.: 'A sensorless method for determining rotor position for switched reluctance motors', IEE Proc. Fifth Int. Conf. Power Electronics and Variable Speed Drives, 1994 pp. 13-17

88. Luenberger D. G., "An Introduction to Observers", IEEE Trans. On Automatic Control, Vol. AC-16, No. 6, Dec. 1971, pp. 171-176.

89. Jansen P. L., Lorenz R. D., "A Physical Insightful Approach to the Design and Accuracy Assesment of Flux Observers for Field Oriented Induction Motor Drives", IEEE Trans. Ind. Appl., Vol. 30, No. 1, Jan./Feb. 1994, pp. 101-110.

90. Lumbsdaine A. and Lang J.H.: 'State observers for variable reluctance motors', IEEE Trans., 1990, IE-37, pp. 133-142.

91. Elmas, C., Zelaya-De La Parra, H., "Position sensorless operation of a switched reluctance drive based on observer", IEE EPE Conf. Proc., pp. 82-87, 1993.

92. Husain I., Sodhi S., Ehsani M., 'A Sliding Mode Observer Based Controller for Switched Reluctance Motor Drives', IEEE Industry Applications Society Annual Meeting, 1994, pp. 635-642.

93. Misawa E. A., Hedrick J. K., "Nonlinear Observers: A State of the art Survey", ASME J. Dyn. Syst. and Meas., Vol. 111, No. 3, 1979, pp. 344-352.

94. Zadeh L.A., "Fuzzy sets," Information and Control, vol. 8, pp. 338-353, 1965.

95. Mandani E.H., 'Twenty Years of Fuzzy Control: Experiences Gained and Lessons Learnt', IEEE International Conference on Fuzzy Systems (FUZZ-IEEE), 1993, pp. 339-344.

96. Marks R.J., 'Intelligence: Artificial versus Computational', IEEE Trans. Neural Networks, September 1993

97. C.C. Lee, "Fuzzy logic in control systems: fuzzy logic controller, Part I," IEEE Trans. Syst. Man and Cybernetics, vol 20, pp. 404-418, Mar./April 1990

98. C.C. Lee, "Fuzzy logic in control systems: fuzzy logic controller, Part II," IEEE Trans. Syst. Man and Cybernetics, vol 20, pp. 419-435, Mar./April 1990

99. Zadeh L.A., 'Fuzzy Logic = Computing with Words', IEEE Trans. on Fuzzy Systems, Vol. 4, No. 2, May 1996, pp. 103-111.

100. Yen J., Langari R., Zadeh L.A., "Industrial Applications of Fuzzy Logic and Intelligent Systems", IEEE Press, Piscatway, 1995.

101. Gilberto C.D., Sousa, Bose B.K., "A fuzzy set theory based control of a phase controlled converter dc machine drive", IEEE Trans. Industry Applications, vol. 30, no. 1, Jan/Feb. 1994.

102. Rao D.H., Saraf S.S., "Study of Defuzzification methods of fuzzy logic controller for speed control of dc motor", 1996 International Conference on Power Electronics, Drives and Emergy Systems For Industrial Growth, New Delhi , Jan 1996.

103. Grabowski P. Z., "Direct Torque Neuro-Fuzzy Control of Induction Motor Drives", IEEE IECON'97, New Orleans, pp. 557-562, Nov. 1997.

104. Mir S.A., Zinger D.S., Elbuluk M.E., "Fuzzy controller for inverter fed induction machines", IEEE Trans. Industry Applications, vol. 30, no. 1, Jan/Feb. 1994.

105. Ta-Cao M., Le-Huy, H., "Model Reference Adaptive Fuzzy Controller and Fuzzy Estimator for High Performance Induction Motor Drives", IEEE IAS Annual Meeting, 1996, Vol. 1, pp. 380-387

106. Johnson J. P., Rahman K. M., Ehsani M., "Application of a Clustering Adaptive Fuzzy Logic Controller in a Brushless DC Drive", IEEE IECON'97, New Orleans, pp. 1001-1005, Nov. 1997.

107. Abut N., Cakir N., Inanc A. B., Yildiz M., Bilgin M., "Switched Reluctance Motor Drive by Using Fuzzy Controller", IEEE IECON'97, New Orleans, pp. 348-353, Nov. 1997.

108. Sharma V.K., Singh B., Murthy S.S., Chandra A., Al-Haddad K., "Performance analysis of fuzzy logic based speed controller for switched reluctance motor drive", 1996 International Conference on Power Electronics, Drives and Emergy Systems For Industrial Growth, New Delhi , Jan 1996.

109. Panda S. K., Zhu X. M., Dash P. K., "Fuzzy Gain Scheduled PI Speed Controller for Switched Reluctance Motor Drive", IEEE IECON'97, New Orleans, pp. 348-353, Nov. 1997

110. Zadeh L.A., "Similarity relations and fuzzy orderings", Inform. Sci., Vol. 3, 1971, pp. 177-200.

111. Zadeh L.A., "Fuzzy Algorithm", Inform. Control, vol 12, pp. 94-102, 1968.

112. Kiska J.B., Kochanska M.E., Sliwinska D.S., "The influence of some parameters on the accuracy of fuzzy model", Industrial Applications of Fuzzy Control, Amsterdam, 1985, pp. 187-230.

113. Langari R., Yen J., "Introduction to Fuzzy Logic Control", Industrial Applications of Fuzzy Logic and Intelligent Systems, IEEE Press, 1995, pp. 3-39.

114. Castro, J.L., "Fuzzy Logic Controllers Are Universal Approximators", IEEE Trans. Syst. Man Cyber., Vol. 25, No. 4, April 1995, pp. 629-635.

115. Dave R. N., Krishnapuram R., "Robust Clustering Methods: A Unified View", Ieee Trans. Fuzzy Stsems, vol. 5, no. 2, pp. 270-293, May 1997.

116. Pacini P. J., Kosko B., "Fuzzy Signal Detection in Impulsive Noise", in Fuzzy Engineering by B. Kosko, Prentice Hall International, pp. 329-357, 1997.

117. Kim H. M., Kosko B., "Fuzzy Filters for Impulsive Noise", in Fuzzy Engineering by B. Kosko, Prentice Hall International, pp. 251-257, 1997.

118. Kosko B., Neural Networks and Fuzzy Systems, Prentice Hall, 1991.

119. Benveniste A., Astrom K. J., "Meeting the Challenge of Computer Science in the Industrial Applications of Control: An Introductory Discussion on the Special Issue", IEEE Trans. Automatic Control, vol. 38, no. 7, pp. 1004-1011, 1993

120. Mamdani E.H., "Applications of fuzzy algorithms for simple dynamic plant," Proc. IEE, 121, no. 12., pp. 1585-1588, 1974

121. Consoli A., Testa A., "Performance Evaluation of Fuzzy Controlled Electrical Drives", IEEE IAS Tutorial Course Notes, Neuro-Fuzzy Drive/Motion Control, IAS Annual Meeting 1996, pp. 4-32.

122. Frenz T., Schroder D., "Learning Unknown Nonlinearities Using a Discrete Observer in Combination with Neural Networks", IEEE PESC, 1995, pp. 1800-1806

123. Elmas C., Sagirogiu S., Colak I., Bai G., "Modeling of a Nonlinear Switched Reluctance Motor Drive Based on Artificial Neural Networks", IEE PEVSD, Conference Publication No.399, 1994, pp. 7-12.

124. Abe S., Lan M., " Fuzzy Rules Extraction Directly from Numerical Data for Function Approximation", III Trans. System Man and Cybernetics, Vol. 25, No. 1, Jan 1995, pp. 119-129.

125. Kosko B., "Fuzzy Systems as Universal Approximators", IEEE Transactions on Computers, vol. 43, no. 11, 1329-1333, November 1994.

126. Buckley J. J., "Sugeno type controllers are universal controllers", Fuzzy Sets and Systems, 1993, pp. 299-303.

127. Nguyen H. T., Kreinovich V., "On approximation of controls by fuzzy systems", Proceedings of the Fifth International Fuzzy Systems Association World Congress, Seoul, pp. 1414-1417, July 1993.

128. Wang L. X, "Fuzzy systems are universal approximators", Proceedings of the IEEE International Conference on Fuzzy Systems, San Diego, CA, pp. 1163-1169, 1992.

129. Sousa G.C.D., Bose B., "A Fuzzy Set Theory Based Control of a Phase-Controlled Converter DC Machine Drive", IEEE Trans. IA, Vol. 30, No. 1, 1994, pp. 34-44.

130. "Why Use Fuzzy Logic", a publication of Aptronix Corporation, availiable on line at http://www.aptronix.com/fide/whyfuzzy.htm

131. Simoes M. G., Bose B. K., "Application of Fuzzy Logic in the Estimation of Power Electronic Waveforms", IEEE IAS Conf. Rec., 1993, pp. 853-861.

132. Bose B. K., "Expert System, Fuzzy Logic, and Neural Network Applications in Power Electronics and Motion Control", IEEE Proc., Vol. 82, No. 8, Aug. 1994, pp. 1303-1323.

133. Inoue K., Nakaoka M., "New generic Fuzzy Algorithms-based Auto-tuning Implementation for DC brushless Servo Systems and its Evaluations", IEE PEVSD Conf Publ. No. 399, 1994, pp. 96-100.

134. Lea R. Kreinovich V., "Intelligent Control Makes Sense Even Without Expert Knowledge: An Explanation", APIC'95 (A supplement to the International Journal of Reliable Computing), El Paso, 1995.

135. Berenji H.R, Khedkar P., "Learning and tuning fuzzy logic controllers through reinforcements", IEEE Trans. Neural Networks, Vol. 3, Sep. 1992, pp. 724-740.

136. Jang R., "Self-learning fuzzy controllers based on temporal back propagation, IEEE Trans. Neural Networks, Vol. 3, 1992, pp. 714-723.

137. Ashrafzadeh F., Nowicki E.P., Salmon J.C., "A self-organising and self-tuning fuzzy logic controller for field oriented control of induction motor drives", IEEE Industry Applications Society Annual Meeting, 1995, pp. 1656-1662.

138. Wang L, "Design and Analysis of Fuzzy Identifiers of Nonlinear Dynamic Systems", IEEE Trans. Automatic Cont., Vol. 40, No. 1, Jan. 1995, pp. 11-23.

139. Shigeo A., Lan M., "Fuzzy Rules Extraction Directly from Numerical Data for Function Approximation, IEEE Trans. Syst. Man Cyb. Vol. 25, No. 1, Jan. 1995, 119-129.

140. Wang L., "Adaptive Fuzzy Systems and Control: Design and Stability Analysis, Prentice Hall, 1994.

141. Barayani P., Korondi P., Hashimoto H., "Fuzzy inversion based on piecewise linearization and rule base reduction", EPE"97, Trondheim, , pp. 2.459-2.464, 1997

142. Kosko B., *Fuzzy Engineeering*, Prentice Hall, 1997.

143. Kreyzig, *Engineering Mathematics,* Prentice Hall.

144. Viot, G., "Fuzzy Logic in C", Dr. Dobbs Journal, pp. 40-49, February 1993.

145. Kim D., Kim C., "Forecasting Time Series with Genetic Fuzzy Predictor Ensemble", IEEE Trans. Fuzzy Systems., vol. 5, no. 4, November 1997.

146. Jang J., R., Sun C., "Predicting chaotic time series with fuzzy IF-THEN rules", 2nd Int. Conf. Fuzzy Syst., San Fransisco, vol. 2, pp. 1079-1084, Mar. 1993.

147. Ye Z., Gu L., "A fuzzy system for trading the Shanghai stock market", *Neural, Genetic and Fuzzy Systems for Chaotic Financial Markets,* G. J. Deboeck, Ed., New York, Wiley, 1994, pp. 207-214.

148. J.M. Mendel, "Fuzzy logic systems for engineering", Proc. IEEE, vol. 83, pp. 345-378, March 1995

149. L. X. Wang and J. M. Mendel, "Generating fuzzy rules by learning from examples", Proc. 6th IEEE Int. Symp. on Intell. Contr., pp. 263-268, 1991

150. J.L. Castro, "Fuzzy logic controllers are universal approximators", IEEE Trans. Syst. Man and Cybernetics, vol 25, pp. 629-636, April 1995

151. Ilic-Spong M, Miller, T. J. E., MacMinn S. R., Thorp J. S., "Instantaneous torque control of electric motor drives", IEEE Transactions, vol. PE-2, 55-61

152. Lovatt H. C., Stephenson J. M., "Computer-optimised current waveforms for switched-reluctance motors", IEE Proc. Electr. Power Appl., vol. 141, no. 2, March 1994.

153. Sutton R. F., Modeling Human Operators, New York, Wiley, 1991.

154. Kandel A., Fuzzy Expert Systems, Florida, CRC Press, 1992.

155. Lyons J.P., MacMinn S.R., Preston M.A., "Flux/Current methods for SRM rotor position estimation", IEEE Industry Applications Society Annual Meeting, 1991, pp. 482-487.

156. Harris, W. D. and Lang J. H., "A simple motion estimator for variable reluctance motors", Proc. IAS Annual Meeting, Pittsburgh, PA, Oct. 2-7, 1998, pp. 281-286.

157. Jones S. R., Dragner B.T., "Performance of a High Speed Switched Reluctance Starter/Generator System Using Electronic Position Sensing", 1995 IEEE PESC, pp. 249-253.

158. Ferreira C. A., Jones S. R., Dragner B. T., "Design and Implementation of a Five-hp, Switched Reluctance , Fuel Lube, Pump Motor Drive for a Gas Turbine Engine", IEEE Trans. Power Electronics, Vol. 10, No. 1, January 1995, pp. 55-60

159. Kreyszig E., "Advanced Engineering Mathematics", 6th Edition, John Wiley & Sons, 1988.

160. Mohan N., Undelaned T. M., Robbind W. P., "Power Electronics - Converters, Applications, and Design", J. Wiley, New York, 1995, pp. 79-117.

161. A. Cheok, S. Kawamoto, T. Matsumoto, H. Obi, "AC drive with reference to traction drives", IEE APSCOM'97 Conf. Proc., Hong Kong, Nov. 1997.

162. Abe S., Lan M., "Fuzzy Rules Extraction Directly from Numerical Data for Function Approximation", IEEE Trans. Syst. Man Cyber., Vol. 25, No. 1, January 1995.

163. P. J. Huber, "Robust Statistics", New York, Wiley, 1981.

164. B. Kosko, Fuzzy Engineering, Prentice Hall, 1996.

165. G. C. Mouzouris, J. M. Mendel, "Dynamic Non-Singleton Fuzzy Logic Systems for Nonlinear Modelling", IEEE Trans. Fuzzy Systems, vol. 5, no. 2, pp. 199-208, May 1997.

166. R. N. Dave, R. Krishnapuram, "Robust Clustering Methods: A Unified View", IEEE Trans. Fuzzy Systems, Vol. 5, No. 2, pp. 270-293, May 1997.

167. F. R. Hampel, E. M. Ponchotti, P. J. Rowsseuw, W. A. Stahel, Robust Statistics: The Approach Based on Influence Functions", New York, Wiley, 1986.

168. Hamming R. W., *Digital Filters*, 2nd ed., Prentice Hall, 1983.

169. Parks, T. W., Burrus, C. S., "Digital Filter Design", pp. 209-213, John Wiley & Sons, New York, 1987.

170. Meshkat, S. "Advanced DSP Motion Control Systems - Part 1: Self Tuning Techniques", PCIM, vol. 22, no. 4, pp. 47-56, April 1996.

171. I. Takahashi, Y. Noguchi, "A new quick response and high efficiency control strategy of an induction motor", IEEE Trans. Industry Applications, Vol. IA-22, No. 5, Sept./Oct. 1986, pp. 820-827

172. M. P. Kazmierkowski, "Improved Direct Torque and Flux Vector Control of PWM Inverter-Fed Induction Motor Drives", IEEE Trans. Industrial Electronics, Vol. 42, No. 4, Oct. 1995, pp. 310-318.

173. V. Lovati, M. Marchesoni, M. Oberti, P. Segarich, "Implementation of a sensorless stator flux oriented asynchronous motor drive with high performances at low speed operation", IEEE Power Electronics Specialists Conference Records, 1996, pp. 1427-1433.

174. A. M. Walczyna, "Problems of Application of Direct Flux and Torque Control Methods to High Power VSI-Fed Drives Operating at Low Speed", IEEE Industrial Electronics Conference IECON'94, 1994, pp. 293-298

175. H. Kubota, K. Matsuse, "The Improvement of Performance at Low Speed by Offset Compensation of Stator Voltage in Sensorless Vector Controlled Induction Machines", IEEE Power Electronics Specialists Conference Records, 1996, pp. 257-261.

176. Ertugrul N., Acarnley P.P., French C.D., "Real Time Estimation of Rotor Position in PM Motors During Transient Operation", EPE Conference Proceedings, Brighton, U.K., 13-16 Sept. 1993.

177. Mitsubishi Electric IPM Manual, MELCO Europe, 1986

178. Balinga, B. J., "Switching speed enhancement in insulated gate transistors by electron irradiation", IEEE Trans. Electron Devices, vol. ED-31, pp. 1790-1795, 1984.

179. Cailleaux H., Le Pioufle B., Multon B., Sol C., "A Precise Analysis of the Phase Commutation for the Torque Non-Linear Control of a Switched Reluctance Motor. Torque Ripple Minimization", IEEE Conf. IECON'93, Hawai, pp. 1985-1990, Dec. 1993.

180. Cameron D. E., Lang J. H., Umans S. D., "The Origin and Reduction of Acouistic Noise in Doubly Salient Variable-Reluctance Motors", IEEE. Trans. Ind. Appl., vol. 28, no. 6, 1992.

181. Husain, I., Ehsani, M.,"Error Analysis in Indirect Rotor Position Sensing of Switched Reluctance Motors", IEEE Trans. On Industrial Electronics, Vol. 41, No. 3, June 1994, pp. 301-307

182. Rehman, S., Taylor, D.G., "Issues in Position Estimation of SR motors", IEEE PESC Conference Records, pp. 337-343.

183. Nordin, K. H., Novotny, W. D., Zinger, D. S., "The influence of motor parameter deviation in feedforward field oriented controls", IEEE Trans. On Industry Appl., Vol. IA-21, No. 4, Aug./Sep/, 1985, pp. 1009-1015.

184. Walivadekar, V. N., Pillai, S. K., Sadistap, S. S., Bhandhari, R., "PC Based Data Acquisition for Meaurement of Switched Reluctance Motor (SRM)", 1996 Int. Conf. PEDES, New Delhi, pp. 957-963, Jan. 1996.

185. Richter E., "High Temperature Lightweight Switched Reluctance Motors and Generators for Future Engine Applications", Proc. 1988 American Control Conference, June 15-17, pp. 1846-1851, 1988.

186. MacMinn, S. R., Jones W.D., "A very high speed switched reluctance starter generator for aircraft engine applications", Proc. NAECON 89, May 1989, Dayton Ohio.

187. Radun, A. V., "High Power Density Switched Reluctance Motor Drive for Aerospace Applications", 1989 Conf. Rec. IEEE-IAS Annual Meeting, Oct 1989, pp. 574-578.

188. Iserman I., "On the Design and Control of Mechatronic Systems – A Survey", IEEE Trans. Ind. Elec., Vol. 43, No. 1, pp. 4-15, Feb. 1996.

189. Dickerson, J. A., Kosko, B., "Fuzzy Function Approximation with Supervised Ellipsoidal Learning", Proc. World Congress on Neural Networks, Portland, pp 9-17, 1993

190. Corder R. J., "A High-Speed Fuzzy Processor", Proc. 3rd IFSA Congress, 1989

191. Moghbelli H.H., 'Prediction of the instantaneous and steady state torque of the switched reluctance motor using FEM with experimental results comparison', Electric Machines and Power, Vol. 19, 1991, pp. 287-302.

192. Omekanda A., Broche C., Crappe M., Baland, R., 'Prediction of the steady state performance of the switched reluctance motor using quadratic biem-FEM field solutions in the linear model', ICEM, 1994, Paris, pp. 59-64.

193. Prescot J.C., El-Kharashi A.K., 'A method for measuring self-inductance applicable to large electrical machines', Proc. IEE, Vol. 106, Pt. A, April 1959, pp. 169-173

194. Krishnan R., Majeru P., 'Measurement and instrumentation of a switched reluctance motor', IEEE Industry Applications Society Annual Meeting, 1989, pp. 116-121.

195. Acarnley P.P., Aggarwal R., 'Inductance and static torque measurements in small reluctance type machines', UPEC88, Nottingham, UK, Sept. 1988.

196. Williams T., Carter R., 'Measurement of Machine Inductances using an Operational Amplifier Integrator', International journal of Electrical Engineering Education', Vol. 10, 1972/73, pp. 177-181.

197. Ray W.F., Erfan F., 'A new method of flux or inductance measurement for switched reluctance motors', Power Electronics and Variable Speed Drives, IEE Conference Publication No. 399, 1994, pp. 137-140.

198. Ferrero A., Racati A., 'A digital method for the determination of the magnetic characteristic of variable reluctance motors', IEEE Trans. Instrumentation and Measurement, Vol. 39, no. 4, August 1990, pp. 604-8.

199. Walivadekar V.N., Pillai S.K., Sadistap S.S., Bhandhari R., 'PC Based Data Acquisition System for Measurement of Switched Reluctance Motor (SRM)', Int. Conf. Power Electronics, Drives & Energy Systems for Industrial Growth, New Delhi, pp. 957-963., 1996

200. Ramanarayanan V., Venkatesha L., Panda D., 'Flux-linkage characteristics of switched reluctance motor', Int. Conf. Power Electronics, Drives & Energy Systems for Industrial Growth, New Delhi, pp. 281-285., 1996

201. Lee P.W., Pollock C., 'Flux linkage estimation in electrical machines', ICEM'94, Paris, September 1994, pp. 463-467.

202. Chai H.D., 'A mathematical model for single-stack step motors', IEEE Trans. PAS, 1975, Vol. 94, pp. 1508-1517.

203. Singh G., Kuo B.C., 'Modeling and simulation of variable-reluctance step motors with application to a high-performance printing system', IEEE Trans. IA, 1975, Vol. 11, pp. 373-383.

204. Buja G.S., Valla M.I., 'Control Characteristics of the SRM drives. Part II: Operation in the Saturated Region', IEEE Trans. Indus. Elec., Vol. 41 No. 3, June 1994, pp. 316-325.

205. Ilic-Spong M., Mak, F.K., 'Non-linear torque control of electric motor drives: Part II', IEEE PESC, 1986, pp. 465-475.

206. Torrey D.A., 'Excitation of variable-reluctance motor drives', Electrical Machines and Power Systems, Vol. 19, 1991, pp. 713-729.

207. Torrey D.A., Lang J.H., 'Modeling a non-linear variable-reluctance motor drive', IEE Proc. B, 1990, Vol. 137, No. 5, pp. 314-326.

208. Tormey D.P., Torrey D.A., 'A comprehensive design procedure for low torque-ripple variable-reluctance motor drives', IEEE IAS conference, Dearborn, MI, USA, Sept 1991, pp. 244-251.

209. Bolognani, S., Buja, G.S., Valla M.I., 'Switched-reluctance motor performance analysis based on an improved modeling of it's magnetic characteristics', Electr. Mach. Power Syst., 1991, Vol 19, pp. 425-438.

210. Byrne J.V., O'Dwyer J.B., 'Saturable variable reluctance machine simulation using exponential functions', Proc. Int. Conf. Stepping Motors and Systems, 1976, pp. 11-16.

211. Pickup I.E.D., Tipping D., 'Method for predicting the dynamic response of a variable reluctance stepping motor', Proc. IEE, 1973, Vol 120, No. 7, pp. 757-765.

212. Pulee, D. W. J., Petersen I. R., "A generalised approach to torque and current computation in switched reluctance motors", EPE'97, Trondheim, 1997, pp. 3.547-3.551.

213. Elmas C., Sagiroglu S., Colak I., Bal G., 'Modeling of a non-linear switched reluctance drive based on artificial neural networks', Power Electronics and Variable Speed Drives, IEE Conf. Publ. 339, 1994, pp. 7-12.

214. Moghbelli, H.H., Adams, G.E., Hoft, R.G., 'Prediction of the instantaneous and steady state torque of the switched reluctance motor using FEM with experimental results comparison', Electrical machines and Power Systems, Vol 19, 1991, pp. 287-302.

215. Moallem M., Ong C.M., 'Predicting the Torque of a Switched Reluctance Machine from it's Finite Element Field Solution', IEEE Trans. Energy Conversion, Vol. 5, No. 4, December 1990, pp. 733-739.

216. Integrated Systems, 3260 Jay Street, Santa Clara, CA 95054

217. Moreira J.C., Lipo T.A., 'Simulation of a Four Phase Switched Reluctance Motor Including the Effects of Mutual Coupling', Electrical Machines and Power Sys

218. Arkadan A.A., Kielgas B.W., 'Switched reluctance motor drive systems dynamic performance prediction and experimental verification', IEEE Trans. Energy Conversion, Vol. 9, No. 1, pp. 36-42.

219. Stephenson J.M., Corda J., 'Computation of torque and current in doubly salient reluctance motors from non-linear magnetisation data', IEE Proc. B, Vol. 126, No. 15, May 1979, pp. 393-396.

220. Casanellas F., 'Losses in PWM inverters using IGBTs', IEE Proc B, Vol. 141, N0. 5, September 1994, pp. 235-239.

221. Holling G., "Digital Signal Processing Basics", Power Conversion and Intelligent Motion, Nov 1996, pp. 39-44.

222. Drafts B., "Current Sensing Solutions for Power Conversion and Intelligent Motion Applications", PCIM magazine, vol. 21, no. 9, pp. 53-58, Sept. 1995

223. Undeland T.M., Mohan N., "Overmodulation and Loss Consideration in High Frequency Modulated transistorized Induction Motor Drives", IEEE Trans. Power Elec., Vol. 3, No. 4, Oct. 1988, pp. 447-452.

224. Mitsubishi Electric Europe, "3rd Generation IGBT and Intelligent Power Modules Applications Manual", 1995

225. B. J. Baliga, "Power Semiconductor Devices for Variable Speed Drives", in "Power Electronics and Variable Frequency Drives", edited by B. K. Bose, IEEE Press, 1997

226. Allocco J.M., Whistler R.J., "Laminated Bus Bars Reduce Inductance and Manufacturing Costs of Power Distribution Circuits", Power Conversion & Intelligent Motion, Nov. 1996, pp. 54-56.

227. C. A. Dimino, R. Dodballapur, J. A. Pomes, "A Low Inductance, Simplified Snubber, Power Inverter Implementation", HFPC proceedings, pp. 502-509, April 1994.

228. International Rectifier Application Note IR AN-983 page 105

Publications

1. Cheok A. D., Ertugrul N., "Sensorless rotor position detection techniques in switched reluctance motor drives", Australasian Universities Power Engineering Conference, 27-29 September 1995, Perth, Australia.

2. Cheok A. D., Ertugrul N., "A Model Free Fuzzy Logic-based Rotor position Sensorless Switched Reluctance Motor Drive", IEEE Industry Applications Society Annual Meeting, San Diego, pp. 76-83, 4-10 October 1996.

3. Cheok A. D., Ertugrul N., "High Robustness and Reliability of a Fuzzy logic Based Angle Estimation Algorithm for Practical Switched reluctance Motor Drives", IEEE Power Electronics Specialist Conference, Fukuoka, 1998. (Accepted)

4. Ertugrul N., Cheok A. D., "Indirect Angle Estimation in Switched Reluctance Motor Drives Using Fuzzy Logic Predictor/Corrector", IEEE Power Electronics Specialist Conference, Fukuoka, 1998. (Accepted)